NASA Technical Memorandum 103226

Solid State Technology Branch of NASA Lewis Research Center Second Annual Digest

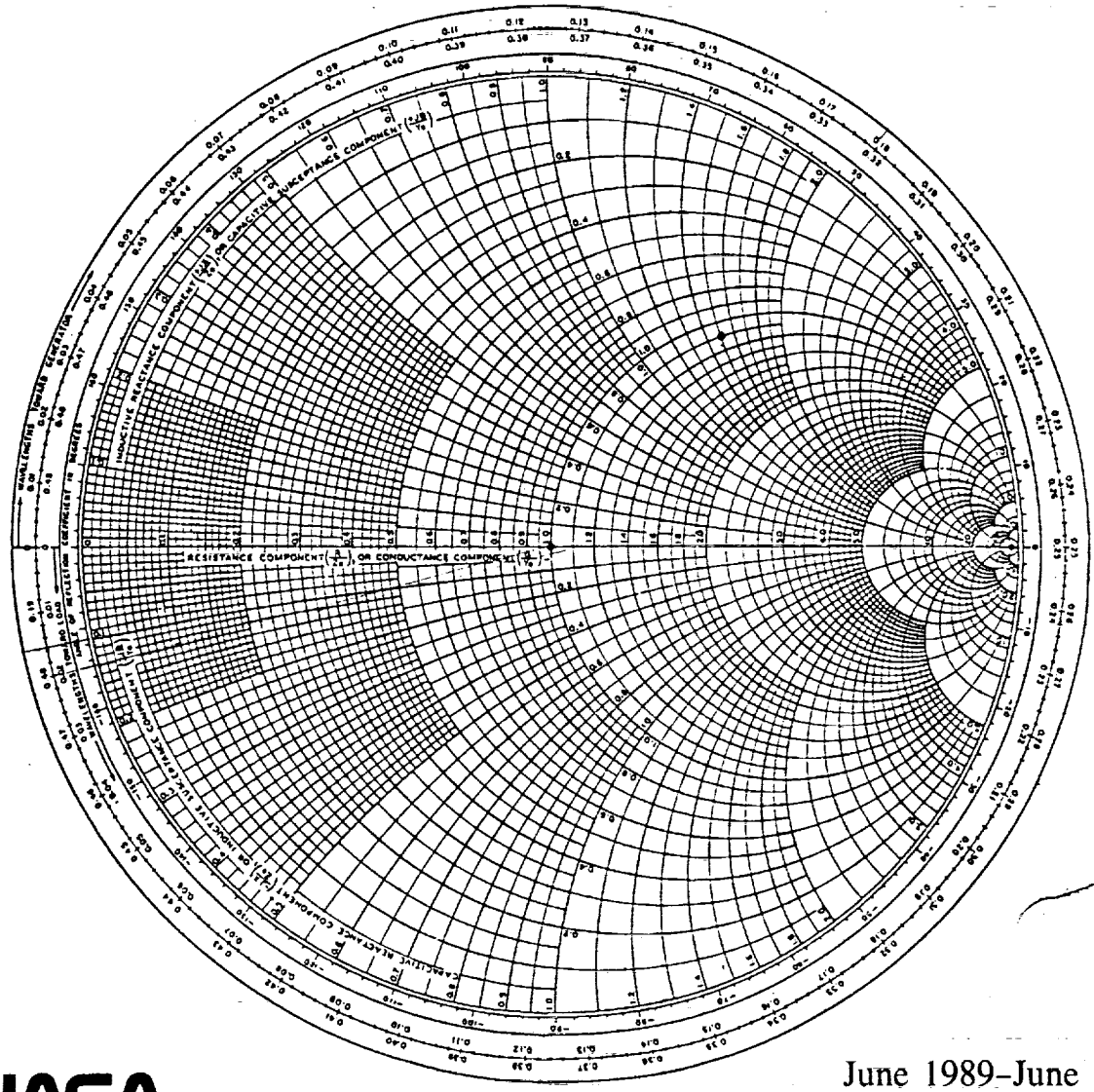

June 1989–June 1990
Lewis Research Center

SOLID STATE TECHNOLOGY BRANCH OF NASA LEWIS RESEARCH CENTER SECOND ANNUAL DIGEST

CONTENTS

III. Superconducting Films

IV. Semiconductor Material Characterization

PREFACE TO THE SECOND ANNUAL SOLID STATE TECHNOLOGY BRANCH DIGEST

The last year has seen a significant growth in the size of the Solid State Technology Branch with the addition of three new persons, two with EE degrees and one with a physics degree. This growth is a reflection of the increase in in-house research activities. Specifically, although not yet indicated in publications, the year saw a large increase in interest in low-temperature electronics: superconductor-based, semiconductor-based, and ultimately, hybrid superconductor/semiconductor circuitry. In most areas, work has continued at approximately the same level as in the previous year.

The present volume represents a collection of papers and presentations authored by members of the branch between June 1989 and June 1990. As in last year's inaugural version of this digest, the papers are organized into four sections. Section I deals with research in microwave circuits and includes full integrated circuits, the demonstration of optical/RF interfaces, and the evaluation of some contractually developed hybrid circuitry. Examination of the review paper on solid-state amplifiers will reveal that Lewis contractors have made significant strides in solving the problems of interstage matching and device development in high efficiency multistage mm-wavelength power amplifiers. In the optical/RF interface area, the papers reveal that work has moved, to a large extent, to the arena of subsystem demonstrations. Consequently, most of this work has been transferred to a more system-oriented organization here at Lewis.

Section II indicates developments in coplanar waveguide and its use in breadboard circuits. This includes both an in-house 30-GHz demonstration array and a 2-GHz investigation for an ATDRSS-type array.

Section III presents one of the most active areas within the branch for the last year. This collection of papers and presentations on high temperature superconductivity includes a wide range of subjects, from thin film deposition to transport measurements of films characteristics, RF surface resistance measurements, substrate permittivity measurements, measurements of microstrip line characteristics at cryogenic temperatures, patterning of superconducting films, and evaluation of simple passive microstrip circuitry based on YBaCuO films.

Finally, in section IV of the digest, those papers on materials and material characterization (other than superconductors) are included. These represent work with a wide variety of materials, including carbon films, silicon carbide, GaAs/AlGaAs, and HgCdTe.

In addition to these articles, it seems worth noting the publication of three books by Solid State Branch personnel in the last year: "Optical Control of Microwave Devices," a textbook on microwave-optical interactions by R. Simons, a branch-sponsored contractor; "Characterization of Amorphous Carbon Films," a comprehensive collection of articles by internationally recognized authors which J. Pouch and S. Alterovitz edited and contributed to; and "Synthesis and Properties of Boron Nitride," a similar collection, also done by Pouch and Alterovitz.

I. MONOLITHIC MICROWAVE INTEGRATED CIRCUITS

NASA Developments in Solid State Power Amplifiers

Regis F. Leonard
NASA Lewis Research Center

Over the last ten years, NASA has undertaken an extensive program aimed at development of solid state power amplifiers for space applications. Historically, the program may be divided into three phases. The first efforts were carried out in support of the Advanced Communications Technology Satellite (ACTS) program, which is developing an experimental version of a Ka-band commercial communications system. These first amplifiers attempted to use hybrid technology. The second phase was still targeted at ACTS frequencies, but concentrated on monolithic implementations, while the current third phase is a monolithic effort, but focusses on frequencies appropriate for other NASA programs and stresses amplifier efficiency.

I. 20 GHZ HYBRID AMPLIFIERS

As required by the ACTS program, the first solid state amplifiers developed by NASA Lewis were at 20 GHz. Two of the units (designed and built by TRW and Texas Instruments) utilized GaAs MESFET technology, while a third was based on GaAs IMPATT devices. All were based on discrete devices and external power combining to achieve the required power levels. The results of these three efforts are shown in Table 1.

TABLE 1.
PERFORMANCE OF HYBRID 20 GHZ AMPLIFIERS

	TI GaAs FET	TRW GaAs FET	TRW IMPATT
BANDWIDTH (GHZ)	2.5	1.5	0.220
GAIN (dB)	30	39.	29.0
POWER OUTPUT (W)	9.0	8.2	15.5
EFFICIENCY (%)	<8.	<8.	10.

As a result of these three efforts, all of which ended about 1984, and all of which were aimed at the production of a single port amplifier which would be appropriate as a tube replacement, NASA concluded that solid state amplifiers were not yet at a level where a 20 GHz single port amplifier at this power level was feasible for space applications. This decision was based primarily on the efficiency achieved at that time. Efforts since then have concentrated on the development of improved devices (efficiencies better than 30%) and their incorporation into monolithic low power (< 1 watts) amplifiers.

II. 20 GHZ MONOLITHIC MESFET POWER AMPLIFIERS

This work has been carried out under contract and has been aimed at several potential applications. The first round of

developments was again centered out at 20 GHz. The target application again was an ACTS-like commercial satellite, requiring multiple, steerable beams. The development of appropriate monolithic power amplifiers (and receivers and phase shifters) would permit such a system to be implemented using phased array antennas rather than the extensive network of ferrite phase shifters and power dividers used by ACTS. This phase of the NASA program, carried out between approximately 1983 and 1986, produced two 20 GHz monolithic amplifiers, each designed and built by Texas Instruments, and each based again on GaAs MESFET technology. The first of these, a variable power module, was a four stage amplifier which utilized dual gate FETs to achieve power variations while maintaining efficiency. A summary of its performance compared to design goals is shown in Table 2.

TABLE 2
TEXAS INSTRUMENTS 20 GHZ VARIABLE POWER AMPLIFIER

	DESIGN GOAL	PERFORMANCE
BANDWIDTH (GHZ)	2.5	2.5
MAX POWER OUTPUT (W)	0.5	0.25
EFFICIENCY AT MAX OUTPUT (%)	15	---
GAIN (dB)	20	20
4TH STAGE GATE WIDTH (MM)	----	1.2

The second 20 GHz chip was focussed entirely on the production of the maximum possible 20 GHZ power in a monolithic chip. Once more the contractor was Texas Instruments. This effort resulted in a three stage amplifier using single gate FETs. The performance of this chip is summarized in Table 3.

TABLE 3.
TEXAS INSTRUMENTS 20 GHZ HIGH POWER AMPLIFIER

	DESIGN GOAL	PERFORMANCE
BANDWIDTH	2.5	2.5
MAX POWER OUTPUT (W)	2.5	>2.0
EFFICIENCY AT MAX POWER (%)	20	16
GAIN (dB)	15	18
LAST STAGE GATE WIDTH (MM)	----	3.6

It is clear, however, that both of these units, although they constituted a benchmark achievement at this frequency, suffered from the same problem as the earlier hybrid implementations of solid state technology. Their efficiencies make their use marginal for space applications, except in very limited numbers, such as would be required if they were used as a driver for a higher efficiency final stage. An attempt to use multiple chips with any kind of combining would lead to prohibitively large prime power requirements.

III. HIGH EFFICIENCY MONOLITHIC POWER AMPLIFIERS

At the present time NASA Lewis is sponsoring the development of four monolithic power amplifier chips. One of these at 15 GHz is a candidate for use in the proximity communications system of the space station. Two at 32 GHz are for possible use in the space (transmitter) portion of the deep space communications network. The fourth at 60 GHz is intended for application to intersatellite communications, such as might be required by Advanced TDRSS or lunar/Mars exploration.

The space station proximity communications system is intended to provide communications within a radius of several 10's of kilometers of the space station. Users would include free flying experimental platforms, the orbital maneuvering vehicle (OMV), and astronauts in EVA. The original planning for this system utilized frequencies in Ku-band. It is not clear at this time whether that assignment will be maintained, inasmuch as there exist possible interferences with commercial, fixed satellite services. Nevertheless, several chips have been developed at 13-15 GHz to accommodate this application. The most challenging of these was a variable power amplifier intended primarily for use by astronauts during EVA. The system design requires approximately 1 watt of output power. Power variability is necessary because of the wide variation in range experienced by the astronaut. Of course, high efficiency is also a prime consideration. The development of the chip was undertaken by Texas Instruments in January 1987. Their design is a four stage monolithic circuit using dual gate GaAs MESFET technology. The chip is shown in Figure 1.

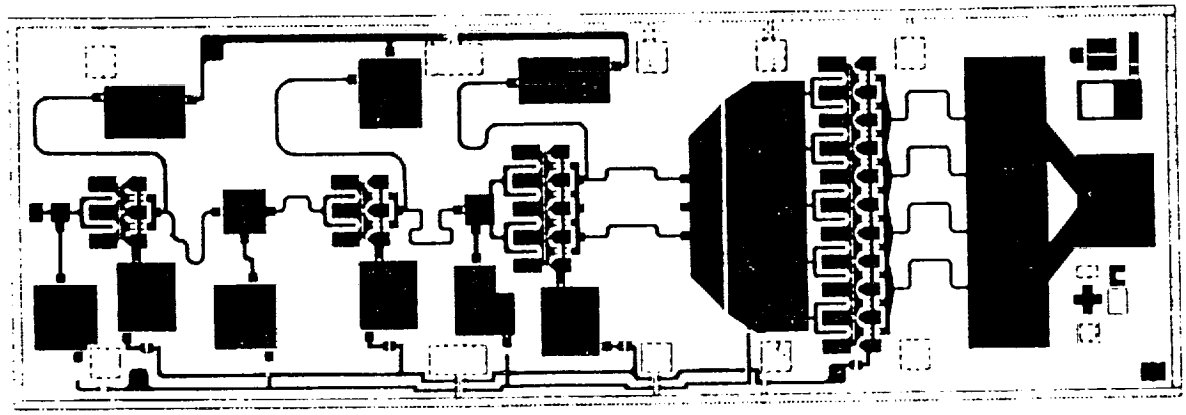

FIGURE 1. 15 GHZ MONOLITHIC VARIABLE POWER AMPLIFIER

The performance of the amplifier, compared to the design goals, is shown in Table 4.

TABLE 4.
15 GHZ HIGH EFFICIENCY VARIABLE POWER AMPLIFIER

	DESIGN GOAL	PERFORMANCE
BANDWIDTH (GHZ)	2.0	20
GAIN (dB)	15.0	29.6
MAX POWER OUTPUT (W)	1.0	.92
EFFICIENCY AT MAX POWER (%)	35	30.
FINAL STAGE GATE WIDTH (MM)	---	1.5

Both the power output and the efficiency achieved by this program essentially meet the system requirements formulated originally by the space station designers. The only problem at the present time is that the chip operates at a center frequency of 17 rather than 14 GHz.

In another application the NASA deep space communications network is considering a conversion to Ka-band. The primary motivation for such a change is the significant increase in antenna gain (for a fixed aperture size) and the corresponding decrease in power requirements (for a fixed data rate). Increased antenna gain, however, implies smaller beams and therefore more stringent pointing requirements. Such a situation, of course, is ideal for implementation of an electronically steerable phased array, which does not disturb other critically-pointed spacecraft instruments in the way a mechanically steered antenna would. To support breadboard evaluations of such a system, 32 GHz power amplifier modules are under development. The contractors executing these efforts are Texas Instruments and Hughes Aircraft. The TI work has been under way since May, 1985, and is near completion, while the Hughes effort was initiated in June 1988.

TI proposed and originally designed amplifiers using GaAs MESFET technology, but was directed, after approximately 18 months work, to concentrate on heterojunction devices. Specifically, they have investigated AlGaAs/GaAs HEMT structures and pseudomorphic InGaAs/GaAs structures. At this point it is clear that the pseudomorphic technology outperforms both the AlGaAs HEMT and the GaAs MESFET technology by a significant margin at 32 GHz. The specific pseudomorphic structure which TI has adopted is shown in Figure 2.

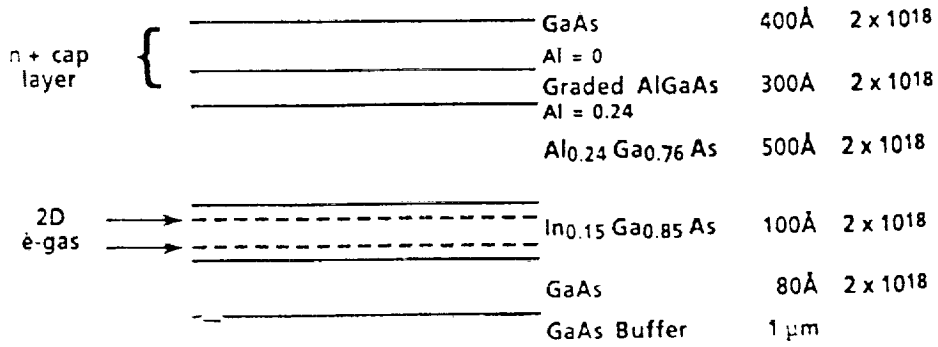

FIGURE 2. Texas Instruments' Pseudomorphic Power Amplifier Structure

The performance parameters for two of the pseudomorphic chips developed under this program are shown in Table 5.

TABLE 5.
TEXAS INSTRUMENTS 32 GHZ MONOLITHIC POWER AMPLIFIER PERFORMANCE

	3-STAGE AMP	1-STAGE
AMP		
BANDWIDTH (GHZ)	2.0	2.0
GAIN (dB)	23	4.6
GATE LENGTH (uM)	0.25	0.25
FINAL STAGE GATE WIDTH (MM)	.25	.25
POWER OUTPUT (mW)	190	460
EFFICIENCY (%)	30	24

The layouts of the two chips are shown in Figures 3 and 4.

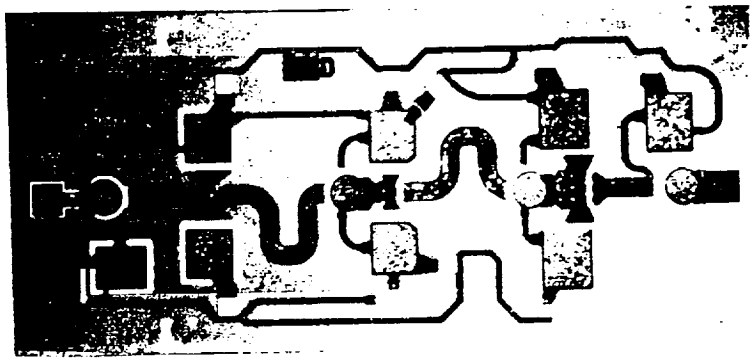

FIGURE 3. TI's 3-STAGE MONOLITHIC 32 GHZ AMPLIFIER

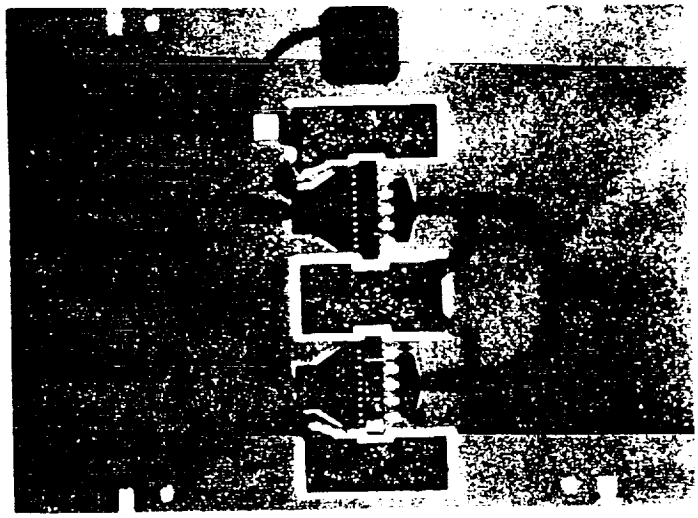

FIGURE 4. TI's ONE-STAGE MONOLITHIC 32 GHZ POWER AMPLIFIER

In a parallel 32 GHz effort Hughes Aircraft Corporation's Microwave Products Division and Malibu Research Laboratories are collaborating on the development of a 32 GHz variable power amplifier. The design goals for this chip are shown in Table 6.

TABLE 6.
DESIGN GOALS FOR HUGHES 32 GHZ VARIABLE POWER AMPLIFIER

BANDWIDTH (GHz)	2.0
MAX POWER OUTPUT (mW)	150
EFFICIENCY AT MAX POWER(%)	40
GAIN AT 1 DB COMP. (dB)	15.0

The Hughes contract, like most such developments at this time is to be carried out in several phases. These will consist of (1) the optimization of a single gate device design, (2) the development of a single stage amplifier, (3) the development of a dual gate device, (4) the design, fabrication, and test of a three-stage, single gate amplifier, and finally, (5) a three stage dual gate amplifier. In the 16 months that the Hughes team has been under contract, they have carried out the first two phases. The epitaxy which they have selected for the basic device is similar to that utilized by TI, except that Hughes has elected not to dope the active layer. It does,however, utilize a single active InGaAs layer with donors on each side. The layout and performance parameters for the basic 32 GHZ device are shown in Figure 5.

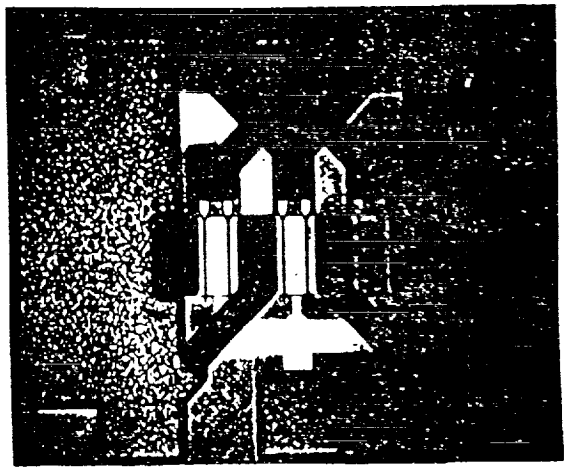

FREQUENCY	32.0
GAIN*	4(5) dB
POWER OUTPUT*	222(123)mW
EFFICIENCY*	23(41)%
GATE WIDTH	300 uM
GATE LENGTH	0.2 uM

*tuned for max power(eff)

Figure 5. Layout and Performance of Hughes 32 GHz Power MODFET

This device has been incorporated into a single stage amplifier, whose performance is shown in Table 7. This amplifier is intended as the third stage of the final monolithic module.

TABLE 7.
Performance of Hughes 32 GHz Single Stage Amplifier

GAIN (dB)	5.5
POWER OUTPUT (mW)	125
EFFICIENCY (%)	21

These results represent the first iteration of this chip, and significant improvement is expected before the program ends.

In addition, under the same contract, Hughes is developing a 60 GHz monolithic power amplifier. The justification for this program is eventual application in intersatellite links. Although NASA's plans for the Advanced Tracking and Data Relay Satellite (ATDRS) do not presently call for 60 GHz crosslinks, it seems likely that if such technology were available it would eventually find application in that area. The performance goals for the program, are shown below in Table 8.

TABLE 8. Performance Goals for Hughes' Pseudomorphic 60 GHz Power Amplifier

BANDWIDTH (GHz)	2.0
MAX POWER OUTPUT (W)	0.1
GAIN (dB)	15
EFFICIENCY (%)	30.

At 60 GHz Hughes is using the same basic pseudomorphic device structure as at 32 GHz, although the gate lengths have been shortened somewhat (0.1 to 0.15 uM). The layout and the performance achieved for a single stage amplifier are shown in Figure 6. As in the 32 GHz module, the amplifier shown is intended as the third (high power) stage of the completed monolithic amplifier.

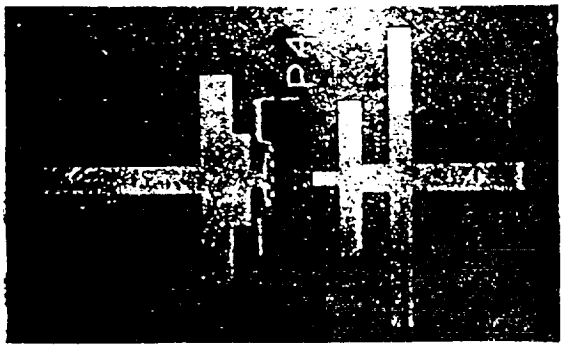

POWER OUT	112 mW
GAIN	6 dB
EFFICIENCY	26%

FIGURE 6. Hughes Single Stage Monolithic 60 GHz Amplifier

IV. FUTURE ACTIVITIES

The 32 GHz power amplifier modules developed by Texas Instruments and described here are scheduled to be incorporated into a breadboard transmitter array antenna which will also utilize phase shifters developed under NASA Lewis sponsorship. This work is being carried out at NASA's Jet Propulsion Laboratory, where a two dimensional array is expected to be completed late in calendar year 1990.

The Hughes work at both 32 Ghz and 60 Ghz is probably at least a year away from being used even in a breadboard system. Although the contract is scheduled for completion in early 1991, it has

yet to address what has been one of the major difficulties in the fabrication of a multistage power amplifier - inadequate large signal device models. It has been a common experience for a designer to develop excellent individual stage amplifiers, which meet all the requirements of the overall power and gain budget, only to find that the multistage module performance falls far short of the program requirements. Consequently, it appears optimistic to expect that Hughes will complete their development by 1991. 1992 would appear to be more realistic. At that time, it is anticipated that a 60 GHz breadboard array will be built, either at JPL or at NASA Lewis. As with the Ka-band array, it will utilize monolithic phase shifters which are being developed in parallel at Hughes.

NASA Technical Memorandum 101960

Performance of Five 30 GHz Satellite Receivers

Robert J. Kerczewski, George E. Ponchak,
and Robert R. Romanofsky
Lewis Research Center
Cleveland, Ohio

Prepared for the
1989 IEEE MTT-S International Microwave Symposium
Long Beach, California, June 13–15, 1989

NASA

PERFORMANCE OF FIVE 30 GHz SATELLITE RECEIVERS

Robert J. Kerczewski, George E. Ponchak, and Robert R. Romanofsky

National Aeronautics and Space Administration
Lewis Research Center
Cleveland, Ohio 44135

Technology development contracts funded by NASA have resulted in five 30 GHz satellite receivers of various design. This paper presents and discusses the results of tests performed at NASA Lewis Research Center to determine the operating characteristics of the receivers and their ability to perform in a digital satellite link.

Introduction

For the past 10 years, NASA has been developing technology intended to enhance the performance of future satellite communication systems. This work has focused on systems operating at 30 GHz uplink and 20 GHz downlink frequencies. A major part of this technology thrust is the development of 30 GHz low noise satellite receivers. As a result of technology development contracts, five receivers of various design have been delivered. These receiver models have undergone extensive testing at NASA Lewis Research Center to determine their operating characteristics and their performance in a satellite communication system transmitting high rate digital data. In the following sections, the design of the receivers will be described, and the results of performance measurements will be presented and discussed.

30 GHz Low Noise Satellite Receiver Designs

The delivery of completed hardware from the five development contracts spanned the time period of 1982 through 1987. Two parallel contracts, under the management of NASA Lewis, were completed in late 1982 by LNR Communications, Inc. and ITT Defense Communications Division. Figure 1 shows the basic functional design of these receivers.[1] Both LNR and ITT used an image-enhanced diode mixer for the receiver front end, followed by a FET IF amplifier. The designs varied in method of local oscillator (LO) generation and operating frequency. The resulting hardware consisted of a complete receiver unit, requiring only dc bias and an LO reference.

NASA Goddard Space Flight Center initiated a contract with Hughes Aircraft Company, Microwave Product Division, which resulted in the delivery of completed receiver models in the fall of 1984. One receiver was sent to NASA Lewis for evaluation under the Lewis satellite communication system component test program. As shown in Fig. 2, the Hughes design consists of a hybrid combination of GaAs FET microwave integrated circuits (MIC's) developed by Hughes for this project.[2] The receiver front end is a 30 GHz GaAs FET low noise amplifier (LNA) MIC, which is followed by an MIC mixer and an IF amplifier. The LO is an internally generated 22 GHz FET dielectric resonator oscillator. The complete receiver package requires only a dc bias.

These three receivers are generally intended for use in 30/20 GHz satellite communication systems with single-feed satellite receive antenna systems. Such an antenna system may consist of a single feed horn or a feed-horn cluster which would permit a beam-hopping system. This system would consist of an array where different groups of feed horns are switched on to provide receive coverage scanning geographically isolated areas. In all these cases, the received signal is collected and combined to provide an input signal to a single receiver.

For electronically scanned antenna systems, a multi-element phased array antenna is used. This system consists of an array of antenna elements, each connected to an individual receiver which includes controllable phase shifters and variable gain amplifiers. Control of these elements allows the antenna beam to be spatially scanned. Each receiver processes only a portion of the signal incident on the antenna. The receiver outputs are then combined into single received signal. For this type of system, a monolithic microwave integrated circuit (MMIC) receiver is required. Therefore, a development program was initiated by NASA Lewis in 1982. Contracts were awarded to Hughes Aircraft Co., Microwave Products Division[5] and Honeywell Sensors and Signal Processing Lab[6] for the development of a 30 GHz monolithic receiver. The receivers consist of an LNA, mixer, gain control amplifier (GCA), and phase shifter. Although both contractors were to meet the same program goals, Hughes and Honeywell used different design approaches. Honeywell performed all amplification and phase shifting at 30 GHz, while Hughes did the phase shifting at the LO frequency and the GCA at the IF. Extra filtering and amplification were added by NASA Lewis to create a complete satellite

receiver in order to allow testing. The block diagrams of the Honeywell and Hughes MMIC receivers are shown in Fig. 3 and 4, respectively.

Test Results

To determine their performance in a high data rate digital satellite transmission system, the receivers were tested in the automated measurement system shown in Fig. 5. The system simulates an end-to-end satellite communications link, operating at a data rate of 220 Mbps. The modulation type is serial minimum shift keying (SMSK). Discrete amounts of noise are added at the system output to allow measurement of the BER as a function of Eb/No.[4] An example of the results of such a measurement is shown in Fig. 6 for the five receivers tested at an input power level of -30 dBm.

A summary of the test results obtained is given in Table I. The RF test data is presented in detail in Refs. 1 to 3, 5 and 6. The BER data given represents the degradation of the measured curve, in dB, compared to the theoretical curve, at a BER of 10^{-6}. For a typical system, the receiver with the highest gain and lowest noise figure should give the lowest BER. At the lower power levels, the BER performance is directly related to the noise figure of the receiver. A BER of 10^{-6} could not be obtained for the Honeywell receiver below a -50 dBm input and for the Hughes MMIC receiver below -30 dBm input because of their high noise figure. The Hughes MMIC receiver performed poorly because the LNA operated optimally at 32-34 GHz; at 30 GHz, the noise figure was very high and no gain was obtained. The Honeywell MMIC receiver used a two-stage LNA. Honeywell's final design will use a six-stage LNA, which will provide a significant gain increase and noise figure reduction. In NASA's tests, the MMIC receivers, consisting of two or more interconnected MMIC fixtures, suffered significantly from interstage mismatch problems.

At higher power levels, the noise figure was not a factor in BER performance except for the Hughes MMIC receiver. The most important factor above -50 dBm was the frequency response of the combined receiver and test system. Due to the various output operating frequencies of the receivers, it was not always possible to test them at their optimum design frequency and the band center of the test system simultaneously. Therefore, the variation of BER results between the receivers at the higher power levels does not necessarily indicate significant performance differences. We consider any BER degradation less than 3.0 dB to indicate acceptable receiver performance.

Conclusion

In general, digital satellite communication systems are required to provide a maximum BER of 10^{-6}. The Hughes MMIC receiver is the only one which did not meet this criteria at the power levels tested. The other receivers met this criteria with a maximum Eb/No degradation of 2.6 dB for an input power of -30 dBm. System performance degradation is observed when the receiver input power is reduced to the noise figure limit of the receiver. Thus, the receiver noise figure is a limiting factor in system performance. The three hybrid receivers performed well for input powers as low as -50 dBm.

The MMIC receivers performed poorly relative to the hybrid receivers. Since an MMIC scanning antenna system would combine the outputs of many MMIC receivers, the system Eb/No obtained would be higher than for each individual receiver. Therefore, adequate system performance may still be obtained with these receivers. In addition, further improvements in MMIC design and optimization are likely to improve performance.

References

1. Conroy, M.J., and Kerczewski, R.J., "Testing of 30 GHz Low Noise Receivers," Eleventh Communications Satellite Systems Conference, AIAA, 1986, pp. 326-340(NASA TM-87171).

2. Watkins, E.T., and Schellenberg, S.M., "Hybrid Microwave Integrated Circuit Ka-Band Low Noise Receiver," (NASA Contract NAS5-26731) Hughes Aircraft Co., Microwave Products Division, Torrance, CA, 1984.

3. Ponchak, G.E., and Romanoffsky, R.R., "Monolithic Microwave Integrated Circuit Technology for Advanced Space Communication," NASA TM-100829, 1988.

4. Kerczewski, R.J., Daugherty, E.S., and Kramarchuk, I., "Automated Measurement of the Bit-Error Rate as a Function of Signal-to-Noise Ratio for Microwave Communications Systems," NASA TM-89898, 1987.

5. Bauhahn, P., Geddes, J., Sokolov, V., and Contolatis, T., "30 GHz Monolithic Receive Module," NASA CR-180849, 1988.

6. Liu, C.S., Asher, P.G., Wang, S.K., and Chang, C.D., "30 GHz Monolithic Receive Module," (NASA Contract NAS5-26731) Hughes Aircraft Co., Microwave Products Division, Torrance, CA, 1987.

TABLE I. - SUMMARY OF TEST RESULTS FOR FIVE 30 GHz SATELLITE RECEIVERS

Parameter	Receiver				
	LNR Communications 1982	ITT Defense Communications 1982	HAC Microwave Products Divison 1984	Honeywell Sensors and Signal Process Lab 1987	HAC Microwave Products Division
Input band, GHz	27.5 to 30.0	27.5 to 30.0	27.5 to 30.0	27.5 to 30.0	27.5 to 30.0
Output band, GHz	3.7 to 6.2	2.3 to 4.8	5.5 to 8.0	4.5 to 7.0	3.0 to 5.5
LO frequency, GHz	23.8	25.2	22.0	23.0	24.5
Gain (maximum), dB	22	19	41	13	-5.2
Gain variation over 2.5 GHz, dB	3.8	4.8	5.2	5.2	5.0
Noise figure (minimum), dB	5.8	6.8	3.7	14.0	>20
Input VSWR (Max. over 2.5 GHz)	2.3:1	3.4:1	[a]1.3:1	3.6:1	>10:1
Output VSWR (Max. over 2.5 GHz)	1.7:1	1.4:1	2.3:1	8.5:1	3.8:1
1 dB Compression point midband (input), dBm	-7	-8	-27	-3	-2
BER degradation, -30 dBm In, HPA saturated, dB	1.1	2.0	2.6	0.9	6.8
BER degradation, -40 dBm In, HPA saturated, dB	1.0	2.1	1.5	2.5	----------
BER degradation, -50 dBm In, HPA saturated, dB	1.2	2.5	2.5	18.4	----------
BER degradation, -60 dBm In, HPA saturated, dB	3.8	6.6	2.5	----------	----------
Dynamic range at -10 dBm input, dB	N/A	N/A	N/A	>13	>18
Insertion phase envelope as a function of gain, deg	N/A	N/A	N/A	±10	±15
Gain envelope as a function of phase state, dB	N/A	N/A	N/A	±2	±2
Phase shift/ phase shift increment, deg	N/A	N/A	N/A	360/ 11.25	180/ Continuous
Design topology	Hybrid	Hybrid	Hybrid - MIC	Multiple-chip MMIC	Multiple-chip MMIC

[a]Hughes measurement

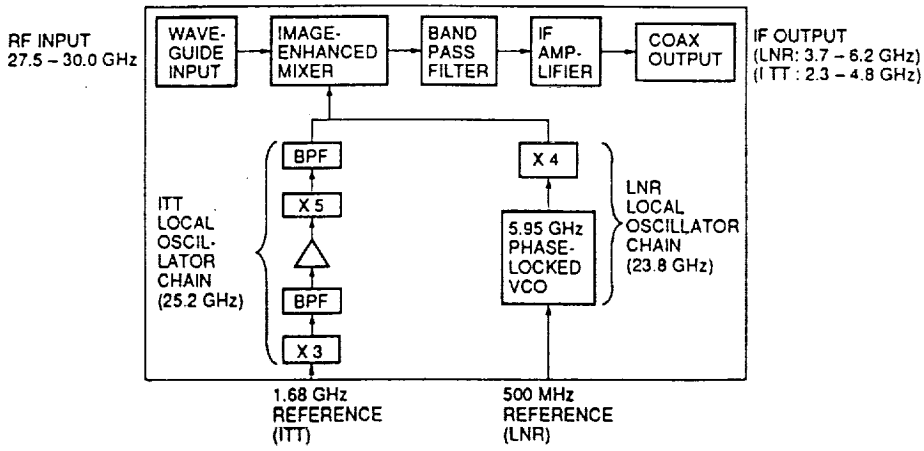

Figure 1. - Functional block diagram for the LNR Communications, Inc., and ITT Defense Communications 30 GHz low noise receivers.

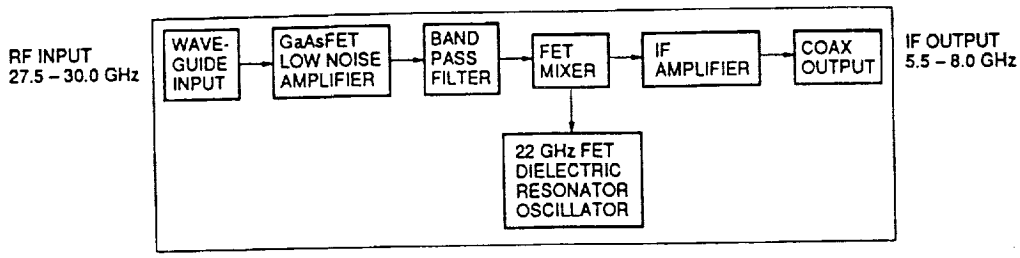

Figure 2. - Functional block diagram for the Hughes Hybrid – MIC 30 GHz low noise receiver.

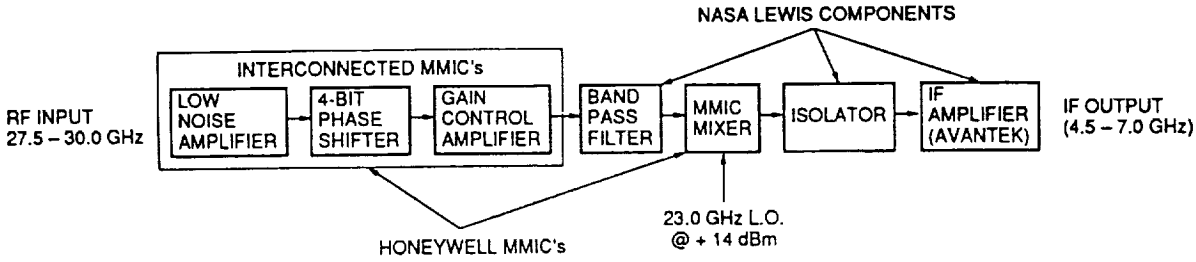

Figure 3. - Honeywell MMIC receiver test configuration.

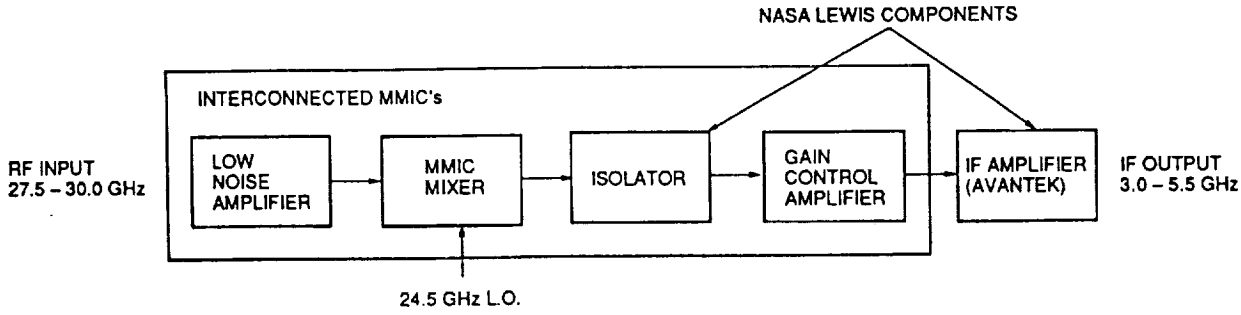

Figure 4. - Hughes MMIC receiver test configuration.

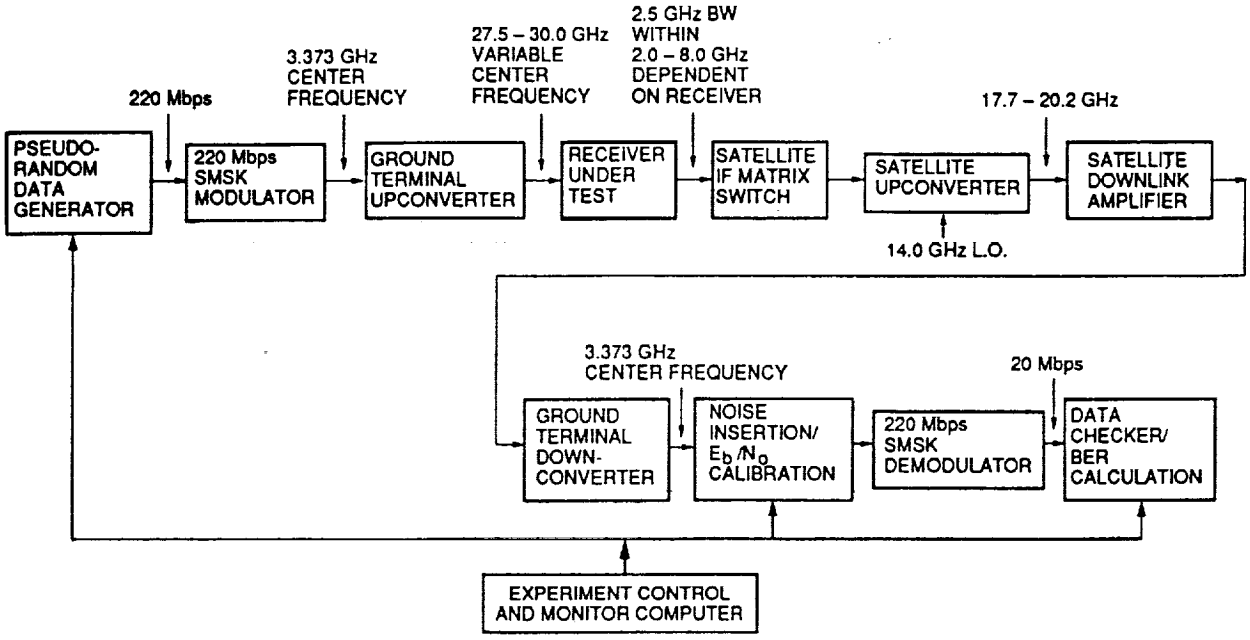

Figure 5. - Block diagram of the receiver BER measurement system.

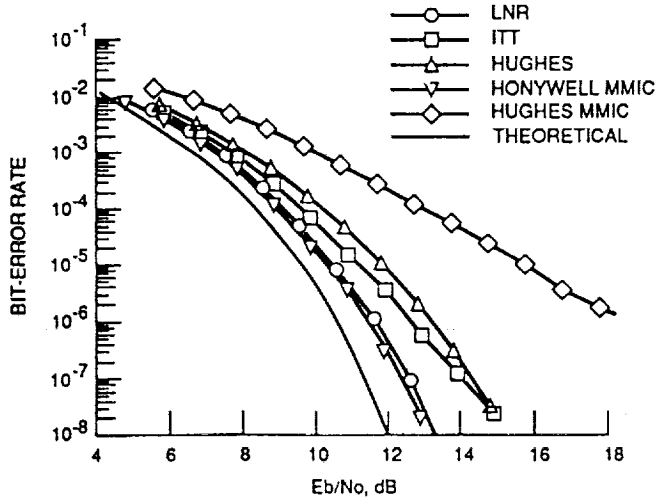

Figure 6. - Measured BER curves, for the LNR, ITT Hughes Hybrid-MIC, Honeywell MMIC, and Hughes MMIC receivers. Input power to the receivers is -30 dBm, and the satellite high power amplifier is in saturation.

NASA Technical Memorandum 102550

Optical Control of an 8-Element Ka-Band Phased Array Using a High-Speed Optoelectronic Interconnect

M.A. Richard and P.C. Claspy
Case Western Reserve University
Cleveland, Ohio

K.B. Bhasin
Lewis Research Center
Cleveland, Ohio

and

M. Bendett
Honeywell, Inc.
Bloomington, Minnesota

Prepared for the
1990 AP-S International Symposium
sponsored by the Institute of Electrical and Electronic Engineering
Dallas, Texas, May 7-11, 1990

NASA

OPTICAL CONTROL OF AN 8-ELEMENT Ka-BAND PHASED ARRAY ANTENNA USING A HIGH-SPEED OPTOELECTRONIC INTERCONNECT

M. A. Richard and *P. C. Claspy, Department of Electrical Engineering,
Case Western Reserve University, Cleveland, OH,
K. B. Bhasin, National Aeronautics and Space Administration,
Lewis Research Center, Cleveland, OH,
and M. Bendett, Honeywell, Inc.,
Sensors and Signals Technology Center, Bloomington, MN

ABSTRACT

Optical distribution of control signals in electronically steered phased array antennas is being considered. This paper describes a demonstration experiment in which a high speed hybrid GaAs optoelectronic integrated circuit (OEIC) was used to control an eight element phased array antenna. The OEIC, which accepts a serial optical control signal as input and converts it to 16 demultiplexed parallel outputs, was used to control the monolithic GaAs phase shifters of a Ka-band patch panel array antenna. Antenna pattern switching speeds of 2.25 μs, limited by interface circuitry, were observed.

E-5365

1. INTRODUCTION

Because of advantages such as low weight and high beam steering speeds offered by phased array antennas, future NASA missions such as Mars Rover and Mission Planet Earth call for the use of such antennas for purposes of communication and radiometry.[1] While the development of steerable microwave frequency phased arrays has been stymied in the past by the lack of small phase shifters and power amplifiers, recent advances in GaAs monolithic microwave integrated circuit (MMIC) technology have resulted in the development of high quality integrated power amplifiers and phase shifters.[2] With these advances, large arrays, on the order of 100 to 1000 elements, are becoming feasible.

The use of such a large number of elements at millimeter wave frequencies presents unique challenges in the distribution of RF and control signals to each element because of the small element spacings involved. As a way to surmount this problem, various fiber optic-based solutions have been proposed and investigated. Optical fibers hold much promise for use in large phased arrays because of their light weight, low attenuation, mechanical flexibility, large bandwidth, and immunity to cross talk and EMI. As the operational frequencies of arrays increase, the amount of available space for interconnection of elements decreases, so multiplexing of control signals onto a single fiber would clearly be advantageous. This would allow beam control data to be brought from a data source and be distributed locally to the phase shifters and amplifiers while simultaneously achieving a reduction in weight and space consumed.[3] When this is done, the input data rate becomes high even though the rate to an individual control line may be low. In this paper we describe the use of a single optical fiber to distribute control data to the phase shifters of an eight-element array.

---

*NASA Resident Research Associate at Lewis Research Center.

2. EXPERIMENTAL ARRANGEMENT

A system consisting of a phased array antenna, an optoelectronic integrated circuit (OEIC) controller, and optical source and fiber, and the necessary electronics, shown schematically in Fig. 1, was set up to demonstrate optical control of a phased array antenna. The OEIC, which has been described in a previous publication,[4] is a hybrid device that requires a serial optical bit stream input, as well as electrical clock and synchronization inputs, and produces 16 parallel, demultiplexed, electrical outputs and a data valid (clock divided by 16) output. It is capable of operation at speeds up to approximately 300 Mb/sec.

The antenna, shown in Fig. 2, was developed by Honeywell[5] for another program, and is a narrow band, eight element system that is tuned to 28.2 GHz. It has an eight-way corporate feed network that divides the input power equally among eight phase shifters that, in turn, feed the eight radiating elements, each of which consists of 10 patches spaced by 1.94 cm. Each phase shifter is a 4-bit device that has 16 possible delay settings in 22.5° increments from 0° to 337.5°.[6,7] The 64 control lines are brought out to two ribbon connectors on opposite sides of the antenna. A phase look-up table was available to permit compensation for path length differences within the feed network in establishing an antenna beam direction. As a result of process tolerances the pinchoff voltages of the FET's in the antenna phase shifters ranged from -5 V to -6 V, and a voltage control circuit to accommodate this was obtained from Honeywell.

Since the OEIC and the antenna phase shifters were not designed to be directly interfaced, voltage level shifting was required between the two systems. The OEIC was therefore used to control an electronic switch which, in turn controlled the voltages applied to the phase shifters. Rather than controlling all 32 bits of the array (8 shifters × 4 bits/shifter), eight bits were strategically selected so that by changing only these bits the antenna pattern could be switched between normal to the plane of the antenna and 20° from the normal to the plane. For the optical control experiment an oscillator/amplifier combination was used to feed a 28.2 GHz signal, at +21 dBm, to a 25 dB horn that served as a transmitter radiator. An HP 8018 data source was programmed to output a sequence of data so that the demultiplexed outputs of the OEIC, that controlled the previously selected eight antenna phase shifter bits, would alternate between high and low levels at 200 KHz. The array was centered on and perpendicular to the horn axis, with a separation of 3 m.

3. EXPERIMENTAL RESULTS

Toggling the phase shifters between the two states caused the array pattern to alternately point directly toward the transmitter, then 20° from it, with the result that the output signal from the antenna alternated from a maximum to nearly zero, as shown in Fig. 3. In the figure the top trace is one OEIC output data line and the lower trace is the amplified detector output. (In the lower trace the response speed was limited by the time constant of the detector that was used to record the antenna output.) In this experiment the clock frequency was 50 MHz, the average optical power to the OEIC was 200 μW and the beam switching rate was 3.2 μs. By rearranging the data pattern the switching rate could be reduced to 2.25 μs, but in all cases the maximum switching speed was limited by the interface circuitry.

4. CONCLUSIONS

In this paper we have reported the results of an experiment involving the optical control of a 28.2 GHz phased array antenna. In this work an eight element antenna was controlled by the demultiplexed output of a single optically fed controller, demonstrating the feasibility of applying such devices to the antenna control problem. The speed of switching was limited by the interface circuitry to 2.25 μs.

The authors wish to acknowledge the assistance and support of Doug Carlson, Mark Vickberg, and Vladimir Sokolov of Honeywell's Sensors and Signals Technology Center.

---

1. K. B. Bhasin and R. R. Kunath, "Optically interconnected phased arrays," SPIE Advances in kSemiconductors and Superconductors: Physics and Device Applications Conference, Newport, CA, March 1988. Also published as NASA Technical Memorandum 100855, 1988.
2. Microwave Integrated Circuits, J. Frey and K. B. Bhasin, eds. (Artech House, 1985).
3. K. B. Bhasin, et. al., "Optical techniques to feed and control GaAs MMIC modules for phased array antenna applications," 11th Communications Satellite Systems Conference, pp. 506-513, AIAA, New York, 1986. Also published as NASA Technical Memorandum 87218, 1986.
4. P. C. Claspy, M. Richard, K. B. Bhasin, M. Bendett, G. Gustavson, and W. Walters, "A high-speed GaAs MESFET Optical Controller," IEEE Photonics Tech. Lett., vol. 1, pp. 389-391, 1989.
5. V. Sokolov and M. Komen, "Electronically Steerable Patch Panel Array Antenna," Honeywell Final Report, Report No. AFATL-TR-87-19, Air Force Armament Laboratory, Eglin Air Force Base, FL, April 1987.
6. V. Sokolov, P. Bauhahn, J. Geddes, A. Contolatis, and C. Chao, "A Ka-Band GaAs Monolithic Phase Shifter," IEEE Trans. Electron Devices, vol. ED-30, pp. 1855-1861, 1983.
7. P. Bauhahn, C. Butter, V. Sokolov, and A. Contolatis, "30 GHz Multi-bit Monolithic Phase Shifter," IEEE Microwave Theory Tech 1985 Symposium Proc. pp. 4-7, May 1985.

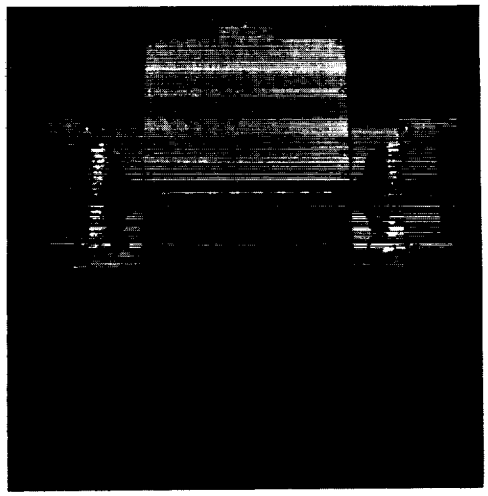

Fig. 1. The 8-element Ka-band phased array antenna.

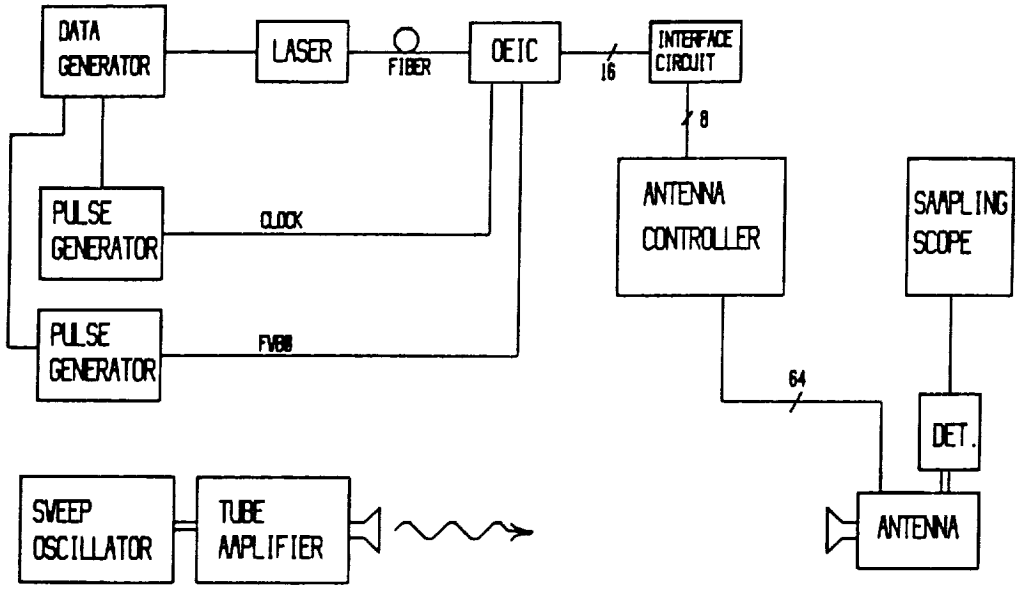

Fig. 2. Experimental arrangement.

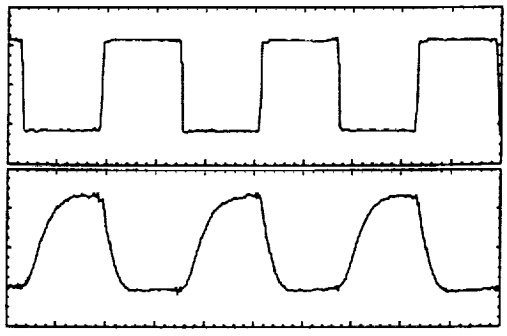

Fig. 3. Antenna switching results. Top trace: Single data line of antenna control signal. Vertical scale: 60μV/div.; Bottom trace: Detector output. Vertical scale: 4 mV/div. Horizontal scale for both traces: 2 μs/div.

NASA Technical Memorandum 103110

Performance of a 300 Mbps 1:16 Serial/Parallel Optoelectronic Receiver Module

M.A. Richard and P.C. Claspy
Case Western Reserve University
Cleveland, Ohio

K.B. Bhasin
Lewis Research Center
Cleveland, Ohio

and

M.B. Bendett
Honeywell, Inc.
Bloomington, Minnesota

Prepared for the
Technical Symposium on Optical Engineering and Photonics
in Aerospace Sensing
sponsored by the Society of Photo-Optical Instrumentation Engineers
Orlando, Florida, April 16–20, 1990

NASA

Performance of a 300 Mbps 1:16 serial/parallel optoelectronic receiver module

M.A. Richard, P.C. Claspy

Case Western Reserve University, Department of Electrical Engineering
Cleveland, OH 44106

K.B. Bhasin

NASA Lewis Research Center
21000 Brookpark Rd., Cleveland, OH 44135

M.P. Bendett

Honeywell, Inc.
Bloomington, MN

E-5434

ABSTRACT

Optical interconnects are being considered for the high speed distribution of multiplexed control signals in GaAs MMIC-based phased array antennas. This paper describes the performance of a hybrid GaAs optoelectronic integrated circuit (OEIC), along with a description of its design and fabrication. The OEIC converts a 16-bit serial optical input to a 16 parallel line electrical output using an on-board 1:16 demultiplexer and operates at data rates as high as 305 Mbps. The performance characteristics as well as potential applications of the device are presented.

INTRODUCTION

The advantages of large directly radiating phased array antennas for rapid beam scanning are well known, but conventional hardware is heavy and bulky, and architectures for implementing these arrays have resulted in cumbersome, topologically complex, and high loss internal distribution systems. GaAs monolithic microwave integrated circuits (MMIC's), which have undergone extensive development and which could be used as array output modules, represent a major step toward improved and light weight arrays[1]. Yet, the interconnection of these devices into a beam formation network (BFN), is still a rather formidable problem. Conventional methods carrier and control signal distribution to the radiating elements suffer from cross talk and electromagnetic interference between elements. To alleviate these problems, several optics-based signal distribution methods have been proposed as solutions. Among the propose methods are those which use fiber optics to interconnect the BFN's[2-5], and those which use optical processing within the BFN's.[6-9]

The work described here is addressed toward the meeting of needs of fiber optic interconnected BFN's. The GaAs MMIC's in a phased array antenna are relatively complex. They include a variable phase shifter and a variable power amplifier which permit the creation of the aperture phase and amplitude distribution that is appropriate to the desired radiated beam configuration. Some proposed architectures also include a local oscillator and a mixer at each antenna element.[10,11] In fiber optic interconnected systems, optical fibers would be used to carry the control signals to the variable phase shifters and amplifiers as well as the signal to be transmitted

and the local oscillator phase locking signal. All control signals for the array including phase shifter and amplifier control signals could be multiplexed onto one optical channel as seen in Fig. 1. Although the actual rate at which a single phase shifter or power amplifier requires data may be low, the large number of elements involved necessitates a high overall data transfer rate, and thus a wide bandwidth channel will be required. Some demonstrations of the use of optical interconnects in phased array applications, using discrete components, have been reported[12], and Crow et. al., have reported a demultiplexing OEIC[13]. In this paper we report on the design and fabrication of a hybrid, high speed GaAs MESFET integrated circuit optical receiver/demultiplexer.

The constructed device is a hybrid optoelectronic integrated circuit (OEIC). Two GaAs circuits, an optical receiver and a demultiplexer, are packaged together in a 34-pin flatpack with a fiber pigtail attached for optical input. The inputs to the OEIC are a 16 bit optical serial data stream at 830 nm, an electrical high-speed clock, and a synchronization signal (FWBO). The outputs are 16 parallel TTL-level electrical outputs and an input clock divided by 16.

DESIGN AND FABRICATION

A PIN photodiode was chosen in place of the conventional MSM photodetector because of its superior noise performance, its speed capability, and its enhanced photosensitivity. It also has the advantage over the MSM or NPN structures commonly used for monolithic integration in that it can be operated in the photovoltaic mode if necessary since it is an asymmetric device. It was implemented using an interdigitated structure (2 μm finger width, 5 μm finger spacing) with an overall size of 40 μm x 60 μm. To achieve high speed and sensitivity a multi-stage differential amplifier is used to boost the signal from the detector up to logic levels. This amplifier consists of a transimpedance input stage followed by two additional capacitively coupled stages, each with a gain of approximately 10 dB. A constant output level is achieved by using a digital amplifier output section. The output from the receiver chip is fed into the 1:16 demultiplexer, that employs direct coupled FET logic (DCFL) circuitry. Although this does not necessarily provide the optimum speed and power dissipation characteristics, it permits circuit construction using established design rules which have been proven during previous development programs. In order to keep the electrical power consumption as low as possible and to reduce the number of high speed circuits, the demultiplexer design incorporated a high speed front end followed by lower speed stages. The outputs of the demultiplexer chip were designed to drive a TTL load and therefore are the major power consumers in the OEIC.

Optical input to the circuit is achieved through the use of a pigtailed optical multimode fiber with a 50 μm core. The fiber is mounted flush on top of the optical receiver wafer. By polishing the end of the fiber at a 58 degree angle, total internal reflection occurs and the light is forced to exit through the side of the fiber. This scheme allows the use of a planar photodiode without the need to bring the fiber in perpendicular to the device. In addition, some focusing of the light is provided by the fiber's curved surface.

All of the circuits were designed using Honeywell GaAs E/D MESFET design and layout rules, and the entire OEIC is amenable to monolithic integration on a single chip. The design was implemented using Honeywell's GaAs Self-Aligned Gate MESFET

process, which is based on selective ion implantation into 3-inch GaAs substrates. Efforts were made initially to fabricate the integrated optical detectors using the standard E/D MESFET implants. In the final fabrication, however, the process was modified to add deep n+ and p+ implants for the PIN detector to permit more efficient collection of carriers that are photogenerated below the wafer surface. The basic process uses 1 μm gate length FET's with V_T's of -0.6 V for Dmode and +0.3 V for Emode devices. Photolithography is accomplished using a projection aligner with die-by-die alignment. (A cross-sectional view of a wafer at various points in the fabrication process is shown in Fig. 2) In this process, Be and Si are implanted through a thin Si_3N_4 implant cap to form the p-buried layer as well as the enhancement and depletion channels, as shown in Fig. 2a. After channel activation the anneal cap is stripped and the refractory metal gate is sputter-deposited and patterned using reactive ion etching. This gate metal then serves as the self-aligned implant mask for the n+ source and drain implants of the FET's, with photoresist masking outside the device areas. (Fig. 2b) Finally, the PIN detector is photolithographically defined and the deep n+ and p+ implants are made, then annealed with a Si_3N_4 cap, using a rapid optical annealer. Ohmic contacts are formed by evaporation using a AuGe-based metal and then lifted off and sintered (Fig. 2c), and interconnect metallization consists of two-level metals defined by a dielectric-assisted liftoff (DAL) technique. This DAL process, together with filled VIA's for interlevel interconnects, permits a complete planarity of the chip topology, which is important in obtaining a high yield for LSI/VLSI fabrication. Both interconnect levels have sheet resistances less than 0.07 ohms per square, which provides for low IR drops and small RC time constants in complex high-speed circuits.

OPERATION

For testing and characterization the completed circuits were packaged in a 34 lead flatpack with a fiber pigtail. These flatpacks were then mounted in a test fixture for an initial performance test. The test fixture is a circuit board with a card edge connecter for the power supply inputs, and coaxial connections for the RF inputs and demultiplexer outputs. A compression clamp connects the flatpack leads to the circuit board tracings. An HP 8080 serial word generator was used to directly modulate an Ortel laser through an HP bias tee, which in turn fed into the optical controller. The word generator was programmed to cycle a 64 bit word output in an NRZ format, and by viewing the demultiplexer outputs on an HP sampling oscilloscope the operation of the device was confirmed. Because of the 1:16 demultiplexer, each output of the controller cycled a 4 bit word. The maximum clock frequency of the controller, limited by the demultiplexer, was found to be 305 MHz. Due to the oscilloscope's 50 Ω inputs, the waveforms were limited to an amplitude of less than 800 mV. Fig. 3 shows three of the 16 output channels along with the data valid line as viewed with a sampling oscilloscope. In this plot the clock frequency was 240 MHz, and the input data was a repeated 64 bit word.

The controller requires less than 200 μW of optical input power. Although tests at Honeywell have demonstrated that powers as low as 1 μW are sufficient, equipment limitations precluded operation of the device at such low optical powers. The electrical power consumption of the controller was found to be always less than 370 mW, and was measured to be as low as 120 mW in some cases. Because most of the power is consumed by the TTL drivers, the terminations of the output leads affected the power consumption greatly.

Initial tests of the device showed that the outputs had uncertainties. A clean output with a definite bit pattern could only be obtained by adjusting the clock frequency to certain values. In addition, the bit pattern sent to a specific output did not necessarily appear on that output. The latter problem was immediately identified as a timing problem in the synchronization (FWBO) signal; the FWBO pulses were not arriving at the proper moment so that the demultiplexer would know which bit was the first. Because the data was input through the laser, fiber and detector/amplifier while the FWBO was input directly into the demultiplexer, the FWBO arrived before the corresponding data. Likewise, the output uncertainty problem was found to be caused largely by the timing of the high speed clock input, which was out of phase with the optically input data because of propagation path length differences. These problems were overcome by using a pulse generator with a variable delay control to regenerate both the clock and FWBO signals shifted in time.

APPLICATIONS

The optical controller described in this paper was developed primarily for use as a phased array antenna controller. As such, the use of the device has been demonstrated in the control of monolithic Ka-Band phase shifter,[14] and in the control of a 30 GHz 8-element phased array antenna.[15] However, many other applications are conceivable as shown in Fig. 4. The built in demultiplexer makes this OEIC suitable for many high data rate transfer applications including neural networks, signal processing interconnections, and integrated modulator/detector arrays.

CONCLUSION

We have described a hybrid MESFET optical controller capable of data rates as high as 300 Mbps. The device uses less than 370 mW of electrical power and requires less than 200 μW of optical power. Because of the on-board demultiplexer, the OEIC has many potential applications beyond its intended phased array antenna application. A fully monolithic version of this device has been fabricated and will be tested in the near future. This device shows that optical and digital technologies are monolithically integratable, and any additional circuitry such as coding or clock recovery that can be fabricated using E/D MESFET design can easily be added to address a specific application.

REFERENCES

1. K.B. Bhasin and D.J. Connolly, "Advances in Monolithic Microwave Integrated Circuit Technology for Space Communications Systems," IEEE Trans. Microwave Theory Tech., vol. MTT-34, pp. 994-1001, 1986.

2. A.M. Levine, "Fiber Optics for Radar and Data Systems," SPIE Proceedings, vol. 150, pp. 992-998, 1978.

3. J. Austin and J.R. Forrest, "Design Concepts for Active Phased-Array Modules," IEE Proceedings F, vol. 127, pp. 290-300, 1980.

4. K.B. Bhasin, G. Anzic, R.R. Kunath, and D.J. Connolly, "Optical Techniques to Feed and Control GaAs MMIC Modules for Phased Array Antenna Applications," 11th Annual AIAA Communications Satellite Systems Conference, AIAA, New York, pp. 506-514, 1986.

5. R.R. Kunath and K.B. Bhasin, "Optically Controlled Phased Array Antenna Concepts Using Monolithic Microwave Integrated Circuits," 1986 International IEEE AP-S Symposium Digest vol. 1, pp. 353-355.

6. G.A. Koepf, "Optical Processor for Phased-Array Antenna Beam Formation," Proc. SPIE, vol. 477, pp. 75-81, 1984.

7. P.G. Sheehan and J.R. Forrest, "The Use of Optical Techniques for Beamforming in Phased Arrays," Proc. SPIE, vol. 477, p. 82-89, 1984.

8. R.A. Soref, "Voltage-Controlled Optical/RF Phase Shifter," J. Lightwave Tech., vol. LT-3, pp. 992-998, 1985.

9. L.P. Anderson, F. Boldissar, and D.C.D. Chang, "Antenna Beamforming using Optical Processing," Proc. SPIE, vol. 886, pp. 228-232, 1988.

10. P.R. Herczfeld, A.S. Daryoush, A. Rosen, A.K. Sharma, and V.M. Contarino, "Indirect Subharmonic Optical Injection Locking of a Millimeter-Wave IMPATT Oscillator," IEEE Trans. Microwave Theory Tech., vol. MTT-34, pp. 1371-1376, 1986.

11. I.D. Blanchflower and A.J. Seeds, "Optical Control of Frequency and Phase of GaAs MESFET Oscillator," Electron. Lett., vol. 25, pp. 359-360, 1989.

12. A. Paolella and P.R. Herczfeld, "Optical Gain Control of a GaAs MMIC Distributed Amplifier," Microwave Optical Tech. Lett., vol. 1, pp. 13-16, 1988.

13. J.D. Crow, C.J. Anderson, S. Bermon, A. Callegari, J.F. Ewen, J.D. Feder, J.H. Greiner, E.P. Harris, P.D. Hoh, H.J.Hovel, J.H. Magerlein, T.E. Mckoy, A.T.S. Pomerene, D.L. Rogers, G.J. Scott, M. Thomas, G.W. Mulvey, B.K. Ko, T. Ohashi, M. Scontras, and D. Widiger, "A GaAs MESFET IC for optical multiprocessor networks," IEEE Trans. Electron Devices, vol. 36, pp. 263-268, 1989.

14. K.B. Bhasin, P.C. Claspy, M.A. Richard, R.R. Romanofsky, M. Bendett, G.Gustafson, W. Walters, "Control of a GaAs Monolithic Ka-Band Phase Shifter Using a High-Speed Optical Interconnect," To be published in IEEE Trans. Microwave Theory Tech., May, 1990.

15. M.A. Richard, P.C. Claspy, K.B. Bhasin, and M. Bendett, "Optical Control of an 8-Element Ka-Band Phased Array Antenna Using a High-Speed Optoelectronic Interconnect," To be published in IEEE AP-S Proceedings, 1990.

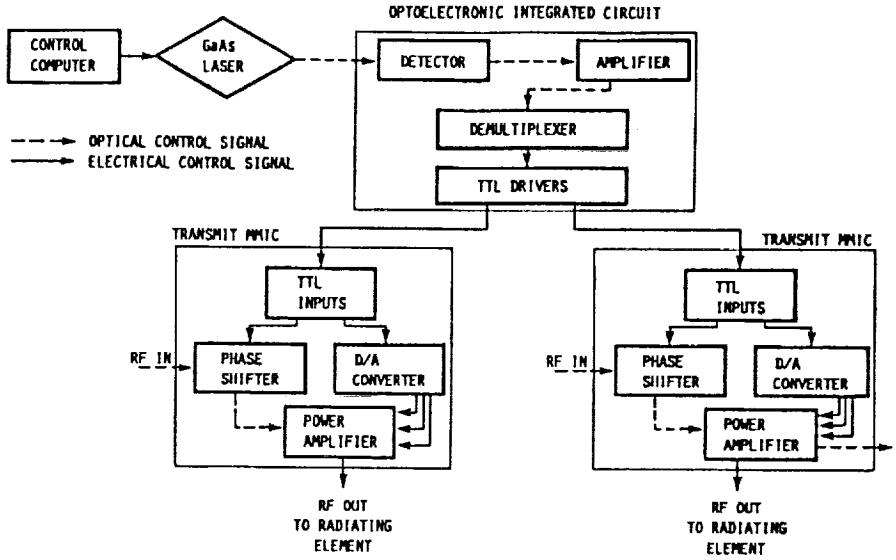

Fig. 1. A possible signal multiplexing scheme.

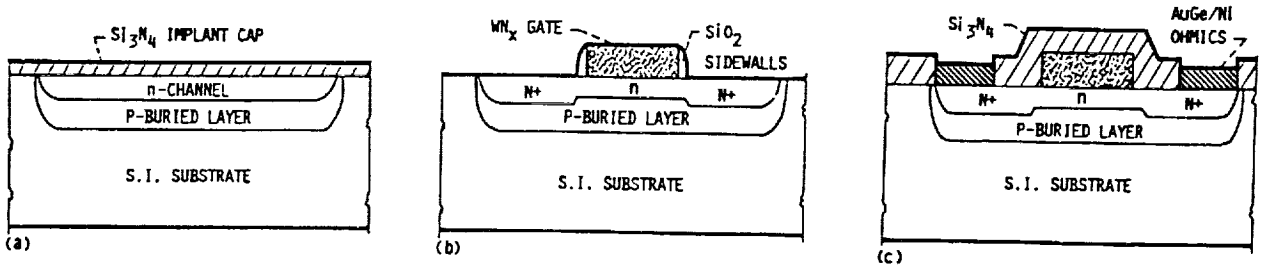

Fig. 2. Fabrication steps: (a) n, n^-, p implantation through Si_3N_4 cap, (b) WN metallization, N^+ implant self-aligned using SiO_2 side-wall spacers, (c) ohmic contact metallization.

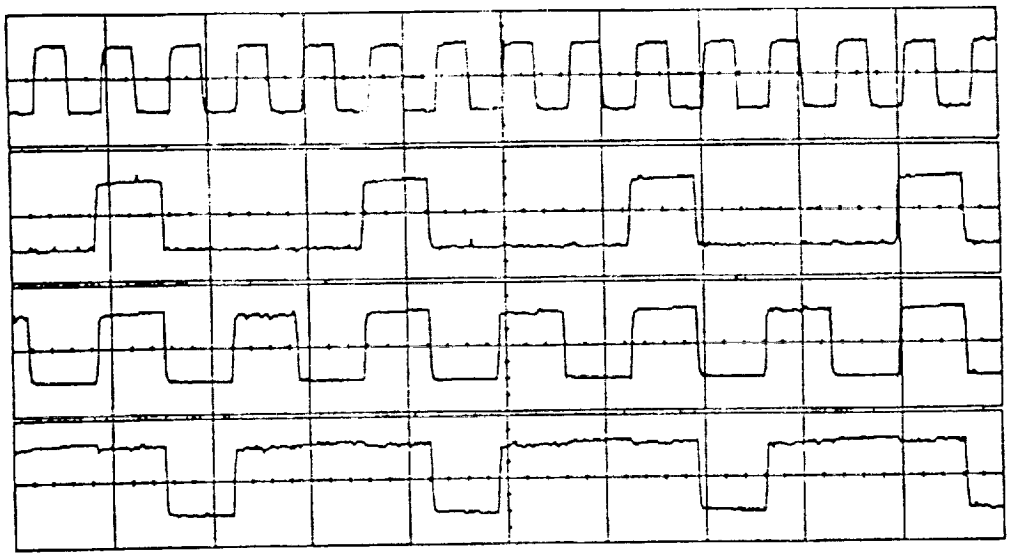

Fig. 3. Outputs of the OEIC. The top trace is the output clock divided by 16 while the lower three traces are data outputs. The input data is a 64 bit repeating word at a clock rate of 240 MHz. The ordinate for each trace is 200 mv/div. while the timebase is 100 ns/div.

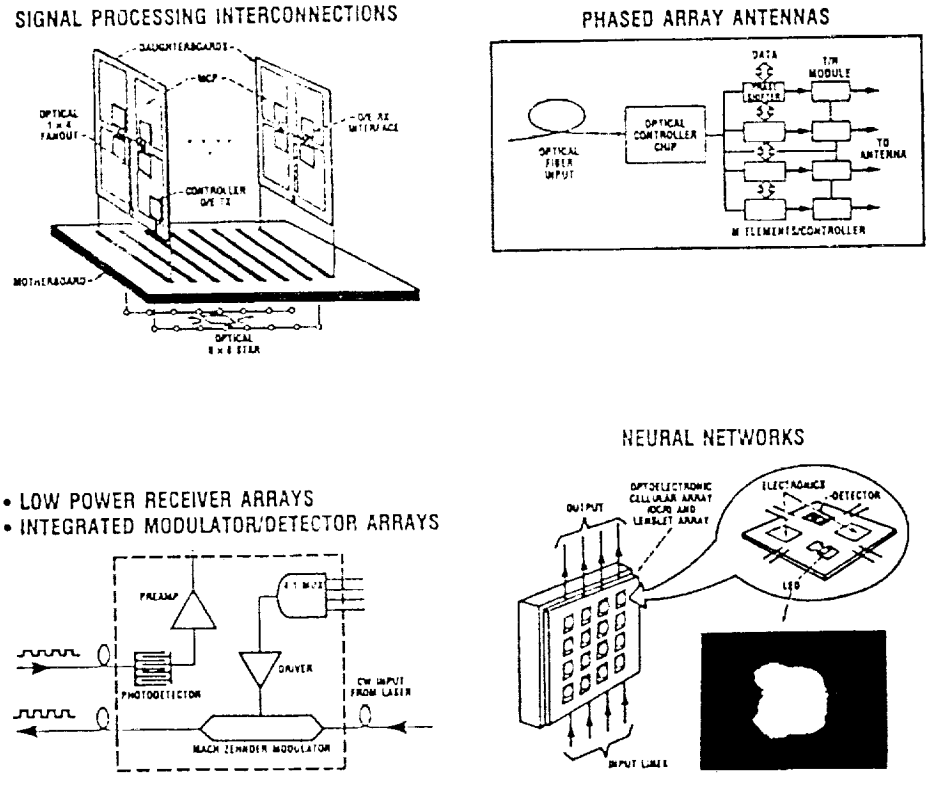

Fig. 4. Potential applications of OEIC include signal processing interconnections, phased array antennas, detector arrays, and neural networks.

NASA Technical Memorandum 101485

Microwave Characteristics of GaAs MMIC Integratable Optical Detectors

Paul C. Claspy
Lewis Research Center
Cleveland, Ohio

Scott M. Hill
Case Western Reserve University
Cleveland, Ohio

and

Kul B. Bhasin
Lewis Research Center
Cleveland, Ohio

Prepared for the
1989 IEEE MTT-S International Microwave Symposium
Long Beach, California, June 13–15, 1989

NASA

MICROWAVE CHARACTERISTICS OF GaAs MMIC INTEGRATABLE OPTICAL DETECTORS

Paul C. Claspy*
NASA Lewis Research Center
Cleveland, Ohio 44135

Scott M. Hill
Case Western Reserve University
Cleveland, Ohio 44106

and

Kul B. Bhasin
NASA Lewis Research Center
Cleveland, Ohio 44135

Summary

Interdigitated photoconductive detectors have been fabricated on microwave device structures, making them easily integratable with MMIC's. Detector responsivity as high as 2.5 A/W and an external quantum efficiency of 3.81 were measured. Response speed was nearly independent of electrode geometry, and all detectors had usable response at frequencies to 6 GHz. A small signal model of the detector, based on microwave measurements is also developed.

Introduction

Over the past few years technology advances have occurred which have increased the possibility that in the near future phased array antennas composed of monolithic microwave integrated circuits (MMIC's) will become a practical reality.[1] To take maximum advantage of the potential size reduction that this advance represents it will be essential to effect a similar size reduction in the chip-to-chip high frequency interconnects that the system will require. Various authors have suggested that fiber optic links, which are small and lightweight, may be a viable alternative to coaxial cables and waveguides for this application.[2] If these links are to be practical, however, high frequency optical transmitters and receivers must be available, and it would be particularly desirable that optical components be process- and material-compatible with GaAs heterostructure MMIC's so that they can be integrated onto the same chip.

In this paper we report the results of a study of the optical and electrical characteristics of interdigitated photoconductive detectors of various geometries that were fabricated on a HEMT-type heterostructure material. The operating wavelength was chosen to be 820 nm.

*P.C. Claspy is a National Research Council - NASA Senior Research Associate. Permanent address: Department of Electrical Engineering and Applied Physics, Case Western Reserve University, Cleveland, Ohio 44106.

Detector Fabrication

The detectors were fabricated on the MBE-grown GaAlAs/GaAs heterostructure material shown schematically in Fig. 1. A typical detector is shown in Fig. 2. Interdigitated electrode geometries, with finger spacings ranging from 1 to 4 μm, were used because they increase the effective active area of the detector while keeping the transit distance small. Since the GaAlAs window that remains after fabrication is essentially transparent to the incident 820 nm radiation, almost all of the photon absorption, and therefore the electron-hole pair generation, occurs within the undoped GaAs layer. For testing, the detectors were mounted directly on the Teflon insulation of a specially prepared length of semi-rigid coaxial cable, with short wire-bonded leads to the center conductor and the shield.

Optical Response Measurements

Frequency domain response measurements were made over the range 0.01 to 10 GHz using the system shown schematically in Fig. 3, and normalized responses of detectors of three different geometries are shown in Fig. 4. The detectors exhibit nearly identical response dispersion, with a 3 dB cutoff frequency at approximately 185 MHz. The gain decays at about 12 dB/decade in the decade between 100 MHz and 1 GHz, with a small plateau at 510 MHz, then falls off at 20 dB/decade after a larger plateau at 1 GHz. The shape of the response suggests that device characteristics are limited by trapping effects.[3]

Detector responsivities at 500 MHz, R(500 MHz), were measured using an Ortel SL620 diode laser, and lie in the range 0.13 to 0.31 A/W. On the basis of measurements at 500 MHz, the low frequency responsivity of the 1 by 1 μm detector was calculated to be 2.5 A/W. The (internal) quantum efficiency of this detector is 5.4%, and the external quantum efficiency is 3.81, all of which are comparable to results reported for GaAs detectors.

Microwave Impedance Measurements and Model

DC and AC impedance characteristics of the detectors were studied under various levels of illumination. DC I-V curves for our detectors were taken using white light illumination, and a typical result is given in Fig. 5. The DC resistance of the detectors is low and constant for small bias, smoothly increases as the bias is increased, becoming very large at high bias as a result of carrier velocity saturation. The decrease of resistance with increasing optical power is also shown in Fig. 5.

The reflection coefficient, S_{11}, was measured over the frequency range 0.5 to 5.5 GHz at various bias levels and incident white light intensities using an HP-4910 Network Analyzer. Some results of these measurements are shown in Figs. 6 to 8. Figure 6 shows that S_{11} decreases with detector feature size, Fig. 7 shows that it increases with bias voltage, at moderate illumination, and Fig. 8 shows that it decreases with increasing illumination, at moderate bias.

A small-signal, high frequency model, consisting of a parallel RC combination with an inductance in series with each node of the RC network, as shown in Fig. 9(a), was developed from the measured S_{11} results. The model, which is similar to that developed by Wojtczuk and Ballantyne[4] leads to a complex impedance given by

$$Z = \frac{R(V,\Phi) + j\omega\{(L_1 + L_2) - CR^2(\omega,\Phi)\}}{1 + \omega CR^2(V,\Phi)} \qquad (1)$$

where the resistance, $R(V,\Phi)$, is a function of both the DC bias and the illumination.

The light intensity primarily affects R, which at low bias drops from well over 100 Ω at ambient to only a few tens of ohms at high intensity. Therefore, at low bias and high light level the low resistance effectively short-circuits the device capacitance, reducing the impedance to

$$Z = R + j\omega(L_1 + L_2), \qquad (2)$$

as shown in Fig. 9(b). The AC resistance was observed to increase significantly with bias, so that at high bias the complex impedance eventually simplifies to

$$Z = \frac{R}{\omega CR^2} - \frac{j}{\omega C}, \qquad (3)$$

as shown in Fig. 9(c). This change from inductive to capacitive behavior suggests the possibility of a zero reactance operating point by the elimination of any RC or R/L time constants if the detector is time constant limited. The impedance of the zero reactance point is determined by setting the imaginary part of Eq. (1) equal to zero. Then, if $(\omega CR^2) << 1$, the impedance reduces to

$$Z = \sqrt{(L_1 + L_2)/C}, \qquad (4)$$

which for our devices is about 250 Ω at somewhat less than 3 V bias.

Summary and Conclusion

The high frequency characteristics of interdigitated photoconductive detectors fabricated on a HEMT structure have been presented. The fabrication process was completely compatible with that used to fabricate MODFET's making these detectors easily integrable for MMIC usage. It should be noted that while the detectors did not exhibit an extremely high bandwidth, they did possess usable response well into the GHz range, and the change from inductive to capacitive reactance with bias suggests the possibility of a zero reactance operating point. In conclusion, then, the combination of fabrication compatibility and performance characteristics makes these devices interesting for interconnection applications.

References

1. J. Frey, and K.B. Bhasin, eds., Microwave Integrated Circuits, 2nd Ed. Dedham, MA: Artech House, 1985.

2. K.B. Bhasin, G. Anzic, R.R. Kunath, and D.J. Connolly, "Optical Techniques to Feed and Control GaAs MMIC Modules for Phased Array Antenna Applications," in AIAA 11th Annual Communications Satellite Systems Conference, New York: AIAA, pp. 506-514, 1986 (NASA TM-87218).

3. G.J. Papaionannou, and J.R. Forrest, "On the Photoresponse of GaAs MESFET's: Backgating and Deep Traps Effect," IEEE Trans. Electron Devices, vol. ED-33, no. 3, pp. 373-378, Mar. 1986.

4. S.J. Wojtczuk, and J.M. Ballantyne, "Impedance Properties and Broad-Band Operation of GaAs Photoconductive Detectors," J. Lightwave Tech., vol. LT-5, no. 3, pp. 320-324, Mar. 1987.

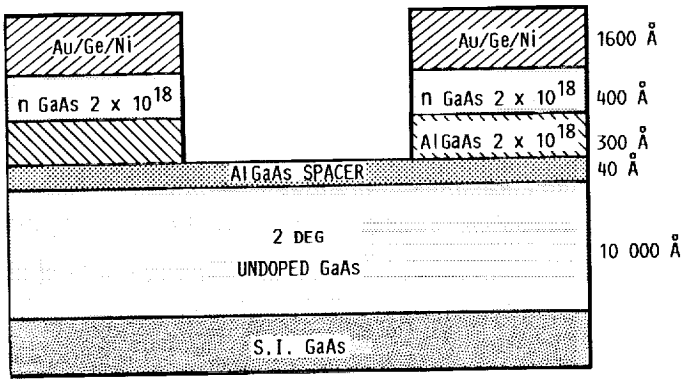

Fig. 1. Schematic cross section of photodetector material.

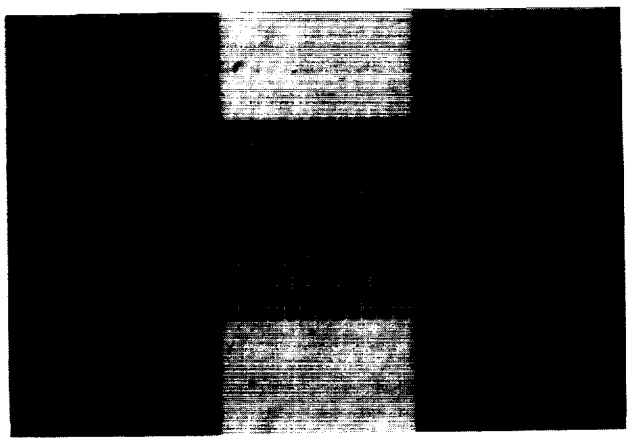

Fig. 2. 1 μm x 1 μm detector.

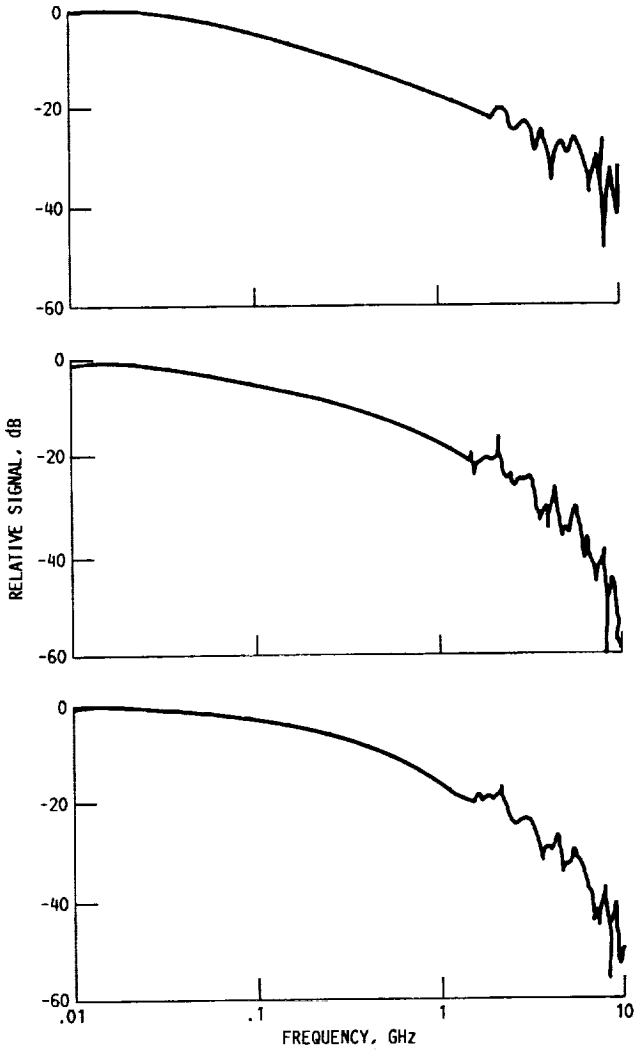

Fig. 4. Normalized frequency response of typical detectors.
(a) 1 μ x 1 μm; (b) 2 μm x 2 μm;
(c) 2 μm x 2 μm.

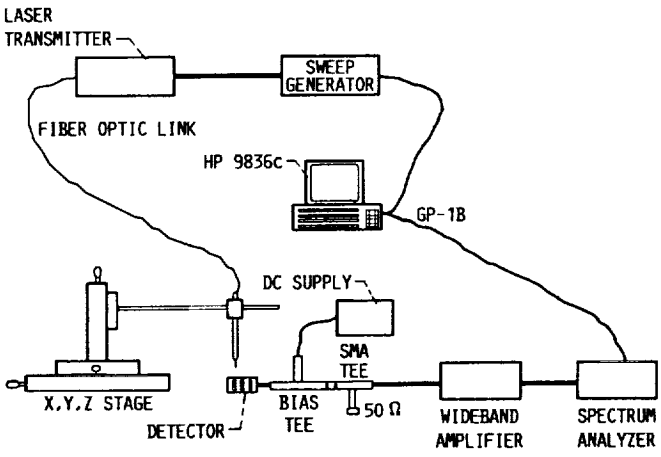

Fig. 3. Frequency domain measurement system.

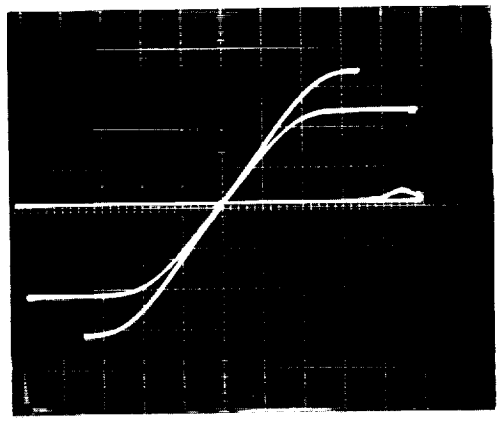

Fig. 5. I-V characteristic curve for 1 μm x 1 μm detector.

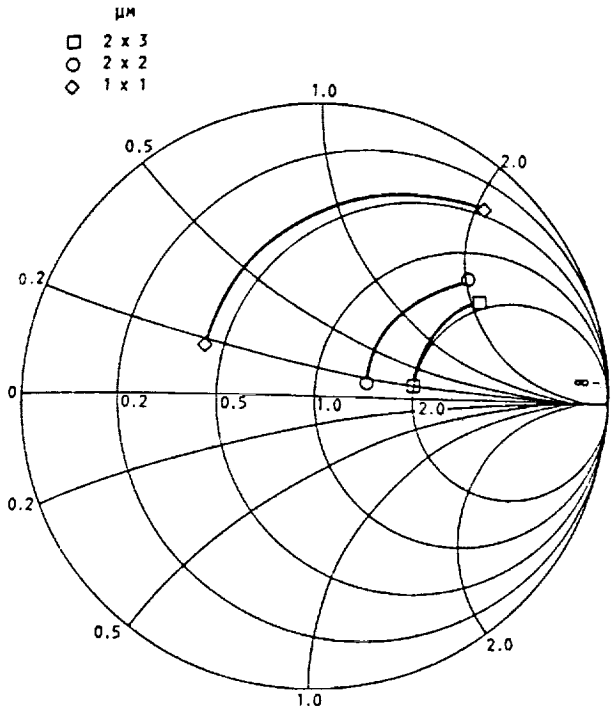

Fig. 6. Effect of electrode geometry on S_{11}.

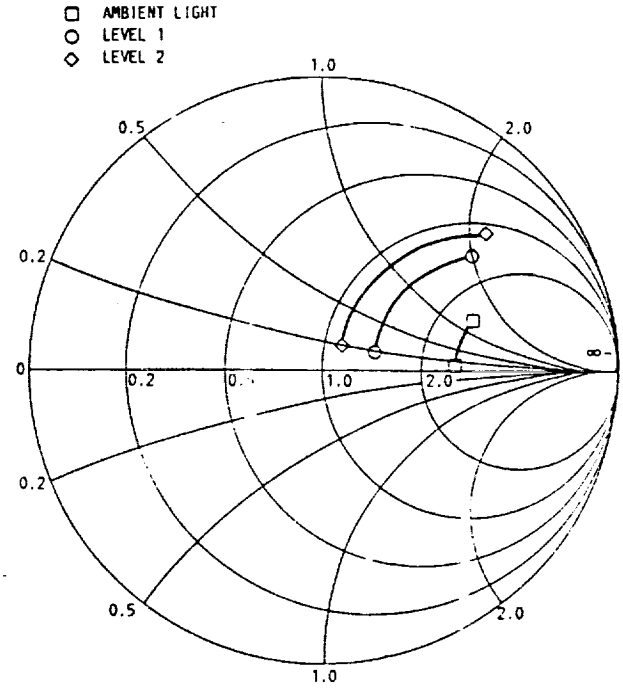

Fig. 8. Effect of illumination on S_{11} for 2 μm x 2 μm detector.

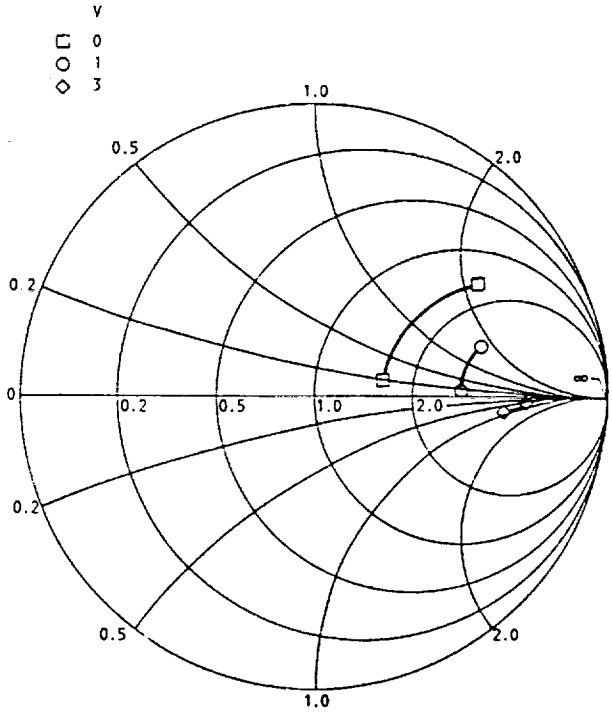

Fig. 7. Effect of bias voltage on S_{11} for 2 μm x 3 μm detector.

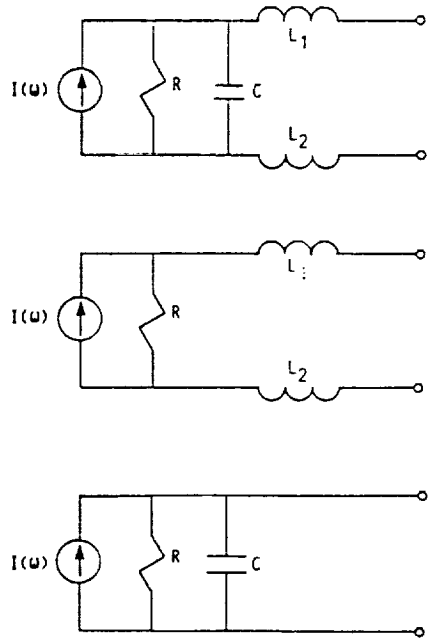

Fig. 9 Detector equivalent circuit models. (a) General equivalent circuit; (b) Low bias equivalent circuit; (c) High bias equivalent circuit.

A High-Speed GaAs MESFET Optical Controller

P. C. CLASPY, SENIOR MEMBER, IEEE, M. RICHARD, K. B. BHASIN, SENIOR MEMBER, IEEE, M. BENDETT, MEMBER, IEEE, G. GUSTAFSON, AND W. WALTERS

Abstract—**Optical interconnects are being considered for control signal distribution in phased array antennas. This paper describes a packaged hybrid GaAs optical controller with a 1:16 demultiplexed output that is suitable for this application. The controller, which was fabricated using enhancement/depletion mode MESFET technology, operates at demultiplexer-limited input data rates up to 305 Mbits/s and requires less than 200 μW optical input power.**

INTRODUCTION

PHASED array antennas are being considered for microwave and millimeter wave communication systems that will be used on future satellites and space vehicles [1]. The requirement for control of the phase and amplitude of signals at each of the several hundred monolithic microwave integrated circuits (MMIC's) that would constitute such an array necessitates the transfer of a large amount of control data to phase shifters and amplifiers in a short period of time when the beam direction is to be changed. One possible method of transmitting these data, with a concurrent reduction in weight and power consumption over more conventional methods, is to multiplex the control signals onto optical carriers, transmit the resulting signals to optical receiver–demultiplexers on the antenna, and distribute the demultiplexed control signals locally [2]. The requirements imposed upon optical links for this application are different from those imposed by telecommunications applications because of the short distances involved and the burst nature of the data. Furthermore, this type of link places an emphasis on reducing power, weight, and size over considerations such as dispersion and attenuation. Therefore, integration of the complete receiver/demultiplexer can provide a significant enhancement of the system.

Over the past several years, various authors have reported optoelectronic integrated circuits ranging from a diode–preamplifier combination [3] to detector–amplifier circuits [4] to an optical receiver with clock recovery [5]. In this letter, we report on the design, fabrication, and characteristics of a packaged hybrid integrated circuit optical controller consisting of two integrated submodules. As shown schematically in Fig. 1, the integrated submodules of our controller

Manuscript received July 11, 1989; revised August 30, 1989.

P. C. Claspy is a National Research Council Senior Research Associate at the National Aeronautics and Space Administration, Lewis Research Center, Cleveland, OH, on leave from Case Western Reserve University, Cleveland, OH.

M. Richard is with Case Western Reserve University, Cleveland, OH.

K. B. Bhasin is with the National Aeronautics and Space Administration, Lewis Research Center, Cleveland, OH.

M. Bendett, G. Gustafson, and W. Walters are with Sensors and Signal Processing Laboratory, Honeywell, Inc., Bloomington, MN.

IEEE Log Number .

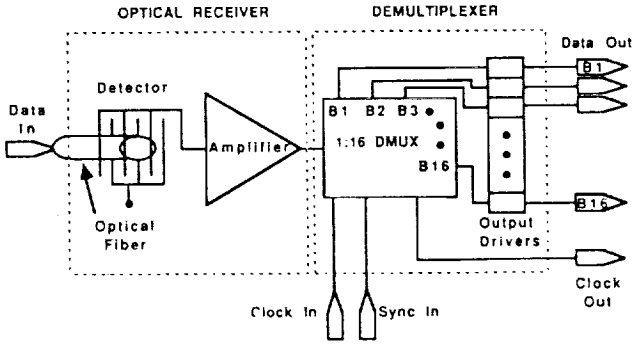

Fig. 1. Block diagram of the controller.

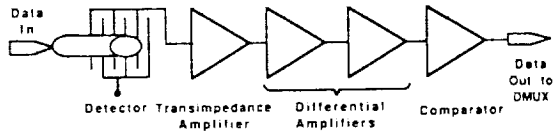

Fig. 2. Block diagram of the optical receiver section of the controller.

are an optical receiver, consisting of a photodetector and a three-stage amplifier with a comparator-based output, and a demultiplexer with output line drivers. The required input signals to the controller are an 830 nm optical serial data stream to the detector and electrical clock and synchronization signals to the demultiplexer. The output is 16 parallel TTL-compatible data streams and a clock at 1/16 of the input clock rate.

FABRICATION

Since the intended application of the controller is in satellite-based systems, low power consumption was a primary design criterion. To ensure this low power consumption as well as for process simplicity and reproducibility we chose to employ enhancement/depletion mode (E/D-mode) GaAs MESFET technology for both the receiver and the demultiplexer. This common technology will also permit future monolithic integration of the controller. The fabrication was based upon a refractory metal self-aligned gate process which is similar to a submicron process that was previously reported [6]. The only modifications to that process were that a 1 μm gate length was used here and that deep n+ and p+ implant steps were added so that the p-i-n photodiodes could be fabricated.

CIRCUIT DESIGN

The receiver section, shown schematically in Fig. 2, consists of an interdigitated p-i-n photodiode, a three-stage amplifier, and an output comparator. The optical input is laterally coupled through the cladding of a multimode fiber (50 μm

1041-1135/89/1100-0389$01.00 © 1989 IEEE

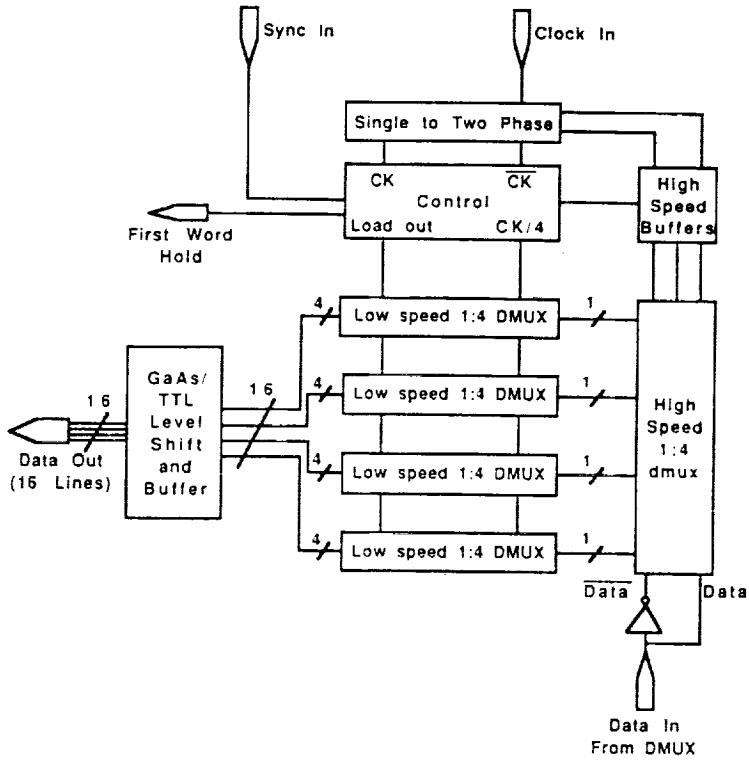

Fig. 3. Block diagram of the demultiplexer-output driver section of the controller.

core) to the photodiode. The fiber is mounted with its axis parallel to the wafer surface and the fiber end is polished at a 58° angle to ensure total internal reflection. The light exits through the curved side of the fiber, which provides some focusing onto the detector [7]. The three-stage amplifier consists of a transimpedance input amplifier followed by a two-stage high-gain differential amplifier to increase sensitivity while allowing high speed. Capacitive coupling is used between amplifier stages to reduce sensitivity to dc offsets resulting from mismatch between the complementary amplifier stages. Each stage of the amplifier produces a gain of 8–11 dB, and the power consumption of the amplifier is less than 100 mW.

The demultiplexer was designed using direct-coupled FET logic (DCFL) in a multistage circuit which operates at input data rates greater than 200 Mbits/s. Fig. 3 is a block diagram of the circuit, which has a high-speed front end followed by lower speed stages. This design reduces power consumption and limits the number of circuits that must be tightly coupled to the high-speed clock. It was used largely because it is based upon existing circuitry, although it does not necessarily provide optimum power and speed characteristics. The output drivers were designed for TTL levels and as a result they are the most power-consuming portion of the chip. The power dissipation in this stage is dependent upon the output logic states and upon the specific voltage level required of the TTL load driver.

Operation

The packaged controllers were tested in a fixture that permits separate observation of any of the 16 data output channels. To characterize the controller, the data output (NRZ format) from a word generator was used to directly modulate the output of a laser diode, which in turn provided data input to the receiver section. Concurrently, the clock and first word bit zero ($\overline{\text{FWB0}}$) from the word generator were input as electrical signals directly to the demultiplexer section of the controller, as shown schematically in Fig. 1.

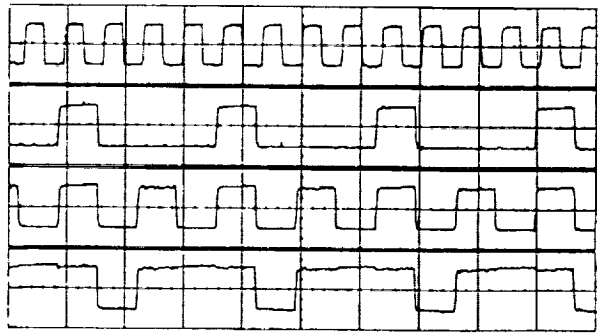

Fig. 4. Example of controller outputs. Top trace is the output clock and the remaining traces are three output data channels. The input data was a 64 bit word stream at a clock rate of 240 MHz. The ordinate for each trace is 200 mV/div and the abscissa is 100 ns/div.

The demultiplexed outputs of the controller were observed with a sampling oscilloscope, and an example of three of these, along with the output clock, is shown in Fig. 4. In this example, the input clock was 240 MHz and the input data was a repeated 64 bit word. By adjusting the dc operating point of the laser and the level of the ac drive power to it, the minimum average optical power required by the controller

was found to be less than 200 μW. The maximum clock rate of the tested controller, which is limited by the demultiplexer, was measured to be 305 MHz.

Conclusion

In this paper, we have described the design and operating characteristics of a packaged hybrid low-power GaAs MESFET demultiplexing optical controller that is suitable for use in controlling a phased array antenna. The two submodules of the controller were fabricated using identical technologies, making monolithic integration possible. The controller operates at input clock speeds greater than 300 MHz, and it requires less than 200 μW of optical power as the input signal and less than 370 mW of electrical power.

References

[1] K. B. Bhasin and D. J. Connolly, "Advances in monolithic microwave integrated circuit technology for space communications systems," *IEEE Trans. Microwave Theory Tech.*, vol. MTT-34, pp. 994-1001, 1986.

[2] K. B. Bhasin, G. Anzic, R. R. Kunath, and D. J. Connolly, "Optical techniques to feed and control GaAs MMIC modules for phased array antenna applications," in *Proc. 11th Annu. AIAA Commun. Satellite Syst. Conf.*, AIAA, New York, 1986, pp. 506-514.

[3] R. M. Kolbas, J. Abrokwah, J. K. Carney, D. H. Bradshaw, B. R. Elmer, and J. R. Biard, "Planar monolithic integration of a photodiode and a GaAs preamplifier," *Appl. Phys. Lett.*, vol. 43, pp. 821-823, 1983.

[4] M. Ito, T. Kumai, H. Hamaguchi, M. Makiuchi, K. Nakai, O. Wada, and T. Sakurai, "High-speed monolithically integrated GaAs photoreceiver using a metal-semiconductor-metal photodiode," *Appl. Phys. Lett.*, vol. 47, pp. 1129-1131, 1985.

[5] J. D. Crow, C. J. Anderson, S. Bermon, A. Callegari, J. F. Ewen, J. D. Feder, J. H. Greiner, E. P. Harris, P. D. Hoh, H. J. Hovel, J. H. Magerlein, T. E. Mckoy, A. T. S. Pomerene, D. L. Rogers, G. J. Scott, M. Thomas, G. W. Mulvey, B. K. Ko, T. Ohashi, M. Scontras, and D. Widiger, "A GaAs MESFET IC for optical multiprocessor networks," *IEEE Trans. Electron Devices*, vol. 36, pp. 263-268, 1989.

[6] K. L. Tan, H. K. Chung, G. L. Grung, and S. M. Shin, "A submicron self-aligned gate GaAs MESFET technology for low power subnanosecond static RAM fabrication," in *Tech. Dig., 1987 GaAs IC Symp.*, IEEE, 1987, pp. 121-124.

[7] P. R. Haugen, S. Rychnovsky, A. Husain, and L. D. Hutcheson, "Optical interconnects for high speed computing," *Opt. Eng.*, vol. 25, pp. 1076-1085, 1986.

Control of a GaAs Monolithic *Ka*-Band Phase Shifter Using a High-Speed Optical Interconnect

K. B. BHASIN, SENIOR MEMBER, IEEE, P. C. CLASPY, SENIOR MEMBER, IEEE, M. A. RICHARD, R. R. ROMANOFSKY, MEMBER, IEEE, M. BENDETT, MEMBER, IEEE, G. GUSTAFSON, AND W. WALTERS

Abstract — **The use of a high-speed optical interconnect in the control of a *Ka*-band GaAs monolithic phase shifter is described. A 16 b serial control signal was used to modulate the output of a laser transmitter, and the transmitted optical signal was detected and demultiplexed into 16 parallel electrical outputs using a high-speed hybrid GaAs optoelectronic integrated circuit (OEIC). Four of the parallel output lines were interfaced to the 4 b phase shifter, and high-speed, optically controlled switching of the phase shifter was observed at clock frequencies to 30 MHz using an interferometric technique.**

I. Introduction

GaAs monolithic microwave integrated circuits (MMIC's), which could be used as array output modules, represent a major step toward improved, lightweight directly radiating phased array antennas for space communications applications [1]. The interconnection of these MMIC modules into a beam forming network (BFN), however, still represents a rather formidable topological problem that requires innovative solutions. In an effort to overcome these problems a variety of optics-based BFN's have been proposed [2]–[4].

The GaAs MMIC's in a phased array antenna are relatively complex. They include a variable phase shifter and a variable power amplifier which permit the creation of the aperture phase and amplitude distribution that is appropriate to the desired radiated beam configuration. Some proposed architectures also include a local oscillator and a mixer at each antenna element [5], [6]. In fiber-optic-interconnected systems, optical fibers would be used to carry the control signals to the variable phase shifters and amplifiers as well as the signal to be transmitted and the local oscillator phase locking signal. Our research is addressed toward the meeting of needs for distribution of digital control signals within a phased array antenna. Because of the inherent wide bandwidth and low loss of optical fibers, all control signals for the variable phase shifter and amplifier on a MMIC module, or for several modules, could be multiplexed onto one optical channel, as shown schematically in Fig. 1, if appropriate optical receiver/demultiplexers were available. Even though the required data input rate to an individual phase shifter or amplifier control line may be modest, the overall multiplexed data rate from the controller will be high, and a wide bandwidth channel will be required. Some proof-of-concept demonstrations of the use of optical interconnects in the context of a phased array, using discrete components, have been reported [7]. In this paper we present the results of the application of a high-speed GaAs MESFET integrated circuit optical receiver/demultiplexer to the optics-based control of a monolithic *Ka*-band phase shifter.

II. The Optoelectronic Integrated Circuit

The optoelectronic integrated circuit (OEIC) that was used in the control of a MMIC phase shifter has been described in a previous publication [8]. It consists of two integrated submodules that were packaged together in a 34 lead flat pack, with a fiber pigtail for optical input, as shown in Fig. 2. The input chip is the receiver section, consisting of an interdigitated p-i-n photodetector and a three-stage amplifier, and the output chip includes a demultiplexer and output drivers [14]. The inputs to the OEIC are a 16 b serial optical data stream and an electrical bit clock and synchronization signal. The outputs are 16 parallel TTL level data streams and the input clock divided by 16. As reported in our previous paper, the demultiplexer-limited maximum clock frequency of the controller is 305 MHz. The minimum frequency is determined by the capacitive coupling between the amplifier stages, so the minimum data rate is dependent upon the pattern of the data being sent.

III. Optical Control of a *Ka*-Band Phase Shifter

To demonstrate the potential use of the OEIC in a phased array context, the demultiplexed outputs of the optical controller

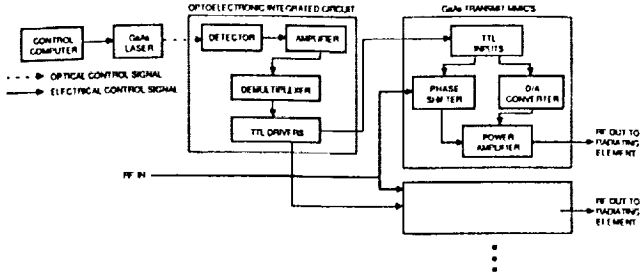

Fig. 1. Schematic diagram of an optically interconnected phased array.

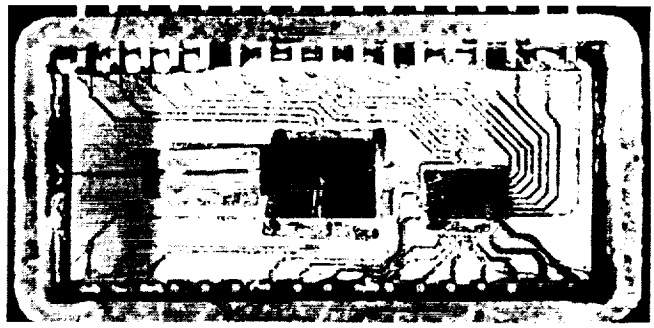

Fig. 2. The packaged optoelectronic integrated circuit.

Manuscript received October 26, 1989; revised November 23, 1989.

K. B. Bhasin and R. R. Romanofsky are with the Lewis Research Center, National Aeronautics and Space Administration, Cleveland, OH 44135.

P. C. Claspy and M. A. Richard are with the Department of Electrical Engineering, Case Western Reserve University, Cleveland, OH 44106.

M. Bendett, G. Gustafson, and W. Walters are with the Sensors and Signal Processing Laboratory, Honeywell, Inc., Bloomington, MN 55420.

IEEE Log Number 9034519.

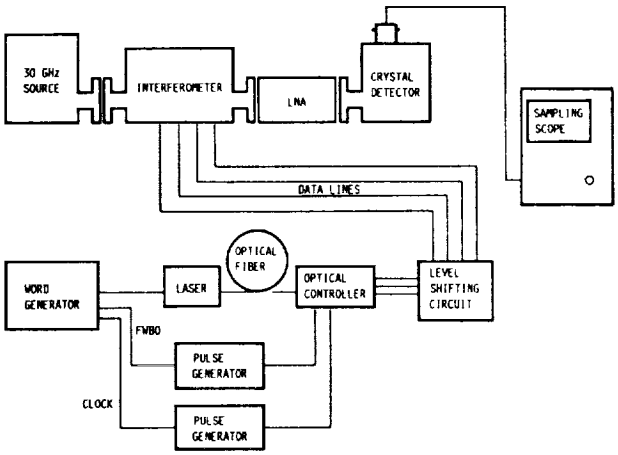

Fig. 3. Block diagram of the microwave interferometer.

were interfaced to the inputs of a 30 GHz 4 b monolithic phase shifter that was produced by Honeywell under a separate contract with NASA, and that has been described in previous publications [9]. The 4 b required by the phase shifter control three switched lines, each of which requires a bit and its complement, and one loaded line. Since the phase shifter and the optical controller were developed under separate programs and therefore were not designed with the interfacing of the two in mind, a voltage level shifting interface circuit was required. The interface circuit consisted of inverting gates to generate the complements and CMOS analog multiplexers to shift the optical controller's TTL outputs to the phase shifter's required 0 V and -6 V inputs, and was the speed-limiting element for this demonstration.

An interferometric technique was devised to allow real-time measurement of fast changes in the effect of the phase shifter on the phase of a *Ka*-band signal. As shown schematically in Fig. 3, the phase shifter was inserted in one leg of an interferometer. A 30 GHz microwave signal of -8 dBm was applied to the input of a 10 dB power splitter. The higher power output from the splitter was fed through the phase shifter input into the output port of a 3 dB power splitter that was used as a power combiner, while the lower power output was input directly into the second port of the power combiner. To compensate for the 9 dB insertion loss of the phase shifter, a 30 GHz low-noise amplifier [10] was connected to the output of the test setup. A crystal detector attached to the output of the combiner indicated the level of output power. To set the initial condition of the system, the propagation time through the phase shifting leg of the interferometer was adjusted, by changing the bit settings on the phase shifter, until the detector indicated maximum power output, corresponding to constructive interference between the two recombined signals. Beginning with this configuration, switching the 180° bit of the phase shifter caused the power output to fall to zero, indicating complete destructive interference, while switching the 45° and 90° bits caused intermediate levels of destructive interference.

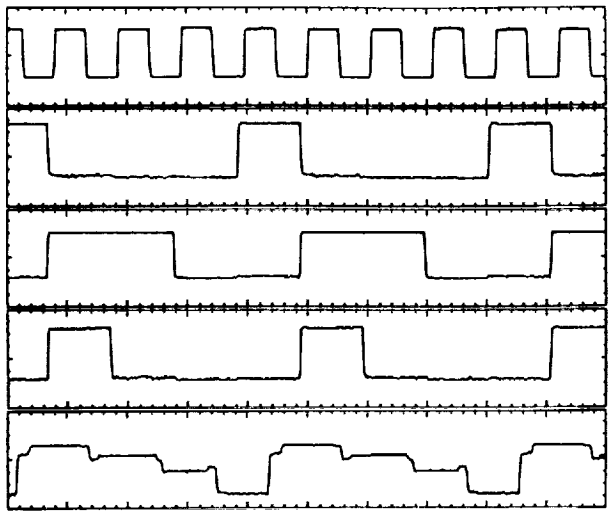

Fig. 4. Controller and interferometer outputs when three phase shifter bits are controlled at a high-speed clock frequency of 30 MHz. The top trace is the clock divided by 16, the center three traces are the OEIC output data, and the lower trace is the interferometer output. The ordinate scale is 200 mV/div for the top four traces and 1 mV/div for the lower trace. The abcissa scale for all traces is 500 ns/div.

Three demultiplexed outputs from the OEIC were used, along with their complements, to control the 180°, 90°, and 45° switched lines of the phase shifter. Since the data input to the controller are through the laser, fiber, and detector, while the clock and synch (FWB0) are input directly to the demultiplexer as electrical signals, problems with timing can cause uncertainties in the output waveforms. To eliminate this problem, a delayable triggered pulse generator was used to adjust the delay of the two electrical signals and synchronize them with the optical input. For this experiment the average input optical power was 250 μW and the high-speed (input) clock was kept at 30 MHz in order to stay within the limitations of the level-shifting circuitry. Different input data patterns were used to control each phase shifter input bit so that combinations of delay lines could be inserted into the path and their effects observed. An example of the success in combining the OEIC with the phase shifter to control the phase of a 30 GHz signal is given in Fig. 4, where one set of input data patterns, along with the resulting interferometer outputs and the output clock, is shown. It should be noted that there are constant delays between the clock and data and between the data and the interferometer response. The former are the result of different propagation times for data and clock in the OEIC, while the latter are the result of delays in the CMOS level-shifting circuit, as are the irregularities in the interferometer signal.

IV. Conclusions

In this paper we have described the first experiment in which a *Ka*-band monolithic phase shifter is controlled through a high-speed fiber-optic interconnect. The interface between the serially encoded optical control signal and the electrically controlled phase shifter uses a new optoelectronic integrated circuit that converts the serial optical input into 16 parallel optical outputs. Switching of the 4 b phase shifter at instrumentation-limited input clock frequencies to 130 MHz was observed in real time using a novel interferometric technique. The optical control of a phase shifter in this manner represents a significant step toward the development of an optically controlled phased array antenna.

REFERENCES

[1] K. B. Bhasin and D. J. Connolly, "Advances in monolithic microwave integrated circuit technology for space communications systems," *IEEE Trans. Microwave Theory Tech.*, vol. MTT-34, pp. 994–1001, 1986.

[2] A. M. Levine, "Fiber optics for radar and data systems," *SPIE Proc.*, vol. 150, pp. 992–998, 1978.

[3] J. Austin and J. R. Forrest, "Design concepts for active phased-array modules," *Proc. Inst. Elec. Eng.*, pt. F, vol. 127, pp. 290–300, 1980.

[4] K. B. Bhasin, G. Anzic, R. R. Kunath, and D. J. Connolly, "Optical techniques to feed and control GaAs MMIC modules for phased array antenna applications," in *Proc. 11th Ann. AIAA Commun. Satellite Syst. Conf.* (New York), 1986, pp. 506–514.

[5] P. R. Herczfeld, A. S. Daryoush, A. Rosen, A. K. Sharma, and V. M. Contarino, "Indirect subharmonic optical injection locking of a millimeter-wave IMPATT oscillator," *IEEE Trans. Microwave Theory Tech.*, vol. MTT-34, pp. 1371–1376, 1986.

[6] I. D. Blanchflower and A. J. Seeds, "Optical control of frequency and phase of GaAs MESFET oscillator," *Electron. Lett.*, vol. 25, pp. 359–360, 1989.

[7] A. Paolella and P. R. Herczfeld, "Optical gain control of a GaAs MMIC distributed amplifier," *Microwave Opt. Technol. Lett.*, vol. 1, pp. 13–16, 1988.

[8] P. C. Claspy *et al.*, "A high speed GaAs MESFET optical controller," *IEEE Photon. Technol. Lett.*, vol. 1, pp. 389–391, 1989.

[9] V. Sokolov, J. J. Geddes, A. Contolatis, P. E. Bauhahn, and C. Chao, "A *Ka*-band GaAs monolithic phase shifter," *IEEE Trans. Microwave Theory Tech.*, vol. MTT-31, no. 12, pp. 1077–1088, 1983.

[10] V. Sokolov, J. Geddes, and P. Bauhahn, "GaAs monolithic receivers for 30/20 GHz satellite communications," presented at IEEE Eascon 86, Washington, DC, Sept. 1986.

II. COPLANAR WAVEGUIDE DEVELOPMENT

COAX-TO-CHANNELISED COPLANAR WAVEGUIDE IN-PHASE N-WAY, RADIAL POWER DIVIDER

Indexing terms: Waveguides, Transmission lines

A novel nonplanar, wideband power divider which makes use of a coax-to-CCPW transition is demonstrated. The transition utilises a coaxial transformer whose outer conductor is slotted along the length for RF power division and also for exciting the CCPWs in equal amplitude and phase at the radial junction. The measured (8–16 GHz) excess insertion loss at the output ports is 0·5 dB for a four-way divider. The amplitude and phase balance are within 0·5 dB and 5°, respectively. The power divider should find applications in the feed network of phased arrays.

Introduction: Channelised coplanar waveguides (CCPW)[1] are a new variant of the conventional coplanar waveguide (CPW).[2] The CCPW has all the advantages of conventional CPW and also has lower radiation loss. In the conventional CPW, the loss of power by radiation to free space occurs from the printed circuit and the substrate. By embedding the substrate in a channel, the radiation loss from the substrate is suppressed. A practical CPW circuit such as a power divider also has several bend and step type discontinuities which can excite higher order CPW modes and surface wave modes. These modes can propagate if the cross-sectional geometry is favourable and may reduce the isolation between adjacent circuits besides giving rise to insertion loss spikes. The metal channel of the CCPW also acts as an effective barrier against interference through the substrate.

We demonstrate a novel power divider which uses a nonplanar coax-to-CCPW transition. The new design has advantages over the conventional planar, in-line Wilkinson type,[3] power divider. It eliminates the need for right angle bends which require dielectric overlays for phase velocity correction.[4] It eliminates the unreliable and nonreproducible bondwires which are used to tie the two ground planes to the same potential. It is also capable of simultaneously exciting multiple odd or even number CCPWs in equal amplitude and phase.

Radial junction: A coax-to-CCPW in-phase, four-way radial power divider is shown in Fig. 1. The junction is formed by the intersection of four CCPW lines. Power is coupled to this junction from a coaxial cable whose outer conductor is slotted along the z direction to form four coupled transmission lines. The centre pin of the coaxial line meets the intersecting CCPW centre conductors and the four coupled outer conductors meet the CCPW ground planes. The electric current at the open end of the coax is divided into the four CCPW lines illustrated in Fig. 2. This arrangement has the advantage of holding the ground planes at the same potential and exciting the four CCPW lines in equal amplitude and phase without the need for bond wires. Each of the four CCPW lines, Fig. 3, has an impedance of 135 Ω at the junction. The net impedance seen by the coaxial line is approximately 34 Ω. A quarter wave coaxial dielectric transformer ($\varepsilon_r = 4$) was used at the junction to match the 50 Ω coaxial line to the 34 Ω CCPW junction impedance. The characteristic impedance of the quarter wave coaxial dielectric transformer section as determined from Reference 5 is approximately 40 Ω. The characteristic impedance ($Z_0 = V^2/P$) of the CCPW line at the output ports was set to 70 Ω to provide a good match to the 50 Ω coaxial connector.[4]

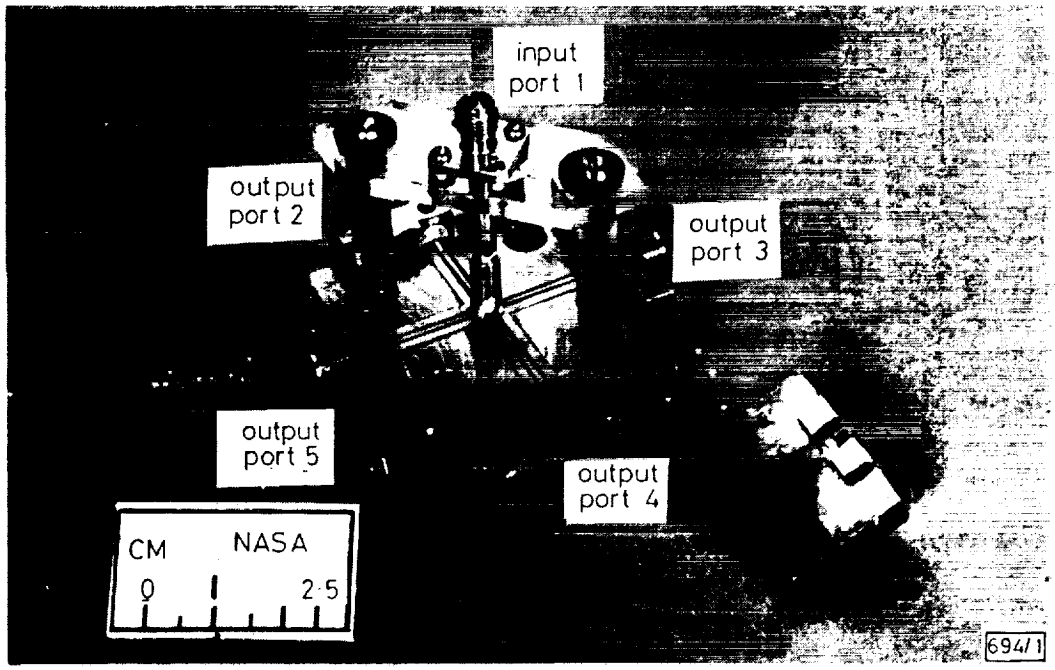

Fig. 1 *Coax to CCPW in-phase, four-way, radial power divider*

Each of the three pairs of slits in the ground plane of the CCPW (Fig. 3) acts as a tuning stub to improve the CCPW to coaxial connector impedance match over the measured frequency range.

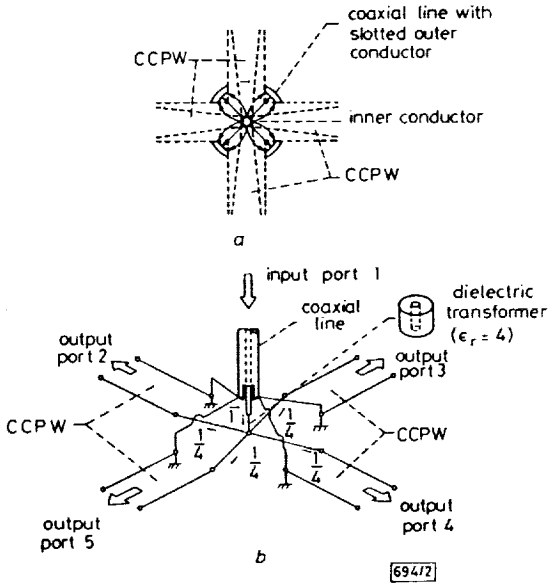

Fig. 2 *Radial power divider characteristics*
a Electric field distribution at end of slotted coaxial line
b Equivalent circuit of junction

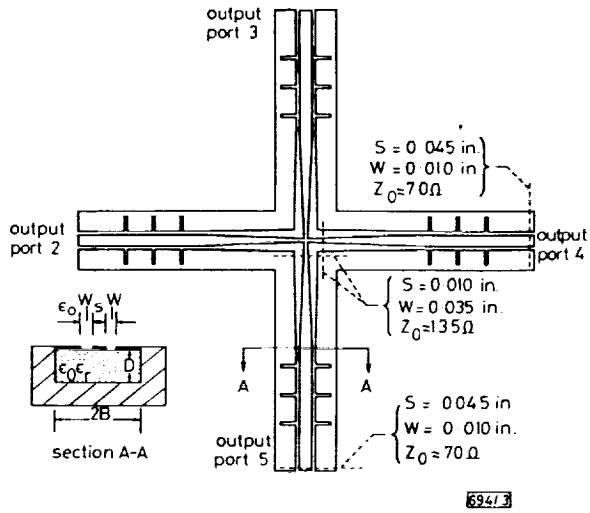

Fig. 3 *Coax to CCPW in-phase, four-way, radial power divider details*

Experimental results: The measured amplitude of the power coupled to one of the output ports over an octave bandwidth (8–16 GHz) is shown in Fig. 4 and is typical of the junction. The −6·5 dB measured amplitude at the output ports is in good agreement with the −6·0 dB expected for a 1 : 4 ideal lossless junction. The additional loss of 0·5 dB includes the CCPW to coaxial transformer and two coaxial connector losses. Also superimposed on Fig. 4 is the return loss of the input port which is greater than 10 dB. The amplitude and phase balance of this circuit are within 0·5 dB and 5°, respectively. These values are a function of the mechanical structure itself since all the ports are identical. The isolation between the ports is approximately 10 dB.

Conclusion: The design, implementation and characterisation of a *N*-way, in-phase, radial power divider which employs a novel coax-to-CCPW transition has been demonstrated. This is the first successful implementation of a copolanar waveguide power divider. The low loss and wide bandwidth characteristics of the divider would facilitate the implementation of

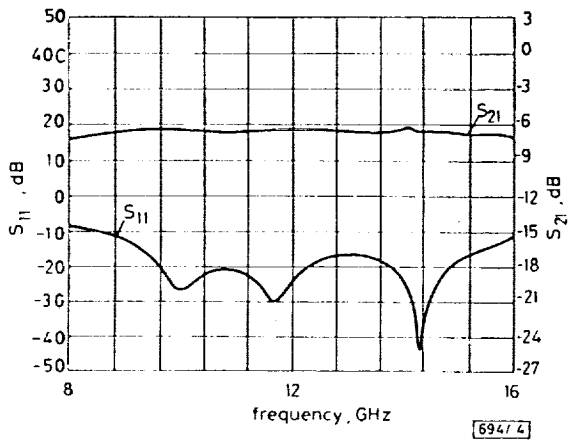

Fig. 4 *Measured coupled power and return loss*

a CCPW feed network in a phased array antenna system. The divider is observed to possess excellent amplitude and phase balance.

R. N. SIMONS
G. E. PONCHAK

NASA Lewis Research Center, 21000 Brookpark Road
Cleveland, OH 44135, USA

1st February 1990

References

1 SIMONS, R. N., PONCHAK, G. E., MARTZAKLIS, K. S., and ROMANOFSKY, R. R.: 'Channelized coplanar waveguide: Discontinuities, junction and propagation characteristics'. Digest IEEE MTT-S Int. Microwave Symposium, 1989, Vol. III, pp. 915–918
2 WEN, C. P.: 'Coplanar waveguide: A surface strip transmission line suitable for nonreciprocal gyromagnetic device applications', *IEEE Trans.*, 1969, **MTT-17**, pp. 1087–1090
3 EDWARDS, T. C.: 'Foundations for microstrip circuit design' (John Wiley, New York, 1981), p. 244
4 SIMONS, R. N., and PONCHAK, G. E.: 'Modeling of some coplanar waveguide discontinuities', *IEEE Trans.*, 1988, **MTT-36**, pp. 1796–1803
5 DUNCAN, J. W., and MINERVA, V. P.: '100 : 1 bandwidth balum transformer', *Proc. IRE*, 1960, **48**, pp. 156–164

NASA Technical Memorandum 102477

A New Rectangular Waveguide to Coplanar Waveguide Transition

George E. Ponchak
Lewis Research Center
Cleveland, Ohio

and

Rainee N. Simons
Case Western Reserve University
Cleveland, Ohio

Prepared for the
1990 IEEE MTT-S International
Microwave Symposium
Dallas, Texas, May 8-10, 1990

NASA

A NEW RECTANGULAR WAVEGUIDE TO COPLANAR WAVEGUIDE TRANSITION

George E. Ponchak
NASA Lewis Research Center
Cleveland, Ohio 44135

Rainee N. Simons*
Case Western Reserve University
Cleveland, Ohio 44106

ABSTRACT

A new rectangular waveguide to coplanar waveguide transition is described. The transition uses a ridge in one of the broad walls of the waveguide and a nonradiating slot in the opposite wall to split and rotate the electromagnetic fields of the rectangular waveguide TE10 mode into the CPW fields.

INTRODUCTION

Coplanar waveguide (CPW) is an attractive transmission line for microwave integrated circuits since the ground planes are on the same side of the substrate as the conducting strip (1). This permits the integration of both series as well as shunt circuit elements without the need for back side processing and via holes. A second important advantage of CPW which has recently emerged is in the design of microwave probes for on-wafer characterization of field effect transistors and for fast, inexpensive evaluation of microwave integrated circuits (2).

In order to fully utilize these advantages, transitions between CPW and other microwave transmission media are required. A coaxial connector to CPW transition in which the center pin and the ground connection of the coaxial connector make contact with the CPW center strip and ground planes respectively has been demonstrated at 18 GHz (3). By reducing the diameter of the coaxial connector, the upper frequency of these transitions has been extended to 50 GHz. Further reduction of the coaxial connector dimensions to increase the frequency of operation may be limited by the fragility of the connectors. Also, millimeter wave sources use rectangular waveguide at the output ports. Therefore, there is a need to develop rectangular waveguide to CPW transitions for applications at V-Band (50 to 75 GHz) and W-Band (75 to 110 GHz).

A waveguide to CPW transition has been reported by Bellantoni, et al. (4). The transition uses a finline taper to concentrate the electric fields and a wire bond to split the electric currents between the two ground planes. The difficulty with the design is positioning the wire bond such that the two slots are excited in equal magnitude and phase. A further difficulty with finline transitions is the occurrence of resonances created by the transition (4,5). This paper presents the design and characteristics of a new rectangular waveguide to CPW transition which uses a ridge in one of the broad walls of the waveguide and a nonradiating slot in the opposite wall. This arrangement transforms the rectangular waveguide TE10 mode into the CPW mode with equal magnitude and phase excitation of the slots. The transition is capable of providing full waveguide bandwidth.

TRANSITION DESIGN

Figure 1 is a schematic of the transition. The printed circuit board shown in Fig. 1(a) forms the bottom wall of the rectangular waveguide. On this printed circuit board, a nonradiating slot is etched which gradually tapers to a width equal to $S + 2W$, where S and W are the width of the CPW center strip and slot, respectively. The cosine tapered ridge shown in Fig. 1(b) protrudes from the top wall of the waveguide and extends down to the printed circuit board metalization at the end of the taper. The ridge width is matched to the width of the center strip conductor, S, of the CPW. The electric field distribution at cross sectional planes along the transition is illustrated in Fig. 2. One can easily visualize that the ridge and the nonradiating slot gradually split the electromagnetic fields of the TE10 waveguide mode and rotate them through 90° to match the fields of the CPW.

TEST RESULTS FOR K BAND TRANSITION

A transition has been designed for K band. The printed circuit portion of the transition has been fabricated on a 0.125 in. thick 5880 RT/Duroid substrate with single sided copper cladding. The ridged waveguide portion of the transition is copper. The cosine taper is 1.5 in. long or approximately 1.5 λ_g at the center frequency. The S and W of the CPW are 0.032 and 0.008 in. respectively yielding a 75 Ω transmission line. For testing, the two transitions were connected back to back through a 0.8 in. length of CPW transmission line. The characteristics for this transition are shown in Fig. 3. The return loss is greater than 11 dB

*NASA Resident Research Associate at Lewis Research Center (work funded by NASA Grant NAG3-816).

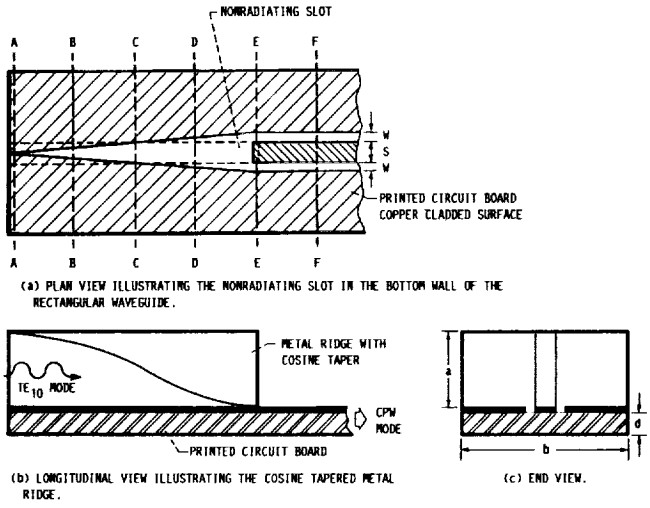

(a) PLAN VIEW ILLUSTRATING THE NONRADIATING SLOT IN THE BOTTOM WALL OF THE RECTANGULAR WAVEGUIDE.

(b) LONGITUDINAL VIEW ILLUSTRATING THE COSINE TAPERED METAL RIDGE.

(c) END VIEW.

FIGURE 1. - SCHEMATIC OF THE TRANSITION.

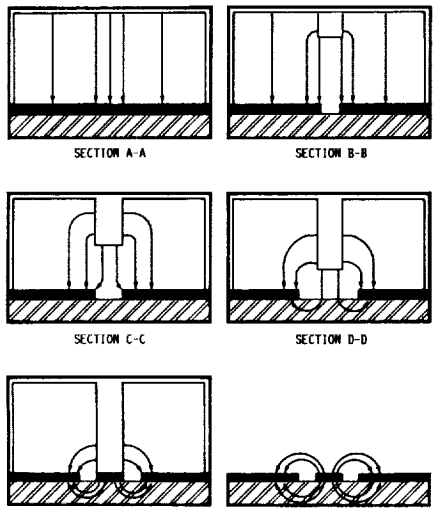

FIGURE 2. - ELECTRIC FIELD DISTRIBUTION AT VARIOUS CROSS-SECTIONS ALONG THE TRANSITION.

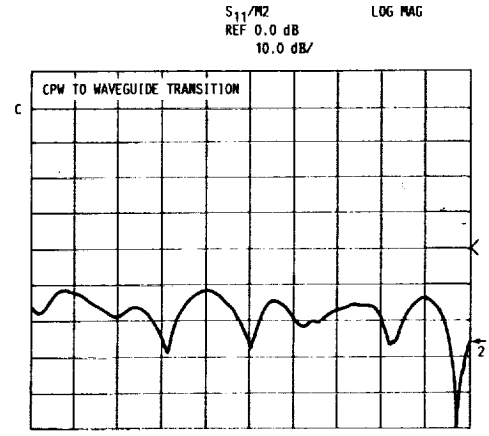

(a) INPUT RETURN LOSS AS MEASURED AT THE WAVEGUIDE PORT.

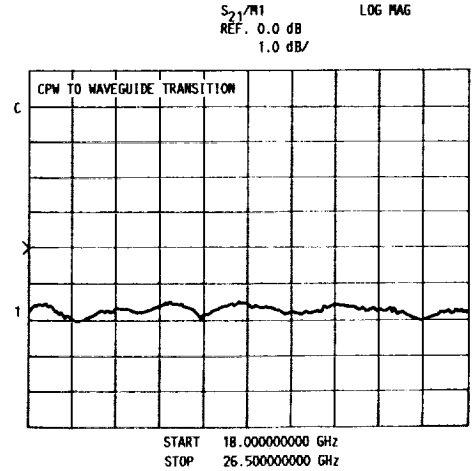

(b) MEASURED INSERTION LOSS OF TWO TRANSITIONS CONNECTED BACK TO BACK.

FIGURE 3.

across the band. The average insertion loss for the back-to-back transitions is 1.75 dB with 0.25 dB ripple.

CONCLUSIONS

A new rectangular waveguide to CPW transition has been developed with full waveguide bandwidth. This transition should permit the use of CPW based circuits in the millimeter wave frequency range and the development of microwave probes above 50 GHz for fast and inexpensive testing of the millimeter wave circuits.

REFERENCES

(1) C.P. Wen, "Coplanar Waveguide: A Surface Strip Transmission Line Suitable for Nonreciprocal Gyromagnetic Device Applications," IEEE Trans. Microwave Theory Tech., vol. MTT-17, no. 12, pp. 1087-1090, 1969.

(2) K.E. Jones, E.W. Strid, and K.R. Gleason, "mm-Wave Wafer Probes Span 0 to 50 GHz," Microwave J., vol. 30, no. 4, pp. 177-183, 1987.

(3) M. Houdart and C. Aury, "Various Excitation of Coplanar Waveguide," in IEEE MTT-S International Microwave Symposium Digest, 1979, pp. 116-118.

(4) J.V. Bellantoni, R.C. Compton, and H.M. Levy, "A New W-Band Coplanar Waveguide Text Fixture," in IEEE MTT-S International Microwave Symposium Digest, 1989, pp. 1203-1204.

(5) G. Begemann, "An X-Band Balanced Fin-Line Mixer," IEEE Trans. Microwave Theory Tech., vol. MTT-26, no. 12, pp. 1007-1011, 1978.

NASA Technical Memorandum 102289

Channelized Coplanar Waveguide Pin-Diode Switches

G.E. Ponchak
Lewis Research Center
Cleveland, Ohio

and

R.N. Simons
Case Western Reserve University
Cleveland, Ohio

November 1989

NASA

CHANNELIZED COPLANAR WAVEGUIDE PIN-DIODE SWITCHES

G.E. Ponchak
National Aeronautics and Space Administration
Lewis Research Center
Cleveland, Ohio 44135

and

R.N. Simons*
Case Western Reserve University
Cleveland, Ohio 44106

SUMMARY

Three different types of p-i-n diode, reflective CPW switches are presented. The first two switches are the series and the shunt mounted diode switches. Each has achieved greater than 15 dB of isolation over a broad bandwidth. The third switch is a narrow band, high isolation switched filter which has achieved 19 dB of isolation. Equivalent circuits and measured performance for each switch is presented.

INTRODUCTION

Coplanar waveguide, CPW, on a dielectric substrate consists of a center strip conductor with semi-infinite ground planes on either side (ref. 1). Channelized coplanar waveguide, CCPW, consists of CPW transmission line placed in a metal enclosure (ref. 2). Because the ground planes and the center conductor are on the same side of the substrate, shunt as well as series mounting of circuit components can be done without the need for wraparounds or via-holes. The improvements in circuit yield and the reduction in inductance for ground paths over microstrip based circuits should permit microwave integrated circuits, MIC's, to be fabricated at higher frequencies and less expensively. However, the extent of applications of CPW circuits is limited due to the unavailability of circuit elements and models which can be incorporated into CAD programs.

Microwave switches are a basic circuit element for phase shifters and radiometers. A CPW switchable attenuating medium propagation, SAMP, switch has been demonstrated by Fleming et al. (ref. 3). This device is useful for GaAs MMIC circuits but it is not easily incorporated into MIC's on passive substrates such as alumina or duroid. P-i-n diodes are good microwave switches since the impedance of the diode can be changed from a very high value to nearly zero in a short time (refs. 4 and 5).

This paper presents for the first time CPW p-i-n diode, reflective switches. Three basic switches are presented. The first is a shunt mounted diode switch. This switch is similar to fin line shunt mounted diode switches (ref. 4). The second switch is a series mounted diode across a gap in the center strip conductor. The last switch is a novel design which converts a CPW interdigital coupler with bandpass filter characteristics into a spurline, bandstop filter.

---

*NASA Resident Research Associate at Lewis Research Center.

The three switches have been fabricated on CCPW transmission lines. All of the circuits have been fabricated on RT/Duroid 5880 substrates with Metelics Corporation beam lead diodes, MBP-1030-B11. Figure 1 is the equivalent circuit

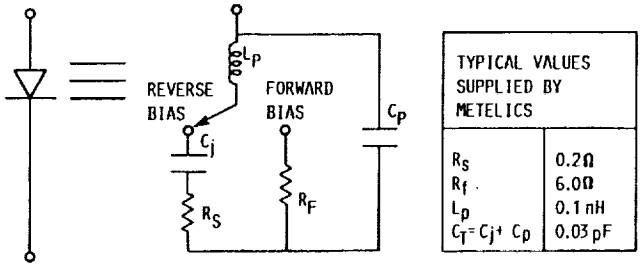

FIGURE 1. - P-I-N DIODE EQUIVALENT CIRCUIT AND TYPICAL CIRCUIT ELEMENT VALUES.

of the diode with the circuit element values supplied by Metelics. Although no tuning to resonate off the diode parasitics was done, the CPW slots were made equal to the length of the packaged diode to minimize the package inductance, Lp. Testing of the switches has been done on an HP 8510 automatic network analyzer with bias tees to supply the dc bias to the diodes. The test fixture is comprised of a 2 in. length of CCPW with a 0.045 in. center strip and 0.010 in. slot. Connection to 3.5 mm coax cables is made through a pair of coaxial connectors. Tuning notches in the ground plane have been used to improve the coax-to-CCPW characteristics over selected frequency bands. The test fixture has a total insertion loss of 0.5 dB and a return loss greater than 15 dB for the frequencies reported in this paper.

P-I-N DIODE SHUNT SWITCH

In a shunt mounted configuration, a pair of diodes are placed in parallel across the slots of the CCPW transmission line (fig. 2). When the diodes are

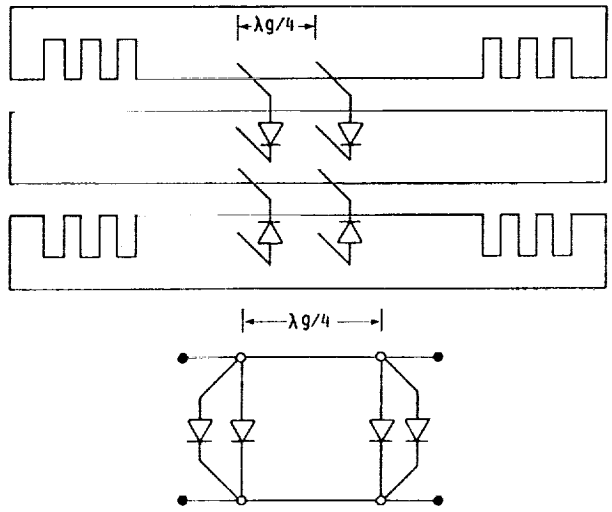

FIGURE 2. - SCHEMATIC AND EQUIVALENT CIRCUIT OF CPW P-I-N DIODE SHUNT SWITCH.

forward biased, each slot is loaded by the forward bias impedance of the diode; at 10 GHz, the impedance across the slot is approximated by $Rf + j\omega Lp \approx 8.7\ \Omega \ll Zo$. The shunt impedance for CPW, with two parallel slots, is therefore 4.35 Ω. This low impedance loading the slot reflects the propagating wave. When the diode is reverse biased, each slot is loaded by an impedance approximated by $1/(j\omega Ct) \approx 530\ \Omega \gg Zo$. This is an equivalent shunt impedance of 265 Ω for CPW. This load results in a small attenuation. Using expressions by Watson (ref. 6) modified for two parallel shunt elements, an isolation of 16 dB and an insertion loss of 0.04 dB is predicted.

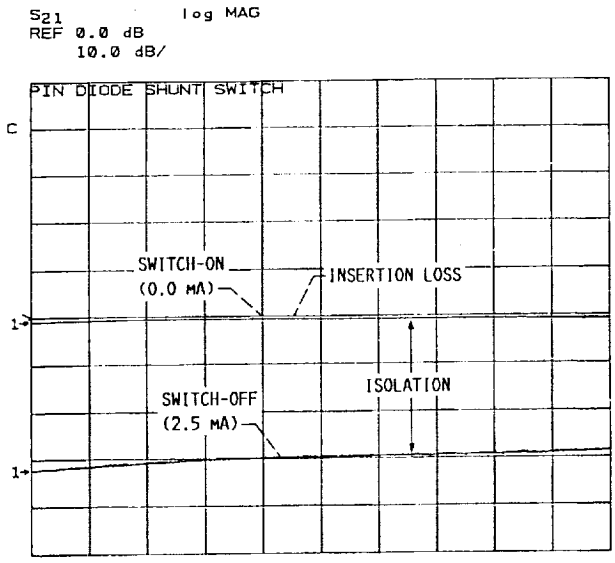

(a) MEASURED INSERTION LOSS AND ISOLATION.

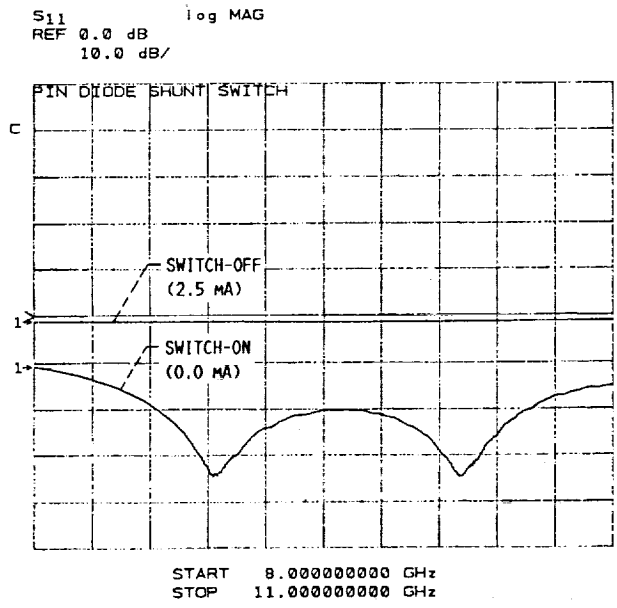

(b) MEASURED RETURN LOSS.

FIGURE 3. - CPW P-I-N DIODE SHUNT SWITCH WITH TWO PAIRS OF DIODES.

An insertion loss less than 1 dB and an isolation of 15 dB has been measured over the frequency band of 8 to 11 GHz. The return loss was less than 10 dB across the band. By incorporating more than one pair of diodes across the slots with a $\lambda g/4$ separation, higher isolation can be achieved. Typically, two pairs of diodes have resulted in an isolation of 30 dB over the 8 to 11 GHz frequency band with little increase in insertion loss, this is shown in figure 3(a). Figure 3(b) shows the return loss which is less than 10 dB across the band.

P-I-N DIODE SERIES SWITCH

In the series mounted diode configuration, a diode is mounted across an 0.008 in. gap in the center strip conductor of the CCPW line (fig. 4). The

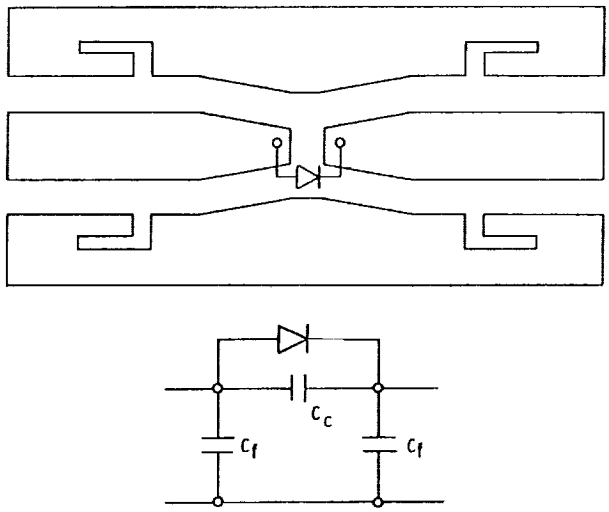

FIGURE 4. - SCHEMATIC AND EQUIVLENT CIRCUIT OF CPW P-I-N DIODE SERIES SWITCH.

center strip has been tapered to the width of the beam lead diode to provide a better match to the width of the diode package. The gap appears as an equivalent capacitive π network (ref. 7). When the diode is forward biased, the coupling capacitance is shorted by the low diode impedance and the wave is transmitted. Reverse biasing the diode results in an impedance across the gap which can be approximated by $1/[j\omega(Ct + Cc)] >> Zo$ at 10 GHz. Therefore, the propagating signal is reflected as if from an open circuit. A measured insertion loss of 1 dB and an isolation of 15 dB has been obtained from 0.045 to 8 GHz (fig. 5(a)). The return loss over this band is less than 10 dB (fig. 5(b)). The gap impedance is not large enough at higher frequencies to provide good isolation. The gap can be lengthened to decrease Cc but the increase in inductance from the longer diode leads will ultimately limit the gap separation. Resonating out these reactances is required for higher frequency operation (ref. 6).

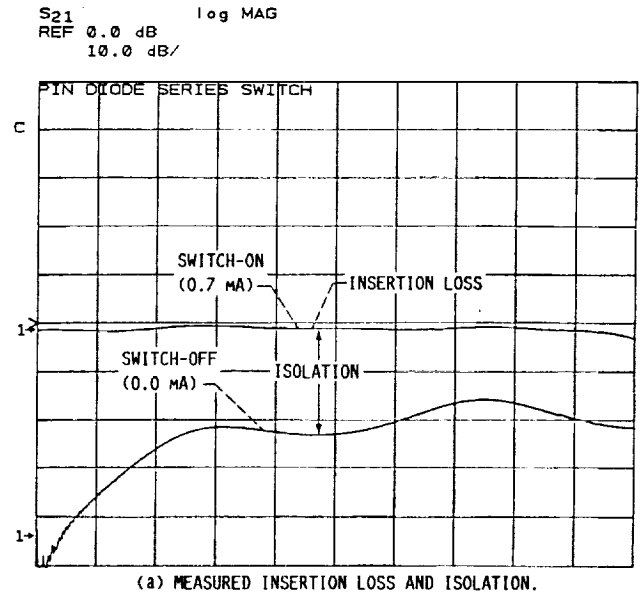

(a) MEASURED INSERTION LOSS AND ISOLATION.

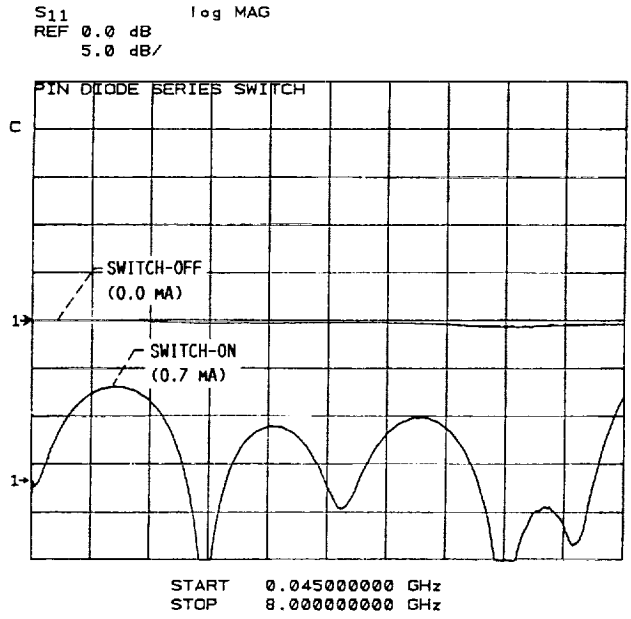

(b) MEASURED RETURN LOSS.

FIGURE 5. - CPW P-I-N DIODE SERIES SWITCH.

P-I-N DIODE SPDT SWITCH

To realize a SPDT switch, a CCPW Tee-junction with gaps in the center strip conductor at the junction was formed (fig. 6). Diodes were mounted across the gaps in parallel. As shown in figure 7, the measured insertion loss is 1 dB and the isolation is greater than 15 dB over the octave bandwidth of 2.25 to 5.5 GHz. The return loss was less than 10 dB.

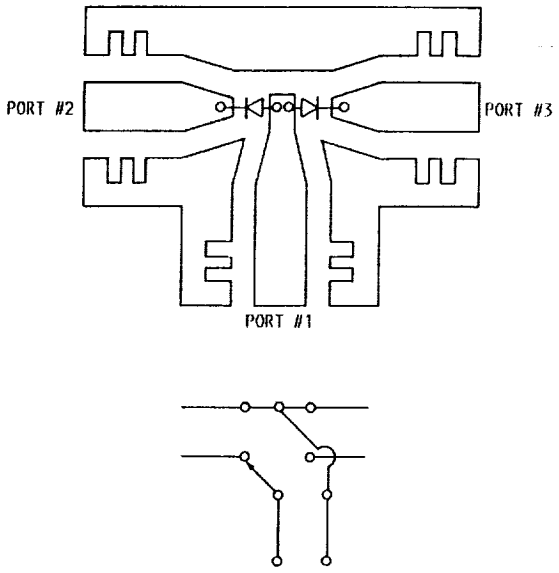

FIGURE 6. - SCHEMATIC AND EQUIVALENT CIRCUIT OF SERIES MOUNTED P-I-N DIODE CPW SPDT SWITCH.

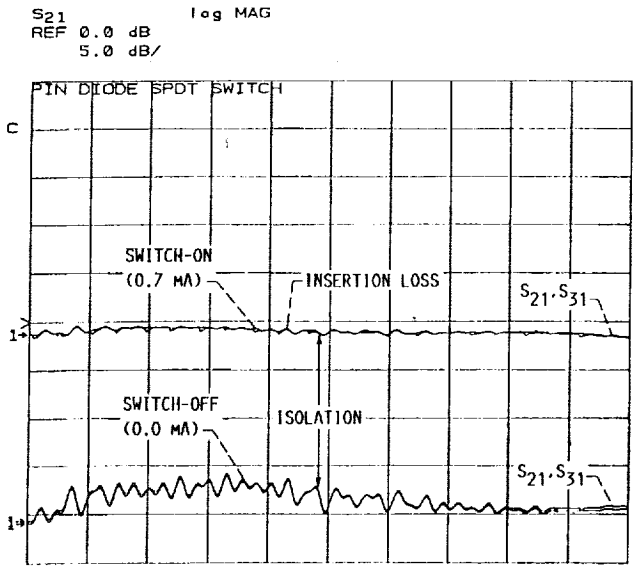

FIGURE 7. - MEASURED INSERTION LOSS AND ISOLATION OF SERIES MOUNTED PIN DIODE CPW SPDT SWITCH.

P-I-N DIODE SWITCHED-SERIES-STUB SWITCH

A diode is mounted across the open end of a $\lambda g/4$ stub which is in series with the center strip conductor of the CCPW as shown in figure 8. When the diode is unbiased, the stub is terminated in an effective open circuit and therefore appears as a series short circuit. Hence, the wave propagates with negligible attenuation. This is the on-state of the switch. When the diode is forward biased, the stub is terminated in an effective short circuit which

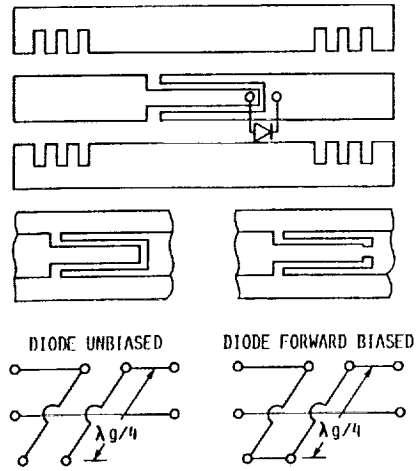

FIGURE 8. - SCHEMATIC AND EQUIVALENT CIRCUIT OF CPW P-I-N DIODE SWITCHED-SERIES-STUB SWITCH.

therefore appears as a series open circuit. The wave is therefore reflected; this is the off-state of the switch. The diode reactances result in an effective lengthening of the stub and can easily be compensated for. A measured insertion loss of 1.0 dB and an isolation of 19 dB has been obtained at 9 GHz (fig. 9(a)). Figure 9(b) shows the return loss.

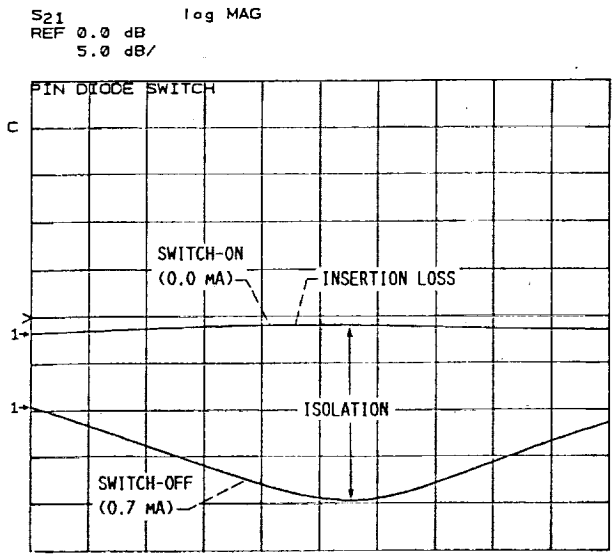

(a) MEASURED INSERTION LOSS AND ISOLATION.

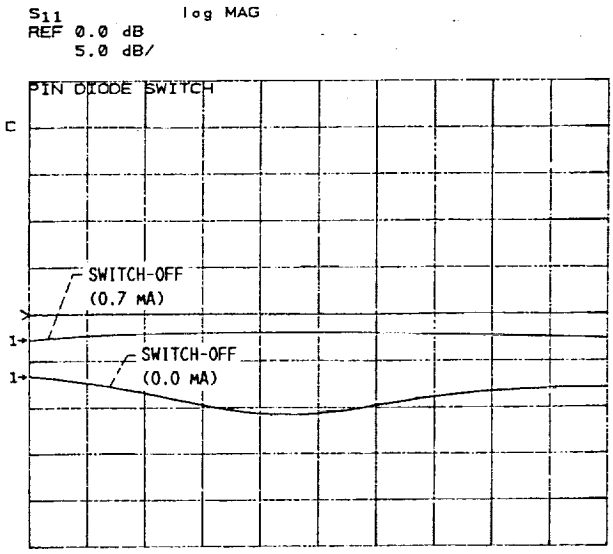

(b) MEASURED RETURN LOSS.

FIGURE 9. - CPW P-I-N DIODE SWITCHED-SERIES-STUB SWITCH.

CONCLUSIONS

P-I-N diode reflective switches are easily realizable on CCPW transmission line and therefore CPW transmission line. Each of the three type of switches presented are practical for specific applications. The performance of the

switches could be improved through typical tuning of the diode reactances once the necessary CPW circuit models become available.

REFERENCES

1. Wen, C.P., "Coplanar Waveguide, A Surface Strip Transmission Line Suitable for Nonreciprocal Gyromagnetic Device Applications," 1969, IEEE Trans. Microwave Theory Tech., vol. MTT-17, pp. 1087-1090.

2. Simons, R.N., Ponchak, G.E., Martzaklis, K.S., and Romanofsky, R.R., "Channelized Coplanar Waveguide: Discontinuities, Junctions, and Propagation Characteristics,: 1989, IEEE MTT-S International Microwave Symposium Digest, IEEE, Piscataway, NJ, pp. 915-918.

3. Fleming, P.L., Smith, T., Carlson, H.E., and Cox, W.A., "GaAs SAMP Device for Ku-Band Switching," 1979, IEEE Trans. Microwave Theory Tech., vol. MTT-27, pp. 1032-1035.

4. Bhat, B., and Koul, S.K., Analysis, Design and Applications of Fin Lines, Artech House, Norwood, MA, 1987.

5. White, J.F., Microwave Semiconductor Engineering, Van Nostrand Reinhold Co., New York, 1982.

6. Watson, H.A., Microwave Semiconductor Devices and Their Circuit Applications, McGraw-Hill Book Company, New York, 1969.

7. Simons, R.N., and Ponchak, G.E., "Modeling of Some Coplanar Waveguide Discontinuities," IEEE Trans. 1988, Microwave Theory Tech., vol. MTT-36, pp. 1796-1803.

NASA Technical Memorandum 102494

Experimental Investigations on Channelized Coplanar Waveguide

Rainee N. Simons
Case Western Reserve University
Cleveland, Ohio

George E. Ponchak
Lewis Research Center
Cleveland, Ohio

Konstantinas S. Martzaklis
University of Akron
Akron, Ohio

and

Robert R. Romanofsky
Lewis Research Center
Cleveland, Ohio

April 1990

NASA

EXPERIMENTAL INVESTIGATIONS ON CHANNELIZED COPLANAR WAVEGUIDE

Rainee N. Simons*
Case Western Reserve University
Cleveland, Ohio 44106

George E. Ponchak
National Aeronautics and Space Administration
Lewis Research Center
Cleveland, Ohio 44135

Konstantinos S. Martzaklis†
University of Akron
Akron, Ohio

Robert R. Romanofsky
National Aeronautics and Space Administration
Lewis Research Center
Cleveland, Ohio 44135

SUMMARY

This paper presents a new variant of coplanar waveguide (CPW) which has been termed channelized coplanar waveguide (CCPW). Measured propagation characteristics for CCPW such as $\varepsilon(\text{eff})$ and unloaded Q as a function of geometrical parameters and frequency are presented. The measured and modeled $\varepsilon(\text{eff})$ are also compared. Equivalent circuit model element values are presented for a CCPW open circuit and a CCPW right angle bend. A CCPW matched T-junction, matched 1:3 junction, and a novel coax-to-CCPW in-phase, N-way, radial power divider are also demonstrated.

E-5285

INTRODUCTION

Coplanar waveguide, CPW, on a dielectric substrate consists of a center strip conductor with semi-infinite ground planes on either side (ref. 1). A variant of CPW is grounded coplanar waveguide, GCPW, which has an additional ground plane on the opposite side of the substrate to facilitate heat removal and packaging (ref. 2). These transmission lines have several advantages which make them ideally suited for microwave integrated circuits. The disadvantage of CPW and GCPW is that the structure can support spurious modes besides the CPW mode since the transverse dimensions may be several wavelengths.

This paper presents a new variant of CPW. The new structure has side walls which, together with the ground plane, constitute a channel and hence is

---

*NASA Resident Research Associate at Lewis Research Center (work funded by NASA Grant NAG3-816).
†Student Co-op at NASA Lewis Research Center.

appropriately termed as channelized coplanar waveguide, CCPW. A shielding structure may also be used to further confine the electromagnetic fields. This structure is shown in figure 1. The enclosure of the CPW transmission line eliminates radiation loss and spurious surface modes created at discontinuities. Also, because the basic transmission line structure is CPW, CCPW maintains the inherent advantages over microstrip for easy shunt as well as series mounting of active and passive components.

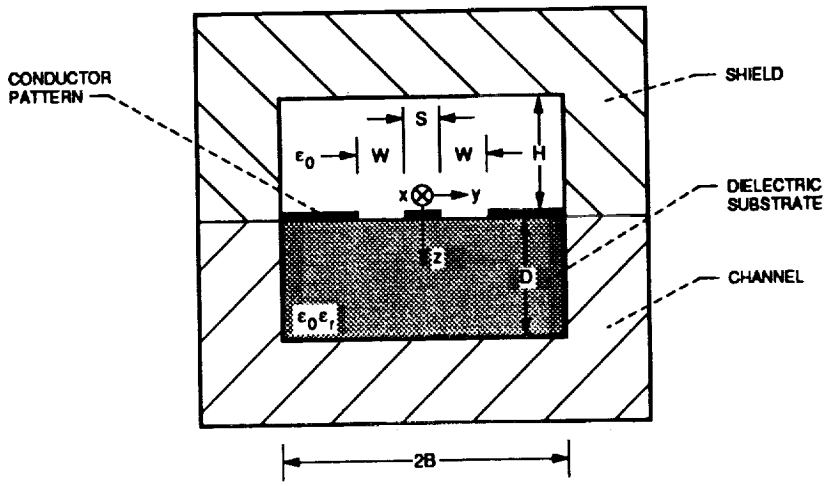

Figure 1. - Schematic of channelized coplanar waveguide (CCPW).

To maintain a single CPW mode of propagation, CCPW must be designed to suppress the dielectric filled rectangular waveguide mode, the microstrip mode, and the rectangular coax mode. The channel width, 2B, is chosen such that the rectangular waveguide mode is cutoff. The microstrip and rectangular coax modes are suppressed by the proper selection of the slot width, W, the center strip width, S, and the substrate thickness, D. The ratios W/D and S/D must be sufficiently small to suppress the microstrip mode. The ratio (S + 2W)/2B must be small to suppress the rectangular coax mode.

This paper presents lumped element circuit models for several CCPW discontinuities, together with their element values as a function of frequency. The discontinuities characterized are an open circuit and a right angle bend. The measured frequency dependence of the effective dielectric constant, $\varepsilon(eff)$, and the unloaded quality factor, Q, are also presented for CCPW lines fabricated on $\varepsilon(r) = 2.2\pm0.02$ RT/Duroid 5880, $\varepsilon(r) = 6.0\pm0.15$ RT/Duroid 6006, and $\varepsilon(r) = 10.2\pm0.25$ 3M Epsilam-10 substrates. This is followed by the design and characterization of a CCPW matched T-junction and a matched 1:3 junction. Lastly, the performance of a novel Coax-to-CCPW in-phase, N-way, radial power divider circuit is presented.

METHOD OF MEASUREMENTS

A resonator technique similar to that described by Richings (ref. 3) and Stephenson and Easter (ref. 4) was used. The $\lambda/4$ end coupled stubs could not be etched off as in the case of microstrip since this would alter the CCPW open end parameters. Hence, a four resonator set had to be fabricated for each frequency to determine the end effects.

This will contribute some errors to the results because the resonator lengths and gaps will not be identical for the two $\lambda/2$ and λ resonators. In addition, S and W varied slightly for each resonator set since the resonators were not processed in parallel. The circuit dimensions were measured to ±0.0002 in. The coupling gaps were varied to maintain a coupling coefficient, β, less than 1. For most of the resonator sets, $\beta \leq 0.3$. This is a sufficient condition to minimize the loading of the resonator for transmission lines with $Q \geq 100$ as are reported in this paper. The Q was determined through a technique given in reference 5.

EFFECTIVE DIELECTRIC CONSTANT

The ε(eff) was measured over the frequency range of 3 to 18 GHz for several unshielded CCPW lines and the results are shown in figure 2. The CCPW lines have been modeled using reference 6 and the ε(eff) is plotted for each CCPW line. ε(eff) of GCPW calculated from the closed form expression of Ghione

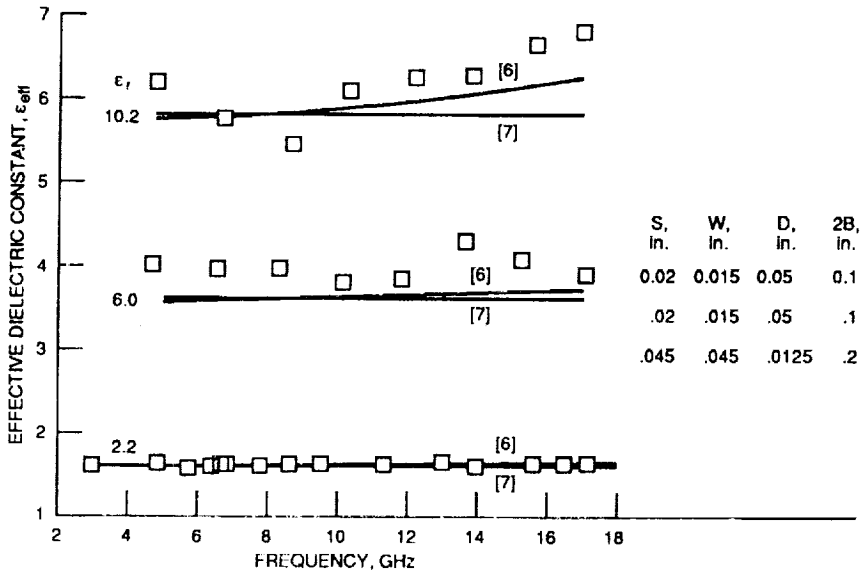

Figure 2. - Measured effective dielectric constant for unshielded CCPW as a function of frequency.

and Naldi (ref. 7) is also plotted for comparison. For the low dielectric substrate, either reference 6 or 7 could be used to predict ε(eff). For the higher dielectric substrates, both methods predicted lower ε(eff) than what was measured.

Effect of Substrate Thickness

ε(eff) was measured as a function of frequency for unshielded CCPW lines fabricated on substrates with D in the range of 0.062 to 0.250 in. The CCPW parameters S, W, 2B, and ε(r) were held fixed at 0.045 in., 0.010 in., 0.200 in., and 2.2, respectively. No variation in ε(eff) was observed for the thicker substrates, $W/D \leq 1/12.5$. ε(eff) of the thinner substrate, $W/D \approx 1/6$, was 0.7 percent higher than the other measured cases. This agrees with the calculated ε(eff) (ref. 6) and results in reference 2. The increase in ε(eff) is due to a microstrip mode.

To verify this, an RF probe was used to sample the electric fields under the center of the strip at the plane of the bottom conductor, the probe placement is shown in figure 3. Since odd mode CPW propagation has zero electric fields at this point, any fields measured by the probe must be due to a microstrip mode. The sampled field was measured for the thickest substrate and this value was used as a calibrated zero. No microstrip mode was measured as D was decreased until W/D ≈ 1/6, when an increase in the sampled field amplitude of ≈3 dB was measured.

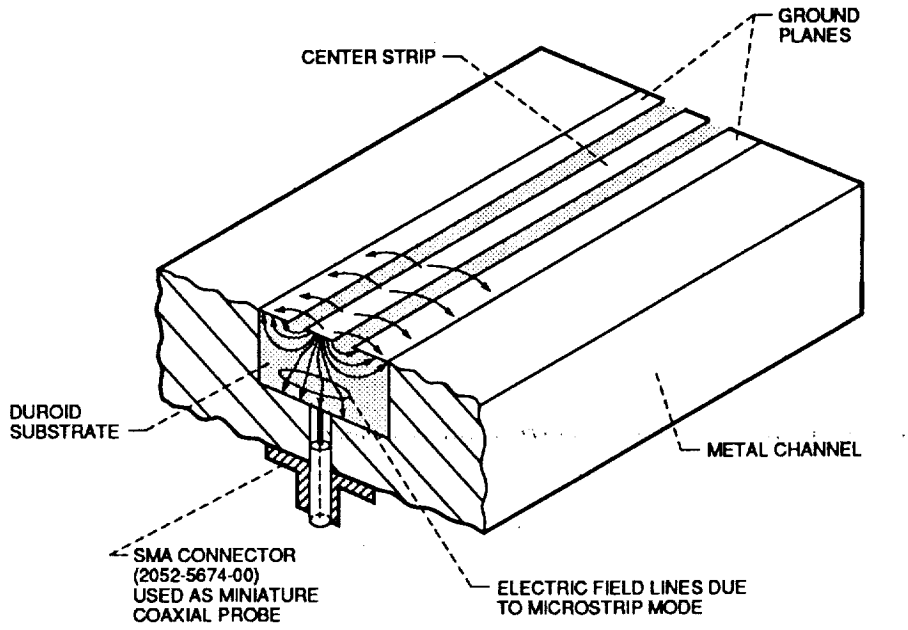

Figure 3. - Probe placement to sample the electric fields due to the microstrip mode.

Effect of Cover Height

$\varepsilon(eff)$ was measured for shielded CCPW lines with cover heights of H = D, 2D, and 4D. Resonators were tested with $\varepsilon(r)$, D, S, and W equal to 2.2, 0.125 in., 0.045 in., and 0.010 in., respectively. Resonators were also fabricated on D = 0.050 in., $\varepsilon(r)$ = 6 and 10.2 substrates. In all the cases, the change in $\varepsilon(eff)$ from the unshielded case was negligible.

LOSS MEASUREMENTS

Effect of S and Shielding

Figure 4 shows the measured Q for resonators of length λ as a function of S for a fixed frequency. The Q of the unshielded resonators decreases with increasing S while the Q of the shielded resonators increases with increasing S. Therefore, radiation loss increases as S increases.

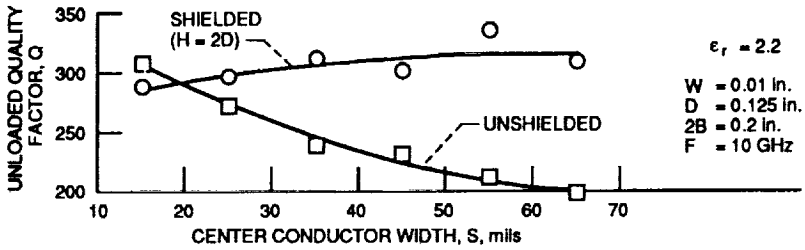

Figure 4. - Measured unloaded quality factor, Q, for CCPW as a function of the center conductor width, with and without a shielding enclosure.

Effect of Frequency and Shielding

Figure 5 shows the measured Q over the frequency range of 3 to 18 GHz for λ resonators both with and without shielding. The reduction in Q with increasing frequency for the unshielded case is due to the increase in radiation loss. With shielding, the Q is observed to increase with frequency or the attenuation per unit wavelength decreases. A change in the cover height from H = 2D to H = D showed no measurable difference in Q.

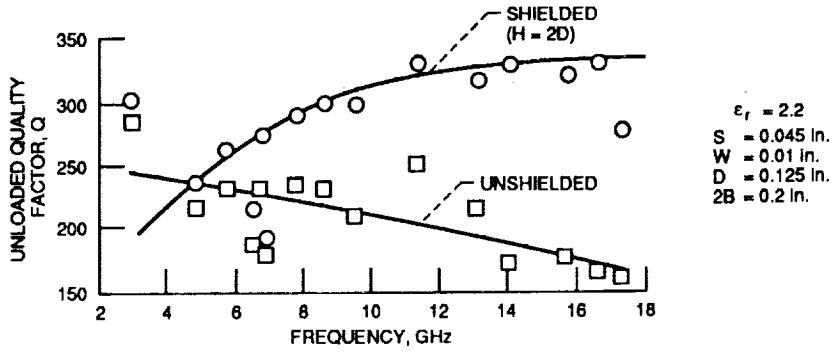

Figure 5. - Measured unloaded quality factor, Q, for CCPW as a function of frequency, with and without a shielding enclosure.

Effect of D and $\varepsilon(r)$

The effect of varying D in the range of 0.062 to 0.250 in. on Q was measured. No measurable variation in Q over the frequency range of 8 to 18 GHz was observed. CCPW resonators on the higher $\varepsilon(r)$ substrates had lower Q's. This is expected since the higher dielectric substrates concentrate more of the fields in the lossy substrate.

CHANNELIZED CPW OPEN CIRCUIT

When a CPW line is terminated in an open circuit, there is an excess fringing of the electromagnetic fields which gives rise to a capacitance, Cf (ref. 8). This capacitance is equivalent to a short length of a transmission line, Lo, terminated in a perfect open circuit as illustrated in figure 6. The open end line extension for the unshielded CCPW de-embedded from the resonator data is shown as a function of frequency in figure 7. Although strict dimensional standards were used to select resonators, a large spread in Lo was present. The exact cause of this spread, particularly at the lower frequencies, is unexplained. There was no variation in Lo for resonators with a

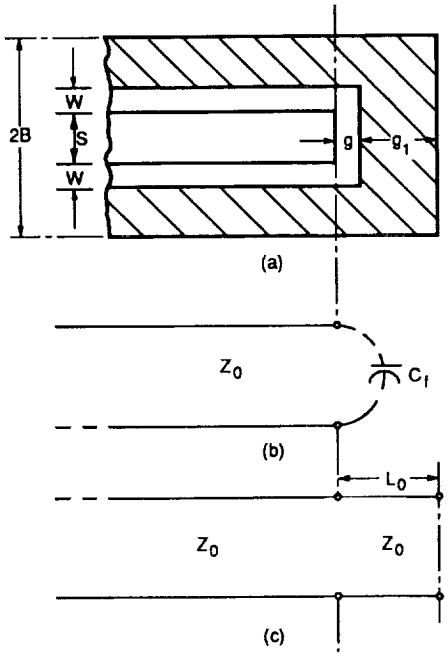

(a) Schematic of a CCPW open circuit.
(b) Equivalent end fringing capacitance, C_f.
(c) Equivalent CCPW end-effect length, L_0.
Figure 6. - CCPW open circuit.

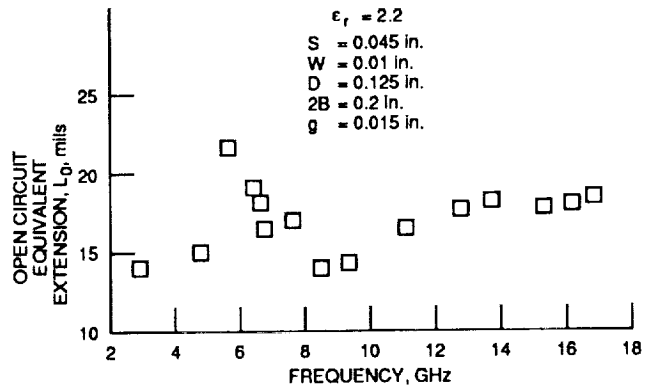

Figure 7. - Experimentally determined open circuit equivalent end-effect length as a function of frequency.

cover height of H $\geq$ 2D since its presence has negligible effect on the fringing fields. Also, Lo was found to be independent of the distance between the open circuit and the end of the substrate, g1.

CHANNELIZED CPW RIGHT ANGLE BEND

A CCPW right angle bend and its equivalent circuit are shown in figure 8. The capacitance, C, is created by the accumulation of excess charge at the corners in the two slots and the resulting excess electric fields to the ground plane. The current flow interruption creates the excess inductance which can be equated to a length of transmission line, L. Radiation from the corner is represented by the shunt conductance, Gr.

To experimentally determine the capacitance, C, a voltage antinode has to be placed at the discontinuity. This is realized by placing a right angle bend at the center of an open circuit terminated resonator of length λ. To

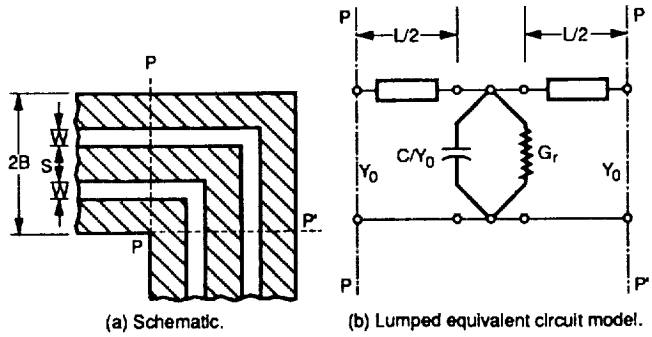

(a) Schematic. (b) Lumped equivalent circuit model.

Figure 8. - CCPW right angle bend.

determine the inductance, a voltage node has to be placed at the discontinuity. This is realized by placing a right angle bend in the center of a $\lambda/2$ resonator. The C and L are determined from the measured resonant frequencies using the following two equations (ref. 4):

$$L_n = \frac{nv}{2f_n \sqrt{(\varepsilon(eff))}} - (l_n + Lo + Lg) \tag{1}$$

$$C/Yo = \frac{1}{\pi f_2} \tan\left[\frac{\pi f_2 \sqrt{\varepsilon(eff)}\, L_2}{v}\right] \tag{2}$$

where

$f_n \equiv$ resonant frequency of the $n\lambda/2$ resonator

$Lg \equiv$ gap equivalent extension

$L_n \equiv$ Extension due to the parasitic reactance, either resulting from a voltage antinode for an $n = 2$ resonator or a voltage node for an $n = 1$ resonator

$Lo \equiv$ open circuit equivalent extension

$l_n \equiv$ physical length of the $n\lambda/2$ resonator

$n \equiv$ order of resonance

$v \equiv 3 \times 10^8$ m/sec

The radiation conductance, Gr, was calculated by deriving a lumped element equivalent circuit model for the shielded and unshielded resonators incorporating a right angle bend (ref. 5). The difference in the resonator circuit conductance is then attributed to an equivalent radiation conductance. The model is valid near the resonant frequency. Table I presents the normalized capacitance C/Yo, L, and the normalized radiation conductance Gr/Yo as a function of the frequency. The radiation conductance is very small at low frequencies, however, it increases rapidly with frequency.

TABLE I. - CCPW RIGHT ANGLE BEND DISCONTINUITY

[S = 0.045 in., W = 0.010 in., $\varepsilon(r) = 2.2$, 2B = 0.200 in.]

Frequency, GHz	L, mil	C/Yo, pF·Ω	Gr/Yo
2.97	22.622	4.219	0.0003635
4.92	26.241	4.353	.0014154
9.74	30.972	3.192	.010823
13.49	27.867	2.950	.011765
17.84	31.794	3.848	---------

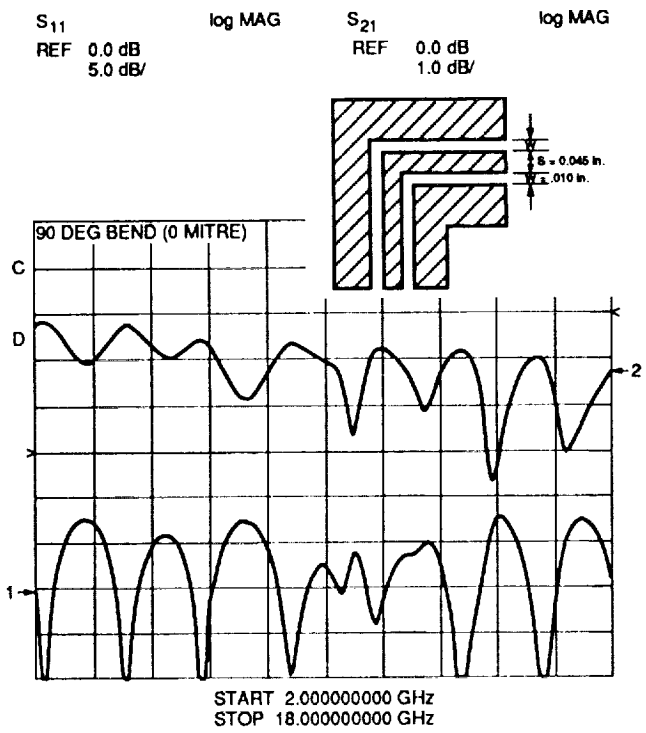

(a) Uncompensated right angle bend.

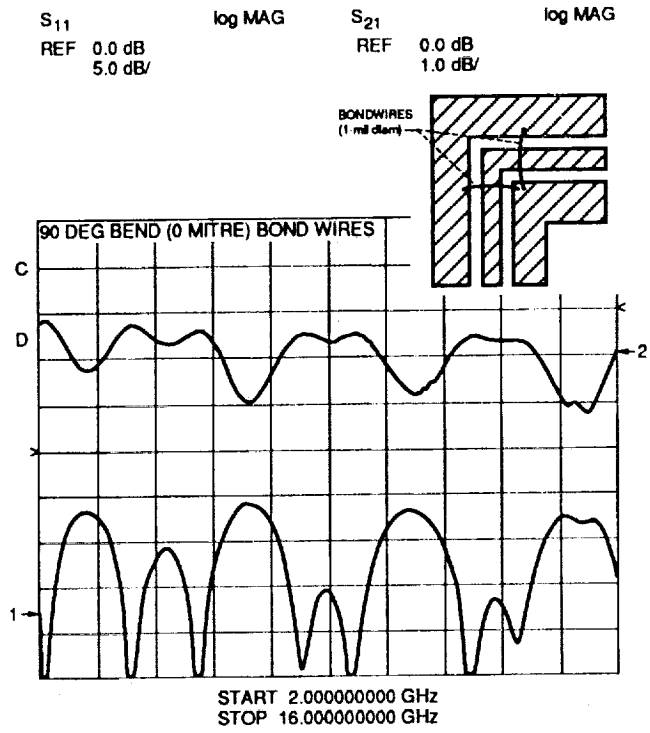

(b) Right angle bend with bond wires.

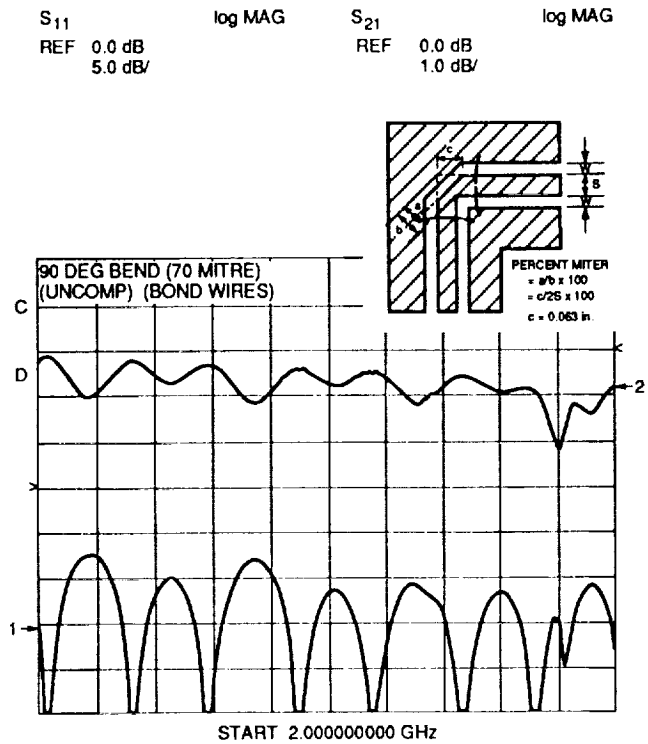

(c) Right angle bend with bond wires and 70 percent miter.

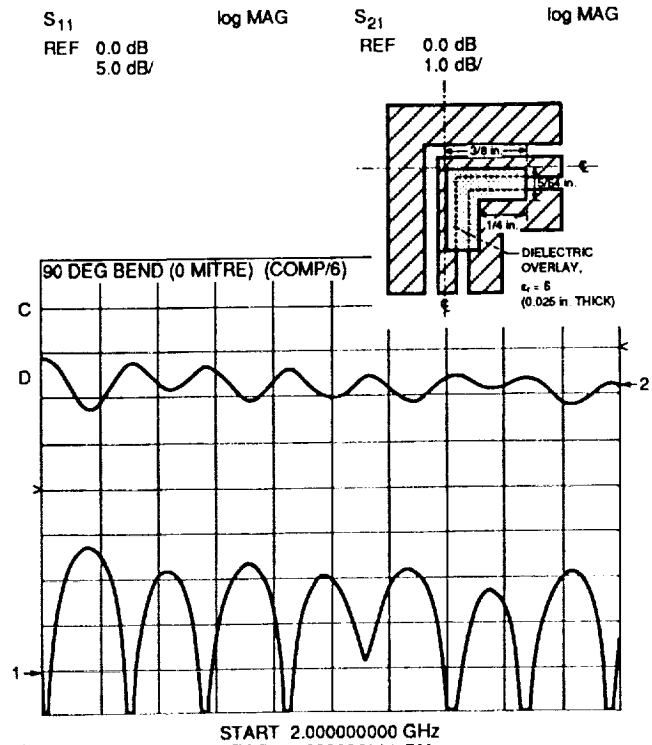

(d) Right angle bend with dielectric overlay.

Figure 9. - Measured RF characteristics for CCPW right angle bends with configurations inset.

The path length differences between the two slots at the CCPW right angle bend degrade the RF characteristics. Therefore, compensating techniques such as miters (ref. 9) and dielectric overlays (ref. 8) were investigated. Figure 9 illustrates a CCPW right angle bend and three possible compensating techniques and shows the measured insertion and return loss for each of the bends. The use of bond wires (fig. 9(b)), to hold the ground planes to the same potential at the element reference planes reduced the resonances in the insertion loss characteristics. To further reduce the path length difference, miters as large as 70 percent were tried. The miter and bond wires eliminated most of the resonances (fig. 9(c)). Finally, a dielectric overlay was placed on the inner slot (fig. 9(d)). The overlay slows the signal travelling along the inner slot so the signal emerging from each of the slots after the right angle bend is in phase. As shown in figure 9(d), the insertion loss and the return loss were less than 1.0 dB and greater than 10 dB, respectively, over a 2 to 18 GHz band. This agrees with the characteristics of a straight thru circuit.

CHANNELIZED CPW MATCHED T-JUNCTION

A pen-plot of a CCPW matched T-junction is shown in figure 10. At the T-junction, the characteristic impedance of the two side arms, Z1, are in parallel and the net impedance the input arm sees is Z1/2. Therefore, for impedance matching, the characteristic impedance, Z0, of the feed arm was set equal to Z1/2. To accomplish this, the output arms were tapered to an impedance of ≈135 Ω and the input arm was tapered to ≈67 Ω. At the coax-to-CCPW transitions, the CCPW impedance was ≈70 Ω to provide a good match to the 50 Ω coaxial line (ref. 8). When a shielding cover of height H = D was used, an insertion loss and return loss of 0.5 dB and 10 dB, respectively, were measured up to 12.5 GHz. A pair of bond wires were added to hold the ground planes at the junction at the same potential (refs. 10 and 11). This increased the bandwidth to 16.5 GHz. The measured insertion loss and return loss of the T-junction with bond wires are presented in figure 11. When the bond wires were used, the measured insertion loss and return loss was independent of the use of a cover.

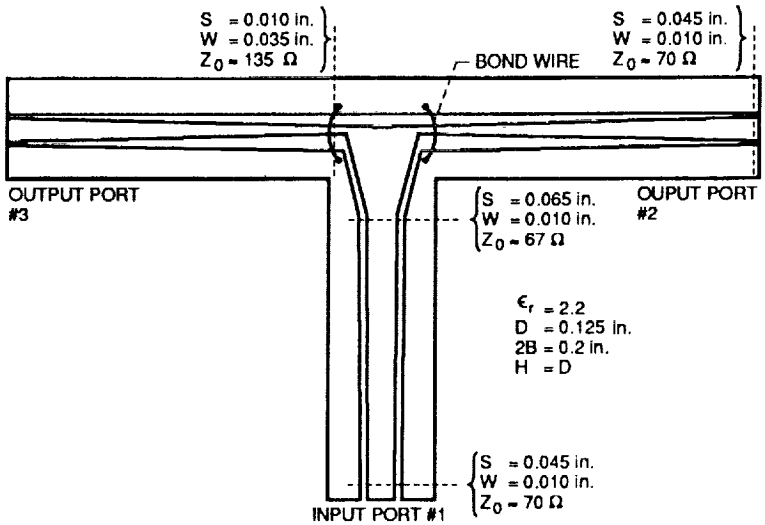

Figure 10. - Pen-plot of a CCPW matched T-junction.

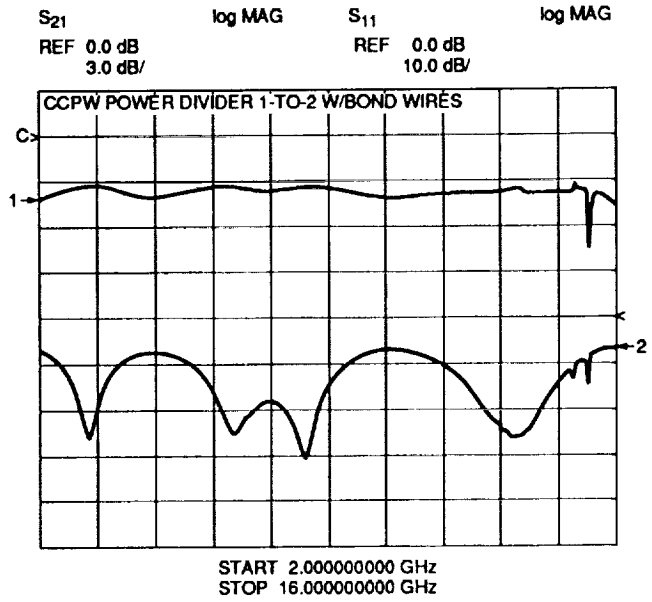

Figure 11. - Measured amplitude of the power coupled to one of the output ports and the return loss of the input port for a CCPW matched T-junction.

CHANNELIZED CPW MATCHED 1:3 JUNCTION

A pen-plot of a CCPW matched 1:3 junction is shown in figure 12. The output arms have been tapered to ≈135 Ω at the junction. The input arm was tapered to 45 Ω for impedance matching. When a shielding enclosure of height H = D was used, a return loss greater than 10 dB and low insertion loss was measured through 12.5 GHz. However, a maximum phase imbalance between ports 2 and 3 of ≈70° exists at 12.5 GHz.

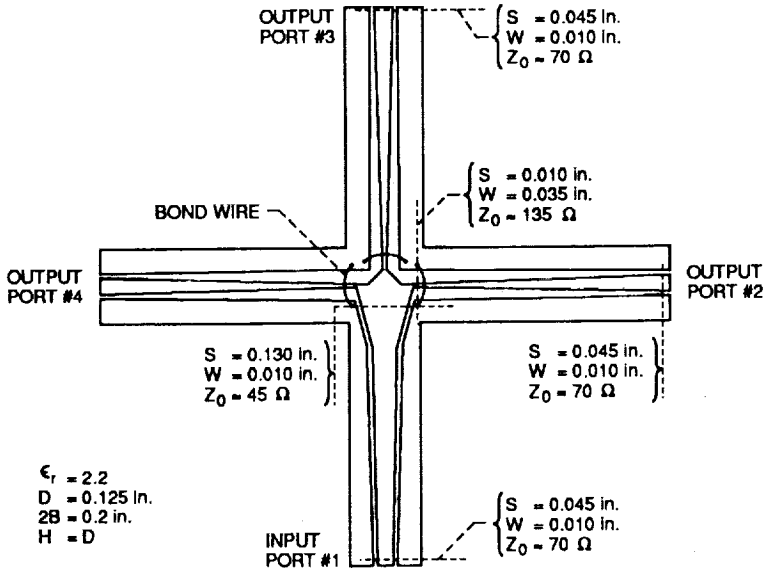

Figure 12. - Pen-plot of CCPW matched 1-to-3 junction.

The use of three bond wires as shown in figure 12 increased the bandwidth to 16.0 GHz. In addition, the bond wires reduced the phase imbalance between ports 2 and 3 by 20° at 12.5 GHz. The measured insertion loss and return loss of the three-way junction with bond wires are presented in figure 13. The average measured amplitude of -5 dB at the output ports agrees well with the expected -4.8 dB. There was negligible amplitude and phase imbalance between ports 2 and 4. A maximum of 1 dB of amplitude imbalance was measured between ports 2 and 3. The phase imbalance between ports 2 and 3 increased linearly from ≈0° at 2 GHz to 70° at 16 GHz. The use of a shielding enclosure with the bond wires did not result in any further improvement in the characteristics.

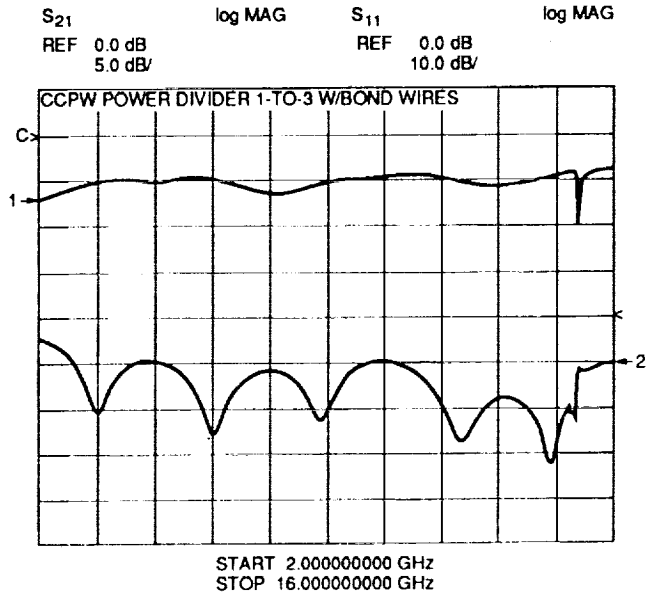

Figure 13. - Measured amplitude of the power coupled to one of the output ports and the return loss of the coaxial input port for a CCPW matched 1-to-3 junction.

COAX-to-CHANNELIZED CPW IN-PHASE N-WAY RADIAL POWER DIVIDER

A coax-to-CCPW in-phase, four-way radial power divider is shown in figure 14. The junction is formed by the intersection of four CCPW lines. Power is coupled to this junction from a coaxial cable whose outer conductor is slotted along the z direction to form four coupled transmission lines. The center pin of the coaxial line meets the intersecting CCPW center conductors while the four coupled outer conductors meet the CCPW ground planes. Therefore, the electric current at the open end of the coax is divided into the four CCPW lines as illustrated in figure 15. This arrangement has the advantage of holding the ground planes at the same potential and exciting the four CCPW lines in equal amplitude and phase without the need for bond wires. Each of the four CCPW lines, figure 16, has an impedance of 135 Ω at the junction. Therefore, the net impedance seen by the coaxial line is ≈34 Ω. A quarter wave coaxial dielectric transformer ($\varepsilon(r) = 4$) was used at the junction to match the 50 Ω coaxial line to the 34 Ω CCPW junction impedance. Each of the three pairs of slits in the ground plane of the CCPW acts as a stub and helps improve the CCPW to coaxial connector impedance match over the measured frequency range.

ORIGINAL PAGE
BLACK AND WHITE PHOTOGRAPH

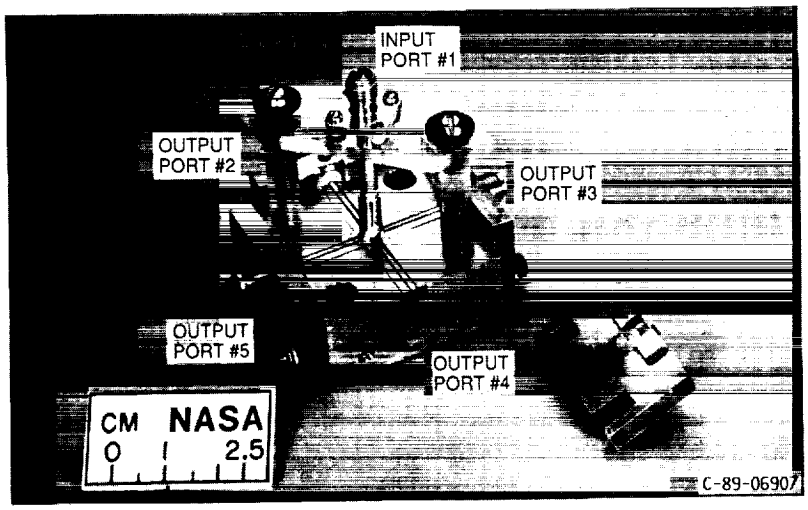

Figure 14. - Coax-to-CCPW in-phase, four-way, radial power divider.

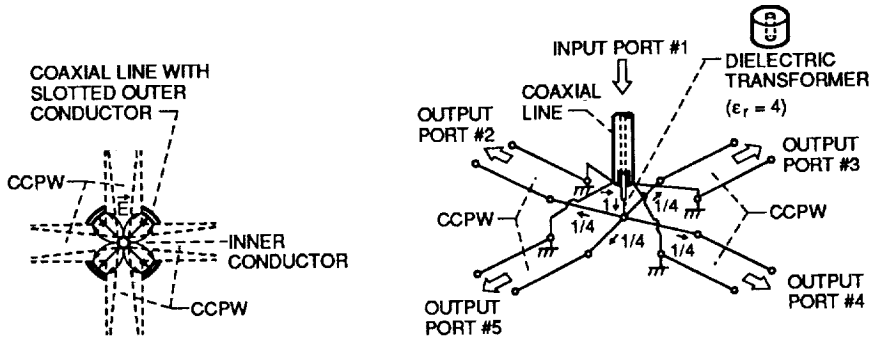

(a) Electric field (E) distribution at the end of the slotted coaxial line.

(b) Equivalent circuit of the junction showing the input RF current (I) being divided into the four ports.

Figure 15. - Coax-to-CCPW junction.

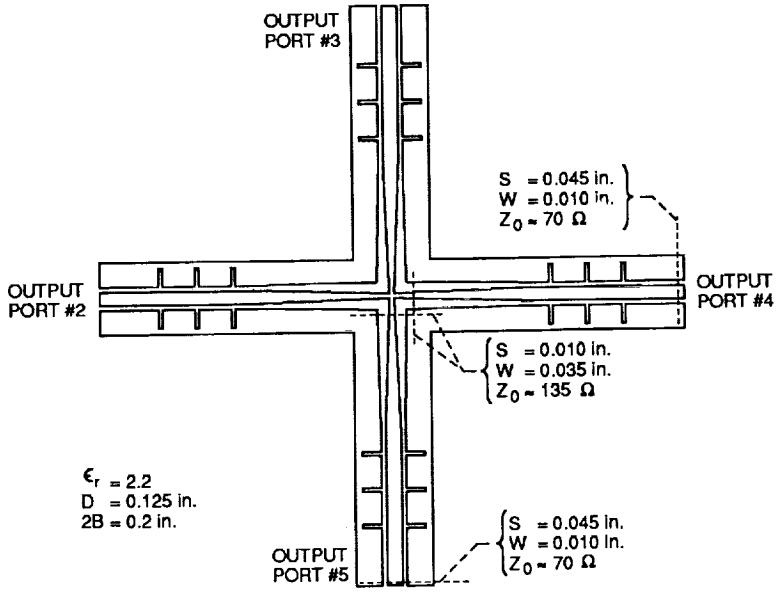

Figure 16. - Pen-plot of the coax-to-CCPW in-phase, four-way, radial power divider.

The measured amplitude of the power coupled to one of the output ports over an octave bandwidth is shown in figure 17 and is typical of the junction. The -6.5 dB measured amplitude at the output ports is in good agreement with the -6.0 dB expected for a 1:4 junction. The additional loss includes the CCPW to coaxial transformer and connector losses. Also superimposed on figure 18 is the return loss of the input port. Figure 18 is a measurement of the amplitude and phase balance for the four output ports; the amplitude and phase balance are within 0.5 dB and 5°, respectively. These values are a function of the mechanical structure itself since all of the ports are identical. The isolation between the ports is ≈10 dB.

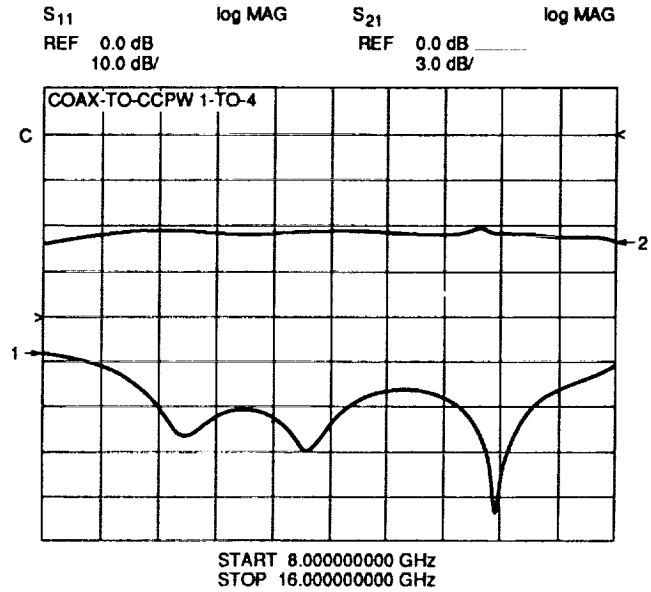

Figure 17. - Measured amplitude of the power coupled to one of the output ports and the return loss of the coaxial input port for a four-way radial power divider.

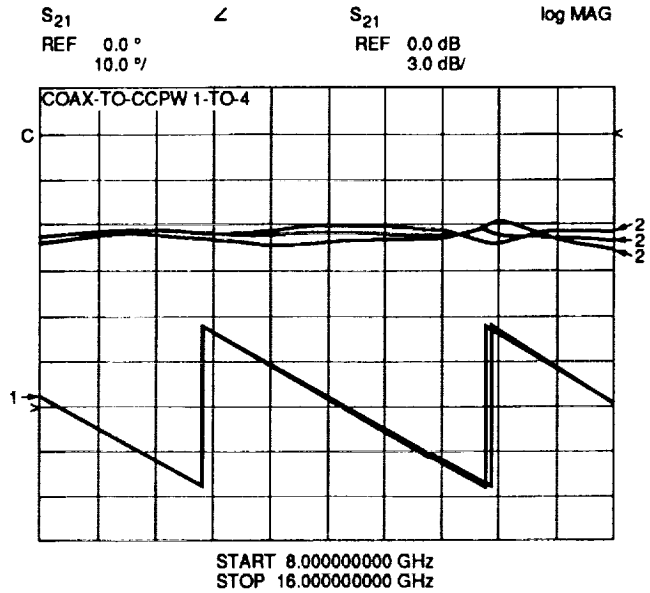

Figure 18. - Measured amplitude and phase balance for a coax-to-CCPW four-way power divider.

A coax-to-CCPW two-way radial power divider with the same basic structure as that described above was fabricated. The outer conductor of the coaxial line was slotted to form two coupled transmission lines. A dielectric transformer was not used with this structure. The measured amplitude at the output ports and the return loss at the coax input port are presented in figure 19. The amplitude imbalance for this circuit is less than 0.5 dB and the phase imbalance is less than 5°. Again, these values are dependent on the mechanical realization of the power divider.

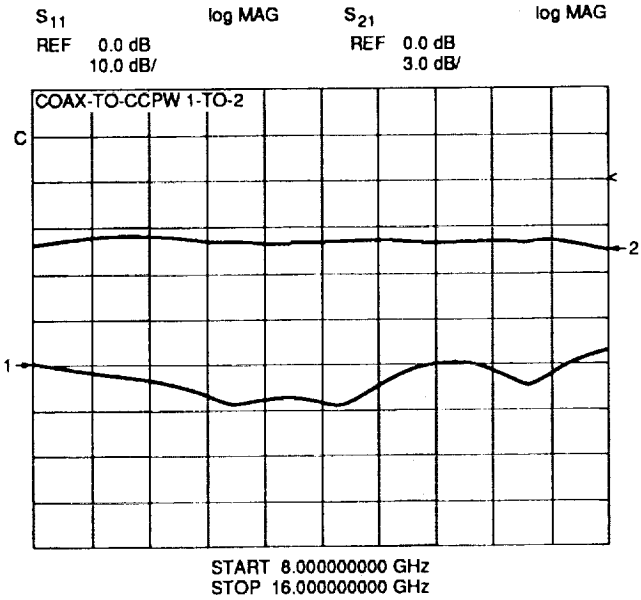

Figure 19. - Measured amplitude of the power coupled to one of the output ports and the return loss of the coaxial input port for a two-way radial power divider.

CONCLUSIONS

A new variant of CPW which has been termed CCPW has been demonstrated. The propagation characteristics of this structure show it to be useful for wide bandwidth, low loss microwave circuits where the favorable size advantage of CCPW over rectangular waveguide may be needed. Equivalent circuit model element values are presented for a CCPW open circuit and a CCPW right angle bend. A matched CCPW T-junction, a matched 1:3 junction, and a novel coax-to-CCPW in-phase, N-way, radial power divider are also demonstrated. These exhibit low loss and wide bandwidth and hence should facilitate the implementation of CCPW in microwave signal distribution networks such as in a phased array antenna system.

REFERENCES

1. Wen, C.P.: Coplanar Waveguide: A Surface Strip Transmission Line Suitable for Nonreciprocal Gyromagnetic Device Applications. IEEE Trans. Microwave Theory Tech., vol. MTT-17, no. 12, Dec. 1969, pp. 1087-1090.

2. Shih, Y.C.; and Itoh, T.: Analysis of Conductor-Backed Coplanar Waveguide. Electron. Lett., vol. 18, no. 12, June 10, 1982, pp. 538-540.

3. Richings, J.G.: An Accurate Experimental Method for Determining the Important Properties of Microstrip Transmission Lines. Marconi Rev., vol. 37, no. 195, 1974, pp. 209-216.

4. Stephenson, I.M.; and Easter, B.: Resonant Techniques for Establishing the Equivalent Circuits of Small Discontinuities in Microstrip. Electron. Lett., vol. 7, no. 19, Sept. 23, 1971, pp. 582-584.

5. Romanofsky, R.R.: Analytical and Experimental Procedures for Determining Propagation Characteristics of mm-Wave GaAs Microstrip Lines. NASA TP-2899, 1989.

6. Simons, R.N.: Suspended Coupled Slotline Using Double Layer Dielectric. IEEE Trans. Microwave Theory Tech., vol. MTT-29, no. 2, Feb. 1981, pp. 162-165.

7. Ghione, G.; and Naldi, C.: Parameters of Coplanar Waveguides with Lower Ground Plane. Electron. Lett., vol. 19, no. 18, Sept. 1, 1983, pp. 734-735.

8. Simons, R.N.; and Ponchak, G.E.: Modeling of Some Coplanar Waveguide Discontinuities. IEEE Trans. Microwave Theory Tech., vol. MTT 36, no. 12, Dec. 1988, pp. 1796-1803.

9. Douville, R.J.P.; and James, D.S.: Experimental Study of Symmetric Microstrip Bends and Their Compensation. IEEE Trans. Microwave Theory Tech., vol. MTT-26, no. 3, Mar. 1978, pp. 175-182.

10. Houdart, M.: Coplanar Lines: Application to Broadband Microwave Integrated Circuits. 6th European Microwave Conference, Microwave Exhibitions and Publishers Ltd., Sevenoaks, England, 1976, pp. 49-53.

11. Stegens, R.E.: Coplanar Waveguide FET Amplifiers for Satellite Communications Systems. Comsat Tech. Rev., vol. 9, no. 1, Spring 1979, pp. 255-267.

NASA Technical Memorandum 102522

Coplanar Waveguide Fed Phased Array Antenna

R.N. Simons
Sverdrup Technology, Inc.
NASA Lewis Research Center Group
Cleveland, Ohio

G.E. Ponchak and R.Q. Lee
National Aeronautics and Space Administration
Lewis Research Center
Cleveland, Ohio

N.S. Fernandez
University of Puerto Rico
Rio Piedras, Puerto Rico

Prepared for the
1990 IEEE AP-S International Symposium
and URSI Radio Science Meeting
Dallas, Texas, May 7–11, 1990

NASA

COPLANAR WAVEGUIDE FED PHASED ARRAY ANTENNA

R.N. Simons
Sverdrup Technology, Inc.
NASA Lewis Research Center Group
Cleveland, Ohio 44135

G.E. Ponchak and R.Q. Lee
National Aeronautics and Space Administration
Lewis Research Center
Cleveland, Ohio 44135

N.S. Fernandez*
University of Puerto Rico
Rio Piedras, Puerto Rico 00931

SUMMARY

A K-band four element linear phased array has been designed and tested. Coplanar waveguide (CPW) is used for the microwave distribution system. A CPW to twin strip transition is used to interface with the printed dipole antennas. MMIC phased shifters are used for phase control.

E-5327

INTRODUCTION

Coplanar waveguide (CPW) is a transmission line which consists of a center strip and a semi-infinite ground plane on either side of it (ref. 1). CPW is useful for integrating MMIC's together to form a microwave distribution network since the ground planes are readily accessible on the top side of the substrate. Grounded CPW (GCPW) is a variant of CPW which incorporates an additional ground plane on the back side of the substrate (ref. 2). This additional ground plane can serve as a heat sink and provide mechanical strength. In addition, this ground plane serves as a shield between stacked antennas boards to improve isolation.

Several CPW fed antennas have been reported in the literature. A GCPW fed coplanar stripline antenna constructed by widening the center strip of the GCPW to form a rectangular patch has been reported (ref. 3). This antenna produces a linearly-polarized pattern normal to the plane of the substrate. Coplanar waveguide fed slot antennas which are the complement to printed dipole antennas have also been reported (ref. 4). This antenna also radiates in a direction normal to the plane of the substrate. Although end-fire antennas are required for many large phased arrays, no CPW fed end-fire antennas have been reported yet in the literature.

*Summer Student Intern at Lewis Research Center.

In this paper we demonstrate a K-Band four element, printed dipole linear array which uses GCPW for the feed network and the integration of the MMIC phase shifters. This array radiates in the end fire direction and is suitable for large two-dimensional arrays.

CIRCUIT DESCRIPTION

The microwave distribution network and antennas is shown in figure 1. The microwave distribution network is fed by a single coaxial transmission line. The microwave signal is then split equally onto four GCPW transmission lines by three GCPW T-junctions. Wire bonds were used to tie the ground planes of the GCPW at the bends and T-junctions. The insertion loss for the one-to-four power divider is shown in figure 2. The MMIC phase shifters are DC isolated from the rest of the network by a pair of GCPW couplers. The couplers have been optimized to have a passband at the antenna operating frequency. The GCPW was tapered to provide a better match to the line width of the microstrip lines on the MMIC. The insertion loss for the two couplers with a GaAs 50 microstrip through connection in place of the phase shifters was 2.0 dB. The transition from the unbalanced GCPW to the balanced coplanar strip transmission line was made through a coplanar balun (ref. 5). The circuit was fabricated on 0.0625 in. thick CuFlon material.

The phase shifters shown in figure 3(a) were developed by Hughes Aircraft Corporation under contract to NASA (ref. 6). The phase shifters are reflection type and utilize a Lange coupler and two reverse biased varactor diodes to provide continuous 180° phase shift. The phase shifters were characterized individually before integration with the antenna network. By applying bias voltages from 0 to 4 V, 170° of phase shift was obtained as shown in figure 3(b) with an average insertion loss of 6.15 dB. Amplitude control can be added by the addition of MMIC amplifiers, variable attenuators, or switches.

ARRAY PERFORMANCE CHARACTERISTICS

The measured radiation pattern for a single GCPW fed printed dipole antenna is shown in figure 4(a). As expected, the pattern is broad due to the low gain of the antenna. The measured radiation pattern for the four element linear array is shown in figure 4(b). The pattern was measured with identical GaAs 50 Ω microstrip through lines in place of the phase shifters. The E-plane and H-plane patterns have 3-dB beam widths of 15° and 40°, respectively. The E-plane pattern has a shift in the main lobe which is probably due to path length differences in the feed network. The radiation pattern of the array with the MMIC phase shifters is in the process of being made.

CONCLUSIONS

A K-Band four element linear array of printed dipole antennas which demonstrates the advantages of CPW for MMIC integration and microwave signal distribution has been fabricated and tested. The radiation characteristics for the antenna is excellent.

REFERENCES

1. C.P. Wen, "Coplanar Waveguide: A Surface Strip Transmission Line Suitable for Nonreciprocal Gyromagnetic Device Applications," IEEE Trans. Microwave Theory Tech., vol. MTT-17, no. 12, pp. 1087-1090, 1969.

2. Y.C. Shih and T. Itoh, "Analysis of Conductor-Backed Coplanar Waveguide," Electron Lett., vol. 18, no. 12, pp. 538-540, 1982.

3. J.W. Greiser, "Coplanar Stripline Antenna," Microwave J., vol. 19, no. 10, pp. 47-49, 1976.

4. A. Nesic, "Slotted Antenna Array Excited by a Coplanar Waveguide," Electron. Lett., vol. 18, no. 6, pp. 275-276, 1982.

5. R.E. DeBrecht, "Coplanar Balun Circuits For GaAs FET High-Power Push-Pull Amplifiers," IEEE G-MTT International Microwave Symposium Digest, New York: IEEE, pp. 309-311, 1973.

6. L.C.T. Liu, et al., "A 30-GHz Monolithic Receiver," IEEE Trans. Microwave Theory Tech., vol. MTT-34, no. 12, pp. 1548-1552, 1986.

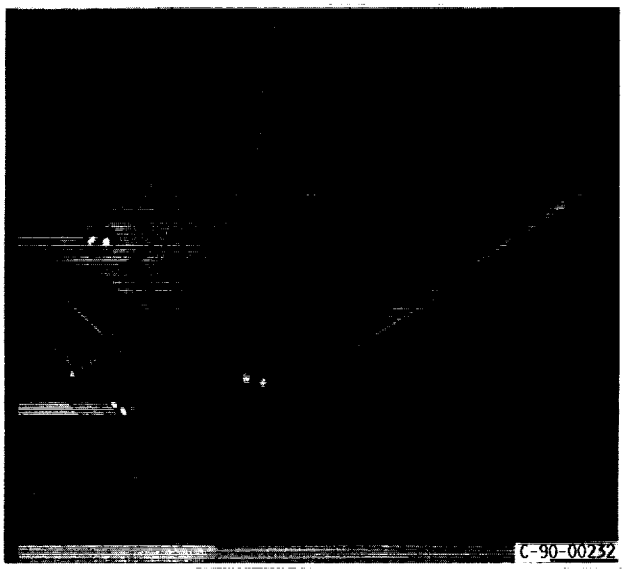

FIGURE 1. - GCPW FED FOUR ELEMENT PRINTED DIPOLE PHASED ARRAY.

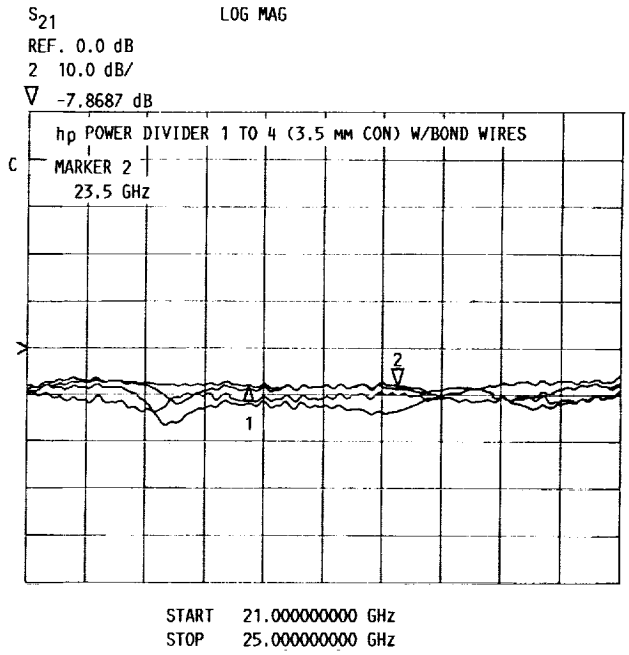

FIGURE 2. - GCPW ONE-TO-FOUR POWER DIVIDER AMPLITUDE CHARACTERISTICS.

(a) PHASE SHIFTER CONFIGURATION.

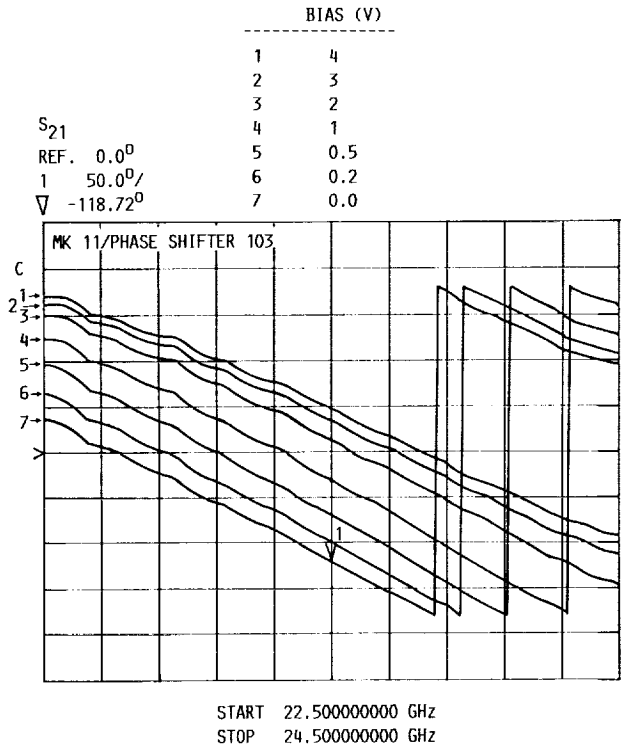

(b) MEASURED PHASE SHIFT AS A FUNCTION OF THE FREQUENCY FOR DIFFERENT VOLTAGES.

FIGURE 3. - GaAs MMIC PHASE SHIFTER.

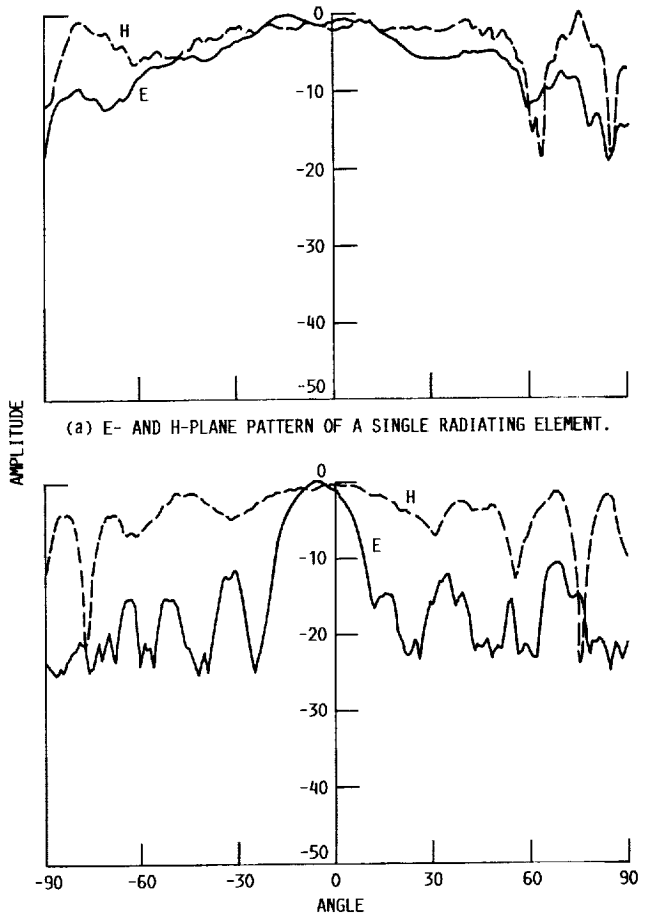

(a) E- AND H-PLANE PATTERN OF A SINGLE RADIATING ELEMENT.

(b) E- AND H-PLANE PATTERN OF THE FOUR ELEMENT ARRAY AT 21.3 GHz.

FIGURE 4. - MEASURED RADIATION PATTERN.

III. SUPERCONDUCTING FILMS

Microwave Conductivity of Laser Ablated $YBa_2Cu_3O_{7-\delta}$ Superconducting Films and Its Relation to Microstrip Transmission Line Performance

K.B. Bhasin, J.D. Warner
National Aeronautics and Space Administration
Lewis Research Center
Cleveland, Ohio

C.M. Chorey
Sverdrup Technology, Inc.
Lewis Research Center Group
Brook Park, Ohio

B.T. Ebihara, R.R. Romanofsky, and V.O. Heinen
National Aeronautics and Space Administration
Lewis Research Center
Cleveland, Ohio

F.A. Miranda and W.L. Gordon
Case Western Reserve University
Cleveland, Ohio

Preprint for the Advances in Material Science and Applications of High Temperature Superconductors sponsored by NASA Goddard Space Flight Center Washington, D.C., April 2-6, 1990

NASA

MICROWAVE CONDUCTIVITY OF LASER ABLATED $YBa_2Cu_3O_{7-\delta}$ SUPERCONDUCTING FILMS AND ITS RELATION TO MICROSTRIP TRANSMISSION LINE PERFORMANCE

K.B. Bhasin,* J.D. Warner,* C.M. Chorey,† B.T. Ebihara,* R.R. Romanofsky,* V.O. Heinen,* F.A. Miranda‡, and W.L. Gordon‡

*NASA Lewis Research Center
Cleveland, Ohio 44135

†Sverdrup Technology, Inc., Lewis Research Center Group
Brook Park, Ohio 44142

‡Department of Physics, Case Western Reserve University
Cleveland, Ohio 44106

ABSTRACT

We report on the values of the microwave conductivity in the normal (σ_N) and superconducting ($\sigma^*=\sigma_1-j\sigma_2$) states of two laser ablated $YBa_2Cu_3O_{7-\delta}$ thin films at 35 GHz, in the temperature range from 20 to 300 K. The films (0.7 and 0.4 μm) were deposited on $LaAlO_3$ by laser ablation. The conductivity was obtained from the microwave power transmitted through the films and assuming a two-fluid model. Values of $\sigma_N \sim 2.3 \times 10^5$ S/m at room temperature for both films, and of $\sigma_1 \sim 6.3 \times 10^5$ and 4.6×10^5 S/m at temperatures around 80 K were obtained for the 0.7 and 0.4 μm films respectively. For σ_2 values of 4.9×10^6 and 5.4×10^6 S/m were obtained for the 0.7 and 0.4 μm films at 80 K. The expected conductor losses and Q-factor of a superconducting ring resonator were calculated using these conductivity values. The theoretical values were then compared with the experimental results obtained for a resonator fabricated from one of these films.

The discovery of high transition temperature (T_c) superconductors has raised the possibility of a new class of microwave and millimeter wave devices operating at temperatures considerably higher than liquid helium temperatures. Therefore, materials properties such as microwave conductivity (σ), critical current density (J_c), microwave surface resistance (R_s), transport anisotropies, thermal expansion, and others have to be well characterized and understood. To date, measurements of R_s at microwave and millimeter wave frequencies and of J_c of $YBa_2Cu_3O_{7-\delta}$ superconducting oxides have been very abundant.[1-3] Nevertheless, reports on the microwave conductivity of these new oxides have been rare.[4,5] The need for more data on the microwave conductivity of these oxides arises from the fact that knowledge of this parameter provides a way to calculate other relevant properties such as the normal skin depth (δ_n) and the magnetic penetration depth in the superconducting state (λ_s). From the practical application point of view, it provides valuable aid for the design of microwave devices and circuits, based on superconducting microstrip lines.[6,7]

In this paper we report on the microwave conductivity of laser ablated $YBa_2Cu_3O_{7-\delta}$ superconducting thin films at 35 GHz in the temperature range from 20 to 300 K. The values of the conductivities were obtained from the microwave power transmitted through the film, assuming a two-fluid model. The expected conductor losses and Q-factor of a superconducting ring resonator were calculated using

these conductivity values. The theoretical values were then compared with the experimental results obtained for a resonator fabricated from one of these films.

The pulsed laser ablation technique is similar to that reported by other researchers.[8,9] The deposition was performed at a substrate temperature of 750° C at an ambient oxygen pressure of 170 mtorr. The laser wavelength was 248 nm, the pulse length and rate were 20 to 30 ns and 4 pps* respectively. During this process the distance between the target and the sample was kept at 7.5 cm and the laser fluence on the target was maintained at 2.0 J/cm^2 per pulse. The laser beam was continually scanned 1 cm across the target using an external lens on a translator. When the deposition was finished, the oxygen pressure was raised to 1 atm and the temperature was lowered to 450° C at a rate of 2° C/min. The temperature was held at 450° C for two hrs before it was lowered to 250° C at the same rate already mentioned. Finally, the heater power was turned off and the sample was allowed to cool to 40° C or less before it was removed from the chamber. This deposition process is explained in more detail in reference 10.

Two $YBa_2Cu_3O_{7-\delta}$ superconducting thin films, deposited by laser ablation on $LaAlO_3$, have been considered in this study. The films' thicknesses were 0.7 and 0.4 μm respectively. $LaAlO_3$ is a convenient substrate because of its perovskite crystal structure and its lattice constant of a=3.792 Å which match very well with the lattice constant of the $YBa_2Cu_3O_{7-\delta}$ superconducting oxide. Also, its low dielectric constant (~22) makes it suitable for microwave device applications. The films were analyzed by X-ray diffraction, dc resistance versus temperature measurements and scanning electron microscopy (SEM). Transitions temperatures (T_c, R=0) of 89.7 and 86.0 K were measured for the 0.7 and 0.4 μm thin films respectively. The dc resistance versus temperature curves are shown in fig.1. The X-ray diffraction pattern revealed that both films are single phased with a strong c-axis orientation. Both films exhibit a very smooth surface as observed from scanning electron micrographs. A grain size of ~¼ μm was observed for both films.

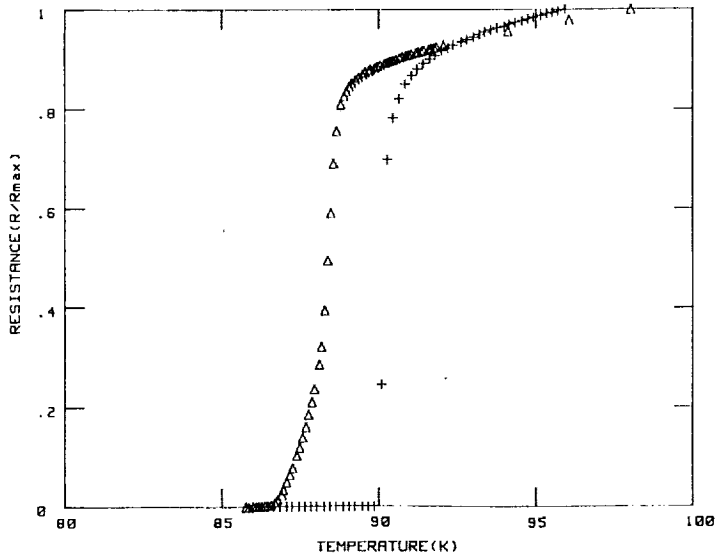

FIGURE 1. dc resistance versus temperature of 0.7 μm (+) and 0.4 μm (Δ) laser ablated $YBa_2Cu_3O_{7-\delta}$ thin films on $LaAlO_3$.

*Pulses per second.

The power transmission measurements were performed using an HP-8510 network analyzer connected to a helium gas closed cycle refrigerator by Ka-band (26.5 to 40.0 GHz) waveguides. All the measurements were taken under vacuum ($<10^{-3}$ torr) in a custom designed vacuum chamber. Inside the vacuum chamber the sample was clamped between two waveguide flanges mounted on top of the cold finger of the refrigerator. The waveguides were made of stainless steel to minimize heat conduction from the external waveguide arrangement and their inner surfaces were gold-plated to reduce microwave energy losses. Vacuum was maintained at the waveguide feedthroughs by means of 'O' rings and mica sealing windows. The temperature of the sample was monitored using silicon diode sensors mounted on the waveguide flanges supporting the sample. All the measurements were taken during sample cooling.

The measured temperature dependence of the transmitted power through the sample for both films under consideration is shown in fig.2 . Note that for the 0.7 μm film, both the onset temperature for the transition from the normal to the superconducting state (~91 K) and the transition temperature T_c (89.7 K), are clearly observed in this measurement. For the thinner film a sharp drop in transmitted power is observed below the onset temperature, with an attenuation of approximately 20 dB at temperatures around 80 K. The most relevant feature of the power versus temperature curve for this film is the sudden increase in transmitted power at temperatures below 80 K. This feature is an indication of the formation of a leakage source (micro-crack or pinhole) which broadens as the temperature decreases allowing more power to leak through the film. At temperatures below 50 K the amount of power leaking through the film reaches a constant value suggesting no significant variation of the leakage sources as a function of temperature in this temperature region.

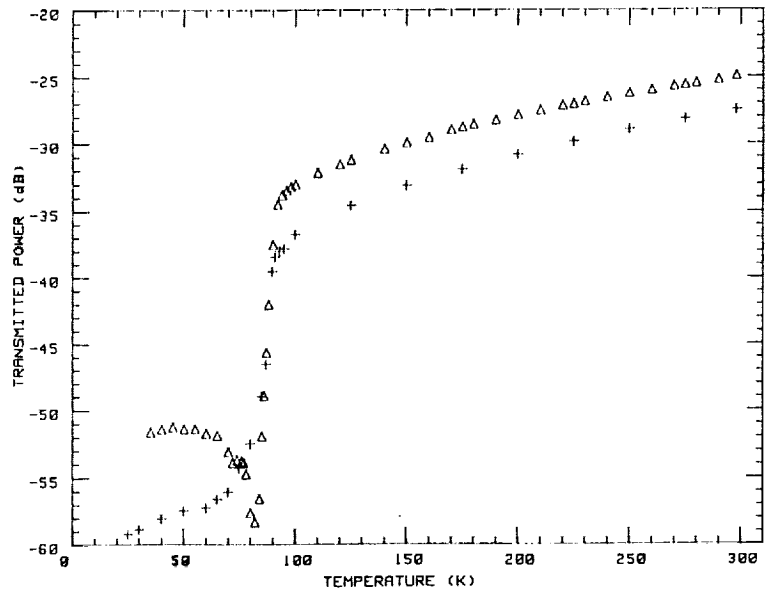

FIGURE 2. Transmitted power versus temperature of 0.7 μm (+) and a 0.4 μm (Δ) laser ablated $YBa_2Cu_3O_{7-\delta}$ thin films on $LaAlO_3$ at 35 GHz.

The normal state microwave conductivity, σ_N, was obtained from the power transmitted through the sample in the normal state, P_N, according to the expression[5]

$$\sigma_N=(-RP_N + [(RP_N)^2-4GP_N(HP_N-8n^2)]^{\frac{1}{2}})/2GP_NdZ_c \quad (1)$$

where

$$G=(n^2+1)+(n^2-1)\cos(2k\ell) \quad (1.a)$$
$$R=2(3n^2+1)+2(n^2-1)\cos(2k\ell) \quad (1.b)$$
$$H=n^4+6n^2+1-(n^2-1)^2\cos(2k\ell) \quad (1.c)$$

with Z_c the characteristic impedance of the waveguide, d the film thickness, ℓ and n the substrate thickness and the index of refraction respectively, and k the wave number. At temperatures below the beginning of the transition, the microwave conductivity takes the form $\sigma^*=\sigma_1-j\sigma_2$, where σ_1 is the conductivity due to the remaining normal electrons and σ_2 is the conductivity due to the superconducting electron pairs. We have calculated σ_1 by using $\sigma_1=\sigma_N(T/T_c)^4$, as defined under the two-fluid model approximation. Values of σ_2 were obtained using the relation[5]

$$\sigma_2/\sigma_c= -\beta/(2\sigma_c dZ_c) + \{[(\beta/2)^2-\gamma]/(\sigma_c dZ_c)^2 -\alpha\sigma_1/\sigma^2 dZ_c -(\sigma_1/\sigma_c)^2 +\ldots \ldots (P_c/P_s)[1+\alpha/\sigma_c dZ_c + \gamma/(\sigma_c dZ_c)^2\}^{\frac{1}{2}} \quad (2)$$

with P_s the power transmitted through the film for $T<T_c$, σ_c and P_c are the conductivity and transmitted power respectively at $T=T_c$, $\alpha=R/G$, $\gamma=H/G$ and $\beta=[-2n(n^2-1)\sin(2k\ell)]/G$.

Figure 3 shows the temperature dependence of σ_r ($\sigma_r=\sigma_N$ for $T>T_c$ and $\sigma_r=\sigma_1$ for $T<T_c$) for the samples under study. The conductivities (~2.3 X 10^5 S/m) at room temperature are in close agreement for the two films considered. These values also compare favorably with reported values for the dc conductivity in this type of film.[11] Hence, using the value of σ_N we found a typical resistivity, ρ, of about 435 $\mu\Omega$-cm at room temperature and of 133 and 160 $\mu\Omega$-cm at temperatures around 100 K, for the 0.7 and 0.4 μm films respectively. These resistivity values are on average a factor of 1.5 greater than the values for ρ (ρ~290 $\mu\Omega$-cm at 300 K and ρ~95 $\mu\Omega$-cm at 100 K) obtained from surface resistance (R_s) measurements in strongly c-axis oriented $YBa_2Cu_3O_{7-\delta}$ thin films on $SrTiO_3$ as reported by Klein, et al.[12] The normal conductivity of both films exhibit a metallic behavior with decreasing temperature, reaching values of ~7.7 X 10^5 S/m for the thicker film and of ~6.3 X 10^5 S/m for the thinner one, at the onset temperature. Below T_c, the values of σ_1 were obtained using the value of the conductivity at the onset temperature in the expression $\sigma_1=\sigma_N(T/T_c)^4$. Values for σ_1 of ~6.3 X 10^5 and 4.6 X 10^5 S/m were obtained at 85 K for the 0.7 μm and 0.4 μm films respectively. At temperatures around 50 K and below the values for σ_1 for the 0.7 μm film has decreased by one order of magnitude. Because the 0.4 μm film exhibited leakage of microwave power below 80 K, no data are shown below this temperature.

Figure 4 shows the imaginary part of σ^* for both films. For the 0.7 μm film, values for σ_2 of ~4.9 X 10^6 and 7.0 X 10^6 S/m were obtained at temperatures around 80 and 50 K respectively. These values are greater than those obtained for $YBa_2Cu_3O_{7-\delta}$ laser ablated films deposited on MgO and ZrO_2.[5] Due to the leakage sources formed in the 0.4 μm film, we were unable to obtain values of σ_2 at

temperatures below 80 K. A value of 3.5 X 10^6 S/m was obtained just below the onset temperature (~92 K) and of 5.4 X 10^6 S/m at 85 K. Note that the increase of σ_2 with decreasing temperature corresponds to an increase in electron pairs which implies a reduction of the normal carrier density.

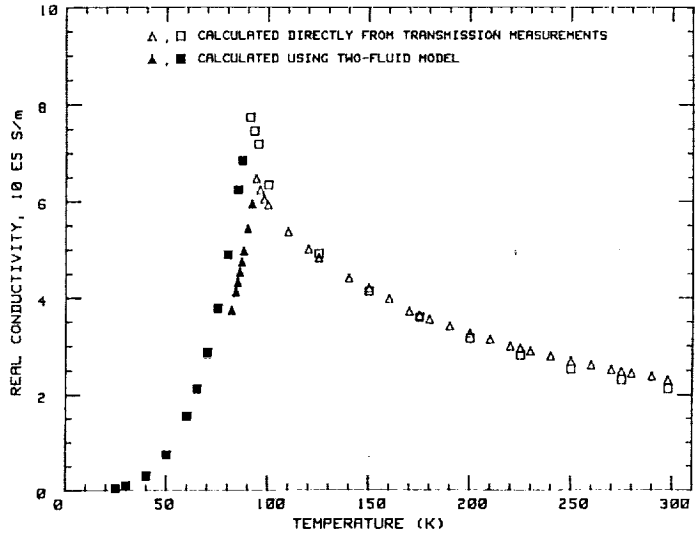

FIGURE 3. Real part of the conductivity, σ_1, versus temperature for 0.7 μm (□) and 0.4 μm (Δ) laser ablated $YBa_2Cu_3O_{7-\delta}$ thin films on $LaAlO_3$ at 35 GHz; $\sigma_1=\sigma_N$ for $T>T_c$ and $\sigma_1=\sigma_1$ for $T<T_c$. Open symbols represent values of the conductivity calculated directly from power transmission measurements and filled symbols represent values of the conductivity calculated using the two-fluid model.

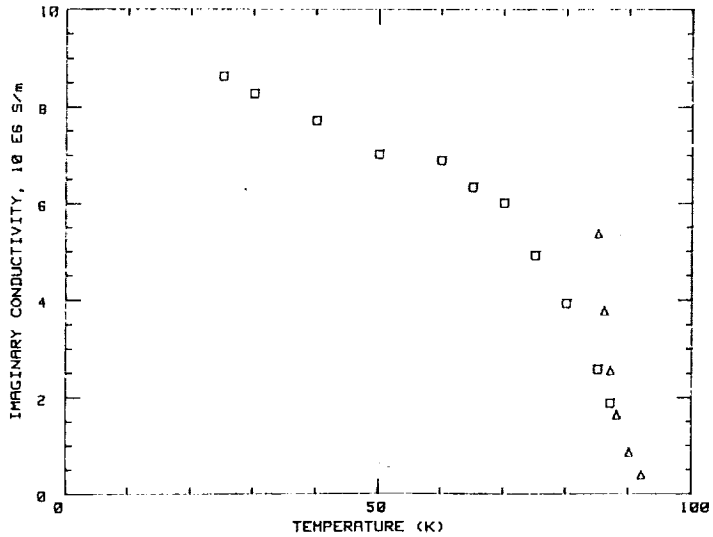

FIGURE 4. Imaginary part of the conductivity, σ_2, versus temperature for 0.7 μm (□) and 0.4 μm (Δ) laser ablated $YBa_2Cu_3O_{7-\delta}$ thin films on LaAlO3 at 35 GHz.

The values of σ_1 and σ_2 have been used to estimate values for the magnetic penetration depth λ and the surface resistance R_s.[13] Values of λ_o=0.67 μm and R_s~9mΩ at 77 K were obtained. These values are in close agreement with those obtained by other researchers.[12]

The conductivity values have been used to calculate the Q-factor of a ring resonator, which has a superconducting strip and a normal conducting ground plane. This resonator is shown in figure 5 and consists of a microstrip ring with a circumference that is three wavelengths in length at the design frequency of 35 GHz. Straight lengths of superconducting strip provide input to the ring with coupling achieved by small capacitive gaps. The substrate is 10 milli-inch thick lanthanum aluminate; and the characteristic impedance of the line is 45 ohms.

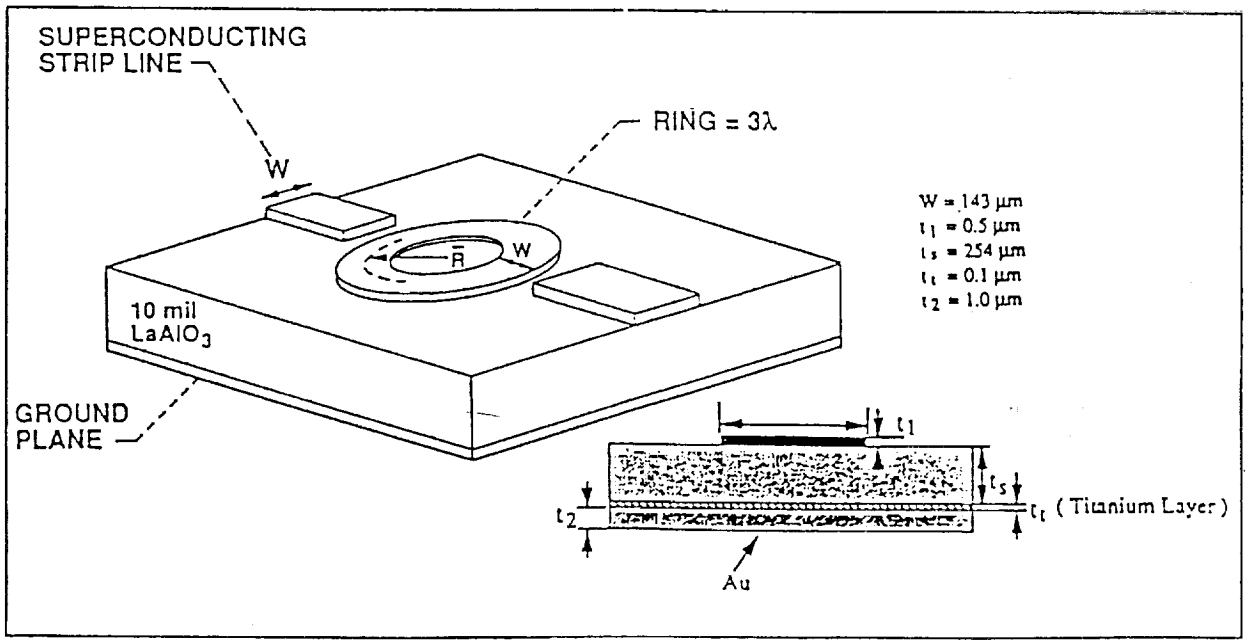

FIGURE 5. 35 GHz ring resonator microstrip transmission line circuit.

The "Q" of the ring is determined by two major loss mechanisms, 1) dielectric loss in the substrate and 2) resistive losses in the conductors. Radiation loss is assumed to be negligible in this case since the resonator, when being measured experimentally, is shielded by a section of waveguide below cutoff which acts to suppress radiation by the circuit. Dielectric losses can be calculated using:

$$\alpha_d = 3.15\ (q^*\epsilon/\epsilon_{eff})\ (\tan\delta/\lambda g)\quad \text{Nepers/m} \qquad (3)$$

where α_d[14] is the attenuation constant due to dielectric loss, 'q' is a geometrical 'filling factor', ϵ and ϵ_{eff} are the static and effective dielectric constants, tanδ is the dielectric loss tangent and λ_g is the transmission line wavelength. In these calculations we have used a value of 5.8 x 10^{-4} for tanδ[15] but it should be noted that authoritative values for the loss tangent have not been established.

The conductor losses were calculated by the Phenomenological Loss Equivalence Method (PEM), an analytical solution for loss in microstrip lines that accounts for thin conductors. The attenuation due to the loss in the conductors is given by :

$$\alpha_c = Z_{ri}/(2*Z_c) \quad \text{Nepers/m} \tag{4}$$

where Z_{ri} is the real part of the internal impedance of the strip and ground plane and Z_c is the characteristic impedance of the line. The internal impedance (Z_i) is obtained through the PEM where:

$$Z_{ix} = Z_{sx} * G_x * \coth(Z_{sx} * \sigma_x * G_x * A) \tag{5}$$

G_x is a geometrical factor, A the cross sectional area of the strip, Z_{sx} is the surface impedance and σ_x the conductivity of the conductor material of the strip or ground plane (x denotes different values for strip and ground plane). The σ values are obtained from the transmission data and the surface impedance is calculated from them. The "Q" of the ring is calculated as:

$$\frac{1}{Q} = \frac{2(\alpha c + \alpha d)}{\beta} \tag{6}$$

where β is the propagation constant of the line.

Using values of the conductivity obtained form the .7μm film and the tanδ as noted above, the "Q" values were calculated and compared to results obtained from a resonator made from a film fabricated under similar conditions (figure 6). Also shown are the measured "Q" values for a resonator with a normal metal (gold) strip and ground plane. While the superconducting strip performs better than the normal metal, the measured "Q" values do not follow those predicted by the calculations using the transmission conductivity values.

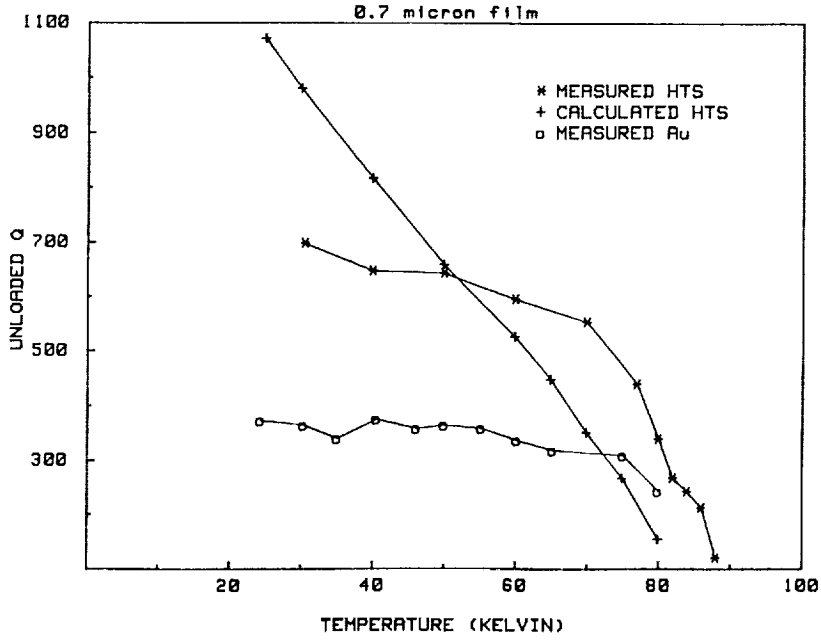

FIGURE 6. Measured and calculated values of unloaded Q for superconducting and normal resonators.

In summary, we have obtained the microwave conductivity at 35 GHz of laser ablated $YBa_2Cu_3O_{7-\delta}$ thin films in the temperature range from 20 to 300 K. The conductivity values at room temperature are in close agreement with dc values reported for the same type of material. Comparing the values for σ_1 and σ_2 for both films with those previously reported for laser ablated $YBa_2Cu_3O_{7-\delta}$ thin films on MgO and ZrO_2 suggest that $LaAlO_3$ is a superior substrate for microwave applications. From these conductivity values, values for the zero-temperature magnetic penetration depth λ_o and the surface resistance R_s, fundamental in the design of microwave devices and circuits, have been obtained. We have used the conductivity values to obtain conductor losses and Q-factors of a microwave transmission line. However, predicted and experimentally observed values are not in good agreement. Further work is needed in developing an accurate correlation between measured conductivity values and microstrip performance.

ACKNOWLEDGEMENT

We would like to gratefully acknowledge Mr. K. S. Kong and Prof. T. Itoh of the University of Texas at Austin for their calculation of the Q values of the ring resonator.

REFERENCES

1. J. P. Carini, A. M. Awasthi, W. Beyermann, G. Gruner, T. Hylton, K. Char, M. R. Beasley and A. Kapitulnik, "Millimeter-wave surface resistance measurements in highly oriented $YBa_2Cu_3O_{7-\delta}$ thin films", Phys. Rev. B. 37 (16), 9726-9729 (1988).

2. N. Klein, G. Muller, H. Piel, B. Roas, L. Shultz, U. Klein and M. Peiniger, "Millimeter wave surface resistance of epitaxially grown $YBa_2Cu_3O_{7-x}$ thin films", Appl. Phys. Lett. 54 (8), 757-759 (1989).

3. H. Kupfer, C. Keller, K. Salama and V. Selvamanickam, "Inductive current measurements in an oriented grained $YBa_2Cu_3O_x$ superconductor", Appl. Phys. Lett. 55 (18), 1903-1905 (1989).

4. P. H. Kobrin, W. Ho, W. F. Hall, P. J. Hood and A. B. Harker, Presented at the M^2S-HTSC Conference, Stanford Ca., July 24-28, 1989. To be published in Physica C.

5. F. A. Miranda, W. L. Gordon, K. B. Bhasin, V. O. Heinen, J. D. Warner and G. J. Valco, NASA TM-102345 (1989) and to be published in "Superconductivity and Applications", Plenum Press Publishing Corporation (1990).

6. F. Huret, D. Kinowski, P. Pribetich and P. Kennis, "Spectral domain analysis of a microstrip thin superconducting line laid on GaAs substrate", Microwave and Optical Tech. Lett. 2 (6), 205-208 (1989).

7. K. B. Bhasin, C. M. Chorey, J. D. Warner, R. R. Romanofsky, V. O. Heinen, K. S. Kong, H. Y. Lee and T. Itoh, NASA TM-102526 (1990).

8. A. Inam, M. S. Hedge, X. D. Wu, T. Venkatesan, P. England, P. F. Miceli, E. W. Chase, C. C. Chang, J. M. Tarascon and J. B. Watchman, "As-deposited high

T_c and J_c superconducting thin films made at low temperatures", Appl. Phys. Lett. 53 (10), 908-910 (1988).

9. B. Roas, L. Schultz, and G. Endres, "Epitaxial growth of $YBa_2Cu_3O_{7-x}$ thin films by a laser evaporation process", Appl. Phys. Lett. 53 (16), 1557-1559 (1988).

10. J. D. Warner, J. E. Meola and K. A. Jenkins, NASA TM-102350 (1989).

11. R. T. Collins, Z. Schlesinger, R. H. Koch, R. B. Laibowitz, T. S. Poaskett, P. Freitas, W. J. Gallacher, R. L. Sandstrom and T. R. Dinger, "Comparative study of superconducting energy gaps in oriented films and polycrystalline bulk samples of Y-Ba-Cu-O", Phys. Rev. Lett. 59 (6), 704-707 (1987).

12. N. Klein, G. Muller, S. Orbach, H. Piel, H. Chaloupka, B. Roas, L. Schultz, U. Klein and M. Peiniger, "Millimeter wave surface resistance and London penetration depth of epitaxially grown $YBa_2Cu_3O_{7-x}$ thin films", Physica C 162-164, 1549-1550 (1989).

13. F. A. Miranda, W. L. Gordon, K. B. Bhasin, J. D. Warner and V. O. Heinen, "Microwave Conductivity of Laser Ablated $YBa_2Cu_3O_{7-\delta}$ Superconducting Thin Film on $LaAlO_3$ Substrate", submitted to Appl. Phys. Lett.

14. R. A. Pucal, D. J. Masse, C. P. Hartwig, "Losses in Microstrip", IEEE Trans. Microwave Theory and Tech., vol. MTT-16, no. 6, 342-350 (1968).

15. R.W. Simon, C. E. Platt, A. E. Lee, G. S. Lee, K. P. Daly, M. S. Wire, J. A. Luine and M. Urbanik, "Low -loss substrate for epitaxial growth of high-temperature superconductor thin films", Appl. Phys. Lett., vol. 53 (26) 2667-2679 (1988).

16. H. Y. Lee and T. Itoh, "Phenomenological Loss Equivalence Method for Planar Quasi-TEM Transmission Line with a Thin Normal Conductor or Superconductor," IEEE Trans. Microwave Theory and Tech., Vol. MTT-37, no. 12, 1904-1909 (1989).

NASA Technical Memorandum 102345

Millimeter Wave Transmission Studies of $YBa_2Cu_3O_{7-\delta}$ Thin Films in the 26.5 to 40.0 GHz Frequency Range

F.A. Miranda and W.L. Gordon
Case Western Reserve University
Cleveland, Ohio

K.B. Bhasin, V.O. Heinen,
and J.D. Warner
Lewis Research Center
Cleveland, Ohio

and

G.J. Valco
The Ohio State University
Columbus, Ohio

Corrected Copy

Prepared for the
Third Annual Conference on Superconductivity and Applications
sponsored by The New York State Institute on Superconductivity
Buffalo, New York, September 19–21, 1989

NASA

MILLIMETER WAVE TRANSMISSION STUDIES OF $YBa_2Cu_3O_{7-\delta}$ THIN FILMS IN THE 26.5 TO 40.0 GHz FREQUENCY RANGE.

F.A. Miranda and W.L. Gordon
Department of Physics, Case Western Reserve University,
Cleveland, Ohio 44106

K.B. Bhasin, V.O. Heinen and J.D. Warner
National Aeronautics and Space Administration,
Lewis Research Center, Cleveland, Ohio 44135

G.J. Valco
Department of Electrical Engineering,
The Ohio State University,
Columbus, Ohio 43210

E-5053

ABSTRACT

Millimeter wave transmission measurements through $YBa_2Cu_3O_{7-\delta}$ thin films on MgO, ZrO_2 and $LaAlO_3$ substrates, are reported. The films (0.2 to 1.0 μm) were deposited by sequential evaporation and laser ablation techniques. Transition temperatures T_c, ranging from 89.7 K for the laser ablated film on $LaAlO_3$ to approximately 72 K for the sequentially evaporated film on MgO, were obtained. The values of the real and imaginary parts of the complex conductivity, σ_1 and σ_2, are obtained from the power transmitted through the film, assuming a two fluid model. The magnetic penetration depth is evaluated from the values of σ_2. These results will be discussed together with the frequency dependence of the normalized power transmission, P/P_c, below and above T_c.

INTRODUCTION

Millimeter wave measurements of the new high T_c superconductors are of fundamental importance due to the potential applicability of these oxides in the fabrication of devices operational in these frequency ranges.[1] Through these measurements, information on the nature of superconductivity in these new superconductors can be obtained from the temperature dependence of parameters such as the surface resistance,[2-6] and the complex conductivity.[7-9] Another important question is the applicability of millimeter wave measurements for the characterization of superconducting thin films. While dc resistance versus temperature measurements give no further information once the zero resistance state is achieved, millimeter wave transmission and absorption measurements provide a sensitive, contactless technique, which yield important information about the microstructure of superconducting films[10]

and their behavior at temperatures below the critical temperature (T_c). Millimeter and microwave absorption studies in low and high T_c superconductors have been performed using resonant cavities.[10-16] Usually, those studies applying millimeter or microwave transmission analysis, have reported results at just one particular frequency.[8,9]

In this work we have measured the power transmitted through $YBa_2Cu_3O_{7-\delta}$ thin films at frequencies within the frequency range from 26.5 to 40.0 GHz and at temperatures from 20 to 300 K. From these measurements and assuming a two fluid model, we have obtained values of the normal and complex conductivities above and below T_c respectively. The zero temperature magnetic penetration depth has been obtained using the value of the imaginary part of the complex conductivity, σ_2.

ANALYSIS

We have applied the two fluid model due to its simplicity and because in the past it has given good results for the microwave properties of metallic type II superconductors in cases for $\hbar\omega << E_{gap}$.[17] Since the energy gap for $YBa_2Cu_3O_{7-\delta}$ superconductors corresponds to frequencies in the terahertz range, we expect the model to be applicable in the frequency range studied. In this phenomenological model, the complex conductivity is defined as

$$\sigma = \sigma_1 - i\sigma_2 \tag{1}$$

with

$$\sigma_1 = \sigma_c t^4 \qquad \text{and} \qquad \sigma_2 = \sigma_c(1 - t^4)/\omega\tau \ . \tag{2}$$

Here, σ_c is the normal conductivity at $T = T_c$, $\omega = 2\pi f$ is the angular frequency, t is the reduced temperature T/T_c, and τ is the mean carrier scattering time. Thus, to determine either σ_1 or σ_2 we need to know the transition temperature T_c and the value of σ_c. Furthermore, the value of τ must be known beforehand if σ_2 is to be obtained from Eq. (2).

In this study, the value of T_c was determined from the standard four-point probe versus temperature measurements. To determine the normal and complex conductivities, we used the method applied by Glover and Tinkham.[18] In this method, the transmission of a normally incident plane wave through a film of thickness d(<< wavelength or skin depth) deposited on a substrate of thickness ℓ and index of refraction n, is measured. Following the notation of Glover and Tinkham[18] the power transmission is given by

$$\mathbf{T} = \frac{8n^2}{A + B\cos 2k\ell + C\sin 2k\ell} \tag{3}$$

where

$$A = n^4 + 6n^2 + 1 + 2(3n^2 + 1)g + (n^2 + 1)(b^2 + g^2)$$

$$B = 2(n^2 - 1)g - (n^2 - 1)^2 + (n^2 - 1)(b^2 + g^2)$$

$$C = 2(n^2 - 1)nb$$

$$k = n\omega/c$$

and

$$y = g - ib = YZc = (G - iB)Z_c = (\sigma_1 - i\sigma_2)dZ_c$$

is the dimensionless complex admittance per square of the film in units of the characteristic admittance, Z_c^{-1}, of the wave guide ($Z_c = Z_o/\sqrt{1 - (f_c/f)^2}$, $Z_o = 377\ \Omega$, mks; $Z_o = 4\pi/c$, cgs; f_c = cutoff frequency of the TE mode wave guide and f is the operational frequency).

In the normal state, Eq. (3) becomes

$$T_N = \frac{8n^2}{\sigma_N^2 d^2 Z_c^2 Q + \sigma_N dZ_c R + P} \tag{4}$$

where

σ_N = normal conductivity

$Q = (n^2 + 1) + (n^2 - 1)\cos 2k\ell$

$R = 2(3n^2 + 1) + 2(n^2 - 1)\cos 2k\ell$

$P = n^4 + 6n^2 + 1 - (n^2 - 1)^2 \cos 2k\ell.$

The normal state conductivity of the film can be expressed conveniently in terms of the power transmission as

$$\sigma_N = \frac{-R\mathbf{T}_N \pm \sqrt{R^2\mathbf{T}_N^2 - 4Q\mathbf{T}_N(P\mathbf{T}_N - 8n^2)}}{2Q\mathbf{T}_N dZ_c} \tag{5}$$

where only the expression with the + sign has physical relevance. It is convenient to use the ratio $\mathbf{T}_S/\mathbf{T}_N$ in the analysis of the superconducting state, where $\mathbf{T}_S$ refers to the transmission in the superconducting state given by Eq. (3). Thus,

$$\frac{\mathbf{T}_S}{\mathbf{T}_N} = \frac{\sigma_N^2 d^2 Z_c^2 Q + \sigma_N dZ_c R + P}{A + B\cos 2k\ell + C\sin 2k\ell} \tag{6}$$

Solving (6) for the imaginary part, σ_2, of the conductivity, and using the value of σ_N at $T = T_c$ we have

$$\sigma_2/\sigma_c = -\beta/2\,\frac{1}{\sigma_c dZ_c} + \left\{\frac{1}{(\sigma_c dZ_c)^2}\left[(\beta/2)^2 - \gamma\right] - \frac{\alpha\sigma_1}{\sigma_c^2 dZ_c} - \left(\frac{\sigma_1}{\sigma_c}\right)^2 + (\mathbf{T}_c/\mathbf{T}_S)\left[1 + \frac{\alpha}{\sigma_c dZ_c} + \frac{\gamma}{(\sigma_c dZ_c)^2}\right]\right\}^{1/2} \tag{7}$$

where σ_c and $\mathbf{T}_c$ are the conductivity and the transmissivity at $T = T_c$, and

$$\alpha = \frac{1}{D}\,[6n^2 + 2 + 2(n^2 - 1)\cos 2k\ell]$$

$$\beta = \frac{1}{D}\,[-2n(n^2 - 1)\sin 2k\ell]$$

$$\gamma = \frac{1}{D}\,[n^4 + 6n^2 + 1 - (n^2 - 1)\cos 2k\ell]$$

$$D = n^2 + 1 + (n^2 - 1)\cos 2k\ell \ .$$

Thus, from the relation for σ_1 in Eq. (2), and Eq. (7), the real and imaginary parts of the complex conductivity can be determined.

The magnetic penetration depth, λ, can be obtained from the London expression

$$\lambda = \left(\frac{1}{\mu_o \omega \sigma_2}\right)^{1/2} \tag{8}$$

which can be written in terms of the superfluid density N_S, as

$$\lambda = \left(\frac{m}{\mu_o N_S e^2}\right)^{1/2} \tag{9}$$

where m is the effective mass of the charge carriers. From the two fluid model

$$\frac{N_S}{N} = 1 - t^4 \tag{10}$$

where $N = N_n + N_S$ is the total number of carriers per unit volume, we have

$$\lambda = \left[\frac{m}{\mu_o N e^2}\right]^{1/2} (1 - t^4)^{-1/2} = \lambda_o\,(1 - t^4)^{-1/2} \tag{11}$$

From this expression the zero-temperature penetration depth, λ_o, can be obtained. Because Eq. (9) applies to homogeneous superconductors, the values of λ_o obtained in this method are larger than those that would be obtained for homogeneous films.

Our measurements were made on thin films (0.2 to 1.0 μm thickness) of $YBa_2Cu_3O_{7-\delta}$ on $LaAlO_3$, MgO and ZrO_2 substrates. The substrates were generally between 0.025 and 0.100 cm thick. The deposition techniques used for the preparation of the films used in this study are described in Refs. 19 and 20. For the laser ablated films, X-ray diffraction data showed that the films were c-axis oriented on $LaAlO_3$ and partially c-axis oriented for those on MgO and ZrO_2. They had T_c's ranging from 89.7 K for the film on $LaAlO_3$ to 79 and 78 K for those deposited on MgO and ZrO_2 respectively. The film deposited by sequential evaporation on MgO had a T_c of approximately 72 K.

The power transmission measurements were made using a Hewlett-Packard model HP-8510 automatic network analyzer connected to a modified closed cycle refrigerator by Ka-band (26.5 to 40.0 GHz) waveguides. Inside the vacuum chamber of the cryosystem, the sample was clamped

between two waveguide flanges which were in direct contact with the cold head of the refrigerator. The power transmitted through the sample was obtained by measuring the scattering parameters as described in Ref. 21. The temperature gradient of the waveguide flanges between the top and bottom of the sample, was estimated to be 2.5 K or less at 90 K. The system was properly calibrated with short, open, load and through calibration standards before each measurement cycle was started.

RESULTS

Figures 1 and 2 show the temperature dependence of the normalized power transmitted through $YBa_2Cu_3O_{7-\delta}$ thin films deposited by laser ablation on $LaAlO_3$ and MgO respectively. The data are normalized with respect to the transmitted power at the critical temperature T_c. The measurements of the power transmitted through the films were started at room temperature and then carried out during sample cooling. In Fig. 1, it can be observed that the rapid decrease in transmitted power occurs at T_c. This is typical of films with a high degree of homogeneity, where all the regions of the film undergo the superconducting transition simultaneously. This is not the case for the film considered in Fig. 2, for which the transmitted power starts to decrease rapidly at temperatures just below an onset temperature (~90 K) approximately 11 K above its transition temperature of 79 K. This behavior may be associated with the presence of inhomogeneities, resulting in a distribution of transition temperatures. For temperatures below T_c both films are characterized by a smooth decrease of the power transmitted through them.

The behavior shown in Figs. 1 and 2 for the power transmitted through the film-substrate combination, as a function of decreasing temperature, was also observed for the laser ablated film on ZrO_2 and for

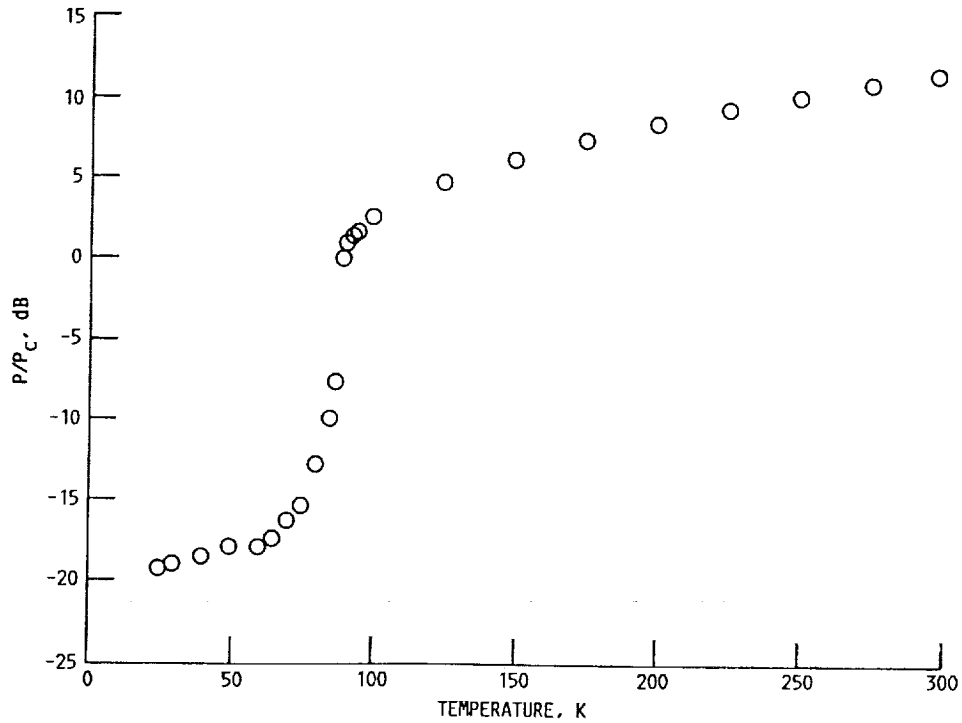

FIGURE 1. - NORMALIZED TRANSMITTED POWER VERSUS TEMPERATURE FOR A LASER ABLATED $YBa_2Cu_3O_{7-\delta}$ THIN FILM (0.7 MICRONS) ON $LaAlO_3$ AT 37.0 GHz.

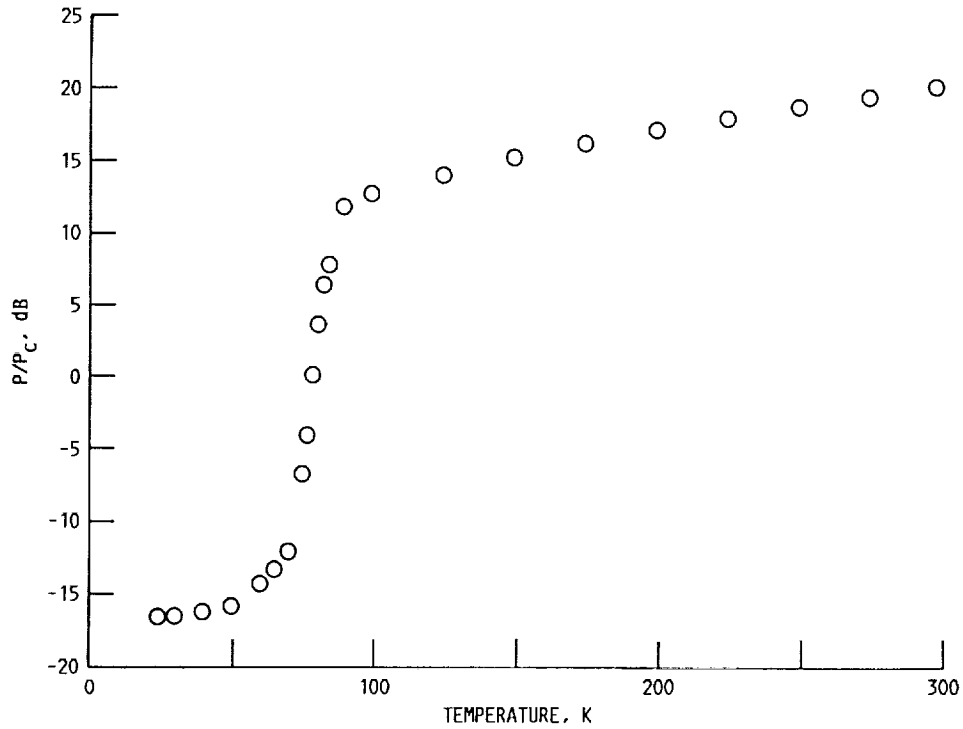

FIGURE 2. - NORMALIZED TRANSMITTED POWER VERSUS TEMPERATURE FOR A LASER ABLATED $YBa_2Cu_3O_{7-\delta}$ THIN FILM (0.2 MICRONS) ON MgO AT 28.5 GHz.

the sequentially evaporated film on MgO. For the latter film the transmission data suggest a lower film quality when compared to the film deposited on MgO by laser ablation. The films on ZrO_2 and sequentially evaporated on MgO also show a wide transition region. This temperature behavior was verified to be frequency independent for the frequencies employed in this study, and our analysis suggest that it is related to the degree of homogeneity and quality of the films.

Figures 3 to 10 and Table I, show the results for the conductivity above and below T_c, and at different frequencies, for the various films considered in this study. Figures 3 and 4 show the real and imaginary parts of the conductivity, σ_r and σ_2 respectively, corresponding to the $YBa_2Cu_3O_{7-\delta}$ film deposited on $LaAlO_3$ by laser ablation. The value for the normal conductivity at room temperature, 2.0×10^5 S/m, compares reasonably well with reported values of the dc conductivity in this type of film.[22,23] The cusp in σ_r at the transition temperature can be observed clearly in Fig. 3 and again indicates the high level of homogeneity and quality of this film. The imaginary part of the conductivity increases as a function of decreasing temperature, as can be seen in Fig. 4. Values of 5.17×10^6 S/m and 6.80×10^6 S/m are obtained at 70 and 40 K respectively. Using Eq. (8) we find $\lambda = 0.81$ μm at 70 K and $\lambda = 0.70$ μm at 40 K. From the value of λ at 40 K we found $\lambda_o = 0.69$ μm.

Figures 5 to 10 show the real and imaginary parts of the complex conductivity for the laser ablated films on MgO and ZrO_2, and for the sequentially evaporated film on MgO. Note that the normal to the superconducting transition region has been clearly identified in Figs. 5, 7 and 9. In the absence of a physical model which can account for the

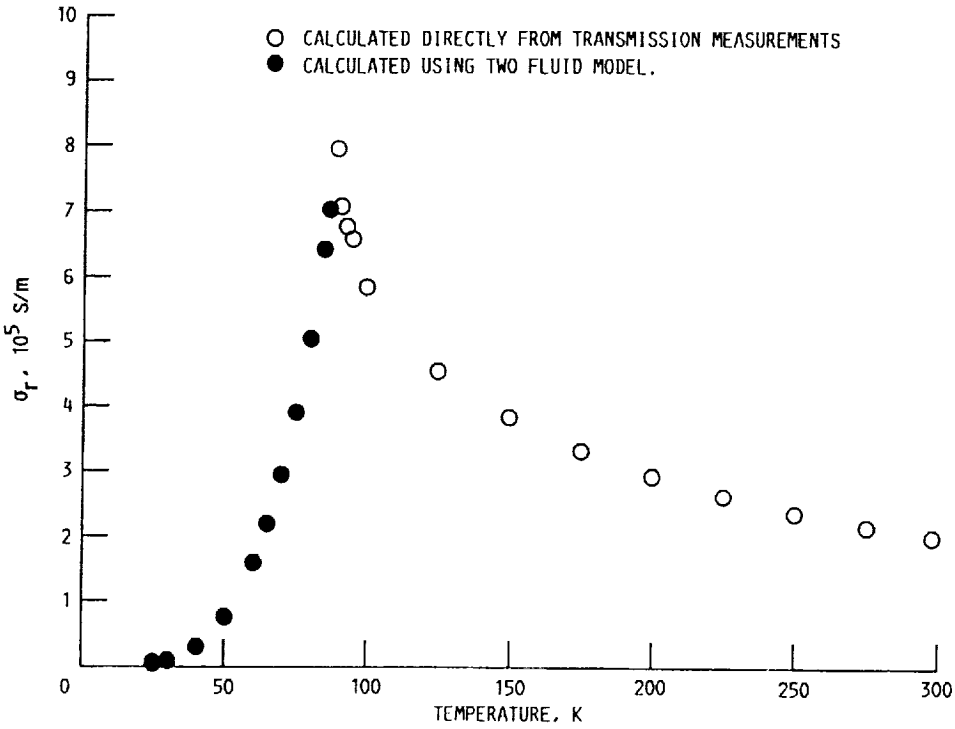

FIGURE 3. - REAL PART OF THE CONDUCTIVITY, σ_r, VERSUS TEMPERATURE FOR A LASER ABLATED $YBa_2Cu_3O_{7-\delta}$ THIN FILM (0.7 MICRONS) ON $LaAlO_3$ AT 37.0 GHz. $\sigma_r = \sigma_N$ FOR $T > T_c$ AND $\sigma_r = \sigma_1$ FOR $T < T_c$.

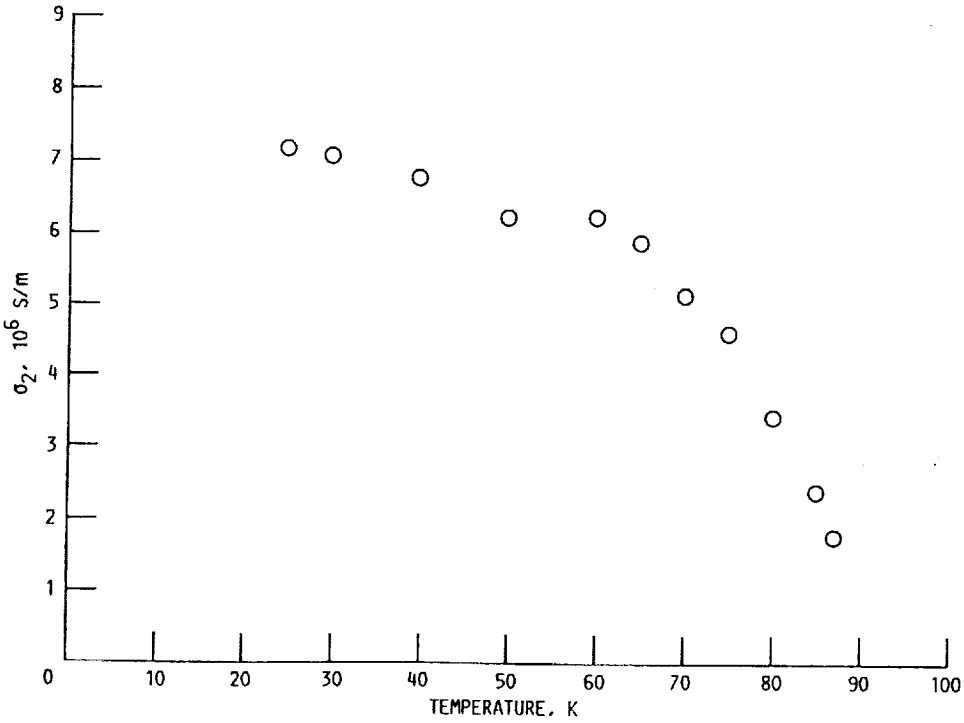

FIGURE 4. - IMAGINARY PART OF THE CONDUCTIVITY, σ_2, VERSUS TEMPERATURE FOR A LASER ABLATED $YBa_2Cu_3O_{7-\delta}$ THIN FILM (0.7 MICRONS) ON $LaAlO_3$ AT 37.0 GHz.

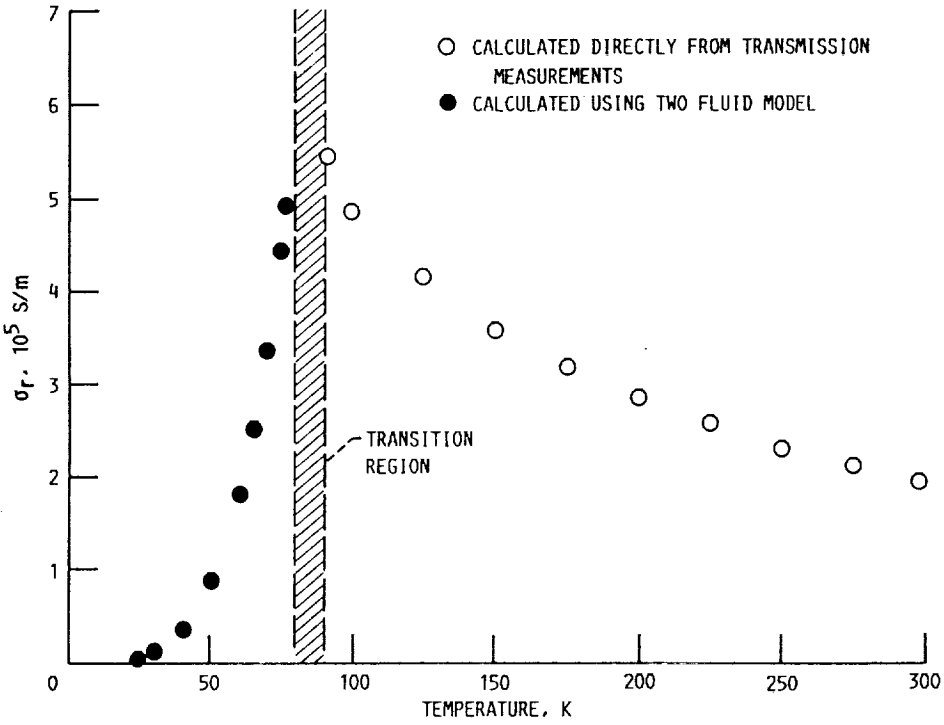

FIGURE 5. - REAL PART OF CONDUCTIVITY, σ_r, VERSUS TEMPERATURE FOR A LASER ABLATED $YBa_2Cu_3O_{7-\delta}$ THIN FILM (0.2 MICRONS) ON MgO AT 28.5 GHz. $\sigma_r = \sigma_N$ FOR $T > T_c$ AND $\sigma_r = \sigma_1$ FOR $T < T_c$.

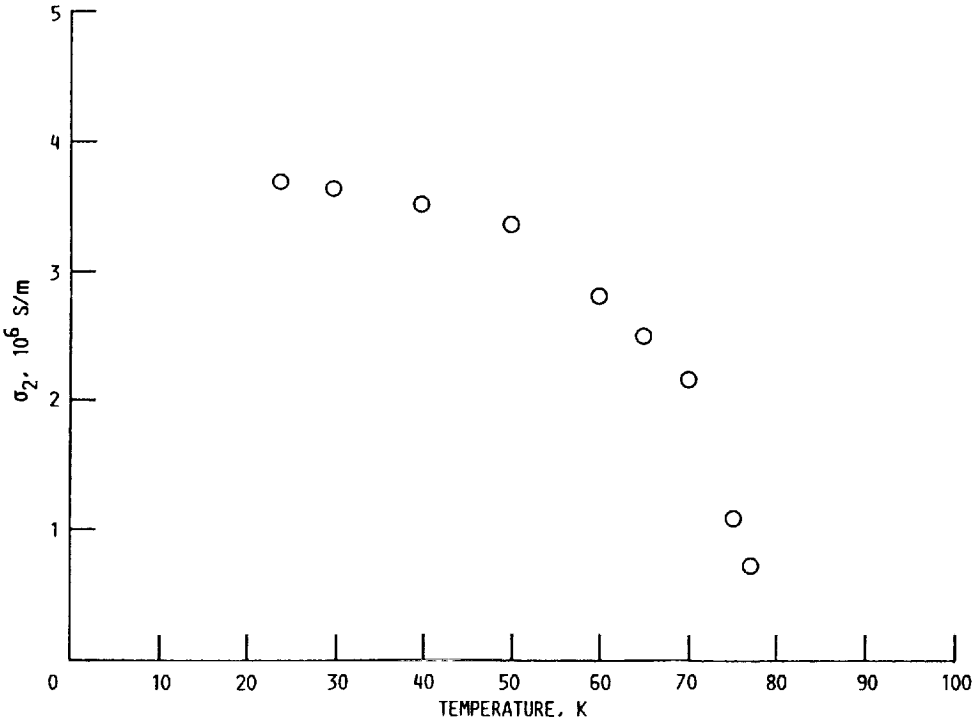

FIGURE 6. - IMAGINARY PART OF THE CONDUCTIVITY, σ_2, VERSUS TEMPERATURE FOR A LASER ABLATED $YBa_2Cu_3O_{7-\delta}$ THIN FILM (0.2 MICRONS) ON MgO AT 28.5 GHz.

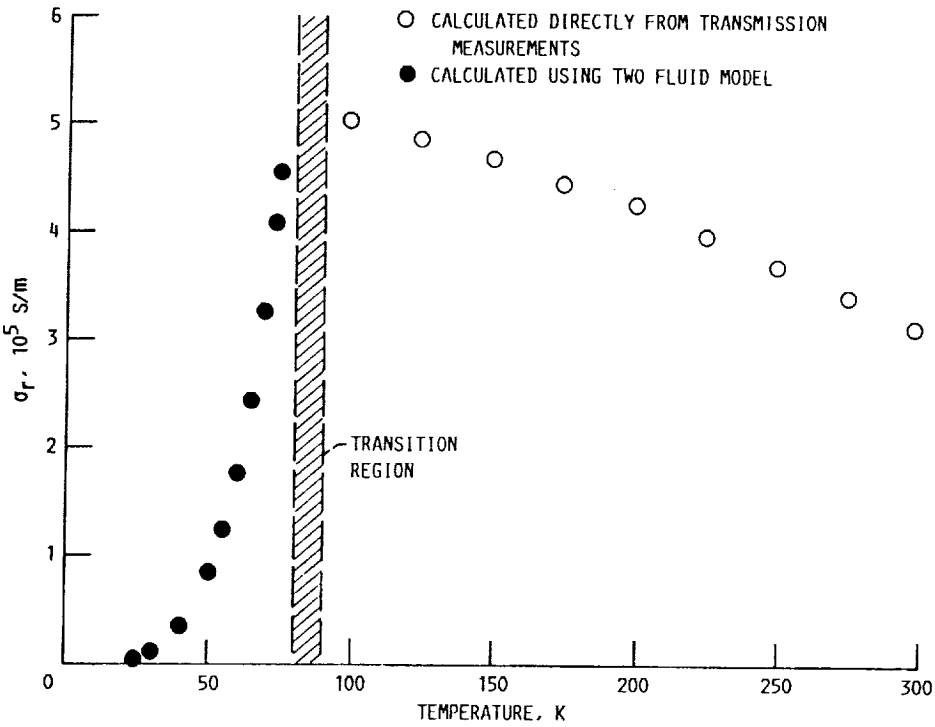

FIGURE 7. - REAL PART OF THE CONDUCTIVITY, σ_r, VERSUS TEMPERATURE FOR A LASER ABLATED $YBa_2Cu_3O_{7-\delta}$ THIN FILM (0.75 MICRONS) ON ZrO_2 AT 37.0 GHz. $\sigma_r = \sigma_N$ FOR $T > T_c$ AND $\sigma_r = \sigma_1$ FOR $T < T_c$.

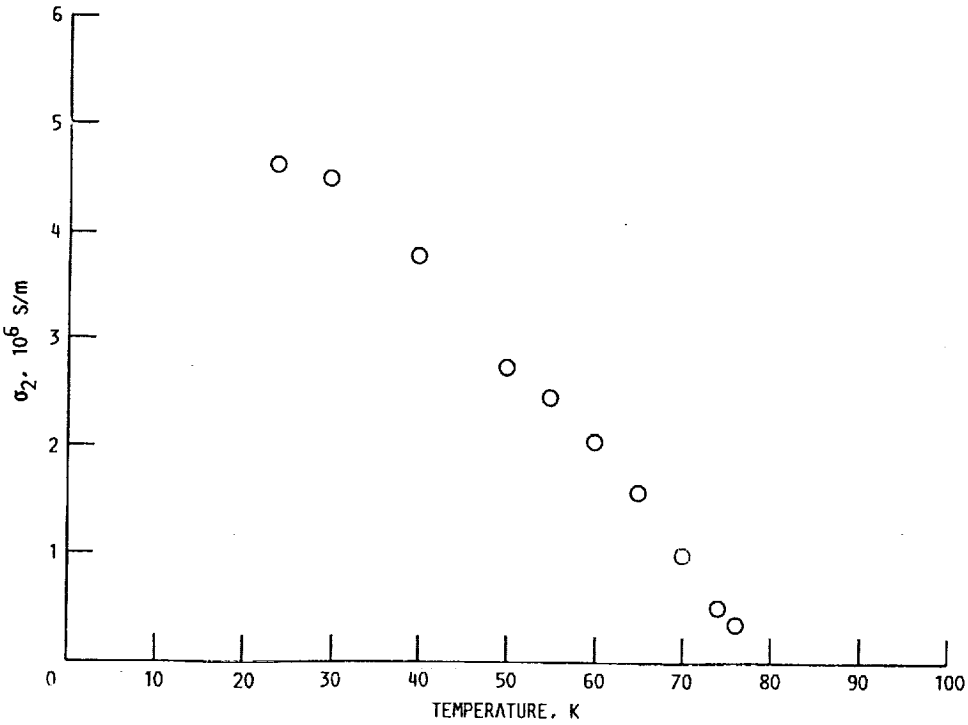

FIGURE 8. - IMAGINARY PART OF THE CONDUCTIVITY, σ_2, VERSUS TEMPERATURE FOR A LASER ABLATED $YBa_2Cu_3O_{7-\delta}$ THIN FILM (0.75 μm) ON ZrO_2AT 37.0 GHz.

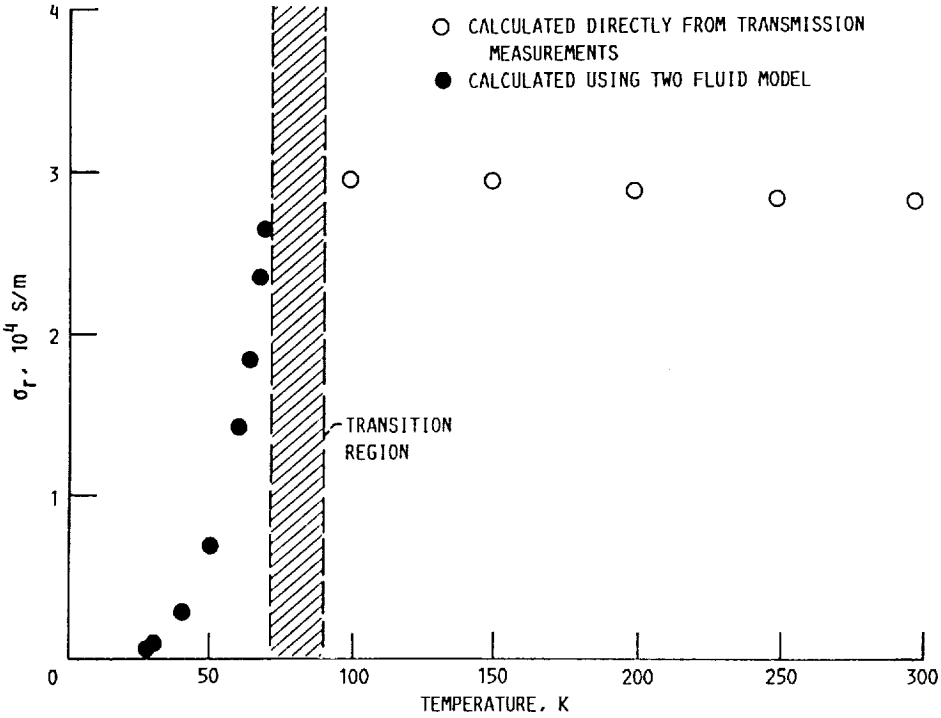

FIGURE 9. - REAL PART OF THE CONDUCTIVITY, σ_r, VERSUS TEMPERATURE FOR A SEQUENTIALLY EVAPORATED $YBa_2Cu_3O_{7-\delta}$ THIN FILM (1.0 MICRON) ON MgO AT 33.0 GHz. $\sigma_r = \sigma_N$ FOR $T > T_c$ AND $\sigma_r = \sigma_1$ FOR $T < T_c$.

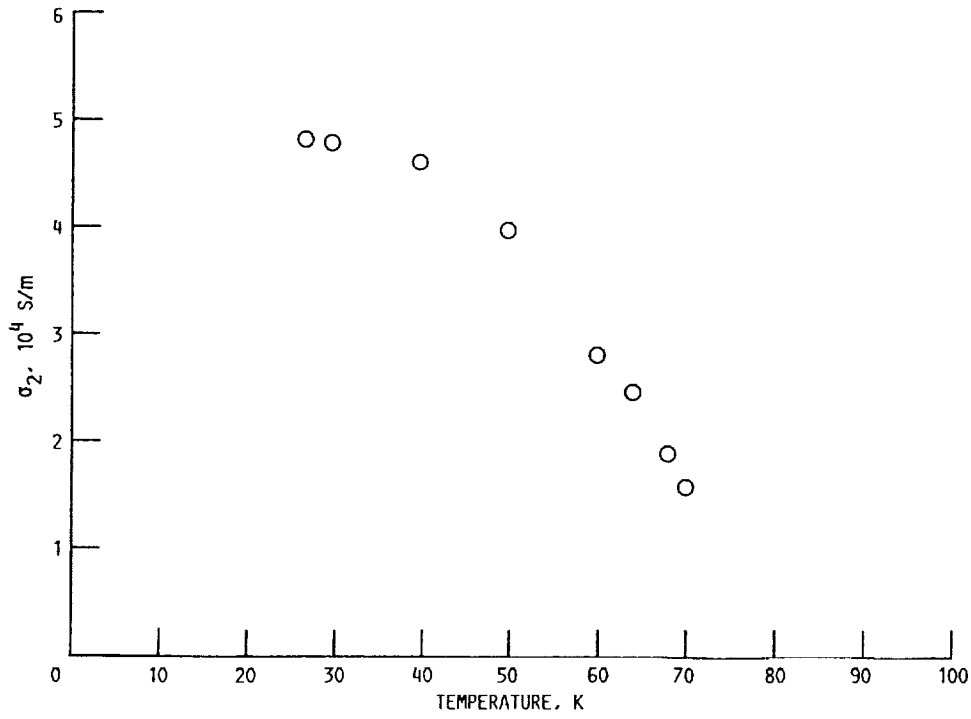

FIGURE 10. - IMAGINARY PART OF THE CONDUCTIVITY, σ_2, VERSUS TEMPERATURE FOR A SEQUENTIALLY EVAPORATED $YBa_2Cu_3O_{7-\delta}$ THIN FILM (1.0 MICRON) ON MgO AT 33.0 GHz.

TABLE I. - MILLIMETER WAVE CONDUCTIVITIES (σ_1,σ_2) AND ZERO TEMPERATURE PENETRATION DEPTH (λ_o) AT 35.0 GHz FOR $YBa_2Cu_3O_{7-\delta}$ THIN FILMS DEPOSITED ON DIFFERENT SUBSTRATES BY LASER ABLATION (LA) AND SEQUENTIAL EVAPORATION (SE)

Parameter	Substrates			
	MgO		$LaAlO_3$	ZrO_2
	SE	LA	LA	LA
σ_1 (70K)	3.0×10^4 S/m	3.9×10^5 S/m	3.3×10^5 S/m	1.7×10^5 S/m
σ_2 (70K)	1.9×10^4 S/m	1.1×10^6 S/m	6.4×10^6 S/m	1.1×10^6 S/m
σ_1 (40K)	3.1×10^3 S/m	4.1×10^4 S/m	3.5×10^4 S/m	1.9×10^4 S/m
σ_2 (40K)	7.1×10^4 S/m	4.0×10^6 S/m	7.7×10^6 S/m	3.6×10^6 S/m
λ_o	6.8 μm	0.91 μm	0.67 μm	0.96 μm

distribution of normal and superconducting material in the transition region, we can not accurately determine the normal conductivity down to the transition temperature T_c. Therefore, we have considered the critical conductivity to be the conductivity at or just above the onset temperature. Since the two fluid model approximation is based upon the assumption that the normal to the superconducting state transition is a sharp one, as for the film on $LaAlO_3$, the values of σ_1 obtained using $\sigma_c = \sigma_{onset}$ in Eq. (2) will be less than those expected for a sharp transition. The magnitude of this difference will depend upon the width ΔT of the transition region and the overall film quality. To estimate the size of the discrepancy between using σ_c at T_{onset} and σ_c at T_c, one can extrapolate σ_r above T_{onset} to T_c. When this is done, the σ_c obtained is 12 percent larger for the laser ablated film on MgO, 3.3 percent for the laser ablated film on ZrO_2 and 1.7 percent larger for the sequentially evaporated film on MgO. In the better films the discrepancy between σ_{onset} and the extrapolated value of σ_r at T_c, is larger due to the larger slope of σ_r for temperatures above the onset temperature as can be seen in Figs. 5, 7, and 9. This discrepancy becomes smaller as T_{onset} nears T_c, as for the film on $LaAlO_3$.

Figures 6, 8 and 10 show the imaginary part of the complex conductivity for the laser ablated films on MgO and ZrO_2, and for the sequentially evaporated film on MgO. Using Eq. (8) we obtain values for λ of 1.1, 0.95, and 9.1 μm, at 40 K, for the laser ablated films on MgO and ZrO_2 and for the sequentially evaporated film on MgO respectively. Additional values for the conductivities and for λ_o at 35.0 GHz are given in Table I. The value for λ_o obtained for the laser ablated film on $LaAlO_3$, compares favorably with that reported by Kobrin, et al.[24] ($\lambda_o \sim 0.48$ μm, at 60.0 GHz) for ion-beam sputtered $YBa_2Cu_3O_{7-\delta}$ films on $LaAlO_3$.

CONCLUSIONS

Millimeter wave power transmission studies have been performed on $YBa_2Cu_3O_{7-\delta}$ thin films at frequencies within the frequency range from 26.5 to 40.0 GHz and at temperatures from 20 to 300 K. The normal, σ_N, and complex, $\sigma_1 - i\sigma_2$, conductivities have been determined for laser ablated films on $LaAlO_3$, MgO and ZrO_2. The conductivities of films on MgO grown by laser ablation and sequential evaporation have been compared. From the results obtained in this study, it is apparent that at least for films deposited on MgO, films deposited by laser ablation appear to have a higher quality than those deposited by the sequential evaporation technique. We have also shown that millimeter wave transmission and conductivity measurements can be used as a test of thin film quality. It was observed that for a film with a narrow transition region, the two fluid model should be more applicable than for those films with a wide transition region. Finally, values for the zero-temperature magnetic penetration depth have been determined from the obtained values of σ_2 .

ACKNOWLEDGMENT

The authors are pleased to acknowledge helpful suggestions by Dr. S. Sridhar and Dr. J. Halbritter. Our thanks to Dr. S. Alterovitz, Dr. M. Stan and Dr. T. Eck for helpful discussions.

REFERENCES

1. Hartwig, W.; and Passow, C.: RF Superconducting Devices -- Theory, Design, Performance, and Applications. Applied Superconductivity, vol. 2, V.L. Newhouse, ed., Academic Press, New York, 1975, pp. 541-639.

2. Martens, J.S.; Beyer, J.B.; and Ginley, D.S.: Microwave Surface Resistance of $YBa_2Cu_3O_{6.9}$ Superconducting Films. Appl. Phys. Lett., vol. 52, no. 21, 23 May 1988, pp. 1822-1824.

3. Carini, J.P., et al.: Millimeter-Wave Surface Resistance Measurements in Highly Oriented $YBa_2Cu_3O_{7-\delta}$ Thin Films. Phys. Rev. B, vol. 37, no. 16, 1 June 1988, pp. 9726-9729.

4. Newman, H.S., et al.: Microwave Surface Resistance of Bulk Tl-Ba-Ca-Cu-O Superconductors. Appl. Phys. Lett., vol. 54, no. 4, 23 Jan. 1989, pp. 389-390.

5. Klein, N., et al.: Millimeter-Wave Surface Resistance of Epitaxially Grown $YBa_2Cu_3O_{6-x}$ Thin Films. Appl. Phys. Lett., vol. 54, no. 8, 20 Feb. 1989, pp. 757-759.

6. Sridhar, S.; Shiffman, C.A.; and Handed, H.: Electrodynamic Response of $Y_1Ba_2Cu_3O_y$ and $La_{1.85}Sr_{0.15}CuO_{u-s}$ in the Superconducting State. Phys. Rev. B, vol. 36, no. 4, 1 Aug. 1987, pp. 2301-2304.

7. Cohen, L., et al.: Surface Impedance Measurements of Superconducting $YBa_2Cu_3O_{6+x}$. J. Phys. F: Met. Phys., vol. 17, 1987, pp. L179-L183.

8. Ho, W., et al.: Millimeter-Wave Complex-Conductivity Measurements of Bi-Ca-Sr-Cu-O Superconducting Thin Films. Phys. Rev. B, vol. 38, no. 10, 1 Oct. 1988, pp. 7029-7032.

9. Nichols, C.S., et al.: Microwave Transmission Through Films of $YBa_2Cu_3O_{7-\delta}$. To be published in Phys. Rev. B.

10. Tyagi, S., et al.: Low-Field AC Susceptibility and Microwave Absorption in YBaCuO and BiCaSrCuO Superconductors. Physica C, vol. 156, 1988, pp. 73-78.

11. Maxwell, E.; Marcus, P.M.; and Slater, J.C.: Surface Impedance of Normal and Superconductors at 24,000 Megacycles per Second. Phys. Rev. vol. 76, no. 9, 1 Nov. 1949, pp. 1332-1347.

12. Pippard, A.B.: The Surface Impedance of Superconductors and Normal Metals at High Frequencies. Proc. R. Soc. A, vol. 203, no. 1072, 7 Sept. 1950, pp. 98-118.

13. Gittleman, J.I.; and Bozowski, S.: Transition of Type-I Superconducting Thin Films in a Perpendicular Magnetic Field: A Microwave Study. Phys. Rev., vol. 161, no. 2, 10 Sept., 1967, pp. 398-403.

14. Durny, R., et al.: Microwave Absorption in the Superconducting and Normal Phases of Y-Ba-Cu-O. Phys. Rev. B, vol. 36, no. 4, 1 Aug. 1987, pp. 2361-2363.

15. Tyagi, S., et al.: Frequency Dependence of Magnetic Hysteresis in the Field-Induced Microwave Absorption in High-T_c Superconductors at $T << Tc$. To be published in Phys. Lett. A.

16. Jackson, E.M., et al.: Study of Microwave Power Absorption in Yttrium-Barium-Copper Based High Temperature Superconductors and Allied Compounds. To be published in Supercond. Sci. Technol.

17. Gittleman, J.I.; and Rosemblum, B.: Microwave Properties of Superconductors. IEEE Proc., vol. 52, no. 10, Oct. 1964, pp. 1138-1147.

18. Glover III, R.E.; and Tinkham, M.: Conductivity of Superconducting Films for Photon Energies Between 0.3 and 40 KTc. Phys. Rev., vol. 108, no. 2, 15 Oct. 1957, pp. 243-256.

19. J.D. Warner, J.E. Meola and K.A. Jenkins: "Study of Deposition of YBa2Cu3O7-x on Cubic Zirconia," NASA TM-102350 (1989).

20. G.J. Valco, N.J. Rohrer, J.D. Warner and K.B. Bhasin: "Sequentially Evaporated Thin Y-Ba-Cu-O Superconducting Films on Microwave Substrates" NASA TM-102068 (1989).

21. Miranda, F.A., et al.: Measurements of Complex Permittivity of Microwave Substrates in the 20 to 300 K Temperature Range From 26.5 to 40.0 GHz. NASA TM-102123, 1989.

22. Gurvitch, M.; and Fiory, A.T.: Resistivity of $La_{1.825}Sr_{0.175}CuO_4$ and $YBa_2Cu_3O_7$ to 1100K: Absence of Saturation and Its Implications. Phys. Rev. Lett., vol. 59, no. 12, 21 Sept. 1987, pp. 1337-1340.

23. Collins, R.T., et al.: Comparative Study of Superconducting Energy Gaps in Oriented Films and Pollycrystalline Bulk Samples of Y-Ba-Cu-O. Phys. Rev. Lett., vol. 59, no. 6, 10 Aug. 1987, pp. 704-707.

24. Kobrin, P.H., et al.: Millimeter-Wave Complex Conductivities of Some TlBaCaCuO and $YBa_2Cu_3O_{7-f}$ Films, Presented at the M^2s-HTSC Conference, Stanford, CA, July 24-28, 1989. To be published in Physica C.

NASA Technical Memorandum 102123

Measurements of Complex Permittivity of Microwave Substrates in the 20 to 300 K Temperature Range From 26.5 to 40.0 GHz

Felix A. Miranda and William L. Gordon
Case Western Reserve University
Cleveland, Ohio

and

Vernon O. Heinen, Ben T. Ebihara,
and Kul B. Bhasin
Lewis Research Center
Cleveland, Ohio

Prepared for the
1989 Cryogenic Engineering Conference
sponsored by the University of California, Los Angeles
Los Angeles, California, July 24–28, 1989

NASA

MEASUREMENTS OF COMPLEX PERMITTIVITY OF MICROWAVE SUBSTRATES IN THE 20 TO 300 K TEMPERATURE RANGE FROM 26.5 TO 40.0 GHz

Felix A. Miranda and William L. Gordon
Case Western Reserve University
Cleveland, Ohio

Vernon O. Heinen, Ben T. Ebihara, and Kul B. Bhasin
National Aeronautics and Space Administration
Lewis Research Center
Cleveland, Ohio

SUMMARY

A knowledge of the dielectric properties of microwave substrates at low temperatures is useful in the design of superconducting microwave circuits. In this paper, we report the results of a study of the complex permittivity of sapphire (Al_2O_3), magnesium oxide (MgO), silicon oxide (SiO_2), lanthanum aluminate ($LaAlO_3$), and zirconium oxide (ZrO_2), in the 20 to 300 K temperature range, at frequencies from 26.5 to 40.0 GHz. The values of the real and imaginary parts of the complex permittivity were obtained from the scattering parameters, which were measured using a HP-8510 automatic network analyzer. For these measurements, the samples were mounted on the cold head of a helium gas closed cycle refrigerator, in a specially designed vacuum chamber. An arrangement of wave guides, with mica windows, was used to connect the cooling system to the network analyzer. A decrease in the value of the real part of the complex permittivity of these substrates, with decreasing temperature, was observed. For MgO and Al_2O_3, the decrease from room temperature to 20 K was of 7 and 15 percent, respectively. For $LaAlO_3$, it decreased by 14 percent, for ZrO_2 by 15 percent, and for SiO_2 by 2 percent, in the above mentioned temperature range.

E-4903-1

INTRODUCTION

The successful application of thin films, made with the new high temperature superconductor oxides, in the development of microwave circuits, rest considerably on the dielectric properties of the different substrates used for film deposition. For microwave applications, it is desirable to have substrates with low dielectric constant and loss tangent, (ref. 1) if good performance from microwave components is expected.

Until now, Y-Ba-Cu-O films deposited on $SrTiO_3$, have shown the highest quality when compared with films deposited on other substrates. Nevertheless, due to its extremely temperature dependent dielectric constant, with a value for 300 at room temperature, around 1000 at 77 K, and over 18000 at helium temperatures, and its considerably high loss tangent, (ref. 2) its microwave applicability is rather limited. Although other materials as MgO, $LaAlO_3$, and ZrO_2 are now being used as substrates, information about their dielectric properties at temperatures below room temperature, and for some of them even at room temperature, is rather scarce.

In this paper, we report on the measurements of the microwave complex permittivity of MgO, Al_2O_3, $LaAlO_3$, ZrO_2, and SiO_2, in the 20 to 300 K temperature range and as a function of frequency. The measurements were taken following a method previously reported by other authors (refs. 3 to 5). This method allows the determination of both parts of the complex permittivity in a rather simple way, and is very convenient for cases in which a fast determination of the dielectric constant of a material is needed. Nevertheless, the method has a high uncertainty in the measurement of the imaginary part of the complex permittivity for materials with very low loss tangent.

ANALYSIS

In order to determine the value of the real and imaginary parts of the complex permittivity for the various substrates under consideration, we have followed the method proposed by Nicolson and Ross, (ref. 3) as modified by Wier, (ref. 4) and following the implementation suggestions of reference 5. In an ideal case, consider a piece of material installed in a rectangular wave guide with characteristic impedance Zo, as shown in figure 1.

After solving the corresponding boundary conditions at $x = 0$ and $x = d$, the scattering parameters, $S_{11}(\omega)$ and $S_{21}(\omega)$, can be related with the reflection, Γ, and transmission, T, coefficients, as follows,

$$S_{11} = \frac{(1 - T^2)\Gamma}{1 - \Gamma^2 T^2}, \qquad S_{21} = \frac{(1 - \Gamma^2)T}{1 - \Gamma^2 T^2} \tag{1}$$

The reflection coefficient, when the length of the material is infinite, is given by

$$\Gamma = \frac{Z - Z_o}{Z + Z_o} = \frac{\sqrt{\frac{\mu r}{\epsilon r}} - 1}{\sqrt{\frac{\mu r}{\epsilon r}} + 1} \tag{2}$$

Also, the transmission coefficient, when the length of the material is finite, is given by,

$$T = \exp(-j\omega \sqrt{\mu\epsilon}\, d) = \exp[(-j\omega/c) \sqrt{\mu_r \epsilon_r}\, d] \tag{3}$$

Thus, the reflection and transmission coefficients can be derived by measuring $S_{11}(\omega)$ and $S_{21}(\omega)$, and in turn they can be used to obtain the value of the permittivity.

The experimental configuration used for the measurements of the reflection, $S_{11}(\omega)$, and transmission, $S_{21}(\omega)$, scattering parameters for the samples under consideration, is shown in figure 2. The measurements were made using an HP-8510 automatic network analyzer, properly connected by an arrangement of Ka-band (26.5 to 40.0 GHz) wave guides, to a cooling system. The cooling system consist of a CTI-Cryogenics closed cycle helium refrigerator, associated with a Lake Shore Cryotronics temperature controller, model DRC 91C, which allows measurements to be taken at the required low temperatures.

The measurements were performed under vacuum ($<10^{-3}$ torr), in an aluminum vacuum chamber specifically designed to fit on the top of the external shield of the refrigerator and to give access to the set up of wave guides connecting the network analyzer with the refrigerator. In order to preserve the vacuum inside the chamber, two mica windows were placed at its ends. The material for the windows was selected due to its very low loss and transparency in this frequency range.

In order to measure the scattering parameters, the sample was held in a sample holder which was suspended between two wave guide flanges, as shown in figure 3. The wave guide flanges were in direct contact with a copper plate, which in turn was attached to the cold head of the refrigerator. The two supporting wave guides inside the vacuum chamber, were specially designed to be used at low temperatures. They are made of stainless steel, a relatively poor thermal conductor. A gold plating of their internal surfaces was performed, in order to reduced the microwave losses. Finally, in an attempt to reduce the errors induced in the measurements, possibly due to linear thermal contractions of the wave guides as the temperature decreases, the system was calibrated at all the temperatures at which measurements were taken. These calibrations were stored, so that they could be recalled to be used in later measurements.

RESULTS

The thickness of the substrates used in this study, varies from 0.285 mm for MgO, to 1.641 mm for SiO_2. The thicknesses for the Al_2O_3, $LaAlO_3$, and ZrO_2 samples are 0.496 mm, 0.432 mm, and 0.494 mm respectively. Figures 4 to 7 and table I show the measurement results for the real part of the complex permittivity of the samples, at room temperature and at 20 K. The value for the dielectric constant of MgO at room temperature agrees well with values quoted by other researchers (refs. 6, 7, 9). For Al_2O_3 and SiO_2, the values of the dielectric constant obtained at room temperature, are also in good agreement with the values quoted by Zahopoulos (ref. 8) and Von Hippel (ref. 7) respectively. Although for ZrO_2 there appear to be no data for comparison in this frequency range, the value for its dielectric constant at room temperature is consistent with the one reported by Gorshunov, et al., (ref. 9) at frequencies within 10^{11} to 10^{12} Hz. In the case of $LaAlO_3$, the value obtained for its dielectric constant at room temperature is not consistent with the value of 15.3 reported by Simon, et al. (ref. 1). Due to this discrepancy, measurements were performed in four different $LaAlO_3$ samples, each one made from different batches, in order to determine if the disagreement was due to intrinsic properties of the sample. The value of the dielectric constant obtained from these measurements was practically the same for all the samples and was consistent with our previously determined value. Nevertheless, since not much information for the value of the dielectric constant of this substrate is available yet, additional experimental verification will be appropriate.

Table I shows the real and imaginary parts of the complex permittivity, at four different temperatures and at 32.9 GHz. A decrease in the value of the real part of the complex permittivity is clearly observed in all the substrates under consideration. For MgO and Al_2O_3, a decrease of 6 and 14 percent down to 70 K, and of 7 and 15 percent down to 20 K respectively, is observed. For $LaAlO_3$ and ZrO_2, the value of the real part of the complex permittivity is lowered by 10 and 13 percent respectively, at temperatures around 70 K, and

goes down 14 percent for $LaAlO_3$ and 15 percent for ZrO_2, at 20 K. For SiO_2, the dielectric constant is lowered by 1 percent at 70 K and by 2 percent for temperatures around 20 K.

From comparison of the data of table I with that of the references mentioned, it can be seen that there is relatively good agreement for the real part of the complex permittivity but wider variation for the imaginary part. For example, a comparison of the value for the loss tangent for MgO at room temperature, 8×10^{-2}, obtained from the data in table I, with the value quoted by Von Hippel, 3×10^{-4}, reveals a difference of two orders of magnitude. Due to this fact, it is very difficult to observe a particular temperature and frequency dependence for this parameter. This is an intrinsic limitation of the technique, when applied in the calculation of the imaginary part of the complex permittivity for materials of low loss tangent, as mentioned in the introduction.

The frequency of 32.9 GHz was selected for construction of table I as being typical of the largest variations with temperature. Finally, for these measurements, the statistical error in the real part of the complex permittivity is ± 0.02, while the variation in the imaginary part is larger.

CONCLUSIONS

The real and imaginary parts of the complex permittivity for MgO, Al_2O_3, $LaAlO_3$, ZrO_2 and SiO_2 have been measured. A decrease in the value of the real part of the complex permittivity, with decreasing temperature, was observed in all the substrates. Nevertheless, no considerable change was observed as a function of frequency. The results obtained in this study show that, at least from the stand point of the dielectric constant, the substrates considered appear to be better suited than $SrTiO_3$, for use with the new high temperature superconductors in microwave applications.

REFERENCES

1. Simon, R.W., et al.: Low-Loss Substrate for Epitaxial Growth of High-Temperature Superconductor Thin Films. Appl. Phys. Lett., vol. 53, Dec. 26, 1988, pp. 2677-2679.

2. Padamsee, H., Green, K., Gruschus, J., Kirchgessner, J., Moffat, D., Rubin, D.L., Sears, J., Shu, Q.S., Buhrman, R., Lathrop, D., Noh, T.W., Russek, S., and Sievers, A.: "Superconductivity and Applications" (To be published).

3. Nicolson, A.M.; and Ross, G.F.: Measurement of the Intrinsic Properties of Materials by Time Domain Techniques. IEEE Trans. Instrum. Meas., vol. 19, no. 4, Nov. 1970, pp. 377-382.

4. Weir, W.B.: Automatic Measurement of Complex Dielectric Constant and Permeability at Microwave Frequencies. Proc. IEEE, vol. 62, no. 1, Jan. 1974, pp. 33-36.

5. Hewlett Packard Product Note No. 8510-3, The Measurement of Both Permittivity and Permeability of Solid Materials. pp. 5954-1535 (1985).

6. Hossain, M.D.: Microwave Dielectric Properties of Ti^{4+}/MgO and Ni^{2+}/MgO. Appl. Phys. A., vol. 36, no. 1, Jan. 1985, pp. 63-65.

7. Von Hippel, A.R.: Dielectric Materials and Applications. The MIT Press, Cambridge, MA, 1954.

8. Zahopoulos, C., Kennedy, W.L.; and Sridhar, S.: Performance of a Fully Superconducting Microwave Cavity Made of the High Tc Superconductor $Y_1Ba_2Cu_3O$. Appl. Phys. Lett., vol. 52, no. 25, June 20, 1988, pp. 2168-2170.

9. Gorshunov, B.P., et al.: Submillimetre Properties of High-Tc Superconductors. Physica C, vol. 153-155, pt. 1, 1988, pp. 667-668.

TABLE I. - COMPLEX PERMITTIVITY OF MICROWAVE SUBSTRATES AT 32.9 GHz

[ϵ'_r = real part of complex permittivity. ϵ''_r = imaginary part of complex permittivity.]

Substrate	MgO		Al_2O_3		$LaAlO_3$		ZrO_2		SiO_2	
Temperature, K	ϵ'_r	ϵ''_r	ϵ'_r	ϵ''_r	ϵ'_r	ϵ''_r	ϵ'_r	ϵ''_r	ϵ'_r	ϵ''_r
300	9.88	0.556	9.51	0.675	21.9	1.70	25.4	1.72	3.82	0.516
150	9.45	.726	8.52	.925	21.6	1.48	23.6	1.75	3.80	.159
70	9.26	.351	8.19	.695	19.7	2.98	22.0	2.50	3.78	.688
20	9.19	.420	8.11	.613	18.8	3.71	21.6	2.23	3.75	.298

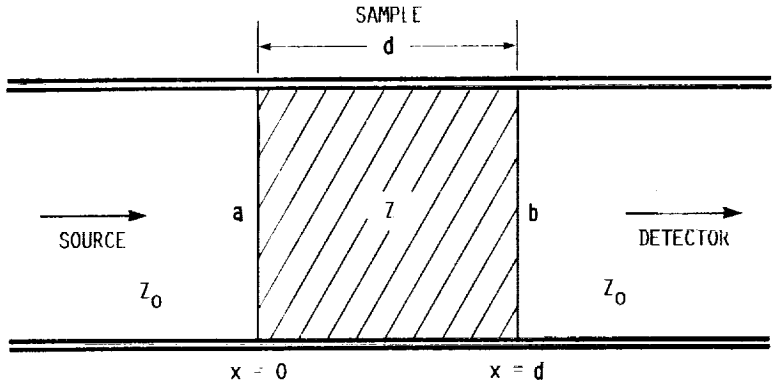

FIGURE 1. - WAVEGUIDE WITH FILLED MATERIAL.

ORIGINAL PAGE
BLACK AND WHITE PHOTOGRAPH

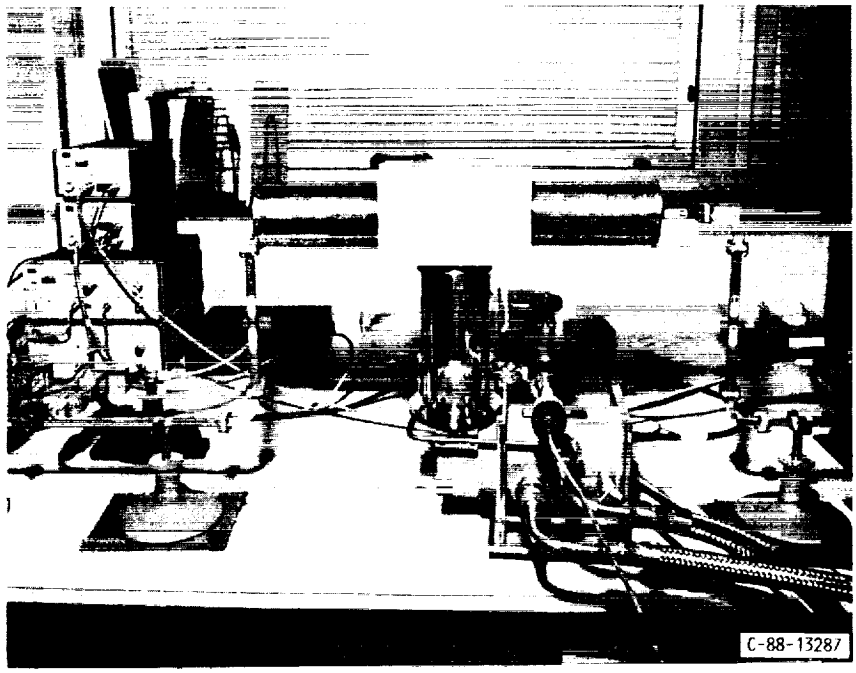

FIGURE 2. - EXPERIMENTAL SETUP.

ORIGINAL PAGE IS
OF POOR QUALITY

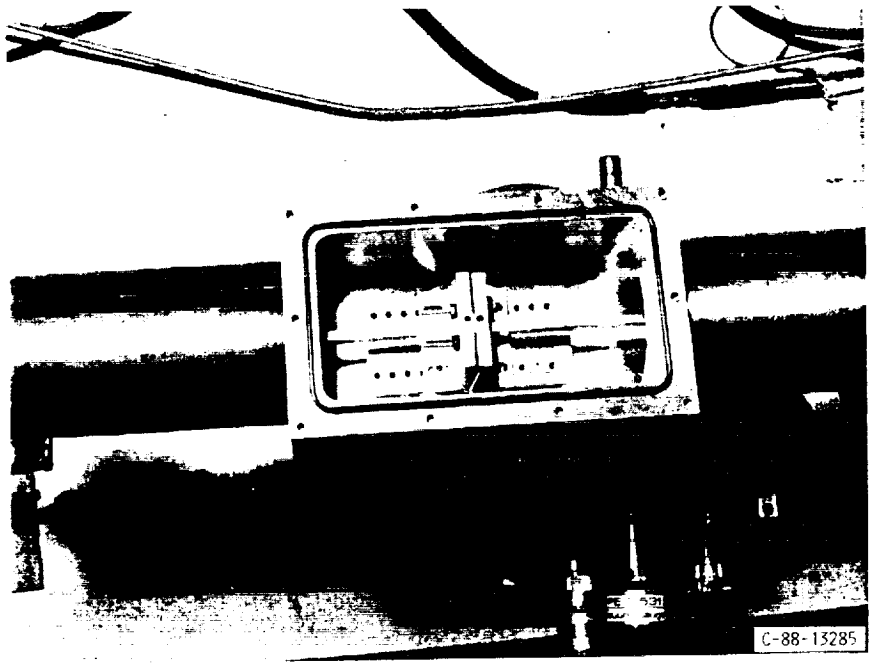

FIGURE 3. - SAMPLE SUSPENSION SETUP.

ORIGINAL PAGE
BLACK AND WHITE PHOTOGRAPH

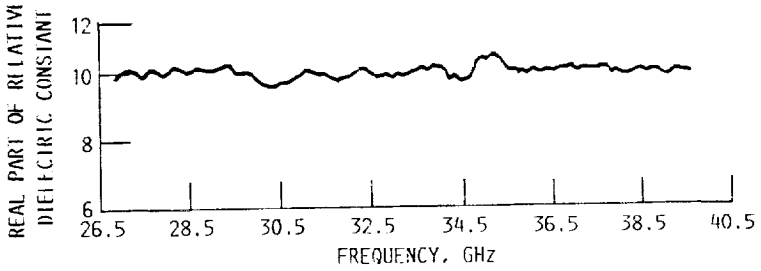

FIGURE 4. - MgO SUBSTRATE AT ROOM TEMPERATURE.

ORIGINAL PAGE IS
OF POOR QUALITY

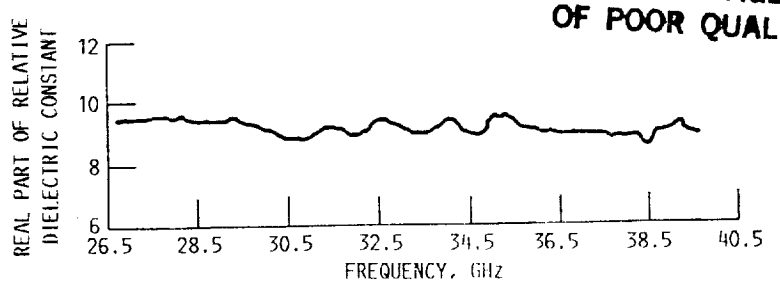

FIGURE 5. - MgO SUBSTRATE AT 20 K.

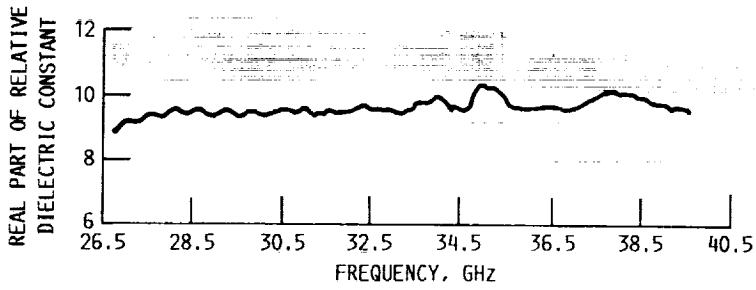

FIGURE 6. - SAPPHIRE SUBSTRATE AT ROOM TEMPERATURE.

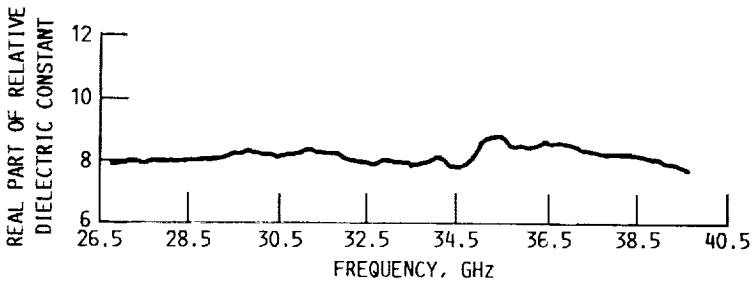

FIGURE 7. - SAPPHIRE SUBSTRATE AT 20 K.

NASA Technical Memorandum 102571

Millimeter Wave Surface Resistance of $RBa_2Cu_3O_{7-\delta}$ (R = Y,Eu,Dy,Sm,Er) Superconductors

F.A. Miranda, W.L. Gordon, and T.G. Eck
Case Western Reserve University
Cleveland, Ohio

K.B. Bhasin, J.D. Warner and K.A. Jenkins
Lewis Research Center
Cleveland, Ohio

Prepared for the
March Meeting of the American Physical Society
Anaheim, California, March 12–16, 1990

NASA

MILLIMETER WAVE SURFACE RESISTANCE OF $RBa_2Cu_3O_{7-\delta}$ (R = Y,Eu,Dy,Sm,Er) SUPERCONDUCTORS

F.A. Miranda, W.L. Gordon, and T.G. Eck
Department of Physics
Case Western Reserve University
Cleveland, Ohio 44106

K.B. Bhasin, J.D. Warner, and K.A. Jenkins
National Aeronautics and Space Administration
Lewis Research Center
Cleveland, Ohio 44135

E-5395

SUMMARY

We report on the measurements of the millimeter wave surface resistance (R_S) at 58.6 GHz of bulk samples of $RBa_2Cu_3O_{7-\delta}$ (R = Y,Eu,Dy,Sm,Er) and of $YBa_2Cu_3O_{7-\delta}$ superconducting films, in the temperature range from 20 to 300 K. The bulk samples were prepared by cold pressing the powders of $RBa_2Cu_3O_{7-\delta}$ into 1 in. diameter disks which were sintered at 925 °C in one atmosphere of oxygen. The thin films were deposited on $SrTiO_3$ and $LaGaO_3$ substrates by pulsed laser ablation. Each sample was measured by replacing the end wall of a gold-plated TE_{013} circular mode copper cavity with the sample and determining the cavity quality factor Q. From the difference in the Q-factor of the cavity, with and without the sample, the R_S of the sample was determined.

INTRODUCTION

Investigation of the properties of the high transition temperature (T_c) superconductors at millimeter wave frequencies is important not only to evaluate their potential for practical microwave applications but also in an attempt to determine the extent to which the standard microscopic theories are able to describe the phenomena of superconductivity in these new materials. From the application point of view, the main interest is to determine how well these materials will perform when implemented to transmission lines and microwave devices in comparison with the most commonly used normal metals (Cu and Au) and lower T_c superconductors currently in use. A parameter which directly provides this information is the surface resistance (R_S). To date, a considerable amount of work has been done on measurements of the R_S both in bulk and thin film high T_c superconductors at different temperatures and frequencies (refs. 1 to 6). Nevertheless, to the best of our knowledge, no measurements of R_S have been reported at frequencies around 60 GHz. In this paper, we report on the measurements of the surface resistance of R-Ba-Cu-O (R = Y,Eu,Dy, Sm,Er) bulk superconductors and $YBa_2Cu_3O_{7-\delta}$ superconducting thin films at 58.6 GHz and at temperatures from 20 to 300 K.

EXPERIMENTAL

The bulk samples were made from cold pressed (20,000 psi) sintered powders made from starting powders of BaO_2 (99.89 percent pure), CuO (99.99 percent pure) and R_2O_3 (R = Y,Eu,Dy,Sm,Er), (99.99 percent pure). The powders were ground together by hand, fired at 925 °C in flowing oxygen (O_2, 99.995 percent pure) for 6 hr, and were cooled to 450 °C at the rate of 2 °C/min. The material was then held at 450 °C for 6 hr before being cooled to room temperature at 2 °C/min. Afterwards, the powders were reground and refired using the same procedure. After the second firing x-ray diffraction showed that the powders were in the superconducting phase. Then the powders were ground and pressed into disks of 1 in. diameter and 1/4-in. thickness and fired at 925 °C.

The pulsed laser ablation technique used for the deposition of the film is similar to that used by other researchers (refs. 7 and 8). The deposition was performed at a substrate temperature of 750 °C at an ambient oxygen pressure of 170 mtorr. The laser wavelength was 248 nm, the pulse length was 20 to 30 ns, and the pulse rate was 4 pps. During deposition, the distance between the target and the sample was kept at 7.5 cm and the laser fluence on the target was maintained at 2.0 J/cm^2 per pulse. During this process, the laser beam was scanned up and down 1 cm over the target using an external lens on a translator. At the end of the deposition process, the oxygen pressure was raised to 1 atm, and the temperature was lowered to 450 °C at a rate of 2 °C/min. The temperature was held at 450 °C for 2 hr before it was lowered to 250 °C at a rate of 2 °C/min. The heater power was turned off and the sample was allowed to cool down to 40 °C or less before it was removed from the chamber. A more detailed description of the deposition technique is given in reference 9.

Surface resistance measurements of both types of samples were made at 58.6 GHz applying the same experimental technique. Using an HP-8510 network analyzer and Ginzton's impedance method (refs. 10 and 11) the Q-factor of the cavity was determined from the reflection coefficient. In each case the end wall of the cylindrical cavity (TE_{013} mode) was replaced by the superconducting sample, and R_s was calculated from the difference in Q values of the bare cavity and the cavity with the sample in place. All the measurements were taken at temperatures from 20 to 300 K, and under a vacuum of less than 10 mtorr.

RESULTS

The dc resistance versus temperature measurements were performed using a standard four probe method. For the bulk samples the transition temperatures (T_c, $R_{dc} = 0$) were distributed between 91.8 K (Eu-Ba-Cu-O) to 79.0 K (Y-Ba-Cu-O and Sm-Ba-Cu-O), as can be seen from dc resistance versus temperature curves shown in figures 1(a) and (b). All the samples had densities from 50 to 60 percent of the ideal, and from SEM micrographs grain sizes of approximately 5 μm were observed. Figure 2 exhibits the measured Q-factor for the cavity as a function of temperature for cases in which its end wall had been replaced by each of the bulk samples under study. It is observed that the Y, Eu, and Dy based samples show a clear increase of the Q-factor at temperatures below T_c, while a rather discrete change is noticed for the Sm-based sample. No change in the rate of increase of Q with decreasing temperature, at temperatures below T_c, is observed for the Er-Ba-Cu-O sample.

Therefore, these observations appear to suggest that although the cold pressing method yields bulk samples with reasonably good T_c values, is does not guarantee obtaining samples with low R_s values. Clear evidence of this is observed in particular in the Er-based sample, and to less extent in the Eu-based sample. The behavior of the Q-factors for the different samples considered is in fair agreement with the concept that the losses in these ceramics appear to be dominated by the weak coupling between grains (ref. 12), especially for grains close to the surface where most of the losses take place.

Figure 3 shows the experimental values of the surface resistance for the Y-, Dy- and Eu based bulk samples. Also plotted is the experimental surface resistance for the gold-plated copper cavity for comparison. It is observed that the R_s for the $YBa_2Cu_3O_{7-\delta}$ sample is smaller than that for the other bulk samples, at temperatures below T_c. The R_s values for the samples at temperatures below T_c are beyond a factor of 2 smaller than the values in the normal state. Nevertheless, none of the samples showed an R_s better than that of the gold-plated cavity even at temperatures below T_c. The fact that the surface resistance obtained for these samples is not comparable with that of gold at any temperature is evidence of the poor quality of the surface of samples prepared by the preparation process considered in this study.

Figure 4 shows the dc resistance versus temperature curves corresponding to $YBa_2Cu_2O_{7-\delta}$ superconducting films deposited on $SrTiO_3$ and $LaGaO_3$ substrates by laser ablation. Zero dc resistance was attained at 90.0 and 88.9 K for the films on $SrTiO_3$ and $LaGaO_3$, respectively. The x-ray diffraction pattern revealed that both films are predominantly c-axis oriented, while SEM micrographs showed that both films are polycrystalline, as can be seen from figure 5. Figure 6 shows the measured Q-factor for the cavity as a function of temperature for cases in which its end wall had been replaced by the $YBa_2Cu_3O_{7-\delta}$ films. A clear increase in the Q-factor is observed for both films at temperatures below T_c, with the rate of increase of the Q-factor with decreasing temperature being higher for the film on $SrTiO_3$ than for the one on $LaGaO_3$ down to 50 K. At temperatures below 50 K we are limited by the resolution of our measurements. Therefore, contrary to what was observed in the bulk material, the value of T_c appears to be directly related with lower microwave losses.

The measured $R_s(T)$ curves for the two films under study are shown in figure 6, in addition to the curve corresponding to the gold-plated copper cavity. The R_s of the films is comparable in the normal state, while the R_s for the film on $SrTiO_3$ was lower than that for the film on $LaGaO_3$ at temperatures just below T_c. Using the normal skin depth formula $R_s = (\omega\mu_o\rho/2)^{1/2}$ a typical resistivity ρ at 300 K of approximately 118 and 158 $\mu\Omega$-cm is obtained for the film $SrTiO_3$ and $LaGaO_3$, respectively. In the superconducting state the films on $SrTiO_3$ and $LaGaO_3$ exhibit a drop of R_s to effective values of 103 and 144 mΩ at 77 K, and 82 and 116 mΩ at 70 K, respectively. The surface resistance at 77 K for the film on $SrTiO_3$ is less than that of the gold-plated cavity, while for the film on $LaGaO_3$ R_s is the same as for the gold-plated cavity. Nevertheless, the value of R_s at 77 K for both films is higher than the theoretical R_s value expected for copper at the same temperature and frequency.

Since we are operating at a fixed frequency, we cannot study the frequency dependence of R_s directly from our measurements. Nevertheless, a comparison

of the R_S values with those reported by other researchers in similar types of films and at different frequencies, may be helpful to formulate a frequency dependence trend for R_S. Thus, using the results obtained by Klein, et al. (ref. 13) for c-axis textured layers samples of $YBa_2Cu_3O_{7-\delta}$, and fitting their data to a quadratic frequency dependence for R_S, gives an R_S value of 102 mΩ at 58.6 GHz and 77 K. This value agrees very well with our experimentally obtained value of 103 mΩ at the same temperature. A similar approach was used for the film on $LaGaO_3$. Using the values for R_S at 22, 86, and 148 GHz and at 70 K reported by Cooke, et al. (ref. 14) for a $YBa_2Cu_3O_{7-\delta}$ superconducting film deposited by magnetron sputtering on $LaGaO_3$, we were able to find by interpolation an R_S value of 106 mΩ at 58.6 GHz. This value is within experimental uncertainty of our measured value of 116 mΩ. These results indicate that our value fit well with the nearly quadratic dependence for R_S ($R_S \alpha \omega^n$, $n = 2.06 \pm 0.14$) reported by Cooke, et al. (ref. 14). Our results, as well as those obtained by the above mentioned researchers, indicates that the quadratic dependence observed for R_S is consistent with the experimental behavior observed in low T_c superconductors and also with the predictions of the BCS theory.

CONCLUSIONS

There appears to be no direct correlation between the surface resistance R_S and the transition temperature T_c in the $RBa_2Cu_3O_{7-\delta}$ bulk superconducting samples obtained by the cold pressing preparation method. Therefore, the dominating factors which control the microwave losses can only be guessed at. Some of the possible factors which could control the losses are: the weak coupling at grain boundaries, the purity of the sample and the possible segregation of composition at the surface. Two main factors can contribute to the presence of weak coupling. The first is the intrinsic mismatch of the lattice and the segregation of impurities to the grain boundaries, while the second could be reactions with the ambient environment (i.e., water vapor and CO_2). This environmental reactions primarily occur at the surface and would not appreciably affect the bulk properties in a short time period. If the losses are due to either the reaction of the surface with the environment or due to porosity, then a different pressing process to make denser pellets should give samples with lower microwave losses.

For the $YBa_2Cu_3O_{7-\delta}$ superconducting films on $SrTiO_3$ and $LaGaO_3$ we found from a correlation of the R_S values obtained for both films with those obtained for similar films measured by other researchers at different frequencies, that these values are consistent with the frequency dependence for R_S observed in classical superconductors, and also with the predictions of the BCS theory.

In summary, we have measured the R_S of bulk $RBa_2Cu_3O_{7-\delta}$ (R = Y,Dy,Eu, Sm,Er) superconducting samples and found that none of them performed as well as gold. Also, for the 1.2 μm thin films of $YBa_2Cu_3O_{7-\delta}$ on $SrTiO_3$ and $LaGaO_3$ we obtained values of R_S significantly lower than gold at temperatures below 70 K, but we are limited by the resolution of our measurement in accurately determining R_S values below 50 K.

REFERENCES

1. Cohen, L., et al.: Surface Impedance Measurements of Superconductivity $YBa_2Cu_3O_{6+x}$. J. Phys. F: Met. Phys., vol. 17, 1987, pp. L179-L183.

2. Sridhar, S.; Shiffman, C.A.; and Hamoleh, H.: Electrodynamic Response of $Y_1Ba_2Cu_3O_y$ and $La_{1.85}Sr_{0.15}CuO_{4-\delta}$ in the Superconducting State. Phys. Rev. B, vol. 36, no. 4, Aug. 1, 1987, pp. 2301-2304.

3. Martens, J.S.; Beyer, J.B.; and Ginley, D.S.: Microwave Surface Resistance of $YBa_2Cu_3O_{6.9}$ Superconduting Films. Appl. Phys. Lett., vol. 52, no. 21, May 23, 1988, pp. 1822-1824.

4. Carini, J.P., et al.: Millimeter-Wave Surface Resistance Measurements in Highly Oriented $YBa_2Cu_3O_{7-\delta}$ Thin Films. Phys. Rev. B, vol. 37, no. 16, June 1, 1988, pp. 9726-9729.

5. Newman, H.S., et al.: Microwave Surface Resistance of Bulk Ti-Ba-Ca-Cu-O Superconductors. Appl. Phys. Lett., vol. 54, no. 4, Jan. 23, 1989, pp. 389-390.

6. Klein, N., et al.: Millimeter Wave Surface Resistance of Epitaxially Grown $YBa_2Cu_3O_{7-x}$ Thin Films. Appl. Phys. Lett., vol. 54, no. 8, Feb. 20, 1989, pp. 757-759.

7. Inam, A., et al.: As-Deposited High T_c and T_c Superconducting Thin Films Made at Low Temperatures. Appl. Phys. Lett., vol. 53, no. 10, Sept. 5, 1988, pp. 908-910.

8. Roas, B.; Schultz, L.; and Endres, G.: Epitaxial Growth of $YBa_2Cu_3O_{7-x}$ Thin Films by a Laser Evaporation Process. Appl. Phys. Lett., vol. 53, no. 16, Oct. 17, 1988, pp. 1557-1559.

9. Warner, J.D.; Meola, J.E.; and Jenkins, K.A.: Study of Deposition of $YBa_2Cu_3O_{7-x}$ on Cubic Zirconia. NASA TM-102350, 1989.

10. Ginzton, E.L.: Microwave Measurements. McGraw-Hill, 1957, p. 406.

11. Romanosky, R.R.: Analytical and Experimental Procedures for Determining Propagation Characteristics of Millimeter-Wave Gallium Arsenide Microstrip Lines. NASA TP-2899, 1989.

12. Hylton, T.L., et al.: Weakly Coupled Grain Model of High-Frequency Losses in High T_c Superconducting Thin Films. Appl. Phys. Lett., vol. 53, no. 14, Oct. 3, 1988, pp. 1343-1345.

13. Klein, N., et al.: Millimeter Wave Surface Resistance and London Penetration Depth of Epitaxially Grown $YBa_2Cu_3O_{7-x}$. Physica C, vol. 162, Dec. 1989, pp. 1549-1550.

14. Cooke, D.W., et al.: Surface Resistance of $YBa_2Cu_3O_7$ Films Deposited on $LaGaO_3$ Substrates. Physica C, vol. 162, Dec. 1989, pp. 1537-1538.

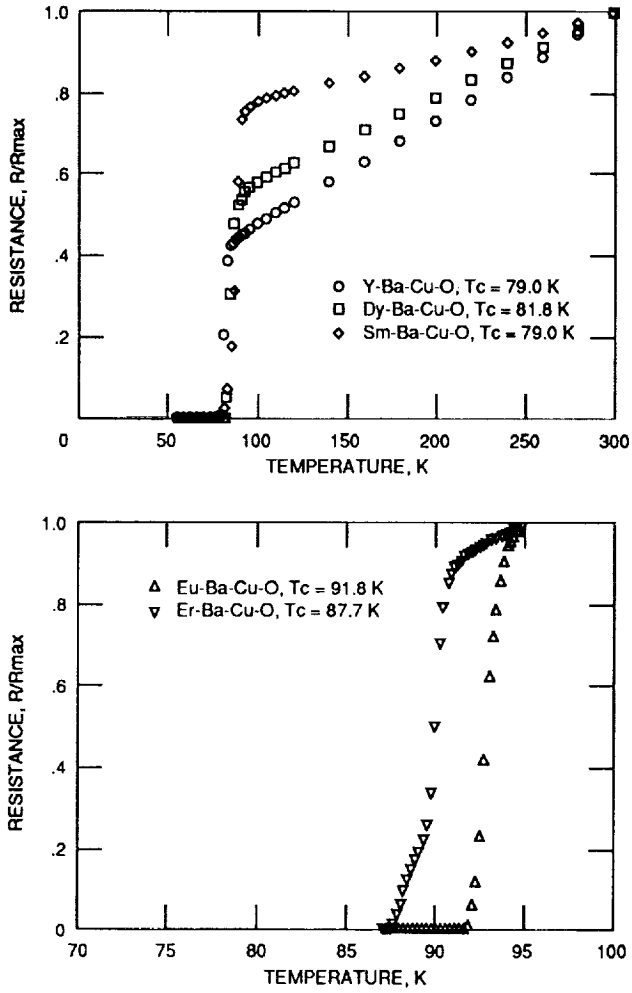

Figure 1. - dc resistance versus temperature measurements of bulk superconducting samples.

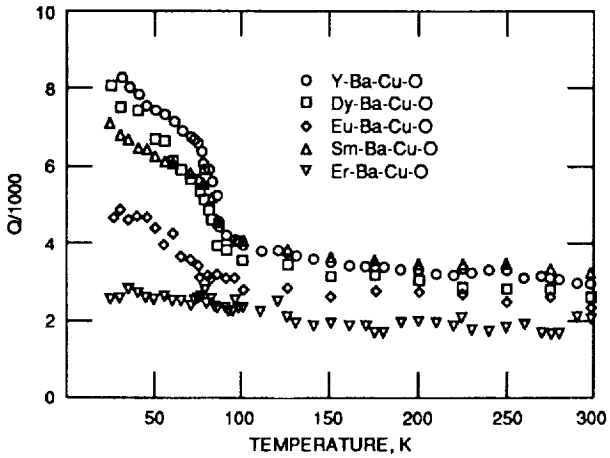

Figure 2. - Measured Q of the cavity, with one end wall replaced by the bulk sample, as a function of temperature.

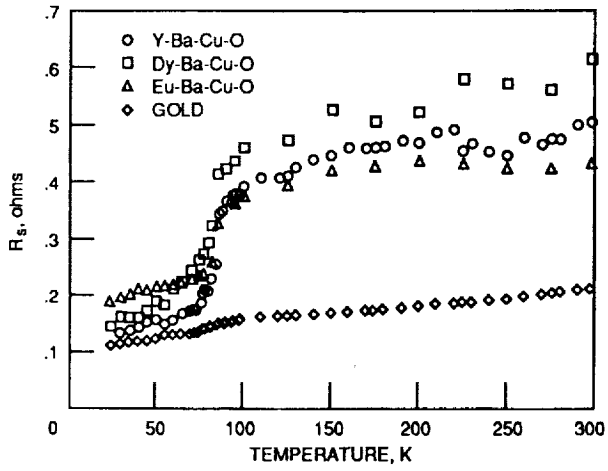

Figure 3. - Surface resistance R_s as a function of temperature and at 58.6 GHz, for bulk superconducting samples.

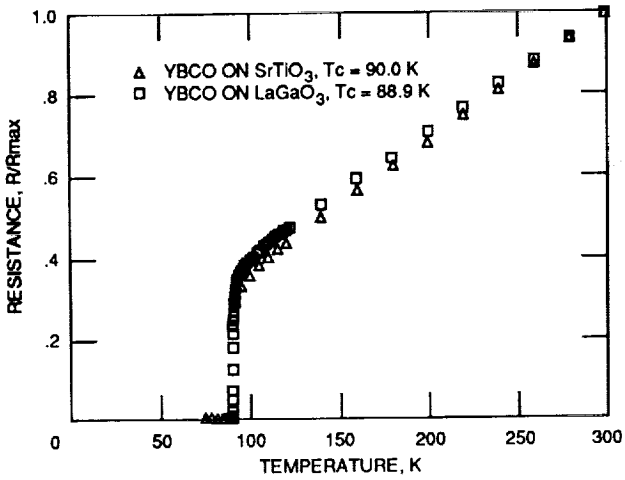

Figure 4. - dc resistance versus temperature measurements of laser ablated $YBa_2Cu_3O_{7-\delta}$ superconducting films on $SrTiO_3$ and $LaGaO_3$ substrates.

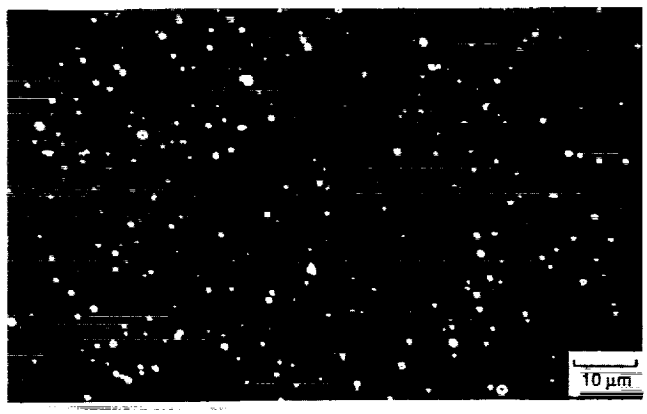

(a)

(b)

Figure 5. - Scanning electron micrographs of laser ablated $YBa_2Cu_3O_{7-\delta}$ superconducting films on $SrTiO_3$ (a) and $LaGaO_3$ (b) substrates.

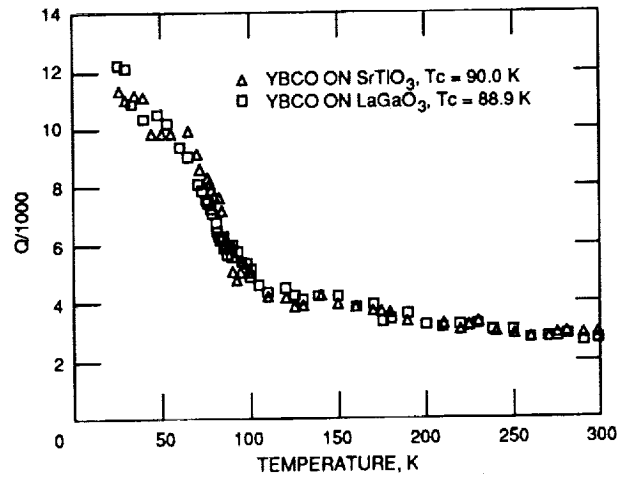

Figure 6. - Measured Q of the cavity, with one end wall replaced by the thin film, as a function of temperature.

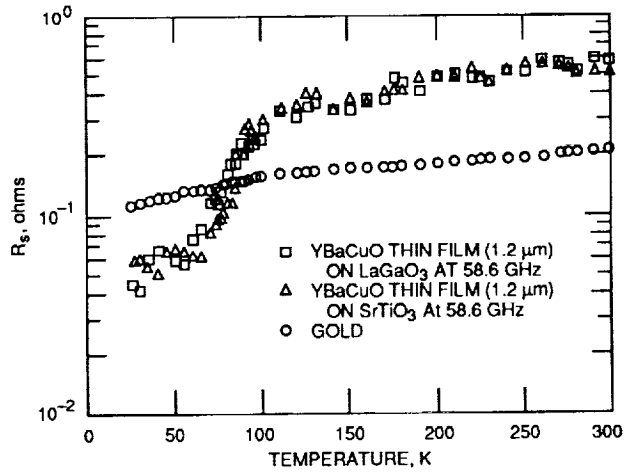

Figure 7. - Surface resistance (R_s) at 58.6 GHz versus temperature for 1.2 μm films of $YBa_2Cu_3O_{7-\delta}$ deposited by laser ablation onto $SrTiO_3$ and $LaGaO_3$ substrates, and for gold-plated cavity.

NASA Technical Memorandum 102346

Growth and Patterning of Laser Ablated Superconducting $YBa_2Cu_3O_7$ Films on $LaAlO_3$ Substrates

J.D. Warner, K.B. Bhasin, N.C. Varaljay, and D.Y. Bohman
National Aeronautics and Space Administration
Lewis Research Center
Cleveland, Ohio

and

C.M. Chorey
Sverdrup Technology, Inc.
NASA Lewis Research Center Group
Cleveland, Ohio

ERRATA

NASA Technical Memorandum 102436

GROWTH AND PATTERNING OF LASER ABLATED SUPERCONDUCTING $YBa_2Cu_3O_7$ FILMS ON $LaAlO_3$ SUBSTRATES

J.D. Warner, K.B. Bhasin, N.C. Varaljay, D.Y. Bohman, and C.M. Chorey
February 1990

Cover and page 8: The NASA report number 102346 should be replaced by 102436.

Prepared for the
36th National Symposium and Topical Conference
sponsored by the American Vacuum Society
Boston, Massachusetts, October 23–27, 1989

NASA

GROWTH AND PATTERNING OF LASER ABLATED SUPERCONDUCTING $YBa_2Cu_3O_7$, FILMS ON $LaAlO_3$ SUBSTRATES

J.D. Warner, K.B. Bhasin, N.C. Varaljay, D.Y. Bohman,
NASA Lewis Research Center Cleveland, OH 44135

C.M. Chorey*
Sverdrup Technology, Inc., NASA Lewis Research Center Group,
Cleveland, OH 44135

ABSTRACT

A high quality superconducting film on a substrate with a low dielectric constant is desired for passive microwave circuit applications. In addition, it is essential that the patterning process does not effect the superconducting properties of the thin films to achieve the highest circuit operating temperatures. We have grown $YBa_2Cu_3O_7$ superconducting films on lanthanum aluminate substrates using a laser ablation technique with resulting maximum transition temperature (T_c) of 90 K. The films were grown on $LaAlO_3$ which was at 775 °C and in 170 mtorr of oxygen and slowly cooled to room temperature in 1 atm of oxygen. These films were then processed using photolithography and a negative photoresist with an etch solution of bromine and ethanol. Results are presented on the effect of the processing on T_c of the film.

I. INTRODUCTION

Laser-ablated, high-temperature superconducting (HTS) $YBa_2Cu_3O_7$ films have been made on many substrates including $SrTiO_3$, MgO, $LaGaO_3$, and ZrO_2.[1-7] These substrates were used because they either had very small interaction with the HTS films during growth or annealing or because the substrates with HTS films had potential electronic applications. In this paper, we report on the growth and patterning of thin $YBa_2Cu_3O_7$ films on $LaAlO_3$ for microwave applications. $LaAlO_3$ was chosen as a substrate because of its relatively low dielectric constant of 22[8] and because of it moderate loss tangent of $8x10^{-5}$ at 10 GHz[9].

Lines varying in width from 10 to 20 μm were patterned using photolithography and wet etching techniques. To determine if the etching or lithography process had influenced the transition temperature of the films. A ring resonator circuit operating at 35 GHz was also fabricated, since the resonator allows the determination of loss and dispersive properties of microstrip transmission line. From the measurement of the quality factor "Q" of a resonator circuit one can determine the microwave losses of the HTS films as compared with those of gold on the same substrates.

*Work done under NASA contract #NAS3-25266; Regis Leonard, monitor.

II. Film Growth

The laser ablation technique used to grow the films on substrates of $LaAlO_3$ is similar to the techniques reported in the literature.[1-7] The details of the geometry of the laser ablation is shown in Fig. 1. The substrates (15 by 15 by 0.25 mm) with orientation (001) were mounted onto a stainless steel plate with a diameter of 63 mm. The plate was heated from the backside using a resistive heater made from Kanthal A-1 wire (made by Kanthal, Inc.). The temperature was measured with a type K thermocouple which was welded to the plate. The thermocouple was 2 mm away from the sample. The sample chamber was evacuated to $3x10^{-7}$ torr, or lower, using a liquid nitrogen cold trapped diffusion pump before the sample was warmed up to 500 °C. A continuous flow of oxygen (120 sccm) was then introduced into the chamber, and the sample heated to 775 °C. During deposition the chamber pressure was 170 mtorr; the laser wavelength was 248 nm; the energy density was 1.5 (J/cm^2)/pulse; the pulse rate was 4 pps; and the distance between the target and the sample was 8 cm. The laser beam was rastered up and down 1 cm over the target using an external lens on a translator. The angle between the laser beam and the normal to the target was 45°. The target used was a sintered 25-mm-diameter pellet of $YBa_2Cu_3O_{7-x}$. After deposition the oxygen pressure was raised to 1 atm, and the temperature was lowered to 450 °C at a rate of 2 °C/min. The temperature was held at 450° C for 2 hr before it was lowered to 250 °C at a rate of 2 °C/min. The heater power was then turned off, and the sample was allowed to cool to 40 °C or less before it was removed the chamber.

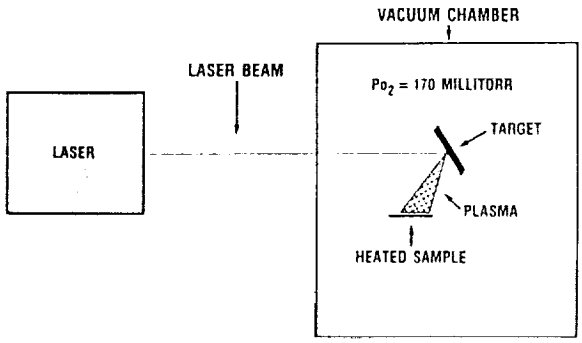

Figure 1. - Schematic of the laser ablation experiment.

The thickness of the HTS films on $LaAlO_3$ was estimated by measuring the thickness of a film grown on quartz plate that was shadow masked. The quartz plate had been placed 1 mm below the bottom of the $LaAlO_3$ on the substrate holder such that the sweep of the plasma plumb was along the line connecting the centers of the quartz and the $LaAlO_3$.

The best film had a T_c of 89.8 K immediately after deposition as determined by a standard four point resistance measurement. Its resistance versus temperature behavior is shown in Fig.2. From the intercept of the extrapolated resistance at 0 K and from the resistance above T_c, one can see that the film is c-axis aligned. This is confirmed by only having the (001) peaks in the x-ray diffraction data (Fig. 3). The surface morphology of the HTS on $LaAlO_3$ is shown in Fig. 4. The surface is very smooth with some small structure. We do not observe large numbers of HTS particulates due to the laser ablation process.

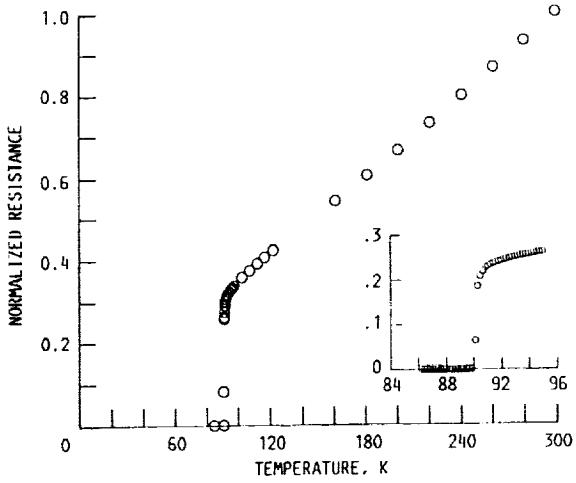

Figure 2. - Normalized resistance of laser ablated $YBa_2Cu_3O_x$ film on $LaAlO_3$.

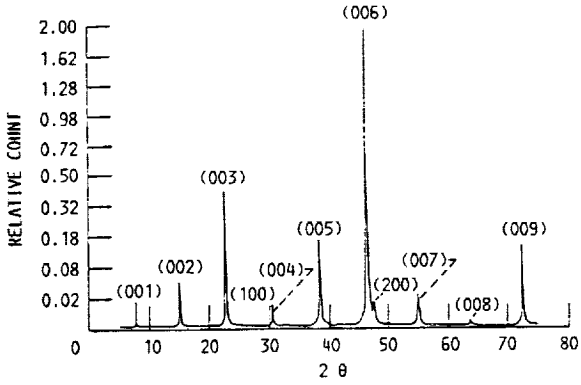

Figure 3. - X-ray diffraction pattern of laser ablated $YBa_2Cu_3O_x$ film on $LaAlO_3$.

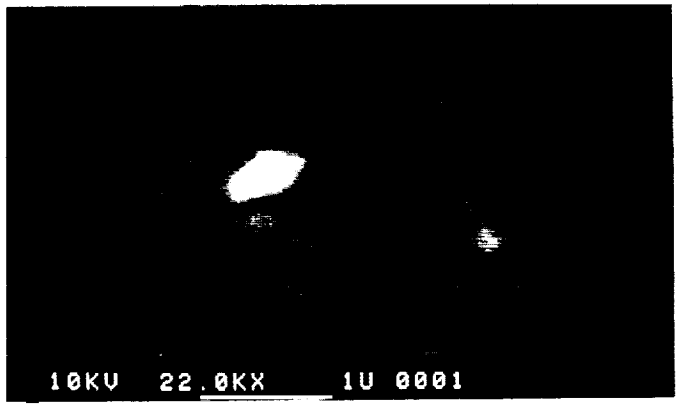

Figure 4. - Scanning electron micrograph of laser ablated $YBa_2Cu_3O_x$ Film on $LaAlO_3$.

PATTERNING

Films on $LaAlO_3$ and $SrTiO_3$ were patterned using photolithography and wet etching. The negative photoresist (752), its developer (802), and the associated rinse (n-butyl acetate) used were obtained from KTI. The photoresist strippers used were Losalin IV (from E.C. Merke), acetone, toluene, and ethanol. Each step of the process was checked to see if it had an effect on the T_c of the HTS films. The results of the different processing steps on T_c are shown in table I. The full process of patterning the HTS films was to spin on the negative photoresist to a thickness of 2 μm, followed by a soft bake at 90° C for 1 hr, and then to expose the photoresist. After developing the photoresist, the film was etched for 500 s in 1 percent molar of bromine in ethanol. After etching, the films were rinsed in ethanol and the photoresist was removed with the Losalin IV photoresist stripper which was at 70 °C. We did not observed any drop in the T_c of the HTS films.

Table I Effect of Photolithography Process on T_c of $YBa_2Cu_3O_x$ Films

Exposure to negative photoresist	None
Soft baking of photoresistat 90 °C for 1 hr)	None
Exposure to photoresist developer and rinse	None
Exposure to different stripping solvents after patterning[a]:	
Boiling ascetone (58 °C) for 10 min	None
Boiling ethanol (78 °C) for 10 min	None
Boiling toluene (111 °C) for 10 min	None
Losalin IV (760 °C) for 5 min	None

[a]Only boiling ethanol and Losalin IV sucessfully removed exposed phoresist.

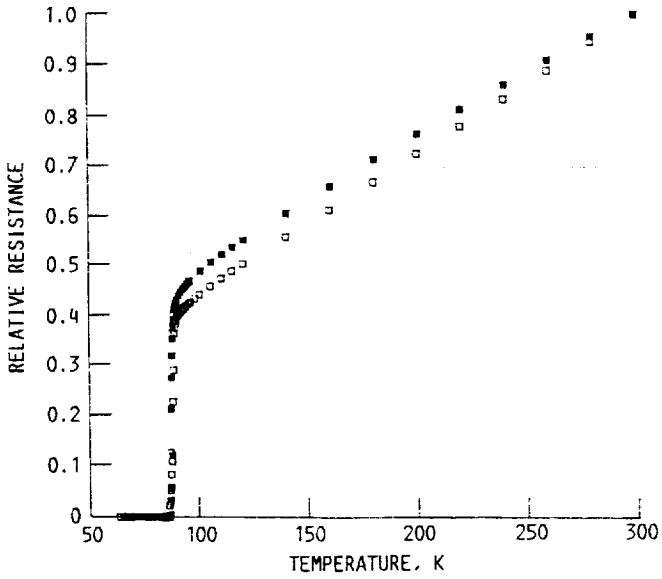

Figure 5. - Normalized resistance of a laser ablated $YBa_2Cu_3O_x$ film on $SrTiO_3$. The film □ is before processing while the film ■ is after exposure to negative photoresist.

The films used to determine the effect of the various fabrication steps had transition temperatures between 77 and 85 K. Fig. 5 shows the effect of exposing the film directly to the photoresist stripper Losalin IV at 70° C. No change in T_c occurred, but the slope of the resistance versus temperature curve did change. Fig. 6 shows the T_c of the film on $LaAlO_3$ before patterning and after it was patterned into a ring resonator, that had operated at 33 GHz, and after it had

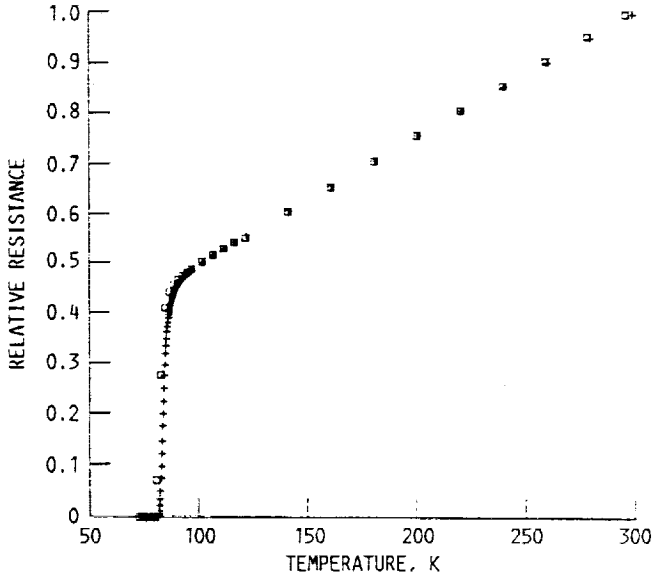

Figure 6. - Comparison of normalized resistance of a laser ablated $YBa_2Cu_3O_x$ film on $LaAlO_3$ before processing □ and after being fabricated into a 35-GHz ring resonator +.

silver contacts evaporated onto it and annealed at 500° C for 1 hr. There is no apparent difference in the T_c or the resistance versus temperature behavior between the film before and after processing.

To test the laser ablation technique's ability to produce uniform film thickness and the variation of T_c across the film, Hall bars with silver contacts were fabricated (Fig. 7). The width of the bar is 10 μm. The film thickness is not very uniform over the 5- by 10-mm area. The time needed to etch the film until the substrate was exposed varied by a factor of 2 from one edge to the other edge of the substrate. However, the T_c did not vary from region to region (table II).

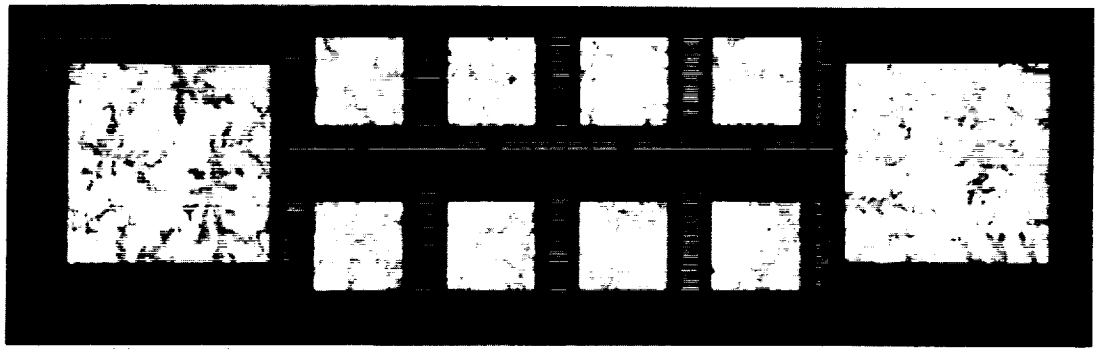

Figure 7. - Finished Hall bar of $YBa_2Cu_3O_x$ film on $SrTiO_3$ substrate.

Table II Variation of on $SrTiO_3$ as Measured With Patterned Hall Bars

Before patterning	70.8 K
10- μm lines after patterning	71.0, 71.5, 72.5 K
20- μm lines after patterning	75.3, 75.5, 76.5 K

Conclusions

Laser-ablated, high-temperature superconducting films on $LaAlO_3$ and $SrTiO_3$ have been grown. The best films had a T_c of 90 K and have their c-axis aligned to the substrate. There is no variation of T_c across the films, but there is a variation of film thickness. These films have been patterned with negative photoresist and a bromine/ethanol etch. There is no detectable degradation of T_c by any step of the fabrication process even though the films were heated to 122° C in toulene.

This fabrication process should be able to be used to make most of the passive and one layer structures without any degradation of the transition temperature.

REFERNCES

1. J.D. Warner, J.E. Meola, and K.A. Jenkins, NASA TM-102350, 1989.

2. D. Dijkkamp, T. Venkatesan, X.D. Wu, S.A. Shaheen, N. Jisrawi, Y.H. Min-Lee, and W.L. Mclean, M. Croft, Appl. Phys. Lett. **51**, 619 (1987).

3. X.D. Wu, D. Dijkkamp, S.B. Ogale, A. Inam, E.W. Chase, P.F. Miceli, C.C. Chang, J.M. Tarascon, and T. Venkatesan, Appl. Phys. Lett. **51**, 861 (1987).

4. J. Narayan, N. Biunno, R. Singh, O.W. Holland, and O. Auciello, Appl. Phys. Lett. **51**, 1845 (1987).

5. L. Lynds, B.R. Weinberger, G.G. Peterson, and H.A. Kransinski, Appl. Phys. Lett. **52**, 320 (1988).

6. T. Venkatesan, C.C. Chang, D. Dijkkamp, S.B. Ogale, E.W. Chase, L.A. Farrow, D.M. Hwang, P.F. Miceli, S.A. Shwarz, J.M. Tarascon, X. D. Wu, and A. Inam, J. Appl. Phys. **63**, 4591 (1988).

7. A.M. Desantolo, M.L. Mandich, S. Sunshine, B.A. Davidson, R.M. Fleming, P. Marsh, and T.Y. Kometani, Appl. Phys. Lett. **52**, 1995 (1988)

8. F.A. Miranda, W.L. Gordon, V.O. Heinen, B.T. Ebihara, and K.B. Bhasin, NASA TM-102123, 1989.

9. R.W. Simon, C.E. Platt, A.E. Lee, G.S. Lee, and K. Daly, Appl. Phys. Lett., **53**, 2677 (1988).

COMPLEX PERMITTIVITY OF LANTHANUM ALUMINATE IN THE 20 TO 300 K TEMPERATURE RANGE FROM 26.5 TO 40.0 GHZ

F. A. Miranda and W. L. Gordon
Case Western Reserve University
Cleveland, Ohio 44106

K. B. Bhasin, B. T. Ebihara, and V. O. Heinen
Lewis Research Center
Cleveland, Ohio 44135

C. M. Chorey
Sverdrup Technology, Inc.
NASA Lewis Research Center Group
Cleveland, Ohio 44135

KEY TERMS

Complex permittivity, superconductors, lanthanum aluminate substrates, microwave measurements

ABSTRACT

Dielectric constants of microwave substrates are required in the design of superconducting microwave circuits at various temperatures. In this paper, we report the results of a study of the complex permittivity of the newly developed lanthanum aluminate ($LaAlO_3$) substrate, in the 20 to 300 K temperature range at frequencies from 26.5 to 40.0 GHz. The value of the complex permittivity was obtained by measuring the sample scattering parameters using a microwave waveguide technique. It is observed that, while the dielectric constant did not change appreciably with frequency, its value decreased by approximately 14 percent from room temperature to 20 K.

INTRODUCTION

The discovery [1] of high transition temperature (T_c) oxide superconductors has opened up a wealth of attractive possibilities, among which, their application in the preparation of thin films to be used in the development of microwave circuits. Therefore, a good knowledge of the dielectric properties of microwave substrates used for film deposition is of paramount importance. Substrates with low dielectric constant and loss tangent [2] are indispensable in order to develop highly reliable microwave components.

At the moment, Y–Ba–Cu–O superconducting thin films deposited in $SrTiO_3$ substrates have shown the best quality when compared with films deposited in other substrates. Unfortunately, its microwave applicability is very limited because of the strong temperature dependence of its dielectric constant —with a value of 300 at room temperature, of 1000 at 77 K, and over 18,000 below 4 K—and its relatively high loss tangent [3].

The recently developed $LaAlO_3$ substrate is actually being used in the fabrication of high T_c superconducting thin films. Nevertheless, the value of its dielectric constant at room temperature and at low temperatures is still not well established. In this paper, we report on the measurements of the microwave complex permittivity of $LaAlO_3$ in the 20 to 300 K temperature range and as a function of frequency.

ANALYSIS

The method for the derivation of the complex permittivity from the sample scattering parameters was first proposed by Nicolson and Ross [4] and modified later for rectangular waveguide applications by Weir [5]. Essentially, for a piece of material properly introduced in a rectangular waveguide with characteristic impedance Z_0 (as shown in Figure 1), the solution of the boundary conditions at $x = 0$ and $x = d$ allows the scattering parameters $S_{11}(\omega)$ and $S_{21}(\omega)$ to be related with the reflection (Γ) and transmission (T) coefficients in the following way:

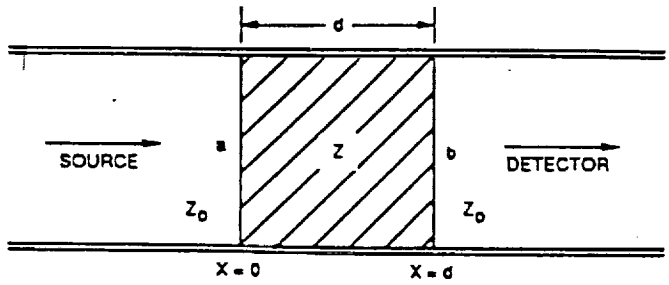

Figure 1 Waveguide with filled material

$$S_{11} = \frac{(1 - T^2)\Gamma}{1 - \Gamma^2 T^2}, \qquad S_{21} = \frac{(1 - \Gamma^2)T}{1 - \Gamma^2 T^2} \tag{1}$$

where

$$\Gamma = \frac{Z - Z_0}{Z + Z_0} = \sqrt{\frac{(\mu_r/\epsilon_r) - 1}{(\mu_r/\epsilon_r) + 1}} \tag{2}$$

and

$$T = \exp(-j\omega\sqrt{\mu\epsilon}\, d) = \exp\left[\left(-j\frac{\omega}{c}\right)\sqrt{\mu_r\epsilon_r}\, d\right] \tag{3}$$

In Equations (2) and (3), Z is the impedance of the sample, d is its thickness, and μ_r and ϵ_r, its relative permeability and permittivity, respectively. Therefore, one can obtain Γ and T from $S_{11}(\omega)$ and $S_{21}(\omega)$, and, in turn, they can be used to determine the permittivity.

The measurements of the reflection, $S_{11}(\omega)$, and transmission, $S_{21}(\omega)$, scattering parameters were performed using an HP-8510 automatic network analyzer, conveniently connected through an arrangement of Ka-band (26.5 to 40.0 GHz) waveguides to a cryogenic system, which allows measurements to be taken at the desired low temperatures. The cryogenic system consists of a closed-cycle helium refrigerator combined with a temperature controller, and an aluminum vacuum chamber, specially designed to fit on top of the external shield of the refrigerator and to give access to the arrangement of waveguides. A vacuum of less than 1.0×10^{-2} torr was maintained throughout the whole measurement procedure. During the actual measurements, the $LaAlO_3$ substrate was suspended perpendicular to the microwave source between two waveguide flanges in such a way that both the transmitted and reflected power can be detected.

Finally, the dielectric constant of $LaAlO_3$ was also measured at room temperature using the well-established parallel-plate capacitor technique, and the value obtained was compared with the one acquired using the scattering parameters method. The capacitor was made with a 10-mil lanthanum aluminate substrate as the filling dielectric, and its plates were made by evaporating gold such that a 1-cm disk was formed on its front surface, with its back surface being completely coated.

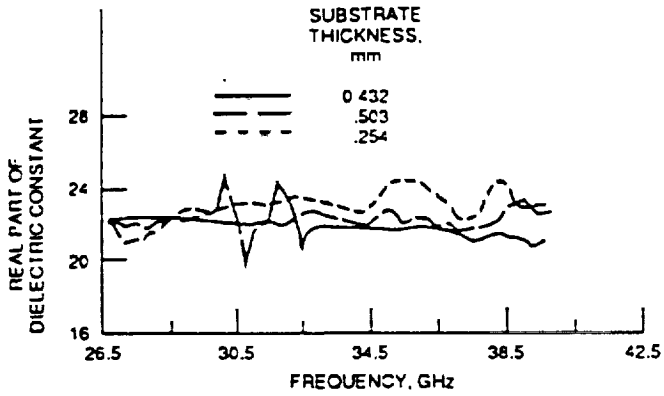

Figure 2 Real part of complex permittivity of $LaAlO_3$ substrates at room temperature

TABLE 1 Complex Permittivity of $LaAlO_3$ at 28.6 GHz

Temperature, K	Real Part of Complex Permittivity, ϵ'	Imaginary Part of Complex Permittivity, ϵ''
300	22.0	1.10
150	20.8	1.10
70	19.7	1.07
20	18.9	0.20

RESULTS

Figure 2 and Table 1 show the results for the room temperature measurements of the dielectric constant for three $LaAlO_3$ substrates. The substrates are 0.254, 0.432, and 0.503 mm thick and were made from different batches of $LaAlO_3$. The value of the dielectric constant is consistent for the three samples, and it has a typical value of approximately 22 ± 1. Hence, neither the difference in thickness nor the fact that the samples come from different batches appears to be an important factor in the determination of the value of the dielectric constant for this substrate. It is also noticed that the frequency dependence for this parameter in the band under consideration is a weak one. We believe that the discontinuities and small variations observed in Figures 2 and 3 are due to systematic errors in the calibration and not to intrinsic properties of the samples.

Although the values of the dielectric constant obtained for the three samples under consideration are in good agreement, they differ considerably from the one reported by Simon et al.

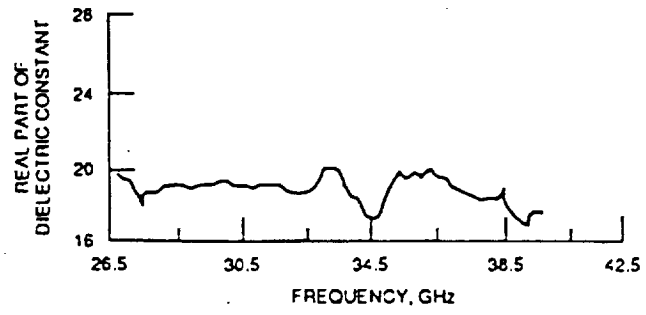

Figure 3 Real part of complex permittivity of $LaAlO_3$ substrate at 20 K

[2]. In view of this discrepancy, we performed measurements on magnesium oxide (MgO), sapphire (Al_2O_3), and silicon oxide (SiO_2), which are substrates with well-known values for the dielectric constant at room temperature. The results of our measurements were consistent with those reported by other researchers [6–8]. Furthermore, we obtained the value of the dielectric constant ϵ of $LaAlO_3$ using a parallel-plate capacitor and the following relations:

$$\epsilon = \frac{\text{measured capacitance}}{\text{ideal vacuum capacitance}} = \frac{C_{\text{measured}}}{C_{\text{ideal vacuum}}} \quad (4)$$

$$C_{\text{ideal vacuum}} = \frac{\epsilon_0 \times \text{area disk}}{\text{plate separation}} = \frac{\epsilon_0 \pi r^2}{d} \quad (5)$$

$$C_{\text{measured}} = \text{measured value} - \text{edge capacitance} \quad (6)$$

and

$$\frac{\text{edge capacitance}}{\text{perimeter}} = -0.229 + 0.105(\epsilon) + 0.214 \log\left(\frac{2\pi r}{d}\right) \quad (7)$$

The value obtained using this approach was $\epsilon \approx 20 \pm 1$ at 1 MHz. Although this value is a little lower than the one derived using the scattering parameters technique, the two values still are in a better agreement than with the results of [2]. Further, because of the relatively low frequency at which this value was measured, it provides an additional indication of the small variation of the dielectric constant of $LaAlO_3$ as a function of frequency.

Table 1 shows the real and imaginary parts of the complex permittivity at four different temperatures, and at 28.6 GHz, for the sample represented with the small dashed line in Figure 2. Figure 3 shows the real part of the complex permittivity for this same sample at 20 K. A decrease of 14% in the value of the dielectric constant at temperatures around 20 K is observed. Although this change can be considered as a relatively large one, it is almost meaningless when compared with the temperature dependence of the dielectric constant of $SrTiO_3$. Now, from the data in Table 1, it is seen that the value of the imaginary part of the complex permittivity tends to decrease with decreasing temperature. Nevertheless, a comparison of our results at room temperature for MgO, Al_2O_3, and SiO_2 substrates was not in good agreement with previously reported values [6–8]. Because for these substrates the values for the dielectric constant and the loss tangent at room temperature are well established, our confidence in the values for the imaginary part of the permittivity, not only at room temperature but also at low temperature, is rather limited. Therefore, for cases in which an accurate knowledge of this parameter is indispensable and mainly when dealing with low-loss substrates, other techniques must be applied.

CONCLUSIONS

The complex permittivity of the newly developed $LaAlO_3$ substrate has been measured. A decrease in the value of the real part of the complex permittivity with decreasing temperature was observed. No considerable change was noticed in this parameter, neither as a function of frequency nor due to difference in thicknesses and batch of origin. The values obtained for the imaginary part of the complex permittivity, both at room temperature and at low temperature, appear not

to be very accurate, mainly due to limitations of the applied technique when used with very low-loss substrates. The results obtained in this study suggest that, at least from the standpoint of the dielectric constant, the $LaAlO_3$ substrate is better suited than $SrTiO_3$, for use with the new high-temperature superconductors in microwave applications.

REFERENCES

1. J. G. Bednorz and K. A. Muller, "Possible High T_c Superconductivity in the Ba-La-Cu-O System," *Z. Phys. B*, Vol. 64, 1986, pp. 189-193.
2. R. W. Simon, C. E. Platt, A. E. Lee, G. S. Lee, K. P. Daly, M. S. Wire, J. A. Luine, and M. Urbanik, "Low-Loss Substrate for Epitaxial Growth of High-Temperature Superconductor Thin Films," *Appl. Phys. Lett.*, Vol. 53, No. 26, Dec. 26, 1988, pp. 2677-2679.
3. H. Padamsee, K. Green, J. Gruschus, J. Kirchgessner, D. Moffat, D. L. Rubin, J. Sears, Q. S. Shu, R. Buhrman, D. Lathrop, T. W. Noh, S. Russek, and A. Sievers, "Superconductivity and Applications," unpublished.
4. A. M. Nicolson and G. F. Ross, "Measurement of the Intrinsic Properties of Materials by Time Domain Techniques," *IEEE Trans. Instrum. Meas.*, Vol. IM-19, No. 4, Nov. 1970, pp. 377-382.
5. W. B. Weir, "Automatic Measurement of Complex Dielectric Constant and Permeability at Microwave Frequencies," *Proc. IEEE*, Vol. 62, No. 1, Jan. 1974, pp. 33-36.
6. M. D. Hossain, "Microwave Dielectric Properties of Ti^{4+}/MgO and Ni^{2+}/MgO," *Appl. Phys. A*, Vol. 36, No. 1, 1985, pp. 63-65.
7. A. R. Von Hippel, "*Dielectric Materials and Applications*," The MIT Press, Cambridge, MA, 1954.
8. C. Zahopoulos, W. L. Kennedy, and S. Sridhar, "Performance of a Fully Superconducting Microwave Cavity Made of the High T_c Superconductor $Y_1Ba_2Cu_3O_{7-x}$," *Appl. Phys. Lett.*, Vol. 52, No. 25, June 20, 1988, pp. 2168-2170.

Received 9-14-89

Microwave and Optical Technology Letters, 3/1, 11-13

CCC 0895-2477/90/$4.00

PERFORMANCE AND MODELING OF SUPERCONDUCTING RING RESONATORS AT MILLIMETER-WAVE FREQUENCIES

K.B. Bhasin, C.M. Chorey*, J.D. Warner, R.R. Romanofsky and V.O. Heinen

NASA Lewis Research Center
21000 Brookpark Road
Cleveland, OH 44135

*Sverdrup Technology/LeRC Group
2001 Aerospace Parkway
Cleveland, OH 44142

K. S. Kong, H. Y. Lee and T. Itoh
Department of Electrical and Computer Engineering
The University of Texas at Austin
Austin, TX 78712

ABSTRACT

Microstrip ring resonators operating at 35 GHz have been fabricated from laser ablated YBCO thin films deposited on lanthanum aluminate substrates. They were measured over a range of temperatures and their performance compared to identical resonators made of evaporated gold. Below 60° Kelvin the superconducting strip performed better than the gold, reaching an unloaded 'Q' ~1.5 times that of gold at 25° K. A shift in the resonant frequency follows the form predicted by the London equations. The Phenomenological Loss Equivalence Method is applied to the ring resonator and the theoretically calculated Q values are compared to the experimental results.

INTRODUCTION

Recent observations of low surface resistance at microwave and millimeter wave frequencies in thin superconducting films [1] suggest their use for low loss/high Q microstrip circuits. Of interest is the surface resistance exhibited by these films across a wide frequency range. To date, measurements of surface resistance in the Ka band and above have been by the cavity technique. This technique fails to model microstrip losses completely because it neglects substrate losses and fails to adequately probe the film-substrate interface. Microstrip resonators patterned from thin films on microwave substrates allow direct measurement of microstrip losses. Several groups have made such measurements at lower microwave frequencies.[2,3,4] In this paper we report on the direct measurement of losses by Ka band microstrip resonators made from laser ablated YBCO films on lanthanum aluminate. Also, we calculate the Q values of the structure using the Phenomenological Loss Equivalence Method and invoking superposition of the internal impedances of the strip and ground plane of the microstrip line. The calculated Q value of the ring resonator with a superconducting strip and a normal conducting ground plane is compared with the experimental results.

GROWTH AND PATTERNING

The superconducting films were deposited by laser ablation of a sintered YBCO pellet onto a heated (700°C) lanthanum aluminate substrate in a 100 mtorr oxygen atmosphere and then slowly cooled to room temperature in 1 atmosphere of oxygen.[5] Films with very smooth surfaces and Tc's of 89.8 have been produced; X-ray analysis has shown that they are c-axis aligned. The microstrip resonators were patterned by standard photolithography using negative photoresist and a 'wet' chemical etchant. This etchant was either a 3% solution of bromine in ethanol or dilute phosphoric acid in water. A metal ground plane was deposited by first evaporating 100 Å of Ti for adhesion followed by 1 micron of gold. In addition to the resonator, each chip also had a test bar for direct Tc testing of the patterned film. Identical resonators were fabricated entirely from gold (both strip and ground plane) using evaporation and lift-off to define the strip.

The resonators were measured using a Hewlett-Packard 8510 Network Analyzer, operating in WR-28 waveguide. The microstrip circuit was mounted in a tapered ridge waveguide to microstrip test fixture which was mounted at the second stage of a two stage, closed cycle helium refrigerator. Circuit temperatures reached approximately 20°K and were monitored by a silicon diode sensor mounted in the test fixture. The entire cold finger and test fixture were enclosed in a custom designed vacuum can. Microwave coupling to the test fixture was through 6 inch sections of WR-28 waveguide made of thin wall stainless steel to minimize heat conduction. Vacuum was maintained at the waveguide feedthroughs by means of 'O' rings and mica sealing windows.

THEORETICAL CALCULATION OF Q

The theoretical Q values were calculated using the Phenomenological Loss Equivalence Method (PEM).[6] This method is applicable to cases where the strip conductor thickness is on the order of a skin depth (for a normal metal) or a penetration depth (for a superconductor). The Incremental Inductance Rule, which is often used to calculate microstrip losses, can only be applied in the case of shallow field penetration, which is not satisfied in this study. Also, PEM has the advantage of simple calculation compared with other numerical techniques such as the Finite Element Method. The technique proceeds on the basis of separately calculating the internal impedances of the strip and the ground plane through use of an equivalent isolated strip, and then adding these impedances to the external impedance of the microstrip structure. First, the ground plane is assumed to be a perfect conductor so that there is no magnetic field penetration into it as shown in figure 1. A geometric factor (G1) for the strip line is then obtained from the magnetic field penetration into it. This G1 factor is used to obtain an equivalent strip; from which the internal impedance of the microstrip line under the assumption of perfect ground plane can be obtained as

$$Z_{i1} = G_1 \bullet Z_{s1} \bullet \coth(Z_{s1} \bullet \sigma_1 \bullet A \bullet G_1)$$

where Z_{s1}, σ_1 and A are the surface impedance, the conductivity of the material and the cross sectional area of the strip, respectively. Next we consider the strip as a perfect conductor as shown in figure 1. Then a geometric factor (G2) is obtained for the field penetration into the ground plane. With the value G2, we obtain the internal impedance of the ground plane based on the assumption of a perfect strip,

$$Z_{i2} = G_2 \bullet Z_{s2} \bullet \coth(Z_{s2} \bullet \sigma_2 \bullet A \bullet G_2)$$

where Z_{s2} and σ_2 are surface impedance and conductivity of the ground, respectively. The internal impedance of the microstrip line is obtained by adding Z_{i1} and Z_{i2}. We add this internal impedance to the external inductance and calculate the propagation constant of the microstrip line by using a transmission line model. It should be emphasized that (1) and (2) are applicable to any field penetration depth.

The conductor losses of the structure in fig. 2 were calculated by applying the method explained above. Then, the Q values of each resonator were calculated by additional consideration of substrate loss; radiation loss was assumed negligible. For the calculation, the value of 5.8x10-4 was used for the loss tangent. Since the current is more concentrated on the strip, the implementation of a superconductor in the strip has more influence on the loss.

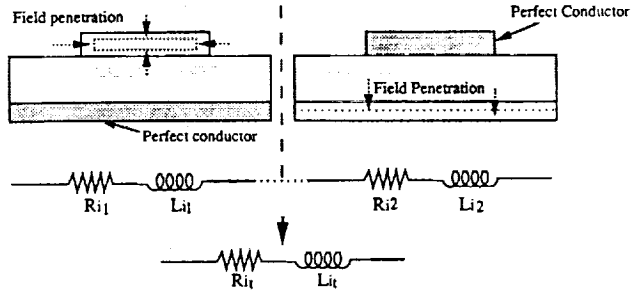

Figure 1. Field penetration in the strip and ground plane; for PEM calculation.

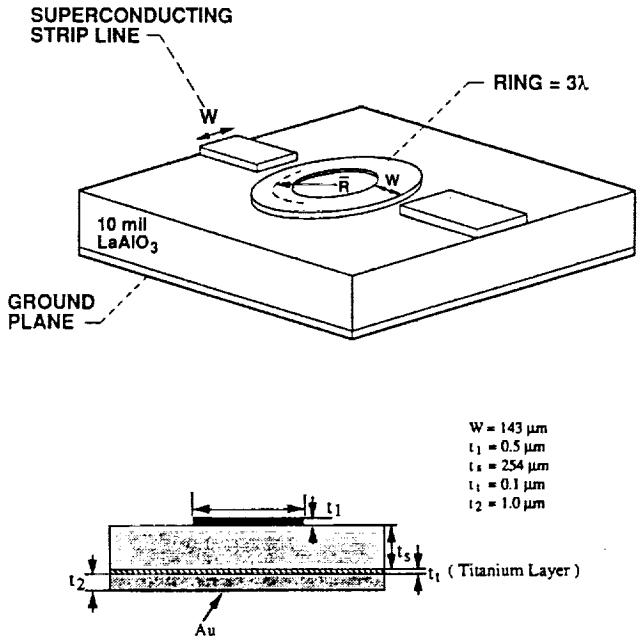

Figure 2. 35GHz Ring Resonator Structure.

The extent of the effect of implementing a superconductor in the microstrip line can be different for different geometries.

RESULTS AND DISCUSSION

In figure 3 are shown plots of S11 for a superconducting resonator at several temperatures. This plot is of the reflected power from the resonator in the test fixture and is thus a measure of the loaded 'Q'. Two features are apparent; 1) the coupling changes with temperature (in this case, starting at near critical coupling just below Tc and going to overcoupled at lower temperatures), and 2) the resonant frequency shifts with temperature. The change in the resonant frequency vs temperature is plotted in figure 4 along with the resonant frequencies of a gold resonator. The variation observed in the gold resonator follows the form expected from thermal contraction in the substrate. But since accurate data on lanthanum aluminate is not readily available, precise comparisons are not possible. The variation seen in the superconducting resonator is a consequence of the dependence of the internal impedance of the strip on the changing normal/superconducting electron densities. The internal inductance of a superconducting strip over a ground plane is given by:[7]

$$L_{int} = \mu_o \cdot \lambda \cdot \coth(t/\lambda)$$

Assuming the Gorter-Casimir temperature dependence of λ:

$$\lambda(T) = \frac{\lambda_o}{[1-(T/Tc)^4]^{\frac{1}{2}}}$$

the form of the resonant frequency variation based on the changing line inductance matches the experimental observations. However, attempts at numerical fitting to extract λ_o, result in λ_o in excess of 1 micron, indicating that the film quality may not be at its highest.

The best circuit to date has been from a 6500 Å film with a post-processing Tc of 79°K. The unloaded Q of this circuit is plotted against temperature in figure 5 along with the unloaded Q of an identical gold resonator. The Q of the superconducting circuit rises sharply below Tc, exceeding the Q of the gold circuit at ~60°K and reaching a value of 1.5 times that of the gold resonator at 25°K. Comparing the experimental results with the calculated values in the same figure, we see that for the gold resonator, the PEM calculation matches the experimental fairly well. The measured superconducting 'Q', however, is much lower than the calculated values. Several reasons can be given for this. First, the values for the complex conductivity of the superconductor used in the PEM calculation were obtained by microwave reflectance/transmission measurements on separate laser ablated films.[8] It is likely that the quality of those films was higher than the resonator film, in part because these films were

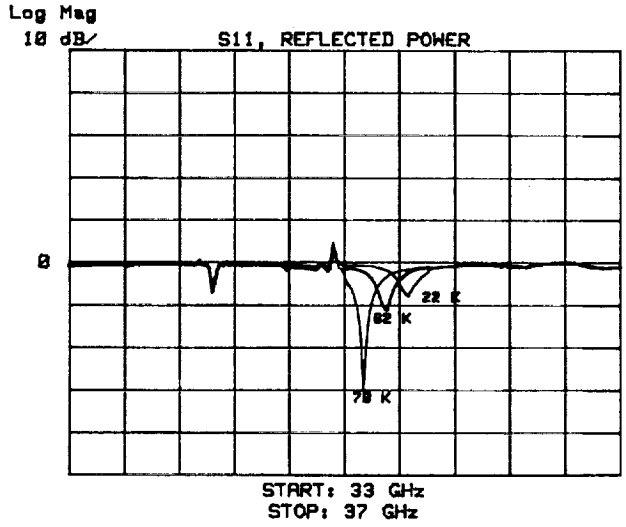

Figure 3. S11 of the superconducting resonator in its test fixture, at three temperatures.

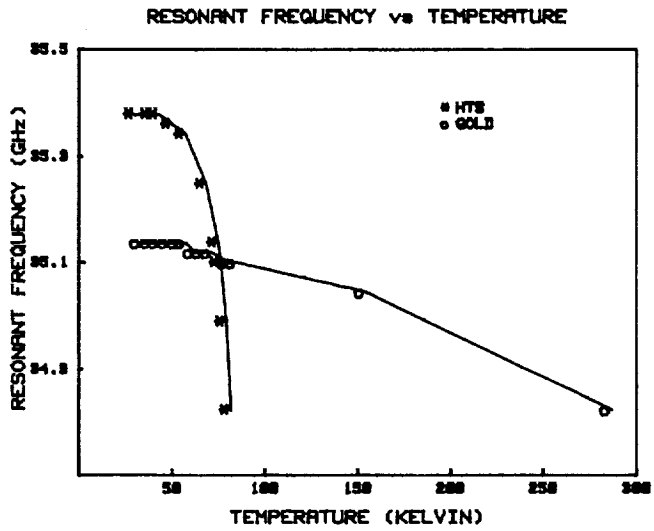

Figure 4. Resonant frequency vs temperature for superconducting and normal strips.

unpatterned. In addition, substrate losses in the PEM were calculated on the basis of tanδ=5.8×10E-4 but accurate values for lanthanum aluminate are not available so the actual value may be higher or lower. It seems likely that improvements in the measured Q are possible with increased film quality.

CONCLUSIONS

Ring resonator circuits were fabricated from laser ablated YBCO superconducting films on lanthanum aluminate to determine transmission line losses at millimeter wave frequencies. At 25°K the unloaded Q of the superconducting resonator was 1.5 times the Q of identical resonators made of gold. A shift in the resonant frequency with temperature follows the form predicted by the London equation. Using the PEM we calculated the Q values of the ring resonator with a thin YBCO strip and a gold ground plane. The theoretical results were compared with experimental results of the ring resonator of that structure. The calculated results predict higher values of Q than those actually observed, but improved film quality should increase measured Q values.

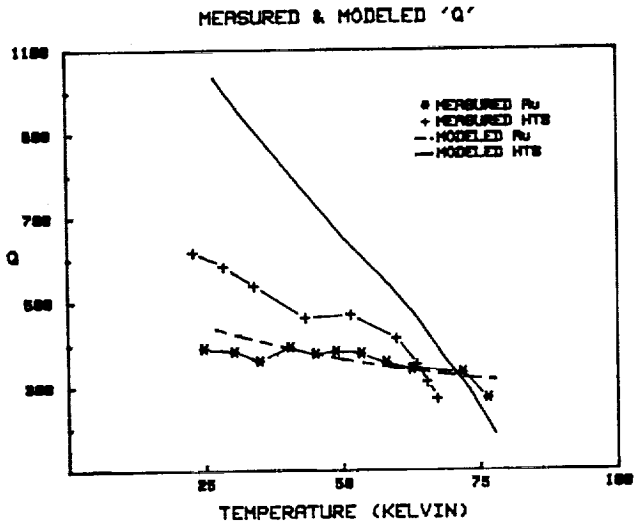

Figure 5. Measured and calculated values of unloaded Q for superconducting and normal resonators.

REFERENCES

1. N. Klein, G. Muller, H. Piel, B. Roas, L. Schultz, U. Klein and M. Peiniger, "Millimeter Wave Surface Resistance of Epitaxially Grown YBCO Thin Films," Appl. Phys. Lett. Vol. 54, pp 757-759.

2. A. A. Valenzuela and P. Russer, "High Q Coplanar Transmission Line Resonators of YBCO on MgO," Appl. Phys. Lett., Vol. 55, pp. 1029-1031, 1989.

3. B. R. McAroy, G. R. Wagner, J. D. Adam, J. Talvacchio and M. Driscoll, "Superconducting Stripline Resonator Performance," IEEE Trans. Magn., Mag. Vol. 25, pp. 1104-1106 (1989).

4. J. H. Takemoto, F. K. Oshita, H. R. Fetterman, P. Kobrin, and E. Sovoro, "Microstrip Ring Resonator Technique for Measuring Microwave Attenuation in High-Tc Superconducting Thin Films," IEEE Trans. Microwave Theory and Tech., Vol. MTT-37, pp. 1650-1652, 1989.

5. J. D. Warner, K. B. Bhasin, N. C. Varaljay, D. Y. Bohman and C. M. Chorey, "Growth and Patterning of Laser Ablated Superconducting YBCO Films on LaAlO3 Substrates," NASA TM-102336.

6. H. Y. Lee, and T. Itoh, "Phenomenological Loss Equivalence Method for Planar Quasi-TEM Transmission Line with a Thin Normal Conductor or Superconductor," IEEE Trans. Microwave Theory and Tech., Vol. MTT-37, no. 12, pp. 1904-1909, 1989.

7. James Swihart, "Field Solution for a Thin-Film Superconducting Strip Transmission Line," Journal Appl. Phys., Vol 32, no. 3, pp. 461-469, 1961.

8. F. A. Miranda, W. L. Gordon, K. B. Bhasin, V. O. Heinen, and J. Valco, "Millimeter Wave Transmission Studies of YBCO Thin Films in the 26.5 to 40 GHz Frequency Range," Proc. Third Annual Conf. on Superconductivity and Applications, to be published by Plenum Press 1990, and NASA TM-102345.

Ka-BAND PROPAGATION CHARACTERISTICS OF MICROSTRIP LINES ON GaAs SUBSTRATES AT CRYOGENIC TEMPERATURES

R. R. Romanofsky, J. C. Martinez, B. J. Viergutz, and K. B. Bhasin
National Aeronautics and Space Administration
Lewis Research Center
Cleveland, Ohio 44135

KEY TERMS

Microstrip line, GaAs substrate, relative permittivity, resonators, low temperature microwave measurements, Q-factor

ABSTRACT

Effective permittivity and loss characteristics of gold microstrip lines on GaAs substrates were obtained by characterizing GaAs linear resonators at cryogenic temperatures (300 to 20 K) from 30–40 GHz. A slight decrease in effective permittivity and a significant reduction in loss were observed with lower temperatures.

INTRODUCTION

Microstrip is a geometrically simple transmission line that has found widespread use in GaAs monolithic microwave integrated circuits (MMIC). Because of the two-wire configuration, it has no lower cutoff frequency. However, upper frequency limitations are imposed due to surface waves and transverse resonance modes that can propagate under certain conditions [1]. The dominant mode of propagation is quasi-TEM (transverse electromagnetic).

Detailed information on propagation characteristics of transmission lines on GaAs at cryogenic temperatures is unavailable. Accurate theoretical analysis is hindered by the inhomogeneous geometry of microstrip, which causes a field discontinuity at the air–dielectric interface. This information is required for the accurate modeling and matching network design of cryogenically cooled GaAs MMICs. Also, such information will prove useful in developing hybrid superconducting/GaAs MMIC circuits. This promising technology will exploit the inherent benefits of superconducting electronics, such as low loss and low noise performance, and simultaneously enhance the active device characteristics due to the cryogenic operating temperature.

DESIGN AND FABRICATION

50-ohm linear open circuit $n\lambda/2$ microstrip resonators were fabricated on 2-in. semiinsulating GaAs wafers along the (100) crystallographic plane in the $[0\bar{1}0]$ direction. The end (fringing) effect was eliminated by using two lines: a short line of length l_1 with a fundamental resonance at f_1 and a long line of length $l_2 = 2l_1$ with a harmonic resonance of $f_2 \approx f_1$. The resonators were coupled to a feed line via a critical symmetric gap. The gap dimensions ranged from 0.0015–0.00175 in. for the 0.010-in.-thick wafers.

A pattern electroplating technique was established to fabricate the GaAs microstrip resonators. Initially, 200 Å of titanium and 1000 Å of gold were sequentially deposited onto the wafers by evaporation. A layer of positive photoresist was then spin coated onto the wafer and subsequently exposed to UV light through a negative (dark-field) chrome/glass mask. At this point, the desired pattern had been transferred to the substrate. The wafer was then developed, which established windows corresponding to the circuit pattern. The electroplating process entailed submersing the wafer in an aqueous gold–potassium–cyanide solution. A platinum–titanium anode was connected to a constant current source and the wafer (cathode) was grounded. A current density of 3 mA/in.^{2} was maintained to ensure a high quality film. Finally, the thin underlying gold and titanium layers were removed by chemical etch. The wafers were then lapped and polished to 0.010 in. in order to obtain the correct characteristic impedance and surface finish. A titanium–gold ground plane was evaporated onto the wafer reverse. A fully fabricated resonator pair is shown in Figure 1.

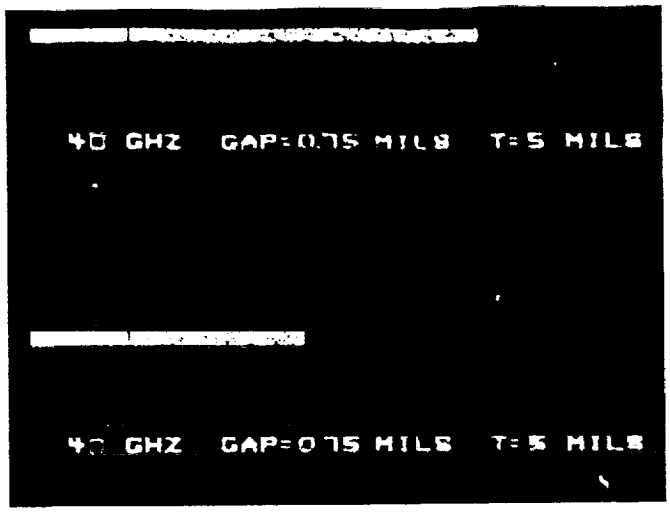

Figure 1 A fully fabricated resonator pair, short line of length l_1 with a fundamental resonance at f_1 and a long line of length $l_2 = 2l_1$, with a harmonic resonance of $f_2 = f_1$. The gap is approximately 0.75 mil

EXPERIMENTAL RESULTS

Swept frequency measurements were performed using an automatic network analyzer system [2] connected to a closed cycle helium refrigerator. A cosine tapered ridge guide test fixture was placed inside the refrigerated chamber and the resonator chip was mounted beneath the ridge using pressure contact (Figure 2). The technique is based on the measurement of reflection coefficients ($S11$) for each microstrip resonator pair. From these data, total loss and effective permittivity can be determined. Raw data yield the loaded quality factor Q_L. Calculation of the unloaded quality factor Q_0 required derivation of the gap coupling coefficient and modeling of the resonator as a transformer coupled RLC tank circuit. Based on the analogous input impedance and accounting for coupling loss, the correct Q_0 was evaluated. Because the devices were enclosed in the waveguide below cutoff, radiation was considered negligible. A complete description of the techniques employed is provided in reference 3.

A number of microstrip resonator pairs were successfully characterized. Figure 3 depicts the measured response of a resonator tested at 300 and 20 K, respectively. Two phenomena were observed upon cooling to cryogenic temperatures. First, there was a consistent shift in the resonant frequency of approximately −2%. The second involved a dramatic change in the loaded quality factor, a consequence of the temperature dependence of loss and a reduction in coupling coefficient. Figure 4 illustrates the temperature dependence of effective permittivity at approximately 31.5 GHz, revealing a trend to diminish slightly upon cooling. Table 1 provides loss data as a function of temperature, demonstrating a 0.15-dB/cm improvement as the material is cooled from 300 to 20 K. It is important to convey that the data for the unshielded resonators contain a large radiation component and should not be interpreted as the loss that would occur along a uniform microstrip line.

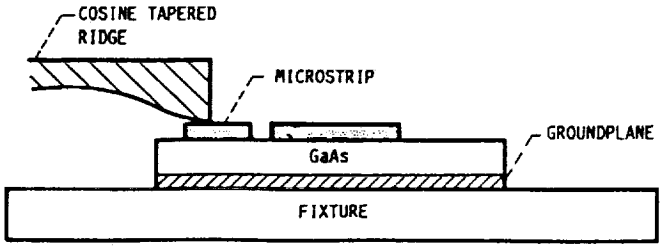

Figure 2 Schematic of cosine tapered ridge guide fixture arrangement

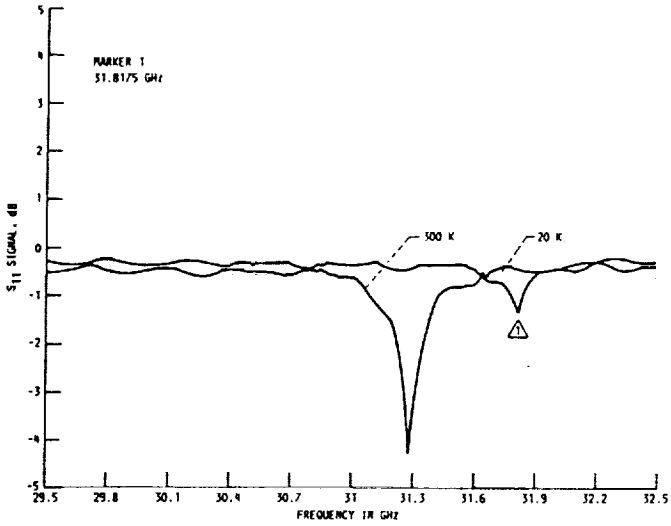

Figure 3 Measure response of a resonator tested at 300 and 20 K

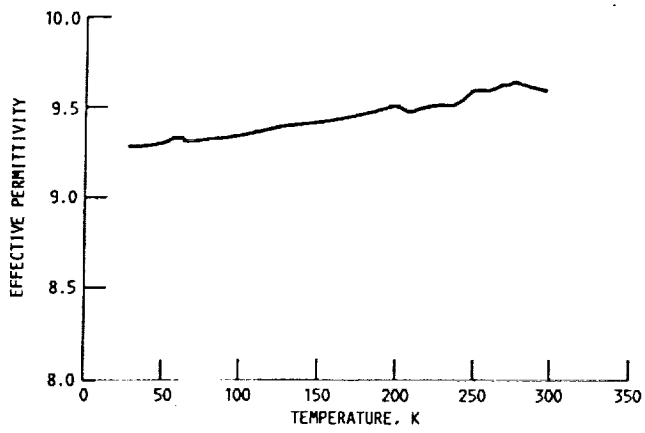

Figure 4 Temperature dependence of effective permittivity of 10-mil-thick GaAs substrate at approximately 31.5 GHz

TABLE 1

Frequency, GHz	Temperature, K	Q_0, Shield	Q_0, Open	Loss, dB/cm
30.2620	300	205	—	0.45
30.5635	300	197	—	0.47
31.6975	300	211	—	0.43
39.0720	300	—	24	4.37
39.1060	300	—	18	5.83
31.0252	77	271	—	0.34
31.9675	77	254	—	0.36
30.8575	20	297	—	0.31

CONCLUSION

Q values from 30–40 GHz were obtained for GaAs microstrip resonators at cryogenic temperatures. It was found that the Q values increased by a factor of approximately 1.25 at 77 K and a factor of 1.5 at 20 K when compared to room temperature data. Also, there is a small but definite decrease in dielectric constant as temperature decreases.

Eventually, as high temperature superconducting technology evolves and merges with GaAs MMIC, such information will be necessary for effective device design. At present, the in situ film processing temperatures exceed the tolerance of GaAs circuitry, due to materials problems ranging from semiconductor diffusion to metal migration.

REFERENCES

1. T. C. Edwards, *Foundations for Microstrip Circuit Design*, Wiley, New York, 1981.
2. J. E. Aitken, "Swept Frequency Microwave Q-Factor Measurement," *Proc. IEE*, Vol. 123, September 1976, pp. 855–862.
3. R. R. Romanofsky, "Analytical and Experimental Procedures for Determining Propagation Characteristics of Millimeter-Wave Gallium Arsenide Microstrip Lines," NASA Report No. TP-2899, 1989.
4. S. Withington, "Cryogenic Performance of Microstrip Substrates," *Electron. Lett.*, Vol. 19, October 13, 1983, pp. 887–888.

Received 1-2-90

Microwave and Optical Technology Letters, 3/4, 117–119

CCC 0895-2477/90/$4.00

TRANSPORT MEASUREMENTS ON GRANULAR Y-BA-CU-O FILMS

M. A. Stan*, S. A. Alterovitz, D. Ignjatovic, and K. B. Bhasin
NASA-Lewis Research Center, 21000 Brookpark Road Cleveland, OH 44135 USA

G. C. Valco and N. J. Rohrer, Department of Electrical Engineering, The Ohio State University Columbus, OH 43210 USA

The critical current in granular YBaCuO films has been measured at temperatures very near the critical temperature, T_c. The critical current is proportional to $(1-T/T_c)^2$ for $T<.9\ T_c$. The current-voltage (I-V) characteristics of the films have also been measured as a function of temperature and indicate that the observed deviation from the $(1-T/T_c)^2$ dependence for $T > .9T_c$ is a natural consequence of the constant field criterion (e.g. .25 μV/mm) used to define the critical current.

1. Introduction

Reports [1,2] have shown that the measured critical current, I_c, near T_c is proportional to $(1-T/T_c)^2$ for $T < .9T_c$ and exhibits a weaker temperature dependence for temperatures nearer to T_c. Our I_c data exhibits qualitatively the same behavior and we will show, with the aid of the (I-V) characteristics, that the variation in the power law near T_c is a result of the measurement criterion. Next we discuss several different criteria for defining the onset of dissipation as it applies to I_c measurements. Finally we show that *i*) the temperature dependence of the I_c can be obtained by fitting the I-V data taken at different temperatures to the simple expression $V=A(I-I_c)^m$, *ii*) the temperature dependence of I_c obtained using this procedure is in good agreement with that of the measured data.

2. Experimental

The superconducting films were prepared by sequential evaporation of Cu,Y, and BaF_2 onto (100) $SrTiO_3$. The films were deposited onto .5 cmx1.0 cm substrates and had a nominal thickness of 1 μm prior to annealing. Details of the film preparation and annealing have been published elsewhere.[3] Scanning-electron-micrographs of the film surface showed irregularly shaped grains .5 μm in size having no epitaxy with the substrate.

A d.c. four probe method was used for all transport measurements. Electrical contact to the films was made by In-soldering to previously deposited 1μm Ag electrodes extending across the short dimension of the films. The critical temperature for the film described below was 62.3K, determined with a measuring current density of $.2A/cm^2$.

3. Results and Discussion

In Fig. 1 the upper four sets of I_c data were obtained using different voltage criteria. The solid lines are guides to the eye. The lowest line in Fig. 1 was obtained from a least-squares fit of the I-V data and will be discussed later in this section. Notice that the upper four curves have a slope of 2 at low temperatures, and show a departure from the straight line behavior at different temperatures depending upon the voltage criterion. The departure from $(1-T/T_c)^2$ as $T \to T_c$ can be understood with the aid of the I-V data in Fig. 2. Here we show a sequence of I-V data obtained at six different

*Also Department of Physics, Kent State University, Kent, Ohio, 44242 USA

0921-4534/89/$03.50

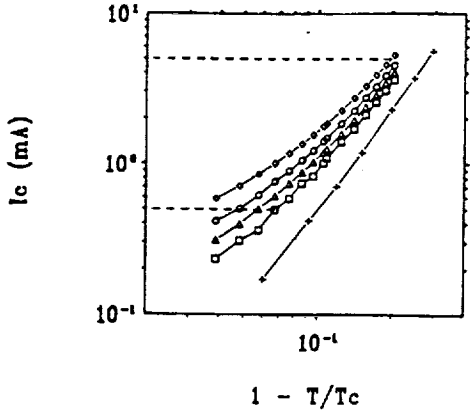

Fig. 1 I_c against $(1-T/T_c)$ obtained using different criteria. From top to bottom 2.5 μV/mm, 1μV/mm, .5μV/mm, .25μV/mm, and data obtained from a least-squares fit of the I-V data to $V=A(I-I_c)^m$.

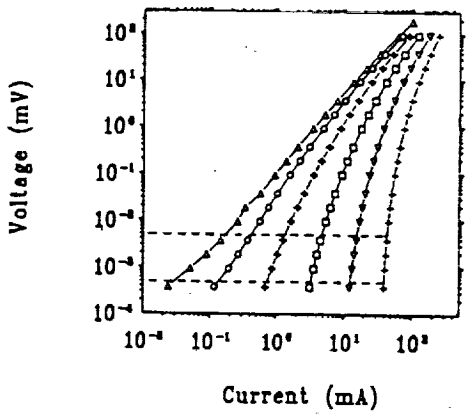

Fig. 2 Voltage against current obtained at a sequence of temperatures. From right to left: 20, 40, 51, 58, 62, and 64K.

temperatures. The upper and lower dashed lines represent the 2.5 μV/mm and .25μV/mm criteria respectively, and a vertical line drawn from the intersection of these lines with the data yields the I_c. At 20K the two criteria result in the same I_c while at 58K they yield numbers differing by a factor of two. The important parameter for evaluating the accuracy of a constant voltage criterion is apparently the logarithmic derivative dlog V/ dLog I. The smaller the logarithmic derivative at the chosen voltage criterion the more one overestimates I_c. Since dLogV/dLogI is rapidly diminishing as $T \to T_c$ it is inevitable that one overestimates I_c which results in the apparent weakening of the temperature dependence near T_c. In principle one would have to define I_c at the same value of the logarithmic derivative (i.e. lower voltages) in order to maintain the same level of accuracy. Since this method is not practical one could use the less stringent resistive criterion whereby a supercurrent is present if $V_c/I_c < R(T_c)$, where V_c is the voltage criterion, and $R(T_c)$ is the smallest detectable resistance in the T_c measurement. In Fig. 1 the top and bottom dashed lines represent the lowest quotable values of I_c for the 2.5 μV/mm and .25μV/mm criteria respectively.

We believe there is yet another way to obtain the temperature dependence of I_c. It has previously been shown that the I-V data can be described by $V=A(I-I_c)^m$ where I_c and m are temperature dependent[4]. By performing a least-squares fit of our data to this relation we obtain I_c and m as a function of temperature. The I_c data obtained in this way are the points on the lowest line in Fig. 1. The exponent is 2.2, in good agreement with the measured data satifying the resistive criterion, and I_c vanishes at 63.8K. In conclusion, we found that I_c is proportional to $(1-T/T_c)^2$ for $T \sim T_c$.

REFERENCES

1) S. B. Ogale, D. Dijkkamp, and T. Venkatesan, Phys. Rev. B36, (1987) 7210

2) J. M. C. de Vries, M. A. M. Gijs, G. M. Stollman, T. S. Baller, and G. N. A. Vern, J. Appl. Phys. 64 (1988) 426.

3) G. J. Valco, N. J. Rohrer, J. D. Warner, and K. B. Bhasin, A.I.P. Proceedings No. 182 (1989) 147.

4) P. England, T. Venkatesan, X. D. Wu, and A. Inam, Phys. Rev. B38 (1988) 7125.

ELECTRICAL TRANSPORT MEASUREMENTS ON POLYCRYSTALLINE SUPERCONDUCTING Y-Ba-Cu-O FILMS

M. A. Stan, S. A. Alterovitz, and D. Ignjatovic

NASA - Lewis Research Center
Cleveland, Ohio

ABSTRACT

The current-voltage, I-V, characteristics of polycrystalline Y-Ba-Cu-O films have been measured as a function of temperature. The I-V characteristics are interpreted using a model based upon an array of weak links with a statistical distribution of critical currents. In addition, we find evidence that the supercurrents flow in nearly independent filaments near T_c. Various criteria are discussed with respect to the definition of the transport critical current, I_c, in these films. A temperature dependence for I_c has also been deduced from the I-V data by appealing to an empirical scaling law. We propose that this temperature dependence, $I_c \propto (1-T/T_c)^{2.2}$, is representative of the weaker links within the critical current distribution.

INTRODUCTION

The T_c measurement is the most commonly used method for the characterization of superconducting materials. However, I_c is a more effective parameter in determining technological usefulness. In particular it is desirable to measure the temperature dependence of I_c in order to illuminate the mechanism limiting I_c, such as depairing in a single crystal sample, or perhaps tunnelling through grain boundaries in a polycrystalline sample. In the presence of a magnetic field, single crystal high temperature superconducting (HTS) samples have been shown to exhibit flux creep[1], while, in polycrystalline samples a variety of effects ranging from weak link limited I_c behavior at low magnetic fields to flux flow limited I_c behavior in high magnetic fields[2] have been

observed. Implicit in any of these I_c measurements is some criterion for the definition of I_c. The selection of a criterion for I_c has been particularly difficult in the HTS materials because, in many instances, the resistive transition is not sharp. Several attempts to standardize the criteria for I_c in the presence of a magnetic field have been proposed[3,4]. However, for thin films in zero magnetic field, a constant field criterion ranging from 0.1 μV/mm to 1 μV/mm is widely used. While this criterion may be satisfactory for epitaxial thin films, where the critical supercurrent density, J_c, is of the order of 10^6 A/cm^2 at 77 K and the transition is sharp, the meaning of an I_c obtained in this way for polycrystalline films is not clear, owing to the broadness of the resistive transition in these films. The lack of a consensus on the temperature dependence of I_c, and in particular, the exponent in the expression $(1-T/T_c)^n$ $(1.5 \leq n \leq 2.0)$, could be symptomatic of the arbitrariness of an I_c obtained from a constant voltage criterion[5,6,7,8]. While the various exponents reported for the temperature dependence of I_c may relate in some way to the microstructure in the films, we believe that one must first understand the mechanism responsible for the transition in order for the measured I_c to have meaning.

To our knowledge, only one attempt has been made to understand the resistive transition in HTS polycrystalline films. This was the work of England et al.[9], where they suggested that the films underwent a phase locking transition similar to that found in compacted polycrystalline Ta samples[10]. Within this model, the phase, θ_i, of the wave function of each of the grains is uncorrelated from grain to grain when $T > T_c$ (T_c being defined at $R = 0$). At T_c, the phase difference, $\theta_i - \theta_j$, between the neighboring grains becomes fixed because the thermal fluctuations ($k_B T_c$) are exceeded by the Josephson coupling energy ($hi_c/2e$). Here i_c is the intergrain critical current. The strongest evidence for this mechanism in polycrystalline HTS films came from the I-V data at T_c, where it was shown that $V(T_c) \propto I^2$. The quadratic dependence of V on I is a prediction of the phase locking model[10].

Recently the resistive transition of sintered Y-Ba-Cu-O wires in a magnetic field has been modeled by Evetts et al.[11] using extensions to the conventional model given for superconducting multifilamentary composites[12]. The extended model, hereafter referred to as the Weak Link Filament Array (WLFA) model, treats the sample as an array of weak links with a normal distribution of I_c's. Essential features of our I-V data are discussed in terms of this model. The implications of this model with respect to defining I_c are then discussed. Finally, by appealing to an empirical scaling law for the I-V data, we can

deduce a temperature dependence for an I_c which is representative of the weakest links in the I_c distribution.

EXPERIMENTAL

Sample Preparation

The films were prepared by sequential evaporation of Cu, Y, and BaF_2 onto (100) $SrTiO_3$. The films had a superstructure period of three, for a total of twelve layers, and a nominal thickness of 1 μm prior to annealing. Details of the deposition parameters and annealing have been published elsewhere[13]. Scanning electron micrographs of the films showed rectangular shaped grains with dimensions of 0.3 μm X 1.0 μm having no epitaxy with the substrate. X-ray diffraction analysis of the films indicated a polycrystalline nature with some a-axis texturing, as well as the presence of $BaCuO_2$ and Y_2O_3 phases. Electrical contact to the films was made by depositing a 1 μm layer of Ag through a shadow mask, resulting in four equally spaced 0.1 cm wide strips traversing the short dimension ($\simeq$ 0.3 cm) of the sample. The contacts were subsequently annealed in dry O_2 at 500° C for approximately two hours resulting in contact resistances of 10 $\mu\Omega$ or less. Wires were then attached to the Ag strips via In-soldering.

Electrical Transport Measurement

Transport measurements in low magnetic fields (0 - 70 Oe) were made in a ^{4}He closed cycle refrigerator with an externally mounted Cu wire Hemholtz coil around the sample chamber. The samples were attached to an OFHC copper holder and housed in an OFHC copper radiation shield. Cooling of the assembly was done by convection through 1 atm (STP) of ^{4}He gas to the refrigerator cold head ($\simeq$ 16 K). The sample temperature was determined by a Si diode which is epoxied into the sample holder, and has a rated accuracy of $\pm$ 0.25 K over the temperature interval of the measurements.

All the transport measurements discussed below were made using the conventional four-probe method. The T_c measurement of the films was made with a typical measuring current density of 0.2 A/cm^2 and a voltage sensitivity of approximately 10 nV. This voltage sensitivity was obtained using a nanovoltmeter in conjunction with signal averaging.

TRANSPORT DATA AND DISCUSSION

Nine samples were measured, but we will present detailed results on one typical film. A common feature of the films is that they have a zero resistance temperature, T_c, in the range 60 K - 70 K. The films exhibit a metallic nature above the onset temperature of 90K but the resistance is not linear in temperature, presumably because of the various grain orientations and presence of other phases.

I-V data, obtained at six different temperatures, is displayed in Fig. 1. The T_c of this film was 62.3 K. The upper and lower horizontal dashed lines in Fig. 1 represent I_c voltage criteria of 2.5 μV/mm and 0.25 μV/mm, respectively. A vertical line drawn from the intersection of one these lines with the I-V data yields a value for I_c. At 20 K the two criteria yield essentially the same I_c while at 58 K they yield numbers differing by a factor of two. Obviously, an important parameter in defining I_c is the logarithmic derivative dLog(V)/dLog(I) commonly referred to as the n value of the resistive transition. The smaller the n value at the chosen voltage criterion the more sensitive I_c is to the voltage criterion. Because the n value is temperature dependent and approaches one at T_c, it is inevitable that this type of criterion will give I_c a weaker temperature dependence the nearer one gets to T_c. This effect is

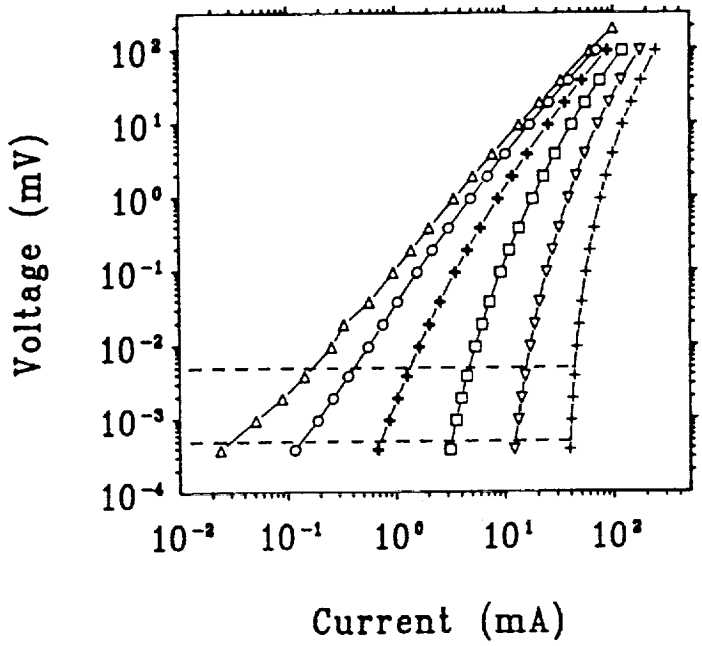

Fig. 1 Voltage against current obtained for a sequence of temperatures. From right to left: 20 K, 40 K, 51 K, 58 K, 62 K, and 64 K.

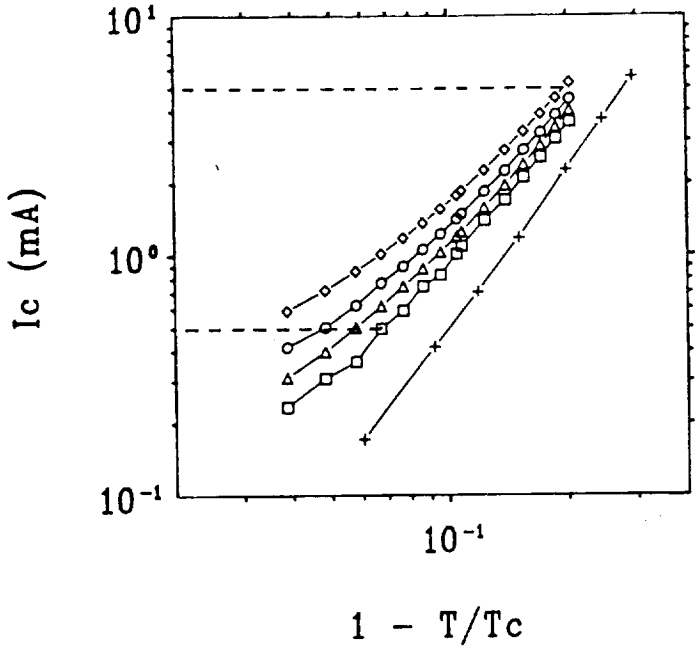

Fig. 2 I_c against $(1-T/T_c)$ obtained using different criteria. From top to bottom: 2.5 μV/mm, 1 μV/mm, 0.5 μV/mm, 0.25 μV/mm, and data from a least-squares fit of the I-V data to $V = A(I-I_c)^n$.

demonstrated in the I_c vs. $1-T/T_c$ characteristic shown in Fig. 2. The upper four sets of I_c data in Fig. 2 were obtained using different voltage criteria. The solid lines are guides to the eye. The lowest line in Fig. 2 was obtained from a data fitting procedure and will be described later. Notice that the upper four data sets are straight lines at the low temperature end of the graph with a slope of $\simeq 2$. The data show a departure from linear behavior at different temperatures depending upon the voltage criterion. One final note with regard to the constant voltage criterion concerns the lowest meaningful I_c measurement. To be self consistent with the T_c measurement the I_c data must be greater than or equal to V_c/R_c, where R_c is the smallest detectable resistance in the T_c measurement and V_c is the voltage criterion used in the I_c measurement. The upper and lower horizontal dashed lines in Fig. 2 represent the lowest self consistent values of I_c for the I_c voltage criteria of 2.5 μV/mm and 0.25 μV/mm, respectively. Failure to make the T_c and I_c measurements consistent with one another may result in assignment of I_c values to very resistive samples[14]. Regardless of the I_c criterion, one must first understand the nature of the resistive transition before one can attach any physical significance, such as tunneling, to I_c measurements on polycrystalline HTS films.

It has long been recognized that the broad resistive transitions into the flux flow state in type-II superconductors can be explained in terms of the variation in the local I_c along the sample length, where the flux-flow voltage is determined by that fraction of material whose I_c is lower than the applied current[15,16]. The I-V characteristic is then determined by

$$V = \left(\frac{\rho}{A}\right) \int_0^I \int_{i_{cm}}^{i} f(i_c)\, di_c\, di \qquad (1)$$

where $f(i_c)$, ρ, and A are the critical current distribution function, the flux-flow resistivity, and the cross-sectional area, respectively. The lower limit, i_{cm}, on the second integral in Eq. 1 is the smallest i_c in the distribution.

In type-II multifilamentary composites the transition into the flux-flow state is broad as a result of a distribution of localized constrictions along the individual filaments. For such structures the empirical relation $V \propto I^n$ seems to characterize the resistive transition quite well. Recently a theoretical understanding of this relation was obtained by Plummer and Evetts[12] by assuming the constrictions were normally distributed. The calculations were made using Eq. 1 and were based on either independent filaments or nearest neighbor coupling. There are three important results which apply for either limit: the scaling law $V \propto I^n$ is a natural consequence of a normal distribution of inhomogeneities; the n value is proportional to $(\langle I_c \rangle/\sigma)^{5/3}$ where $\langle I_c \rangle$ and σ are the mean critical current and the width of the distribution, respectively; and the measured I_c, obtained by a constant voltage criterion, will increasingly underestimate $\langle I_c \rangle$ as the n value decreases.

Recently, Evetts[11] has been successful in qualitatively explaining the resistive transition of sintered Y-Ba-Cu-O wires in a magnetic field using the WLFA model. The WLFA model is an extension of the independent filament model to include long range coupling and the tunnelling nature of the weak links. In the WLFA model, the conductor geometry is essentially a multiply connected weak link network. However, in low density samples near the percolation threshold, there are many junctions in series between parallel interconnections and one has, effectively, an array of independent filaments, in complete analogy to the multifilamentary composite system. If a normal distribution of junction I_c's is assumed, n bears the same significance to $\langle I_c \rangle$ and σ that it does in the multifilamentary composite system.

In the multiply connected limit of the WLFA model it is argued[11] that there is a length scale, Λ, in the direction perpendicular to the direction of applied current, which is used to describe the degree to which junctions within Λ switch to the normal state at the same current. For low values of magnetic field, temperature, and current the network is isotropic and Λ extends across the entire sample. If M represents the number of connected junctions within Λ, then it is argued that the n value is increased by a factor $\sqrt{M}$, as compared to the single filament result, and the effective width of the normal distribution becomes $\sigma/\sqrt{M}$. In the WLFA model Λ falls with increasing current since larger applied currents require larger transverse balancing currents which in turn increase the probability that the transverse junctions will be broken. The reduction in Λ manifests itself as a current dependent reduction of the n value, a result which is qualitatively different from multifilamentary composite systems where n is independent of the current. At this point we caution the reader that when the junctions are multiply connected Eq. 1 no longer applies, and one must resort to numerical techniques[11] in order to obtain an I-V relation.

Referring once again to Fig. 1, we believe that the I-V data qualitatively exhibits the main features of the WLFA model. These features are: the larger the n value, the larger the current required to drive the film normal, and at

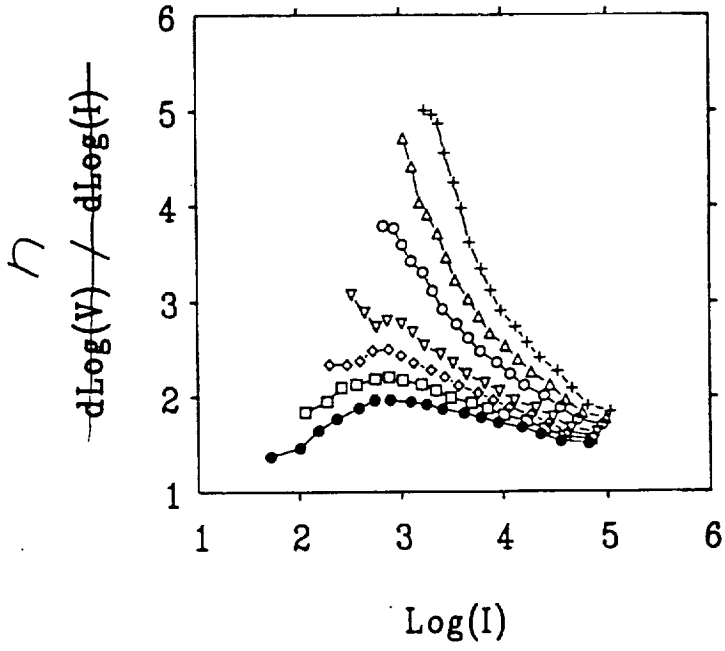

Fig. 3 Logarithmic derivative of the I-V data for a sequence of temperatures near T_c. From top to bottom: 54 K, 56 K, 58 K, 60 K, 61 K, 62 K, and 63 K.

a given temperature, the n value falls monotonically with increasing current. In addition, the I-V data shows evidence near T_c that the films are nearly in the independent filament limit, i.e. that the films are made up of independent chains of weak links. If one looks closely at the low voltage portion of the I-V characteristic for the two left most curves, a tail in the data is evident. The data designated by the open circles was obtained at T_c and the left most data about 1 K higher. To make the tail more prevalent we plot the n value against Log(I) in Fig. 3 for seven different temperatures spaced 1 K apart, with the lowest temperature being at the top of the graph. It is evident that the tail appears very abruptly within approximately 1 K of the T_c value determined in the resistivity measurement. In the experiments of Evetts et al.[11], where the magnetic field was varied and the temperature held constant, the same feature was observed to appear suddenly at a field of 2 mT for sintered Y-Ba-Cu-O wires immersed in LN_2. An obvious explanation for the tail is that the measured voltage contains an ohmic component and a nonlinear component. The ohmic component could be a result of tunnel junctions, which have been driven normal, in series with the nonlinear component from the remaining portion of the weak link connected filaments. The fact that an ohmic component of the voltage exists near T_c implies that the weak links are not multiply connected. If the junction array was multiply connected there would always be a superconducting path across the sample and the ohmic contribution from the normal

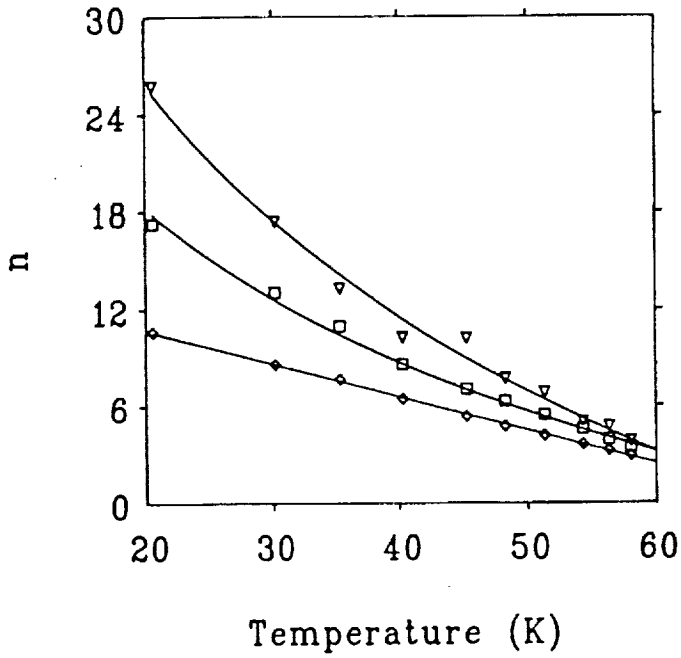

Fig. 4 Resistive transition n value against temperature obtained using different criteria. From top to bottom: 0.4 μV, 4 μV, and 40 μV.

junctions would not be visible.

An implication of the WLFA model on the measurement of the intergranular critical current is that the measured I_c is nearly equal to $\langle I_c \rangle$ at any given voltage criterion provided that the n value at the voltage criterion is large. However, when n becomes small one tends to underestimate $\langle I_c \rangle$ at any given voltage criterion. The latter point indicates that the I-V curves are being controlled by the weakest links, a result also deduced from magnetic field measurements[2]. In WLFA model, or more specifically, if the I-V characteristic results from switching of the weakest links which have a statistical distribution, we expect the temperature dependence of I_c, as determined using a constant field criterion, to be a convolution of the junction and statistical distribution temperature dependencies, casting doubt on interpretations of the temperature dependence based solely on the tunnelling model.

Continuing under the assumption that n is determined by $\langle I_c \rangle$ and σ, we plot in Fig. 4 the n value vs. temperature at three different voltage criteria spanning two orders of magnitude. The solid lines are guides to the eye. For large n values the dependence of n with temperature is of a nonlinear nature, while the small n values show a more or less linear temperature dependence. When n is large the I_c distribution is sharp and we expect that many weak links will be broken simultaneously resulting in a rapid reduction of n with increasing temperature. Small n values indicate a broad I_c distribution therefore few weak links switch co-operatively and n has a weaker temperature dependence.

Although the WLFA model provides no analytical expression for the I-V characteristic, and the temperature dependence of I_c obtained using a constant voltage criterion is open to question in light of a statistical interpretation of the I-V data, we have been very successful in obtaining the temperature dependance of I_c by appealing to the empirical relation $V = A(I-I_c)^m$, first applied to such films by England, et al.[9]. In this relation I_c and m are temperature dependent, and m was found to vary continuously from approximately $m = 3$ at low temperature to $m(T_c) = 2.2 \pm 0.1$, and finally to $m = 1$ at 90 K. This empirical relation has been applied with similar success on both Tl and Bi films[7,8] to describe the I-V data. We also find that the I-V characteristic of our films is reasonably described by this relation. In Fig. 5 we show the results of a least-squares fit of the data from Fig. 1 to the equation $V = A(I-I_c)^m$. The solid lines represent the least-squares fit at each temperature. In Fig. 6 we show the temperature dependence of the exponent, m, determined from the least-squares fit for the entire range of temperatures in which the I-V data were obtained. After performing least-squares fits on five

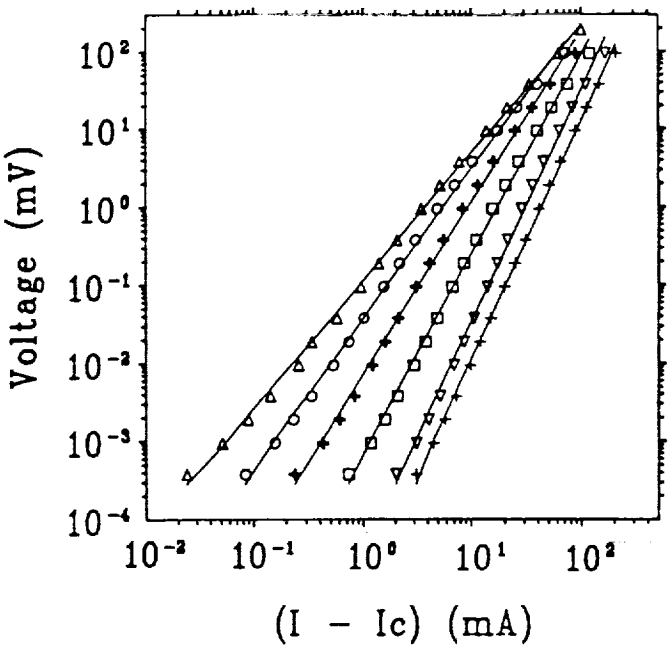

Fig. 5 Voltage against excess current obtained for a sequence of temperatures. From right to left: 20 K, 40 K, 51 K, 58 K, 62 K, and 64 K.

such films we find that the value of m in the low temperature limit, $m(20\ K) = 3.13 \pm 0.05$ is determined with far more confidence than $m(T_c) = 1.90 \pm 0.28$. It would seem that this is a natural consequence of the fact that $(dm/dT)_{20K} << (dm/dT)_{Tc}$. The I_c data of Fig. 5 are plotted in Fig. 2 and are denoted with a + symbol. This fitted data shows a simple power law behavior, with an exponent of 2.22, for all temperatures. The power law temperature dependence is seen at low temperatures in the upper four I_c data sets where the constant voltage criterion is expected to provide a more accurate value for I_c. The temperature dependence of I_c, deduced from the least-squares fitting procedure, on three separate films is shown in Fig. 7. The slope of the lines is 2.20 ± 0.05. The fit in Fig. 7 illustrates two points. The first point is that the temperature dependence is the same even for films whose J_c's differ by more than an order of magnitude, and second, that the power law fits the data from near T_c down to the lowest temperature measured (20 K). If one accepts that the I-V characteristic is controlled by a distribution of weak links, as described by the WLFA model, then the I_c obtained from fitting the I-V data to $V \propto (I-I_c)^m$ is characteristic of the weakest links in the distribution. It is not clear whether the $(1-T/T_c)^2$ dependence of I_c, deduced from $V \propto (I-I_c)^m$, is indicative of S-N-S tunnelling[17]. In other words, the temperature dependence of the I_c distribution may be admixed with the weak link

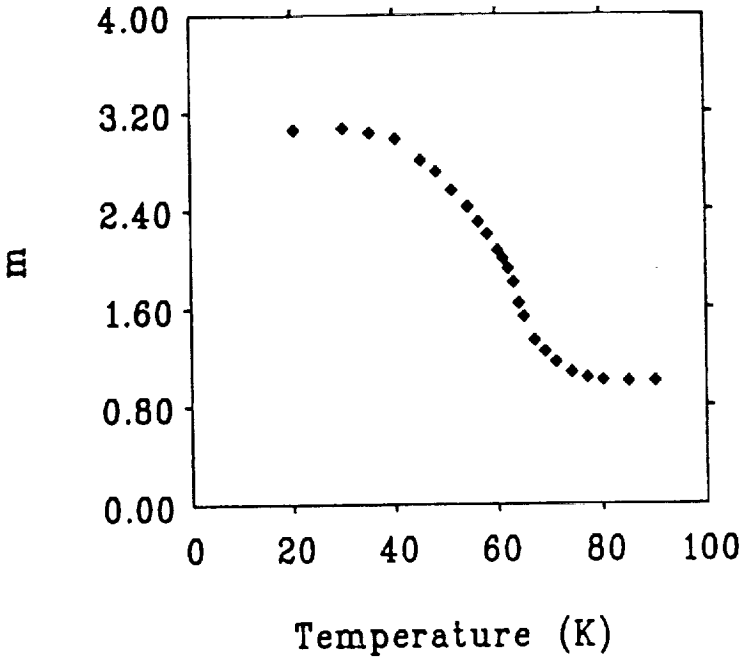

Fig. 6 Temperature dependence of the exponent, m, obtained from a least-squares fit of the I-V data to $V = A(I-I_c)^m$.

temperature dependence. In fact, what is puzzling about the $(1-T/T_c)^2$ dependence of I_c is the wide range of temperatures over which it fits the data, an observation which has been made in Tl- and Bi- based HTS films as well[7,8]. In any type of tunnelling model, whether it is S-N-S, S-I-N-S, or S-I-S, one expects to see a saturation at low temperatures because the energy gap and the decay length both become independent of temperature for $T \leq 0.5T_c$. Our measurements are made down to $T = 0.2T_c$ and still show no evidence of saturation in the I_c data. One other possibility is that there is a distribution of T_c's in the material, but again, it is not clear what type of a temperature dependence in I_c one is expected to observe from such an effect.

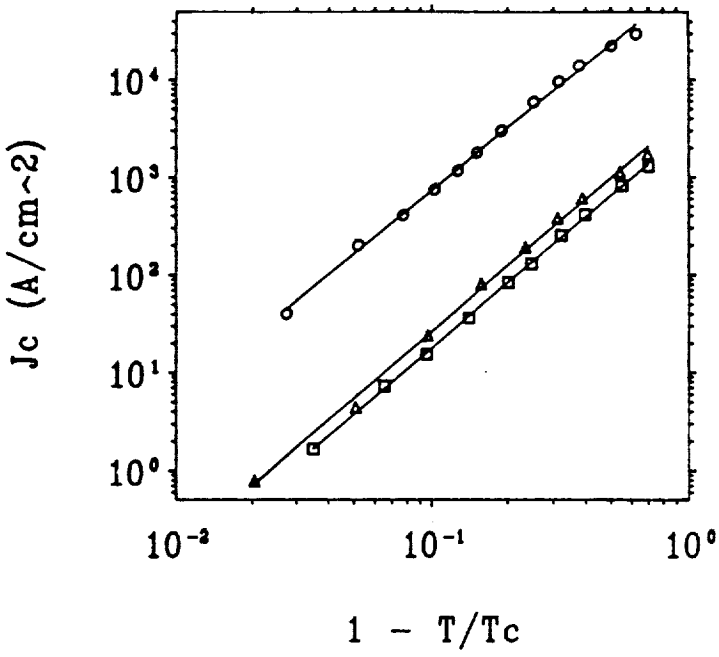

Fig. 7 J_c vs. $(1-T/T_c)$ for three films. In each case J_c was obtained from a least-squares fit of the I-V data to $V = A(I-I_c)^m$. The best fit straight lines through the data have a slope of 2.2.

CONCLUSIONS

We have shown that the I-V characteristics of the polycrystalline HTS films are qualitatively explained within the Weak Link Filament Array model (WLFA). In addition, our films show evidence of being in the filamentary limit of the WLFA model near T_c. The I-V data is well described by the empirical relation $V \propto (I-I_c)^m$ for the temperature range 20 K $\leq$ T $\leq$ 90 K. From this empirical I-V relation we find that $I_c \propto (1-T/T_c)^{2.2}$, and that this temperature dependence is characteristic of the weaker links in the I_c distribution.

ACKNOWLEDGEMENTS

The authors wish to thank Drs. G. J. Valco, Kul B. Bhasin, and Mr. N. J. Rohrer for providing the thin film samples used in these experiments.

REFERENCES

1. T. T. M. Palstra, B. Batlogg, L. F. Schneemeyer, and J. V. Wazczak, Thermally Activated Dissipation in Bi-Sr-Ca-Cu-O, Phys. Rev. Lett., 60:1662 (1988).

2. J. W. Ekin, T. M. Larson, A. M. Hermann, Z. Z. Sheng, K. Togano, and H. Kumakura, Double-Step Behavior of Critical Current vs. Magnetic Field in Y-, Bi-, and Tl- Based Bulk High-Tc Superconductors, (preprint submitted to Physica C).

3. T. T. M. Palstra, B. Batlogg, R. B. van Dover, L. F. Schneemeyer, and J. V. Wazczak, Critical Currents and Thermally Activated Flux Motion in High-Temperature Superconductors, Appl. Phys. Lett., 54:763 (1989).

4. J. W. Ekin, Offset Criterion for Determining Superconductor Critical Current, Appl. Phys. Lett., 55:905 (1989).

5. S. B. Ogale, D. Dijkkamp, and T. Venkatesan, Current Transport in High-T_c Polycrystalline Films of Y-Ba-Cu-O, Phys. Rev. B, 36:7210 (1987).

6. J. W. C. deVries, M. A. M. Gijs, G. M. Stollman, T. S. Baller, and G. N. A. Van Veen, Critical Current as a Function of Temperature in Thin Y-Ba-Cu-O Films, J. Appl. Phys., 64:426 (1988).

7. J. F. Kwak, E. L. Venturini, R. J. Baughman, B. Morosin, and D. S. Ginley, High Critical Currents in Polycrystalline Tl-Ca-Ba-Cu-O Films, Cryogenics, 29:291 (1989).

8. H. E. Horng, J. C. Jao, H. C. Chen, H. C. Yang, H. H. Sung, and F. C. Chen, Critical Current in Polycrystalline Bi-Ca-Sr-Cu-O Films, Phys. Rev. B, 39:9624 (1989).

9. P. England, T. Venkatesan, X. D. Wu, and A. Inam, Granular Superconductivity in R-Ba-Cu-O Thin Films, Phys. Rev. B, 38:7125 (1988).

10. C. Lebeau, J. Rosenblatt, A. Raboutou, and P. Peyral, Current-Voltage Hyperscaling in Arrays of Josephson Junctions, Europhys. Lett., 1:313 (1986).

11. J. E. Evetts, B. A. Glowacki, P. L. Sampson, M. G. Blamire, N. McN. Alford, and M. A. Harmer, Relation of the N-Value of the Resistive Transition to Microstructure and Inhomogeniety for Y-Ba-A_2-Cu_3-O_7 Wires, IEEE Trans. Magn., 25:2041 (1989).

12. C. J. G. Plummer and J. E. Evetts, Dependence of the Shape of the Resistive Transition on Composite Inhomogeneity in Multifilamentary Wires, IEEE Trans. Magn., 23:1179 (1987).

13. G. J. Valco, N. J. Rohrer, J. D. Warner, and K. B. Bhasin, Composition and Processing Effects in Sequentially Evaporated Y-Ba-Cu-O Thin films, A.I.P. Proceedings, 182:147 (1989).

14. S. S. Yom, T. S. Hahn, Y. H. Kim, H. Chu, and S. S. Choi, Exponential Temperature Dependence of the Critical Current in Y-Ba-Cu-O Films, Appl. Phys. Lett., 54:2370 (1989).

15. R. G. Jones, E. H. Rhoderick, and A. C. Rose-Innes, Non-Linearity in the Voltage-Current Characteristic of a Type-2 Superconductor, Phys. Lett. A, 24:318 (1967).

16. J. Baixeras and G. Fournet, Pertes par Deplacement de Vortex dans un Supraconducteur de Type II Non Ideal, J. Phys. Chem. Sol., 28:1541 (1967).

17. J. Clarke, Supercurrents in Lead-Copper-Lead Sandwiches, Proc. Roy. Soc. A, 308:447 (1969).

MICROWAVE CONDUCTIVITY OF SUPERCONDUCTING Bi-Sr-Ca-Cu-O THIN FILMS IN THE 26.5 TO 40.0 GHz FREQUENCY RANGE

F.A. MIRANDA
Case Western Reserve University, Cleveland, Ohio 44106, USA

K.B. BHASIN and V.O. HEINEN
Lewis Research Center, Cleveland, Ohio 44135, USA

R. KWOR and T.S. KALKUR
University of Colorado at Colorado Springs, Colorado Springs, Colorado 80833-7150, USA

Received 30 January 1990

The conductivity σ_N in the normal state and the real and imaginary parts of the conductivity in the superconducting state $\sigma^* = \sigma_1 - i\sigma_2$ of two Bi-Sr-Ca-Cu-O thin films (~ 5000 Å) are reported. The films were deposited on $LaAlO_3$ and MgO substrate by co-evaporation and have a transition temperature T_c of 80 K. The microwave conductivities were obtained from power transmission data, using a two-fluid model. Values for σ_N of 4.1×10^4 and 6.3×10^4 S/m at room temperature were obtained for the films on $LaAlO_3$ and MgO at 28.8 GHz, respectively. Below T_c, values of $\sigma_1 = 5.8 \times 10^4$ and $\sigma_2 = 1.4 \times 10^5$ S/m for the film on $LaAlO_3$ and $\sigma_1 = 7.3 \times 10^4$ and $\sigma_2 = 7.7 \times 10^4$ S/m for the film on MgO were obtained at 28.8 GHz. For the film on $LaAlO_3$, σ_2 decreased with increasing frequency, while for the one deposited on MgO, the behavior was completely opposite. The temperature dependence of the conductivity, both above and below T_c, was the same for both films. From σ_2, values for the magnetic penetration depth λ or 5.6 and 7.6 μm at 75 K were determined for the films on $LaAlO_3$ and MgO, respectively.

1. Introduction

The discovery of high temperature superconductors [1,2] has prompted efforts to develop their microwave applications. The low microwave and millimeter wave losses of these new superconducting oxides make them very attractive for the development of voltage dividers, resonators, phase shifters, and other high frequency analog devices. Microwave studies are of major importance in the view of the limitations of other traditional probes, such as specific heat and ultrasonic attenuation. These are strongly influenced by the phonon system which is heavily populated near the transition temperatures of these new superconductors [3]. In millimeter and microwave characterization, the parameter most often measured has been the surface resistance [3–6]. Less frequently, results have been reported for the complex conductivity [7–9]. A considerable amount of work in this area has been carried out in the Y–Ba–Cu–O superconducting oxide [3–6,9], and now similar measurements are underway in the recently discovered Bi–Sr–Ca–Cu–O [10] and Tl–Ba–Ca–Cu–O [11] superconductors. Although millimeter wave studies of Y–Ba–Cu–O thin films have been performed in the frequency range from 26.5 to 40.0 GHz [12], to the best of our knowledge no similar studies has been performed for Bi–Sr–Ca–Cu–O at these frequencies.

In this communication we are reporting our resulting of the characterization of Bi–Sr–Ca–Cu–O thin films at frequencies from 26.5 to 40.0 Ghz, in terms of the power transmitted through the films, assuming a two-fluid model. Values for the normal and complex conductivities, above and below T_c respectively, have been obtained along with values for the magnetic penetration depth as a function of temperature and frequency.

0921-4534/90/$03.50

2. Analysis

Since a complete understanding of the nature of superconductivity in the high-T_c superconductors is still rather limited, we have assumed that their superconducting state can be described in terms of a two-fluid model. The attributes of simplicity and success in yielding reasonably good estimates of the microwave properties of metallic superconductors for the case $\hbar\omega \ll E_{gap}$ [13] and also for Y–Ba–Cu–O at microwave frequencies [14,15] make this model an appropriate one for describing some of the phenomenological aspects of the behavior of the Bi–Sr–Ca–Cu–O superconductors. In this model the complex conductivity is $\sigma^* = \sigma_1 - i\sigma_2$, with

$$\sigma_1 = \sigma_c t^4, \quad \sigma_2 = \sigma_c (1 - t^4)/\omega\tau . \tag{1}$$

Here, σ_c is the normal conductivity at $T = T_c$, $\omega = 2\pi f$ is the angular frequency, t is the reduced temperature T/T_c, and τ is the mean carrier scattering time. Thus, to determine either σ_1 or σ_2 we need to know the transition temperature T_c and the value of σ_c. Furthermore, the value of τ must be known beforehand if σ_2 is to be obtained from eq. (1).

In order to determine the normal and complex conductivities of the films under study, we have used the method applied by Glover and Tinkham [16]. In this method, the transmission of a normally incident plane wave through a film of thickness d ($\ll$ wavelength or skin depth) deposited on a substrate of thickness l and index of refraction n is measured. Mathematically, the transmitted power can be expressed as

$$P = \frac{8n^2}{A + B\cos 2kl + C\sin 2kl}, \tag{2}$$

where

$$A = n^4 + 6n^2 + 1 + 2(3n^2 + 1)g + (n^2 + 1)(b^2 + g^2),$$

$$B = 2(n^2 - 1)g - (n^2 - 1)^2 + (n^2 - 1)(b^2 + g^2),$$

$$C = 2(n^2 - 1)nb,$$

$$k = n\omega/c,$$

and

$$y = g - ib = YZ_c = (G - iB)Z_c = (\sigma_1 - i\sigma_2)d\,Z_c$$

is the dimensionless complex admittance per square of the film in units of the characteristic admittance Z_c^{-1} of the waveguide (where $Z_c = Z_0/\sqrt{1 - (f_c/f)^2}$, $z_0 = 377\ \Omega$, mks; $Z_0 = 4\pi/c$, cgs; f_c = cutoff frequency of the TE mode waveguide, and f is the operational frequency).

In the normal state, eq. (2) becomes

$$P_N = \frac{8n^2}{\sigma_N^2 d^2 Z_c^2 Q + \sigma_N d Z_c R + J}, \tag{3}$$

where

σ_N = normal conductivity,

$$Q = (n^2 + 1) + (n^2 - 1)\cos 2kl,$$

$$R = 2(3n^2 + 1) + 2(n^2 - 1)\cos 2kl,$$

$$J = n^4 + 6n^2 + 1 - (n^2 - 1)\cos 2kl.$$

The normal state conductivity of the film can be expressed conveniently in terms of the power transmission as

$$\sigma_N = \frac{-RP_N \pm \sqrt{(RP_N)^2 - 4QP_N(JP_N - 8n^2)}}{2QP_N dZ_c}, \tag{4}$$

where only the expression with the + sign has physical relevance. It is convenient to use the ratio P_S/P_N in the analysis of the superconducting state, where P_S refers to the transmission in the superconducting state given by eq. (2). Thus,

$$\frac{P_S}{P_N} = \frac{(\sigma_N dZ_c)^2 Q + \sigma_N dZ_c R + J}{A + B\cos 2kl + C\sin 2kl}. \tag{5}$$

Solving eq. (5) for the imaginary part σ_2 of the conductivity and using the value of σ_N at $T = T_c$ we have

$$\frac{\sigma_2}{\sigma_c} = \left(\frac{-\beta}{2}\right)\frac{1}{\sigma_c dZ_c} + \left\{\frac{1}{(\sigma_c dZ_c)^2}\left[\left(\frac{\beta}{2}\right)^2 - \gamma\right] - \frac{\alpha\sigma_1}{\sigma_c^2 dZ_c} - \left(\frac{\sigma_1}{\sigma_c}\right)^2 + \left(\frac{P_c}{P_S}\right)\left[1 + \frac{\alpha}{\sigma_c dZ_c} + \frac{\gamma}{(\sigma_c dZ_c)^2}\right]\right\}^{1/2}, \tag{6}$$

where σ_c and P_c are the conductivity and the transmissivity at $T = T_c$, and

$$\alpha = (1/D)[6n^2 + 2 + 2(n^2 - 1)\cos 2kl],$$

$$\beta=(1/D)[-2n(n^2-1)\sin 2kl]\,,$$

$$\gamma=(1/D)[n^4+6n^2+1-(n^2+1)^2\cos 2kl]\,,$$

$$D=n^2+1+(n^2-1)\cos 2kl\,.$$

Thus, from the relation for σ_1 in eq. (1), and eq. (6), the real and imaginary parts of the conductivity can be determined.

The magnetic penetration depth λ can be obtained from London's equation

$$\lambda=(1/\mu_0\omega\sigma_2)^{1/2}\,, \tag{7}$$

where μ_0 is the permeability of free space. The magnetic penetration depth can then be written in terms of the superfluid density $\mathcal{N}_s$ as

$$\lambda=(m^*/\mu_0\mathcal{N}_s e^2)\,, \tag{8}$$

where m^* is the effective mass and e is the charge of the charge carriers. From the two-fluid model

$$\frac{\mathcal{N}_s}{\mathcal{N}}=1-t^4\,, \tag{9}$$

where $\mathcal{N}=\mathcal{N}_n+\mathcal{N}_s$ is the total number of carriers per unit volume, we have

$$\lambda=\left(\frac{m^*}{\mu_0\mathcal{N}e^2}\right)^{1/2}(1-t^4)^{-1/2}=\lambda_0(1-t^4)^{-1/2}\,. \tag{10}$$

From this expression the zero-temperature penetration depth λ_0 can be obtained. Note that since eq. (8) applies to homogeneous superconductors, the values of λ_0 obtained in this way are larger than those that would be obtained for homogeneous films.

Our measurements were made on $Bi_2Sr_2Ca_1Cu_2O_x$ superconducting films of approximately 5000 Å thickness deposited on MgO and $LaAlO_3$ substrates. The MgO and $LaAlO_3$ substrates were 0.113 and 0.025 cm thick, respectively. The films were deposited by co-evaporation in an oxygen atmosphere of 5×10^{-5} Torr. Then the film were post annealed at 725°C in a wet oxygen atmosphere for 30 to 60 min, followed by an anneal at 850°C for a period of 5 to 25 min. A more detailed explanation of the deposition technique is given in ref. [17]. The T_c for both films was approximately 80 K.

The power transmission measurements were made using a Hewlett–Packard model HP-8510 automatic network analyzer connected to a modified helium gas closed cycle refrigerator by Ka-band (26.5 to 40.0 GHz) waveguides. Inside the vacuum chamber of the refrigerator, the sample was clamped between two waveguide flanges which were in direct contact with the cold head of the refrigerator. The power transmitted through the sample was obtained by measuring the trasmission scattering parameter. The temperature gradient between the top and the bottom of the sample was estimated to be less than 1 K at 90 K. The system was properly calibrated with short, open, loads, and through calibration with short, open, loads, and through calibration standards before the beginning of each measurement cycle.

3. Results and discussion

The $Bi_2Sr_2Ca_1Cu_2O_x$ films deposited on $LaAlO_3$ and MgO substrates were inspected with a scanning electron microscope (SEM) and analyzed by X-ray diffraction. The surface morphology of the film deposited on MgO is smoother than for the one deposited on $LaAlO_3$, as can be seen from fig. 1. The voids seen in the SEM picture for the film deposited on the MgO were probably caused by hydrolyzing the CaF_2 and SrF_2 during the first step of the annealing. The hydrolyzation produces HF gas, which probably caused the voids. The same effect had been observed in sequentially evaporated $YBa_2Cu_2O_{7-\delta}$ superconducting films [18]. The films on both substrates are *c*-axis oriented. This can be observed from both the SEM pictures in fig. 1 and the X-ray diffraction data in fig. 2. One must conclude from the ratio of the $(00lm)$ and $(00np)$ peaks in the X-ray diffraction pattern that the $Bi_2Sr_1Ca_1Cu_2O_x$ film on MgO is better *c*-axis aligned than the one on $LaAlO_3$.

Figures 3 and 4 show the transmitted power versus temperature plots, at three different frequencies, for the films considered in this study. The beginning of the superconducting transition is observed clearly in both films and for the three frequencies shown in the figures. Note that the starting point of this transition for both films remains approximately at the same temperature for the frequencies represented, suggesting that, at least for the frequencies and temperature intervals considered here, the frequency dependence of the starting point for the normal to the superconducting state transition is rather small. it is

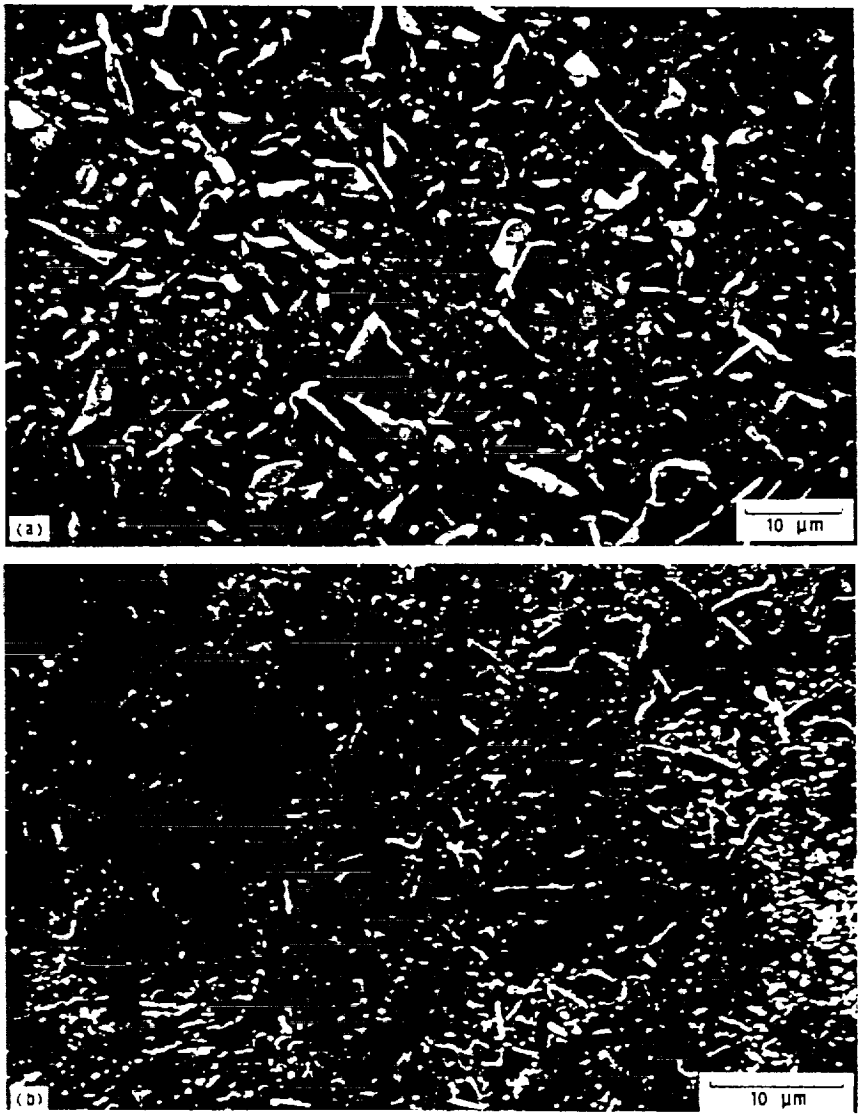

Fig. 1. Scanning electron micrograph for $Bi_2Sr_2Ca_1Cu_2O_x$ thin films (5000 Å) on $LaAlO_3$ (a) and MgO (b) substrates. The bar indicates 10 μm.

also observed that the temperature at which the normal to the superconducting state transition begins ($\sim$90 K) does not coincide with the transition temperature corresponding to zero DC resistance ($\sim$80 K). This behavior is in agreement with the rather broad resistive transition ($\Delta T_c \sim 10$ K) typical of this superconducting system, and it appears to indicate that within this region the sample is in a mixed state where all the superconducting clusters are not interconnected, as previously suggested by other researchers [19]. An interesting feature of the power transmission through the films is its frequency dependence. From fig. 3 it is observed that the power transmitted through the film on $LaAlO_3$ increases with increasing frequency, while the opposite behavior is observed for the film on MgO. Within the fre-

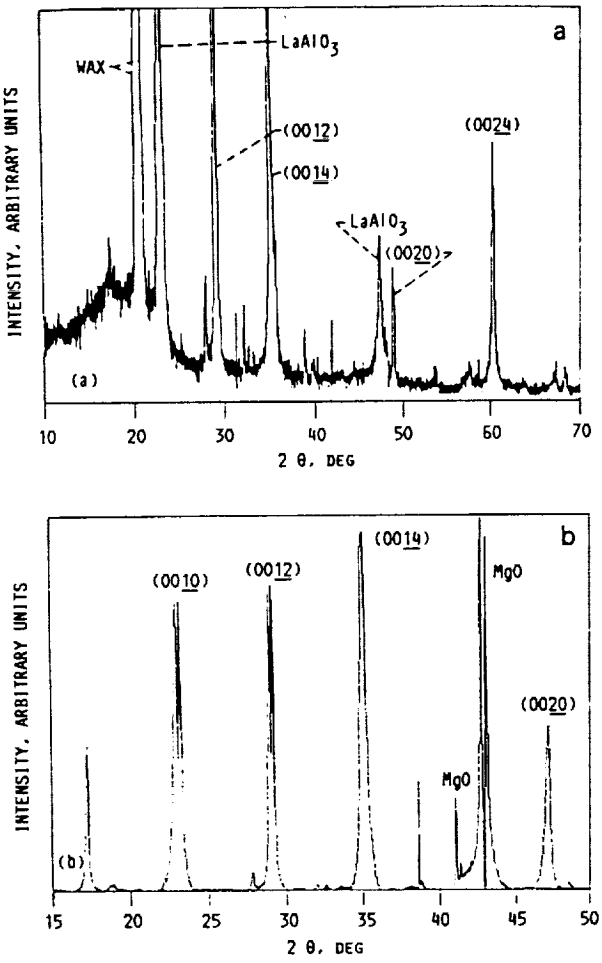

Fig. 2. X-ray diffraction pattern of 5000 Å superconducting BSCCO thin films on $LaAlO_3$ (a) and MgO (b) substrates. The films are the $Bi_2Sr_2Ca_1Cu_2O_x$ (2212) phase with the *c*-axis perpendicular to the $LaAlO_3$ and MgO substrates.

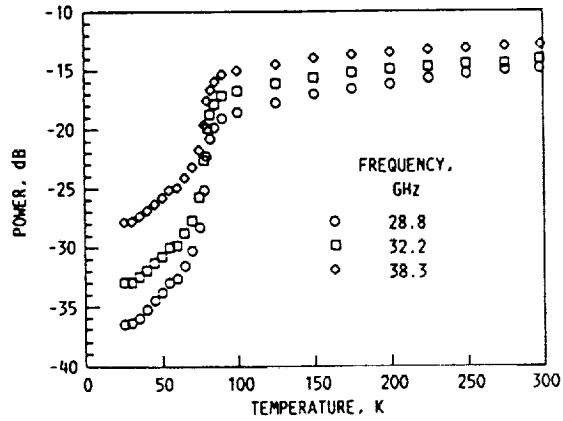

Fig. 3. Transmitted power vs. temperature for a co-evaporated $Bi_2Sr_2Ca_1Cu_2O_x$ thin film (5000 Å) on $LaAlO_3$.

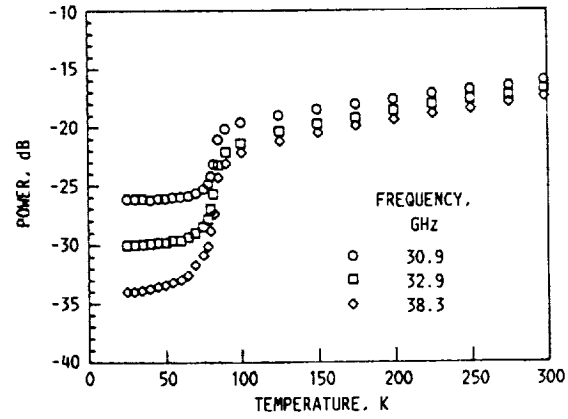

Fig. 4. Transmitted power vs. temperature for a co-evaporated $Bi_2Sr_2Ca_1Cu_2O_x$ thin film (5000 Å) on MgO.

quency range measured there is no frequency dependence in the power transmitted through bare $LaAlO_3$ and MgO substrates. This suggests that the observed frequency dependence is a film–substrate combination effect. No concrete explanation for this behavior is available yet, and further investigations are underway.

Figures 5 and 6 show the real and imaginary conductivities, σ_r and σ_2, respectively, for both films at 28.8 GHz. The values for the normal conductivities at room temperature for the films on MgO and $LaAlO_3$ are 6.3×10^4 and 4.1×10^4 S/m, respectively. Both values are lower than estimated values for the normal direct current conductivity at room temperature ($\sim 2.0\times10^5$ S/m) reported for very high quality $Bi_2Sr_2Ca_1Cu_2O_x$ superconducting films deposited on MgO by sequential electron beam evaporation [20]. No data within the normal to superconducting state transition region, clearly identified in fig. 5, were considered in our analysis. Although studies of this region had been done assuming different models, such as the presence of randomly diluted Josephson junctions [19], there is no simple physical model to account for the distribution of normal and superconducting carriers in this region, a fact that makes the determination of the normal

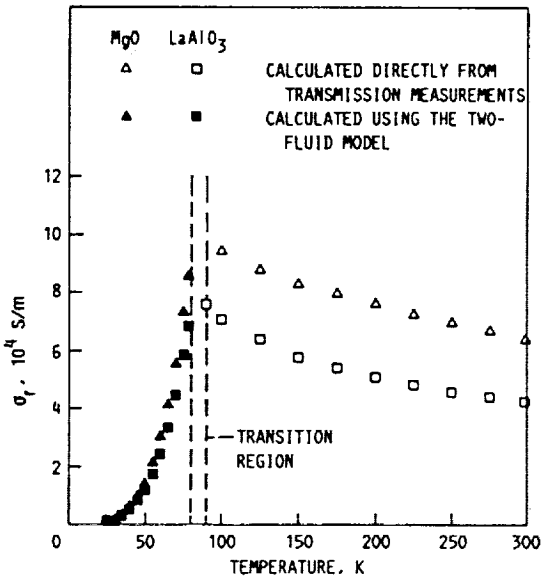

Fig. 5. Real part of the conductivity σ_r vs. temperature for co-evaporated $Bi_2Sr_2Ca_1Cu_2O_x$ thin films (5000 Å) on MgO and $LaAlO_3$ at 28.8 GHz. $\sigma_r = \sigma_N$ for $T > T_c$ and $\sigma_r = \sigma_1$ for $T < T_c$.

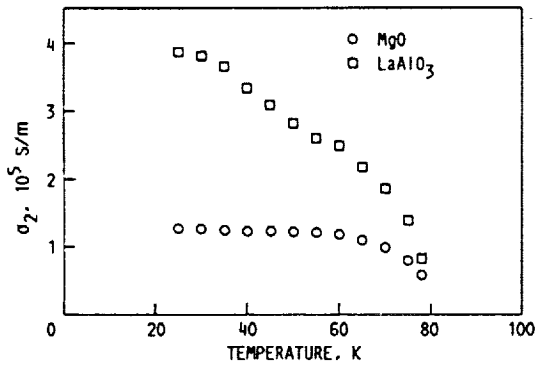

Fig. 6. Imaginary part of the conductivity σ_2 vs. temperature for co-evaporated $Bi_2Sr_2Ca_1Cu_2O_x$ thin films (5000 Å) on MgO and $LaAlO_3$ at 28.8 GHz.

conductivity down to T_c very cumbersome. Therefore, using the same approach applied in a previous work [12], we have considered the critical conductivity to be the conductivity at or just above the onset temperature. Since the two-fluid model assumes that all the regions of the sample become superconducting at once, the values of σ_1 obtained using $\sigma_c = \sigma_{onset}$ in eq. (1) will be smaller than those obtained from $\sigma_c = \sigma_{at\ T_c}$. How much these values differ will depend upon the width ΔT of the transition region and the overall quality of the superconducting properties of the film. For comparison purposes, an extrapolation of σ_r above T_{onset} to T_c was done. This resulted in a σ_c extrapolated 6.0 and 7.2 percent greater than σ_{onset} for the film on MgO and $LaAlO_3$, respectively. It is important to realize that this discrepancy will become smaller for films in which T_{onset} is very close to T_c. Using eq. (1), values of $\sigma_1 = 7.3 \times 10^4$ and $\sigma_1 = 5.9 \times 10^3$ S/m were obtained for the film on MgO at 75 and 40 K, respectively. For the film on $LaAlO_3$ we obtained $\sigma_1 = 5.8 \times 10^4$ and $\sigma_1 = 4.7 \times 10^3$ S/m at 75 and 40 K, respectively.

Figure 6 shows the imaginary part of the complex conductivity at 28.8 GHz for the two films under consideration. Observe that the values of σ_2 corresponding to the film on $LaAlO_3$ are greater than those of the film on MgO. This feature, together with the observation from fig. 5 that σ_1 for the film on MgO is greater than that for the film on $LaAlO_3$, appears to indicate that at this frequency the film on $LaAlO_3$ has better superconducting properties than the one on MgO. This raises an interesting observation that despite the film on $LaAlO_3$ being less c-axis oriented than the film on MgO, as concluded from the X-ray diffraction pattern, it still shows a higher degree of superconductivity. Therefore, the deposition of highly c-axis oriented $Bi_2Sr_2Ca_1Cu_2O_x$ on $LaAlO_3$ promises to yield films with excellent superconducting properties.

The imaginary part of the conductivity increases with decreasing temperature, a behavior expected from the two fluid model approximation. Values of 1.4×10^5 and 3.3×10^5 S/m are obtained for the film on $LaAlO_3$ at 75 and 40 K, respectively. For the film on MgO we obtained values of 7.7×10^4 and 1.2×10^5 S/m for the same temperatures mentioned above. Using eq. (7) we found the magnetic penetration depth λ for the film on $LaAlO_3$ to be 5.6 and 3.7 μm at 75 and 40 K, respectively. From the value of λ at 40 K we found $\lambda_0 = 3.6$ μm. For the film deposited on MgO we found $\lambda = 7.6$ μm at 75 K and $\lambda = 6.1$ μm at 40 K, and a value of λ_0 equal to 5.9 μm. The values of λ obtained for both films are considerably larger than the film's thickness, which implies a strong interaction between the microwave field parallel to the film surface and the substrate. The zero-temperature penetration depths are also large in compari-

son with the values obtained at the same frequencies and temperature for laser ablated $YBa_2Cu_3O_{7-\delta}$ superconducting thin films on $LaAlO_3$ and MgO [12].

Figures 7 to 10 show the real and imaginary conductivities versus temperature at 31.5 and 34.9 GHz. It can be seen that as the frequency increases so does the imaginary part of the conductivity of the film on MgO, while the imaginary part of the conductivity for the film on $LaAlO_3$ decreases with increasing frequency. No significant change as a function of frequency is observed for σ_1. Values for λ of 3.7 and 3.9 μm were obtained for the film on $LaAlO_3$ at 40 K and at 31.5 and 34.9 GHz, respectively. For the film deposited on MgO, λ was equal to 5.4 and 4.7 μm for the same temperature and frequencies.

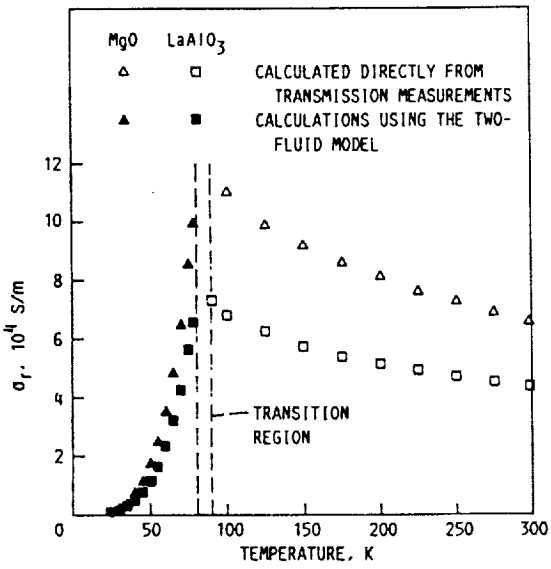

Fig. 7. Real part of the conductivity σ_r vs. temperature for co-evaporated $Bi_2Sr_2Ca_1Cu_2O_x$ thin films (5000 Å) on MgO and $LaAlO_3$ at 31.5 GHz. $\sigma_r=\sigma_N$ for $T>T_c$ and $\sigma_r=\sigma_1$ for $T<T_c$.

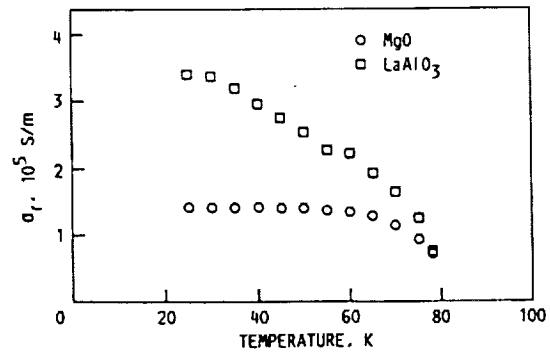

Fig. 8. Imaginary part of the conductivity σ_2 vs. temperature for co-evaporated $Bi_2Sr_2Ca_1Cu_2O_x$ thin films (5000 Å) on MgO and $LaAlO_3$ at 31.5 GHz.

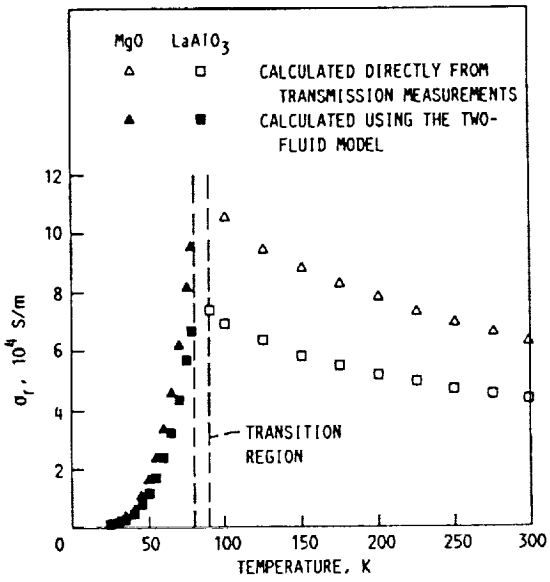

Fig. 9. Real part of the conductivity σ_r vs. temperature for co-evaporated $Bi_2Sr_2Ca_1Cu_2O_x$ thin films (5000 Å) on MgO and $LaAlO_3$ at 34.9 GHz. $\sigma_r=\sigma_N$ for $T>T_c$ and $\sigma_r=\sigma_1$ for $T<T_c$.

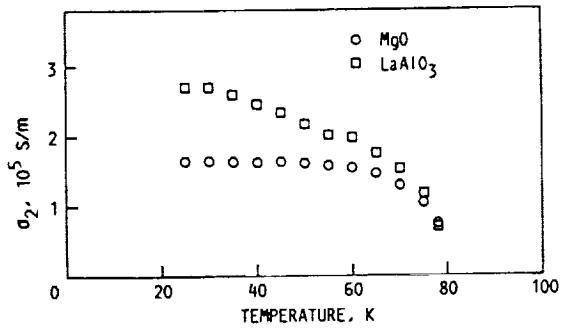

Fig. 10. Imaginary part of the conductivity σ_2 vs. temperature for co-evaporated $Bi_2Sr_2Ca_1Cu_2O_x$ thin films (5000 Å) on MgO and $LaAlO_3$ at 34.9 GHz.

4. Conclusions

Microwave conductivities of superconducting Bi-

Sr–Ca–Cu–O thin films at frequencies within 26.5 to 40.0 GHz and at temperatures from 25 to 300 K were determined. The conductivities, σ_N and $\sigma^* = \sigma_1 - i\sigma_2$, corresponding to the normal and the superconducting state, respectively, were obtained in terms of the transmitted power and a two-fluid model. The results obtained suggest that, at least from the standpoint of the complex conductivity and for the frequency range considered, the film deposited on $LaAlO_3$ shows better superconducting properties than the one deposited on MgO. Values for the magnetic penetration depth, determined using the obtained values of σ_2, were more than five times the film thicknesses, indicating a strong field substrate interaction in this frequency range. This aspect may be of importance in the proper selection of film-substrate combination for microwave devices operating in this frequency range.

References

[1] J.G. Bednorz and K.A. Muller, Z. Phys. B 64 (1986) 189.

[2] M.K. Wu, J.R. Ashburn, C.J. Torng, P.H. Hor, R.L. Meng, L. Gao, Z.J. Huang, Y.Q. Wang and C.W. Chu, Phys. Rev. Lett. 58 (1987) 908.

[3] S. Sridhar and W.L. Kennedy, Rev. Sci. Instrum. 59 (1988) 531.

[4] J.S. Martens, J.B. Beyer and D.S. Ginley, Appl. Phys. Lett. 52 (1988) 1822.

[5] J.P. Carini, A. Awasthi, W. Beyerman, G. Gruner, T. Hylton, K. Char, M.R. Beasley and N.A. Kapitulnik, Phys. Rev. B37 (1988) 9726.

[6] N. Klein, G. Muller, H. Piel, B. Roas, L. Schultz, V. Klein and M. Peiniger, Appl. Phys. Lett. 54 (1989) 757.

[7] L. Cohen, I.G. Gray, A. Porch and J.R. Waldram, J. Phys. F 17 (1987) L179.

[8] W. Ho, P.J. Hood, W.F. Hall, P. Kobrin, A.B. Harker and R.E. Dewames, Phys. Rev. B38 (1988) 7029.

[9] C.S. Nichols, N.S. Shiren, R.B. Leibowitz and T.G. Kazyaka, Phys. Rev. B38 (1988) 11970.

[10] H. Maeda, Y. Tanaka, M. Fukutomi and T. Asano, Jpn. J. Appl. Phys. Lett. 27 (1988) L209.

[11] Z.Z. Sheng and A.M. Hermann, Nature 332 (1988) 138.

[12] F.A. Miranda, W.L. Gordon, K.B. Bhasin, V.O. Heinen, J.D. Warner and G.J. Valco, NASA TM-102345 (1989) and to be published in: Superconductivity and Applications, (Plenum, 1990).

[13] J.I. Gittleman and B. Rosenblum, IEEE Proc. 52 (1964) 1138.

[14] W.J. Radcliffe, J.C. Gallop, C.D. Langham, M. Gee and M. Stewart, Physica C 153 (1988) 635.

[15] J.I. Gittleman and J.R. Matey, J. Appl. Phys. 65 (1989) 688.

[16] R.E. Glover III and M. Tinkham, Phys. Rev. 108 (1957) 243.

[17] T.S. Kalkur, R. Kwor, S. Jernigan and R. Smith,Coevaporated Bi–Sr–Ca–Cu Oxide Superconducting Films and Their Patterning, presented at the Conf. Sci. Technol. Thin Films Supercond., Colorado Springs, CO, 14–18 November, 1988.

[18] G.J. Valco, N.J. Rohrer, J.D. Warner and K.B. Bhasin, NASA TM-101388, and American Institute of Physics Conf. Proc., Vol. 182 (1989) p. 147.

[19] S.C. Gadkary, K.P. Muthe, S.K. Gupta, S.C. Sabharwal and M.K. Gupta, Physica C 160 (1989) 167.

[20] J. Steinbeck, B.Y. Tsaur, A.C. Anderson and A.J. Strauss, Appl. Phys. Lett. 54 (1989) 446.

NASA Technical Memorandum 103180

Sequentially Evaporated Thin Film $YBa_2Cu_3O_{7-x}$ Superconducting Microwave Ring Resonator

Norman J. Rohrer, Hing Y.To, and George J. Valco
Ohio State University
Columbus, Ohio

Kul B. Bhasin
Lewis Research Center
Cleveland, Ohio

Chris Chorey
Sverdrup Technology, Inc.
Lewis Research Center Group
Brook Park, Ohio

Joseph D. Warner
Lewis Research Center
Cleveland, Ohio

Prepared for the
Conference on the Science and Technology of Thin Film Superconductors
sponsored by the U.S. Department of Energy
Denver, Colorado, April 30—May 4, 1990

NASA

SEQUENTIALLY EVAPORATED THIN FILM $YBa_2Cu_3O_{7-x}$ SUPERCONDUCTING MICROWAVE RING RESONATOR

Norman J. Rohrer, Hing Y. To, and George J. Valco

Department of Electrical Engineering
Ohio State University, Columbus, Ohio 43210

Kul B. Bhasin

National Aeronautics and Space Administration
Lewis Research Center, Cleveland, Ohio 44135

Chris Chorey

Sverdrup Technology, Inc.
Lewis Research Center Group, Brook Park, Ohio 44142

Joseph D. Warner

National Aeronautics and Space Administration
Lewis Research Center, Cleveland, Ohio 44135

ABSTRACT

There is great interest in the application of thin film high temperature superconductors in high frequency electronic circuits. A ring resonator provides a good test vehicle for assessing the microwave losses in the superconductor and for comparing films made by different techniques. Ring resonators made of $YBa_2Cu_3O_{7-x}$ have been investigated on $LaAlO_3$ substrates. The superconducting thin films were deposited by sequential electron beam evaporation of Cu, Y, and BaF_2 with a post anneal. Patterning of the superconducting film was done using negative photolithography. A ring resonator was also fabricated from a thin gold film as a control. Both resonators had a gold ground plane on the backside of the substrate. The ring resonators' reflection coefficients were measured as a function of frequency from 33 to 37 GHz at temperatures ranging from 20 K to 68 K. The resonator exhibited two resonances which were at 34.5 and 35.7 GHz at 68 K. The resonant frequencies increased with decreasing temperature. The magnitude of the reflection coefficients is used in the calculation of the unloaded Q-values. The performance of the evaporated and gold resonator are compared with the performance of a laser ablated $YBa_2Cu_3O_{7-x}$ resonator. The causes of the double resonance are discussed.

INTRODUCTION

The advent of high temperature superconductors has drawn attention towards the possibilities of using thin films superconductors in microwave circuits. Several measurement techniques have been employed for characterization of the films including high Q cavities [1], stripline resonators [2] and

ring resonators [3]. The surface resistance of the the YBa2Cu3O7-x superconductor has been investigated on bulk samples, thin films and single crystals [4-6]. In this paper we employ a ring resonator to study the microwave properties of $YBa_2Cu_3O_{7-\delta}$ fabricated by multi-layer sequential evaporation with post-anneal.

DEPOSITION AND ANNEAL PROCEDURES

Electron beam evaporation was used for deposition of Cu, Y, and BaF_2 on $LaAlO_3$. The materials were deposited in that order which was repeated four times for a total of twelve layers. The thicknesses of the individual layers were 507 angstroms for Cu, 473 angstroms for Y, and 1704 angstroms for BaF_2. The details of the deposition process have been previously reported [7,8].

The multilayer stack was subjected to a post anneal to assist in the formation of the proper phase of $YBa_2Cu_3O_{7-x}$. The samples were inserted into a preheated furnace using a slow push. They were annealed at 900 °C for 45 minutes in oxygen bubbled through room temperature water. The temperature was then ramped down to 450 °C where it was held for six hours. Finally, the temperature was ramped down to room temperature. The ambient was dry oxygen during all stages except the high temperature anneal. This procedure resulted in a one micron thick superconducting thin film with an onset temperature of 93 K and a critical temperature of 85 K.

PATTERNING PROCEDURE

The ring resonator was patterned using negative photolithography. KTI 752 photoresist was spun on at a rate of 4,000 rpm for 60 seconds which resulted the photoresist being 1.7 μm thick. The sample was soft baked at 95 °C for 25 minutes and exposed through a dark field mask for five seconds with an illumination power density of 34.8 mW/cm^2. The photoresist was developed for 2 minutes and 45 seconds in 802 developer and rinsed in ethanol. A one percent molar bromine solution in ethanol was used for etching the thin film followed by a 30 second rinse. Finally, the photoresist was removed in SN-10 stripper.

Once the superconductor was patterned, a ground plane was deposited on the back of the substrate using electron beam evaporation. For adhesion, a 1400 angstrom titanium layer was deposited before the one micron gold ground plane.

RESONATOR ANALYSIS

The following dimensions correspond to the resonator shown in Figure 1. H is the substrate thickness.

H = 254 microns	W = 143.3 microns
S = 36 microns	R = $(r_1 + r_2)/2$ = 990 microns

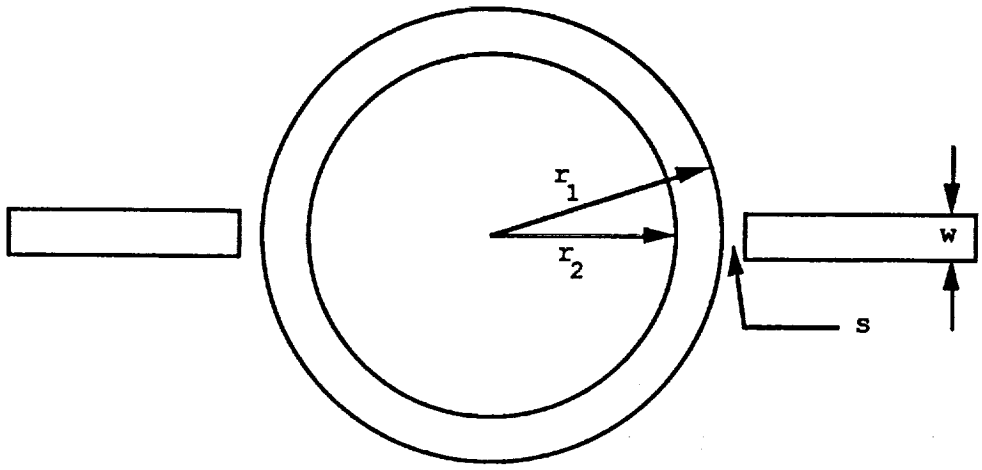

Figure 1: Ring resonator.

The resonator was designed for 50 ohm transmission lines with a resonant frequency of 30 GHz for the first harmonic. At the time of the design, the dielectric constant for $LaAlO_3$ was reported to be 15. Since then a more recent value reported for the dielectric constant is 21.9. This has resulted in a characteristic impedance for this geometry 42.9 ohms. The first harmonic was decreased below K-band. For this reason, we measured at the second harmonic which had a resonant frequency of 35.1 GHz at 25 K.

Microwave Testing

Once fabricated the ring resonator was experimentally tested using an HP 8510B network analyzer. The microwave test setup was configured using waveguides. Thus, a waveguide to microstrip transition was implemented using a cosine tapered ridge transition [9].

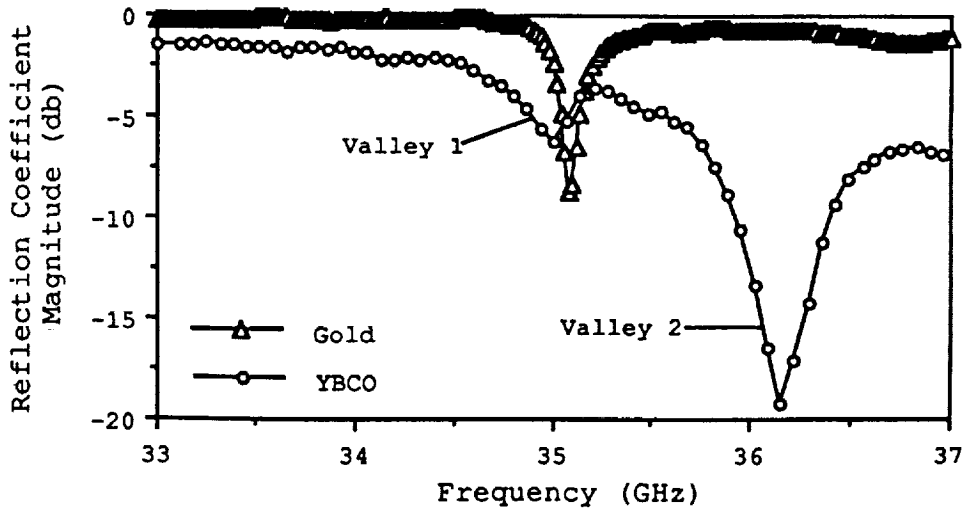

Figure 2: Magnitude of the reflection coefficient for ring resonator's fabricated from gold and $YBa_2Cu_3O_{7-x}$ at 30 K.

The reflection coefficient for the resonators was measured as a function of frequency at temperatures ranging from 20 K to 300 K using a CTI closed cycle cryogenic refrigerator. The superconducting resonator was measured from 20 K to its critical temperature. The resonant frequency superconducting resonator was 35.1 GHz at 25 K. Figure 2 shows the magnitude of the reflection coefficient for both the gold and the superconducting resonator at approximately 30 K.

The superconducting resonator exhibited two resonant valleys. Valley 1 matched the resonant frequency of the gold resonator while valley 2 occurred at 36.1 GHz. As will be discussed below, the occurrence of the second valley can be caused by one section of the ring resonator having a larger impedance than the rest of the ring.

Double Resonance Modeling

A transmission line model was implemented in Touchstone [10] to allow study of the double resonance. The resonator was simulated using transmission lines to match the physical layout and capacitors to model the gap. The capacitance values used were calculated from empirical equations derived in reference [11]. The impedance was increased in a region corresponding to three percent of the ring's circumference located closer to the transmission end. The location of this section for our model was 114° from the input. The impedance of this region was increased from a single line with 42.9 ohms to two parallel lines of 150 ohms each. This simulates a blister centered in the ring's transmission line. Figure 3 presents the results from this model.

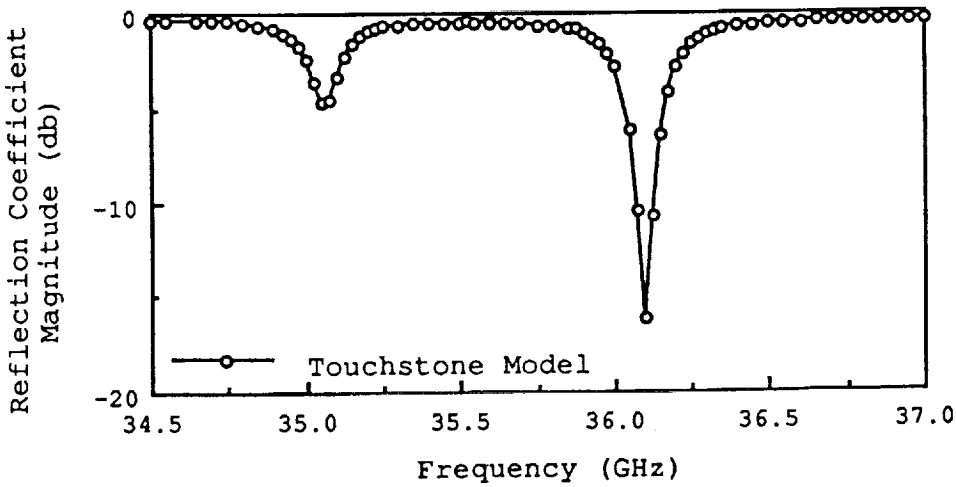

Figure 3: Modeled ring resonator with blister centered in the transmission line. Impedance of the lines around the blister were 150 ohms. Blister was located 1/3 the way around the ring.

The resonant frequencies of the model match directly with the resonant frequencies of the superconducting ring resonator. The width of valley 1 is quite similar, but the width of valley 2 is smaller for the modeled resonator. The reflection coefficient is much lower off resonance for the superconducting resonator. The the depth of the valley's peaks could be

altered by varying the position of the blister around the ring. The position used for the calculation shown in Figure 3 agrees with the location of a blistered region observed in the film of the resonator. The separation of the two valleys could be increased by increasing the impedance of the transmission lines around the blister. The response of the model remained the same for different number of transmission lines used within the high impedance region as long as the parallel combination of the characteristic impedances remained constant.

Resonant Frequency Shifts

The group velocity for a microstrip configuration with superconducting transmission lines varies as a function of temperature for temperatures less than the superconductor's critical temperature. This corresponds directly to a change in wavelength. Thus, the resonant frequency also varies as a function of temperature. The group velocity for a superconducting transmission line with a superconducting ground plane is given by [12]

$$v = \frac{c}{\sqrt{e_{eff(f)}}} \left[1 + \left(\lambda_1/h\right) \coth\left(t_1/\lambda_1\right) + \left(\lambda_2/h\right) \coth\left(t_2/\lambda_2\right)\right]^{-1/2}$$

where λ_1 and t_1 are the transmission line's penetration depth and thickness, respectively, and λ_2 and t_2 are the ground plane's penetration depth and thickness, respectively. If the ground plane is a normal metal, the group velocity is reduced to

$$v = \frac{c}{\sqrt{e_{eff(f)}}} \left[1 + \left(\lambda_1/h\right) \coth\left(t_1/\lambda_1\right)\right]^{-1/2}$$

Note that the first equation is general enough to accommodate microstrip circuitry with superconductors of different penetration depths for the transmission line and ground plane.

Figure 4 shows the calculated resonant frequency for a 0.7 micron thick film as a function of the temperature normalized to the critical temperature. This graph shows three plots. Two plots show the comparison of the resonant frequency with two different penetration depths for a sample with a gold ground plane and a superconducting resonator. The penetration depths were chosen to be on each side of the values experimentally determined by [13]. The third plot represented by the open squares shows the resonant frequency as a function of temperature for a sample with both the ground plane and the resonator being superconducting. Replacing both the transmission lines and the ground plane with a superconductor will decrease the losses in the circuit if the superconductor losses are lower than the gold losses. The resonant frequency for a sample with both a superconducting transmission line and a ground plane will exhibit a larger shift in the resonant frequency as the temperature nears the critical temperature for the superconducting film.

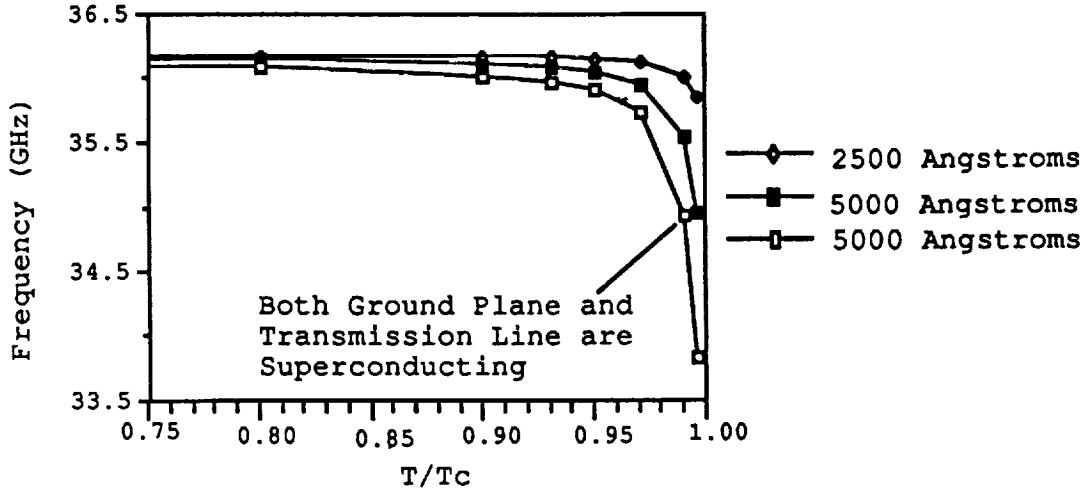

Figure 4: Resonant frequency versus normalized temperature for a 0.7 micron thick film. Different penetration depths are shown as well as an example of both ground plane and transmission lines being superconductors.

The shift in the resonant frequency for the sequentially evaporated superconducting ring resonator exhibited the same shape as the theoretical predictions. The measured resonant frequency as a function of temperature is given in Figure 5.

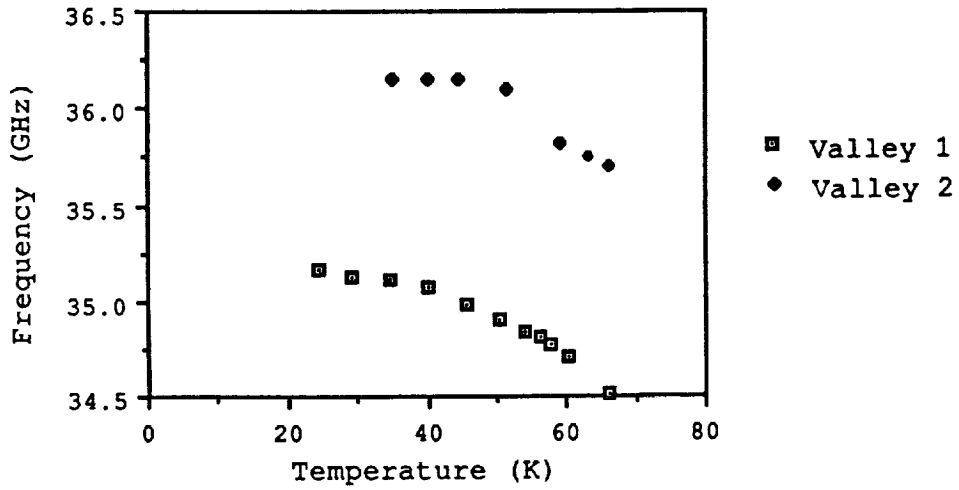

Figure 5: Resonant frequency versus temperature for the superconducting ring resonator. Both valleys are represented.

An attempt was performed to try to match the theoretical equations with the experimental data. The equations resulted in a penetration depth that was much larger than the thickness of the film. This is not reasonable since the film would no longer be superconducting for a large penetration depth. A possible explanation for the large penetration depth is due to the film being granular. This may allow more penetration at between grains.

Unloaded Q Calculation

The unloaded Q of the resonator can be extracted from the reflection coefficient. The model used for the derivation of the equation is a parallel RLC circuit with an ideal transformer in parallel and a series input resistance [14]. This model is for an unterminated resonator. It was used since the resonator was not loaded on the transmission side during our testing.

The derivation of the equations presented here are published in reference [14]. The loaded Q of a resonator is given by

$$Q_L = \frac{f_r}{f_1 - f_2}$$

where f_1 and f_2 are the half power points on each side of the resonant frequency f_r. The values for the half power levels are calculated by

$$p_{1/2} = \frac{1}{2}\left(\left[\frac{k' - 1}{k' + 1}\right]^2 + \left[\frac{\sigma - 1}{\sigma + 1}\right]^2\right)$$

where σ is the coupling loss and k' is the effective coupling coefficient. The coupling loss is calculated far off resonance where the reflection coefficient (Γ_i) is nearly constant.

$$\sigma = \frac{1 - \Gamma_i}{1 + \Gamma_i}$$

The effective coupling coefficient is the sum of the coupling coefficient and the coupling loss. The coupling coefficient can be easily calculated using the reflection coefficient (Γ_r) at the resonant frequency. The coupling coefficient can be calculated by

$$k = \frac{1 - \Gamma_r}{1 + \Gamma_r} \quad \text{or} \quad k = \frac{1 + \Gamma_r}{1 - \Gamma_r}$$

for the undercoupled and overcoupled cases, respectively. The unloaded Q can be calculated from the loaded Q by

$$Q_o = Q_L\left(\frac{1 + k'}{1 + \sigma}\right)$$

The unloaded Q as a function of temperature is shown in Figure 6. The unloaded Q for both valleys of the sequentially evaporated resonator are shown.

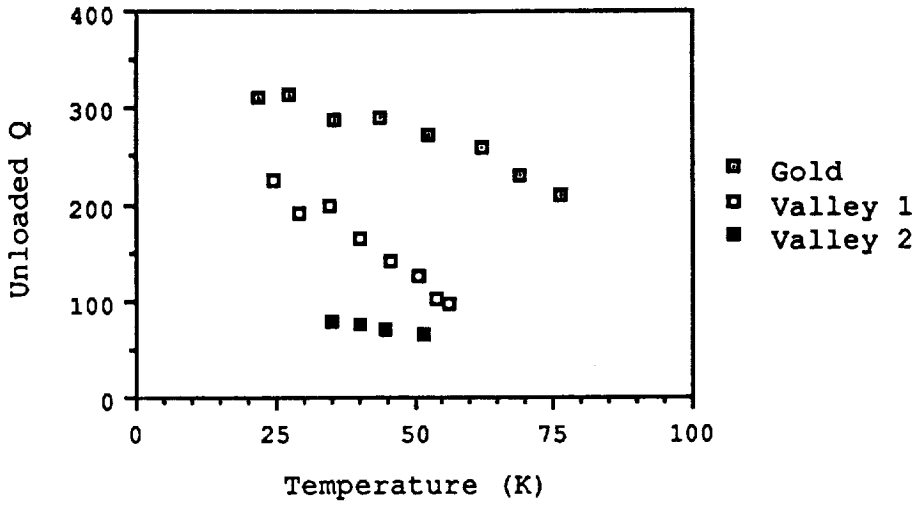

Figure 6: Unloaded Q versus temperature for the gold ring and the superconducting ring. Both valleys are shown for the superconducting ring.

The gold resonator had a larger unloaded Q than our sequentially evaporated film. At lower temperatures the difference between the unloaded Q values narrowed since the superconducting resonator's unloaded Q increased faster then the gold resonator's when compared to valley 1.

Surface Resistance

The surface resistance of the ring resonator can be extracted from the unloaded Q. The surface resistance is given by [15]

$$R_{SS} = R_{SAU} - \frac{4\pi Z_o}{B(C + D)} \frac{\pi}{\lambda} \left(\frac{1}{Q_{oAU}} - \frac{1}{Q_{oS}} \right)$$

where R_{SAU} is the surface resistance of gold, and Q_{oAU} and Q_{oS} are the unloaded Q values of the gold resonator and the superconducting resonator at the same temperature, respectively. The constants B, C, and D are related to the physical dimensions and are given in reference [15].

The surface resistance as a function of temperature for both the gold and the sequentially evaporated films are shown in Figure 7. For comparison a ring resonator was fabricated from a film deposited by laser ablation [16]. The surface resistance calculated for this film is also shown in Figure 7.

The graph shows that the sequentially evaporated film had the highest surface resistance at all temperatures. The gold film's surface resistance was about two-thirds the value of the sequentially evaporated film at 25 K. The laser ablated film had a surface resistance of approximately half that of gold at temperatures less than 50 K. As the temperature neared the critical temperature, the surface resistance of the laser ablated film started to increase rapidly to a value larger than that for gold at 70 K.

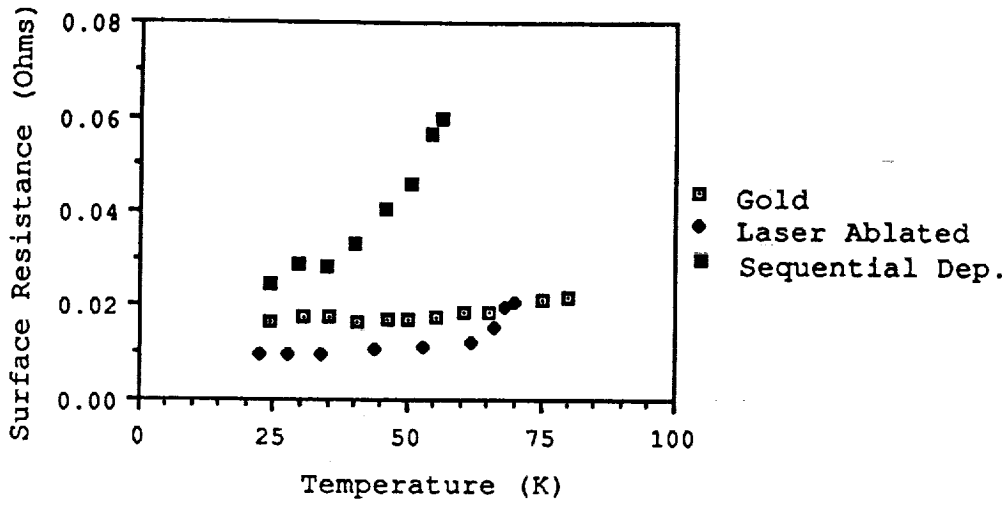

Figure 7: Surface resistance versus temperature for a gold resonator and two superconducting resonators. The superconducting resonators were deposited using different techniques. One was deposited by laser ablation and one by sequential evaporation.

CONCLUSION

A sequentially evaporated $YBa_2Cu_3O_{7-x}$ superconducting thin film was patterned into a ring resonator using negative photolithography. The ring resonators' reflection coefficients were measured using an HP 8510B network analyzer as a function of frequency from 33 to 37 GHz at temperatures ranging from 20 K to 68 K. The resonator exhibited two resonances which were at 34.5 and 35.7 GHz at 68 K. The resonant frequencies increased with decreasing temperature. The double resonance could be explained using a model that allowed for a small section of the ring resonator to have a larger impedance than the rest of the ring resonator. The location of the high impedance section in the model correlated well with the location of a blistered region of the film in the resonator. Once the reflection coefficient data was taken, the unloaded Q was extracted. The superconducting resonator was compared to a gold resonator. The gold resonator had a higher unloaded Q value at all temperatures. This translated into the gold having a lower surface resistance than the sequentially evaporated superconducting film. The surface resistance of the gold was about two-thirds the surface resistance of the sequentially evaporated superconducting film at 25 K. When compared to the laser ablated film, the laser ablated film's surface resistance was about one half that of gold for temperatures less than 50 K.

ACKNOWLEDGEMENTS

Design of the ring resonator was done by Robert Romanofsky and one of the authors (Kul Bhasin). This research was funded by the National Aeronautics and Space Administration, Lewis

Research Center under cooperative research agreement NCC 3-105 and under the graduate student research program NGT 50378.

REFERENCES

1. J. S. Marten, J. B. Beyer, and D. S. Ginley, Appl. Phys. Lett. **52** (21), 1822 (1988).
2. M. DiIorio, A. C. Anderson, and B. Y. Tsaur, Phys. Rev. B., **38** (10), 9726 1988.
3. J. H. Takemoto, F. K. Oshita, H. R. Fetterman, P. Korbin, E. Sovero, **MTT-37**, 1650 (1989).
4. M. K. Wu, J. R. Ashburn, C. J. Torng, P. H. Hor, R. L. Meng, L. Gao, Z. J. Huang, Y. O. Wang, and C. W. Chue, Phys. Rev. Lett., **58**,908 (1987).
5. T. M. P. Percival, J. S. Thorn, and R. Driver, Electron. Lett., **23**, 1225 (1987).
6. I. Sankawa, M. Sato, T. Konaka, M. Dobayashi, and K. Ishihara, Jap. Journ. Appl. Phys., **27** (9), L1637 (1988).
7. G. J. Valco, N. J. Rohrer, J. D. Warner and K. B. Bhasin, High T_c Superconducting Thin Films, Devices and Applications, G. Margaritiondo, R. Joynt and M. Onellion, AIP Conference Proceedings No. 182, pp. 147-154, American Institute of Physics, Atlanta, 1988.
8. G. J. Valco, N. J. Rohrer, J. D. Warner and K. B. Bhasin, Proceedings of the Workshop on High Temperature Superconductivity, pp. 197-203, GACIAC, Hunstville, 1989.
9. R. R. Romanofsky and K. A. Shalkhauser, NASA Technical Paper # 2875, 1989.
10. Commercially available software, EEsof, Westlake Village, CA 91632.
11. R. Garg and J. J. Bahl, Int. Journ. Elect., 45 (1978).
12. J. C. Swihart, Journ. Appl. Phys., **32** (3), 461 (1961).
13. S. M. Anlage, H. Sze, H. J. Snortland, S. Tahara, B. Langley, C. B. Eom, M. R. Beasley, R. Taber, Appl. Phys. Lett. **54** (26) 1989.
14. Robert R. Romanofsky, NASA Technical Paper #2899, 1989.
15. J. Takamoto, F. Oshita, H. Fetterman, IEEE Trans., **MTT-37**, 1650 (1989).
16. K. B. Bhasin, C. M. Chorey, J. D. Warner, R. R. Romanofsky, V. O. Heinen, K. S. Kong, H. Y. Lee, and T. Itoh, To be published in Symp. Digest of the 1990 IEEE Int. Microwave Symp., Dallas, TX.

NASA Technical Memorandum 103144

Photoresponse of $YBa_2Cu_3O_{7-\delta}$ Granular and Epitaxial Superconducting Thin Films

G.J. Valco
Ohio State University
Columbus, Ohio

P. Claspy
Case Western Researve University
Cleveland, Ohio

and

J.D. Warner, N. Varaljay, and K.B. Bhasin
Lewis Research Center
Cleveland, Ohio

Prepared for the
Technical Symposium on Optical Engineering and Photonics
in Aerospace Sensing
sponsored by the Society of Photo-Optical Instrumentation Engineers
Orlando, Florida, April 16-20, 1990

NASA

Photoresponse of $YBa_2Cu_3O_{7-\delta}$ Granular and Epitaxial Superconducting Thin Films

G.J. Valco
Department of Electrical Engineering
Ohio State University, Columbus, Ohio 43210

P. Claspy
Department of Electrical Engineering
Case Western Reserve University, Cleveland, Ohio 44106

J.D. Warner, N. Varaljay and K.B. Bhasin
National Aeronautics and Space Administration
Lewis Research Center, Cleveland, Ohio 44135

ABSTRACT

In this paper we report on the response of thin films of $YBa_2Cu_3O_{7-\delta}$ with either a very grainy or a smooth epitaxial morphology to visible radiation. $SrTiO_3$ substrates were employed for both types of films. The grainy films were formed by sequential multi-layer electron beam evaporation while the epitaxial films were formed by laser ablation. Both films were patterned into "H" shaped detectors via a negative photolithographic process employing a Br/ethanol etchant. The bridge region of the "H" was 50μm wide. The patterned films formed by laser ablation and sequential evaporation had critical temperatures of 74 K and 72 K respectively. The bridge was current biased and illuminated with chopped He-Ne laser radiation and the voltage developed in response to the illumination was measured. A signal was detected only above the critical temperature and the peak of the response coincided with the resistive transition for both types of films although the correspondence was less exact for the grainy film. The details of the responses and their analysis are presented.

1. INTRODUCTION

The discovery of high temperature superconductors has prompted a large amount of research into potential applications. These include their use in detectors for electromagnetic radiation over a wide range of frequencies, including optical frequencies[1-4]. Much of the reported work attributes the observed photoresponse to bolometric effects in which the film is heated by the incident radiation. Some authors have attributed some of their observations, particularly for grainy films with wide transitions, to non-bolometric phenomena but these interpretations have not been universally accepted.

We report here our observations on the photoresponse of two different $YBa_2Cu_3O_{7-\delta}$ films to visible radiation. One film was epitaxial and had a smooth morphology while the other film had a mixed orientation to the substrate and was quite grainy. Both of these films had comparable critical temperatures and transition widths after patterning into test structures.

2. EXPERIMENTAL PROCEDURES

The sequentially evaporated films were deposited by electron beam evaporation. Details on the formation of these films have been reported previously[5,6] but the main parts of the process will be reviewed here. The films were formed from Cu, Y and BaF_2 deposited in that order. Five layers of each were deposited for a total of

fifteen layers. $SrTiO_3$ substrates were used. Following deposition the films were annealed in a hot wall tube furnace to form the superconductor. The samples were slowly pushed into the preheated furnace over a five minute period. They were annealed at 900°C for 15 min. The temperature was lowered to 450°C at -2°C/min and held there for 6 hr. Finally the temperature was lowered to room temperature at approximately 2°C/min. The ambient was oxygen bubbled through room temperature water during the high temperature anneal and dry oxygen at all other times. The thickness of the sequentially evaporated film for these experiments was 0.5 μm. Films produced by this procedure typically have a critical temperature of 85 K, a granular morphology with a "basket weave" texture and mixed orientation.

The epitaxial film was formed by laser ablation from a $YBa_2Cu_3O_{7-\delta}$ target[7]. During deposition the substrate was heated to 630°C and the chamber pressure was 170 mtorr oxygen. The wavelength of the laser was 248 nm, the energy density was 1.5 J/cm^2/pulse and the pulse rate was 4 per second. The laser beam was incident on the target at 15° from the normal. After deposition the oxygen pressure was raised to 1 atm and the temperature was lowered to 450 °C at -2°C/min. It was held there for 2 hr and then slowly lowered to 250°C. The film had a thickness of approximately 0.2 μm and a smooth morphology.

For the photoresponse measurements the films were patterned into an "H" shaped detector. The photolithographic procedure employed KTI 752 negative photoresist. The films were etched in 1:100 bromine:ethanol (molar). The bridge region of the "H" was 50 μm wide.

Electrical contacts were made to each of the four legs of the "H." The metalization for the contacts consisted of 0.7 μm of Ag and 0.3 μm of Au. The Au top layer was used to facilitate wire bonding. The contacts were patterned through a chlorobenzene assisted lift-off procedure employing positive photoresist. Following deposition, the contacts were annealed at 500°C in oxygen[5].

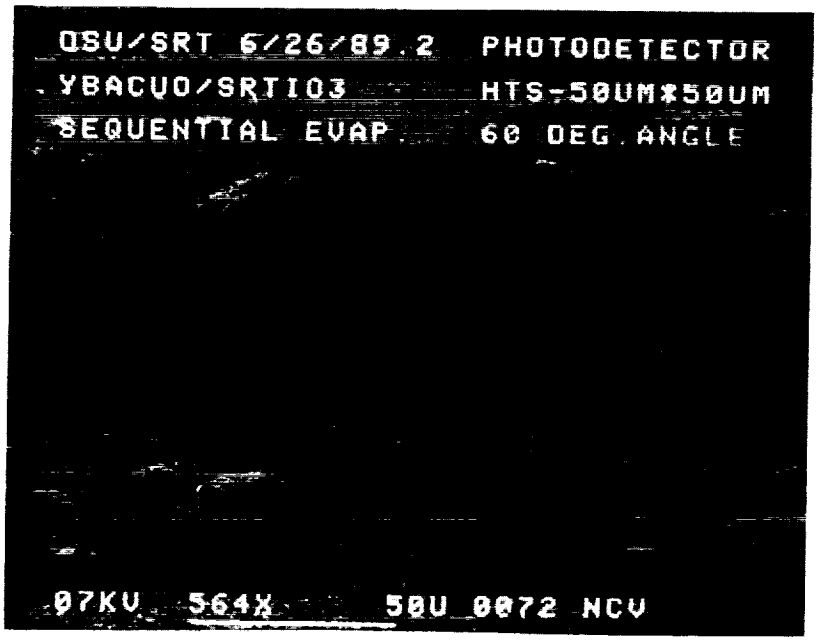

Figure 1. Scanning electron micrograph of a detector fabricated from a sequentially evaporated superconducting film.

Figure 1 shows a scanning electron micrograph of a detector made from the sequentially evaporated film. The darkest region is the superconductor. The four contacts are also visible on the legs of the "H". Also evident in this micrograph are many small blisters in the film. These blisters occasionally form on the sequentially evaporated films during the annealing procedure. They do not occur on all samples formed with nominally the same procedures but unfortunately did form on this sample. Electrical measurements showed continuity and measurements on this sample were carried out in spite of these defects. Figure 2 is a higher magnification micrograph of the bridge region of the same detector. The granular basket weave morphology is apparent. Notice that the basket weave structure is not apparent on the blister, where the film has come out of contact with the substrate.

Figure 2. Higher magnification scanning electron micrograph of the bridge region of the sequentially evaporated detector.

The bridge region of a detector formed from the epitaxial laser ablated film is shown in Figure 3. The film is very smooth, although there are some small particles on the surface. (The large particles are dirt or dust.)

For measurement of the resistance-temperature characteristics and photoresponse of the samples, the substrates were mounted onto the sample holder of a closed cycle He cryostat. Gold wire bonds provided the electrical connections between the four contacts on the detectors and pins on the sample holder. Two of the contacts, one on each side of the bridge were used for current biasing while the other two were connected to either a voltmeter, for resistance measurements, or a lock-in amplifier, for photoresponse measurements.

For the photoresponse measurements the sample was illuminated with chopped He-Ne laser radiation. The light was focused onto the bridge region of the detectors through a window in the housing of the cryostat. To position the beam on the bridge for initial measurements, the temperature was adjusted to approximately the midpoint of the resistive transition. The detector was then illuminated and the position and focus of the beam was adjusted to maximize the detected signal. Additional comments on this will be made later in the paper. The diameter of the focused beam was small

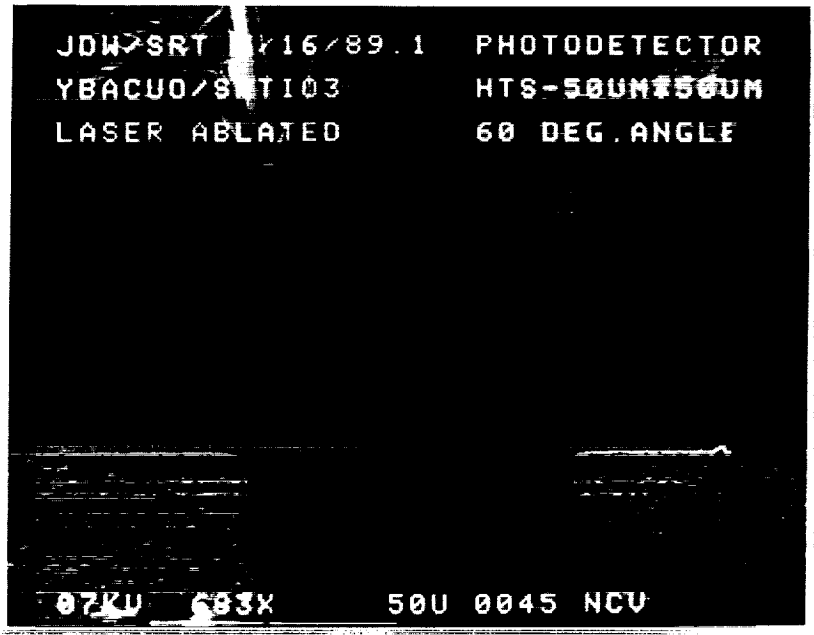

Figure 3. Scanning electron micrograph made from a laser ablated superconducting film.

enough to avoid illumination of the contacts so that spurious signals due to thermocouple effects were prevented. Such signals were observed on occasion for mispositioned beams, but not during actual measurements.

After positioning the beam, the photoresponse was measured as the temperature of the sample was varied. The measurements reported in this paper were made with the illumination chopped at 400 Hz and the sample biased at 100 μA. A few measurements of the photoresponse as a function of chopping frequency up to 4 KHz were made with the temperature fixed. The signal was found to decrease by approximately 40% as the frequency increased over this range. Measurements were also made at several lower bias currents. The response was found to scale with current and those results will not be further reported here.

3. RESULTS

The resistance (R) in ohms, dR/dT in ohms/K and measured signal in μV for the detector made from the epitaxial film are shown as a function of temperature from 70 to 90 K in Figure 4. The curve for dR/dT has been multiplied by a factor of five so that it could be plotted on the same scale as the others. The temperature of the sample was held at 79.4 K during optimization of the beam position. During the measurement it was varied down to approximately 12 K. The only observed response was in the range plotted in the figure. (Neglecting the small and nearly constant response at higher temperatures.) The peak of the photoresponse coincides well with the peak in dR/dT and the two curves agree well. The slight displacement of the two peaks is within the uncertainty in thermometry as the resistance-temperature characteristic and the photoresponse were not measured simultaneously. The agreement indicates a bolometric photoresponse.

Figure 5 is a graph of the resistance, dR/dT and the initial measurement of the

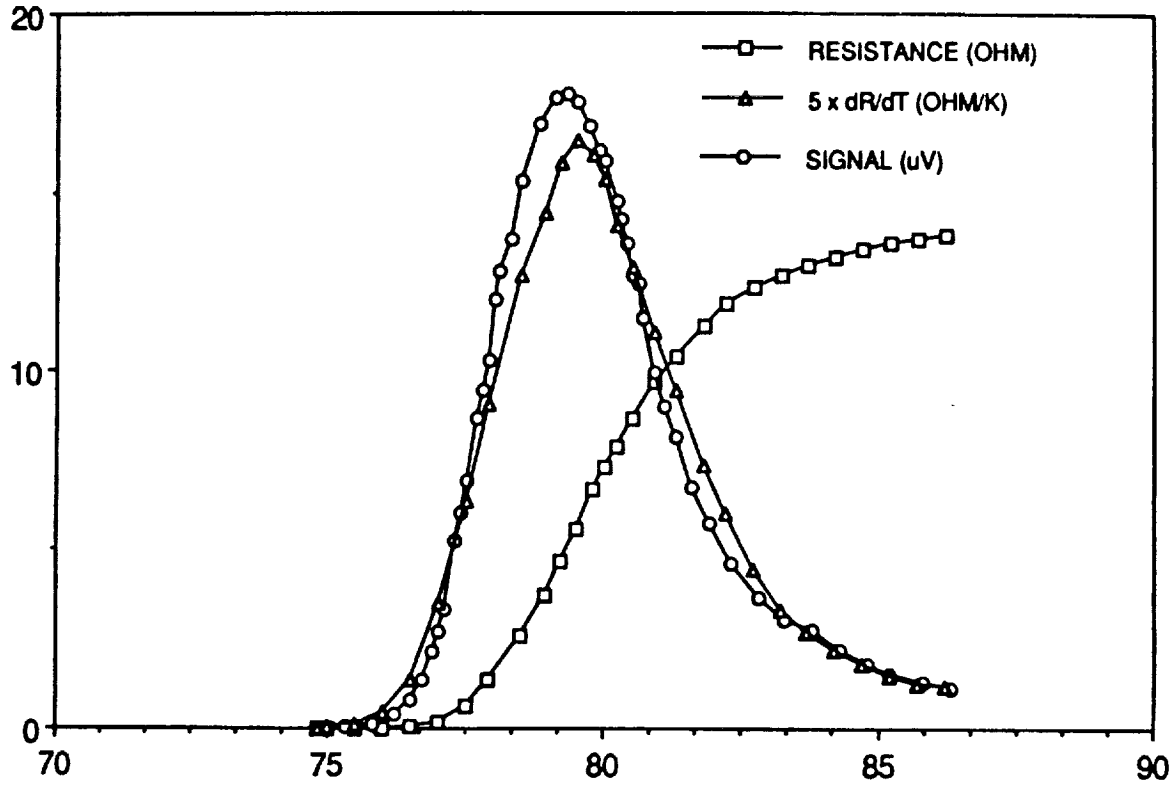

Figure 4. Resistance (squares), 5 x dR/dT (triangles) and photoresponse (circles) of the laser ablated superconducting film. 400 Hz chopping frequency, He-Ne laser illumination, 100 μA bias.

photoresponse signal for a detector made from the sequentially evaporated film. The curve for dR/dT has been multiplied by a factor of 10. The temperature of this sample was held at 78.5 K during optimization of the beam position. As with the epitaxial sample, the temperature was varied down to approximately 12 K and no photoresponse other than that shown in this figure was observed. The agreement between the photoresponse and dR/dT is poor. The maximum of the signal is displaced from the maximum of dR/dT by approximately 3 K to a higher temperature. Notice however that there is a shoulder on the peak of the signal at approximately the temperature of the peak in dR/dT and that there appears to be a shoulder on the peak of dR/dT at the peak in the signal.

In speculating on the possibility of experimental problems that might explain this result, a rough calculation showed that thermal expansion of parts in the cryostat could shift the sample on the order of 10 μm relative to the focused laser beam. The sample was remeasured and, to correct for motion due to expansion, the beam was repositioned every one to two degrees of temperature change.

The remeasured response is plotted in Figure 6. The resistance-temperature characteristic was also remeasured using finer temperature increments. Note that while R and dR/dT are plotted on the same scale in this figure as in Figure 5, the signal is divided by a factor of 2. The measured signal voltage was nearly a factor

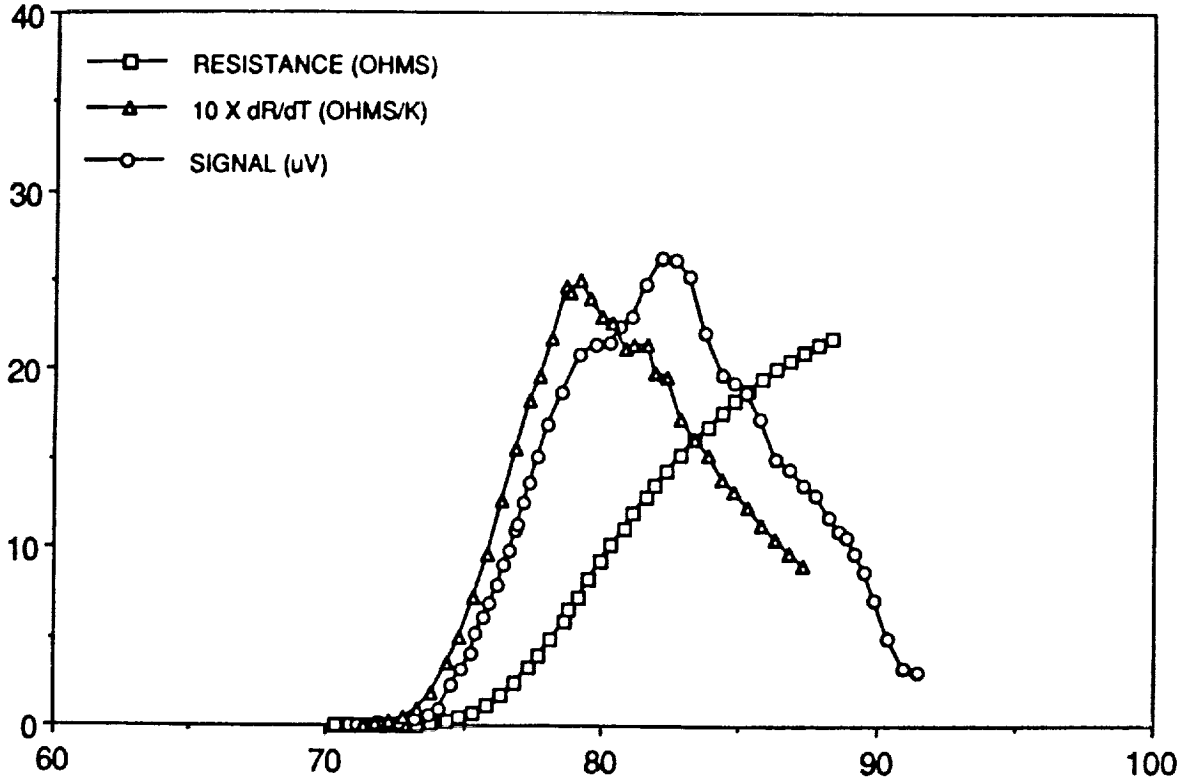

Figure 5. Resistance (squares), 10 x dR/dT (triangles) and initial measurement of the photoresponse (circles) of the sequentially evaporated superconducting film. 400 Hz chopping frequency, He-Ne laser illumination, 100 μA bias.

of three larger when the position of the beam was optimized as the measurement progressed. The agreement between the peak positions was still approximately the same. In addition a shoulder still appeared to exist on the signal peak at about the temperature of the peak in dR/dT and on the dR/dT curve at about the peak in the signal.

4. DISCUSSION

The observed photoresponse of the granular sequentially evaporated film can be explained with two assumptions: 1) That the film is spatially nonuniform with different critical temperatures in different regions, and 2) That the laser beam was not uniformly illuminating the entire bridge area. With these assumptions, as the signal is optimized at a given temperature, the laser beam can be positioned at a location on the film that has a locally high dR/dT, even if it doesn't make a dominant contribution to the total resistance of the film. This can be particularly true if the size of the laser spot is comparable in size to the non-uniformities.

Several simple one dimensional simulations were made to explore this possibility. Three of these will be presented here. In the first two a one dimensional detector was assumed to consist of a series combination of two regions, one with a

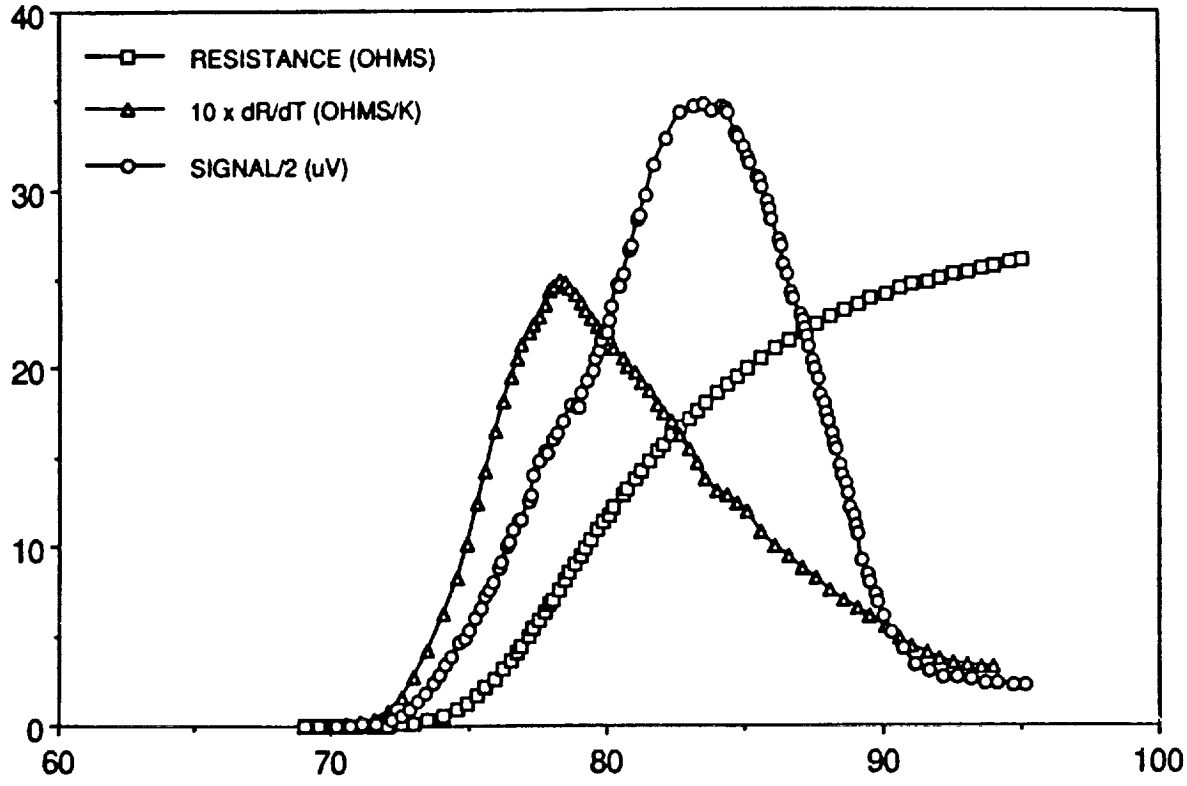

Figure 6. Resistance (squares), 10 x dR/dT (triangles) and remeasured photoresponse/2 (circles) of the sequentially evaporated superconducting film. 400 Hz chopping frequency, He-Ne laser illumination, 100 μA bias.

transition centered about 83 K and another with a transition centered about 79 K. The higher temperature transition was assumed to be broader. The illumination was assumed to result in a temperature increase that had a Gaussian distribution along the detector. The resistance, dR/dT and the signal for two beam positions are plotted in Figures 7 and 8. In Figure 7 the position of the beam was optimized at 77 K resulting in a strong response due to the low T_c region of the detector while for Figure 8 it was optimized at 87 K resulting in a strong response due to the high T_c portion of the detector.

A slightly more sophisticated simulation was also made. The one dimensional detector was assumed to consist of a narrow region of high T_c with broader regions of lower T_c on either side. The simulation was then run with the beam position re-optimized at 1 K intervals. The result in Figure 9 shows many of the features observed in the measurement on the sequentially evaporated film. The peak in the photoresponse is at a higher temperature than the peak in dR/dT and each peak has a shoulder that corresponds with the other, although the shoulders are much stronger here. The cusp in the signal between the peaks results from the sharp boundary between the regions. The parameters of the model could be adjusted to give a better reproduction of the measured data but this simulation demonstrates that a bolometric response in a nonuniform film can explain the observed signal.

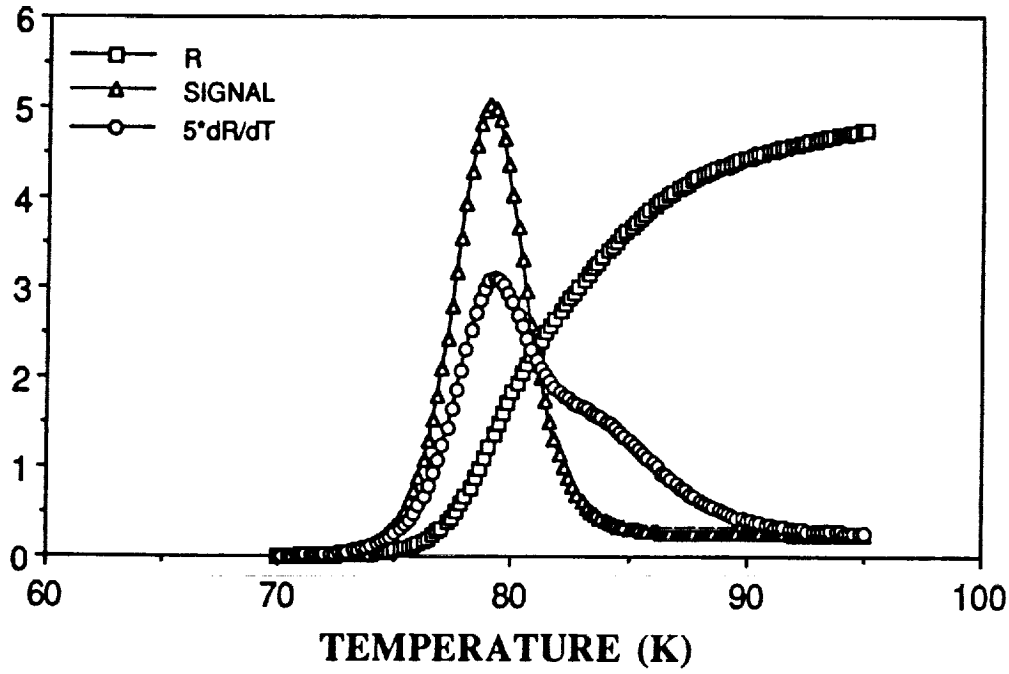

Figure 7. Simulated resistance, 5 x dR/dT and signal of a nonuniform detector. Beam position optimized at 77 K.

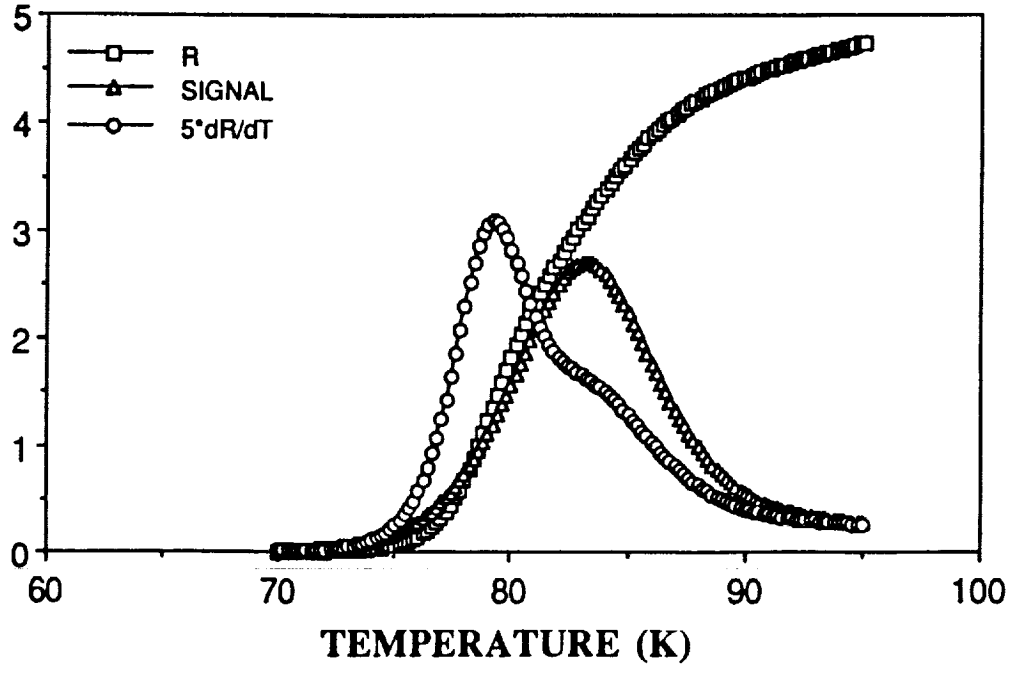

Figure 8. Simulated resistance, 5 x dR/dT and signal of a nonuniform detector. Beam position optimized at 87 K.

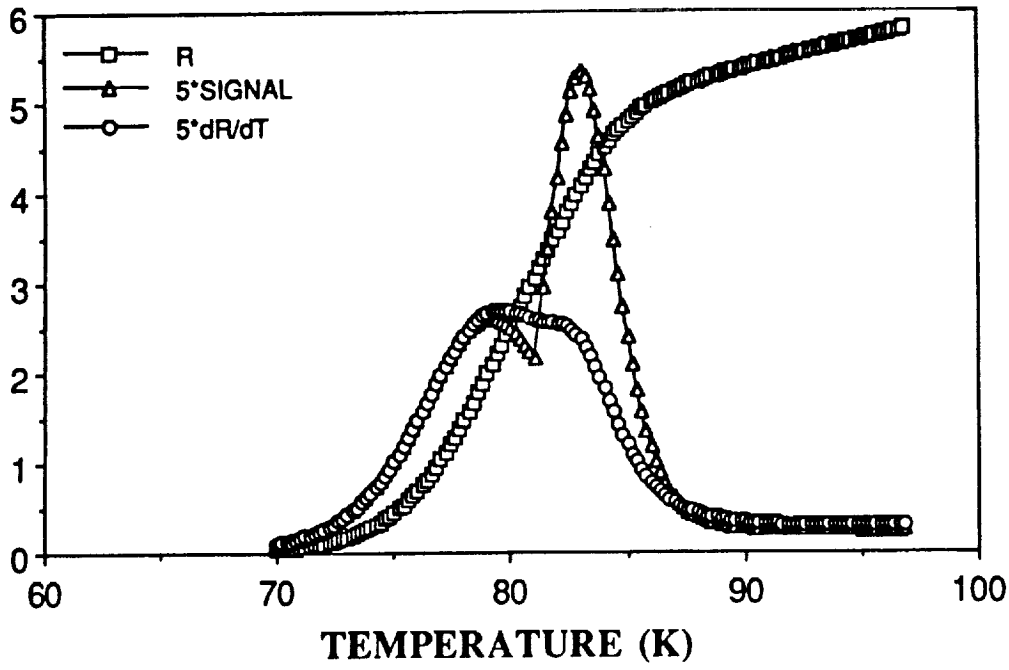

Figure 9. Simulated resistance, 5 x dR/dT and 5 x signal of a nonuniform detector. Beam position re-optimized at 1 K intervals.

5. CONCLUSIONS

The photoresponses of a laser ablated epitaxial film and a granular sequentially evaporated film of $YBa_2Cu_3O_{7-\delta}$ have been measured. For both films the only observed signal occurred for temperatures near the transition temperature. For the epitaxial film there was good correspondence between the measured signal and the temperature derivative of the resistance indicating that the photoresponse was bolometric in nature. The photoresponse of the granular films did not coincide as well with dR/dT, however simulations based on the assumption that the film is nonuniform lead to the conclusion that nonuniformities, coupled with a bolometric effect, are sufficient to explain the observations.

6. ACKNOWLEDGEMENTS

This research was supported by the National Aeronautics and Space Administration, Lewis Research Center under cooperative research agreement NCC 3-105.

REFERENCES

1. M. G. Forrester, M. Gottlieb, J. R. Gavaler and A. I. Braginski, "Optical response of epitaxial films of $YBa_2Cu_3O_{7-\delta}$," Appl. Phys. Lett., 53 (14), pp. 1332-1334, 1988.

2. M. Leung, P. R. Broussard, J. H. Claassen, M. Osofsky, S. A. Wolf and U. Strom, "Optical detection in thin granular films of Y-Ba-Cu-O at temperatures between 4.2 and 100 K," Appl. Phys. Lett., 51(24), pp. 2046-2047, 1987.

3. M. G. Forrester, J. Talvacchio and A. I. Braginski, "Electrical response of high-T_c superconducting films to laser radiation," Proceedings of the Workshop on High Temperature Superconductivity," pp. 241-248, GACIAC, Huntsville, 1989.

4. P. L. Richards, J. Clarke, R. Leoni, Ph. Lerch, S. Verghese, M. R. Beasley, T. H. Geballe, R. H. Hammond, P. Rosenthal and S. R. Spielman, "Feasibility of the high T_c superconducting bolometer," Appl. Phys. Lett., 54(3), pp. 283-285, 1989.

5. G. J. Valco, N. J. Rohrer, J. D. Warner and K. B. Bhasin, "Sequentially evaporated thin Y-Ba-Cu-O superconductor films: composition and processing effects," High T_c Superconducting Thin Films, Devices and Applications, G. Margaritondo, R. Joynt and M. Onellion, AIP Conference Proceedings No. 182, pp. 147-154, American Institute of Physics, Atlanta, 1988.

6. G. J. Valco, N. J. Rohrer, J. D. Warner and K. B. Bhasin, "Sequentially evaporated thin Y-Ba-Cu-O Superconducting Films on Microwave Substrates," Proceedings of the Workshop on High Temperature Superconductivity," pp. 197-203, GACIAC, Huntsville, 1989.

7. J. D. Warner, J. D. Meola and K. A. Jenkins, "Study of Deposition of $YBa_2Cu_3O_{7-x}$ on cubic zirconia," preprint.

NASA Technical Memorandum 103235

High Temperature Superconducting Thin Film Microwave Circuits: Fabrication, Characterization, and Applications

K.B. Bhasin, J.D. Warner, R.R. Romanofsky, and V.O. Heinen
National Aeronautics and Space Administration
Lewis Research Center
Cleveland, Ohio

and

C.M. Chorey
Sverdrup Technology, Inc.
Lewis Research Center Group
Brook Park, Ohio

Prepared for the
Technical Symposium on Optical Engineering and Photonics
in Aerospace Sensing
sponsored by the Society of Photo-Optical Instrumentation Engineers
Orlando, Florida, April 16–20, 1990

NASA

HIGH TEMPERATURE SUPERCONDUCTING THIN FILM MICROWAVE CIRCUITS: FABRICATION, CHARACTERIZATION, AND APPLICATIONS

K.B. Bhasin, J.D. Warner, R.R. Romanofsky, and V.O. Heinen
National Aeronautics and Space Administration
Lewis Research Center
Cleveland, Ohio 44135

and

C.M. Chorey
Sverdrup Technology, Inc.
Lewis Research Center Group
Brook Park, Ohio 44142

SUMMARY

Epitaxial $YBa_2Cu_3O_7$ films have been grown on several microwave substrates. Surface resistance and penetration depth measurements have been performed to determine the quality of these films. In this paper, the properties of these films on key microwave substrates are described. The fabrication and characterization of a microwave ring resonator circuit to determine transmission line losses is presented. Lower losses than those observed in gold resonator circuits were observed at temperatures lower than critical transition temperature.

Based on these results, potential applications of microwave superconducting circuits such as filters, resonators, oscillators, phase shifters, and antenna elements in space communication systems are identified.

E-5515

INTRODUCTION

The discovery of superconductivity in ceramic oxides such as Y-Ba-Cu-O, Bi-Sr-Ca-Cu-O and Tl-Ca-Ba-Cu-O with transition temperatures T_c around 100 K has inspired many researchers around the world to manipulate and to alter these ceramic oxides to form beneficial products for various applications. One important application where high T_c superconductors have begun to show promise is in the area of microwave communication and radar systems. The use of high T_c superconductors in a microwave system requires development of thin films on microwave substrates which then can be patterned into desired microwave circuits such as filters, phase shifters, ring resonators, and delay lines. The superconducting thin films for microwave circuits need to be deposited on low dielectric constant and low loss substrates, have smooth morphology, high critical temperature T_c, high critical current density J_c and low surface resistance R_s. Furthermore, films on the substrates must be evaluated as microstrip or ring resonator circuit to determine the quality factor "Q", and various losses prior to developing microwave circuit applications.

In this paper, we describe the characteristics of high quality Y-Ba-Cu-O thin films on microwave substrates and evaluation of their microwave properties. We discuss the fabrication, characterization, and performance of ring resonator circuits. In conclusion, we present some examples of applications of superconducting microwave circuits.

FABRICATION OF THIN FILMS ON MICROWAVE SUBSTRATES

To obtain high quality $YBa_2Cu_3O_7$ films on suitable substrates the substrate lattice constants must be matched to those of the films and there must not be a detrimental chemical reaction between the substrates and the film. In addition, the film composition must be as close to the correct composition as possible. To date, to obtain the highest quality films several physical and chemical deposition techniques have been used. Many of these require post-annealing at high temperatures. This high temperature anneal causes chemical interactions at the film-substrate interface, making the substrate/film interface unsuitable for microwave applications (ref. 1). See table I for the properties of sequential evaporated films on microwave substrates. To circumvent this problem, an in situ annealing procedure which allows lower growth temperatures have been used to grow epitaxial films using a laser ablation technique (ref. 2).

The details of the geometry of the laser ablation are shown in figure 1(a). The substrates were mounted onto a stainless steel plate with a diameter of 63 mm. The plate was heated from the backside using a resistive heater. The sample chamber was evacuated to 3×10^{-7} torr, or lower, using a liquid nitrogen cold trapped diffusion pump before the sample was warmed up to 700 °C. During deposition the chamber pressure was 170 mtorr; the laser wavelength was 248 nm; the energy density was 1.5 (J/cm^2)/pulse; the pulse rate was two pulses per second; and the distance between the target and the sample was 8 cm. The laser beam was rastered up and down 1 cm over the target using an external lens on a translator. After deposition the oxygen pressure was raised to 1 atm, and the temperature was lowered to 450 °C at a rate of 2 °C/min. The temperature was held at 450 °C and held for 2 hr, then cooled to room temperature.

The best film had a T_c of 89.8 K immediately after deposition as determined by a standard four point resistance measurement. Its resistance versus temperature behavior is shown in figure 1(b). From x-ray diffraction data the film was determined to be c-axis aligned. Critical current density J_c versus temperature is shown in figure 1(c). As can be seen, the value of J_c was greater than 10^6 A/cm^2 at 77 K. The surface morphology of the HTS on $LaAlO_3$ is shown in figure 1(d). The surface is very smooth with some small structure of about 0.25 μ in size. This size of structure has been confirmed by Scanning Tunneling Microscopy. We do not observe large numbers of HTS particulates due to the laser ablation process. In table I, we list the performance of $YBa_2Cu_3O_7$ thin films on various microwave substrates along with properties of these substrates.

SURFACE RESISTANCE

Surface resistance characterization of superconducting film offers valuable information on the film quality for microwave circuit applications. Currently, surface resistance values are obtained by cavity (refs. 3 and 4) and stripline measurements (ref. 5). Correlation between material properties (i.e., dc conductivity above T_c, penetration depth, and T_c) and surface resistance are still not well understood for new high T_c superconducting films. Theoretically, surface resistance of metal conductor is given by

$$R_N = \left(\frac{\omega\mu}{2\sigma}\right)^{1/2} = \frac{1}{\sigma_N \delta_N} \quad (1)$$

where

$$\delta = \left(\frac{2}{\mu\sigma\omega}\right)^{1/2} \text{ is the skin depth.}$$

σ_N is the normal conductivity, μ_o is the magnetic permeability, and ω is the angular frequency. For superconducting films, conductivity is a complex quantity $\sigma = \sigma_1 + j\sigma_2$. For $\sigma_2 >> \sigma_1$ one can obtain the surface resistance of superconducting film

$$R_s = \frac{0.5\sigma_1\omega\mu}{\sigma_2^{3/2}} \quad (2)$$

where σ_2 is related to the penetration depth λ by

$$\sigma_2 = \frac{1}{\omega\mu\lambda^2} \quad (3)$$

From equations (1) and (2)

$$\frac{R_s}{R_N} = \frac{2\sigma_1}{\sigma_N}\left(\frac{\lambda}{\delta_c}\right)^3 \quad (4)$$

Clearly, from this expression to obtain surface resistance for superconducting film lower than for a normal metal, the lowest values of σ_1 and λ are desired. Miranda et al. (ref. 6) have measured microwave transmission in a waveguide for superconducting films as shown in figure 2. From the transmission data, using the two fluid models, σ_1 and λ have been obtained. A summary of results for Y-Ba-Cu-O films on various substrates is shown in table II. The penetration depth value was small for laser ablated film on lanthanum aluminate substrates. Using these values in equation (4), a surface resistance for films on $LaAlO_3$ is calculated. In figure 3, which is adopted from reference 7, we show how the quadratic variation f^2 of the surface resistance varies with frequency for laser ablated Y-Ba-Cu-O films on microwave substrates. The surface resistance is several orders of magnitude lower than that of copper. Clearly surface resistance, penetration depth, and microwave conductivity measurements provide valuable information on the quality of these films for microwave circuits.

BASIC MICROWAVE CIRCUIT - RING RESONATOR

Measurements of surface resistance by the cavity technique fail to model microstrip losses completely because it neglects substrate losses and fails to adequately probe the film-substrate interface. Microstrip resonators patterned from thin films on microwave substrates allow direct measurement of microstrip losses. We have fabricated microstrip ring resonators operating at 35 GHz

from laser ablated YBCO thin films deposited on lanthanum aluminate substrate (ref. 11). Also, several groups have studied resonator circuits at lower frequencies (refs. 5 and 8 to 10). The resonator circuits we fabricated were patterned by standard photolithography using negative photoresist and a 'wet' chemical etchant. This etchant was either a 3-percent solution of bromine in ethanol or dilute phosphoric acid in water. A metal ground plane was deposited by first evaporating 100 Å of Ti for adhesion followed by 1 μ of gold. In addition to the resonator, each chip also had a test bar for directly determining T_c of the patterned film. Identical resonators were fabricated entirely from gold (both strip and ground plane) using evaporation and lift-off to define the strip.

The resonators were measured using a Hewlett-Packard 8510 Automatic Network Analyzer, operating in WR-28 waveguide. The microstrip circuit mounted in a tapered ridge waveguide to microstrip test fixture is shown in figure 4. The design of a cosine tapered ridge used inside the waveguide to couple the incoming signal to microwave circuit is shown in figure 5. The plot of the reflected power from the resonator (which is a measure of the loaded 'Q') is shown in figure 6 for several frequencies. Two features are apparent; (1) the coupling changes with temperature (the coupling coefficient increases with decreasing temperature) and (2) the resonant frequency shifts with temperature. The change in the resonant frequency versus temperature for a superconducting resonator is plotted in figure 7. This change is a consequence of the dependence of the internal impedance of the strip on the changing normal superconducting electron densities. The internal inductance of a superconducting strip over a ground plane is given by (ref. 8):

$$L_{int} = \mu_o \lambda \coth\left(\frac{t}{\lambda}\right)$$

Assuming the Gorter-Casimir temperature dependence of λ:

$$\lambda(T) = \frac{\lambda_o}{\left[1 - \left(\frac{T}{T_c}\right)^4\right]^{1/2}}$$

the form of the resonant frequency variation based on the changing line inductance matches the experimental observations (fig. 7).

The best resonators measured to date have shown unloaded 'Q's ranging from 2500 to 1000 at 20 and 77 K, respectively. This corresponds to a surface resistance value of, at most, 15 mΩ at 77 K at 35 GHz, a value two to three times better than copper at the same temperature and frequency.

POTENTIAL APPLICATIONS

High T_c superconducting thin films have shown lower surface resistance than copper. Low conductor losses for high T_c superconducting ring resonator circuit have been demonstrated. These characteristics are desirable in passive microwave circuits used in communication and radar systems since they reduce loss and size, increase bandwidth, and provide low noise. Complete system

analysis of the impact of the advantages of high T_c superconducting microwave circuits is yet not available. From a block diagram of satellite transponder (fig. 8), we have considered the following examples of potential applications of HTS microwave circuits in satellite communications applications. One can easily project the application of superconducting passive circuits as low loss, high 'Q' filters (ref. 11), high 'Q' resonators, delay lines, power splitter combiners, and resonator stabilized oscillators. Based on results obtained to date on the performance of superconducting microstrip resonator circuits with high 'Q' values.

In addition to these applications, extremely low loss phase shifters using superconducting switches are also feasible. In figure 9, we show a phase shifter which utilizes superconducting-normal-superconducting switches in place of FET/diode switches. The switches are fabricated from high temperature thin films of YBCO. The switches operate in the bolometric mode with the film held near its transition temperature. Radiation from a light source raises the temperature and consequently causes the film to become resistive. If the switches in the reference path are illuminated, they will become resistive. The switches on the opposite side of the device are superconducting. Since each switch is positioned one quarter of a wavelength from the junction, the signal will be reflected from the delay path in phase. A similar phenomenon occurs at the output port. To achieve the desired phase shift, the opposite set of switches is illuminated. Figure 9 shows the predicted behavior for a 180° phase shifter, with exceptional narrow insertion loss envelope and excellent return loss.

In figure 10, we show an example of hybrid semiconductor/superconductor device. It is possible that by combining the excellent low noise properties of GaAs devices with the low loss and low noise properties of superconducting transmission lines one can achieve ultra low noise receivers for satellite communications applications. If these promising concepts of high T_c superconducting devices are actually brought to fruition, then one can conceive their use in low loss, low noise superconducting phased array antenna in space communications systems as shown in figure 11. HTS transmission lines can provide low loss feed network which is a major problem in antenna networks.

SUMMARY OF RESULTS

We have demonstrated that rare-Earth oxide thin superconducting films can be deposited on various microwave substrates with critical temperature T_c above 77 K, critical current densities J_c above 10^6 A/cm^2, and low surface resistance. Films can be easily etched into microwave transmission line circuits. The basic microwave circuit ring resonator fabricated on a $YBa_2Cu_3O_7$ superconducting film on $LaAlO_3$ substrate showed higher 'Q' than gold circuits at 77 K. Such circuits can provide propagation characteristics of microwave signals at the film-substrate interface. Several key HTS circuits such as filters, oscillators, phase shifters, and phased array antennas' feeds are feasible in the near future. For technology to improve further, reproducible, large area films have to be grown on low dielectric constant, low loss microwave substrates. Tradeoffs between superconducting microwave circuits with cryogenic systems and normal metal microwave circuits will have to be quantitatively established to determine their suitability for advanced communication and sensor systems.

REFERENCES

1. Valco, G.J., et al.: Sequentially Evaporated Thin Y-Ba-Cu-O Superconducting Films on Microwave Substrates. NASA TM-102068, 1989.

2. Warner, J.D., et al.: Growth and Patterning of Laser Ablated Superconducting YBCO Films on $LaAlO_3$ Substrates. NASA TM-102436, 1989.

3. Klein, N., et al.: Millimeter Wave Surface Resistance of Epitaxially Grown $YBa_2Cu_3O_7$ Thin Films. Appl. Phys. Lett. vol. 54, no. 8, Feb. 20, 1989, pp. 757-759.

4. Miranda, F.A., et al.: Millimeter Wave Surface Resistance of Laser Ablated Y-Ba-Cu-O Superconducting Films. Accepted for publication in Appl. Phys. Lett., Sept. 1990.

5. Fathy, A., et al.: Microwave Properties and Modeling of High T_c Superconducting Thin Film Meander Line. IEEE MTT-S Internatinal Symposium (Dallas, TX, May 1990) Digest, 1990, pp. 859-862.

6. Miranda, F.A., et al.: Microwave Conductivity of Superconducting Bi-Sr-Ca-Cu-O Thin Films in the 26.5 to 40.0 GHz Frequency Range. Pysica C., vol. 188, 1990, pp. 91-98.

7. Inam, A., et al.: Microwave Properties of Highly Oriented $YBa_2Cu_3O_7$ Thin Films. Appl. Phys. Lett., vol. 56, no. 12, Mar. 19, 1990, pp. 1178-1180.

8. Valenzuela, A.A., and Russer, P.: High-Q Coplanar Transmission Line Resonators of YBCO on MgO. Appl. Phys. Lett., vol. 55, no. 10, Sept. 4, 1989, pp. 1029-1031.

9. McAroy, B.R., et al.: Superconducting Stripline Resonator Performance. IEEE Trans. Magn., vol. 25, no. 10, Oct 1989, pp. 1104-1106.

10. Takemoto, J.H., et al.: Microstrip Ring Resonator Technique for Measuring Microwave Attenuation in High T_c Superconducting Thin Films. IEEE Trans. Microwave Theory Tech., vol. MTT-37, no. 10, Oct. 1989, pp. 1650-1652.

11. Bhasin, K.B., et al.: Performance and Modeling of Superconducting Ring Resonators at Millimeter-wave Frequencies. IEEE MTT-S International Microwave Symposium (Dallas, Tx, May 1990) Digest, 1990, pp. 269-272. (Also NASA TM-102526, 1990).

12. Fiedziuszko, S.J., Holme, S., and Heidmann, P.: Novel Filter Implementations Using HTS Materials. To be published.

TABLE I. - KEY PROPERTIES OF MICROWAVE SUBSTRATE MATERIALS

Material	T_c achieved		Dielectric constant	Loss tangent	Lattice size, Å
	Sequential evaporation, K	Laser ablation, K			
Magnesium oxide (MgO)	70	88	9.65	4×10^{-4}	4.178 (100)
Lanthanum aluminate ($LaAlO_3$)	82	90	22	5.8×10^{-4}	3.792 (110)
Lanthanum gallate ($LaGaO_3$)	—	88	27	2×10^{-3}	3.892 (110)
Sapphire (Al_2O_3)	71	60	9.4 11.6	1×10^{-6}	5.111 ($0\bar{1}\bar{1}$)
Yttria stabilized zirconia (ZrO)	70	89	27	6×10^{-4}	3.8795 (100)
Silicon (Si)	—	—	12	10×10^{-4}	5.43 (100)
Gallium arsenide (GaAs)	—	—	13	6×10^{-4}	5.653 (100)

TABLE II. - MICROWAVE CONDUCTIVITIES (σ_n, $\sigma^* = \sigma_1 - 1\sigma_2$) AND ZERO TEMPERATURE PENETRATION DEPTH (λ_0) at 33.3 GHz FOR LASER ABLATED $YBa_2Cu_3O_{7-\delta}$ SUPERCONDUCTING THIN FILMS

Parameter	YBCO on $LaAlO_3$			YBCO on MgO	YBCO on ZrO_2
	828 Å	1769 Å	5000 Å	3500 Å	1200 Å
σ_n (300 K)	3.0×10^5 S/m	2.2×10^5 S/m	1.5×10^5 S/m	1.4×10^5 S/m	2.8×10^5 S/m
σ_1 (77 K)	2.8×10^5 S/m	2.5×10^5 S/m	1.8×10^5 S/m	1.2×10^5 S/m	2.4×10^5 S/m
σ_2 (77 K)	5.4×10^6 S/m	1.1×10^7 S/m	4.6×10^5 S/m	3.0×10^6 S/m	8.4×10^6 S/m
λ_0	0.43 μm	0.36 μm	0.39 μm	0.53 μm	0.59 μm

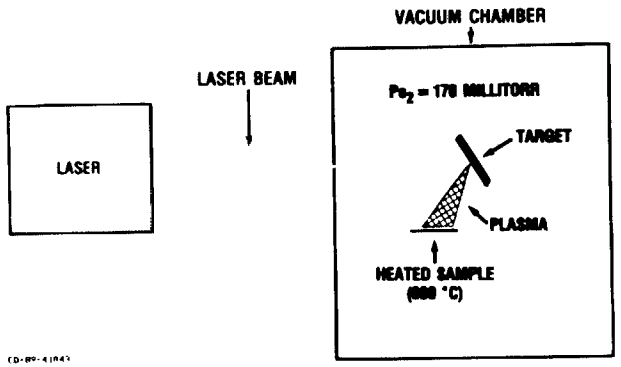

(a) LASER ABLATION TECHNIQUE.

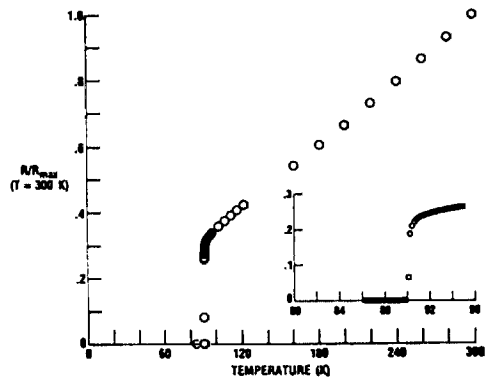

(b) RESISTANCE VERSUS TEMPERATURE OF $YBa_2Cu_3O_7$.

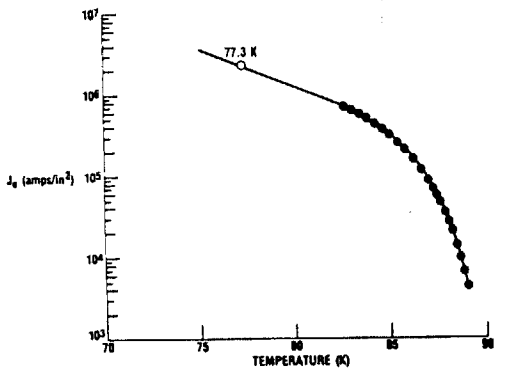

(c) CRITICAL CURRENT DENSITY OF $YBa_2Cu_3O_7$ ON $SrTiO_3$.

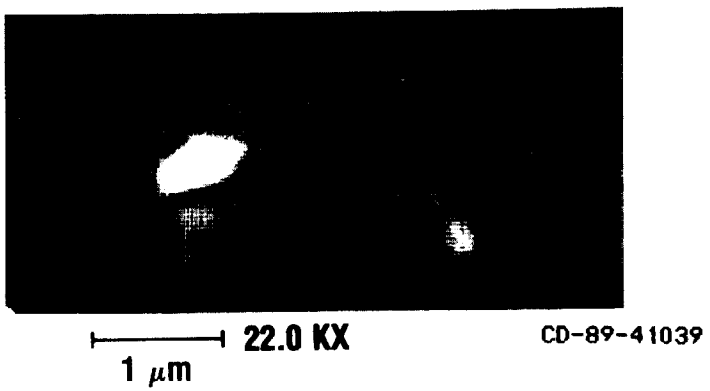

(d) SEM MICROGRAPHS OF $YBa_2Cu_3O_7$ FILM ON $LaAlO_3$.

FIGURE 1.

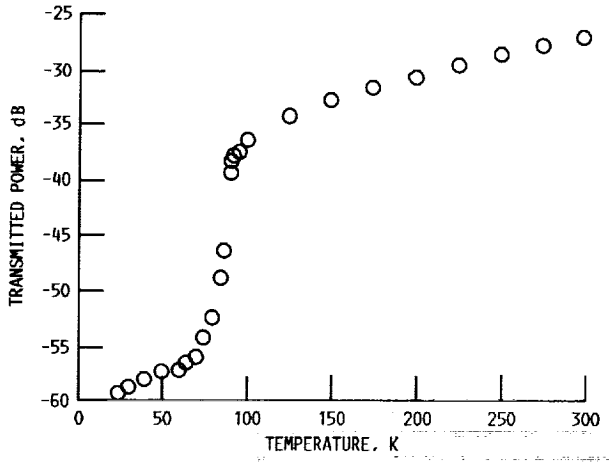

FIGURE 2. - TRANSMITTED POWER IN dB THROUGH A Y-Ba-Cu-O FILM ON $LaAlO_3$ SUBSTRATE AT 37 GHz.

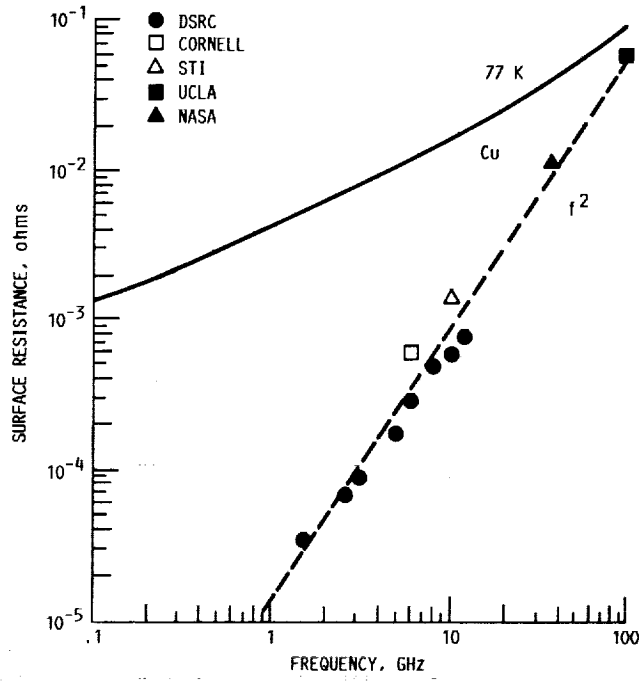

FIGURE 3. - SURFACE RESISTANCE OF LASER ABLATED Y-Ba-Cu-O FILMS ON $LaAlO_3$ SUBSTRATE VERSUS FREQUENCY. ADOPTED FROM APPLIED PHYSICAL LETTERS VOLUME 56, P.P. 1178-1180. NASA DATA OBTAINED BY MICROWAVE CONDUCTIVITY MEASUREMENTS.

ORIGINAL PAGE
BLACK AND WHITE PHOTOGRAPH

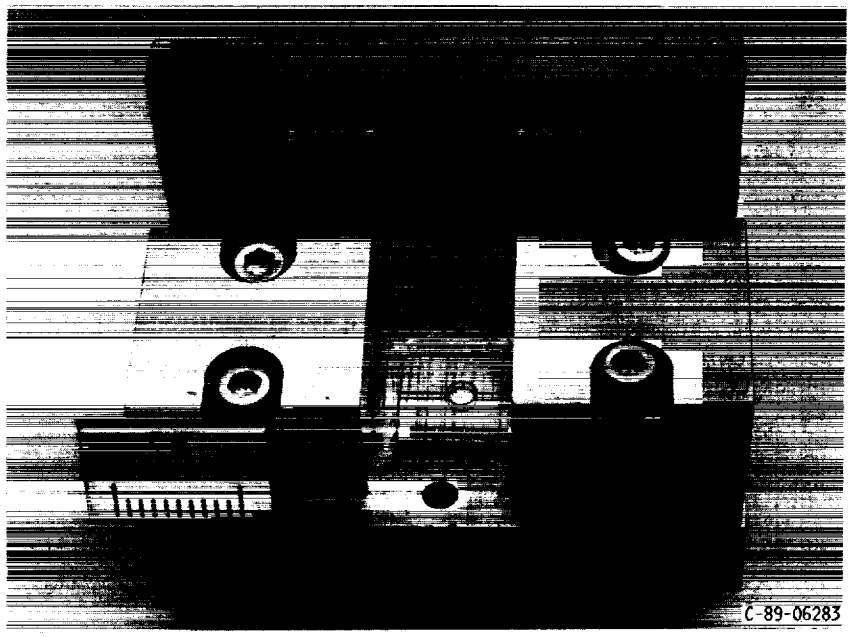

FIGURE 4. - WAVEGUIDE TEST FIXTURE USED FOR THE MEASUREMENT OF "Q" VALUES OF SUPERCONDUCTING RING RESONATORS.

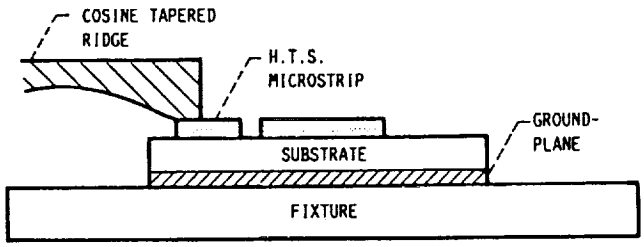

FIGURE 5. Design of the cosine taper ridge inside the waveguide used for waveguide to microstrip. transition

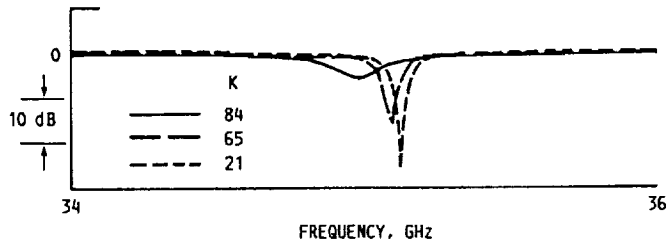

FIGURE 6. Resonances of Y-Ba-Cu-O ring resonator at three temperatures. Note the frequency shift with temperature.

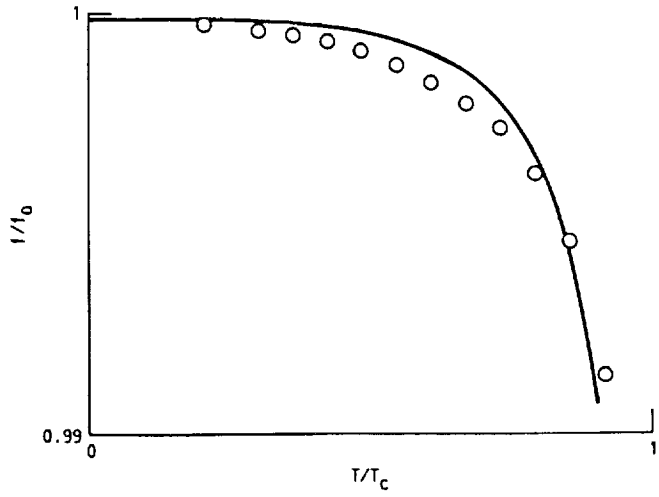

FIGURE 7. Ratio of the observed resonant frequency (f) to the zero temperature frequency (f_o) versus the T/T_c. O represent experimental values. Solid lines represents calculations based on Gorter-Casimir model.

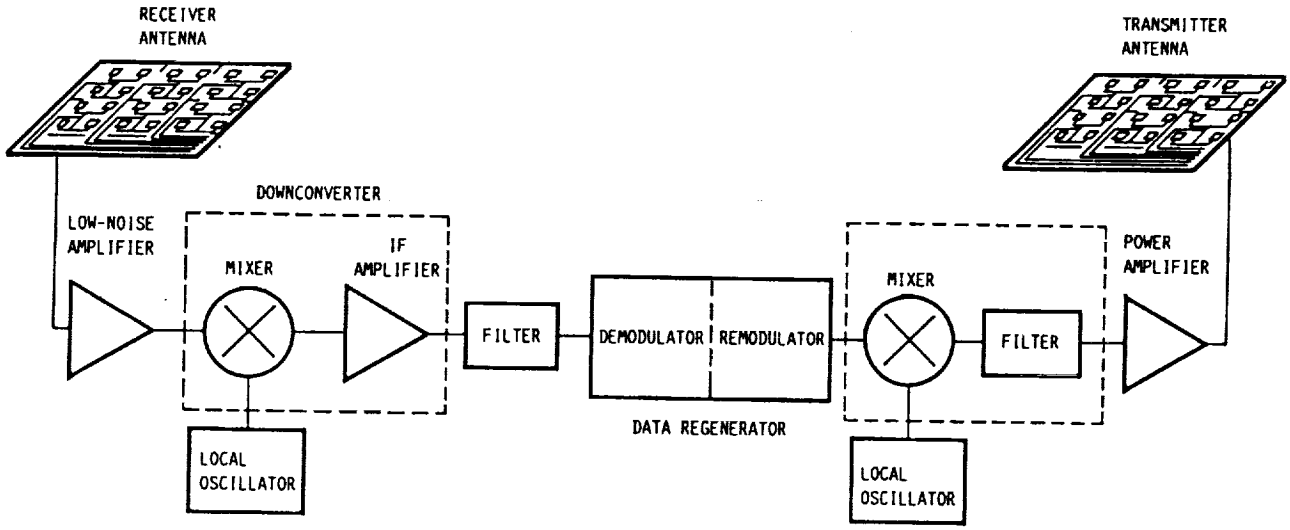

FIGURE 8. Block Diagram of a satellite transponder.

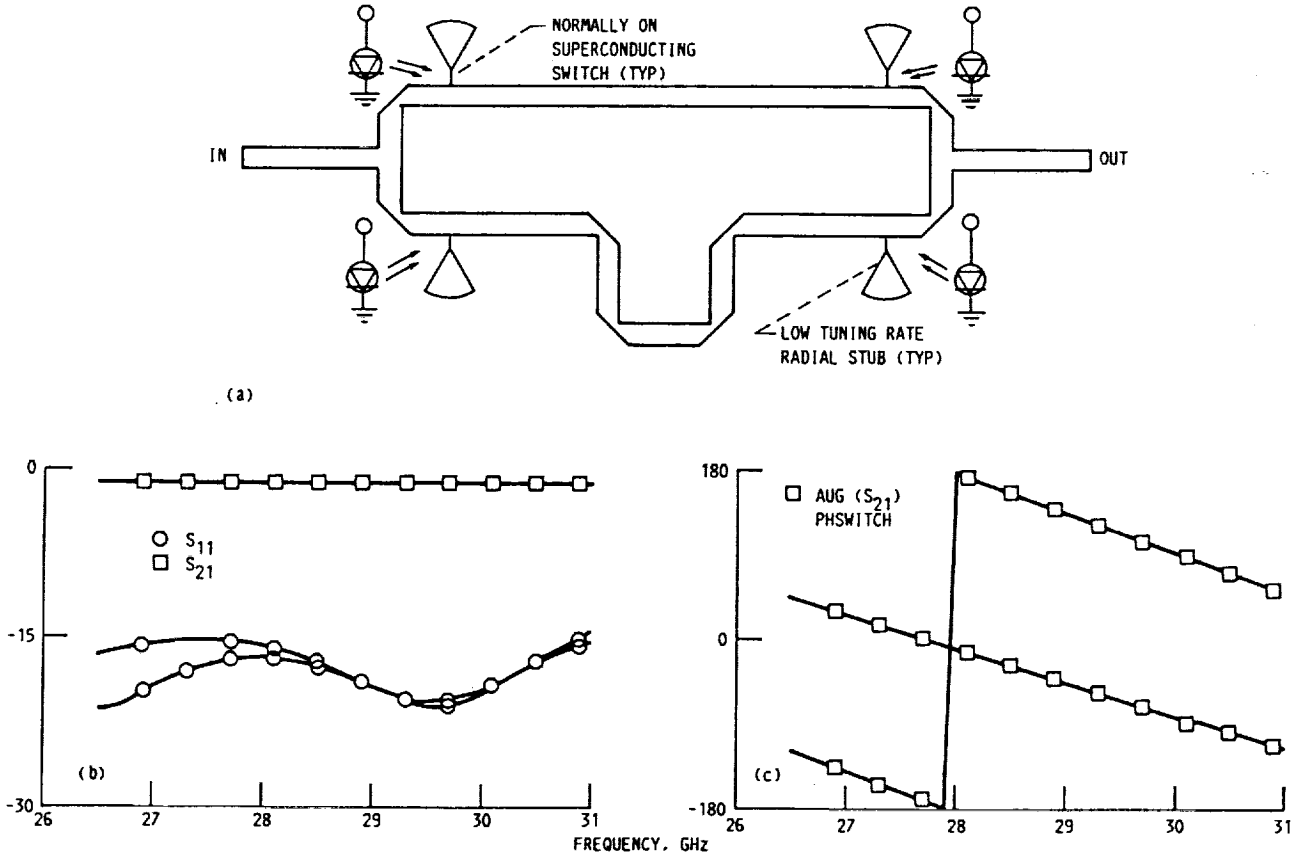

FIGURE 9. (a) Optically controlled High-T_c superconducting switch-line phase shifter. (b) Insertion loss and return loss for both reference and delay states. (c) Insertion phase for reference and delay states.

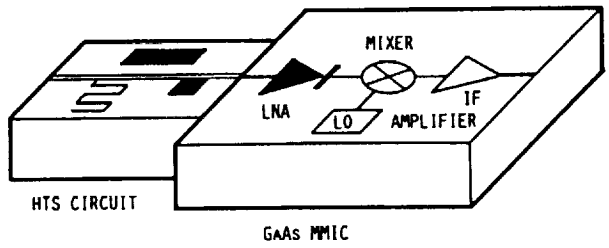

FIGURE 10. Superconducting GaAs MMIC Hybrid Receiver

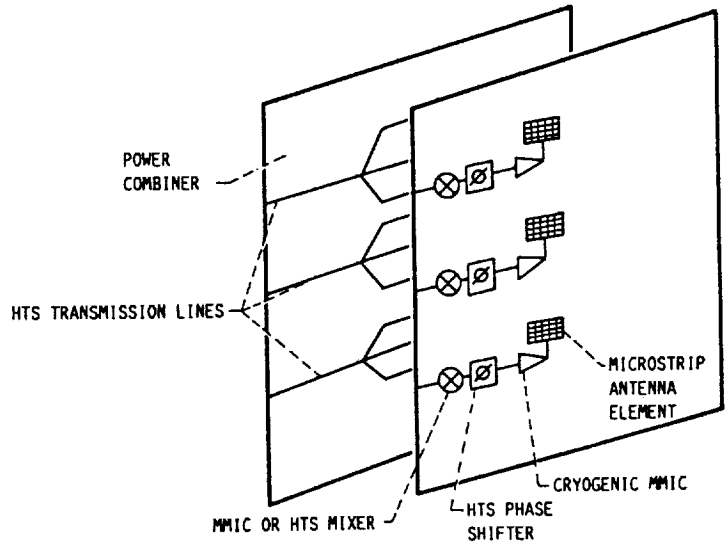

FIGURE 11. Conceptual diagram of a MMIC-Superconducting hybrid phase array antenna.

IV. SEMICONDUCTOR MATERIAL CHARACTERIZATION

Surface and implantation effects on p–n junctions

S E Schacham† and E Finkman

Department of Electrical Engineering and Solid State Institute, Technion—Israel Institute of Technology, Haifa 32000, Israel

Received in accepted form 18 September 1989

Abstract. The contribution of the graded region of implanted p–n junctions is analysed using an exponential profile. Though previously neglected, we have recently shown that this contribution to the saturation current of HgCdTe diodes is significant. Assuming a dominant Auger recombination, an analytical solution to the continuity equation is obtained. An expression for the current generated by the graded region is presented for both ohmic and reflecting boundary conditions. A revised condition for a 'wide' region is derived. When the region is 'narrow', the current differs drastically from that of the zero-gradient case. The effects of the junction depth and the substrate and surface concentrations on the current are investigated. It is shown that the reverse current does not saturate.

1. Introduction

The structure of p–n junctions made by microcircuit fabrication techniques is graded. When generating such junctions either by diffusion or by implantation, the carrier concentration on the diffused implanted region is not constant. This structure has several implications as to the performance and mathematical analysis of such diodes. The non-constant dopant profile gives rise to an electric field throughout the region, which directs the minority carriers back into the junction. The carrier diffusion current is modified and a drift current component is added. The excess carrier lifetime varies according to the local carrier concentration, thus affecting the junction characteristics.

Most methods for analysing I–V characteristics of p–n junctions are based on the depletion approximation. This approximation renders excellent results for an abrupt junction. However, the mathematical analysis of graded junctions cannot rely on the abrupt junction model. As a first-term expansion, the linearly graded junction [1, 2] suffers from serious basic drawbacks and its accuracy is questionable. An exponential carrier profile is a very attractive alternative [3–5]. Accurate numerical calculations for both gaussian and erfc doping gradients can be closely approximated by an exponential function [4]. The latter has several convenient features: in many cases it can be solved analytically, the electric field generated by such a carrier profile is constant, and mathematically this profile is consistent with the depletion approximation [3].

† Mailing address: NASA Lewis Research Center, m.s 54-5, Cleveland, OH 44135, USA.

0268-1242/90/030S41+04 $03.50

The narrow-gap semiconductor $Hg_{1-x}Cd_xTe$ is the leading material for making infrared photodetectors. Depending on the composition ratio x, the various atmospheric windows can be covered. Imaging arrays are produced almost exclusively with photovoltaic devices. These diodes are mostly implemented by ion implantation, usually resulting in an n^+ layer on a p-type substrate [6, 7]. Recent reports have shown that diffusion and heat treatment of an HgCdTe substrate can turn the top layer into a p-region, thus producing a p-on-n junction [8, 9].

The general approach to the analysis of the performance of $Hg_{1-x}Cd_xTe$ diodes took into consideration the substrate only, employing a one-side diffusion model for abrupt junctions. This approach was based on the assumption that the graded region does not contribute to the current [10, 11]. Recently we have proven experimentally that there is a *significant* current component generated by the implanted n^+ graded region of $Hg_{1-x}Cd_xTe$ diodes [12]. Depending on temperature, the ratio between the current produced by the graded region and that generated by the substrate is 0.5–3. Therefore we proceed to investigate this contribution.

The analysis of the effects of implantation conditions and surface treatment on the performance of $Hg_{1-x}Cd_xTe$ photodiodes is the subject of this paper. The implantation parameters determine the carrier gradient and the junction depth. Surface treatment, as manifested by boundary conditions, is an essential part of this analysis. It is well known that for abrupt junctions, reflecting boundary conditions render photodiodes with superior performance, i.e. higher R_0A and lower saturation current [10]. Since the electric field present outside the depletion region directs the minority carriers away

from the surface, this property has to be investigated for a graded region.

2. Current generated by graded region

The current generated by the graded region is derived from the excess carrier distribution. This distribution can be obtained from the continuity equation, taking into account the electric field present outside the depletion layer, and introducing the concentration dependence of the various parameters. Since the graded region is characterised by a high concentration of carriers, we assume the lifetime is dominated by an Auger process. Let us assume that the graded region is n-type over a p-substrate (as is usually the case in HgCdTe). The carrier profile in the graded region is approximated by an exponential function

$$N(x) = N_0 \exp(-\eta x/x_j) \tag{1}$$

where N_0 is the surface concentration, x_j is the junction depth and $\eta = \ln(N_0/N_a)$ where N_0 is the substrate concentration. This distribution results in a constant electric field $E = kT\eta/qx_j$ throughout the graded region. The resulting continuity equation can be solved analytically [13]. If the lifetime is indeed dominated by Auger recombination, a hyperbolic function is obtained for the excess carrier distribution. The current contribution of the graded region has two components: the diffusion term, obtained by taking the derivative of the excess hole distribution at the edge of the depletion region, x_n, and a drift term due to the constant electric field.

The solution of the continuity equation depends on the boundary conditions at the surface. For ohmic contacts, i.e. with no excess carriers at $x = 0$, the saturation current generated by the graded region is given by

$$J_{0n}(\text{ohmic}) = J_x \coth\left(\frac{x_j}{\eta}(L(0)^{-1} - L(x_n)^{-1})\right). \tag{2}$$

The diffusion length L depends on position through the lifetime dependence on concentration; $L(0)$ is its value at the surface, while $L(x_n)$ is the value at the edge of the depletion layer. Here J_x is the 'classical' saturation current for a 'wide' region, i.e. $x_j \gg L$, of an abrupt junction with a constant carrier concentration:

$$J_x = q\frac{D_p \tilde{p}(x_n)}{L(x_n)}.$$

It is important to note that for the case of a dominant Auger recombination, J_x is independent of location and is a material parameter, since the equilibrium minority carrier concentration at the edge of the depletion region, $\tilde{p}(x_n)$, is equal to $n_i^2/N(x_n)$, and since the Auger lifetime depends inversely on the square of majority concentration. Usually, owing to the steep slope of the carrier profile in the graded region, $L(x_n) \gg L(0)$; thus $J_{0n}(\text{ohmic}) \approx J_\infty \coth(x_j/\eta L(0))$. This approximation is valid only if the width of the neutral region, x_n, is not much smaller than x_j (not close to punch-through). Under these approximations, the exact value of x_n is immaterial, even though this width may be smaller than the diffusion length. For a graded junction we have to revise the condition for a 'wide' region to $x_j \gg \eta L(0)$; then J_{0n} (ohmic) approaches J_x. However, when the region is 'narrow', we obtain a drastic reduction in J_{0n} by a factor of $\eta w_n L(0)/x_j L(x_n) = \eta w_n N(x_n)/x_j N_0$ over the abrupt case with a constant concentration N_d equal to $N(x_n)$; w_n is the width of the neutral region for the abrupt junction. Only when the constant concentration of an abrupt junction is of the order of the surface concentration are the currents comparable. When $N_d = N_0$, the factor is $\eta w_n/x_j$.

It should be pointed out that although the final formulation of the saturation current for the graded junction is very similar to that of the abrupt one, this may be misleading. The local carrier concentration is drastically different. The electric field tends to repel the minority carriers back to the junction; thus the carriers have to redistribute in order to comply with the same boundary conditions. The drift component of the current always opposes the diffusion component.

The dual boundary condition is that of a perfectly reflecting surface. Solving the continuity equation with the appropriate limits, and obtaining both the diffusion and the drift terms at the edge of the depletion region, the contribution of the graded region to the saturation current is found to be

$$J_{0n}(\text{reflecting}) = J_x \tanh\left(\frac{x_j}{\eta}(L(0)^{-1} - L(x_n)^{-1})\right). \tag{3}$$

For a steep enough profile, the current can be approximated by $J_{0n}(\text{reflecting}) \approx J_x \tanh(x_j/\eta L(0))$. If the graded region is wide according to the revised definition, the saturation current approaches the same asymptotic value—that of a wide abrupt junction. For a narrow region, the ratio between the current of a graded structure and that of an abrupt junction is the inverse of the ratio derived for ohmic contact. It should be noted that the current for the reflecting boundary is always smaller than J_x, while the current for the ohmic contact is always larger than this value. Thus J_{0n}(ohmic) is *always* larger than J_{0n}(reflecting), just as in the case of an abrupt junction.

Next let us analyse the dependence of the saturation currents on the various device parameters. The effect of the junction depth x_j on J_0 is similar to that for the case of a constant-concentration region [10], i.e. the shallower the junction, the larger is the current for ohmic contact and the opposite for reflecting contact. Again, though, the physical processes involved are much more involved for the graded junction. While for an abrupt junction the only effect of bringing the junction closer to the surface is the increased excess carrier gradient for ohmic contact, thus increasing their diffusion, in a graded junction the shallower junction results also in a larger electric field which opposes the current in the case of ohmic contacts. For reflecting conditions, since no net flow should reach the boundary, the change in the electric field just described must be compensated by an appropriate redistribution of excess carriers. These results are demonstrated

in figure 1, where we have plotted the saturation current as a function of the normalised depth. The exponential profile is compared with two abrupt junctions whose constant concentrations are $N_d = N_0$ ($= 5 \times 10^{17}$) and $N_d = N(x_n)$. The problem is that x_n and $N(x_n)$ change with changing x_j. We took $N_d = 10^{17}$ cm^{-3}, which is a typical value for the smaller x_j; x_n was derived from a recent work by Pimbley [3]. All the calculations were performed for $Hg_{1-x}Cd_xTe$ diodes with composition $x = 0.21$, i.e. with 77 K band gap which covers the second atmospheric window.

Applying this analysis, other important conclusions can be drawn, such as the effect of the surface concentration on the current. Increasing the surface concentration (maintaining N_a and x_j constant) increases the gradient and the electric field while reducing the excess carrier lifetime throughout the graded region. Mathematically, two factors in the argument of the hyperbolic functions are affected: $L(0)$ is inversely proportional to N_0, while η is proportional to its logarithm. Thus increasing the surface concentration reduces J_0 for ohmic boundary conditions and increases it for reflecting conditions. These effects are shown in figure 2.

A similar analysis can be applied to investigate the effects of substrate concentration on the performance of the graded junction. Increasing N_a while maintaining a constant N_0 and x_j is achieved by decreasing the profile gradient, reducing *both* the electric field and the excess carrier lifetime. The consequence is a smaller η; thus the current decreases for ohmic contacts and increases for reflecting surfaces. As N_a approaches N_0, $L(x_n)$ approaches $L(0)$. This effect is enhanced by the widening of the depletion region. The combined result is that the saturation current does not reach J_{0r} as shown in figure 3. For the last two figures we assumed a typical reverse bias of 0.1 V. The exact bias has little implication on this analysis.

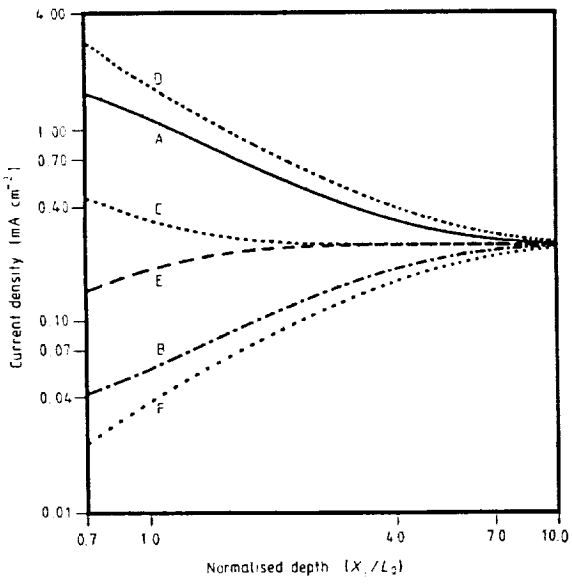

Figure 1. Saturation current generated by an n-region against normalised junction depth, for an exponential profile and for abrupt junctions with $N_d = 5 \times 10^{17} = N_0$ and $N_d = 10^{17} \approx N(x_n)$, for ohmic and reflecting boundary conditions ($Hg_{1-x}Cd_xTe$, $x = 0.21$, $N_a = 10^{16}$): A, graded ohmic; B, graded reflecting; C, constant ohmic, $N_d = N_0$; E, constant reflecting, $N_d = N_0$; D, constant ohmic, $N_d = N(x_n)$; F, constant reflecting, $N_d = N(x_n)$.

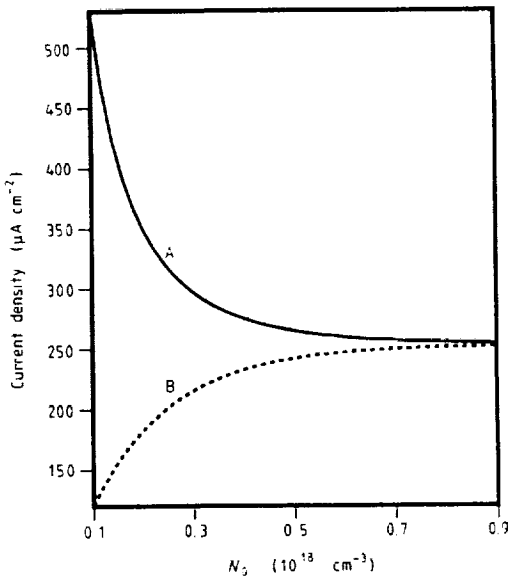

Figure 2. Saturation current generated by an n-region of a graded junction as a function of surface concentration for (A) ohmic and (B) reflecting boundary conditions ($Hg_{1-x}Cd_xTe$, $x = 0.21$, $N_a = 10^{16}$, $x_j = 0.4$ μm, $T = 77$ K, $V = -0.1$ V; Auger recombination).

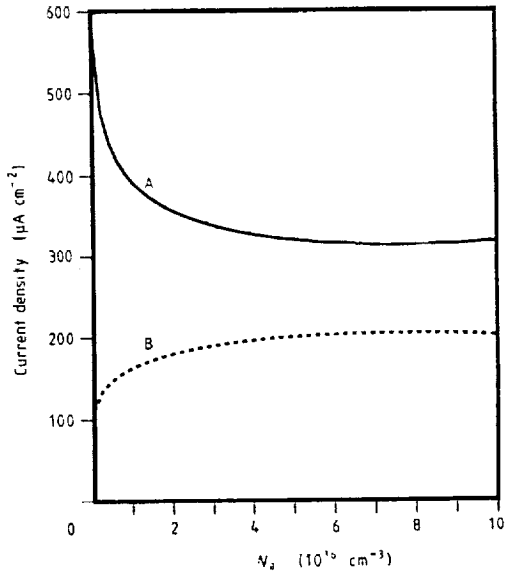

Figure 3. Saturation current generated by an n-region of a graded junction as a function of substrate concentration for (A) ohmic and (B) reflecting boundary conditions ($Hg_{1-x}Cd_xTe$, $x = 0.21$, $N_0 = 4 \times 10^{17}$, $x_j = 0.2$ μm, $T = 77$ K, $V = -0.1$ V; Auger recombination).

Another interesting effect is the dependence of the saturation current on the reverse bias. Even though we assume that the current is not governed by generation and recombination nor by tunnelling, the reverse current may *not* approach a saturation value. This effect, shown in figure 4, is a consequence of x_n moving towards the surface with increasing reverse bias.

3. Conclusions

The current generated by a graded region of a p-n junction differs considerably from that generated by a region of constant carrier concentration. The exact expression for the current component depends on the recombination mechanism, surface treatment, exact carrier profile and substrate concentration. The illustrations provided in this paper are specific to $Hg_{1-x}Cd_xTe$.

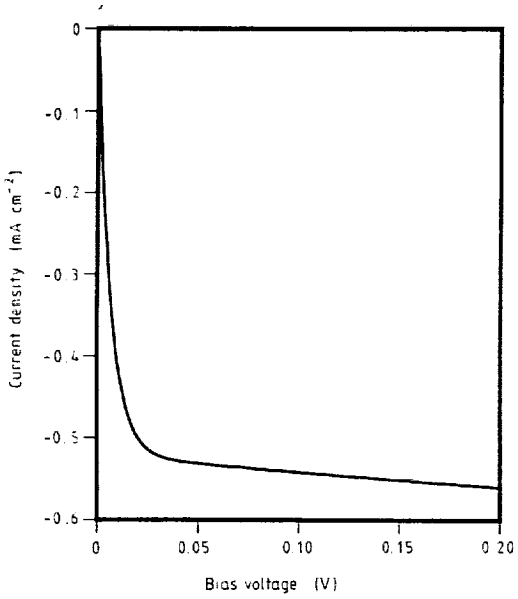

Figure 4. *I–V* characteristic for reverse bias showing the current generated by an n-region of a graded $Hg_{1-x}Cd_xTe$ diode ($x = 0.21$, $N_a = 10^{16}$, $N_0 = 5 \times 10^{17}$, $x_j = 0.1\ \mu m$, $T = 77$ K; ohmic contact). Note that the reverse current does *not* saturate.

dominated by the Auger 1 recombination process, with lifetime inversely proportional to the square of the carrier concentration. As the graded n-type region may very likely be degenerated, the recombination may have a different power law. In this case, as well as in cases dominated by radiative or Shockley Read-type recombination, the current is expressed as a combination of modified Bessel functions [13]. Still, the simplicity of our solution makes it a very attractive tool for investigation of the basic processes involved and how they are influenced by selection of the proper parameters. Finally, the new p-on-n junctions may present a structure for which the analysis is exact since the p-type material does not become degenerate till much higher concentrations. The expressions for the current are obtained merely by replacing the Auger 1 process by an Auger 7.

Acknowledgment

We wish to thank Dr Y L Juravel for his interest in the early stages of this work.

References

[1] e.g. Sze S M 1981 *Physics of Semiconductor Devices* (New York: Wiley)
[2] van Opdorp C and 't Hooft G W 1984 *Solid State Electron.* **27** 261–6
[3] Pimbley J M 1988 *IEEE Trans. Electron Devices* **ED-35** 1957–62
[4] Ghandhi S K 1968 *The Theory and Practice of Microelectronics* (New York: Wiley)
[5] Chawla B R and Gummel H K 1971 *IEEE Trans. Electron Devices* **ED-18** 178–95
[6] Marine J and Motte C 1973 *Appl. Phys. Lett.* **23** 450–2
[7] Kolodny A and Kidron I 1980 *IEEE Trans. Electron Devices* **ED-27** 37–43
[8] Arias J M, Shin S H, Pasko J G, DeWames R E and Gertner E R 1989 *J. Appl. Phys.* **65** 1747–53
[9] Destefanis G L 1988 *J. Cryst. Growth* **86** 700–22
[10] Reine M B, Sood A K and Tredwell T J 1981 *Semiconductors and Semimetals* vol. 18, ed. R K Willardson and A C Beer (New York: Academic) pp 201–311
[11] Tredwell T J and Long D 1977 *Final Tech. Rep., NASA Contract NAS9-14180*
[12] Schacham S E and Finkman E 1989 *J. Vac. Sci. Technol.* A 7 387–90
[13] Schacham S E and Finkman E, to be published

Properties of insulator interfaces with p-HgCdTe

N91-18300

S. E. Schacham[a] and E. Finkman
Kidron Microelectronics Research Center, Department of Electrical Engineering, Technion–Israel Institute of Technology, Haifa 32000, Israel

(Received 4 October 1989; accepted 29 October 1989)

Heat treatment at 70 °C of low carrier concentration *p*-type HgCdTe samples ($p_0 = 8 \times 10^{14}$ cm^{-3}) generates an inverted surface layer. A two day anneal process below 95 °C did not affect the Hall coefficient, whereas an almost complete recovery was obtained by annealing at 120 °C. While bulk electron mobility, obtained from PEM data, remained high (about 9×10^4 cm^2/V s at 77 K), surface mobility is lower by more than an order of magnitude. Surface recombination velocity indicates a continuous improvement with increased temperature, and the activation energy remains equal to the vacancies energy level. The proposed mechanism is that of positive charges in the sulfide migrating towards the interface and generating an image inversion layer.

I. INTRODUCTION

Surface passivations of semiconductor devices are very crucial to the device's performance.[1] Interface properties depend strongly on process parameters. They can result in surface charges, either accumulation or inversion, both undesirable for diodes. Secondly, they set the boundary conditions, as manifested by the surface recombination velocity.[2] Accordingly, the carrier distribution in the semiconductor is set, and the efficiency as photodevices is determined. The interface properties can be modified by subjecting the device to an annealing process.

Various passivations have been employed with narrow bandgap HgCdTe, including anodic oxide, anodic sulfide, and SiO_2 and ZnS coatings. Recently, we investigated interface properties such as surface recombination velocity, mobility, and carrier concentration.[3,4] This data was obtained using several opto-galvanomagnetic experiments, including the photoelectromagnetic effect (PEM) for the determination of surface recombination velocity and electron mobility. The properties of anodic sulfide, anodic oxide, and ZnS coatings were compared. Anodic oxide formed an inverted layer on *p*-type samples, which resembles a two-dimensional layer by virtue of extremely high surface electron mobility.[4] Both anodic sulfide and ZnS coatings rendered surface recombination with identical activation energies.[3] It was concluded that surface traps are related to lattice defects, most probably vacancies. It was also shown that the thickness of the anodic sulfide determines the quality of this passivation. On a carefully prepared sample with a very thin sulfide layer it was possible to obtain a "normal" *p*-type Hall data even at low temperatures on a sample with acceptor concentration as low as 8×10^{14} cm^{-3}.

In this paper we report a further investigation of the properties of the anodic sulfide interface. Following the formation of an inversion layer, several annealing steps lasting from two hours to two days, were applied. The annealing temperature was gradually increased from 70 to 120 °C. Following each step, full optogalvanomagnetic characterizations were performed.

II. EXPERIMENTAL RESULTS AND DISCUSSION

In order to study the formation and annealing of inversion layers, *p*-type $Hg_{1-x}Cd_xTe$ samples with composition ratio of $x \sim 0.22$ and with very low carrier concentrations were passivated by anodic sulfide. The low concentration enables the detection of even minute surface charges. A sample with equilibrium concentration of $p_0 = 8 \times 10^{14}$ cm^{-3}, which previously maintained flatband conditions for three years, was heated to 70 °C in vacuum. After two hours of heating, an inversion layer was formed on its surface. A series of annealing steps were carried out, gradually increasing the annealing temperature. The effect of the annealing process on reducing inversion charges was investigated through the measurement of the Hall coefficient. The experimental results are summarized in Fig. 1. The original measurement shows a classical curve of a *p*-type sample, with a single sign inversion at about 85 K ("as prepared"). Following the formation of the inverted surface layer, the Hall data renders a typical *n*-type curve, in which the Hall coefficient remains negative throughout the entire scanned temperature range. Heating for two days at 70 °C did not change the Hall data at all. Similarly, the effect of a two day anneal at 80 °C on the carrier concentrations is hardly noticeable. Only after a two day anneal at 95 °C can an improvement be detected through a narrow region of positive Hall coefficients, before it reverses its sign again. Heating the sample to 120 °C for two days brought about almost a complete recovery of the Hall coefficient. The data at the range of 20–50 K almost coincides with the original bulk measurements, although at lower temperatures a second sign change is still present.

A heat treatment of 70–80 °C generates an electron inversion layer of about 8×10^{11} cm^{-2}. It seems that the positive charges present in the sulfide layer diffuse towards the interface, segregating there, as is frequently the case with defects accumulating at the interface. Consequently, the concentration of negative charges at the surface of the semiconductor increases. Indeed, in samples with a thicker sulfide layer, a higher surface concentration was measured.[4] Only at higher temperatures, 95 °C and above, does an annealing process

 0734-2101/90/021171-03$01.00

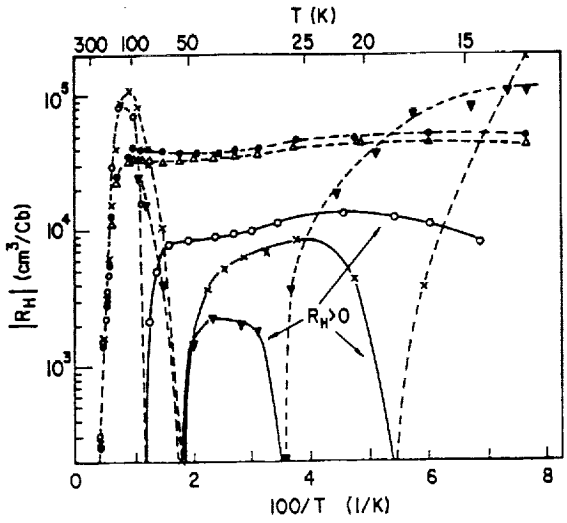

FIG. 1. Hall coefficient of p-HgCdTe, $x = 0.225$, $N_A = 8\times10^{14}$ cm^{-3}, with anodic sulfide. Original well-passivated p-type data ("as prepared"), turns to all negative n-type results following 70 °C anneal. Only above 95 °C does a positive section reappear, and by 120 °C substantial recovery is observed. — $R_H>0$, - - - $R_H<0$; ○ as prepared, ● anneal, 70 °C, △ 2 days, 80 °C, ▼ 2 days, 95 °C, and × 2 days, 120 °C.

start to take place, reducing the concentration of these charges.

The second basic parameter investigated is the electron mobility. Both Hall and PEM experiments were employed. The bulk electron mobility was extracted from fitting the measured PEM current and from the high temperature Hall data. When an extensive inversion layer is present, the Hall experiment provides information about this layer only. Therefore, the Hall mobility extracted from these samples is that of the inversion electrons. The mobility data is presented in Fig. 2. The high-temperature data and the lower mobilities at lower temperatures are obtained from Hall experiments.

The electron mobility in the inversion layer is very low. Surface scatterings reduce the mobility by more than an order of magnitude. This result is in drastic contrast to the anodic oxide passivation of p-type samples, where we have measured very high electron mobilities, *higher* than bulk electron mobilities.[4]

The analysis of the PEM data renders the bulk electron mobility. It is interesting to note that this holds true even for the samples with the extensive inversion layers, whose Hall mobilities are considerably lower than those of the bulk. These latter, obtained from the PEM experiments, are practically unchanged by all the heat treatments, and remain almost identical to the as prepared values. Only the final anneal, at 120 °C, resulted in a slight deterioration of bulk electron mobility. At 77 K the bulk mobility is typically 9×10^4 cm^2/V s which is comparable to electron mobility in n-type material of similar concentration and composition. This is more than twice the mobility in p-type material with concentration of about 10^{16} cm^{-3}.

In the range of 80–150 K, the results obtained combine both bulk and inversion layer effects. At extremely low temperatures, i.e., below 30 K, the surface electron mobility decreases further, which is typical of scattering by defects. Again, it indicates that the defect concentration at the surface is much higher than the bulk.

The surface recombination velocity was derived from the PEM data. Following our previous analysis (Equation 7, Ref. 3), the results shown in Fig. 3 are presented as ST/p_0 versus $1/T$, where S is the surface recombination velocity, p_0 is the bulk equilibrium hole concentration and T is the absolute temperature. The present results are compared to those obtained from samples with anodic sulfide passivation of higher bulk concentration p-type HgCdTe, with $p_0 = 5\times10^{15}$–2×10^{16} cm^{-3} (Ref. 3). We note that all mea-

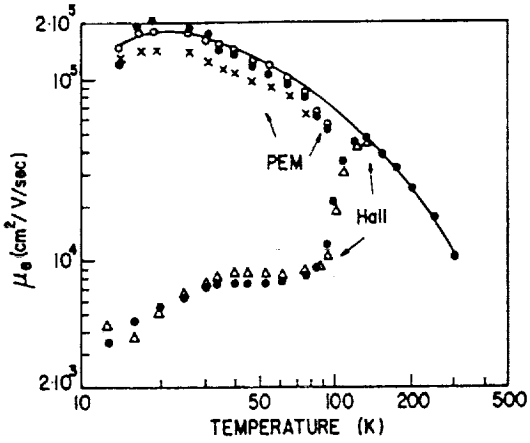

FIG. 2. Electron mobility recorded after the same annealing steps as in Fig. 1. High temperature and low (inversion layer) mobility data is Hall mobility. High mobility at low temperatures (bulk mobility) is derived from PEM experiments. ○ as prepared, ● anneal 70 °C, △ 2 days, 80 °C, and × 2 days, 120 °C.

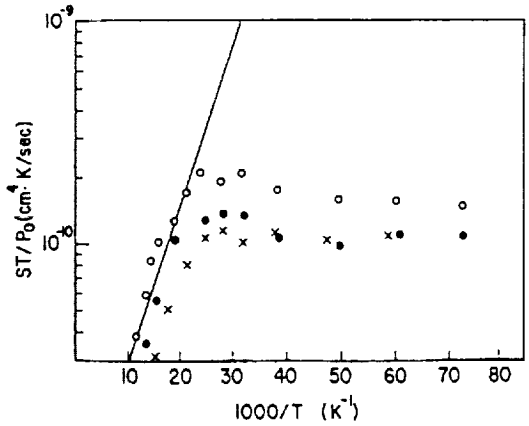

FIG. 3. Surface recombination velocity derived from PEM experiments. Data shows considerable improvement with annealing. Activation energy is 12.5 meV for all cases. ○ as prepared, ● anneal 70 °C, and × 2 days, 120 °C.

surements render the same activation energy, of 12.5 meV, which is identical to the energy level of the cation vacancies. Again, there is a low temperature plateau (unlike samples with zinc sulfide treatment), which indicates pinning of the Fermi energy. However, the surface recombination velocity is substantially lower than that obtained with previous samples (with higher bulk concentrations). It improves with annealing, decreasing from about 800 cm/s at 77 K for the as prepared sample to around 250 cm/s following heat treatments. The overall lower recombination with reduced bulk concentration is again indicative of the correlation of the recombination centers to the vacancies in the substrate.

III. CONCLUSIONS

The effect of heat treatment of HgCdTe samples passivated by anodic sulfide was investigated. It was observed that the as prepared samples show very small band bending at the semiconductor interface. The sulfide, however, is produced with internal positive charges, which create an electron image layer at the HgCdTe surface. This electron inversion charge is observed in samples passivated with a thick (> 100 Å) sulfide. The surface concentration of these electrons depends on the thickness of the sulfide layer. It is suggested that the positive charges are evenly distributed in the "as grown" sulfide. A 70–80 °C anneal produces an inversion layer even in materials with a thin sulfide passivation. It is proposed that this layer is the result of migration of positive charges to the interface and their segregation there. The underlying assumption is that the diffusion coefficient is very high, even at these low temperatures. As a result the density of negative image charges in the HgCdTe surface increases. The positive sulfide charges start to anneal at temperatures above 90 °C, thus the inversion layer diminishes. It is shown that while the Hall and conductivity data obtained from inverted *p*-type materials reveal mainly the properties of the high conductivity inversion layers, the parameters extracted from PEM measurements are those of the bulk.

[a] NASA Lewis Research Center, Mailstop 54-5, Cleveland, OH 44135. This work was done while the author was a National Research Council—NASA Research Associate, on leave from the Technion.

[1] M. B. Reine, A. K. Sood, and T. J. Tredwell, in *Semiconductors and Semimetals*, edited by R. K. Willardson and A. C. Beer (Academic, New York, 1981), Vol. 18, pp. 201–311.
[2] A. Many, Y. Goldstein, and N. B. Grover, *Semiconductor Surfaces* (North-Holland, Amsterdam, 1965).
[3] E. Finkman and S. E. Schacham, J. Vac. Sci. Technol. A 7, 464 (1989).
[4] S. E. Schacham and E. Finkman, Proc. SPIE **1106**, 206 (1989).

SURFACE ELECTRONS IN INVERTED LAYERS OF *p*-HgCdTe

SAMUEL E. SCHACHAM* AND ELIEZER FINKMAN
*NASA Lewis Research Center, Cleveland, OH 44135
Department of Electrical Engineering and Solid State Institute, Technion - Israel Institute of Technology, Haifa 32000, Israel.
*This work was done while this author held a National Research Council – NASA Research Associateship.

ABSTRACT

Anodic oxide passivation of *p*-type HgCdTe generates an inversion layer. Extremely high Hall mobility data for electrons in this layer indicated the presence of a two-dimensional electron gas. This is verified by use of the Shubnikov–de Haas effect from 1.45-4.15K. Data is extracted utilizing a numerical second derivative of DC measurement. Three sub-bands are detected. Their relative occupancies are in excellent agreement with theory and with experimental results obtained on anodic oxide as accumulation layers of *n*-type HgCdTe. The effective mass derived is comparable to expected.

INTRODUCTION

The narrow-gap semiconductor HgCdTe is an important infrared detector material. Most photodiodes are implemented on *p*-type HgCdTe. The performance of these devices is heavily dependent on surface properties. Thus the selection of an appropriate passivation is crucial.

Anodic oxide forms an accumulation layer on *n*-type material. The two-dimensional sub-bands of this passivation have been thoroughly investigated in recent years. Findings obtained using various magnetoresistence measurements [1-7] are in good agreement with data obtained from other narrow-gap non-parabolic semiconductor systems, in particular on HgTe and HgTe/CdTe superlattices [8-10]. It has been shown both in theory [11,12], as well as experimentally [1,5,6] that narrow-gap non parabolic materials possess common features. One characteristic of accumulation and inversion layers on such materials is a large number of occupied sub-bands, as many as five in HgCdTe [5,6]. Ando [12] has shown that a large change in the band-gap energy has little effect on the relative occupancy of the various sub-bands.

In this work we report the use of the Shubnikov–de Haas (SdH) technique to measure the transport properties of electrons in an inversion layer on *p*-type $Hg_{1-x}Cd_xTe$. The inversion film was formed by generating an anodic oxide passivation to a low concentration *p*-type substrate, $N_a - N_d \simeq 8 \cdot 10^{14}\ cm^{-3}$, with composition ratio of $x \simeq 0.22$. The low acceptor concentration enhanced the Hall data of the inverson layer. An extremely high Hall mobility, higher than measured for electrons in *n*-type material of similar composition, triggered our speculation that a 2-dimensional electron gas is present [13]. Since previous measurements concentrated on accumulation layers, it seemed intriguing to examine an inversion film, in particular since the theory of Takada et al. [11] was developed for the latter structure (see remark in [7]).

When a magnetic field is applied perpendicular to a surface layer, the translational motion is quantized into Landau levels. Sweep of the field reveals oscillations periodic with inverse magnetic field due to modulation of the density of states at the Fermi level as the Landau levels increase in energy with increasing field. When several sub-bands are occupied, these SdH measurements generate a waveform which is a superposition of the oscillations for each sub-band. The two-dimensionality of the structure can be verified by a vanishing signal as the sample is rotated by 90°.

EXPERIMENTAL WORK

The measurement of DC magnetoresistence on HgCdTe frequently reveals little information. Seiler and Becker [14] introduced an AC technique where the magnetic field is modulated and phase sensitive detection is employed. The second derivative of the amplitude presents clear data of SdH oscillations [2,5,6,8,10]. An alternative method is using a metal-insulator-semiconductor (MIS) structure and modulating the gate voltage [1,7,15]. Since our experimental setup did not provide for modulation of the magnetic field and Hall bar samples were used, we had to develop appropriate numerical methods in order to extract the oscillatory data. Fourier analysis showed no oscillatory pattern following background subtraction. Instead numerical second derivative of the voltage with respect to the field combined with data smoothing was employed. These were obtained by fitting a small number of points to a second degree polynomial. This process eliminates the background and reveals the SdH oscilations.

Figure 1 shows such a plot of the second derivative versus an inverse magnetic field measured at 1.45 K. Several frequencies of oscillations can be observed, corresponding to various sub-band populations and their harmonics. In figure 2 we separated between these frequencies: trace (a), corresponds to 0.31-0.44 T, with a frequency of 3.75 T; trace (b), corresponds to 0.51-0.79 T, with a frequency of 9.7 T and a change of phase (beat) at 0.66 T; trace (c), corresponds to 1.01-1.16 T and shows superposition of the previous frequency with a 30.4 T waveform.

The effect of increasing temperature is presented in figure 3, in which trace 2c is repeated, this time at 4.15 K. There is an obvious decrease of the amplitude of the 30.4 T oscillation, while the reduction in the 9.7 T component is minimal.

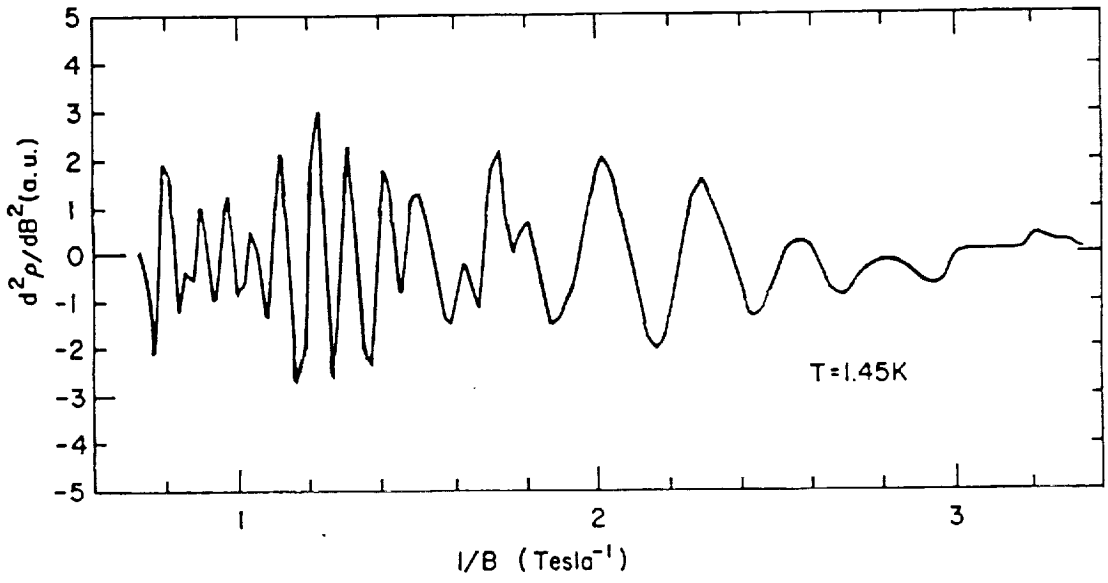

Fig. 1: Numerical second derivative of magnetoresistance measured at 1.45K, showing SdH oscillations of an anodic oxide inversion layer on $p-Hg_{0.78}Cd_{0.22}Te$

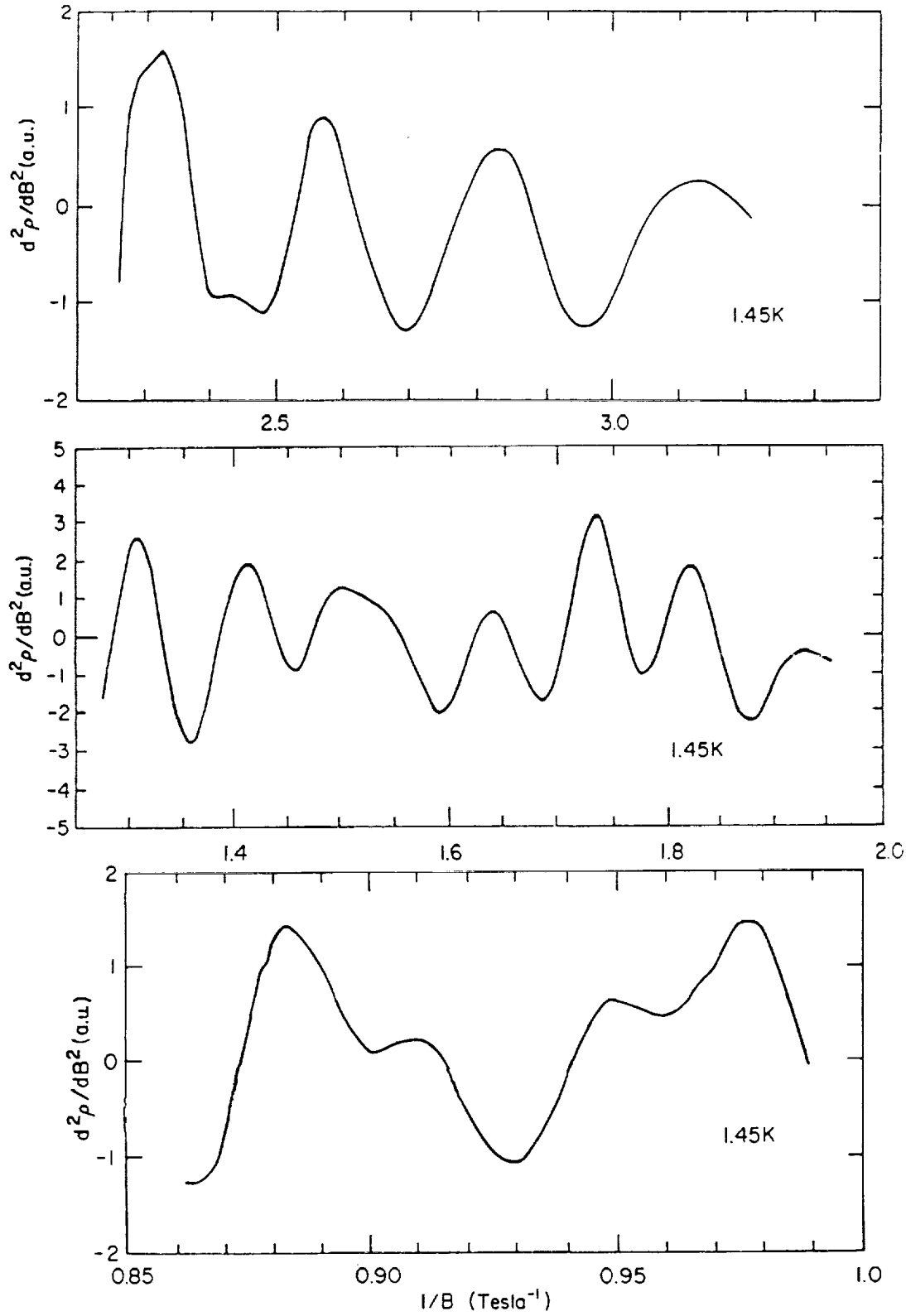

Fig. 2: High resolution data of Fig. 1, revealing 3 oscillation frequencies:
a. 0.31-0.44T, F = 3.75T.
b. 0.51-0.79T, F = 9.7T. Note the phase shift at ~1.52 1/T.
c. 1.01-1.16T, superposition of F = 9.7T and F = 30.4T.

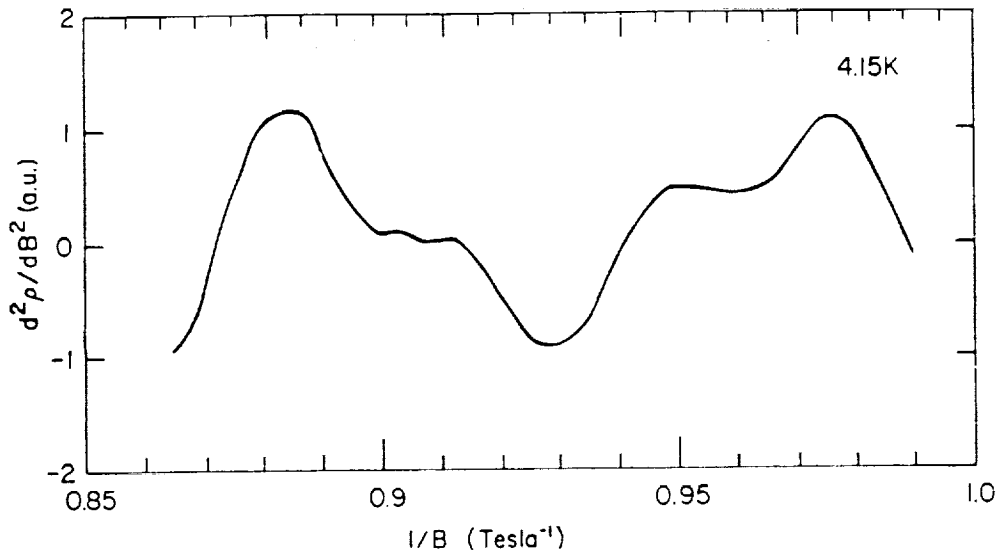

Fig. 3: Same as Fig. 2c, at 4.15, showing substantial decrease of 30.4T component, less of the 9.7 one.

ANALYSIS AND DISCUSSION

The change in the resistivity due to the magnetic field can be expressed as [16]

$$\frac{\Delta\rho}{\rho_0} \propto \sum_n \sum_M T\left[\frac{M \cdot m_r^n}{B}\right]^{1/2} \frac{\exp(-\beta M T_D^n m_r^n/B)}{\sinh(\beta M T m_r^n/B)} \cdot \cos\left[\frac{2\pi M F^n}{B} + \phi^n\right] \qquad (1)$$

where T = temperature, B = magnetic field, F = oscillation frequency, ϕ = phase, T_D = Dingle temperature, m_r = effective mass ratio (m^*/m_0), and $\beta = 2\pi^2 k_B m_0/HB\ e = 14.7$ T/K. The summation on M is over the harmonic frequencies of a given sub-band n. In order to obtain the occupancy of the various sub-bands, the Fourier transform of the data was obtained using an FFT. Figure 4 shows a transform of the second derivative taken at 4.15 K. Similar spectra were obtained for all other measured temperatures. These results highly resemble the data of Beck and Anderson (Fig. 2, Ref. 7), obtained for an accumulation layer. In addition to the three main frequencies, corresponding to three occupied sub-bands, one can easily observe the second and third harmonics of the 3.75 T line (with the third harmonic more intense than the second).

The effective mass of electrons in the various sub-bands can be derived from the reduction in amplitude with increasing temperatures. This dependence can be summarized as $\chi/\sinh\chi$, where $\chi = \beta T m_r/B$. Unfortunately due to the very small effective mass in HgCdTe and due to the superposition of the various lines, it is hard to obtain precise data in the limited temperature range employed. Figure 5 shows a fit for the amplitude of a peak at 1.05 T (0.95 1/T) which corresponds to the first sub-band, with the largest effective mass. The fitted value is $m^* = 0.033\, m_0$. The convex shape of the curve indicates that the argument of the hyperbolic function is indeed small, thus replacing the hyperbolic sine with an exponential function should be done with extreme caution! [9]. The data is summarized in Table I. The uncertainty in the value of the effective masses is large. Moreover, since the ratio of x to its hyperbolic sine approaches rapidly 1 as x approaches 0, the very small effective masses of the second and third subbands renders a ratio which is almost temperature independent, causing a further increase in uncertainty in determination of these values. The accuracy of the derivation may be improved by either a deconvolution of the various frequency components of the waveform, or a simulation this pattern.

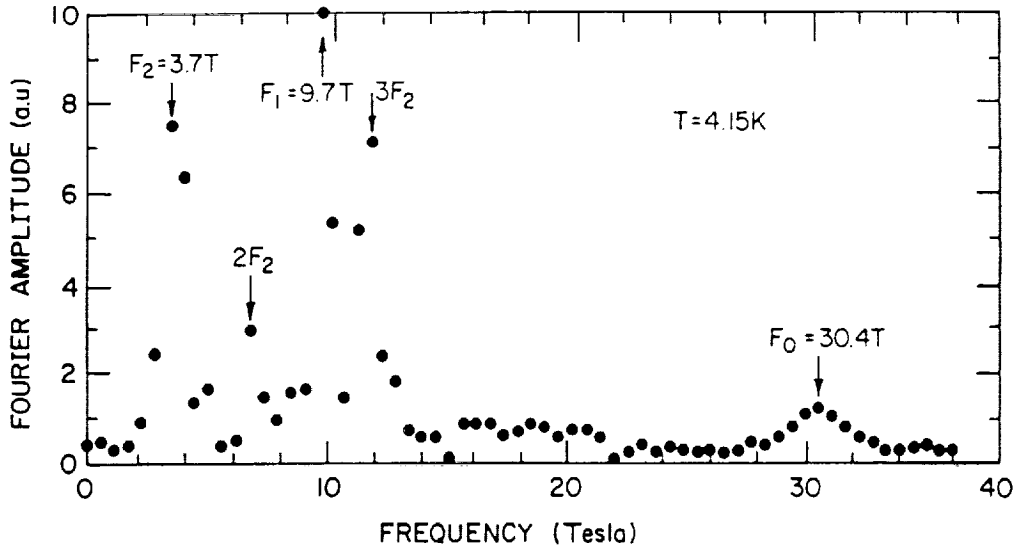

Fig. 4: Fourier transform of SdH oscillations. Clear peaks of 3 fundamental frequencies, due to 3 sub-bands, and harmonics of $F = 3.75$T.

The sub-band occupancy is given by $N_s^n = \frac{2e}{h} \cdot F^n$. Summing up the concentration of the first three sub-bands, and adding 4% for the higher ones [5], we came up with the ratio of the sub-bands occupancy to total surface concentration N_s^T, presented in Table I.

Table I

n	$F^n(T)$	$N_s^n(cm^{-2})$	N_s^n/N_s^T	m_r^n
1	30.4	$1.47 \cdot 10^{12}$	0.693	0.033±0.008
2	9.7	$4.69 \cdot 10^{11}$	0.221	0.018±0.007
3	3.75	$1.81 \cdot 10^{11}$	0.0855	0.011±0.005

The concentration ratios are in excellent agreement with the theory in [12], the results of Beck and Anderson [7] and the various Singleton, Nicholas and Nasir investigations [1-6]. Taking into consideration the composition ratio ($x = 0.22$), our results indeed fit perfectly with a slight difference between those of $x = 0.2$ and $x = 0.3$ [2]. The discrepancy between these data and that of Zhao et al. [1] was recently explained [5].

The effective masses obtained are on the lower edge of the theory [11] and experimental results [6,7]. However, the large uncertainty in present values necessitates further investigation before any conclusions can be drawn.

The two-dimensionality of the data was verified by rotating the sample by 90°. The numerical analysis renders noise with amplitudes one-order of magnitude smaller than the SdH oscillations, for all temperatures tested. No peaks are present in the Fourier transform.

A change of phase, such as we observed at about 0.66 T, has been previously reported for SdH data on various materials, including HgTe films [8]. The last one was observed only at ~1.9 K, and was attributed to strain-effects, rather than to inversion asymmetry, since it was observed at low electron concentration. In this work it is also possible that the beat is a result of the superposition of the two frequencies at 9.7 T (second sub-band) and at 11 T (third harmonic third sub-band).

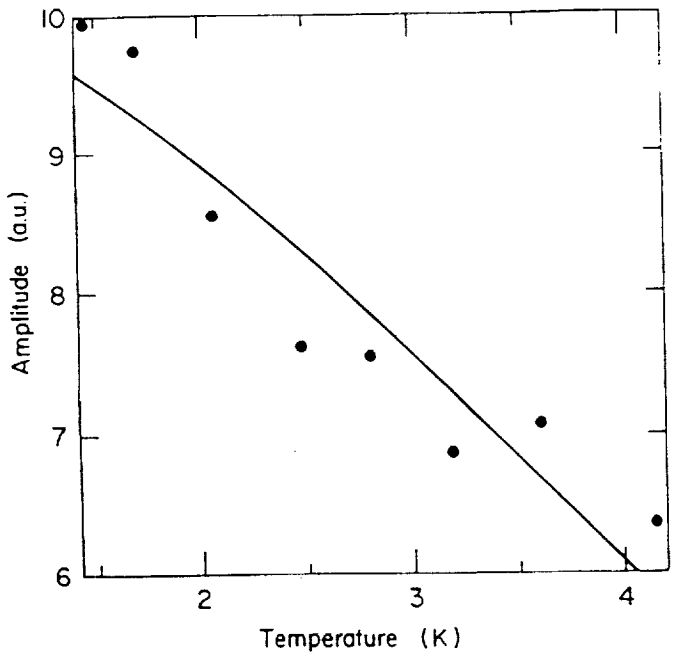

Fig. 5: Measured temperature dependence of peak at 1.05T. Effective mass derived from theoretical fit $m^* = 0.33m_0$.

CONCLUSIONS

The SdH experimental technique performed on an inversion layer, generated by anodic oxidation of a *p*-HgCdTe, proves the existance of a 2DEG and renders data on three sub-bands. The calculated relative occupancies of these sub-bands agree extremely well with theory and experimental results obtained from accumulation layers on *n*-type materials. The analysis should be extended to achieve better accuracies of the effective mass by both measurements at higher temperatures and by mathematical simulation of the data. This also may render scattering times. Experimental work at higher magnetic fields may reveal additional structures.

The numerical analysis performance in this work has proven that it is possible to compensate for limitations in experimental facilities by appropriate mathematical tools.

REFERENCES

1. W. Zhao, F. Koch, J. Ziegler and H. Maier, Phys. Rev. B 31, 2416 (1985).

2. J. Singleton, R.J. Nicholas, F. Nasir and C.K. Sarkar, J. Phys. C 19, 35 (1986).

3. J. Singleton, F. Nasir and R.J. Nicholas, in Optical Properties of Narrow-Gap Low-Dimensional Structures, Vol. 152 in NATO ASI Series B, edited by C.M.S. Torres, J.C. Portal, J.C. Maan and R.A. Stradling (Plenum, New York, 1987), p. 195.

4. J. Singleton, F. Nasir and R.J. Nicholas, Proc. SPIE 659, 99 (1986).

5. F. Nasir, J. Singleton and R.J. Nicholas, Semicond. Sci. Technol. 3, 654 (1988).

6. R.J. Nicholas, F. Nasir and J. Singleton, J. Cryst. Growth 86, 656 (1988).

7. W.A. Beck and J.R. Anderson, J. Cryst. Growth 72, 437 (1985).

8. R.J. Justice, D.G. Leider, W. Zawadzki, R.J. Koestner, M.G. Goodwin and M.A. Kinch, J. Vac. Sci. Technol. A 6, 2779 (1988).

9. L. Ghenim, R.G. Mani and J.R. Anderson, Phys. Rev. B 39, 1419 (1989).

10. D.G. Seiler, G.B. Ward, R.J. Justice, R.J. Koestner, M.W. Goodwin, M.A. Kinch and J.R. Meyer, J. Appl. Phys. 66, 303 (1989).

11. Y. Takada, K. Arai, N. Uchimura and Y. Vemura, J. Phys. Soc. Jpn. 49, 1851 (1980).

12. T. Ando, J. Phys. Soc. Jpn. 54, 2676 (1985).

13. S.E. Schacham and E. Finkman, to be published in Opt. Eng.

14. D.G. Seiler and W.M. Becker, Phys. Rev. 183, 784 (1969).

15. J.C. Thuillier and F. Bazenet, J. Vacuum Sci. Technol. 16, 1417 (1979).

16. E.N. Adams and T.D. Holstein, J. Phys. Chem. Solids 10, 254 (1959).

PLASMA-DEPOSITED AMORPHOUS HYDROGENATED CARBON FILMS AND THEIR TRIBOLOGICAL PROPERTIES

K. Miyoshi, J.J. Pouch and S.A. Alterovitz
National Aeronautics and Space Administration
Lewis Research Center, Cleveland, OH 44135, USA

ABSTRACT

Recent work on the properties of "diamondlike" carbon films and their dependence on preparation conditions are reviewed. The results of the study indicate that plasma deposition enables one to deposit a variety of amorphous hydrogenated carbon (a-C:H) films exhibiting more diamondlike behavior to more graphitic behavior. The plasma-deposited a-C:H can be effectively used as hard, wear-resistant, and protective lubricating films on ceramic materials such as Si_3N_4 under a variety of environmental conditions such as moist air, dry nitrogen, and vacuum.

INTRODUCTION

Carbon films exhibiting unique properties can be formed on different substrates by ion-beam deposition, ion-beam sputtering, and plasma deposition of gaseous hydrocarbons [1 to 8]. The properties are sensitive to the deposition conditions. These resulting films can exhibit high electrical resistivity, semitransparency, mechanical hardness, and chemical inertness. The carbon films show promise as wear-resistant, hard solid lubricating coatings for mechanical systems such as bearings and optical components. In addition, carbon films are useful as gate dielectrics and passivating layers in semiconductor device processing, insulators for metal-insulator-metal fabrication, and masks for nanometer lithography [9 to 11].

This chapter is principally concerned with the chemical, physical, and tribological characteristics of amorphous hydrogenated carbon (a-C:H) films grown on different substrates (Si_3N_4, GaAs, InP, Si, and fused silica) by means of plasma chemical vapor deposition at 30 kHz. The influence of growth conditions on the chemical and physical properties of these films was studied by Auger electron spectroscopy (AES), secondary ion mass spectroscopy (SIMS), x-ray photoelectron spectroscopy (XPS), ellipsometry, and N^{15} nuclear reaction techniques. The nuclear reaction techniques provide the hydrogen concentration information. These analysis techniques and procedures are described in references 12 to 18. Tribological studies have also been conducted with the a-C:H films to better understand those chemical and physical properties of the films that will affect their tribological behavior when in contact with a ceramic material. The friction, wear, and lubricating behavior of the a-C:H films were examined with flat specimens (composed of an a-C:H film and Si_3N_4 substrate) in contact with Si_3N_4 riders in two processes. The first was done in dry nitrogen gas in moist air to determine the environmental effects on friction and resistance to wear of the a-C:H films. The second was done in an ultrahigh vacuum system to determine the effect of temperature on adhesion and friction of a-C:H films.

AMORPHOUS HYDROGENATED CARBON (a-C:H) FILMS

Plasma Deposition

Amorphous hydrogenated carbon films were formed on the different substrates from the 30 kHz ac glow discharge by using a planar plasma reactor [12 to 18]. All substrate materials were first cleaned in acetone and ethanol baths and then rinsed in deionized water. The substrates were placed on the ground anode of the parallel plate reactor in the chamber; the upper electrode was capacitively coupled to the 30 kHz power source. The background pressure was typically 2.7 Pa (20 mtorr). The gas sources were CH_4 and C_4H_{10} (methane and butane, 99.97 percent pure). The deposition gas (CH_4 or C_4H_{10}) was used to flush the system three times prior to each run. The chamber pressure was controlled by the input gas flow rate and pumping speed. The power density and flow rate settings covered the ranges 0.4 to 5 kW m^{-2} (25 to 300 W) and 3 to 9×10^{-5} m^3 min^{-1} (30 to 90 SCCM), respectively. The initial substrate temperature was 25 °C, and it increased a few degrees during each deposition.

The film growth rate varied monotonically with deposition power. Figure 1 illustrates the typical dependence of growth rate on deposition power. The specimens are a-C:H films grown on InP substrates using a CH_4 flow rate of 70 SCCM. This growth rate increases from 5 to 27 nm min^{-1} as the power increases from 25 to 300 W.

Film Characteristics

The AES and XPS measurements indicated that the a-C:H films contained only carbon; no other element was observed to the detection limits (0.1 at. %) of the instrument [12 and 13]. Figure 2 shows a typical AES profile of a-C:H films on the InP and GaAs. Oxygen was not present in the films, but there was a small percentage of oxygen at the carbon-InP interface. This suggests that the CH_4 (methane) plasma removes all of the native oxides from the GaAs surfaces and most of it from the InP surfaces.

Relative counts of hydrocarbon ions sputtered from a-C:H films deposited on the InP substrate were determined by means of SIMS depth-profiling studies performed with 3 keV Ar^+ ions [12]. In figure 3(a) the distribution of ion counts is plotted as a function of mass-to-charge ratio for various deposition conditions using a C_4H_{10} plasma. The predominant ion is CH^+; it is interesting that a higher CH^+ level is obtained from films produced at the higher power densities. Additional ions are presented in figure 3(a): CH_2^+, CH_3^+, C_2H^+, $C_2H_2^+$, and $C_2H_3^+$.

The ion distributions extracted from a-C:H films prepared by a CH_4 (methane) discharge are shown in figure 3(b). Evidently, CH^+ has a higher probability of being sputtered from each film. At 50 SCCM (32.7 Pa), more CH^+ is generated from the a-C:H deposit made at 2.45 kW m^{-2}. In addition, some of the films obtained from the C_4H_{10} discharge (fig. 3(a)) have higher amounts of incorporated C_2H_3 relative to the CH_4-derived films (fig. 3(b)). Figure 3 indicates that the lowest populations are associated with CH_3^+. The ion distributions thus reflect some of the bonding arrangements that result from the interaction of the plasma radicals with the growing film [19 to 21].

A SIMS depth profile (3 keV Ar^+ ions) of carbon deposited onto GaAs using C_4H_{10} is presented in figure 4. The CH_x^+ ($x = 0,1,2,3$) distributions are uniform in the bulk of the film, and they drop to lower levels in the vicinity

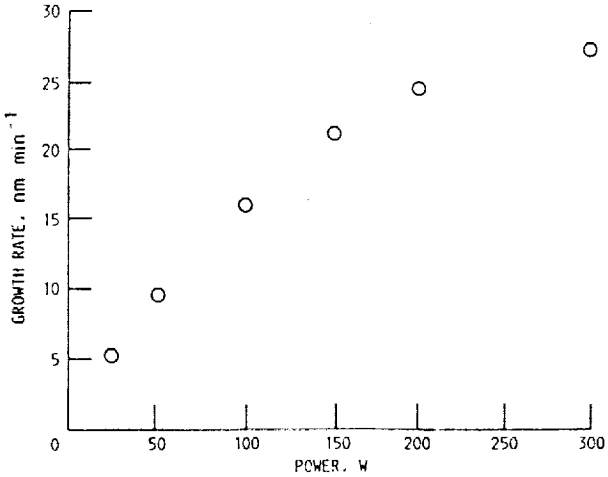

Figure 1.—Growth rate of hydrogenated carbon on *n*-InP as function of deposition power.

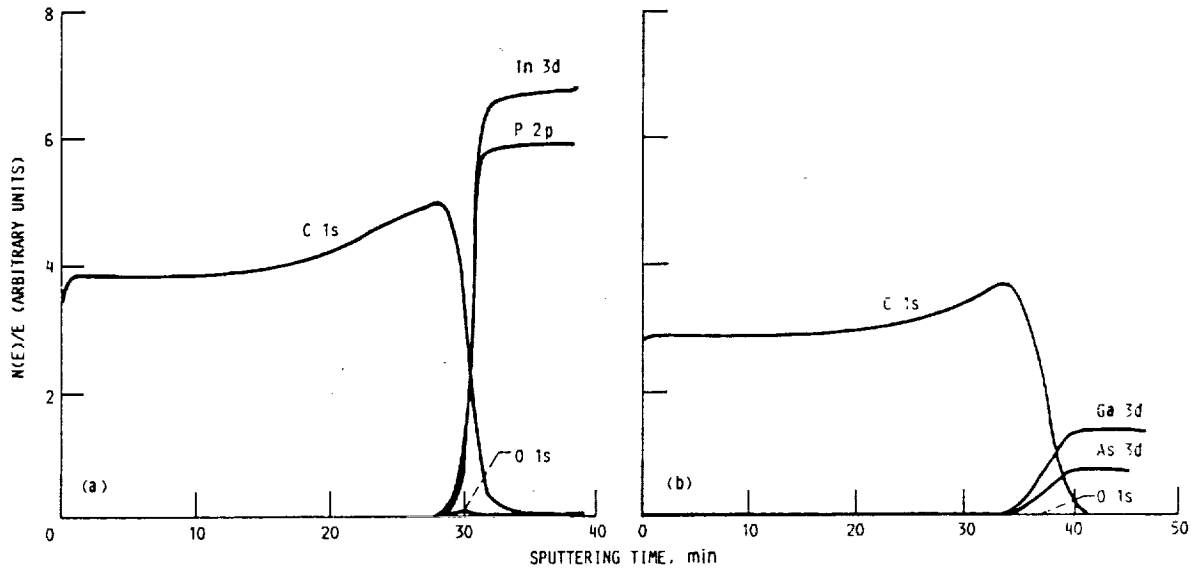

(a) InP.
(b) GaAs.

Figure 2.—Auger electron spectroscopy (AES) profiles of carbon films on InP and GaAs, using 25 mA 3 keV Ar^+ ions.

of the carbon-GaAs interface. Moreover, figure 4 shows oxygen to be present throughout the film. This determination cannot be made with the less-sensitive AES technique. It is apparent that Ga^+ and As^+ are readily detected as the carbon film is sputtered away.

The argon ion etching rate of the a-C:H films is shown as a function of deposition power in figure 5(a). An inverse relationship between argon ion etching rate and deposition power is observed. The etching rate drops from 80 to 50 nm min^{-1} when the deposition power is increased from 25 to 300 W. This suggests that films grown at higher powers are denser than those grown at lower powers. Figure 5(b) shows the nuclear reaction analyses data. The hydrogen concentration in the carbon film decreases slightly with increasing power. The hydrogen concentrations are in the 7.2 to 7.7×10^{22} cm^{-3} range, which gives an approximate value of 0.8 for x in the formula CH_x.

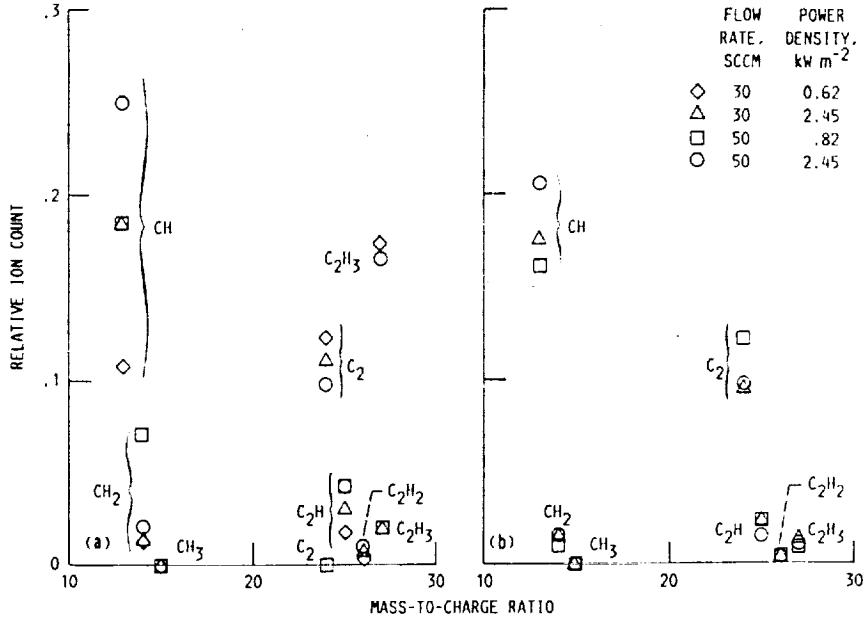

(a) C_4H_{10} plasma.
(b) CH_4 plasma.

Figure 3.—Relative ion count as function of mass-to-charge ratio for carbon deposited onto InP using C_4H_{10} and CH_4 plasmas.

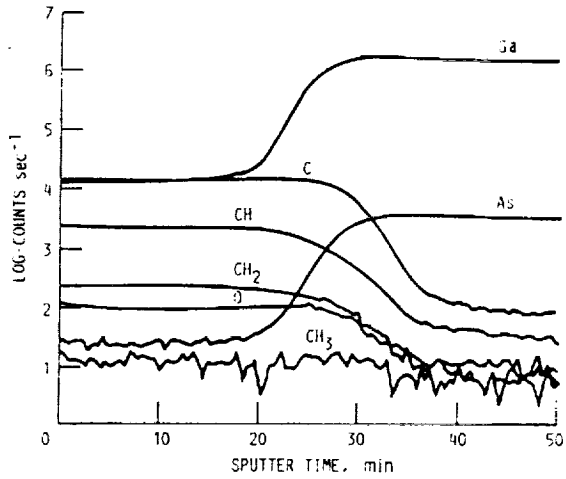

Figure 4.—Secondary ion mass spectroscopy (SIMS) depth profile of carbon on GaAs using 3 keV Ar^+ ion bombardment.

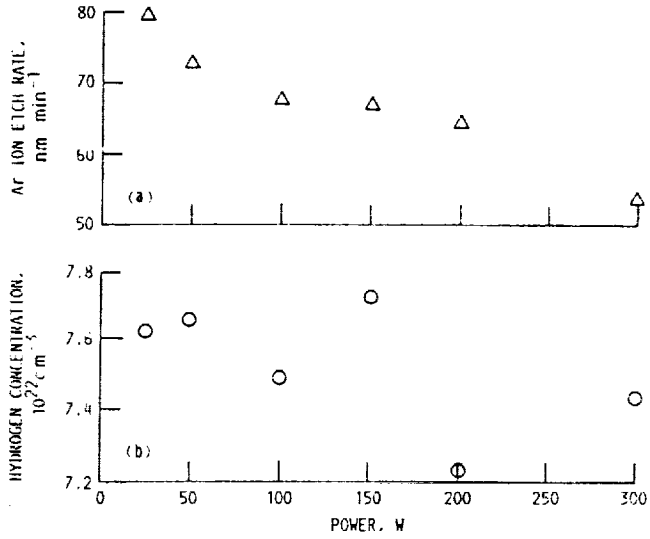

(a) Ar ion etch rate.
(b) Hydrogen concentration.

Figure 5.—Ar ion etching rate and hydrogen concentration as function of deposition power for carbon film grown on *n*-InP.

TABLE I.—COMPOSITION AND PROPERTIES OF HOT-PRESSED SILICON NITRIDE

Nominal composition, wt %	92 Si_3N_4-4MgO-4Y_2O_3
Structural phase	β-Phase
Density, g cm^{-3}	3.27
Vickers hardness, GPa	16.1
Three-point bending strength, MPa	980
Fracture toughness, MN m$^{-3/2}$	9.4
Young's modulus, 10^4 kg mm^{-2}	2.9
Poisson's ratio	0.27
Compressive strength, kg mm^{-2}	330
Thermal expansion coefficient, 10^{-6} °C^{-1}	3.6

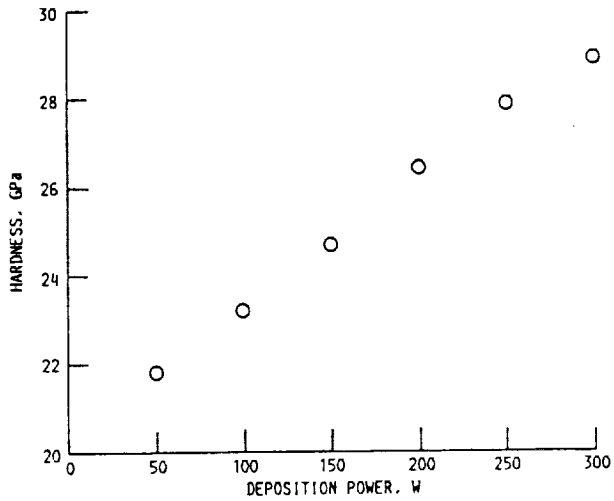

Figure 6.—Vickers hardness as function of deposition power for a-C:H film deposited on Si_3N_4 (hardness measuring load, 0.25 N; hardness of Si_3N_4 substrate, 17.1 GPa).

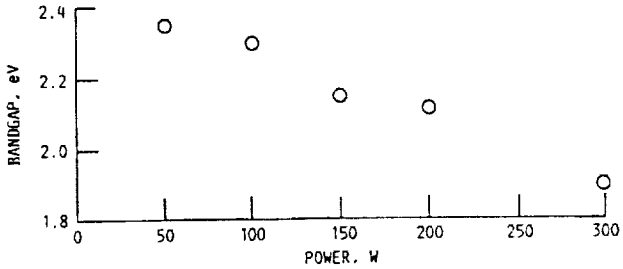

Figure 7.—Optical bandgap as function of deposition power for carbon film grown on *n*-InP.

The microhardness data measured for the carbon films on Si_3N_4 substrate (table I) at various deposition powers are presented in figure 6. The microhardness increases as the power increases. Thus it appears that a decrease in hydrogen concentration is accompanied by an increase in film density and/or c-c bondings, and in hardness.

The optical energy gap is shown as a function of the deposition power in figure 7. A decrease in the optical energy gap is clearly observed with increasing power.

At this stage, we will compare our results with conjecture forwarded by S. Kaplan et al. [22]. They claim that since double-bond hydrogenation is an exothermic process, "graphitic" behavior is favored over tetrahedral bonding in higher energy growth environments. They show evidence of this assumption by comparing a-C:H films made by five different experimental configurations. As a-C:H properties are dependent quite strongly on the many variables encountered in different preparation conditions, it seems that a better test of this assumption is in order. In addition, their results show a rather striking feature: a-C:H films exhibiting more "diamondlike" behavior (i.e., larger bandgap and more tetrahedral bonding) show a steep decrease in their hardness as compared with the more "graphitic" films. Our results confirm this model, including the hardness measurements. The higher the plasma deposition power, the more sp^2 versus sp^3 bonds are made, giving a more "graphitic" film, with smaller bandgap (fig. 7) and higher density and hardness (figs. 5 and 6, respectively).

TRIBOLOGICAL PROPERTIES

In the preceding section there have been indications that a-C:H films have diamondlike behavior in lower energy growth environments as compared with the more graphitic behavior in higher energy growth environments. Therefore, the objective of this section is to compare the tribological properties of a-C:H films made by different deposition powers.

Sliding friction and wear experiments were conducted with a-C:H films deposited on Si_3N_4 flats in contact with hemispherical Si_3N_4 riders (1.6 mm in radius). The a-C:H films on the Si_3N_4 flat substrates were approximately 0.06 μm. The Si_3N_4 used for flat substrates and hemispherical riders was hot pressed, and its composition and some of its properties are presented in table I. Two types of sliding friction experiments were conducted with the a-C:H films [23 to 25]. The first type was conducted in nitrogen and laboratory air atmospheres with a load of 1 N (Hertzian contact pressure, 910 MPa) and at a sliding velocity of 8 mm min^{-1} at room temperature. The specimen rider was made to traverse on the surface of a-C:H film. The motion was reciprocal. The a-C:H films were subjected to multipass sliding by the Si_3N_4 riders. The second type was conducted in ultrahigh vacuum (10^{-8} to 10^{-9} torr) with loads up to 1.7 N (Hertzian contact pressure, 1.5 GPa) and at a sliding velocity of 3 mm min^{-1} at temperatures up to 700 °C. In this case, the a-C:H films were subjected to single-pass sliding by the Si_3N_4 riders.

Environmental Effects on Friction and Wear

Environment significantly changes the friction and wear behavior of solid materials. Friction and wear of a-C:H films are consistent with this generality and depend on water vapor [1 and 26 to 28].

Figure 8 presents typical plots of the coefficient of friction for plasma-deposited a-C:H films at low (50 W) and high (250 W) deposition power as a function of the number of repeated passes in dry nitrogen and humid air environments. The values of coefficient of friction given are typical, but the trends with number of passes are quite reproducible. With the 50-W plasma-deposited a-C:H films, the coefficient of friction was generally found to increase,

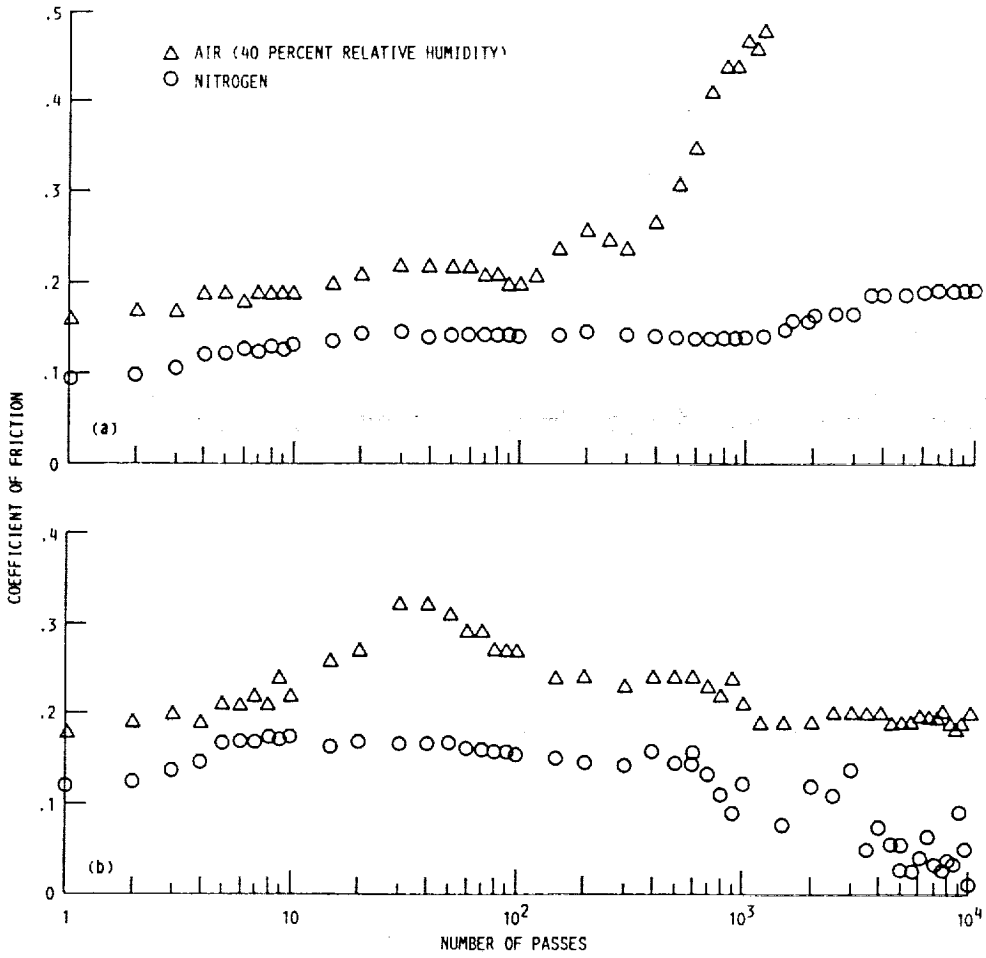

(a) Deposition power, 50 W.
(b) Deposition power, 250 W.

Figure 8.—Average coefficient of friction as function of number of passes of Si_3N_4 rider across a-C:H film surface in laboratory air and in dry nitrogen at deposition powers of 50 and 250 W.

as shown in figure 8(a). This increase, however, was small in a dry nitrogen environment even after it had been in contact with the rider for about 10 000 passes. On the other hand, in humid laboratory air a significant increase in the coefficient of friction occurred at about 500 passes and increased sharply to 1000 passes. The sliding action caused breakthrough of the film and removed it from the sliding contact area at about 1000 passes. Note that among the a-C:H films deposited at various deposition powers (50 to 300 W), the film deposited at 50 W has the lowest initial coefficient of friction (0.08 to 0.09) in the dry nitrogen environment. The value of the coefficient of friction was similar to that of a hemispherical diamond pin (radius, 0.2 mm) in sliding contact with a Si_3N_4 flat. The friction of the diamond was low (0.05 to 0.1) in dry nitrogen. It is well known that diamond has a low coefficient of friction in contact with various types of materials [29].

With the 250-W plasma-deposited a-C:H films (fig. 8(b)), although the coefficient of friction increased with increasing number of passes for about 10 passes in the dry nitrogen environment, it generally decreased in the range 10 to 10 000 passes.

At 600 to 700 passes, the coefficients of friction became very erratic and variable, as presented in figure 8(b). Optical microscopic examination indicated that some wear debris particles formed in the front region of the rider and on the wear track of the a-C:H film. Thus the wear particles so produced were caught up in the sliding mechanism and affected the coefficient of friction.

At 1000 passes and above, the coefficient of friction became low, but still variable (0.01 to 0.1). At this range the coefficients of friction for the 250-W plasma-deposited film were lower than those for the film deposited at 50 W.

In a humid air environment, the coefficients of friction for the 250-W plasma-deposited a-C:H film were higher as compared with those in dry nitrogen by a factor of 1.5 to 3 up to 10 000 passes. The film, however, did not wear off from the substrate even in the humid air environment.

Thus, water vapor greatly increases friction and reduces the wear life of plasma-deposited a-C:H film at low deposition powers. In general, a-C:H films deposited with lower deposition powers were more susceptible to water vapor, when compared with the films deposited with higher deposition power. Particularly, the deposition power greatly affects the wear life of the films in a humid air environment. The greater the deposition power (the more graphitic the film), the greater the wear life in humid air.

Annealing Effects on Friction and Wear

Thermal annealing significantly affects the properties of a-C:H films. For example, an abrupt decrease of the optical bandgap has been observed for the thermal annealing process [14].

Figure 9 presents the optical bandgap of the a-C:H films deposited on the quartz substrates by using 150-W, 70-SCCM-flow-rate CH_4 plasma as a function of annealing time at 400 and 600 °C. The thermal processing of the films was accomplished in nitrogen gas with tungsten halogen light. The main part of the reduction in the optical bandgap is obtained at short annealing time. This fact can also be deduced by the result obtained by laser annealing [30].

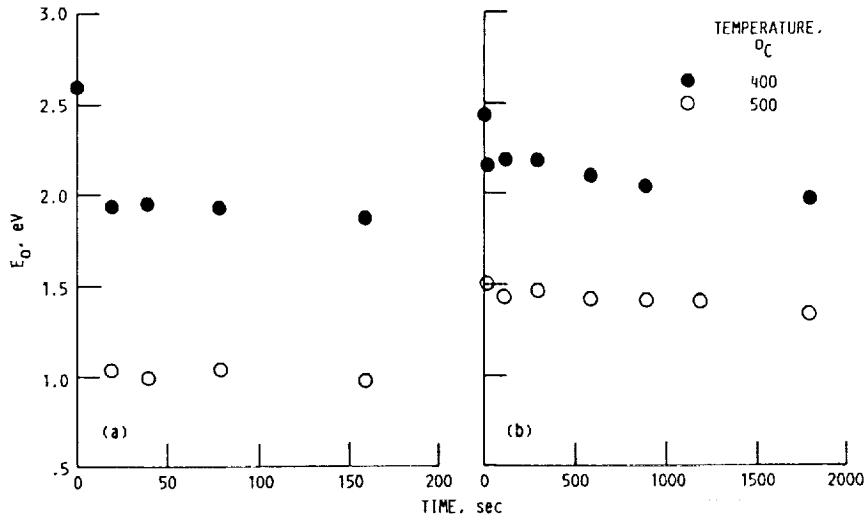

(a) Short annealing time.
(b) Long annealing time.

Figure 9.—Optical energy gap E_o as function of annealing time for a-C:H films on quartz annealed at two temperatures.

when processing time is much shorter than that reported here. The mechanism involved should be a two-step process. There is known to be a two-stage pyrolysis of organic material into graphite [31] for temperatures in this range, namely carbonization and polymerization. The carbonization stage includes loss of volatile matter, which we identify with hydrogen loss in this case [1]. This stage occurs in the temperature range 400 to 600 °C in a-C:H. The polymerization stage includes the formation of graphitic crystallites or sheets. If we assume that the polymerization is a diffusion-dependent process with a relatively long time constant (on the order of 10^3 sec), then we can deduce that the two processes of carbonization and polymerization occur simultaneously in our a-C:H films. The abrupt decrease of the bandgap versus time at very short processing time is due to the hydrogen loss, while the subsequent decrease in optical bandgap is due to an increase in cluster size [31].

Further, absorption in the UV-visible range was measured with a-C:H films on quartz substrates [14]. The absorbance-versus-wavelength plot at 600 °C shows a decrease in peak height and a shift in the peak position. The shift indicates changes in the carbon bonding. The decrease in peak height is attributed mostly to loss of material in this case.

Thermal annealing also changes the friction and wear characteristics of a-C:H films. Figure 10 presents the friction data for annealed a-C:H films in sliding contact with Si_3N_4 riders in dry nitrogen and humid air environments. The

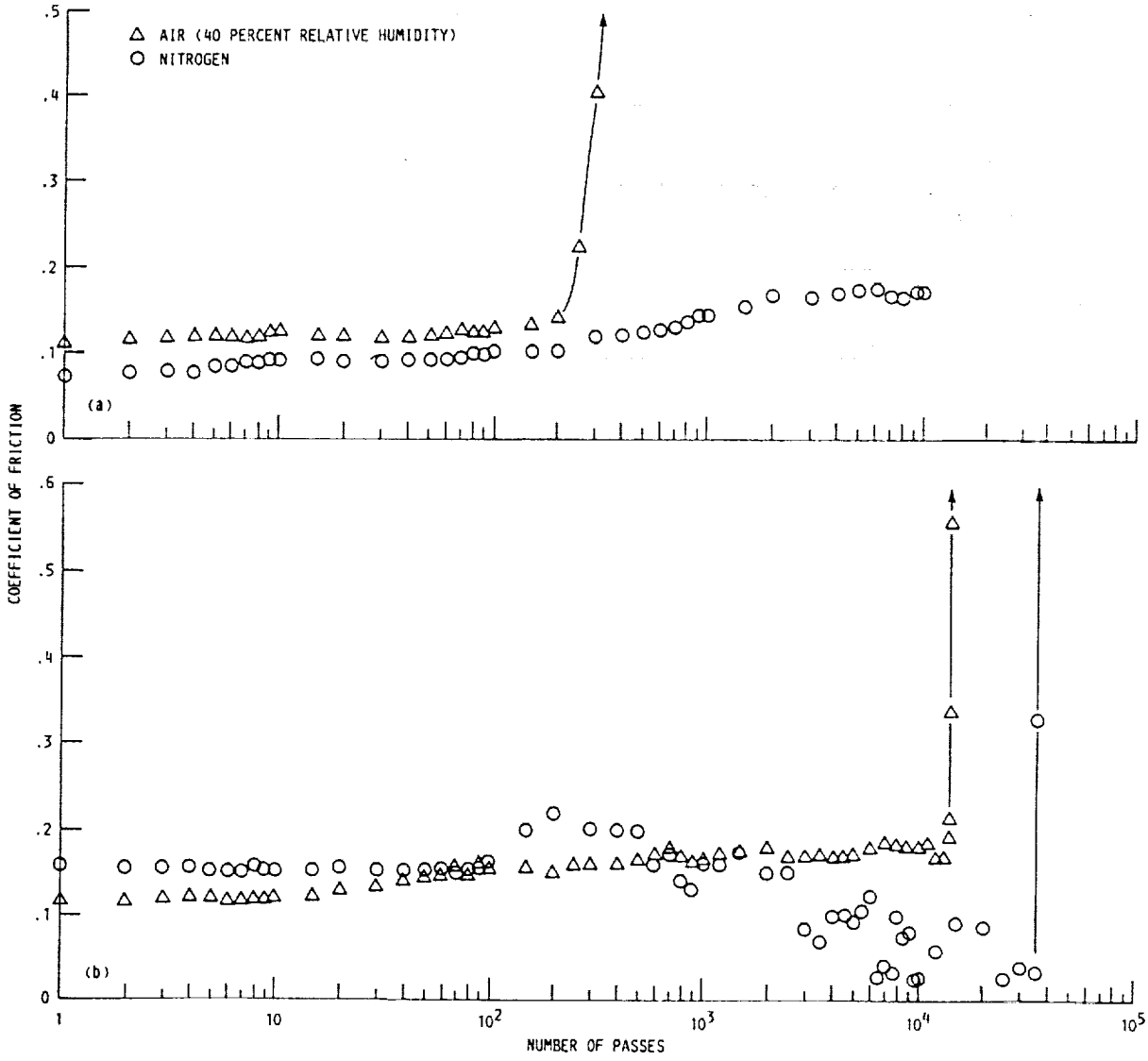

(a) Deposition power, 150 W.
(b) Deposition power, 300 W.

Figure 10.—Average coefficient of friction as function of number of passes of Si_3N_4 rider across a-C:H film surface in laboratory air and in dry nitrogen, after annealing a-C:H in vacuum at 700 °C, at deposition powers of 150 and 300 W.

annealing of the a-C:H films deposited on the Si_3N_4 substrates was accomplished at 700 °C in ultrahigh vacuum (10^{-8} to 10^{-9} torr).

Both in dry nitrogen and in humid air, the initial coefficients of friction for the annealed film deposited at 150 W (fig. 10(a)) were reduced by about a factor of 2 as compared with those for as-deposited film. The annealed film did not wear off from the substrate in dry nitrogen even after it had been in contact with the rider for about 10 000 passes, while in humid nitrogen it wore off at 300 passes and had shorter wear life.

With the a-C:H deposited at 300 W (fig. 10(b)), the results show an interesting feature: the annealed film exhibited more graphitic behavior; that is, at up to 100 passes the initial coefficients of friction in humid air were lower than those obtained in dry nitrogen. This is contrary to the results obtained from the as-deposited a-C:H films (e.g., fig. 10) and the annealed film at 150 W power (fig. 10(a)). Further, in the humid air environment the coefficients of friction were reduced by about a factor of 2 as compared with the as-deposited film. The generally accepted theory (that graphite lubricates because of adsorbed water or gaseous films) seems capable of explaining these results [32 and 33]; namely, the a-C:H film deposited at 300 W is believed to be more graphitic than the films deposited at lower power. Moreover, the annealing of the film gives a more graphitic film. Effective lubrication is possible with the very graphitic film provided both by the high-power plasma deposition and by the annealing process when an adsorbed water vapor film is present. Thus, the annealed a-C:H film deposited at 300 W has very graphitic friction behavior.

Temperature Effects on Adhesion and Friction in Vacuum

An increase in the surface temperature of a-C:H films tends to cause chemical changes, as discussed in the preceding subsection. These chemical changes can alter their friction and wear behavior. For simplicity of discussion, the effect of temperature on tribological properties of concern is investigated in a nonoxidizing environment (i.e., in an ultrahigh vacuum). The in situ friction experiments were conducted in a vacuum with the as-received plasma-deposited a-C:H films in contact with the ion-sputter-cleaned, hemispherical monolithic Si_3N_4 rider specimens.

Typical plots of the coefficient of friction for a-C:H films plasma-deposited at 150 and 300 W as a function of surface temperature are presented in figures 11(a) and (b), respectively. Comparative data for an uncoated Si_3N_4 flat in contact with a hemispherical Si_3N_4 rider are presented in figure 12.

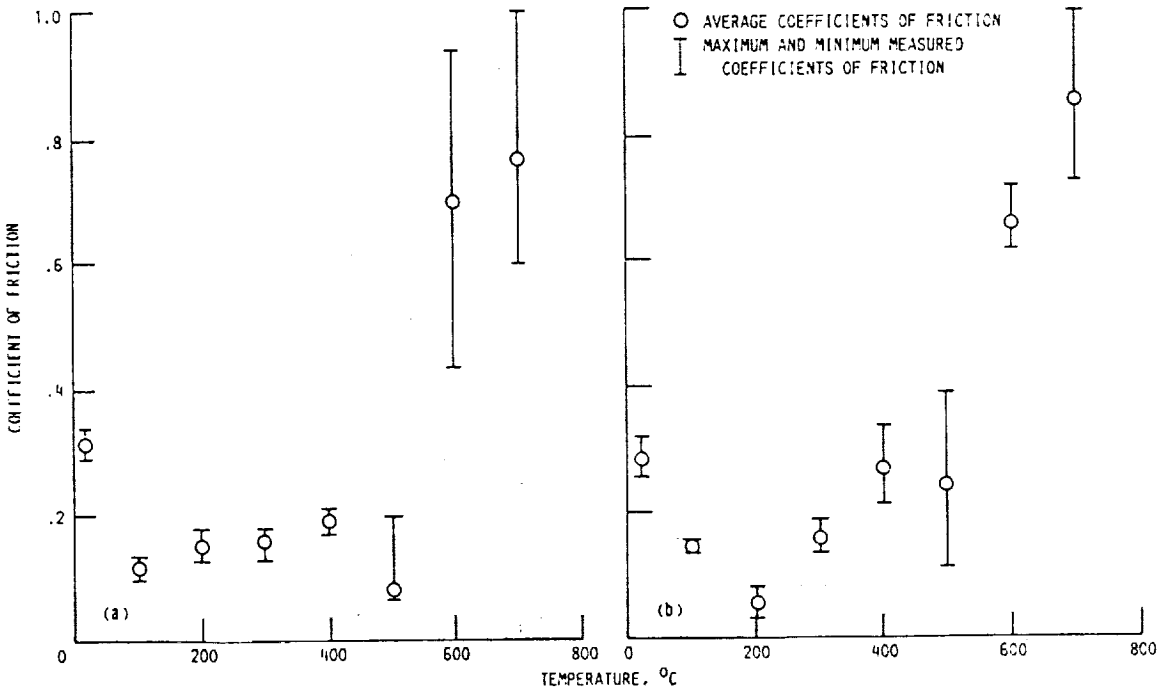

(a) Deposition power, 150 W.
(b) Deposition power, 300 W.

Figure 11.—Coefficients of dynamic friction as function of temperature for a-C:H films in contact with Si_3N_4 rider specimens in vacuum.

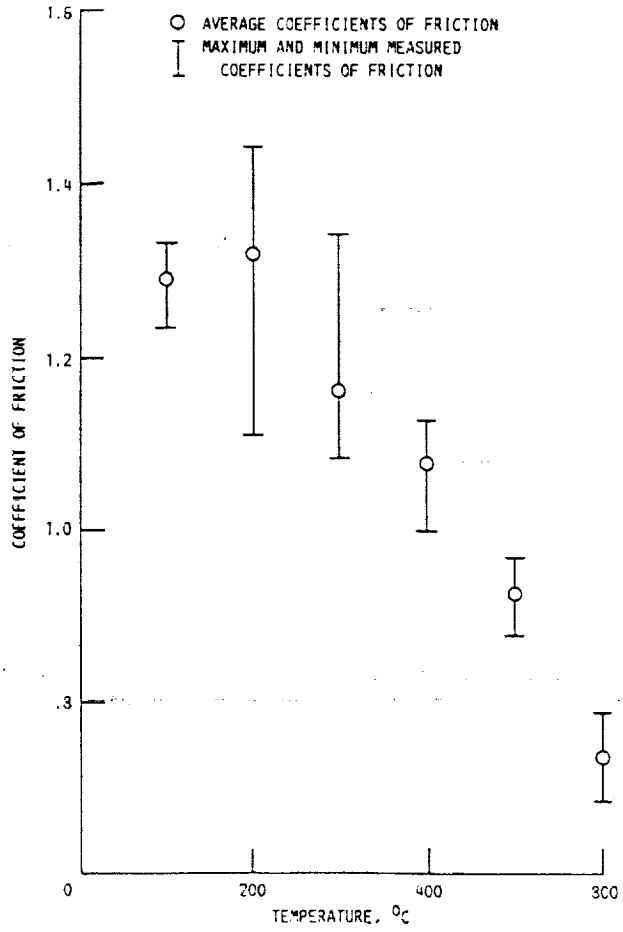

Figure 12.—Coefficients of dynamic friction as function of temperature for Si_3N_4 flats in contact with Si_3N_4 rider specimens in vacuum.

With the 150- and 300-W plasma-deposited a-C:H films (fig. 11), the coefficient of friction remained low at temperatures to 500 °C and rapidly increased with increasing temperatures at 600 °C and above, remaining high in the range of 600 to 700 °C. The mechanism involved in the rapid increase in friction at 600 to 700 °C should be related to the two-step process, namely carbonization and polymerization of a-C:H films, as discussed in the preceding subsection.

When compared with the coefficient of friction for Si_3N_4 in contact with Si_3N_4 itself (fig. 12), the coefficient of friction for a-C:H films in contact with a Si_3N_4 rider (fig. 11) was generally much lower at temperatures to 500 °C. It is also interesting to note that the coefficient of friction for the film deposited at 150 W had a very low coefficient of friction (about 0.08 at 500 °C) even in an ultrahigh vacuum environment (fig. 11(a)), and that the film effectively lubricated Si_3N_4 surfaces. Note that in vacuum the friction behavior of a-C:H film deposited at 50 W was similar to that shown in figure 11(a).

CONCLUDING REMARKS

There are two parts in this chapter, one mainly describing the growth and physical characterization of a-C:H films and the other dealing with the tribological properties. The films can be characterized by several parameters, as described in the first part. The main properties are defined by bonding ratios (sp^2/sp^3) and by hydrogen concentration, which will give the graphitic or diamondlike behavior. The more graphitic behavior is associated with lower bandgap and low mechanical etch rate.

In the second part of the work, the a-C:H films were shown to be capable of tribological applications. Plasma-deposited a-C:H can be effectively used as hard, wear-resistant, and protective lubricating films on ceramic material under a variety of environmental conditions such as moist air, dry nitrogen, and vacuum. More specifically, we

found a very good correlation of the tribological behavior with the physical properties, as described in the first part of the work. For a-C:H films deposited at low power, which are more diamondlike, we found friction behavior similar to that of bulk diamond. The present experiments show that among the a-C:H films deposited at various deposition powers (50 to 300 W), the film deposited at 50 W had the lowest initial coefficient of friction in dry nitrogen. The value of the coefficient of friction (0.08 to 0.09) was similar to that of hemispherical diamond (radius, 0.2 mm) in sliding contact with a Si_3N_4 flat. Conversely, for the a-C:H films deposited at higher power, a graphitic tribological behavior was found. Effective lubrication is possible with the graphitic films like bulk graphite when adsorbed water vapor is present.

Lastly, a simple physical characterization of the films can partially predict the tribological properties.

REFERENCES

1. Angus, J.J., Koidl, P., and Domitz, S.: "Carbon Thin Films," in Plasma Deposited Thin Films, ed. by Mort, J. and Jansen, F. CRC Press Inc., 1986, pp. 89-127.
2. Aisenberg, S., and Chabot, R.: J. Appl. Phys., 1971, **42**, 2953.
3. Holland, L., and Ojha, S.M.: Thin Solid Films, 1978, **48**, L21.
4. Berg, S., and Andersson, L.P.: Thin Solid Films, 1979, **58**, 117.
5. Meyerson, B., and Smith, F.W.: Solid State Commun., 1980, **34**, 531.
6. Moravec, T.J., and Orent, T.W.: J. Vac. Sci. Technol., 1981, **18**, 226.
7. Vora, H., and Moravec, T.J.: J. Appl. Phys., 1981, **52**, 6151.
8. Banks, B.A., and Rutledge, S.K.: J. Vac. Sci. Technol., 1982, **21**, 807.
9. Khan, A.A., Woollam, J.A., Chung, Y., and Banks, B.A.: IEEE Electron Devices Lett., 1983, **4**, 146.
10. Khan, A.A., Woollam, J.A., and Chung, Y.: Solid-State Electron., 1984, **27**, 385.
11. Kikuchi, M., Hikita, M., and Tamamura, T.: Appl. Phys. Lett., 1986, **48**, 835.
12. Pouch, J.J., Warner, J.D., Liu, D.C., and Alterovitz, S.A.: Thin Solid Films, 1988, **157**, 97.
13. Warner, J.D., Pouch, J.J., Alterovitz, S.A., Liu, D.C., and Lanford, W.A.: J. Vac. Sci. Technol. A, 1985, **3**, 900.
14. Alterovitz, S.A., Pouch, J.J., and Warner, J.D.: "Rapid Thermal Annealing of Amorphous Hydrogenated Carbon (a-C-H) Films," in Rapid Thermal Processing of Electronic Materials, MRS Symp. Proc. Vol. 92, ed. by Wilson, S.R., Powell, R., and Davies, D.E., Materials Research Society, 1987, pp. 311-318.
15. Pouch, J.J., Warner, J.D., and Liu, D.C.: Carbon Films Grown from Plasma on III-V Semiconductors, NASA TM-87140, 1985.
16. Pouch, J.J., Alterovitz, S.A., Warner, J.D., Liu, D.C., and Lanford, W.A.: "Optical Properties of Hydrogenated Amorphous Carbon Films Grown from Methane Plasma," in Thin Films: The Relationship of Structure to Properties, MRS Symp. Proc. Vol. 47, ed. by Aita, C.R. and Sreeharsha, K.S., Materials Research Society, 1985, pp. 201-204 (Also, NASA TM-86995).
17. Alterovitz, S.A., Warner, J.D., Liu, D.C., and Pouch, J.J.: "Ellipsometric and Optical Study of Some Uncommon Insulator Films on III-V Semiconductors," in Dielectric Films on Compound Semiconductors, Electrochemical Society Symp. Proc. Vol. 86-3, ed. by Kapoor, V.J., Connolly, D.J., and Wong, Y.H., The Electrochemical Society, Pennington, NJ, 1986, pp. 59-77 (Also, NASA TM-87135).
18. Pouch, J.J., Alterovitz, S.A., and Warner, J.D.: "Optical and Compositional Properties of a-C:H and BN Films," in Plasma Processing, MRS Symp. Proc. Vol. 68, ed. by Coburn, J.W., Gottscho, R.A., and Hess, D.W., Materials Research Society, 1986, pp. 211-216 (Also, NASA TM-87258).
19. Benninghoven, A.: Surf. Sci., 1975, **53**, 596.
20. Wagner, J., Wild, Ch., Pohl, F., and Koidl, P.: Appl. Phys. Lett., 1986, **48**, 106.
21. Kobayashi, K., Mutsukura, N., and Machi, Y.: J. Appl. Phys., 1986, **59**, 910.
22. Kaplan, S., Jansen, F., and Machonkin, M.: Appl. Phys. Lett. 1985, **47**, 750.
23. Miyoshi, K., and Rengstorff, G.W.P.: Corrosion, 1989, **45**, 266.
24. Miyoshi, K., and Buckley, D.H.: Wear, 1986, **110**, 295.
25. Miyoshi, K., Pouch, J.J., Alterovitz, S.A., Pantic, D.M., and Johnson, G.A.: in Wear of Materials, Vol. 2, ed. by Ludema, K.C., ASME, 1989, p. 585.
26. Enke, K., Dimigen, H., and Hubsch, J.: Appl. Phys. Lett., 1980, **36**, 291.
27. Memming, R.: Thin Solid Films, 1986, **143**, 279.
28. Okada, K., and Namba, Y.: J. Vac. Sci. Technol. A, 1989, **7**, 132.
29. Bowden, F.P., and Tabor, D.: "The Friction and Lubrication of Solids—Part II," Clarendon Press, Oxford, 1964, pp. 158-185.
30. Prawer, S., Kalish, R., and Adel, M.: Appl. Phys. Lett., 1986, **48**, 1585.
31. Robertson, J.: Adv. Phys., 1986, **35**, 317.
32. Bisson, E.E.: "Nonconventional Lubricants," in Advanced Bearing Technology, ed. by Bisson, E.E. and Anderson, W.J., NASA SP-38, 1965, pp. 203-258.
33. Bisson, E.E., Johnson, R.L., and Anderson, W.J.: "Friction and Lubrication with Solid Lubricants at Temperatures to 1000 °F with Particular Reference to Graphite," in Proceedings of the Conference on Lubrication and Wear, Institution of Mechanical Engineers, London, England, 1957, pp. 348-354.

Characterization of Multilayer GaAs/AlGaAs Transistor Structures by Variable Angle Spectroscopic Ellipsometry

Kenneth G. MERKEL*, Paul G. SNYDER, John A. WOOLLAM, Samuel A. ALTEROVITZ** and A. K. RAI***

Department of Electrical Engineering, Center for Microelectronic and Optical Materials Research, University of Nebraska-Lincoln, Lincoln, Nebraska 68588-0511, USA

(Received January 7, 1989; accepted for publication March 25, 1989)

Variable angle of incidence spectroscopic ellipsometry (VASE) has been implemented as a means of determining layer thickness, alloy composition, and growth quality of GaAs/AlGaAs samples composed of relatively thick layers as well as superlattices. The structures studied in this work contained GaAs/AlGaAs multilayers with a superlattice "barrier" and were grown for later formation of modulation-doped field effect transistors (MODFETs). Sample modeling was performed by treating the superlattice as a bulk AlGaAs layer of unknown composition. Extremely good data fits were realized when five layer thicknesses and two alloy ratios were allowed to vary in a regression analysis. Room temperature excitonic effects associated with the e-hh(1), e-lh(1) and e-hh(2) transitions were observed in the VASE data.

KEYWORDS: ellipsometry, spectroscopic, variable angle, layer thicknesses, GaAs, AlGaAs multilayer transistors

§1. Introduction

Rapid progress has occurred in the development of modulation-doped and multiple quantum well heterostructure devices. These types of structures have found applications in opto-electronics, digital electronics and microwave analog communications.[1]

These advances have created a requirement for monitoring the accuracy and quality of III-V semiconductor growth processes. Traditional methods for these purposes include cross sectional TEM (XTEM) and photoluminescence.[2,3] XTEM is slow, expensive, and destructive, and photoluminescence (PL) does not yield thickness information for the thicker layers. Generally PL, as well as photomodulation measurements, must be performed at cryogenic temperatures to be maximally useful. This limits the usefulness of these techniques in a manufacturing environment. VASE has been shown to provide an accurate, room temperature, atmospheric pressure, and nondestructive method of characterizing samples containing heterojunction and superlattice layers.[4,5,6] Thus it is logical to extend application of VASE to the more complex structure represented in the present paper. Important additional considerations such as interfacial roughness,[7] wafer homogeneity, and oxide growth can be determined by the VASE process.[8,9] In the present work we determine five layer thicknesses and two (equivalent) alloy ratios, representing one of the more complicated structures yet analyzed by ellipsometry. With these many unknowns the full spectral and variable angle capabilities of the VASE technique are required. Because we are "pushing the technique to the limit," we have included a careful study of the mean square error and correlation, in the present work.

Optical switches and modulators require very large nonlinearities induced optically or electro-optically. These nonlinearities are inherent in excitonic resonances in bulk semiconductors at low temperatures. The observance of excitonic effects in superlattices at room temperature greatly enhances the suitability of their use with other opto-electronic devices.[10] VASE provides important information for these devices, specifically the index of refraction and extinction coefficient at excitonic transition energies in superlattices.[6]

VASE resolves the structural and dielectric properties of multilayered samples by measuring the ratio of the reflection coefficients for light polarized parallel (R_p), and perpendicular (R_s) to the plane of incidence.[11] The ellipsometric parameters can be expressed as

$$\rho = \tan \Psi \exp(i\Delta) = R_p/R_s \qquad (1)$$

Experimentally, Ψ and Δ are measured and results are compared in a regression analysis to Ψ' and Δ' which are calculated using the Fresnel reflection coefficients and effective medium theories. The results of this analysis are values for layer thicknesses, alloy compositions and optical constants as a function of wavelength. In the present paper we use VASE to obtain layer thicknesses and alloy fractions for MODFET structures containing superlattices.

In §2 the experimental set-up is discussed. Section 3 details the VASE modeling procedure. Results are presented in §4 and conclusions in §5.

§2. Experiment

The design of the ellipsometric measuring system used for the present experiment is based upon a design by Aspnes and Studna.[12] The basic ellipsometer is a Gaertner model L119 with the additional capability of setting the angle of incidence, ϕ, over a wide range of values from 20° to almost 90° with an accuracy of ±0.01°. The analyzer rotates at an angular speed of 3600 rpm, and a 75 W Xenon short arc lamp is used as a light source. The

*AFWAL/ELRA, Electronics Technology Laboratory, Wright-Patterson AFB, OH 45433-6543
**NASA Lewis Research Center, Cleveland, Ohio 44135
***Universal Energy Systems, 4401 Dayton-Xenia Road, Dayton, Ohio 45432

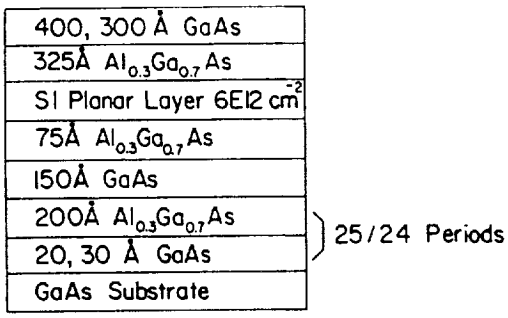

Fig. 1. Superlattice structure for samples #2352, #2207.

output of the arc lamp is passed through a Kratos GM252 monochromator providing a 2500–8500 A spectral range with a typical linewidth of 20 A. The narrow light beam from the monochromator output passes through a polarizer to the sample where it is reflected through a rotating analyzer. A photomultiplier tube (PMT) measures the intensity of the light beam at the output of the analyzer. The PMT output is digitized and collected by a computerized data acquisition system, from which Ψ and Δ are calculated using a Fourier analysis.

The sensitivity of ellipsometric measurements is a strong function of ϕ with maximum sensitivity occurring at the wavelength-dependent, principal (pseudo-Brewster) angle.[11,13] The principal angle can be estimated prior to measurement by modeling the assumed structure for the sample and generating three-dimensional plots of Ψ or Δ vs. wavelength and ϕ. VASE allows measurement at several angles close to the principal angle, as opposed to spectroscopic ellipsometry (SE), in which measurements are made at a fixed, single value of ϕ. For the two samples used in this study, measurements were made at $\phi=75.5°$ and 76.5° (for sample #2207), and at $\phi=76°$ (for sample #2352) which are very near the principal angles over most of the spectral range. The data for these experiments were taken in the 3500 to 8000 A spectral range in increments of 25 A.

The nominal structure of the two measured samples is shown in Fig. 1. The layers were grown by molecular beam epitaxy in a Varian II machine on an undoped liquid encapsulated Czochralski (LEC) GaAs substrate.[13] The substrate was rotated at 7 rpm during deposition with the deposition rates and the Al to Ga ratio calibrated using RHEED intensity oscillations.[8] The superlattice buffer provides a high quality barrier at the quantum well/superlattice interface. The superlattice GaAs wells are nominally 20 A thick for sample #2207 and 30 A thick for sample #2352. The 75 A AlGaAs section is an undoped spacer layer which separates mobile carriers within the 150 A GaAs well from ionized impurities in the 325 A doped AlGaAs layer. A single atomic plane of Si provides "delta" doping for the quantum well, and the 400 A GaAs layer at the top is used as a surface cap.

§3. Modeling

The model used to analyze the VASE data is shown in Fig. 2(a). The optical constants of bulk materials are normally used for the modeling procedure. However, in superlattices the quantum energy subbands, along with the added complexity of wave function overlap, nullifies the use of bulk material properties.[15] Because the optical constants of real superlattices are not independently known, the superlattice was modeled as a single $Al_xGa_{1-x}As$ layer of unknown thickness and composition. A native oxide layer was also incorporated into the model on top of the GaAs cap. Optical constants of $Al_xGa_{1-x}As$ and GaAs were kindly provided by Dr. David Aspnes of Bellcore, Inc., USA.

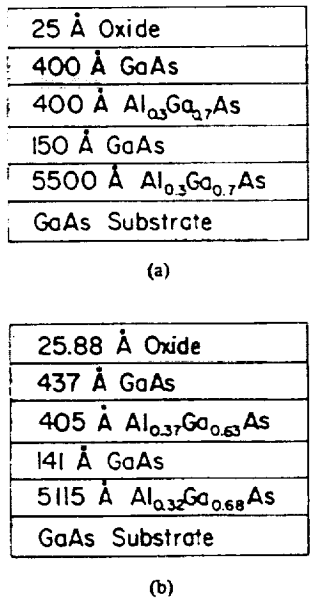

Fig. 2. a) VASE model, and b) final model for sample #2352.

The thicknesses and compositions of the superlattice "equivalent layer" as well as the other layers were solved for in a regression analysis. A Fortran program produces calculated Ψ and Δ values using the model, then minimizes the mean-square (MSE) between the measured and calculated ellipsometric error parameters by using the Marquardt minimization algorithm.[16,17] The MSE is expressed as

$$MSE=1/m\sum_i\{(\Psi_{ci}-\Psi_{ei})^2+(\Delta_{ci}-\Delta_{ei})^2\}^{1/2} \qquad (2)$$

where the subscripts c and e represent the calculated and experimental values respectively and m is the number of measurements. Occasionally the minimization is done with respect to Ψ only, due to the adverse effects on delta values if there is a change in the sense of polarization handedness.

§4. Results

In order to obtain the best possible fits to the experimental data, a number of modeling approaches were utilized. The results of the modeling sequence for both samples are shown in Table I. The initial best fit was over the entire (3500 to 8000 A) spectral range where the MSE was minimized for both Ψ and Δ. Due to the shorter wavelength light being absorbed closer to the surface, the

Table I. Results of VASE and XTEM Analyses (all thicknesses and wavelengths in A).

Sample: #2352								
	t1	t2	t3	x3	t4	t5	x5	MSE
Nominal values	25	400	400	0.30	150	5,500	0.30	—
VASE	26	435	413	0.37	142	5,470	0.32	0.069
90% confidence limits (±)	1	8	16	0.005	10	20	0.001	—
XTEM	460*		420	—	160	5,420	—	—

* combined thickness of layers t1 and t2

Sample: #2207								
	t1	t2	t3	x3	t4	t5	x5	MSE
Nominal values	25	300	400	0.30	150	5,520	0.30	—
VASE	25	286	275	0.35	153	5,115	0.21	0.076
90% confidence limits (±)	2	10	24	0.01	18	37	0.01	—

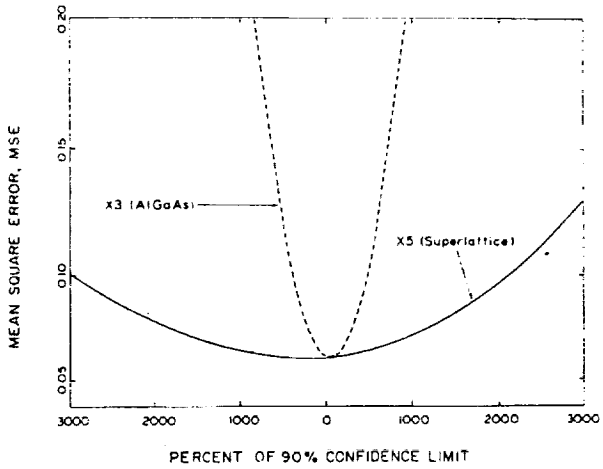

Fig. 3. Mean square error vs. percent of 90% confidence limit added to VASE solution value for the alloy compositions of sample #2352.

analysis range was decreased to 3500–6800 A in order to focus on the layers above the superlattice. Results from the 3500–6800 A analysis were used as input parameters for a Ψ only data analysis over the full spectral range. This ensured that the fitting procedure would be more sensitive to the superlattice parameters. The final model for sample #2352 with corresponding layer thicknesses, composition and MSE is shown in Fig. 2(b). These values are from the Ψ only type data fits shown in Table I. The 90% confidence limits for the final model are also exhibited.

An additional analysis of sample #2352 was conducted using XTEM. The XTEM results (Table I) are in good agreement with those of VASE and serve to verify the accuracy of the VASE layer thickness measurements. The XTEM photograhs showed that the material layers were uniform with abrupt interfaces. A previous study[18] of a less complicated GaAs/AlGaAs system has also demonstrated the concurrence between XTEM and VASE layer thickness determinations.

Of particular importance in the VASE data analysis procedure is ensuring that the MSE (defined by eq. 2) obtained from a set of starting values is the true minimum MSE and not a satellite minimum (defined as a local minimum, but not the lowest minimum). Therefore, the MSE for a variety of starting values were analyzed. The variation of MSE with respect to changes in each particular model variable, keeping all other variables fixed, was obtained for sample #2352. Figure 3 shows changes in MSE for the alloy composition variations as each composition is fixed at a series of values centered near its optimum solved value, and the other composition is fixed at its best fit value. The MSE is presented with respect to the 90% confidence limits of Table I added to or substracted from the VASE "best" solution values. The 90% confidence limit is a statistical measure of the uncertainty of a particular measured parameter. Values for the present experiments are given in Table I. It is evident from the figure that the starting value for a single variable analysis could deviate from the solved value by a factor of approximately 15 times the 90% confidence limit and the best fit MSE would still be realized in the regression analysis. The figure also demonstrates that the 90% confidence limits applied to the VASE solutions lie well within the region for a correct minimum.

Plots of the experimental and calculated VASE data for sample #2352 are shown in Figs. 4(a) and 4(b), and for sample #2207 in Figs. 5(a) and 5(b). A good fit of the calculated data to the general features of the experimental data was obtained. The data are matched particularly well considering that there are seven variables with varying degrees of correlation between them. The good data fits are evidence that replacing the superlattice with an "effective" $Al_xGa_{1-x}As$ layer is a reasonable approach for this specific case, where the AlGaAs barriers are thick when compared to the GaAs quantum well thicknesses.

The broad peaks in the Ψ data at 5800, 6500, 7200 and 7900 A for #2352, and 6000, 6800, and 7500 A for #2207 are mainly the result of optical interference effects from the superlattice region. Spectral features at the shorter wavelengths are dominated by the top layer of GaAs. However, the spectral details at all wavelengths are influenced to some degree by each of the layers; in particular the surface oxide. This is shown by Figs. 6 through 9 which are discussed below.

Figures 6 through 9 were made by fixing the thickness and composition values found from the analysis of sample #2352 and sequentially varying one parameter at a time for a single ϕ. Figures 6 and 7 exhibit how the superlattice effects spectra in the 6000 to 8000 A range. It is apparent from Fig. 6 that increasing the superlattice thickness causes a corresponding increase in the amplitude and a shift to higher wavelengths of the Ψ spectra. However, an increase in the value of superlattice composition is seen to cause an increase in amplitude and decrease in the wavelength shift (Fig. 7). Variation of the thickness of the upper layer of GaAs has a pronounced effect in Ψ between 4400 and 5200 A (Fig. 8), and also causes leveling between maxima and minima at higher wavelengths. Changing the oxide thickness uniformly shifts the amplitude of Ψ over the entire wavelength

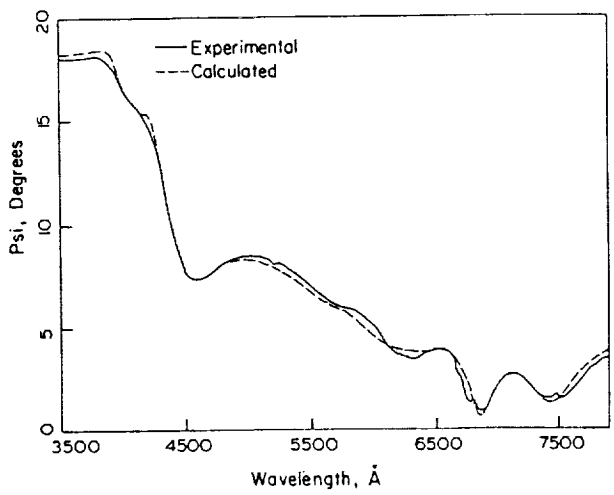

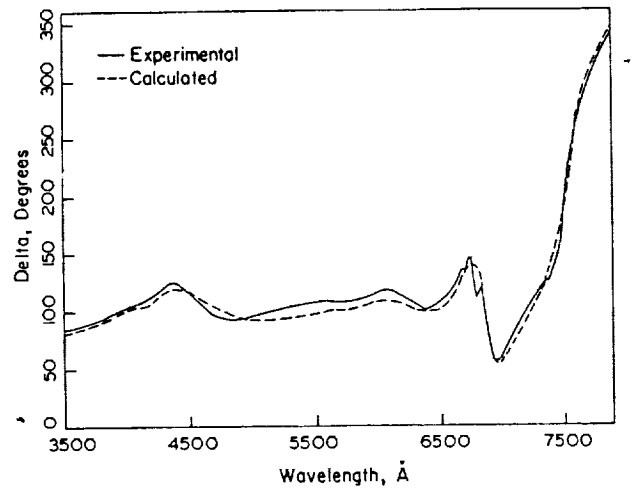

Fig. 4. a) Psi, and b) delta vs. wavelength for sample #2352.

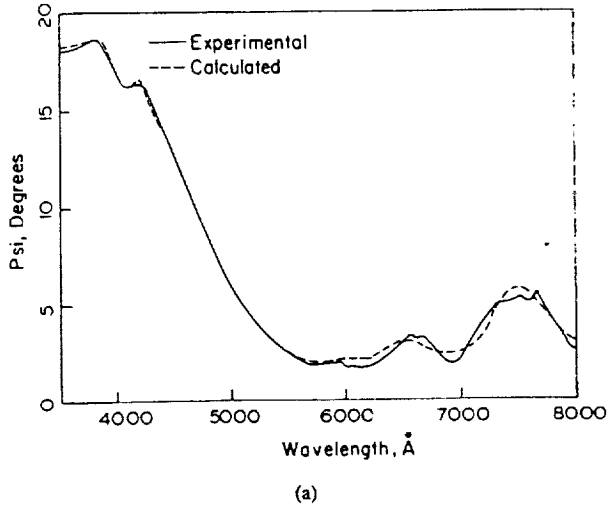

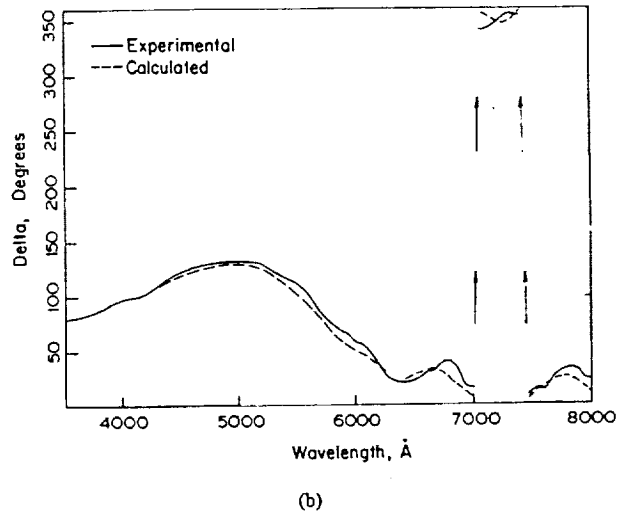

Fig. 5. a) Psi, and b) delta vs. wavelength for sample #2207.

range (Fig. 9).

The growth quality of the superlattice was determined prior to the XTEM analysis by studying interfacial smoothness between layers. In order to appraise roughness, a Bruggeman effective medium approximation was performed on sample #2352 with a 20 A mixture of GaAs and $Al_{0.3}Ga_{0.7}As$ in the model between the 150 A GaAs layer and the superlattice. The solution showed no appreciable change in values for layer thickness of composition. This resulted in an increase in the MSE of only 0.3%, demonstrating that physically there is not a mixture (roughness) layer present. Another modeling trial incorporated an Al_2O_3 layer in between the same layers. This analysis was done to determine if roughness existed due to the burial of oxygen impurities (which are Al composition dependent) in the GaAs portion of the GaAs/AlGaAs interface.[19] The oxide layer solved to less than 2 A with no change in MSE. Thus VASE in addition to XTEM has shown that the superlattice growth quality

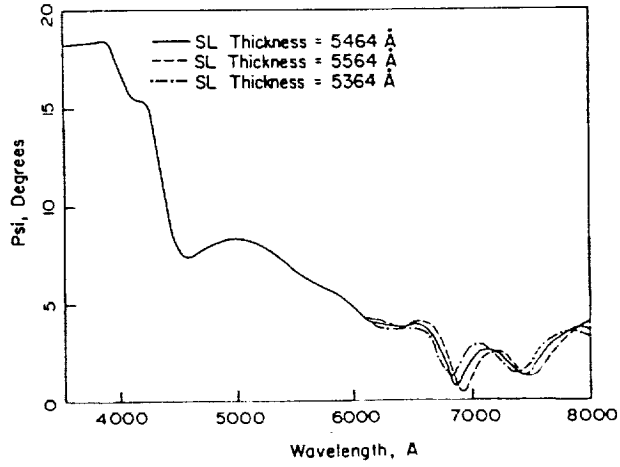

Fig. 6. Generated psi vs. wavelength for sample #2352 with varying superlattice thickness.

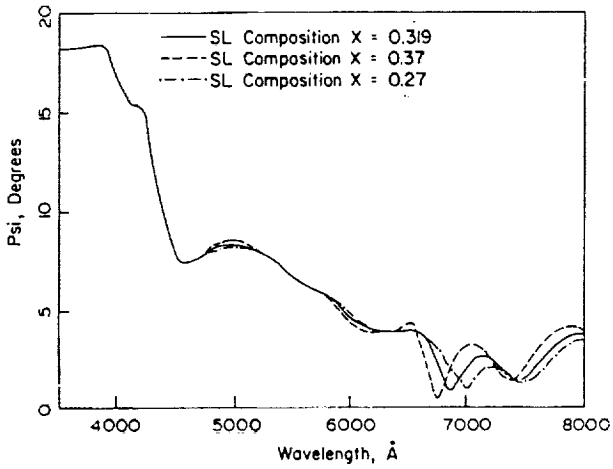

Fig. 7. Generated psi vs. wavelength for sample #2352 with varying superlattice composition.

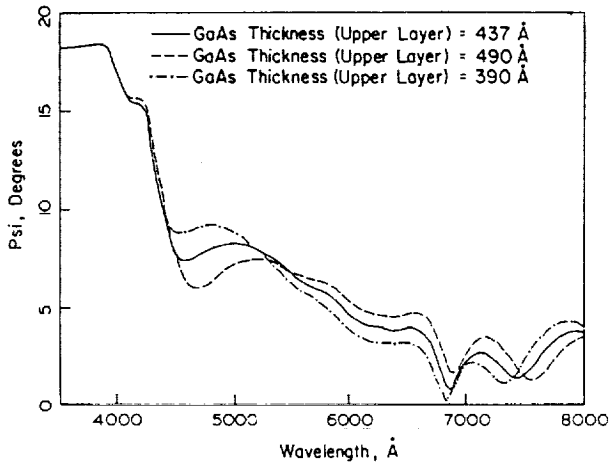

Fig. 8. Generated psi vs. wavelength for sample #2352 with varying thickness of upper GaAs layer.

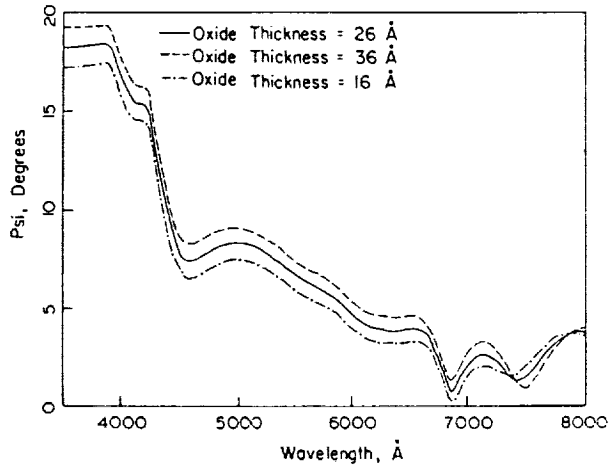

Fig. 9. Generated psi vs. wavelength for sample #2352 with varying surface oxide thickness.

is good since incorporation of a GaAs/AlGaAs mixture or oxide into the regression analysis worsened the fits.

The narrow excitonic structures seen in Fig. 5(a) at 6530 A, 7500 A, and 7700 A, are respectively the second electron to heavy hole, e-hh(2), first electron to light hole, e-lh(1), and first electron to heavy hole, e-hh(1), transitions in the superlattice quantum wells. The exciton energies are in qualitative agreement with values predicted by subtracting the exciton binding energy (9.1 meV in single quantum well GaAs) from the e-hh(1) transition energy of a quantum well with a 30 A well width and a wide $Al_{0.3}Ga_{0.7}$ barrier.[20] This analysis yields: $E_{e\text{-}hh(1)} = 1.582$ (7,840 A). This approach is sufficient due to the barrier width being large in comparison to the well width. It follows that the e-lh(1) and e-hh(2) transitions are the next sharp structure when moving toward higher energies.

The exciton peaks are shown in Fig. 10 for sample #2207 meaasured at 10 A intervals. The presence of the excitonic structure in both samples confirms that the superlattice interfaces are of good quality. The broadness of the excitonic structure can most likely be attributed to slight energy changes in the quantum levels associated with layer thickness variations in the GaAs layers of the superlattice. Also, thermal broadening of approximately 100 A is a factor at room temperature measurements. The exciton lines from levels in the 150 A quantum well are outside of the spectral range shown.

§5. Conclusion

We have found that the superlattices in MODFET/superlattice structures can be effectively incorporated in the VASE modeling sequence by representing the superlattice as a bulk AlGaAs layer of unknown alloy composition. In the future it would be beneficial to make independent measurements of the optical constants of superlattices. This would be an enormous task since each superlattice design would have unique optical properties. Modeling the superlattice as multilayers, each having the bulk GaAs and AlGaAs optical properties, gives poor results. Thus the approach we have taken works

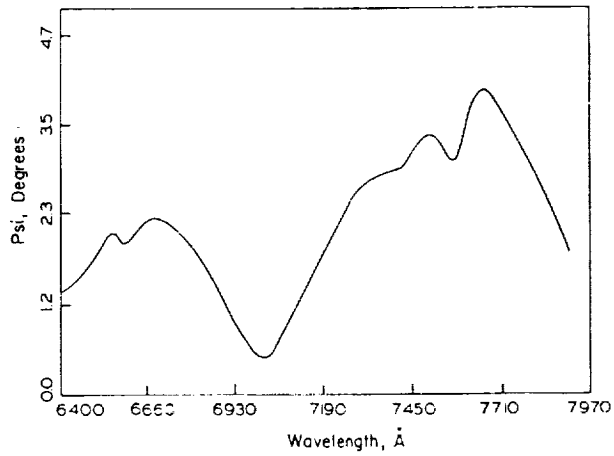

Fig. 10. Excitonic spectra for sample #2207.

reasonably well, and is applicable to any superlattice structure.

Analysis of five layers and two alloy fractions is possible if data are taken near the wavelength dependent pseudo-Brewster angle. Room temperature excitonic effects as well as growth quality determination are realized using the VASE measurement process. Thus the analysis of these structures through VASE can provide an accurate and nondestructive assistance in the production of semiconductor structures for optoelectronic and microwave communication devices.

Acknowledgements

This research was supported by NASA Lewis Research Center grant NAG3-154. The authors would like to thank D. C. Radulescu and L. F. Eastman of Cornell University for providing the samples.

We would also like to thank Dr. David Aspnes for supplying accurate values for the optical dielectric response function vs. photon energy for GaAs and $Al_xGa_{1-x}As$.

References

1) T. J. Drummond, W. T. Masselink and H. Morkoc: Proc. IEEE 74 (1986) 773.
2) O. J. Glembocki, F. H. Pollak and J. J. Song: Proc. of SPIE Vol. 794, see especially invited paper by K. K. Bajaj and D. C. Reynolds on p.2 (1987).
3) Mater. Res. Soc. Symp. Proc. 77 (1987) 755.
4) P. G. Snyder, J. E. Oh, J. A. Woollam and R. E. Owens: Appl. Phys. Lett. 51 (1987) 770.
5) P. G. Snyder, J. E. Oh and J. A. Woollam: Mater. Res. Soc. Proc. 77 (1987) 761.
6) P. G. Snyder, B. N. De, K. G. Merkel, J. A. Woollam, D. W. Langer, C. E. Stutz, R. Jones, A. K. Rai and K. Evans: Superlattices & Microstructures 4 (1988) No. 1, 97.
7) M. Erman, J. B. Theeten, N. Vodjdani and Y. Demay: J. Vac. Sci. & Technol. B1 (1983) 328.
8) S. A. Alterovitz, P. G. Snyder, K. G. Merkel, J. A. Woollam, D. C. Radulescu and L. F. Eastman: J. Appl. Phys. 63 (1988) 5081.
9) H. Burkhard, H. W. Dinges and E. Kuphal: J. Appl. Phys. 53 (1982) 655.
10) D.S. Chemla: *Proc. of Basic Properties of Optical Materials*, ed. A. Feldman (NBS Publication 697, 1985) p. 202.
11) R. M. A. Azzam and N.M. Bashara: *Ellipsometry and Polarized Light* (North-Holland Publishing, New York, N.Y., 1977).
12) D. E. Aspnes and A. A. Studna: Appl. Opt. 14 (1975) 220.
13) P. G. Snyder, M. C. Rost, G. H. Bu-Abbud, J. A. Woollam and S. A. Alterovitz: J. Appl. Phys. 60 (1986) 3293.
14) D. C. Radulescu, G. W. Wicks, W. J. Schaff, A. R. Calawa and L. F. Eastman: J. Appl. Phys. 62 (1987) 954.
15) J. N. Schulman and Y. C. Chang: Phys. Rev. B31 (1985) 2056.
16) D. W. Marquardt: J. Soc. Indus. Appl. Math. 11 (1963) 431.
17) G. H. Bu-Abbud, N. M. Bashara and J. A. Woollam: Thin Solid Films 138 (1986) 27.
18) J. A. Woollam, P. G. Snyder, A. W. McCormick, A. K. Rai, D. C. Ingram, P. P. Pronko and J. J. Geddes: Mater. Res. Soc. Symp. Proc. 77 (1987) 755.
19) T. Achtwich, G. Burri, M. A. Py and M. Ileyems: Appl. Phys. Lett. 50 (1987) 1730.
20) R. L. Greene and K. K. Bajaj: Solid State Commun. 45 (1983) 831.

DIAMONDLIKE CARBON AS A MOISTURE BARRIER AND ANTIREFLECTING COATING ON OPTICAL MATERIALS†

JOHN A. WOOLLAM*, BHOLA N. DE*, AND L. Y. CHEN*
JOHN J. POUCH** AND SAMUEL A. ALTEROVITZ**
*Department of Electrical Engineering, University of Nebraska, Lincoln, NE 68588-0511
**NASA Lewis Research Center, Cleveland, OH 44135

INTRODUCTION

Diamondlike carbon (DLC) is amorphous, hard, semitransparent, and is under consideration for use as a coating material for infrared optics [1] . DLC is also designated as a-C:H to indicate its amorphous nature as well as to indicate the presence of large (20 to 55 percent) amounts of hydrogen in the film.

Two important questions arise with respect to use of DLC in infrared optics. DLC is amorphous, and will the lack of grain boundaries help to keep moisture from penetrating the film? Secondly, application as an antireflecting coating places restrictions on the allowed values of the index of refraction of the film relative to the particular substrate material being used. Will DLC have the correct index range? These two questions are addressed in this paper.

MOISTURE PROTECTION STUDIES

It is very difficult to measure penetration of moisture into thin films. Common surface analysis techniques such as AUGER, and SIMS require ultrahigh vacuum, and therefore can't be used.

We have shown that variable angle spectroscopic ellipsometry (VASE) can be used to determine the thickness of ultrasmall amounts of water on, and in a thin film. This spectroscopy is not commonly known, so a brief description is given [2], [3].

Ellipsometry determines the complex reflection coefficient

$$\rho \equiv R_p/R_s = \tan\psi \exp j\Delta \qquad (1)$$

where R_p and R_s are the complex Fresnel reflection coefficients for components of light parallel (p) and perpendicular (s) to the plane of incidence of the incident and reflected light. Our VASE data were taken from 300 to 850 nm with light incident at an angle ϕ to the normal to the sample. The reflected light polarization state was analyzed with a rotating polarizer. Light intensity was measured with a photomultiplier tube, and the signal digitized, and Fourier analyzed to determine the ψ and Δ parameters of equation 1.

†Research supported by the U.S. Army Materials Technology Laboratory, Contract No. DAAL04-86-C-0030, by NASA Lewis Grant NAG-3-154, and by Control Data Corporation.

Mat. Res. Soc. Symp. Proc. Vol. 152. ©1989 Materials Research Society

The measured complex ratio $\tilde{\rho}$ is related to the optical index of refraction, n, and extinction coefficient, k, of the material under study. If complex materials structures are involved then n and k can be determined for individual layers, and layer thicknesses determined.

Microstructural analysis is performed assuming the nature of the sample under study. For the present samples the model shown is Fig. 1. The t_i are layer thicknesses, and f_2 is the fraction of DLC in a DLC plus H_2O Bruggeman effective medium approximation (EMA) mixture layer. The procedure is to calculate $\tilde{\rho}$ using the Fresnel reflection coefficients for a multilayer parallel stack (and EMA mixed layers), for a given initial set of values for thicknesses and fractions. Next, a regression analysis is performed to minimize the error function (MSE) defined by

$$MSE = \frac{1}{N}\sum_{i=1}^{N} (\psi_i^{exp} - \psi_i^{calc})^2 + (\Delta_i^{exp} - \Delta_i^{calc})^2 \qquad (2)$$

The general set of materials parameters such as dielectric constants, layer thicknesses, and composition fractions giving the minimum MSE are then found. In the present experiments thicknesses and moisture fractions are found.

The films of DLC used for moisture penetration studies were prepared using a 30kHz parallel-plate plasma deposition system. Pure methane at a chamber pressure of 20 microns was used. Power levels of 100, 200, and 300 watts were used, but results for 200 watt are reported here.

Moisture was introduced to the films in two ways; from immersion in 23°C water, and from a steam jet at 100°C.

Example ellipsometric data are shown in Figure 2. The data at 0 hours after H_2O indicate that water was introduced, then the bulk of it allowed to run off a vertical surface. At this time the maximum amount of water remained, and the Δ parameter was lowest. Twenty four hours later some water had evaporated, and Δ increased. After exposure to a heat lamp much of the water on the surface was evaporated (but not all!). After exposure to the laboratory 23°C atmosphere a small amount of moisture from the ambient air deposited, with an associated decrease in Δ .

Using regression analysis of ellipsometric data for this sample, and a two-layer (t_2 = 0 in Fig. 1) model in our ellipsometric analysis, we determined that the water layer was 66-Å thick on top of a 344-Å thick DLC film. The three-layer (t_1, t_2, t_3, in Fig. 1) analysis was consistent with this result: 330 Å of DLC, 29 Å of 50%-50% mixture of DLC and water, and 48 Å of pure water on top.

This type of analysis was performed on a large number of samples, with the same final result: DLC films were not penetrated by water [4] . The DLC surfaces had small amounts of roughness, and moisture was found to penetrate the valleys of this roughness but not further.

ANTIREFLECTION CONDITIONS USING DLC

Substrates on which we deposited DLC included: lexan, silicon, fused silica, KG-3 glass, BK-7 glass, ZnS, GaAs, Ge, and heavy metal fluoride glass. It was desired to know if DLC could be deposited to the proper thicknesses and with the correct indices of refraction for use as an antireflecting coating on each of these substrates.

Antireflecting coatings provide an important method of and enhancing transmission through optical window materials [5].

The reflectivity has a minimum when

$$n_1 d_1 = \lambda_o/4 \qquad (3)$$

where n_1 is the index of refraction of the coating, and d_1 its thickness. The

reflectivity minimum is at its lowest value (zero) when

$$n_1^2 = n_o n_2$$

where n_o is the index for the ambient, which is normally air, so

$$n_1 = \sqrt{n_2} \qquad (4)$$

is required, where n_2 is the index of the substrate at the wavelength of interest.

Table I lists infrared transmitting substrates, their indexes of refraction, the operating wavelengths of interest, and the required DLC thickness and optical index of refraction. The proper index came from use of Eq. 4, and the proper thickness from Eq. 3.

What is noticed immediately from Table I is that the required film index of refraction ranges from 1.2 to 2.8 for the examples listed.

The index of refraction of DLC can be controlled by choosing the proper deposition technique and parameters [1]. The range typically found is for

$$1.6 \leq n_1 \leq 2.3$$

which makes the optimum matching substrates have indices from

$$2.5 \leq n_2 \leq 5.3$$

These values are much higher than the indexes for the glasses under consideration (Table I), but results in a decent match for ZnS, diamond, Ti_2O_2, As_2S_3 glass, Se glass, and results in good matches for Si, Ge, GaAs, and InSb. All are common infrared transmitting materials [6].

The effect of index match or missmatch on reflectance near the antireflecting condition is seen in Figs. 3 and 4 for the substrates indicated.

DISCUSSION AND CONCLUSIONS

We were able, with extreme care in surface preparation, to get DLC to adhere to lexan, silicon, fused silica, KG-3 glass, BK-7 glass, ZnS, GaAs, Ge, and heavy metal fluoride glass. The most difficult adherence problem was with ZnS, for which we were unable to deposit the required thicknes for antireflection (Table I).

Table I Candidate Substrates, and Conditions for Antireflection

Operating Substrate	Index at Wavelength	Operating Wavelength	Required DLC: Thickness	Index
ZnS	2.2	4 micron	676nm	1.48
Fused Silica	1.46	550nm	114nm	1.21
KG3 Glass	1.5	1.06 micron	217nm	1.22
BK7 Glass	1.52	550nm	90nm	1.23
Heavy Metal Fluoride	1.45	4 micron	833nm	1.20
Lexan	1.4	550nm	113nm	1.22
Silicon	3.42	10 micron	1351nm	1.85
GaAs	3.5	4 micron	535nm	1.87
Ge	4.0	4 micron	500nm	2.0
InSb	3.9	10 micron	1269nm	1.97

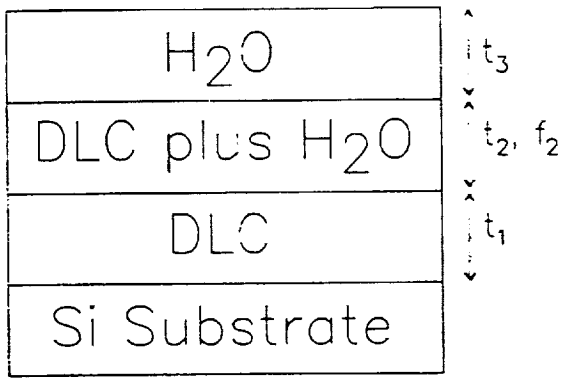

Fig. 1 Model structure assumed.

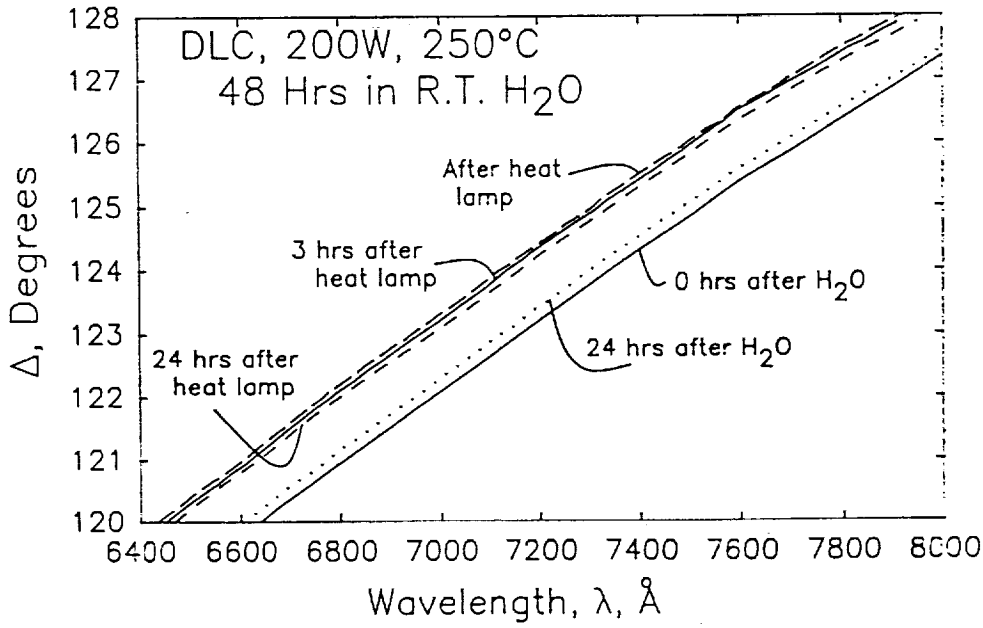

Fig. 2 Change in parameter Δ with moisture changes.

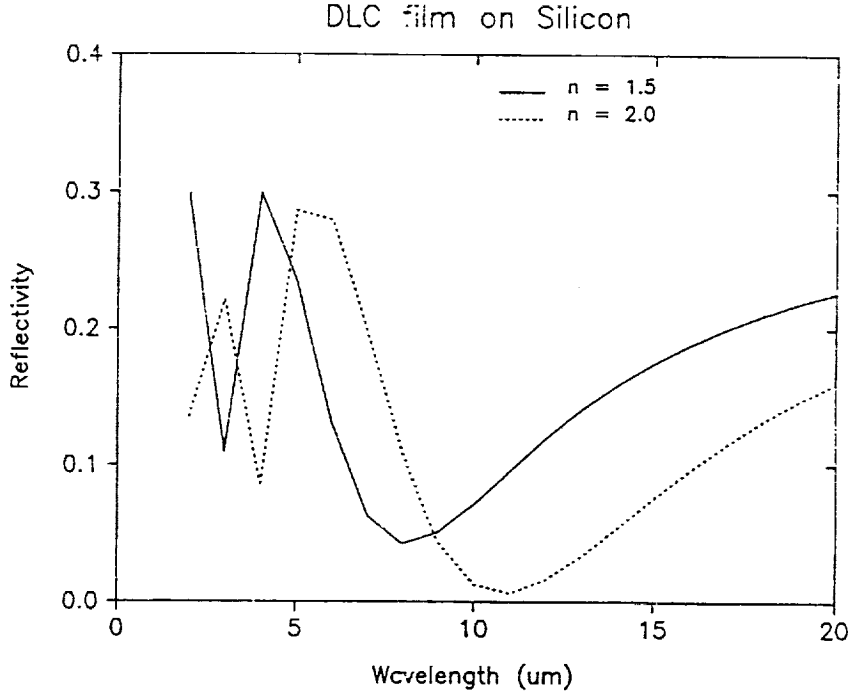

Fig. 3 DLC as an AR coating on Si.

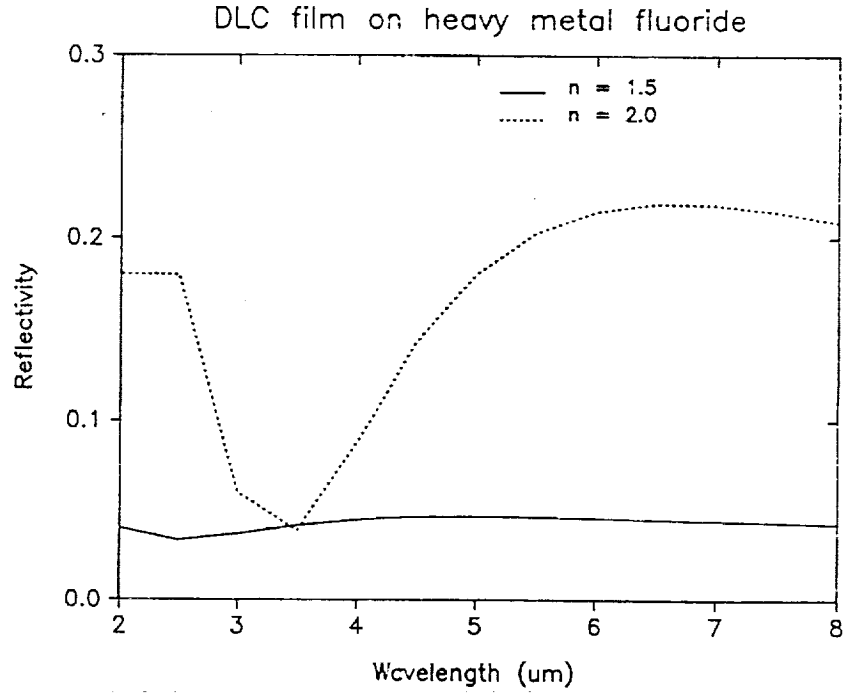

Fig. 4 DLC as an AR coating on heavy metal fluoride glass.

In conclusion, we find that DLC is an effective moisture barrier for use on infrared optics, and with the exception of ZnS we were able to directly deposit DLC on the chosen substrates to the desired thicknesses for antireflection. The indexes of refraction were measured from 300 nm to 10 microns, and found to be in the range from 1.6 to 2.0. Other workers have prepared DLC samples with indices up to 2.3. Thus, we have established a range of conditions for use of DLC as an antireflecting coating. Zero reflectance can be achieved on substrates of Si, Ge, GaAs, and InSb. Low reflectance can be achieved on ZnS, diamond, T_iO_2, As_2S_3 glass, Se glass; but DLC will not be a good antireflecting coating on the common glasses with index near 1.5.

References

[1] J. C. Angus, P. Koidl, and S. Dormitz, in Plasma Deposited Thin Films, edited by J. Mort and F. Jansen (CRC, Boca Raton, FL, 1986), Chapter 4.

[2] J. A. Woollam, P. G. Snyder, and M. C. Rost, Thin Solid Films 166, 317 (1988).

[3] J. A. Woollam, P. G. Snyder, and M. C. Rost, Mat. Res. Soc. Symp. Proc. 93, 203 (1987).

[4] S. Orzeszko, B. N. De, J. A. Woollam, J. J. Pouch, S. A. Alterovitz, and D. C. Ingram, J. Appl. Phys. 64, 4175 (1988).

[5] H. J. Hovel, "Solar Cells', in Semiconductors and Semimetals, Vol. 11, edited by. R. K. Willardson, and A. C. Beer, Academic Press, New York, 1975, page 203.

[6] The Intrared Handbook, edited by W. L. Wolfe and G. J. Zissis, The Infrared Information and Analysis Center, Environmental Research Institute of Michigan, Ann Arbor, MI, 1978.

N91-18303

Thin Film Characterization Using Spectroscopic Ellipsometry

Samuel A. Alterovitz

NASA Lewis Research Center
21000 Brookpark Road
Cleveland, OH 44135

INTRODUCTION

Thin films are widely used in the semiconductor industry. Dielectric, metallic and epitaxially grown semiconducting films, are the building blocks of modern electronics. The versatile, non destructive optical method of ellipsometry is particularly suited for characterization of these thin films. In this paper we will discuss the application of the multiple angle and wavelength (MAW) technique to measure the dielectric function of the film. This technique evaluates unabiguously the complex dielectric function $\epsilon(E)$ of the film without any pre assumtions. For other techniques, a priori knowledge of one or more of the following is required to find $\epsilon(E)$: film components, thickness, functional form of the dielectric function and/or use of the Kramers-Kronig relation. In some cases the effective medium approximation (EMA) was used to determine the volume fraction of the film components. Application of the MAW technique to several semiconducting films was published previously (1). In the following different applications and examples will be given, including metal and insulator films.

EXPERIMENTAL

A rotating analyzer ellipsometer with variable angle of incidence capability was used as described in reference (2). The system is controlled by a 286 type PC computer which also performed the analysis for each sample. The spectral range of 3500-7300Å at 5 angles of incidence was used.In most cases, data was taken in 100Å intervals. The ellipsometric parameters psi and delta were obtained using a Fourier transform. The inversion process is based on the MAW analysis least squares technique (3-5). In most cases, the substrate optical properties were known, and a simple substrate-film-ambient model was used. The inversion process gave the complex dielectric constant at every wavelength measured, and the films thickness.

In many applications, the EMA technique, with its small number of parameters, was a better choice. However, the EMA cannot be used for a film with unknown components, or for a material with no published $\epsilon(E)$ data.

RESULTS

Several type of samples were tested, to cover a variety of cases, including metal film on metal substrate, insulator film on metal, semiconductor on semiconductor and insulator on semiconductor.

A sputtered aluminum film was analyzed in terms of Al_2O_3 on Al. The optical properties of these and all subsequent materials were taken from reference (6). The EMA analysis show that the sputtered Al is really only 70% pure Al with the remainder being voids or Al_2O_3. The top Al_2O_3 layer thickness is of order 20Å. A thin (<20Å) Mo film on stainless steel was measured and analyzed using MAW. Results for the thickness (15Å) are reliable, but the dielectric function does not produce the published Mo results. Two films produced in an attempt to deposit a Ga_2S_3 layer on GaAs during a chemical vapor deposition growth were measured and analyzed. The thickness of the layers were of order 100Å. The dielectric function of the unknown top layer on GaAs was calculated using MAW. The shape of the function was found to be similar to that of GaAs, but included a change in amplitude. We tried EMA, using GaAs and an insulator as components. The final result shown that 89% of the volume is GaAs.

Other examples, including BN films on semiconducting substrates, epitaxial semiconducting films of SiC on Si and III-V on III-V will be given.

ACKNOWLEDGEMENT

I would like to thank the following NASA scientists: Dr. S. V. Pepper for the metal films, Dr. G. A. Landis for the Ga_2S_3 films, Mr. J. A. Powell for the SiC films, I would also like to thank Dr. W. D. Halverson from Spire Corporation for the BN films and Dr. L. P. Erickson from Perkin Elmer Corporation for the AlGaAs on GaAs films.

REFERENCES

1. S. A. Alterovitz, J. A. Woollam and P. G. Snyder, Sol. State Technol. 31 (3), 99 (1988).

2. S. A. Alterovitz, R. M. Sieg, N. S. Shoemaker and J. J. Pouch, MRS Symp. Proc. - to be published.

3. G. H. Bu-Abbud, S. A. Alterovitz, N. M. Bashara and J. A. Woollam, J. Vac. Sic. Technol. A1, 619 (1983).

4. S. A. Alterovitz, G. H. Bu-Abbud, J. A. Woollam and D. C. Liu, J. Appl. Phys. 54, 1559 (1983).

5. G. H. Bu-Abbud, N. M. Bashara and J. A. Woollam, Thin Solid Films 138, 27 (1988).

6. Edward D. Palik, Handbook of Optical Constants of Solids, Academic Press Inc., (1985).

Reprinted with permission of the Electrochemical Society. This paper was originally presented at the 1989 Fall meeting of the Electrochemical Society held in Hollywood, Florida.

N91-18304

Ellipsometric Study of Cubic SiC

S.A. Alterovitz, N.S. Shoemaker, and J.A. Powell

NASA Lewis Research Center, Cleveland, OH 44135, USA

Variable angle spectroscopic ellipsometry (VASE) has been applied to cubic SiC. This technique gives absolute values of the refractive index (n) and the extinction coefficient (k) of a substrate and/or a thin film of an unknown material. The samples were grown by chemical vapor deposition (CVD) on p-type silicon. The substrate was aligned either on the (001) axis or 1° off (001). Several growth temperatures and growth durations were used. The samples were divided into two groups: (a) thick films, of order 10 μm, grown near optimal conditions of temperature, flow and gas ratios; (b) thin films, of order 100Å, grown at various temperatures.

The ellipsometric results for samples in group (a) were analyzed using a two-phase model (substrate and ambient). Results show that for wavelengths in the visible, the refractive index of these CVD samples is equal to that reported for single crystal cubic SiC, within the experimental error, which is on the order of 1%. However, the extinction coefficient has a relatively large value, even above the band gap. The absorption is sample dependent and has a broad peak in the visible. The results for samples in group (b) were analyzed using a three-phase model (substrate, film and ambient). The dielectric functions of the film, deducted from the measured n and k, were further analyzed using the effective medium approximation. The results show that the films contain 30-40 vol.% amorphous silicon, i.e. silicon with only short-range order.

Springer Proceedings in Physics, Vol. 43
Amorphous and Crystalline Silicon Carbide and Related Materials II
Editors: M.M. Rahman · C.Y.-W. Yang · G.L. Harris

OPTICAL DISPERSION RELATIONS FOR "DIAMONDLIKE" CARBON FILMS

Samuel A. Alterovitz*, Robert M. Sieg†, Neil S. Shoemaker‡, and John J. Pouch*
*NASA Lewis Research Center, Cleveland, Ohio 44135
†Undergraduate Student Intern at NASA Lewis Research Center from Cleveland State University, Dept. of Electrical Engineering, Cleveland, Ohio 44106
‡Undergraduate Student Intern at NASA Lewis Research Center from Case Western Reserve University, Physics Dept., Cleveland, Ohio 44115

ABSTRACT

Ellipsometric measurements on plasma deposited "diamondlike" amorphous carbon (a-C:H) films were taken in the visible, (E = 1.75 to 3.5 eV). The films were deposited on Si and their properties were varied using high temperature (up to 750 °C) anneals. The real (n) and imaginary (k) parts of the complex index of refraction N were obtained simultaneously. Following the theory of Forouhi and Bloomer (Phys. Rev. B34, 7018 (1986)), a least squares fit was used to find the dispersion relations n(E) and k(E). Reasonably good fits were obtained, showing that the theory can be used for a-C:H films. Morever, the value of the energy gap Eg obtained in this way was compared to the Eg value using conventional Tauc plots and reasonably good agreement was obtained.

INTRODUCTION

The optical energy band gap of amorphous materials is usually found using a Tauc plot [1], i.e., an extrapolation of $(\alpha nE)^{1/2}$ versus E. Here α is the optical absorption coefficient, n is the refractive index and E is the energy. In many cases, the refractive index is almost constant or is unavailable, and $(\alpha E)^{1/2}$ versus E is used (simplified Tauc). There are several drawbacks to the Tauc theory and procedure. First, the theory relates to absorption only, and cannot give the refractive index through the Kramers-Kronig relation [2]. Second, there is ambiguity on the energy range that the Tauc extrapolation is correct. Below a certain value of α, the absorption falls exponentially. This regime is called the Urbach edge [1]. The onset for this regime varies and values of order $\alpha = 10^3$ cm^{-1} [1] up to $\alpha = 10^4$ cm^{-1} [3] have been used. Empirically, many Tauc plots also start to deviate from a straight line at high α values [4,5].

Recently, an extension of the theory of optical absorption has been published for amorphous materials [2]. Later, the theory was extended to include more than one critical point, and was applied to crystalline semiconductors [6]. In the Tauc plot derivation [1], the main assumptions are a constant matrix element and parabolic density of states for both the valence and the conduction bands. However, if the excited state has a finite lifetime τ, the absorption probability has a damping factor [2] and Tauc plots are theoretically incorrect. The extinction coefficient k ($k = \alpha c\hbar/2E$ where E is the energy) is calculated in [2,6] using the lifetime concept, obtaining.

$$k(E) = \frac{A(E - E_g)^2}{E^2 - BE + C} \qquad (1)$$

Here A is $k(\infty)$ and is proportional to M^2/τ where M is the position matrix element ($M = \langle f|x|i\rangle$); $B = 2(E_{c,crit} - E_{v,crit})$, where $E_{c,crit}$ and $E_{v,crit}$ are energies in the conduction and valence band respectively corresponding to a critical point, i.e., where $k(E_{c,crit} - E_{v,crit})$ is a maximum. C is related to the lifetime τ through $\hbar/\tau = (4C - B^2)^{1/2}$ and

Mat. Res. Soc. Symp. Proc. Vol. 152. ©1989 Materials Research Society

$Eg = E_{c,bottom} - E_{v,top}$, i.e., the optical bandgap. Using the Kramers-Kronig relation, the refractive index was obtained [2]:

$$n(k) = n(\infty) + \frac{B_o E + C_o}{E^2 - BE + C} \qquad (2)$$

Here B_o and C_o are related to A,B and C through simple algebraic formulas, and $n(\infty)$ is a constant.

In this paper we will examine if this new result applies to "diamond-like" carbon, also denoted a-C:H (amorphous hydrogenated carbon). If applicable, the result can give the n(E) function from a known absorption spectrum k(E) and a single refractive index measurement. Also, the functions n(E) and/or k(E) can be used when their analytical form is required, e.g., optimizing antireflection filters. In addition, this paper will discuss the meaning of the experimental constants, A,B, C, and Eg.

Amorphous hydrogenated carbon material is made almost exclusively in form of thin films. The natural choice for an experimental technique is ellipsometry. The multiple angle of incidence, multiple wavelengths (MAW) technique [7 to 9] was used. MAW gives n and k of the film simultaneously at all wavelengths measured, without the use of either a known dispersion relation or application of the Kramers-Kronig analysis. This technique was commonly used to analyze various semiconductor multilayer structures [10,11] when n and k of the constituents were known. Here, the MAW technique is used in a spectroscopic way, to measure unknown n(E) and k(E). The smallest value of k that is accurately determined by ellipsometry is of order 0.005, corresponding to $\alpha \cong 1000\ cm^{-1}$ in the visible. Thus, the Urbach edge regime is almost eliminated from this work. Reflection ellipsometry has the added benefit of measuring the thin film samples on any substrate, in contrast to transmission experiments. As the optical energy bandgap Eg depends on the substrate material [5], possibly due to differences in conductivity, this advantage of ellipsometry can be crucial for actual applications.

EXPERIMENTAL

Samples were prepared on 3 in. diameter Si substrates using a 30 kHz plasma deposition unit. The power P used was in the range 50 to 200 W, with a constant flow rate of $7 \times 10^{-5}\ m^3/min$. Details of the growth chamber are given in [12]. Several samples cut from the 150 W wafer were annealed in nitrogen for 10 sec using a rapid thermal anneal module [5]. The rotating analyzer ellipsometer set-up [13] is essentially similar to the one described in [10]. At each angle of incidence, data was taken in the wavelength range 3500 to 7300 Å, with 100 Å intervals. Five angles of incidence were used, usually in the range 55° to 75°. Each measurement consisted of 100 rev, with 72 points per rev, taken at a rate of ~50 rev/sec. Background subtraction was done at each point. Calibration of the absolute value of the ellipsometric parameters ψ and Δ was done using [14]. The double grating monchromator was controlled by a IBM-AT personal computer that was also used for all data acquistion and analysis. ψ and Δ were obtained by Fourier analysis. The MAW inversion process was done by minimizing experimental ψ and Δ (or $\tan\psi$ and $\cos\Delta$) versus their calculated values [9]. The model used included only the substrate and a homogeneous film. This is a reasonable approximation, as the interface of a-C:H on Si includes only the native oxide and ~5 Å SiC_x [15], and our films were above 1000 Å thick.

RESULTS

Seven samples were measured. Simplified and regular Tauc plots were done for all samples. A representative plot (50 W sample) is given in

Fig. 1, showing a slightly concave result versus the theory. As the annealing temperature and/or deposition power rises, the experimental Tauc function first becomes a straight line and later turns convex. We kept the extrapolation range to the linear part of the experimental function. A summary of the energy bandgaps obtained from regular and simplified Tauc plots, together with sample thicknesses t, are given in Table I. Results of n(E) and k(E) for the 50 and 150 W, 600 °C samples are given in Figs 2 and 3 respectively. Figure 2 shows a rising n versus E while Fig. 3 show a decreasing n(E). All other samples have an interim type of behavior. Grid least square fits to Eq. (1) were done to obtain A,B,C and Eg simultaneously. With these 4 parameters fixed, the value of $n(\infty)$ was set to get the best n(E) fits. The solid lines in Figs. 2 and 3 were calculated using these parameters. Results for all samples are given in Table II, while Eg is also displayed in Table I.

TABLE I a-C:H OPTICAL ENERGY GAPS IN eV

P, W	T,°C	t, A	Sqrt(αE)	Sqrt(αEn)	Grid
50	-	1490	1.90	1.90	1.64
100	-	2305	2.65	2.65	2.70
150	-	2810	2.36	2.36	2.23
200	-	2960	2.02	2.02	1.65
150	400	2560	2.05	2.06	1.90
150	600	1320	1.08	0.89	1.03
150	750	950	0.57	0.39	0.39

TABLE II DISPERSION RELATION PARAMETERS FOR a-C:H FILMS

P, W	T, C	A	B, eV	C, $(eV)^2$	Eg, eV	$n(\infty)$
50	-	.06	6.39	12.67	1.64	1.63
100	-	.01	6.46	10.51	2.70	1.70
150	-	.05	5.90	9.75	2.23	1.67
200	-	.11	5.99	11.73	1.65	1.69
150	400	.06	5.10	7.20	1.90	1.70
150	600	.40	3.66	4.22	1.03	1.58
150	750	.85	1.21	1.85	0.39	1.71

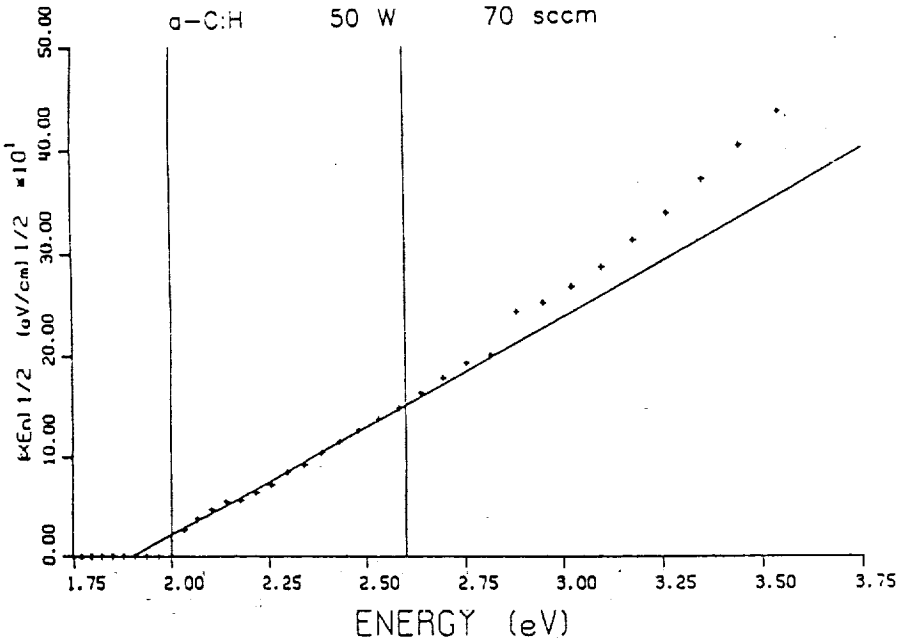

FIGURE 1. TAUC PLOT FOR THE 50 W SAMPLE. VERTICAL LINES SHOW THE FITTING RANGE.

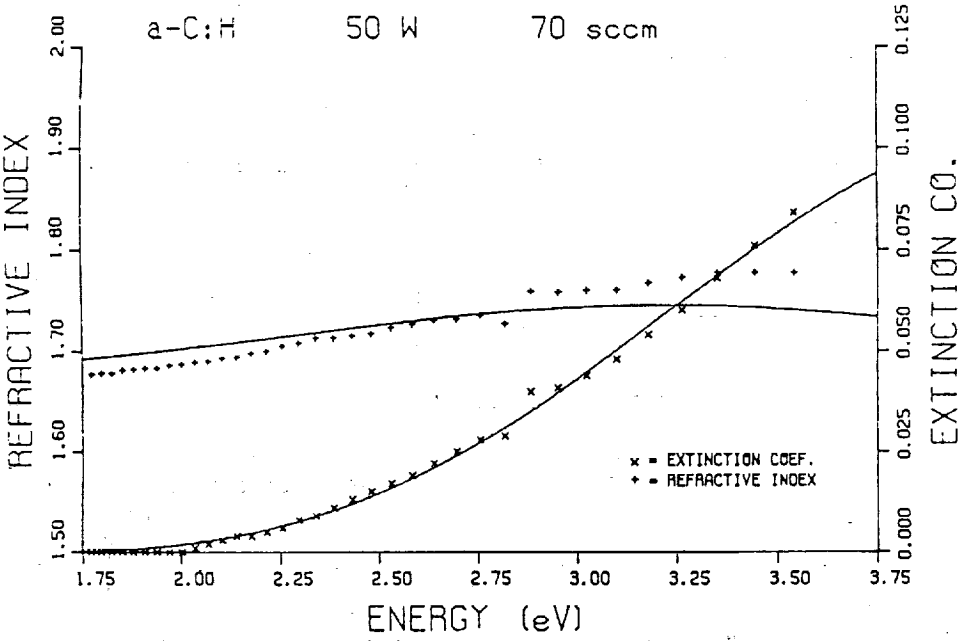

FIGURE 2. REFRACTIVE INDEX AND EXTINCTION COEFFICIENT OF THE 50 W SAMPLE. SOLID LINES ARE DUE TO EQUATIONS (1) AND (2).

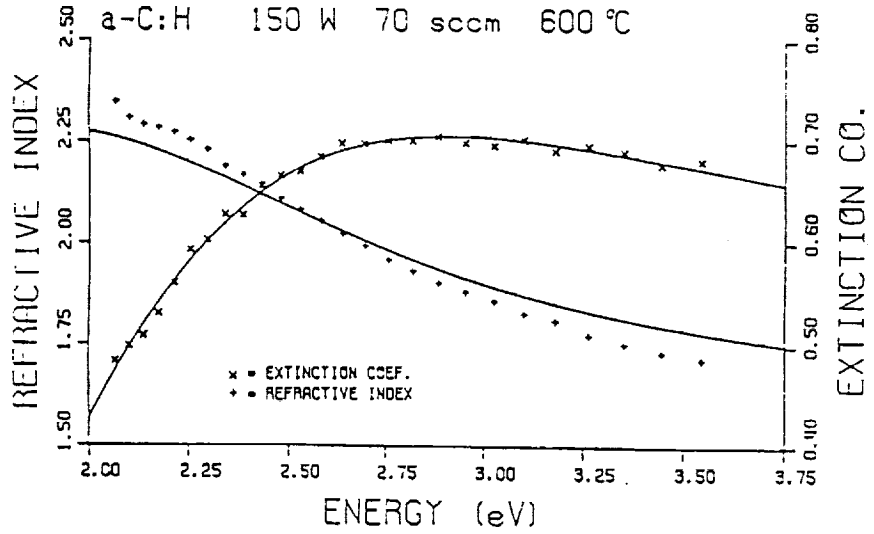

FIGURE 3. REFRACTIVE INDEX AND EXTINCTION COEFFICIENT OF THE 150 W, 600 °C SAMPLE. SOLID LINES ARE DUE TO EQUATIONS (1) AND (2).

DISCUSSION

Optical energy bandgaps Eg found using the two Tauc procedures are identical. However, Eg found using the dispersion relation fits are almost always smaller than the Tauc plots, although the differences are not very large. It is impossible to rule which bandgap is the "correct" one. The dispersion relation functions do take into account, at least qualitatively, the existence of absorption at lower energy than the regular Tauc regime, the Urbach tail. This can be seen by the very small slope of k(E) near Eg, as shown in Fig. 2. However, $\alpha(E)$ is expected to be purely exponential in the Urbach edge [1]. Thus, theoretically, the dispersion relations do not describe this regime. Table I also shows a decrease in Eg with increasing deposition power, (except the 50 W sample) and with increasing annealing temperature, in agreement with prior results [4,5]. The thickness increases with power [16] and decreases with annealing temperature.

The quality of the fits shown in Figs. 2 and 3 is quite good. The n(E) fits are the real test of the theory and the figures show a reasonable agreement between experiment and calculation. All other n(E) experimental curves show an equal or better fit to theory, as they include almost constant n(E) values. In addition, the k(E) fit is definitely better than the Tauc fits.

The value of the A,B,C parameters, as shown in Table II, are essentially constant as function of deposition power, but they change significantly versus annealing temperature. The value of the lifetime $\hbar/\tau$, deduced from $(4C - B^2)^{1/2}$, has quite an amount of scatter. However, all results are around $\hbar/\tau \cong 2$ eV. This is a large value, but it is comparable with other amorphous materials [2]. The values of A are in general lower than for other materials [2], denoting a smaller position matrix element M in a-C:H. There is an order of magnitude increase in M with heating to 750 °C. It would be interesting to correlate this increase with the changes in the composition and crystallivity of a-C:H. The value of B for the room temperature deposited samples, is equal to the lowest values obtained for other materials [2], and drops markedly with annealing temperature. The value of B/2 is characteristic of the critical point bandgap [6], denoting a sharp decrease in this bandgap, in parallel with the sharp Eg drop. However, we did not see signs of a peak in k(E) at E = B/2, as expected for a critical point.

CONCLUSION

Dispersion relations suggested in [2] are obeyed, although the n(E) function does not have a perfect fit. Values of the parameters for the bandgaps B and Eg show reasonable agreement with Tauc plots and with prior results. The position matrix element increases with increasing annealing temperature.

REFERENCES

1. N.F. Mott and E.A. Davis, Electronic Processes in Non-Crystalline Materials, 2nd ed. (Clarendon Press, Oxford, 1979).

2. A.R. Forouhi and I. Bloomer, Phys. Rev. B, 34, 7018 (1986).

3. J. Robertson, Adv. Phys., 35, 317 (1986).

4. S.A. Alterovitz, J.D. Warner, D.C. Liu and J.J. Pouch, J. Electrochem. Soc., 133, 2339 (1986).

5. S.A. Alterovitz, J.J. Pouch and J.D. Warner, in Rapid Thermal Processing of Electronic Materials, edited by S.R. Wilson, R. Powell, and D.E. Davies, (Mater. Res. Soc. Proc. 92, Pittsburgh, PA, 1987) pp. 311-318.

6. A.R. Forouhi and I. Bloomer, Phys. Rev. B, 38, 1865 (1988).

7. S.A. Alterovitz, G.H. Bu-Abbud, J.A. Woollam, and D.C. Liu, J. Appl. Phys., 54, 1559 (1983).

8. G.H. Bu-Abbud, S.A. Alterovitz, N.M. Bashara and J.A. Woollam, J. Vac. Sci. Technol., A, 1, 619 (1983).

9. G.H. Bu-Abbud, N.M. Bashara, and J.A. Woollam, Thin Solid Films, 138, 27 (1986).

10. P.G. Snyder, M.C. Rost, G.H. Bu-Abbud, J.A. Woollam, and S.A. Alterovitz, J. Appl. Phys., 60, 3293 (1986).

11. S.A. Alterovitz, J.A. Woollam, and P.G. Snyder, Sol. State Tech., 31 (3), 99 (1988).

12. J.J. Pouch, J.D. Warner, D.C. Liu and S.A. Alterovitz, Thin Solid Films, 157, 97 (1988).

13. J.A. Woollam Co., Lincoln, NB.

14. D.E. Aspnes and A.A. Studna, Appl. Opt., 14, 220 (1975).

15. R.W. Collins, Appl. Phys. Lett., 52, 2025 (1988).

16. J.J. Pouch, S.A. Alterovitz, J.D. Warner, D.C. Liu, and W.A. Lanford, in Thin Films: The Relationship of Structure to Properties, edited by C.R Aita and K.S. Sreeharsha, (Mater. Res. Soc. Proc. 47, Pittsburgh, PA, 1985) pp. 201-204.

This paper also appears in Mat. Res. Soc. Extended Abstract (EA-19)

Materials Science Forum Vols. 52 & 53 (1989) pp. 577-608

DIAMONDLIKE CARBON APPLICATIONS IN INFRARED OPTICS AND MICROELECTRONICS

J.A. Woollam, B.N. De, S. Orzeszko*, N.J. Ianno and P.G. Snyder (a)
S.A. Alterovitz and J.J. Pouch (b) and
R.L.C. Wu and D.C. Ingram** (c)

(a) Center for Microelectronic and Optical Materials Research, and
Dept. of Electrical Engineering, University of Nebraska
Lincoln, NE 68588-0511, USA
(b) NASA Lewis Research Center, Cleveland, OH 44135, USA
(c) Universal Energy Systems, Dayton, OH 45432, USA

I. Introduction

Numerous authors worldwide have prepared diamondlike carbon (DLC) for various potential applications [1]. The present chapter reviews work done, by ourselves and others on an important aspect of the use of DLC as a protective coating in harsh environments. This article contains new material not previously published, as well as material re-presented, but with a new perspective. The motivation for the original studies was the potential application of DLC on infrared transmitting optics [2], and as protective coatings in microelectronics [3].

There are three sub-topics in this chapter. The first is a description of the preparation of DLC on seven different infrared transmitting materials, and the possibility of using DLC as an anti-reflecting coating at commonly used wavelengths [4]. DLC doesn't bond easily to all materials, and special techniques for bonding have been found both by ourselves and others.

The second topic deals with how well DLC will protect a substrate from moisture penetration. This is an important aspect in numerous uses of DLC, including both infrared optics and integrated circuits [5].

The third sub-topic also involves an environmental aspect, namely the effect of particulate impact on film performance and integrity. For example, an infrared coating may be exposed to a space environment or to conditions of blowing sand or water [2]. It is important to know how well DLC maintains its integrity.

* Now at Nicholas Copernicus University, Torun, Poland.

**Now at Whickham Ion Beam Systems, Ltd., Newcastle-Upon-Tyne, Great Britain.

II. DLC on Infrared Transmitting Materials

Several different infrared substrates were used, including lexan, silicon, fused silica, KG-3 glass, BK-7 glass, ZnS, ZnSe, heavy metal fluoride glass, GaAs, and Ge.

Extensive depositions were carried out using four different systems, including direct ion beam, and three parallel plate capacitively coupled plasma chamber designs.

A. Ion-Beam Deposition

The schematic diagram of the system used to ion beam deposit DLC films is shown in Figure II-1. It consisted of four sections: the ion source, the gas inlet system, the vacuum system, and the target fixture. The ion source was a 2.5 cm Kaufman source made by Ion-Tech Inc. Figure II-2 shows a schematic circuit diagram of the source. The ion beam was produced by a plasma discharge and a typical ion current was 10mA. The ion kinetic energy used in the deposition could be varied from 100 to 1500 eV. The beam profiles of the ion source were extensively characterized under various conditions such as ion energy, and external magnetic and

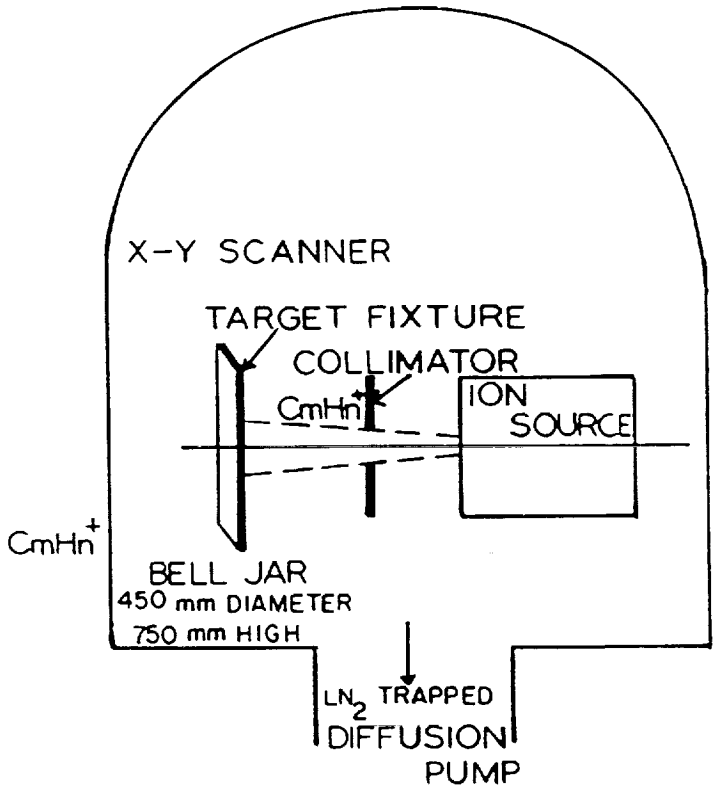

FIGURE II-1. Schematic drawing showing the relationship of the ion source to the target fixture inside the bell jar.

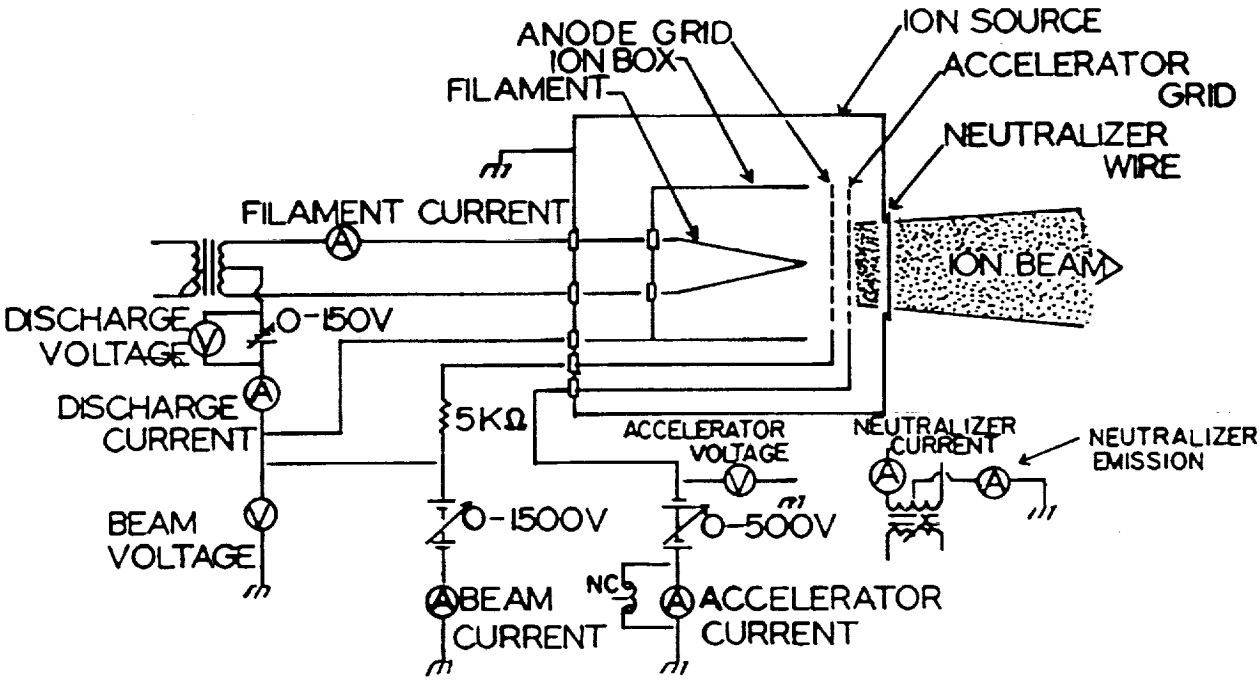

Figure II-2 Circuit diagram of the ion source.

electrostatic fields. In general the beam profile was narrow and peaked.

The sample inlet system permitted introduction of two premixed gases into the ion source. The flow rate of each gas was controlled by an MKS flow controller, and the gases used in this work were methane (99.99%) and hydrogen (99.99%). The background pressure was typically 10^{-6} torr, and the operating pressure was on the order of 10^{-5} - 10^{-4} torr.

The target fixture was mounted about 8 cm from the ion source. Using the present ion source, the directly deposited films were found to be nonuniform. In order to obtain a uniform and large area film, an X-Y scanner was constructed, as shown in Figure II-3. The target plate was able to move approximately $\pm$ 17.5 cm in two orthogonal directions in a plane perpendicular to the beam. This was accomplished using stepping motors controlled by SLO-SYN indexers (430-PI, Superior Electric Co.). The

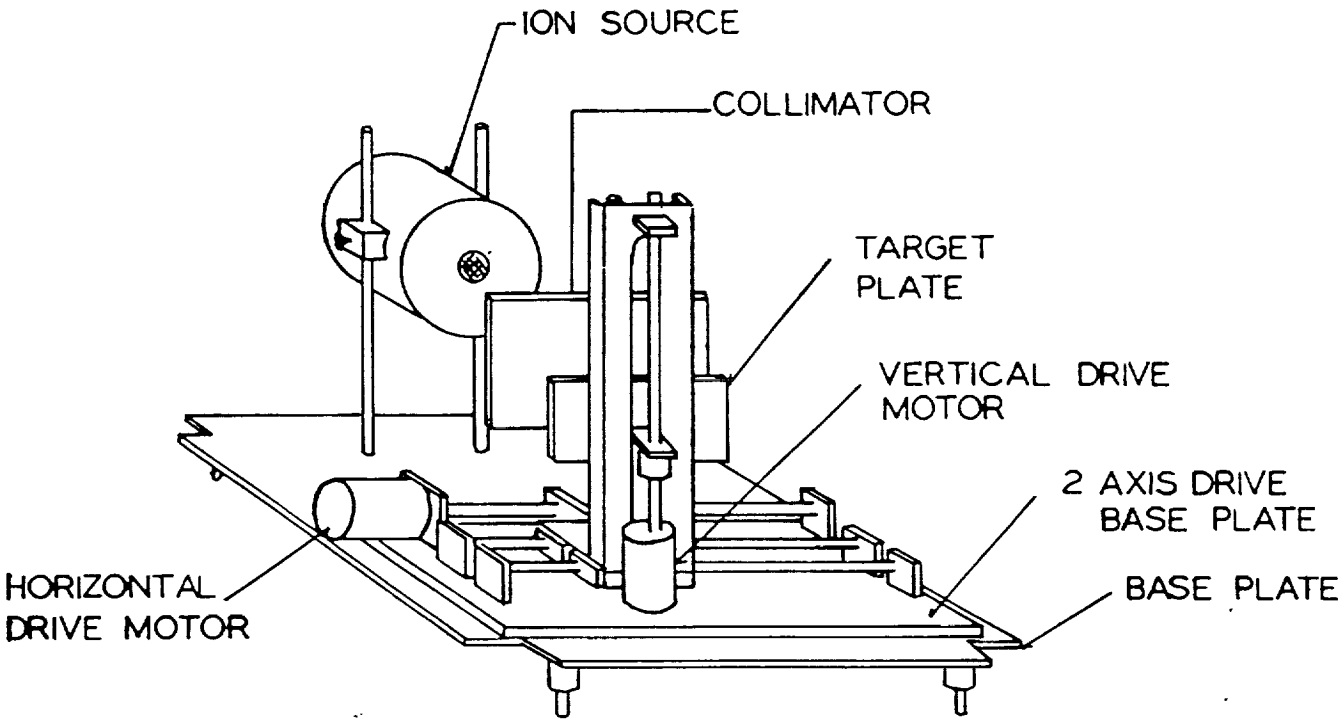

Figure II-3 Schematic layout of the target scanner.

indexers were interfaced to an IBM XT-compatible computer via an RS-232 port, which allowed the user to change parameters, i.e., feed-rate and travel distance, in the indexers. Extensive tests were performed to determine the optimum scan rates. The carbon content of the deposited film was then analyzed for uniformity using Rutherford Backscattering across a 5.5 x 5.5 cm^2 area. The optimum conditions were determined to be 0.04 cm/sec for the X-direction and 1.6 cm/sec for the Y-direction. This set of scan rates was used on all subsequent depositions.

B. RF-Plasma Configuration I

An rf sputtering system was purchased from Cooke Vacuum Corporation, consisting of a cryopumped stainless steel bell jar chamber. Inside the chamber were two parallel plate electrodes which were driven by a 13.56 MHz, 0 to 500 watt rf generator, and a load matching network.

In Configuration I, one electrode was grounded, and the other driven by the rf generator. The driven electrode was much

smaller in area than the grounded electrode, as sketched in Figure II-4. This geometry created an intense plasma above the driven electrode which was accompanied by a large self-induced DC bias. Also, a rather diffuse plasma existed at the ground plane with virtually no DC bias. The substrate was placed on the driven electrode to take advantage of the intense plasma and the high deposition rate. During depositions at low power, the self-induced dc bias was moderate and did not appear to alter the film characteristics. However, significant high energy ion bombardment of the depositing film occurred. We feel the main effect of the ion bombardment was to heat the depositing film and drive out the hydrogen, leaving a low band gap material. This conclusion was based on the results obtained when a deposit was made at 500 watts rf power, 140 microns torr total pressure for 30 minutes. Another deposit was made under the same conditions except the discharge was run for 2 minutes and turned off for 3 minutes until a total time of 30 minutes deposition was achieved. The former deposit exhibited a band gap of approximately 0.2eV. the band gap of the latter film was greater than 1 eV, comparable to that observed in films deposited at low powers. In view of this, the Cooke system was modified such that the areas of the driven electrode and ground plane were approximately equal (Configuration II). This eliminated the self-induced bias and the accompanying heating effect. This modified system allowed a more accurate exploration of the effect of various plasma parameters on the film properties.

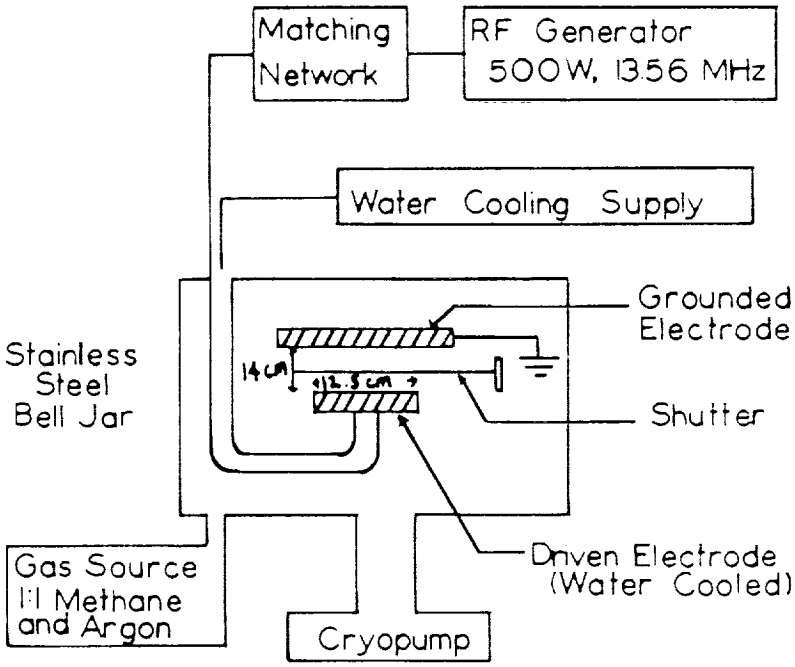

Figure II-4 Configuration I schematic design

c. RF-Plasma Configurations II and III

The reason behind the design for this configuration as discussed above was to eliminate high energy ion impact and loss of hydrogen during deposition. This configuration had a 30 cm diameter stainless cathode on the bottom (Figure II-5), and a 28 cm diameter stainless steel upper electrode with an appropriate ground shield.

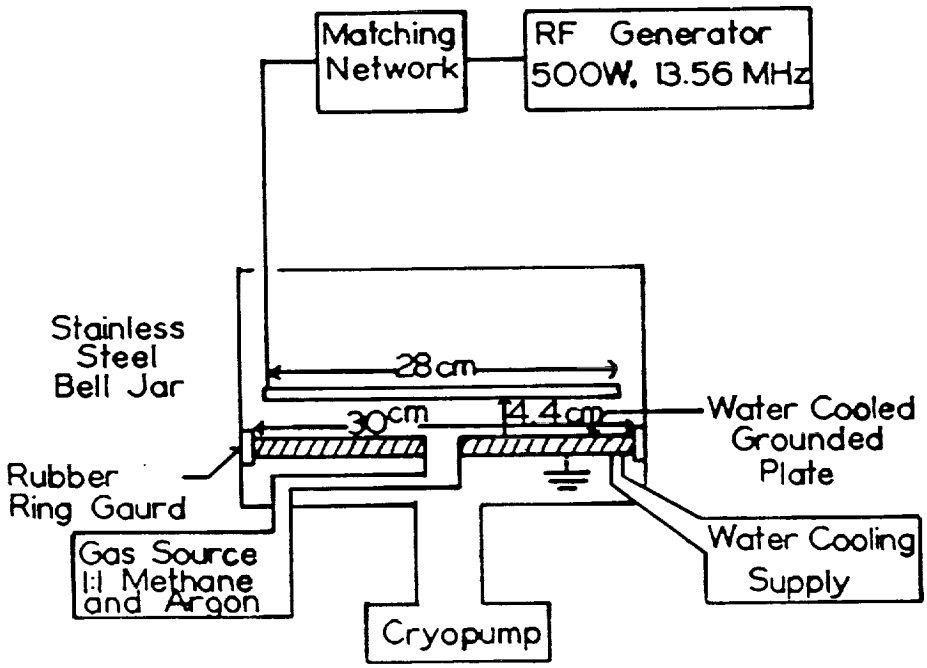

Figure II-5 Configuration II schematic design

The center of the lower grounded electrode was connected to the gas inlet pipe by means of a small plastic tube. A small metal screen was placed over the center of the hole in the lower plate to prevent the gas discharge from igniting in the gas outlet opening. This electrode was also water cooled by a 28 cm diameter stainless steel plate with copper cooling coils soldered to it.

The Configuration II design reduced the self-induced DC bias, by forcing the area of the driven electrode to be approximately equal to the area of the ground plate. This reduced the high energy ion bombardment of the depositing film and the subsequent heating effects. This design provided a uniform gas flow over the lower electrode for a wide range of input gas flow rates and pumping speeds, creating a large area of

uniform deposition for samples placed on this electrode. A rubber ring guard was placed around the outside of the lower electrode to prevent the discharge from igniting around the edges. The frequency was 13.56 MHz.

In Configuration III (used at NASA Lewis) the chamber was similar to II but the plates were of equal area (20 cm diameter), and 2 cm separation. The plasma was pure methane at a pressure of 20 microns. The frequency was 30 kHz.

D. Optimization of Experimental Parameters

The physical properties of the DLC films on various substrates were found to be dependent upon the deposition parameters. Optimum deposition parameters, for each technique, were established and are described below.

1. Ion-Beam Deposition

An attempt was made to optimize the hydrogen content of DLC films by varying the hydrogen-to-methane ratio inside the ion source. A series of experiments were performed using silicon substrates. The hydrogen concentration was varied from 0% to 98%. The deposition conditions were as follows: beam voltage - 1000 V; accelerator voltage - 100 V. The discharge voltage increased from 58 V to 98 V with increasing hydrogen content in order to maintain the source discharge. The filament current was typically 6 A; neutralizer current typically 6 A with 3 mA emission, and the gas flow increased from 1.5 to 10 SCCM with increasing hydrogen content.

The deposited film composition was determined by Rutherford backscattering (RBS) analysis for carbon content and proton recoil detection (PRD) for the hydrogen content. The results are shown in Table II-1. Hydrogen content in the deposited DLC film has been found to be dependent on the hydrogen-to-methane ratio inside the ion source. In particular, increased hydrogen concentration in the ion source has been found to result in an increased hydrogen content in the deposited film. Using pure methane in the process of the present study, the final hydrogen concentration in the DLC film is approximately 30%. With 20% hydrogen in the ion source, the hydrogen concentration in the DLC film is approximately 35% while with hydrogen concentration in the ion source of between 50% and 80%, the final hydrogen concentration in the DLC film is approximately 40% to 41%. Accordingly, variation of the hydrogen concentration in the ion source can be utilized to vary the hydrogen concentration of the deposited DLC film. In general, lower hydrogen concentrations in the DLC film render the coating denser and harder than films having higher hydrogen concentrations. Accordingly, in most applications, the use of pure methane is preferred.

The effect of ion-impact energy on the film quality (uniformity, pinhole, adhesion, and optical properties), on the deposition rate, and on the damage to the substrate was investigated. Two impact ion-energies of 500 and 1000 eV were used to deposit diamondlike carbon on silicon substrates. A pure CH_4 gas was used in these experiments. The gas flow rate was 3 SCCM and the chamber pressure was 9.0×10^{-5} torr. Both films appeared to be uniform and golden in color. The film growth rate, hydrogen content and carbon content were analyzed. The results are shown in Table II-2. Within the uncertainties of the RBS, PRD and Dektak film thickness analyses, the deposition rate and the hydrogen concentration in the film were found to be the same. The cross-sectional transmission electron micrograph of the DLC film at 1000 eV showed no damage on the surface of the silicon substrate. At high energy ion impact, the ion current seemed more intense and the films stuck well to the substrate.

The increase of methane molecules resulted in ion-molecule reactions inside the ion source; higher molecular weights of hydrocarbon ions were produced. The present experiments were carried out at three different pressures: 2.6×10^{-4} torr, 9×10^{-5} torr and 6×10^{-5} torr brought about by controlling the CH_4 flow rate 7.32, 3.00 and 1.32 SCCM. An ion-impact energy of 1000 eV and silicon substrates were used. Uniform golden color films were observed for deposition pressures of 2.6×10^{-4} torr and 9×10^{-5} torr. However, darker films were obtained using a pressure of 6×10^{-5} torr. The carbon and hydrogen content of the films were analyzed, and results are shown in Table II-3.

It can be seen that at the lowest pressure, the hydrogen content in the film was slightly increased. Therefore, if harder films have less hydrogen, it is better to use higher methane pressures.

The effect of substrate material (silicon, fused silica, lexan, KG-3, BK-7 glass, ZnS, ZnSe and HMF) on DLC film growth rate and film quality was investigated using the same experimental conditions: pure CH_4 at flow rates of 3.0 SCCM, 1 KeV ion energy, source pressure of 9×10^{-5} torr, deposition times from 65 to 450 minutes. All films on the above listed substrates were found to be uniform. The film thicknesses were measured using a Dektak instrument. Table II-4 gives the average growth rate of DLC on various substrates over an area of 4.9 cm^2. These were direct ion beam depositions, with the present 2.5 cm diameter ion source.

The effect of cleaning the substrate surface prior to ion deposition of the DLC films was studied extensively. Bonding of the DLC film on various substrates was found to be strongly dependent upon the surface cleaning procedures. The initial cleaning procedures included: (1) washing with 1,1,1 Trichloroethane, (2) washing with acetone, (3) washing with methanol and finally (4) blow drying by dry nitrogen. All samples were cleaned by these four procedures, except the lexan substrate

Table II-1. Effect of Hydrogen in the Source Gas on the Carbon, Hydrogen Contents of Direct Ion Beam Deposited Diamondlike Carbon Films

Sample No.	% Hydrogen in the Source	% Hydrogen in the Film (±5%)	% Carbon in the Film (±5%)
DLC - C	0	30	70
DLC 140	2	40	60
DLC 141	5	36	64
DLC 142	10	38	62
DLC 143	20	35	65
DLC 144	50	40	60
DLC 145	80	41	59
DLC 146	90	NO FILM	NO FILM
DLC 147	90	NO FILM	NO FILM
DLC 149	95	39	61
DLC 148	98	NO FILM	NO FILM

TABLE II-2. Effect of Ion Impact Energy on the Direct Ion Beam Deposited Diamondlike Carbon Films.

Sample No.	Ion Impact Energy (eV)	% Hydrogen in the Film (±5%)	% Carbon in the Film (±5%)	Film Growth Rate A/min±5 A/min
871-365	1000	33.0	67.0	23
871-366	500	37.5	63.5	25

TABLE II-3. Effect of Methane Pressure on the Direct Ion Beam Deposited Diamondlike Carbon Films.

Sample No.	CH_4 Source Pressure (torr)	Flow Rate (SCCM)	% Hydrogen in the Film (±5%)	% Carbon in the Film (±5%)
871-367	6×10^{-5}	1.32	38.4	61.6
871-365	9×10^{-5}	3.0	33	67
871-368	2.6×10^{-4}	7.32	33.4	66.7

TABLE II-4. Diamondlike Carbon Film Growth Rate on Various Substrates.

Substrate	Direct ion beam Deposition Rate (Å/sec)
Lexan	11.5
BK-7	8.3
KG-3	8.3
Silicon	6.3
Fused Silica, Glass	5.7
ZnS, ZnSe	6.8
HMF	6.8

which used only procedures (3) and (4). It was found that DLC films adhered to BK-7, KG-3, ZnS, silicon and lexan substrates quite well, and passed the initial "Scotch" tape tests. However, the DLC film on fused silica and heavy metal fluoride glass failed the "Scotch" tape tests. Thus an attempt was made to investigate the surface cleaning procedures for HMF glass and fused silica. The substrates of HMF and fused silica were cleaned by procedures (1), (2), (3), and (4), and cleaned again by 1000 eV Ar^+ ion beam for 20 minutes prior to DLC deposition. The DLC films on both substrates again failed the "Scotch" tape test. Another cleaning procedure was tried to clean the surface by washing with methanol and drying using a heat gun or dry nitrogen. The DLC films on both substrates were found to stick well to these substrates. The new cleaning procedure was thus adapted for cleaning of HMF and fused silica substrates.

In the present ion-beam deposition technique, the temperature of the substrate was constantly monitored by a temperature tape and was found to be less than $60^{\circ}C$. Since optical materials can be temperature sensitive, no attempt was made to heat the substrate.

2. RF Plasma Discharge: Configuration I

Plasma DLC deposition was extremely successful on glass slides (Thickness $\leq$ 1 micron) and Si-wafers. Occasionally there were problems with pinholes when high power was used. At high power (especially 250 and 500 watts), the film quality became significantly degraded, in terms of the uniformity of the film thickness and the ability to adhere to glass. The thickest films spalled off the edges of the glass slides if the power was too high. As measured from UV-VIS absorption measurements on samples deposited on glass slides, the optical energy gap was about 0.2 eV for the 500-watt sample. Substrate heating was suspected to occur at high rf powers. To test for this postulate, sample K3 was prepared on glass, at 500-watt power, 140 microns pressure, and deposited for 10 minutes (1 minute times 10 with 5 minutes cooling interrupt periods in between); the resulting sample had an optical gap of 1.1 eV, the same value that occurred when low powers were used. This supported the hypothesis that heating caused the drop in optical gap. All subsequent depositions were made with the plasma on for only a few minutes, then the plasma off for 3 to 5 minutes to permit cooling.

All glass samples were cleaned by washing with the following sequence: 1) 1,1,1,-Trichloroethane, 2) acetone, 3) methanol, 4) deionized water, and 5) dry nitrogen blow. All Lexan samples were cleaned by washing with methanol, followed by deionized water, and finally by a dry nitrogen blow.

We noticed that pinholes in films were caused by segregated granular carbon deposits. The pinholes were exposed after the film was blown with dry nitrogen. These granular carbon deposits were probably formed before reaching the substrate, and were likely caused by the excessive amount of carbon atoms in the gas

phase (in the plasma). Thus, it was logical to reduce the carbon atom density within the plasma. That could be achieved in two ways: 1) By reducing the pressure, and 2) by reducing the power.

We chose the second alternative. Thus, all samples were made at 25 watts power and 140 microns pressure. The results were highly successful.

3. Plasma Discharge: Configuration II

A 1:1 mixture of methane and argon and a 13.6 MHz RF power source, capable of delivering up to 500 watts, were used for the generation of the plasma. The plate areas were made almost equal in order to deliver the power with a minimum DC bias voltage between the plates. The maximum DC vias voltage observed was 550 volts. The lower plate was grounded and the upper plate was driven by an RF power supply. A cryopump was used on the chamber.

When the system shown in Figure II-5 was first designed and operated, the rubber guard ring was not present, and the plasma was very unsteady and sometimes passed beyond the lower ground plate to the bottom of the chamber. Also, sometimes it became difficult to start the plasma; even after using the tesla coil and adjusting the matching network of the RF power supply we could not start the plasma, (at the 80 microns base pressure and the flow rate of 12.5 sccm for both methane and argon). Figure II-6 shows more details of the Figure II-5 design which permitted easier ignition of the plasma due to a better gas flow geometry. We made 16 small holes in the plate and closed the gap between the lower ground plate and the chamber using a vacuum compatible rubber strip as shown in Figure II-6. The gas thus entered the plasma region through the center and flowed radially outward. We planned to use the external DC INPUT to start the plasma (instead of the tesla coil), but found that after modifying the system, the gas plasma was generated rather easily by increasing the gas pressure to 100 microns. Sometimes, use of a tesla coil in combination with some adjustment of the matching network of the RF power supply was helpful in starting the gas discharge. The plasma was found to be confined within the volume above the lower ground plate.

Except for Si, Lexan, HMF glass, and ZnS, all the substrates were first ultrasonically cleaned using 1,1,1-Trichloroethane; then washed with acetone, methanol, and deionized water successively and finally dried by blowing dry nitrogen. Lexan was ultrasonically cleaned using methanol, washed with deionized water and finally dried using dry nitrogen. HMF surface was found to be deteriorated by the use of any of the organic solvents mentioned previously. Thus, we visually looked for the cleanest surface of HMF, and dried it in flowing dry nitrogen. The Si surfaces were clean as received; therefore we used only

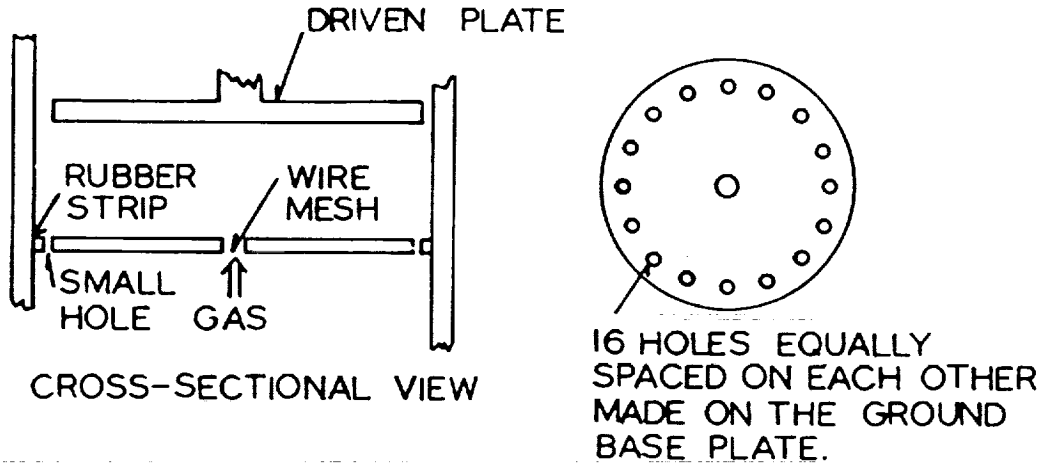

Figure II-6 Cross-sectional view of the plasma discharge

Configuration II.

dry nitrogen to clean them. For ZnS, we followed the same procedure, in order to maximize adhesion.

The best deposition conditions were found to be: 1) flow rate for methane and argon: 13 sccm each, 2) base pressure: 100 microns, 3) power: 200 watts, and 4) DC bias between the two plates: 300 volts.

From the depositions using Configuration I, we found that DLC films on ZnS substrates tended to spall very easily if the film was thicker than a few hundred angstrom units. Because of that, we deposited for 2 minutes (only) on the ZnS substrates, resulting in an estimated film thickness of about 300 Å. We should note that DLC will adhere to ZnS and ZnSe if a thin (300 Å) Ge film is deposited between the semiconductor and the DLC layer [6].

4. 30 kHz Plasma Deposition System: Configuration III

Figures II-7 and II-8 show the strong dependence of deposition rate on substrate temperature, and on power [7]. The configuration for these depositions was similar to Plasma Deposition Configuration II, described above. The plasma was of pure methane gas at a pressure of 20 microns. 100°C substrate temperature and a power level of 200 watts was typical for producing good films.

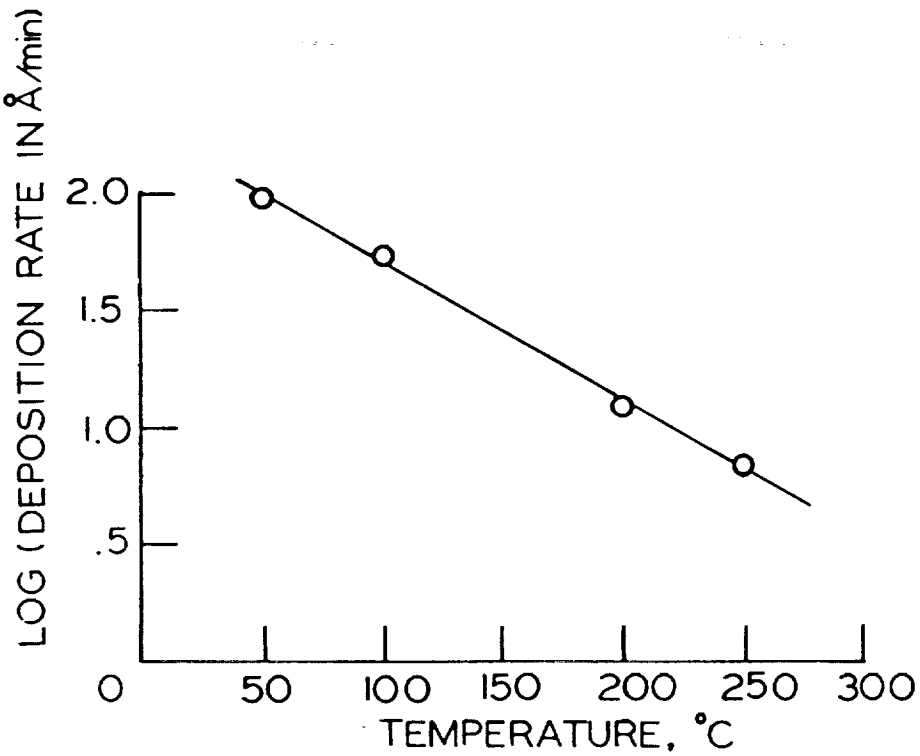

Fig II-7. Logrithmic plot of deposition rate vs temperature

E. Antireflection Conditions Using DLC

As mentioned above, substrates of infrared interest on which we deposited DLC included: lexan, silicon, fused silica, KG-3 glass, BK-7 glass, ZnS, GaAs, Ge, and heavy metal fluoride glass. It was desired to know if DLC could be deposited to the proper thicknesses and with the correct indices of refraction for use as an antireflecting coating on each of these substrates.

Antireflecting coatings provide an important method of enhancing transmission through optical window materials [8].

The reflectivity has a minimum when

$$n_1 d_1 = \lambda_0/4 \qquad \text{II-1}$$

where n_1 is the index of refraction of the coating, and d_1 its thickness. The reflectivity minimum is at its lowest value (zero) when

$$n_1^2 = n_0 n_2 \qquad \text{II-2}$$

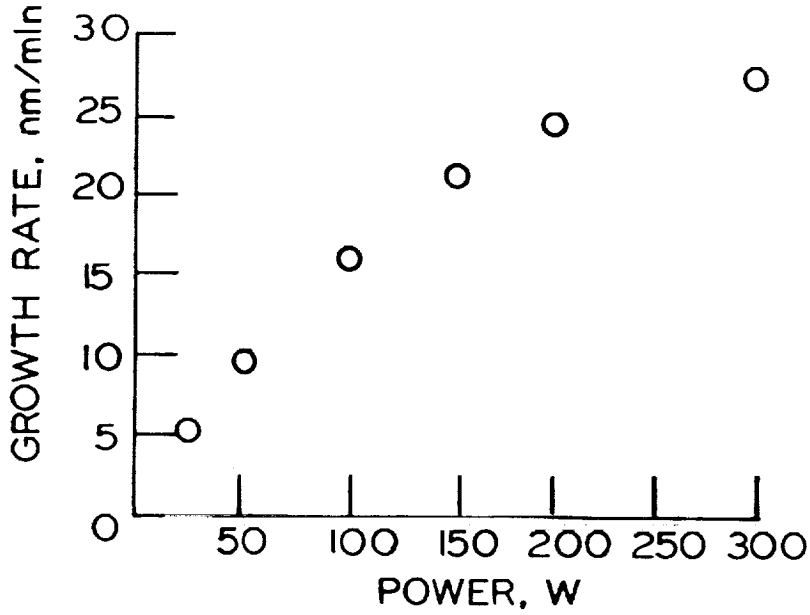

Fig II-8 Growth rate of hydrogenated carbon on n-InP as a function of deposition power.

where n_o is the index for the ambient, which is normally air, so

$$n_1 = \sqrt{n_2}$$

is required, where n_2 is the index of the substrate at the wavelength of interest.

Table II-I lists infrared transmitting substrates, their indexes of refraction, the operating wavelengths of interest, and the required DLC thickness and optical index of refraction. The proper index came from use of Eq. II-3, and the proper thickness from Eq.II-1.

What is noticed immediately from Table II-I is that the required film index of refraction ranges from 1.2 to 2.85 for the examples listed.

The index of refraction of DLC can be controlled by choosing the proper deposition technique and parameters [1]. The range typically found is for

$$1.6 \leq n_1 \leq 2.4 \qquad \text{II-4}$$

which makes the optimum matching substrates have indices from

$$2.5 \leq n_2 \leq 5.8 \qquad \text{II-5}$$

These values are much higher than the indexes for the glasses under consideration (Table II-I), but result in a decent match for ZnS, diamond, TiO_2, As_2S_3-glass, Se-glass, and results in good matches for Si, Ge, GaAs, and InSb. All are common infrared transmitting materials [9].

In conclusion, we find that with the exception of ZnS we were able to directly deposit DLC on the chosen substrates to the desired thicknesses for antireflection. The indexes of refraction were measured from 300 nm to 10 microns, and found to be in the range from 1.6 to 2.0. Other workers have prepared DLC samples with indices up to 2.4. Thus, we have established a range of conditions for use of DLC as an antireflecting coating. Zero reflectance can be achieved on substrates of Si, Ge, GaAs, and InSb. Low reflectance can be achieved on ZnS, diamond, TiO_2, As_2S_3-glass, Se-glass; but DLC will not provide total antireflecting conditions when deposited on the common glasses with index near 1.5.

III. Moisture Protection with DLC

A. Introduction

DLC is amorphous and thus has no grain boundaries through which water might otherwise diffuse. One of the most common uses of thin films is for coatings for moisture protection. Thus DLC seemed to be an ideal candidate material for use as a hermetic seal [5]. Applications, for example, might be to passivate integrated circuits, or to keep water from sensitive infrared transmitting optical windows or lenses.

It is very difficult to measure penetration of liquids into thin films. Common surface analysis techniques such as AUGER, ESCA, and SIMS require ultra high vacuum, and therefore cannot be used.

B. Diagnostics Technique

We have shown that variable angle spectroscopic ellipsometry (VASE) can be used to determine the thickness of ultrasmall amounts of water on, and in a thin film [5]. This spectroscopy is

not commonly known, so a brief description will be given [10]. The interested reader can find more details in references listed.

Ellipsometry determines the ratio of complex reflection coefficient

$$\tilde{\rho} \equiv \tilde{R}_p/\tilde{R}_s = \tan\psi \exp j\Delta \qquad \text{III-1}$$

where $\tilde{R}p$ and $\tilde{R}s$ are the complex Fresnel reflection coefficients for components of light parallel (P) and perpendicular (S) to the plane of incidence of the incident and reflected light.[10] In our VASE technique, data are taken from 300 to 800 nm with light incident at an angle ϕ to the normal to the sample. The reflected light polarization state is analyzed with a rotating polarizer. Light intensity is measured with a photomultiplier tube, and the signal is digitized and Fourier analyzed to determine the ψ and Δ parameters of equation III-1.

The measured complex ratio $\tilde{\rho}$ is related to the optical index of refraction, n, and extinction coefficient, k, of the material under study. If complex materials structures are involved, then n and k can be determined for individual layers, and layer thicknesses determined.

Microstructural analysis is performed assuming the nature of the sample under study. For the present samples the model is shown in Fig. III-1. The t_i are layer thicknesses, and f_2 is the fraction of DLC in a DLC plus H_2O Bruggeman effective medium approximation (EMA) mixture layer. The procedure is to calculate using the Fresnel reflection coefficients for a multilayer parallel stack (and EMA mixed layers), for a given initial set of values for thicknesses and fractions. Next, a regression analysis is performed to minimize the mean square error function (MSE) defined by

$$MSE = \frac{1}{N} \sum_{i=1}^{N} (\psi_i^{exp} - \psi_i^{calc})^2 + (\Delta_i^{exp} - \Delta_i^{calc})^2 \qquad \text{III-2}$$

where "exp" means experimentally measured, and "calc" means calculated. The psi and delta are functions of wavelength λ and angle of incidence ϕ. A large range of both λ and ϕ are chosen so that an "overdetermination" of measurements with respect to the number of unknown parameters is made, and correlation problems avoided. In our analysis programs we can use Eq. (III-2) as formulated, or we can use psi alone or delta alone, or the minimization can be done with respect to $\tan\psi$ and $\cos\Delta$. The final outcome is a set of values for thicknesses, EMA fractions, and optical constants for any of the layers. The optical constants can take on several forms: 1) index of refraction n and extinction coefficient k, 2) real, E1 and imaginary, E2, parts of the optical dielectric function, or 3) the amplitude, position, and width of Lorentz oscillators.

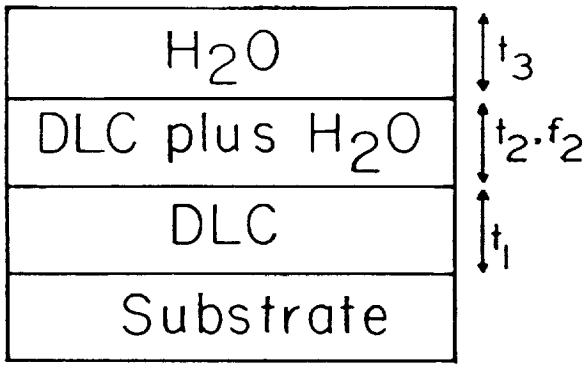

FIG. III-1 Structural model assumed for analysis of moisture. t_i are thicknesses and f_2 is the fraction of H_2O in layer 2.

Since we used the Lorentz oscillator model extensively it will be described further. When the wavelength-dependent n, k (or E1, E2) values are solved for, the number of unknown parameters equals the number of wavelengths times two, plus the number of layers, plus the number of unknown fractions in an EMA. Thus if 10 wavelengths are used and there are two unknown thicknesses there will be (2 X 10) + 2 = 22 unknowns. In the Lorentz oscillator model there are fewer unknowns, since the following equation represents the spectral dependence of optical constants:

$$E = 1 + \sum_{i=1}^{M} Ai \left(\frac{1}{\lambda + P_i + jW_i} - \frac{1}{\lambda - P_i + jW_i} \right), \qquad \text{III-3}$$

where E is the complex dielectric function, and the sum is over the total number of oscillators M. For the presently reported work, the maximum number of oscillators used was one. (In section IV the results of a two oscillators analysis are presented). In Eq. (3), A_i, P_i, and W_i are the amplitude, position, and width of the i^{th} oscillator, respectively, and λ is the photon wavelength. In the oscillator analysis A_i, P_i, and W_i thicknesses and EMA fractions are solved for in the regression analysis. Thus a typical one oscillator DLC analysis has five unknowns: three oscillator parameters and two layer thicknesses; or seven unknowns: three oscillator parameters, three layer thicknesses, and an EMA fraction (see the structural model shown in Fig. III.1).

C. Samples

The films of DLC used for moisture penetration studies were prepared using the 30kHz parallel-plate plasma deposition system (Configuration III) described above [7]. Pure methane and a chamber pressure of 20 microns was used. Power levels of 100, 200, and 300 watts were used, but results for 200 watts are reported here. Substrate temperatures ranged from 23°C to 250°C.

Moisture was introduced to the films in two ways; from immersion in 23°C water, and from a steam jet at 100°C.

D. Results

1. As-deposited films

Fig. III-2 shows the dependence of average (over the 300 to 800 nm range) index of refraction, n on substrate temperature for films made with a plasma power level of 300 watts. In general the index rises from about 1.7 at low temperature to above 1.9 at high temperature. A measurement of hydrogen content in the film by proton recoil analysis showed that lower hydrogen was present in films with a higher index of refraction [11]. Measurements of the optical absorption coefficient showed that the bandgap increased with increasing hydrogen concentration. Similar trends have been seen by other workers as well [1].

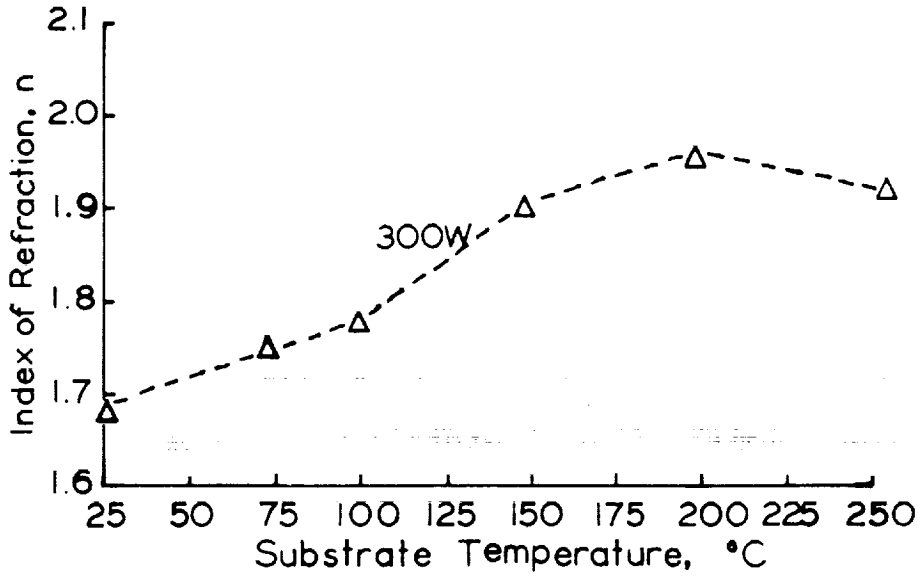

FIG. III-2 Optical index of refraction vs substrate temperature for a power level of 300 Watts.

The environmental stability of DLC films was studied on a large number of samples deposited at various power and temperature values onto polished silicon single-crystal wafers and subjected to immersions in trichlorethane, acetone, ethyl alcohol, sulfuric acid, nitric acid, hydrochloric acid, and hydrofluoric acid. After each immersion samples were subjected to rubber eraser abrasion tests and "scotch tape" pull tests.

These tests served as a comparative measurement. They had no effect on samples deposited with 100 W. For 200 W and 300 W depositions there was partial removal for samples deposited at

room temperature, but there was no effect for substrate temperatures of 74 up to 250°C. Thus DLC samples prepared under all but a few conditions survived very stressing environmental tests.

2. Moisture Introduced

A large number of samples were prepared and investigated for water penetration. The final result was that DLC films were not pentrated by water. The DLC surface had a small amount of roughness, and moisture was found to penetrate the valleys of this roughness, but no further.

Example ellipsometric data are shown in Figure III-3. The data at 0 hours after H_2O indicate that water was introduced, then the bulk of it allowed to run off a vertical surface. At this time the maximum amount of water remained, and the Δ parameter was lowest. Twenty four hours later some water had evaporated, and Δ increased. After exposure to a heat lamp much of the water on the surface was evaporated (but not all!). After exposure to the laboratory 23°C atmosphere a small amount of moisture from the ambient air deposited, with an associated decrease in Δ.

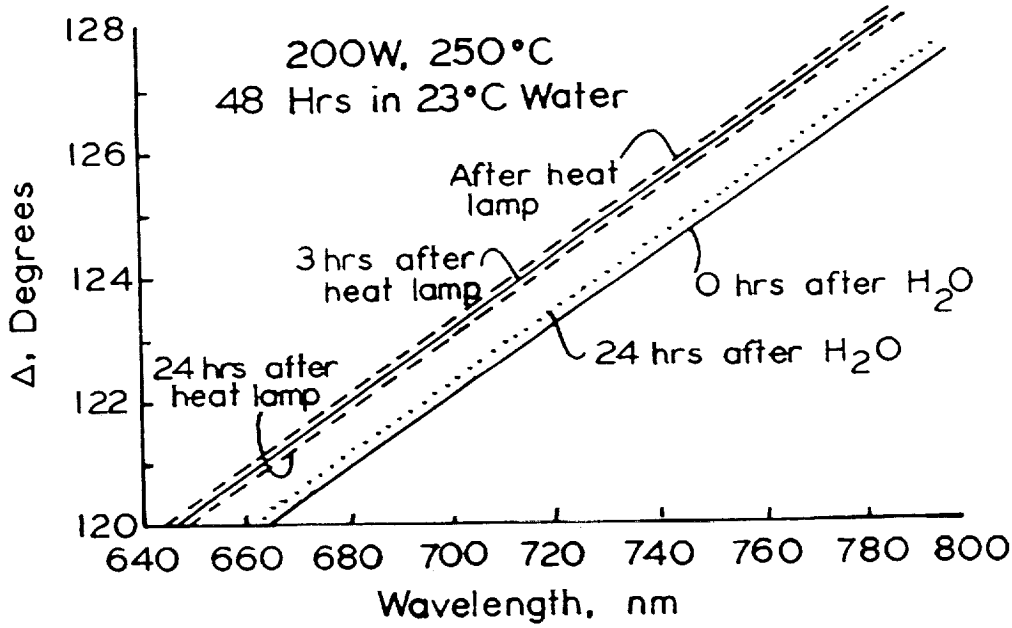

FIG. III-3 Ellipsometric delta parameter vs wavelength at various times after removing the sample from 23°C water. Sample was deposited at 200W, and 250°C, and soaked in room temperature water for 48h. After removing from water, it was kept in a room atmosphere.

Using the "oscillator" regression analysis for this sample, and a two-layer (t_2 = 0 in Fig. III-1) model in our ellipsometric analysis, we determined that the water layer was 66-Å thick on top

of a 344-Å thick DLC film. The three-layer (nonzero t1, t2, t3, in Fig. III.-2) analysis was consistent with this result: 330 Å of DLC, 29 Å of 50%-50% mixture of DLC and water, and 48 Å of pure water on top.

An interesting result was that the heat lamp removed only 12 Å of water and that 54 Å of water still remained! We propose that this thin water layer was being held to the surface by an unusually high surface tension associated with DLC surface micropores.

A detailed analysis of VASE data for all samples, assuming the model of III.2, was carried out. Tables III.1-4 summarize some of the results.

A summary of the results of DLC moisture studies are that: a) Moisture resided mainly on the surface of DLC independent of water temperature. b) In cases where there was an apparent penetration ($\leq$50 Å) it is likely that water was merely filling the void regions of a "rough" surface. The substrates were highly polished oriented single-crystal (semiconductor grade) wafers. 50Å of roughness layer was reasonable for these materials. c) A heat lamp removed water, but not all of it. This suggests that surface micropores provide a strong surface tension for these very thin water layers. d) The amount of water on the surface after wetting (but without further treatment) did not depend on the parameters of DLC deposition such as power or substrate temperature, nor did it depend on the DLC film thickness in any systematic manner. Thus, DLC protects effectively against moisture penetration [5].

IV. Ion-Beam Modified, Ion-Beam Deposited DLC

A. Introduction

In this section we present results of variable angle spectroscopic ellipsometric (VASE) studies of ion beam deposited DLC films [11]. These films have been modified by directing 1 MeV gold ions, as well as 6.4 MeV fluorine ions through the DLC and into the underlying silicon substrates. The percentage of hydrogen in the film was measured vs. fluence using proton recoil analysis. Optical analysis was performed assuming the Lorentz oscillator model, using two oscillators with spectral position, width, and amplitude all variable. This model fit the VASE data extremely well. With ion modification the oscillators shifted to lower photon energy, consistent with reduction in hydrogen concentration and possible increased graphitization.

Ion beam modification of DLC films has not been extensively investigated. The purpose of the present work was to study the effects of high energy ion beam irradiation when the ion beam passed <u>through</u> the DLC films. Two ions (gold and fluorine) and a

Table III-1. 200 Watt, 250°C deposited DLC (3 layer analysis). 23°C water.

DLC thickness	Mixture (50-50) layer thickness	Water layer thickness
330 Å	29 Å	48 Å

Table III-2. 200 Watt, 250°C deposited DLC, 23°C water (3 layer analysis).

Condition	DLC Thickness	Mixture (50-50) layer thickness	Water layer thickness
No water	326 Å	...	...
2 h in water	326 Å	24 Å	37 Å
4 h in water	328 Å	28 Å	51 Å

Table III-3. 200 W, 250°C deposited DLC sample in 100°C water (3 layer analysis).

Condition	DLC thickness	Mixture (50-50) layer thickness	Water layer thickness
No water	338 Å	...	...
2 h in water	337 Å	46 Å	36 Å
4 h in water	339 Å	54 Å	56 Å

TABLE III-4. Best fit ellipsometric solutions for indicated samples (steam jet was used to introduce water).

75°C	100°C	150°C	200°C	250°C
200-W DLC samples without H_2O				
t_1 = 915 Å	t_1 = 810 Å	t_1 = 840 Å	t_1 = 448 Å	t_1 = 252 Å
oscillator parameters	oscillator parameters	oscillator parameters	oscillator parameters	oscillator parameters
11.8;7.7;3.8	13.2;7.9;3.8	14.4;7.9;3.8	14.8;7.9;3.8	12.5;7.4;4.05
MSE = 10	MSE = 11.5	MSE = 7	MSE = 2.5	MSE = 0.18
200-W DLC samples with H2O, oscillator parameters (as given above) fixed				
t1 = 943 Å f2 = 97% MSE = 5.1	t1 = 847 Å f2 = 100% MSE = 8.4			
t3 = 4.5 Å t1 = 936 Å MSE = 2.8	t3 = 3 Å t1 = 847 Å MSE = 8.3	t3 = 74 Å t1 = 904 Å MSE = 13	t3 = 139 Å t1 = 473 Å MSE = 15.1	t3 = 123 Å t1 = 271 Å MSE = 0.21
t2 = 31 Å f2 = 99% t1 = 906 Å MSE = 2.6	t2 = 12 Å f2 = 58% t1 = 841 Å MSE = 8.2			

range of fluences were used. Diagnostics techniques included Rutherford Backscattering, proton recoil, hydrogen analysis, and variable angle of incidence spectroscopic ellipsometry (VASE).

B. Experimental

Samples were prepared in the ion-beam system described in section I above. Methane gas in the 2.5 cm diameter Kaufman type neutralized ion beam gun system (IonTech Corporation) was used, and the chamber had a base pressure of ~10^{-7} Torr. During deposition the chamber pressure rose to the range 10^{-4} to 10^{-5} Torr, and the gas flow rate was 20 sccm. In these experiments all substrates were silicon.

Rutherford Backscattering (RBS) and proton-recoil experiments were performed at Universal Energy Systems using a tandem (1.6 MeV) accelerator (Tandetron Corp.) which was used to provide 1 MeV gold ions, or 6.4 MeV fluorine ions for the ion beam modifications. Fluences ranged from 3 X 10^{14} cm^{-2} to 1 X 10^{16} cm^{-2}.

In the present VASE optical diagnostics, spectral data were taken at several angles of incidence, and the data analyzed with respect to a two oscillator model with all six parameters variable. In addition, the thickness of the DLC film was a variable.

RBS was used to determine the number of carbon atoms per cm^2 in each DLC film. Film thicknesses on these same samples were then determined by ellipsometry. From these combined measurements the film density was determined. The limits of error in RBS measurements were approximately $\pm$10 percent, and in ellipsometry were $\pm$5 percent for DLC films. The combined error of $\pm$15 percent covers the range of values measured on all eight samples. Thus we conclude that the density was 1.5 $\pm$ 0.2 gms/cm^3 independent of thickness for this set of samples. The density could easily depend on deposition technique and parameter setting, however.

C. Fluorine (6.4 MeV) Irradiated Samples

Table IV-I summarizes results of ellipsometric analysis of "fluorine-beam" processed DLC on silicon. The shorthand notation has the following meanings: A, P, and W are the one oscillator amplitude, position (in eV), and width (in eV), respectively. Subscripts I and II refer to first oscillator, and second oscillator in the two oscillator analyses, respectively. "Th" signifies thickness, and the MSE defined by Equation (2) in the last section.

Notice from Table IV-I that irradiation shifted the position of the oscillators to lower photon energy. Another universal trend was for the amplitude in the lower energy oscillator to

increase with fluence.

Figure IV.1 shows the effect of fluorine irradiation on the imaginary part of the dielectric function, E2, analyzed allowing all six oscillator parameters as well as the film thickness to be variables in the regression analyses. The trends are obvious: a downward shift of the E2 maxima in energy, and an increase in the E2 amplitude. At the same time, the higher energy oscillator position decreases (Table IV-1).

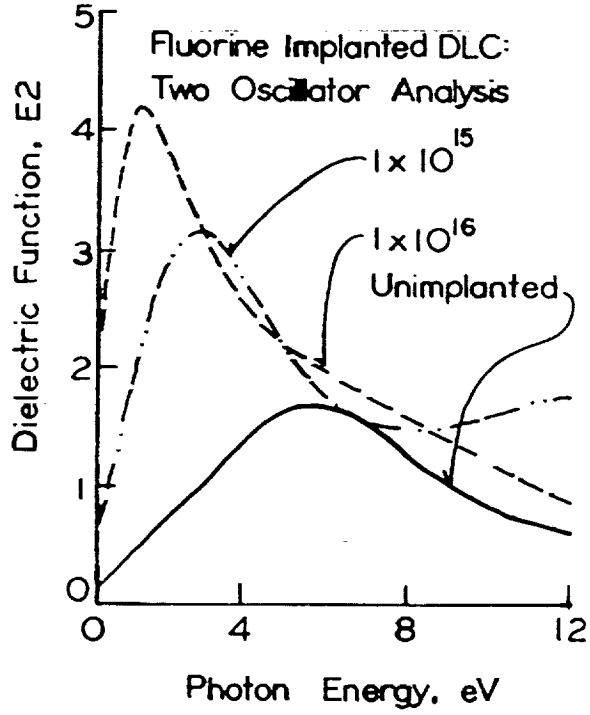

FIG. IV-1 Imaginary part of dielectric function, E_2, for Fluorine Implanted DLC: Two Oscillator Analysis.

In Figure IV.2 the real part of the dielectric function E1 is shown. Again there are shifts to lower energies, and an increase in the amplitude of E1.

The extinction coefficient, k, vs. wavelength for the various fluences are shown in Fig. IV.3. Note the general rise in magnitude of k with increasing fluence. This general increase in k with fluence gives rise to a decrease in optical bandgap, and a decrease in hydrogen content, as determined by proton recoil. The main effects of fluence of both the fluorine and gold species on hydrogen content are shown in Figure IV.4. A nearly linear relationship between energy gap and hydrogen content was found.

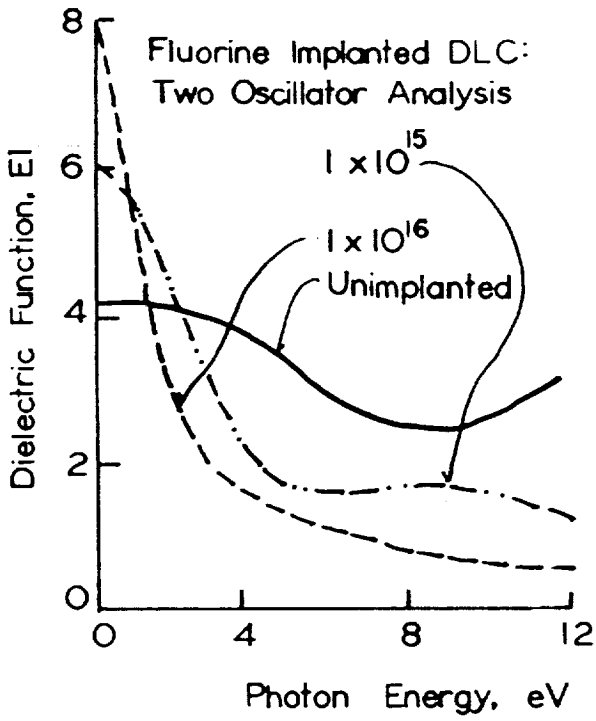

FIG. IV-2 Real part of dielectric function, E_1, for Fluorine Implanted DLC: Two Oscillator Analysis.

D. Gold (1MeV) Irradiated Samples

Results of ellipsometric analysis of samples irradiated with gold ions are shown in Table IV.2. A two oscillator model was used, with all six oscillator parameters variable.

Again there are downward shifts in the oscillator positions with increasing fluence. Other trends were less obvious. By fitting data over our spectral range of 300 to 800 nm, the oscillator analysis allowed us to extend our knowledge of the optical constants over a wider range (with an admitted danger of errors far from the measured range). The results show that the two oscillator model is appropriate for both F and Au irradiation. In both cases the downward shifts are consistent with there being a loss of hydrogen, a decrease in the optical gap, and a tendency towards graphitization.

Table IV-1. Comparison results of 2-osc. model analysis for F-implanted (4.6 MeV) DLC ion beam deposited samples (-fit only; u = unimplanted, I = implanted). Except for thicknesses, all units are electron volts. fluence, cm^{-2} sec.

2-oscillator model - Position of 2nd oscillator variable

	1st oscillator			2nd oscillator			Tk (Å)	MSE
	AI	PI	WI	AII	PII	WII		
0	7.5	5.58	4.0	12.2	17.4	0.44	1221	1.22
3	10.4	3.4	3.6	8.37	14.5	1.64	1307	0.13
10	11.1	2.56	2.92	10.22	12.8	6.0	790	0.015
30	12.8	2.49	2.92	8.6	11.0	7.8	757	0.1
100	22.6	0.68	2.28	18.7	4.57	7.8	2624	0.47

Table IV-2. Results of 2-oscillator models for Au (1 MeV) -implanted DLC ion beam deposited samples (u = unimplanted, I = implanted). Except for thicknesses, all units are electron volts. = fluence, cm^{-2} sec.

2-oscillator model

	1st oscillator			2nd oscillator			Thickness	MSE
	AI	Position	WI	AII	Position	WII		
0	3.34	4.33	1.45	17.0	16.7	0.55	1832 Å	1.18
3	1.40	3.24	0.78	21.4	16.5	0.39	2096 Å	2.60
10	3.60	3.53	1.38	9.9	11.6	1.70	1173 Å	0.34
30	3.50	3.44	1.53	9.7	9.2	2.30	913 Å	0.26
100	3.29	3.33	1.18	12.5	10.8	1.21	1314 Å	0.77

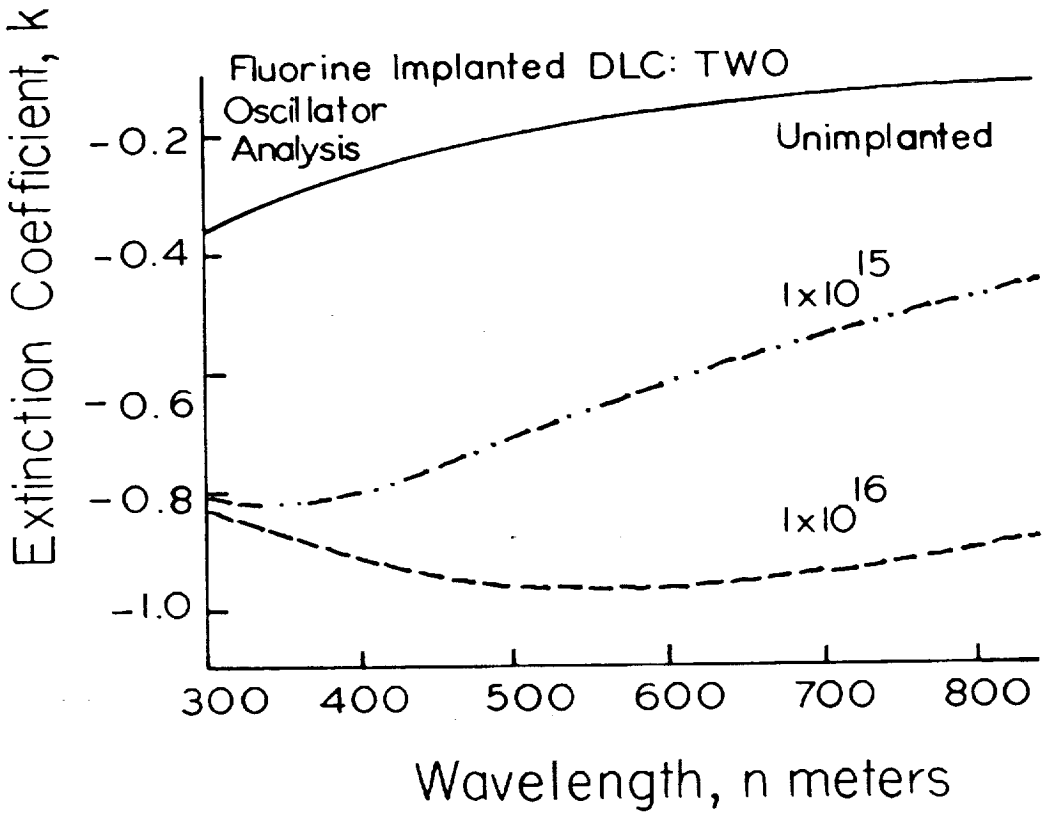

FIG. IV-3 Extinction Coefficient, for Fluorine Implanted DLC: Two Oscillator Analysis.

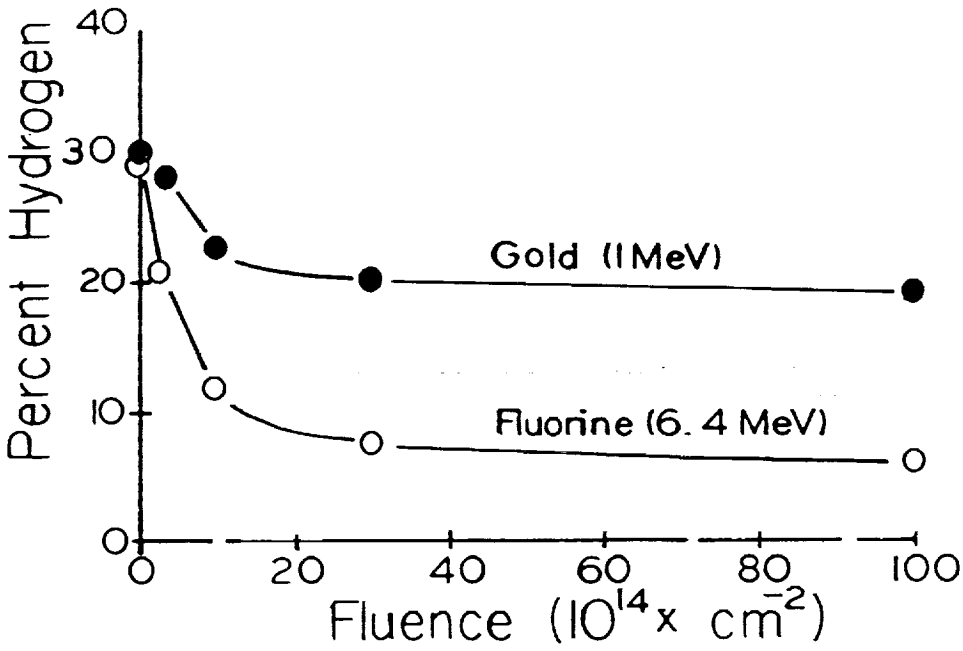

FIG. IV-4 Hydrogen concentration for Au and F implanted DLC.

For gold implants, an optical gap slightly above 1 eV is seen to decrease to about 1 eV with increasing fluence. The effect of irradiation on bandgap isn't as great for Au as it is with F irradiation. However, the loss of hydrogen with gold fluence was not as great as it was for fluorine.

E. Discussion of Results

We found that irradiation with a lighter ion (F) at 6.4 MeV through a DLC film (composed of light elements) had a greater effect on the hydrogen content and optical properties of DLC than did Au irradiation at 1 MeV.

In general a two oscillator model yielded an excellent fit to the optical data, and the two oscillators were centered near 5 eV and 17 eV in the unirradiated samples. These positions shift to lower photon energies with fluence, and proton recoil experiments show that the hydrogen content decreased from near 30% (in unirradiated materials) to near 20% (Au), or near 6% (F) with fluence. The loss of hydrogen was not linear with fluence;

rather there was a near "saturation" of the irradiation effects for fluences above 10^{15} cm^{-2}. We believe that at high fluence the ion beams introduced defect centers produced by electronic energy loss which acted to retrap part of the hydrogen. The magnitude of this effect was reduced with increasing ion mass as the proportion of nuclear to electronic energy loss was increased.

It has been argued [13] from optical absorption, Raman, conductivity, and ESR experiments that irradiation at first had only the effect of lowering the hydrogen content, and then at high fluences it increased the graphitic component in their glow discharge produced carbon films. Similarly, we found a linear relationship between optical bandgap and hydrogen content. However, their 50 keV carbon ions were implanted to a depth of only 100 nm. Rather than the "saturation" effects that we saw, they observed a continuing decrease in hydrogen to less than a few percent at a fluence of 10^{17} cm^{-2}.

The tendency towards lower hydrogen concentration and lower optical gaps was similar to the trend seen with annealing. (The presently reported irradiations were carried out using a cool substrate and low beam currents, so sample heating was not a problem). Thus there appears to be an analogy between the physical effects of irradiation and those of annealing.

References

1. J.C. Angus, P. Koidl, and S. Domitz, in Plasma Deposited Thin Films, edited by J. Mort and F. Jansen (CRC, Boca Raton, FL, 1986). Chapter 4.

2. R.L.C. Wu, D.C. Ingram, and J.A. Woollam, Final Report: "Diamondlike Carbon Coatings for Optical Systems", U.S. Army Materials Technology Laboratory, Contract No. DAAL04-86-C-0030, October 1988.

3. J.A. Woollam, S. Orzeszko, B.N. De, N.J. Ianno, A.R. Massengale, J.J. Pouch, and S.A. Alterovitz, "Diamondlike Carbon Dielectrics for Integrated Circuits", Final Report, Control Data Corporation, December 1987.

4. J.A. Woollam, B.N. De, L.Y. Chen, J.J. Pouch, and S.A. Alterovitz, MRS Proceedings Volume: Optical Materials: Processing and Science, 1989.

5. S. Orzeszko, B.N. De, J.A. Woollam, J.J. Pouch, S.A. Alterovitz, and D.C. Ingram, J. Appl. Phys. 64, 4175 (1988).

6. M.J. Mirtich, D. Nir, D. Swec, and B. Banks, J. Vac. Sci. Technol. A4, 2680 (1986).

7. J.J. Pouch, S.A. Alterovitz, J.D. Warner, D.C. Liu, and W.A. Lanford, Mat. Res. Soc. Symp. 47, 201 (1985).

8. H.J. Hovel, "Solar Cells", in Semiconductors and Semimetals, 11, edited by R.K. Willardson, and A.C. Beer, Academic Press, New York, 1975, p. 203.

9. The Infrared Handbook, edited by W.L. Wolfe, and G.J. Zissis, The Infrared Information and Analysis Center, Environmental Research Institute of Michigan, Ann Arbor, MI, 1978.

10. J.A. Woollam, P.G. Snyder, and M.C. Rost, Thin Solid Films 166, 317 (1988).

11. S. Orzeszko, J.A. Woollam, D.C. Ingram, and A.W. McCormick, J. Appl. Phys. 64, 2611 (1988).

12. S. Prawer, R. Kalish, M. Adel, and V. Richter, J. Appl. Phys. 61, 4492 (1987).

13. M.E. Adel, R. Kalish, and S. Prawer, J. Appl. Phys. 62, 4096 (1987).

BRANCH MEMBERS

Address: NASA Lewis Research Center
21000 Brookpark Road
Cleveland, Ohio 44135

Name	Phone	Mail Stop
Alterovitz, Samuel A., Dr.	(216) 433-3517	54-5
Bhasin, Kul B., Dr.	(216) 433-3676	77-5
Chorey, Chris	(216) 433-3379	77-5
Downey, Alan N.	(216) 433-3508	54-5
Haughland, Edward J., Dr.	(216) 433-3516	54-5
Kascak, Thomas J.	(216) 433-3505	54-5
Leonard, Regis F., Dr.	(216) 433-3500	54-5
Mena, Rafael A.	(216) 433-3383	54-5
Morrison, Carlos R.	(216) 433-8447	54-5
Ponchak, George E.	(216) 433-3504	54-5
Pouch, John J., Dr.	(216) 433-3523	54-5
Romanofsky, Robert R.	(216) 433-3507	54-5
Schacham, Samuel E., Dr.*	(216) 433-3516	54-5
Sil, Ajit K.	(216) 433-8610	54-5
Simons, Rainee N., Dr.	(216) 433-3462	54-5
Stan, Mark A., Dr.	(216) 433-8369	54-5
Stecura, Stephan, Dr.	(216) 433-3264	54-5
Taub, Susan R.	(216) 433-3443	54-5
Vitta, Satish, Dr.*	(216) 433-3504	54-5
Warner, Joseph D.	(216) 433-3677	77-5

Branch Secretary:

Kimberly J. McKee	(216) 433-3514

*NASA Resident Research Associate at Lewis Research Center

Samuel A. Alterovitz received a Ph.D. degree in Solid State Physics in 1971 from Tel Aviv University, Israel. After a 2-year postdoctoral appointment at University of Illinois, Urbana, IL, he joined the staff of the Physics Department at Tel Aviv University where he achieved the rank of tenured associated professor. In both places he worked on properties of superconducting materials, especially critical currents and critical fields. In 1981, he accepted a position in the Electrical Engineering Department at University of Nebraska, Lincoln, NE, as senior engineering research scientist where he worked to develop the ellipsometric technique. In 1983, he transferred to NASA Lewis Research Center where he is now a senior research scientist. He played a key role in developing new materials (e.g., InGaAs) for a new generation of electronic devices for high-speed, low-noise, high-efficiency space applications. He also developed ellipsometry for novel and multilayer structures specializing in insulators, superconductors, and semiconductor materials. He is now working on materials for cryogenic electronics applications, including semiconductors, superconductors, and their combination. Dr. Alterovitz has authored 92 papers in referred journals and 89 meeting presentations and has edited 2 books. He is an active National Research Council postdoctoral adviser.

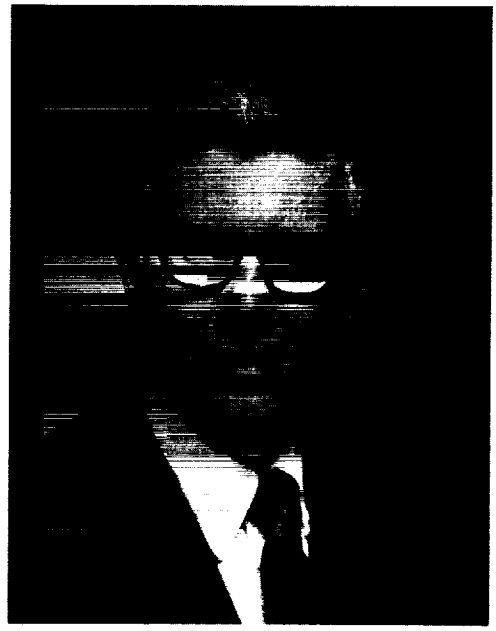

Christopher M. Chorey received a Master's degree in Materials Science in 1987 and a Bachelor's in Electrical Engineering in 1984 from Case Western Reserve University. Through 1987 and 1988, he performed additional graduate work in electrical engineering with Case Western Reserve University, supported by the NASA Lewis Research Center, and concentrated on fabricating and testing AlGaAs based high-frequency electro-optic modulators. In 1989, he joined Sverdrup Technology, Inc., under contract to the NASA Lewis Research Center, and is currently involved in studies of the microwave properties of high-temperature superconductors.

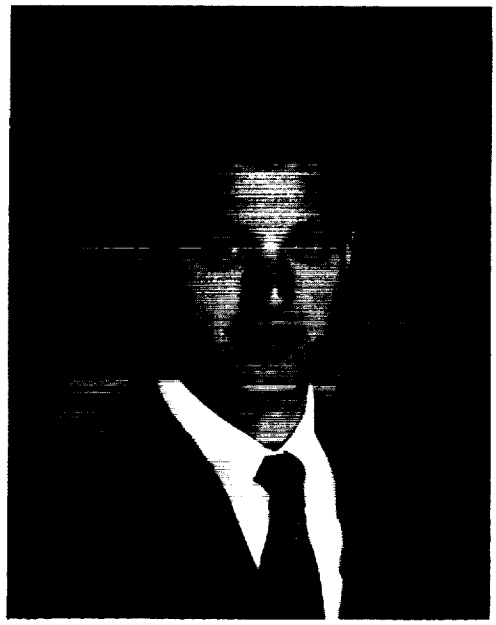

Alan N. Downey received a BEE from Cleveland State University in 1979 and his MSEE from the University of Toledo in 1983. He joined NASA Lewis Research Center in 1977 as a co-op student and joined the Space Communications Division in 1979. From 1979 to 1985, he was engaged in microwave measurements and solid-state technology research, followed by a 3-year hiatus in the Communications Projects Branch as Experiments Manager for the Applications Technology Satellites Program. Mr. Downey returned to the Solid State Technology Branch in July 1989, and his current research interests include the measurement of novel HEMT structures at cryogenic temperatures, coplanar waveguide circuit design, and MMIC applications.

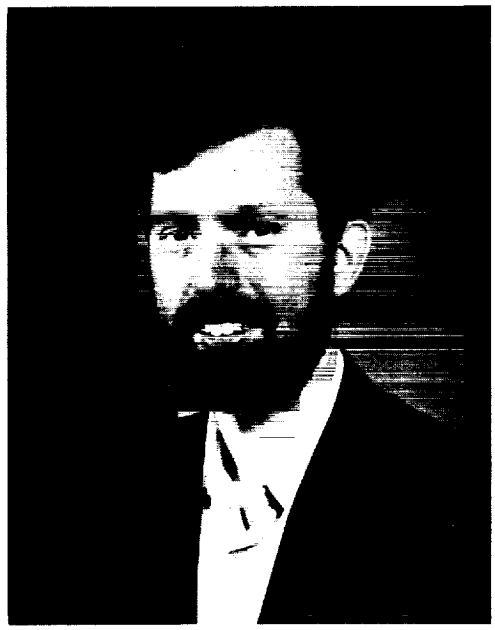

Edward J. Haugland received a B.S. degree in Physics from the University of Minnesota and an M.S. and Ph.D. degree in Solid State Physics from Case Western Reserve University. He joined NASA Lewis Research Center in 1980 as a member of the Solid State Technology Branch. Since that time, he has been involved with experimental research on electrical properties of III-V semiconductor materials and heterostructures and SiC. He was responsible for contracts for the development of high-power IMPATT diodes and MMIC power amplifiers. Dr. Haugland is a member of the American Physical Society.

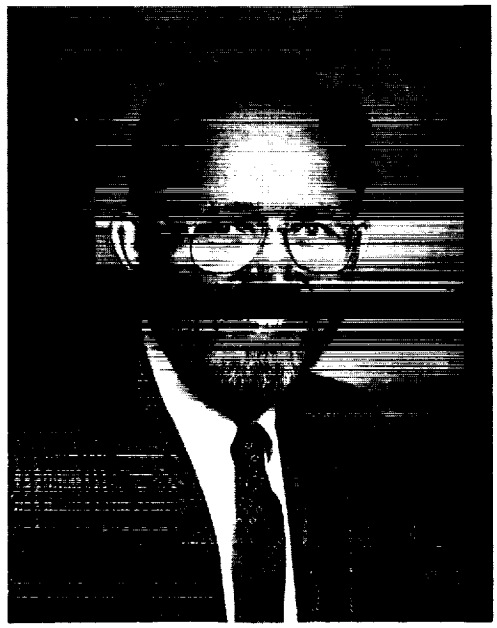

Thomas J. Kascak received a BSEE degree from Case Western Reserve University in 1959 and joined Union Carbide Corporation where he worked with performance and reliability aspects of dry cell and alkaline batteries. Mr. Kascak received an MS degree in Physics in 1965 from John Carroll University, Cleveland, OH. From 1966 to the present, he has been employed at the NASA Lewis Research Center. He has been involved in several work areas from research on thermonic heat to electric power conversion devices. In 1973, he transferred to the Launch Vehicles Division where he had contract management responsibilities dealing with the guidance equipment for the NASA Atlas/Centaur launch vehicle systems. In 1980, he transferred to the Space Electronics Division where he has been involved in various aspects of microwave and millimeter wave solid-state devices and circuits. He was responsible for formulating and managing several NASA sponsored contractual efforts involving MMIC development programs. One of these efforts, a 20-GHz MMIC Transmit Module, resulted in the R&D Magazine IR-100 Award. For the last few years, he was responsible for the set-up of the Division's in-house solid-state facilities. Mr. Kascak has authored papers on thermionic direct energy conversion devices, 20-GHz and 30-GHz MMIC devices, and MMIC-based phased array antennas. Mr. Kascak is a member of the American Vacuum Society (AVS).

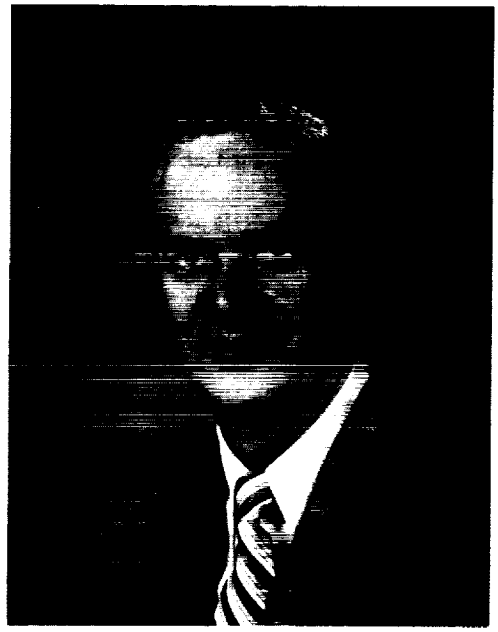

Regis F. Leonard received a Ph.D. degree in Physics from Carnegie Institute of Technology and came to work at NASA Lewis in 1963. Since that time, he has devoted 10 years to basic research in the physics of nuclear structures and 6 years to the development of a unique Lewis facility for the treatment of cancer patients with neutron radiation. For the last 9 years, he has worked in the development of technology in support of NASA's communications programs. This assignment included work on the ACTS proof-of-concept technology program and, as head of the RF Systems Section, the development of an in-house communications system test capability for the ACTS POC hardware. For the last 4 years, he has served as Chief of the Solid State Communications Branch, responsible for NASA's MMIC technology development program, an active in-house solid-state research program, and a sizeable university grant program in supporting basic research as applicable to solid-state electronics.

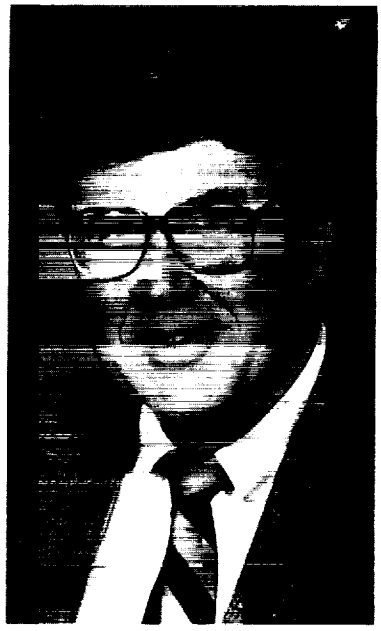

Rafael A. Mena received a B.S. degree in Electrical Engineering in 1988 from the University of Texas at El Paso and an M.S. degree in Solid State Physics in 1990 from Arizona State University. While at Arizona State University, he made theoretical calculations on the effect of a magnetic field on the optical properties of semiconductor alloys. While persuing his degree, he participated in several co-op programs. In the summer of 1987, he was with Arizona Public Service where he conducted an economic study on the installation of underground power lines. The following summer of 1988 he was accepted into the NASA Lewis Summer internship program. During that time, he was involved in a research program to investigate the magnetic field penetration depth of superconducting materials. He returned to NASA Lewis the summer of 1989 where he assisted in the software development for the automation of a secondary ion mass spectrometer. In 1990, he joined the Solid State Technology Branch at NASA Lewis Research Center as a full-time employee. His current interests lie in both the theoretical and experimental investigation of the electrical properties of novel semiconductor materials. Mr. Mena has authored a paper on the work conducted at Arizona State University.

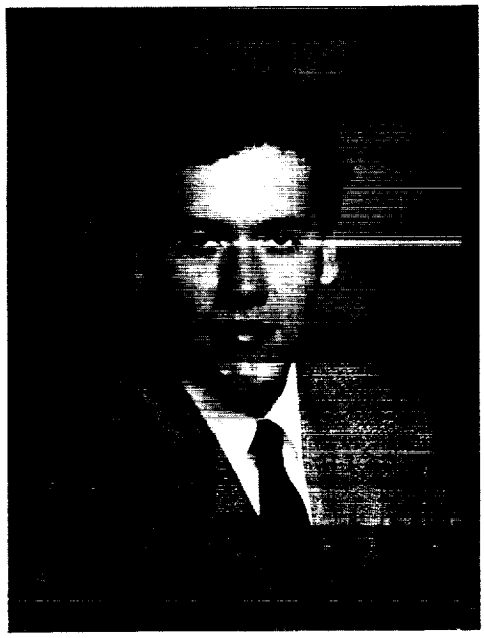

Carlos R. Morrison, a native of Jamaica, West Indies, received his B.S. (Hon.) in Physics in 1986 from Hofstra University where he was elected to membership in the Sigma-Pi-Sigma National Physics Honor Society, the Kapa-Mu-Epsilon National Mathematics Honor Society, and the Society of Physics Students. He received a Master's degree in Physics in 1989 from the Polytechnic Institute of New York (Brooklyn Polytechnic). He joined the NASA Lewis Research Center in September 1989 where he worked for a short time in Reliability and Quality Assurance. He then transferred to the Solid State Technology Branch in January 1990 where he is currently involved in thin film deposition and ellipsometry.

George E. Ponchak received his BEE from Cleveland State University in 1983 and his MSEE from Case Western Reserve University in 1987. He joined the Space Electronics Division of NASA Lewis Research Center in July 1983. Since joining NASA, he has been responsible for research of microwave transmission lines and managing the development of monolithic microwave integrated circuits. Mr. Ponchak has coauthored 18 papers on these topics and has applied for 5 patents related to coplanar waveguide circuits.

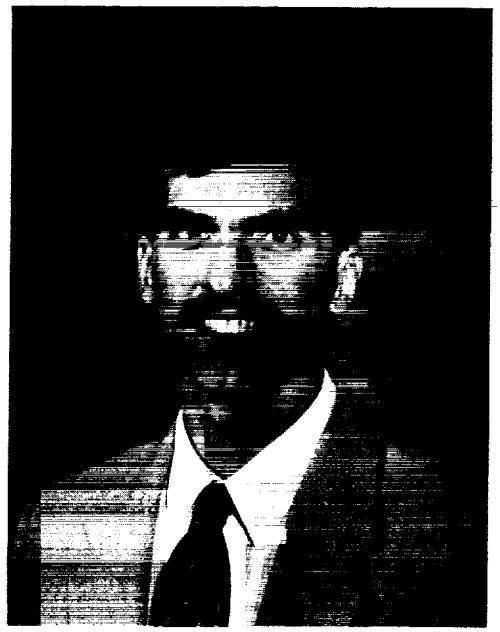

John J. Pouch received his Ph.D. degree in Solid State Physics from Wayne State University, Detroit, MI, in 1981. His research activities at the NASA Lewis Research Center include surface analysis of thin films for microelectronic applications, plasma and reactive ion etching, and plasma deposition.

Robert R. Romanofsky received a Bachelor of Science Degree in Electrical Engineering from the Pennsylvania State University in 1983. From 1983 to 1989, he was employed in the Space Electronics (Communications) Division of the NASA Lewis Research Center. His work was directed toward microwave transmission line research, device characterization and modeling, and microwave applications of high-temperature superconductivity. He has filed for two patents related to millimeter-wave technology. In 1989, Mr. Romanofsky received a Master of Science Degree in Electrical Engineering from the University of Toledo. He is currently detailed at NASA Headquarters, Washington, DC, as the acting program manager for superconductivity and RF communications. He is a member of the Institute of Electrical and Electronics Engineers (IEEE).

Samuel E. Schacham received a B.S. degree in Mathematics and Physics with honors in 1971 and an M.S. degree in Physics in 1973 from Bar Ilan University, Ramat-Gan, Israel. He performed research work on nonlinear optical effects in liquid crystals at the Weitzmann Institute and Bar Ilan University. He received a Ph.D. degree in Biomedical Engineering in 1978 from Northwestern University in Evanston, IL, working on applications of lasers to microendoscopy. From 1978 to 1981, he was the manager of the optic group at Fibronics Ltd., Haifa, Israel. He joined the Department of Electrical Engineering at the Technion, Haifa, Israel. In 1988, he was a visiting scientist at MCNC, Research Triangle Park, NC, working on optical interconnects as part of the packaging group. Presently, he is with NASA Lewis Research Center as a National Research Council Senior Research Associate. His present research interests are in the physical properties of quantum structures and narrow bandgap semiconductors. His list of publications include 40 papers in international scientific journals and referred conferences.

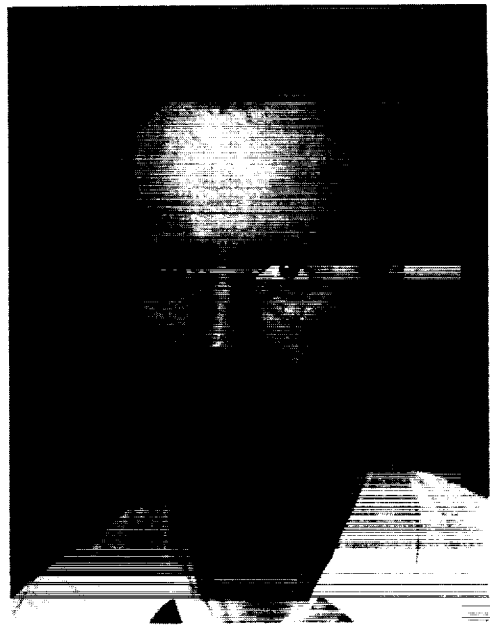

Ajit K. Sil received his B.S. degree from Calcutta University, India. He emigrated to the United States and was employed by Oakwood Downriver Medical Center. He received his second B.S. degree in Electronic Engineering Technology in 1988 from Wayne State University, Detroit, MI. He joined the NASA Lewis Research Center in July 1989 as a member of the Solid State Technology Branch where he is working with microwave integrated circuits and soild-state devices. He is currently working toward his M.S.E.E. at Cleveland State University, Cleveland, OH.

Rainee N. Simons received a B.E. degree in Electronics and Communications from the Mysore University in 1972, an M. Tech. degree in Electronics and Communications from the Indian Institute of Technology, Kharagpur, in 1974, and a Ph.D. degree in Electrical Engineering from the Indian Institute of Technology, New Delhi, in 1983. He was a Senior Scientist Officer at the Indian Institute of Technology, New Delhi. From 1985 to 1987, Dr. Simons was a National Research Council Research Associate and investigated the direct optical control of GaAs microwave semiconductor devices and circuits. He joined the Solid State Technology Branch of the Space Electronics Division at NASA Lewis Research Center. Since 1990, he has been with Sverdrup Technology, Inc., NASA Lewis Research Center group. His research interest includes GaAs microwave semiconductor devices, optical control, and superconductivity. Dr. Simons is the author of a book entitled "Optical Control of Microwave Devices" published by Artech House. He received the distinguished alumni award from his alma mater and is a senior member of IEEE.

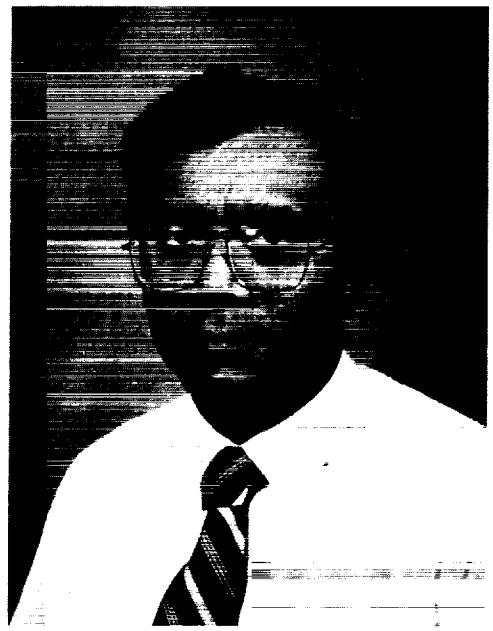

Stephan Stecura received an M.S. degree in Physical Chemistry in 1957 from Western Reserve University and a Ph.D. degree in Solid State Reaction Kinetics-Thermodynamics in 1965 from Georgetown University. From 1958 to 1965, at College Park Metallurgy Center, he studied the kinetics of crystallographic transformations and the high-temperature properties of oxides by high-temperature x-ray diffraction techniques. He designed and built high-temperature x-ray diffraction equipment and was invited to present the high-temperature x-ray diffraction arc-image furnace, capable of reaching 3000 °C in air, at the International Crystallographic Society meeting. Since 1965, he has been with NASA Lewis Research Center. His work on heat pipes led him to determine the corrosion mechanism and the true solubilities of containment metals and alloys in alkali metals. He developed thermal barrier systems for the protection of alloy components at very high temperatures, up to 1600 °C on air-cooled components. Currently, he is studying the properties of superconductng materials and is trying to identify the substrate materials for superconducting films. Dr. Stecura is recognized as an authority on the thermal barrier system technology that he developed. For his work in this field, he has received two IR-100 awards, one major Space Act award, and three major patents. He has written more than 30 original publications and is a member of the American Ceramic Society.

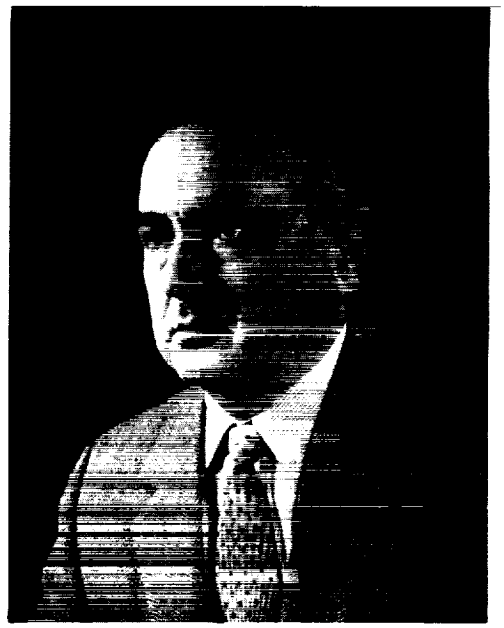

Susan R. Taub received a B.S. in Electrical Engineering Technology in 1988 and a Master of Science in Engineering in 1990 from Temple University. In 1988 and 1989, she worked for AT&T Bell Laboratories, Reading, PA, developing PSPICE compatible models for power MOSFET's. She joined NASA Lewis Research Center's Solid State Technology Branch in 1990 and is currently involved in design and characterization of MMIC's and the investigation of HEMT performance at cryogenic temperatures. Ms. Taub is a member of the Institute of Electrical and Electronics Engineers (IEEE).

ORIGINAL PAGE
BLACK AND WHITE PHOTOGRAPH

Joseph D. Warner received an MS in Physics from Carnegie Melon University in 1977. From 1977 to 1981, he performed research at C.M.U. on magnetic phase transition at low temperature. From 1982 to date, he has been with NASA Lewis Research Center where he characterized various insulators on GaAs and was among the first to demonstrate growth of GaAs by laser-assisted OMCVD at growth temperature below 500 °C. Presently, he has set up a laser ablation experiment to grow high-temperature superconducting thin films. In 1989, he received a NASA Achievement Award for his part in establishing a high-temperature superconductor program at Lewis. Mr. Warner has authored papers on magnetic phase transitions, electrical properties of insulation films on III-V compounds, laser-assisted growth of GaAs and AlGaAs, and properties and growth of high-temperature superconductors. He is a member of the American Physical Society (APS), the American Vacuum Society (AVS), and the Materials Research Society (MRS).

NASA
National Aeronautics and Space Administration

Report Documentation Page

1. Report No.	2. Government Accession No.	3. Recipient's Catalog No.
NASA TM-103226		

4. Title and Subtitle

Solid State Technology Branch of NASA Lewis Research Center
Second Annual Digest
June 1989–June 1990

5. Report Date

6. Performing Organization Code

7. Author(s)

8. Performing Organization Report No.
E-5642

10. Work Unit No.
506-59-4C

9. Performing Organization Name and Address

National Aeronautics and Space Administration
Lewis Research Center
Cleveland, Ohio 44135-3191

11. Contract or Grant No.

13. Type of Report and Period Covered
Technical Memorandum

12. Sponsoring Agency Name and Address

National Aeronautics and Space Administration
Washington, D.C. 20546-0001

14. Sponsoring Agency Code

15. Supplementary Notes

Responsible individual, Ajit K. Sil (216) 433-8610.

16. Abstract

This digest is a collection of papers written by the members of the Solid State Technology Branch of NASA Lewis Research Center from June 1989–June 1990. The papers cover a range of topics relating to superconductivity, MMIC's, coplanar waveguide, and material characterization.

17. Key Words (Suggested by Author(s))	18. Distribution Statement
Microwave Superconducting materials Thin films	Unclassified – Unlimited Subject Category 32

19. Security Classif. (of this report)	20. Security Classif. (of this page)	21. No. of pages	22. Price*
Unclassified	Unclassified	289	A13

*For sale by the National Technical Information Service, Springfield, Virginia 22161